An assessment of the stability of southwest Antarctic Peninsula Ice Shelves

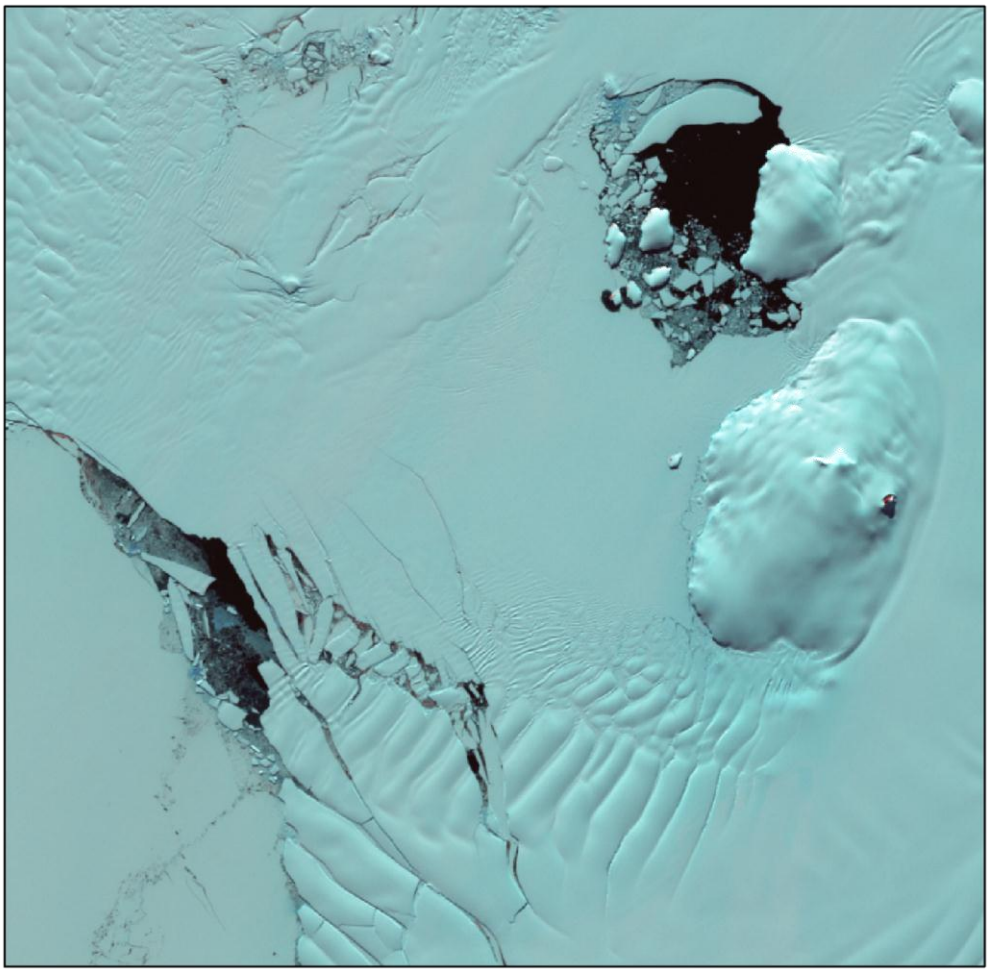

Thomas Owen Holt

PhD Thesis

Institute of Geography and Earth Sciences,

Aberystwyth University

Declaration

This work has not previously been accepted in substance for any degree and is not being concurrently submitted in candidature for any degree.

Signed ..... (candidate)

Date .....

Statement 1

This thesis is the result of my own investigations, except where otherwise stated. Where *__correction services__ have been used, the extent and nature of the correction is clearly marked in a footnote(s). Other sources are acknowledged by footnotes giving explicit references. A bibliography is appended.

Signed ..... (candidate)

Date .....

[*this refers to the extent to which the text has been corrected by others]

Statement 2

I hereby give consent for my thesis, if accepted, to be available for photocopying and for inter-library loan, and for the title and summary to be made available to outside organisations.

Signed ..... (candidate)

Date .....

I hereby give consent for my thesis, if accepted, to be available for photocopying and for inter-library loans after expiry of a bar on access approved by Aberystwyth University.

Signed ..... (candidate)

Date ……..

Abstract

Over the last three decades, Antarctic Peninsula Ice Shelves have shown a pattern of sustained retreat, often ending in catastrophic and rapid breakup. This study provides a detailed analysis of the structures and dynamics of Bach, George VI and Stange Ice Shelves, situated on the southwest Antarctic Peninsula, to determine their current and future stability on the premise that glaciological changes can be identified well in advance of final breakup phases. Spatial extent and glaciological surface features were mapped for each ice shelf from 1973 to 2010 using optical and radar satellite images to assess their structural stability, structural evolution and historical dynamics. A combination of InSAR and feature tracking methods has been used to assess the recent dynamic configurations of the ice shelves from 1989 to 2010, with repeat ICESat measurements used to evaluate their vertical changes from 2003 to 2008. On Bach Ice Shelf, the formation of two large fractures near the ice front is linked to widespread thinning (~2 ma^{-1}) and sustained retreat (~360 km^2). It is postulated that iceberg calving along these fractures will alter the frontal geometry sufficiently to promote enhanced, irreversible retreat within the next decade. On George VI Ice Shelf, acceleration is observed at both ice fronts linked to a release of back-stresses through continued ice loss (1995 km^2 in total). The most significant changes are recorded at its southern ice front, with ice flow accelerating up to 360% between ca. 1989 and ca. 2010, coupled with widespread rifting and a mean thinning rate of 2.1 ma^{-1}. On Stange Ice Shelf, shear-induced fracturing was observed between two flow units, also linked to widespread thinning (~4.2 ma^{-1}) illustrating a response of southwest Antarctic Peninsula Ice Shelves within the proposed limit of viability. A semi-quantitative assessment reveals that the southern margin of George VI Ice Shelf is most susceptible to rapid retreat, whilst its northern ice front, Bach Ice Shelf and the northern front of Stange Ice Shelf are more vulnerable than those situated on the east Antarctic Peninsula.

Acknowledgements

First and foremost I thank my supervisors, Professor Neil Glasser and Dr. Duncan Quincey, for their unwavering support, enthusiasm and all of those Ph.D (and football) meetings. Thank you also for the advice and guidance during the first year of my own academic career.

I am also very grateful to all of those in the Centre for Glaciology and Earth Observation research clusters who have contributed to discussions on the project, and huge thanks especially to Andy Fitzpatrick, Colin Souness and Dan Clewley for being the most entertaining office-mates one could wish for. Your constant laughter, banter and need for hot beverages have been very much appreciated and will never be forgotten!

Thank you also to Professor Helen Fricker, Matt Siegfried and Dr Kelly Brunt at Scripps Institution of Oceanography for allowing access to the pre-processed ICESat GLAS data, and all of the support they have provided. Thank you also to Dr Jennifer Griggs for supplying the ice-shelf thickness data used in the latter parts of this study.

A special thanks to Urs Wegmuller and Charles Werner for their input during the InSAR processing stage, and for the short but hugely beneficial time spent at GAMMA HQ, Berne, Switzerland.

Finally, I would like to thank my Mum and Dad, and the rest of the Holt/Jones/Turvey clan for their constant support throughout my time at Aberystwyth University. And of course, an enormous thank you to Sara for her encouragement and patience over the duration of the Ph.D!

Contents

List of Figures

(summarised captions)

Chapter 5

Chapter 6

Chapter 7

Chapter 9

List of Tables

(summarised captions)

Chapter 7

Chapter 8

Chapter 9

List of Abbreviations

ACC	Antarctic Circumpolar Current
ALOS	Advanced Land Observing Satellite
APC	Antarctic Place-name Committee
ASAR	Advanced Synthetic Aperture Radar
ASTER	Advanced Spaceborne Thermal Emission Reflection Radiometer
CCI	Cross-correlation of Intensity
CDW	Circumpolar Deep Water
DEM	Digital elevation Model
EAIS	East Antarctic Ice Sheet
ERS	European Remote Sensing Satellite
ETM+	Enhanced Thematic Mapper Plus
FFT	Fast-Fourier Transform
GIS	Geographical Information System
GLAS	Geoscience Laser Altimeter System
IBE	Inverse Barometer Effect
ICESat	Ice, Cloud and Elevation Satellite
InSAR	Interferometric Synthetic Aperture Radar
LGM	Last Glacial Maximum
LiDAR	Light Detection and Ranging
MEaSUREs	Making Earth Science data records for Use in Research Environments
MLI	Multi-Look Image
MOA	Mosaic of Antarctica (MODIS MOA)
MODIS	Moderate Imaging Spectrometer
MSS	Multi-spectral Scanner
NIR	Near Infrared
NSIDC	National Snow and Ice Data Centre
ODR	Orbital Data Records
RA	Radar Altimetry
RADAR	Radio Detection and Ranging
RAMP	Radarsat Antarctic Mapping Project
RBV	Return-Beam Vidicon
RDC	Range-Doppler Coordinates
SAM	Southern Annular Mode
SAR	Synthetic Aperture Radar
SLC	Single-Look Complex
SNR	Signal-to-Noise Ratio
SWIR	Short-wave Infrared
TIR	Thermal Infrared
TM	Thermatic Mapper
VIS	Visible Infrared
VNIR	Visible-Near Infrared
WAIS	West Antarctic Ice Sheet
WGS84	World Geodetic System 1984

Chapter 1

Introduction

1. Introduction

1.1 Aims

The aim of this thesis is to:

- Assess the current and future stability of Bach, George VI and Stange Ice Shelves on the south-west Antarctic Peninsula with respect to atmospheric and oceanic changes.

More specifically, the study aims to:

- Quantify the retreat rate and assess the retreat patterns of Bach, George VI and Stange Ice Shelves from the early 1970s to present.
- Analyse their structural and surface-feature evolution, including an evaluation of surface meltwater extent and distribution.
- Calculate multi-annual flow speeds to assess long-term dynamics.
- Examine the vertical response of these ice-shelf systems to atmospheric and oceanic warming.
- Assess the future stability of the ice shelves using a semi-quantitative approach.

1.2 Objectives

In order to achieve these aims, the following objectives are to be met:

- To map and monitor ice-front positions over sub-decadal time scales to achieve a quasi-continuous dataset of retreat patterns and retreat rates using a range of optical and radar satellite-remote sensing imagery.

- To produce detailed and comprehensive sub-decadal glaciological maps of ice-shelf extent, surface structure and surface features, concentrating in particular on those that show ice-shelf dynamics and dynamic changes over time (for example, longitudinal flow structures, fractures, fracture traces and rifts). These will also be produced using a range of optical and radar satellite datasets.

- To calculate flow speeds using Interferometric Synthetic Aperture Radar (InSAR) and feature tracking techniques over multiple time periods, in order to assess the dynamic response of the ice shelves to documented climatic and oceanic variation.

- To use repeat surface-elevation measurements to calculate variations in the ice-shelf surface height over recent years, from which the patterns of ice-shelf-thickness changes can be inferred.

- To combine the above empirical datasets to offer a semi-quantitative, critical assessment of the current stability of Bach, George VI and Stange Ice Shelves, that to date, have been considered stable ice-shelf systems.

- To critically assess the future response of these ice shelves using empirical datasets acquired in this study, and historical patterns observed elsewhere on the Antarctic Peninsula.

1.3 Project Rationale

Glasser and Scambos (2008), Braun *et al.* (2009) and Glasser *et al.* (2011) have documented the structural evolution of Larsen B, Wilkins and Prince Gustav Ice Shelves before, during and after recent ice shelf breakup events in the Antarctic Peninsula. Yet despite these studies illustrating the importance of structural regime on ice-shelf stability,

few studies have set out to detail the structural and dynamic configurations prior to the breakup of ice shelves. Furthermore, the remaining ice shelves are not being critically assessed in terms of their future viability in a rapidly changing climatic and oceanic situation, although Mercer (1978) and Vieli *et al.* (2007) both recognised that glaciological changes occur well in advance of the final collapse stages. The rationale for this project is thus formed around the absence of key data for those ice shelves currently considered stable.

1.4 Ice shelves and their distribution

Ice-shelves are the floating extremities of ice sheets and glaciers in both the Arctic and Antarctic polar regions, fringing roughly 45% of the Antarctic continent and accounting for approximately 90% of the total loss of ice (Vaughan, 1993; MacAyeal *et al.,* 2003; Hooke, 2005; Figure 1.1). They are composed almost entirely of ice that accumulated as part of a grounded ice sheet and entered the ice-shelf zone via tributary glaciers (Vaughan, 1993). Direct surface accumulation via snowfall (Vaughan *et al.,* 2003) and basal accumulation through freezing of sub-ice-shelf water (Thyssen, 1988) can also contribute a significant fraction to the overall ice-shelf mass, particularly in basal cavities (Fricker *et al.,* 2001). The primary sources of ablation from ice shelves is via iceberg calving and basal melting although surface meltwater run-off, sublimation and aeolian processes also account for a fraction of ablation (Vaughan, 1993).

Glasser and Scambos (2008) identified five key reasons for the importance of ice shelves: 1) Because of the high-ablation rates, they play a vital role in the global ice-volume/sea-level system: 2) Ice shelves influence the dynamics of grounded tributary ice that feed them, and therefore are a critical component in ice-sheet mass balance (Rott *et al.,* 2002; Scambos *et al.,* 2004): 3) They play a pivotal role in the global ocean heat budget due to the direct interaction between their basal cavities and the Southern Ocean (Joughin and Padman, 2003; Padman *et al.,* 2012): 4) Ice shelves entrain, transport and deposit significant quantities of glacigenic sediment: and 5) iceberg-calving events from ice shelves have been attributed as the cause of Late Quaternary climatic fluctuations (Hulbe *et al.,* 2004). Thus, understanding ice-shelf configuration, dynamics and mass balance is critical in the assessment and prediction of global climatic and oceanic variations (Alley *et al.,* 2005; Rignot and Kanagaratnam, 2006; Griggs and Bamber, 2011).

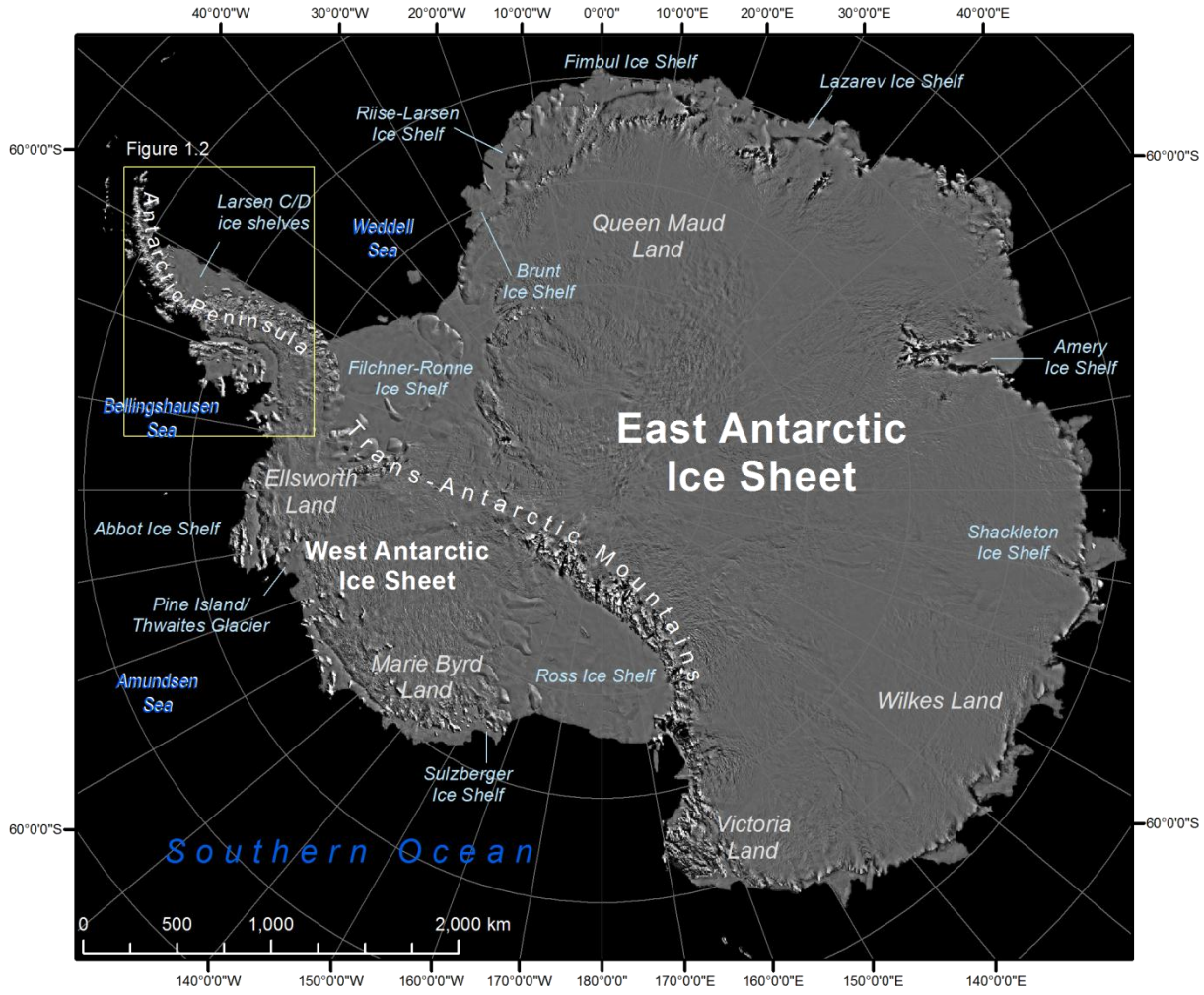

Figure 1.1. Antarctica and key locations as discussed during the thesis. Of particular note are the large ice shelves of Filchner-Ronne and Ross. The Antarctic Peninsula with study ice shelves is shown in more detail in Figure 1.2. Background image = MODIS Image Mosaic of Antarctica (MOA) (Haran *et al.*, 2006).

1.4.1 Ice shelves, climate and oceanic variation

In recent years, many Antarctic Peninsula Ice Shelves have undergone rapid retreat with seven ice shelves dramatically breaking apart over periods of several weeks-to-months (Vaughan *et al.*, 2003; Cook and Vaughan, 2010), namely Prince Gustav Channel Ice Shelf (Rott *et al.*, 1996; Glasser *et al.*, 2011), Larsen Inlet (Skvarca, 1993), Larsen A (Rott *et al.*, 1998; Doake *et al.*, 1998) and Larsen B (Rott *et al.*, 2002; Glasser and Scambos, 2008) on the east of the Antarctic Peninsula, and Jones (Fox and Vaughan, 2005), Wordie (Vaughan, 1993) and Müller (Ward, 1995) Ice Shelves on the west Antarctic Peninsula (Figure 1.2). Additionally, during 1998, 2008 and 2009, the Wilkins Ice Shelf experienced major breakup phases (Braun *et al.*, 2009; Scambos *et al.*, 2009; Cook and Vaughan, 2010;

Padman *et al.*, 2012) that highlighted the on-going cryospheric response to climatic and oceanic variations.

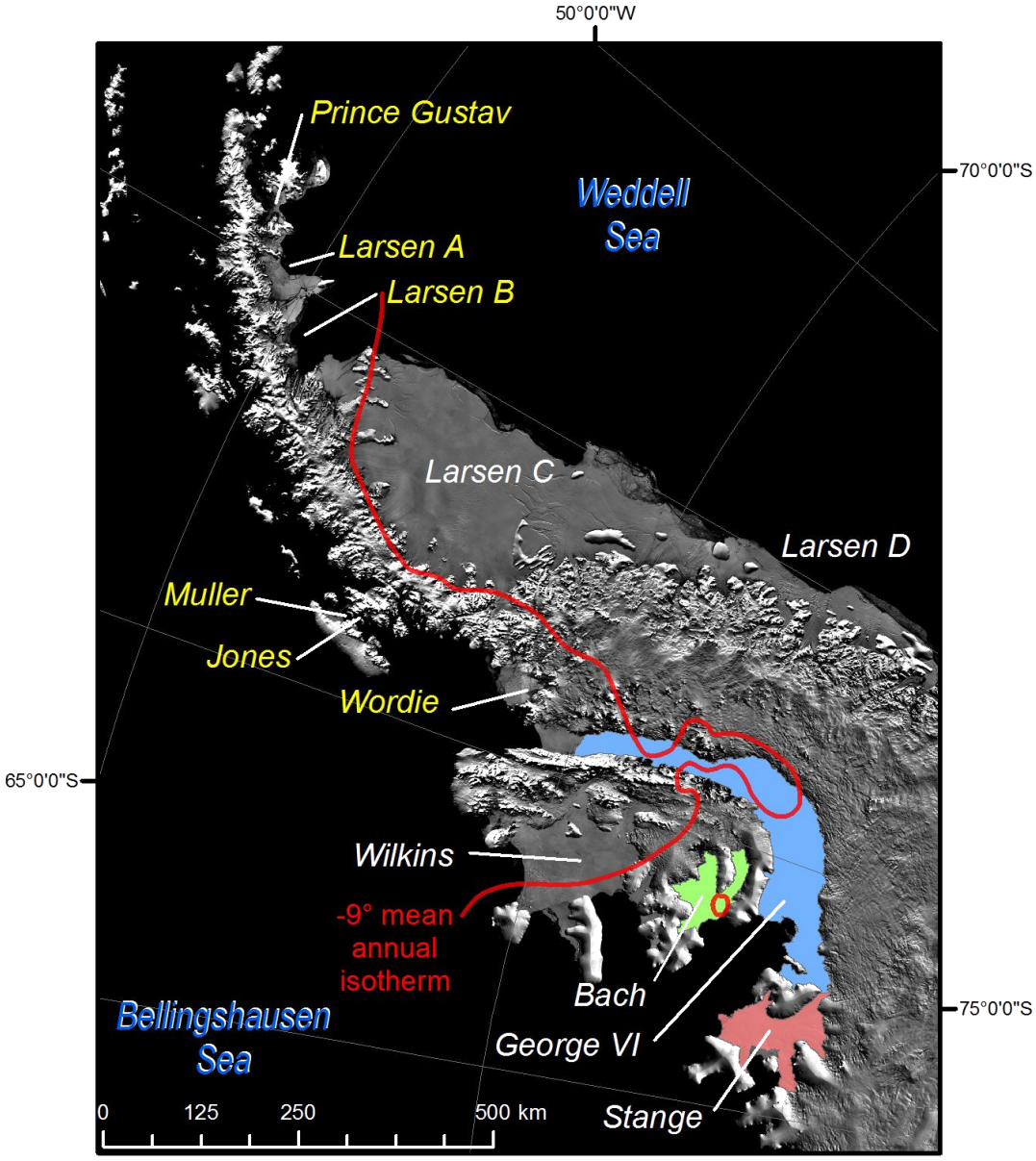

Figure 1.2. Former (yellow text) and current (white text) **i**ce shelves of the Antarctic Peninsula as discussed in the text. Those considered in this study (Bach, George VI and Stange Ice Shelves) are highlighted by coloured polygons. Also shown is the -9°C mean annual isotherm (Morris and Vaughan, 2003). Background image = MODIS Image Mosaic of Antarctica (MOA) (Haran *et al.*, 2006).

The sedimentary record on the continental shelf indicates that some Antarctic Peninsula Ice Shelves (e.g. George VI (Hjort *et al.*, 2001; Gilbert and Domack, 2003; Bentley *et al.*, 2005, 2011; Roberts *et al.*, 2008) and Prince Gustav Channel (Pudsey and Evans, 2001)), retreated in the early-Holocene and may follow an asymmetrical cyclical process involving

rapid disintegration followed by gradual expansion (Glasser and Scambos, 2008). However, there is no such evidence that all Antarctic Peninsula Ice Shelves have followed such cycles during the Holocene; in particular, sedimentary evidence beneath Larsen B and Wilkins Ice Shelves indicate that recent breakup is otherwise unprecedented (Domack *et al.*, 2005).

Many authors report an exceptional increase in near-surface air temperatures across the Antarctic Peninsula region of up to 3°C since the 1950s (King, 1994; King and Harangozo, 1998; Comiso, 2000; Turner *et al.*, 2005), coinciding with an increase of winter precipitation of 50% (Turner *et al.*, 1997). Furthermore, Torinesi *et al.* (2003) report an increase of 0.5 days a^{-1} of mean-melt duration between 1980 and 1999 that, along with temperature increase, has enhanced thinning rates on Antarctic Peninsula Ice Shelves (Vaughan *et al.*, 2003). Rising air temperatures and increased bottom melting (Shepherd *et al.*, 2003) have thus been recognised as principal factors that govern ice-shelf breakup and disintegration. Indeed, the timing of ice-shelf collapse on the Antarctic Peninsula has been linked to the gradual poleward migration of the -9°C mean annual isotherm which is thus considered to be a critical environmental threshold for ice-shelf viability (Mercer, 1978; Vaughan and Doake, 1996; Rott *et al.*, 1996, 1998; Morris and Vaughan, 2003). Climatic changes are discussed in more detail in Chapter 2.

1.5 Terminology of '*ice-shelf collapse*'

Terminology used to describe the removal of ice from ice-shelf systems is not consistent from one publication to another. In this thesis, the following terminology is used to describe ice loss from Antarctic Peninsula Ice Shelves:

Retreat: The normal process by which ice is lost from an ice shelf through iceberg calving. An overall negative-mass-balance is achieved over a specified time period that results in the movement of the ice-front position back towards the grounding line.

Breakup: Sudden, fast release of icebergs of variable size not governed by normal calving mechanisms. May occur on timescales from days to months and can result in a significant removal of shelf ice.

Collapse: The disappearance of an ice shelf over a short period of time (weeks to months). May consist of one or more *breakup* phases within the specified timescale but unlikely to be governed by normal *retreat* processes.

Disintegration: Complete removal of an ice-shelf system over a non-specific timescale. May be governed by more than one *breakup* phase or a single *collapse* phase.

1.6 Thesis Structure

The thesis is structured to first give an overview of the Antarctic Peninsula and its glaciological, climate and oceanic regimes; the key precursors to ice-shelf collapse are presented in order to focus the remainder of the study (Chapter 2). The use of satellite remote sensing in ice-shelf science is then considered, in particular concentrating on the key optical and radar imaging sensors, and other non-imaging sensors, and their application in investigating Antarctic Ice Shelves (Chapter 3). Subsequently, the study sites are briefly introduced (Chapter 4) before giving a thorough account of the data sources used and the principal methods applied (Chapter 5). Chapters 6, 7 and 8 present the results and interpretations of Bach, George VI and Stange Ice Shelves respectively. Subsequently, Chapter 9 contains a discussion on the current and future stability of the three aforementioned ice shelves, with the main conclusions presented in Chapter 10.

Chapter 2

Review of Antarctic Glaciology and Ice-shelf Stability

2. Antarctic glaciology and ice-shelf stability

2.1 Antarctic glaciology

The Antarctic continent lies wholly within the south polar region and measures roughly 14 million km^2 (Sugden, 1982). Approximately 98% of Antarctica is covered in ice, accounting for 90% of the world's ice cover. Antarctica is divided into two large domains, namely the East Antarctic Ice Sheet (EAIS) and the West Antarctic Ice Sheet (WAIS), divided by the Transantarctic Mountains. The EAIS is largely grounded above current sea-level, whereas the WAIS is largely grounded below sea level, with the exception of the Antarctic Peninsula, Ellsworth Land and Marie Byrd Land (Vaughan *et al.,* 2003; see also Figure 1.1). Ice flows out from the central ice divides towards the coastal regions through outlet glaciers and ice streams, many of which terminate into ice shelves that fringe ~45% of the Antarctic coastline. This study concentrates on these peripheral ice shelves, and specifically, those in the southwest Antarctic Peninsula.

2.2 The Antarctic Peninsula

The Antarctic Peninsula is one of three main upland centres on the WAIS. It is fringed by a continental shelf typically less than 100 km wide, but which extends for distances of up to 1000 km into the Weddell Sea embayment. The Antarctic Peninsula favours a wide range of glacial systems, from small valley glaciers and cirque glaciers in the northern-most islands, to larger glacier systems and ice caps in the southern Antarctic Peninsula (Sugden, 1982). The total area of inland ice on the peninsula measures ~300,000 km^2, with an average thickness of 610 m (Drewry *et al.,* 1982). The total ice-shelf extent prior to recent dramatic collapse events was ~145,000 km^2 (Drewry *et al.,* 1982; Drewry, 1983), with the volume of inland ice and shelf ice totalling ~226,600 km^3. Dramatic and rapid responses of the cryosphere in recent decades have highlighted the sensitivity of the glaciological system on the Antarctic Peninsula with respect to climate.

2.2.1 Recent climatic changes in the Antarctic Peninsula

Various authors (e.g. Raper *et al.,* 1984; Jacka and Budd, 1998; Comiso, 2000) have suggested that a polar amplification of atmospheric temperature is noticeable in the Antarctic Peninsula, with Vaughan *et al.* (2003) proposing a recent rapid regional warming trend. Atmospheric warming over the Antarctic Peninsula has greatly impacted upon the glacial ice and sea-ice extent. Rapid regional warming has caused the retreat of glaciers

(Morris and Mulvaney, 1995; Smith *et al.*, 1999a) and a reduction of snow cover (Fox and Cooper, 1998). Summer melt seasons have increased by 0.5 ± 0.3 days per year (Vaughan *et al.*, 2003), and in some cases have doubled since the 1950s (Torinesi *et al.*, 2003). During 1995 and 2002, the warmest summer temperatures on record were observed at Esperanza Station, coinciding with the rapid collapse of Larsen A and Larsen B Ice Shelves respectively (Marshall *et al.*, 2006).

The present-day Antarctic Peninsula can be divided into two distinct climatic zones: 1) polar maritime on the western side and, 2) polar continental on the east (Martin and Peel, 1978). Frequent, relatively warm and saturated weather systems approach the west side of the peninsula over the Bellingshausen Sea, depositing between 1000 and 1500 mm of precipitation per annum (Robin and Adie, 1964). The polar maritime weather patterns on the west deliver mean near-surface air temperatures of between -3°C and -10°C from 63°S to 73°S, whereas temperatures on the eastern side are between 2-10°C lower over a similar latitudinal range (Reynolds, 1981; Vaughan and Doake, 1996). The differences in precipitation and temperature are reflected in the positioning of the equilibrium line altitude (ELA); greater precipitation on the west leads to a much lower ELA (<100 m) than on the east (>400 m) (Ingolfsson *et al.*, 2003).

It has been widely reported that global atmospheric and oceanographic changes have had, and will have, a direct impact on the cryosphere (IPCC, 1990, 1995, 2001, 2007). Of particular concern are the heightened atmospheric temperature increases observed, predicted and modelled in the Polar Regions (Manabe and Stouffer, 1980; Mitchell *et al.*, 1990; Holland and Bitz, 2003; Vaughan *et al.*, 2003; Bekryaev *et al.*, 2010). This 'polar amplification' of temperature increase in Antarctica has been found elsewhere: Raper *et al.* (1984) analysed data from 16 meteorological stations from around Antarctica and established a warming of 2.8°C century^{-1} from 1957-1982. Furthermore, direct measurements taken from various field excursions were analysed by Jones (1995), in conjunction with station data, revealing a general increase of at least 1°C between the first and last decades of the 20th Century. Jacka and Budd (1998) similarly assessed 16 meteorological points (though treating Antarctic Peninsula records as a single data point) from across Antarctica and obtained a mean trend of 1.2 ± 1.4°C century^{-1}, whereas in a later study, Comiso (2000) found a warming trend of 1.2 ± 0.8°C from 21 Antarctic meteorological stations over a 45 year period from 1954 to 1999 (2.7°C century^{-1}).

On the Antarctic Peninsula, temperature trends from Faraday (now Vernadsky), Esperanza and Bellingshausen meteorological stations (Figure 2.1, Figure 2.2) reveal an increase of an order of magnitude greater than global temperature increase (0.6 ± 0.2°C century^{-1}; IPCC, 2007) with other stations around the Antarctic Peninsula also suggesting atmospheric warming on the north eastern coasts (Vaughan *et al.*, 2003). In particular, King (1994), King and Harangozo (1998), Vaughan *et al.* (2001) and Marshall *et al.* (2002) highlighted the marked warming observed on the western coasts of the Antarctic Peninsula, with temperature increase at Faraday (Vernadsky) measured at 2.5°C since 1950. More recently, Turner *et al.* (2005) re-evaluated temperature trends across the northern reaches of the Antarctic Peninsula (Figure 2.2) and highlighted some significant increases in annual and seasonal temperatures from 1951-2000 (Table 2.1) particularly at those three aforementioned stations.

Table 2.1. Annual and seasonal surface temperature trends at selected Antarctic Peninsula stations as reported by Turner *et al.* (2005). **Bold and underlined = significant at 1% level**. **Bold = significant at 5% level**. *Italic = significant at 10% level*. See Figure 2.1 for the location of meteorological stations and Figure 2.2 for trends.

Station	**Temperature trend (°C decade^{-1})**					**Period**
	Annual	**Spring**	**Summer**	**Autumn**	**Winter**	
Rothera	+1.01 ± 1.42	+1.06 ± 1.53	+0.36 ± 0.57	+1.37 ± 1.46	+1.73 ± 2.97	1978-2000
Faraday/ Vernadsky	**+0.56 ± 0.43**	+0.25 ± 0.4*	**+0.24 ± 0.17**	**+0.63 ± 0.60**	**+1.09 ± 0.88**	1951-2000
Bellingshausen	+0.35 ± 0.46	-0.10 ± 0.47	**+0.30 ± 0.20**	+0.51 ± 0.60	+0.58 ± 0.97	1969-2000
Esperanza	*+0.41 ± 0.42*	-0.07 ± 0.57	**+0.43 ± 0.34**	+0.82 ± 1.11	+0.51 ± 0.82	1961-2000
Marambio	-	-0.8 ± 10.5	-	-	+0.81 ± 1.53	1971-2000

**Assumed due to typo in published data (± 0.4.4, Turner et al., 2005, Table 1.)*

The link between climate warming and the retreat of glaciers and ice shelves has been studied over several decades (Mercer, 1978; Splettoesser, 1992; Morris and Mulvaney, 1995; Smith *et al.*, 1999; Scambos *et al.*, 2000; Morris and Vaughan, 2003; Rau *et al.*, 2004; Cook *et al.*, 2005; Cook and Vaughan, 2010; Davies *et al.*, 2012). Most strikingly, the link between atmospheric temperatures and ice-shelf vulnerability was reported by Morris and Vaughan (2003) who suggested that ice shelves at or near the -9°C annual isotherm are most susceptible to rapid retreat. With increasing atmospheric temperatures observed in the region, this thermal limit has progressively migrated south over the Antarctic Peninsula (Figure 2.3)

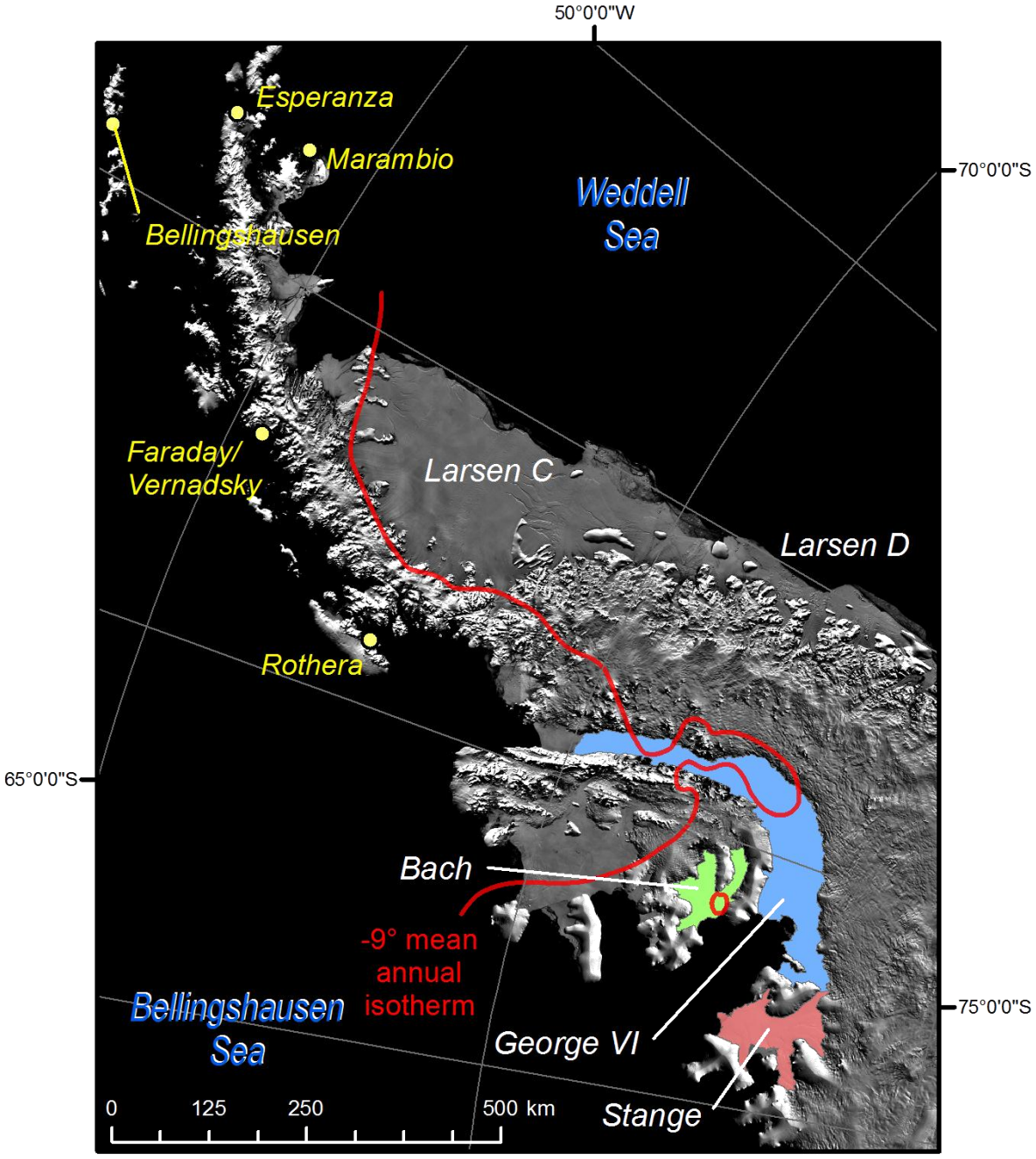

Figure 2.1. Antarctic Peninsula meteorological station locations with respect to the ice shelves studied here. The -9°C mean annual isotherm (Morris and Vaughan, 2003) as discussed in the text is also shown. Background image; MODIS Mosaic of Antarctica (2003) (Haran *et al.*, 2006).

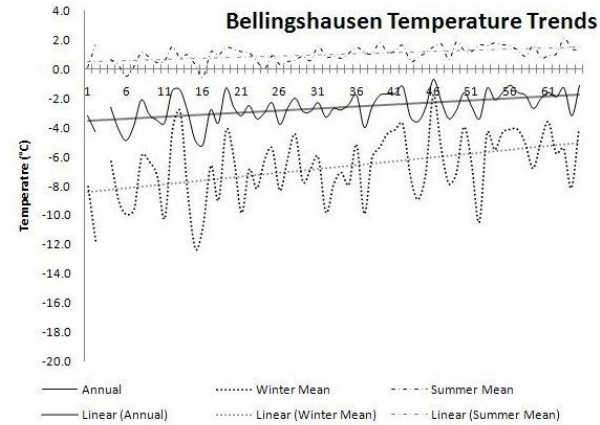

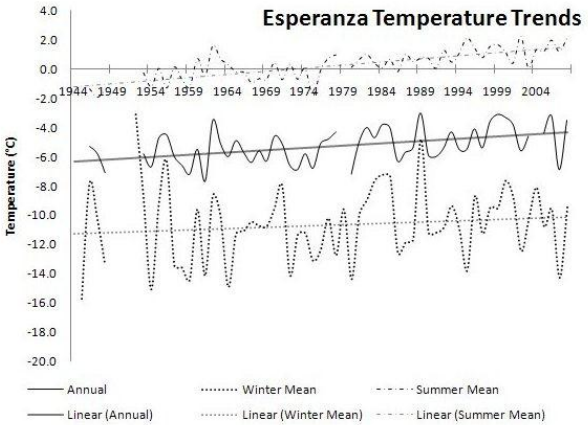

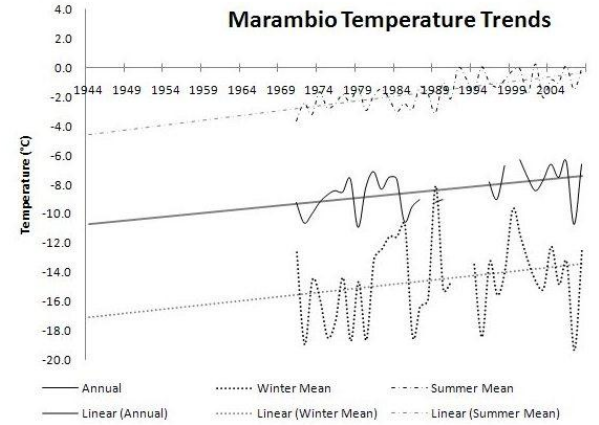

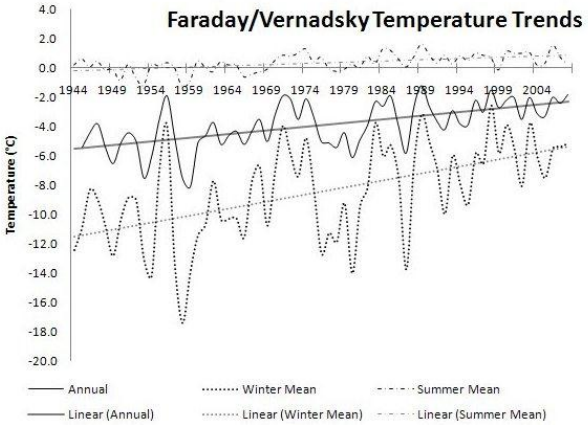

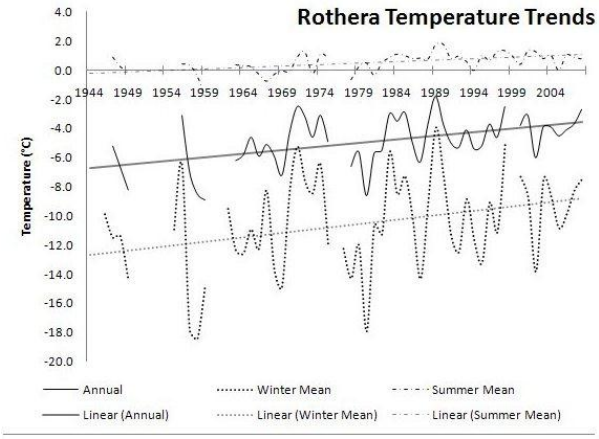

	Bellings-hausen	Esperanza	Marambio	Faraday	Rothera
Min (W) (°C)	-15.50	-20.80	-23.20	-20.10	-23.10
Max (S) (°C)	2.80	3.60	1.50	2.40	2.70
Mean (A) (°C)	-2.63	-5.26	-8.39	-3.89	-4.89
St Dev. (W) (°C)	2.28	2.56	2.79	3.27	3.24
St Dev. (S) (°C)	0.55	1.01	1.05	0.62	0.67
St Dev. (A) (°C)	1.01	1.18	1.31	1.56	1.68
Change (W) (°C)	3.45	1.16	3.68	6.25	4.00
Change (S) (°C)	10.2	2.77	4.28	1.15	1.30
Change (A) (°C)	1.83	2.00	3.37	3.29	3.21

W = winter (June, July, August), S = summer (December, January, February), A = Annual. Temperature change based on linear trend lines.

Figure 2.2. Near-surface air temperature records for Bellingshausen, Esperanza, Marambio, Faraday and Rothera meteorological stations on the Antarctic Peninsula from ca. 1944 to ca. 2008 illustrating the general warming observed across the region. Note the enhanced winter temperatures at Bellingshausen and Faraday in particular. Raw data sourced from http://www.antarctica.ac.uk/met/gjma/temps.html. See Figure 2.1 for meteorological station locations.

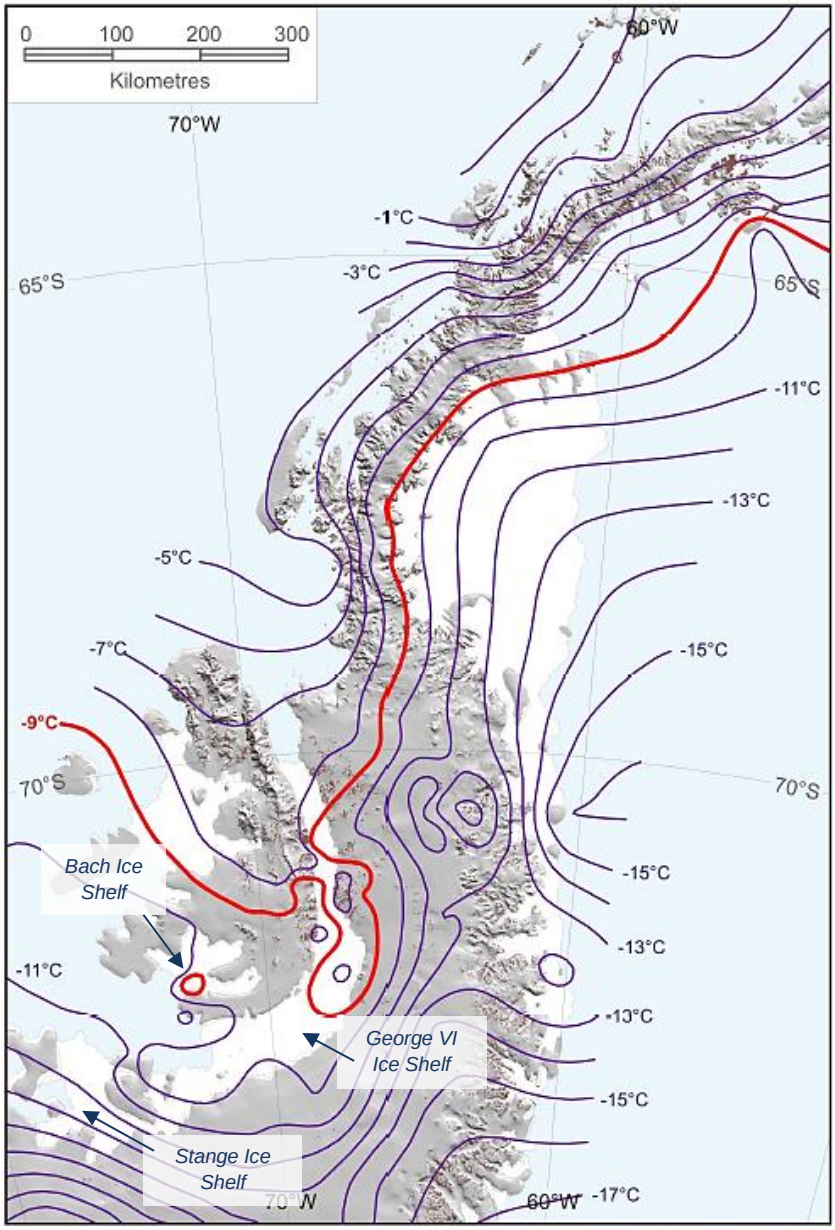

Figure 2.3. Contours of interpolated mean annual temperature in 2000 from meteorological station data, highlighting the position of the critical -9°C isotherm. Note the close proximity to Bach Ice Shelf and the northern extent of George VI Ice Shelf on the west Antarctic Peninsula. Source: Cook and Vaughan (2010) and originally from Morris and Vaughan (2003).

Recent investigations have revealed that the atmospheric circulation of the peninsula region has changed significantly over the last few decades. The principal mode of variability in the southern hemisphere circulation, the Southern Hemisphere Annular Mode (SAM), began a positive phase shift in the mid-1960s (Marshall *et al.*, 2006) which has resulted in reduced atmospheric pressure in the Antarctic Peninsula region. The associated trends are statistically significant during the autumn and summer seasons, and thus are considered a primary variable in the large increase observed in mean annual air

temperatures. Marshall *et al.* (2004) and Jones and Widmann (2004) proposed that natural variability may have played a role in driving these trends, and Carvalho *et al.* (2005) and L'Heureux and Thompson (2006) linked the phase shift with El-Nino Southern Oscillation (ENSO). Several model studies also suggest that anthropogenically enhanced greenhouse gases and ozone depletion is primarily responsible for the SAM phase shift (e.g. Gillet and Thompson, 2003; Shindell and Schmidt, 2004).

Table 2.2. Annual and seasonal surface pressure trends at selected Antarctic Peninsula stations. Source: Turner *et al.* (2005). See Figure 2.1 for location of meteorological stations.

Station	**Pressure trend (hPa decade^{-1})**					**Period**
	Annual	**Spring**	**Summer**	**Autumn**	**Winter**	
Rothera	-0.42 ± 2.22	+0.27 ± 4.89	-2.02 ± 3.39	-0.64 ± 3.52	+0.01 ± 5.28	1978-2000
Faraday/ Vernadsky	-0.03 ± 0.49	-0.08 ± 1.16	-0.31 ± 0.84	+0.55 ± 0.96	-0.27 ± 1.14	1951-2000
Bellingshausen	-0.57 ± 1.08	-0.37 ± 2.14	-1.17 ± 2.05	+0.39 ± 1.49	-0.64 ± 2.32	1969-2000
Esperanza	-0.34 ± 0.52	-0.01 ±0.91	-0.54 ± 0.94	+0.13 ± 1.27	-0.56 ± 1.17	1952-2000
Marambio	-	-	-	-	-1.12 ± 2.39	1971-1998

Table 2.3. Annual and seasonal wind speed trends at selected Antarctic Peninsula stations. Source: Turner *et al.* (2005). **Bold = significant at 5% level**. *Italic = significant at 10% level*. See Figure 2.1 for location of meteorological stations.

Station	**Wind speed trend (knots decade^{-1})**					**Period**
	Annual	**Spring**	**Summer**	**Autumn**	**Winter**	
Rothera	+0.537 ± 1.442	+0.565 ± 1.564	+0.624 ± 1.834	+1.060 ± 2.146	+0.397 ± 1.765	1978-2000
Faraday/ Vernadsky	*+0.275 ± 0.291*	+0.032 ± 0.352	**+0.421 ± 0.416**	+0.272 ± 0.482	+0.291 ± 0.525	1951-2000
Bellingshausen	+0.081 ± 0.485	+0.369 ± 0.682	-0.086 ± 0.518	+0.178 ± 0.693	+0.187 ± 0.578	1969-2000
Esperanza	-	-	-	-	-	-
Marambio	-	-	-	-	-	-

Changes within the pressure systems (Table 2.2) have subsequently strengthened the circumpolar vortex, intensifying the westerlies that impinge upon the north western Peninsula (Table 2.3; Marshall, 2002; Turner *et al.*, 2005). Kwok and Comiso (2002) revealed strong positive correlations between the SAM and near-surface air temperatures, particularly over the Bellingshausen, Amundsen and Weddell seas. It has been proposed

that during the positive phase of the winter SAM, the south Atlantic storm centre is displaced, cutting off the atmospheric branch of the Weddell gyre, subsequently leading to a rise in air temperature over the Weddell Sea and Antarctic Peninsula (van den Broeke and van Lipzig, 2003; Marshall *et al.*, 2006; Thompson and Solomon, 2002). Similarly, towards the west of the peninsula, a strong cyclonic circulation during the positive phase shift of the SAM results in an increased poleward heat flux into the region that, combined with sea-ice divergence away from the coast, leads to warmer Antarctic Peninsula temperatures.

High-resolution modelling (e.g. van Lipzig *et al.*, 2008) indicated that over the northern Antarctic Peninsula, the response of temperature to an increase in westerlies is affected by the high mountain range. The temperature sensitivity to the SAM exhibits a clear contrast between the north-eastern side and the north-western side of the barrier, extending to ~68°S as when denser air is lifted over a barrier it will sink down the leeward side due to gravitational forcing. Both the latent heat release, and the transport of relatively dry air with high potential temperature, results in a warming and drying of the air on the leeside (Beran, 1967; van Lipzig *et al.*, 2008). It is by this process that warmer air temperatures have been observed over eastern Antarctic Peninsula climate stations since 1965 (Marshall *et al*., 2006).

2.2.2 Oceanic regime of the Antarctic Peninsula

2.2.2.1 Circulation patterns and water patterns

The Southern Ocean is the only oceanic domain that encircles the globe. It contains the strong eastward flow of the Antarctic Circumpolar Current (ACC) (White and Peterson, 1996), that is the unifying link for exchanges of water masses at all depths between the world's major oceanic basins (Figure 2.4A) (Schmitz, 1995). Thus, the ACC is a major control on the mean global climate and the transmission of climate anomalies around the world. The Antarctic Circumpolar Wave (the principal flow regime) progresses eastwards at average speeds of 6-8 cm s^{-1}, taking 8-10 years for individual phases to travel around the globe (White and Peterson, 1996). The interconnectivity of the ACC was highlighted by the sea-ice extent anomaly during 1988/89 in the Bellingshausen Sea region of the Antarctic Peninsula; an extraordinary retreat of sea ice was recorded and later attributed to anomalies in the Indian Ocean some five years previous (White and Peterson, 1996).

There are three main water masses that affect the seas surrounding Antarctica (Figure 2.4B):

1) The Antarctic Surface Water that consists of a layer 100 to 150 m thick that has low salinity and a temperature close to freezing point. At its northern extent, temperatures of 1-2°C in winter and 3-5°C in summer are typical, decreasing poleward to approximately -2°C (Sugden, 1982). The Antarctic Convergence zone (or Polar Front), is a shallow frontal feature where the Antarctic surface water meets with the warmer waters of the Southern Ocean, and subsequently sinks. The convergence zone is marked by a horizontal temperature change at the sea surface of 3°C within 30 km (Sugden, 1982).

2) The Circumpolar Deep Water (CDW) lies beneath the Antarctic surface water and consists of a warm (0.5-2°C) layer which is a continuation of the deep ocean water of the Atlantic, Pacific and Indian oceans (Gordon and Goldberg, 1970).

3) Beneath this layer flows the colder Antarctic Bottom Water that instigates from the Antarctic continental shelf (Sugden, 1982).

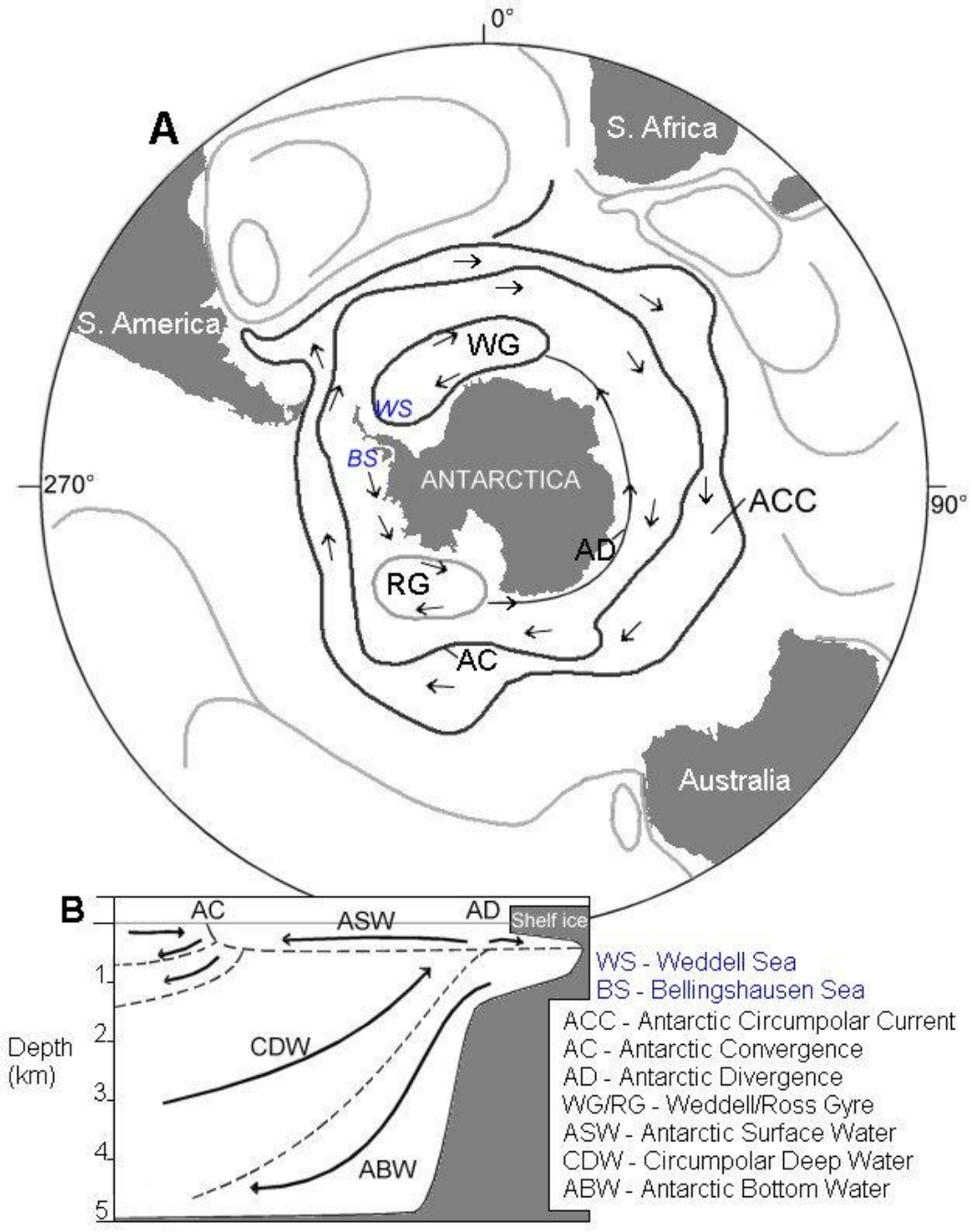

Figure 2.4 A) Oceanic regime of the southern hemisphere and B) water masses of the ACC. Source: Sugden (1982).

The seas immediately adjacent to the Antarctic Peninsula are the Bellingshausen Sea to the west, and the Weddell Sea to the east (Figure 2.4A). The Bellingshausen Sea is affected by the major eastward-flowing ACC and the smaller Antarctic Divergence current that flows westward along the Antarctic continental margin (Figure 2.4A). The Weddell Sea is one of the primary sources of Antarctic bottom water, formed via mixing of CDW with

colder continental shelf or ice shelf waters from the east Antarctic Peninsula (Robertson *et al.*, 2002).

Between 1955 and 1964, a large cold anomaly was recorded in the Bellingshausen Sea to the west of the Antarctic Peninsula. This, however, was replaced in successive years by increasingly warm oceanic temperatures, linked to increasingly warm near-surface air temperatures (Meredith and King, 2005, Figure 2.5). The results presented by Meredith and King (2005) also illustrated the surface intensification of warming oceanic temperatures in the Bellingshausen Sea, to depths of up to 50 m (Figure 2.6). The trend towards higher sea surface temperatures (also Levitus *et al.*, 2000; Robertson *et al.*, 2002; Gille, 2002; Martinson *et al.*, 2008) is coherent with a reported reduction in sea-ice extent in this region (e.g. Zwally *et al.*, 1983; Jacobs and Comiso, 1993, 1997; Comiso, 2000; Stammerjohn *et al.*, 2008; Cavalieri and Parkinson, 2008; Parkinson and Cavalieri, 2012). Indeed, the west coast of the Antarctic Peninsula is also the only region of the continent where a strong correlation between sea-ice extent and atmospheric temperature is observed (Weatherley *et al.*, 1991), and is possibly linked to the physical barrier of the Antarctic Peninsula to east-ward moving air masses (Vaughan *et al.*, 2003; King, 1994).

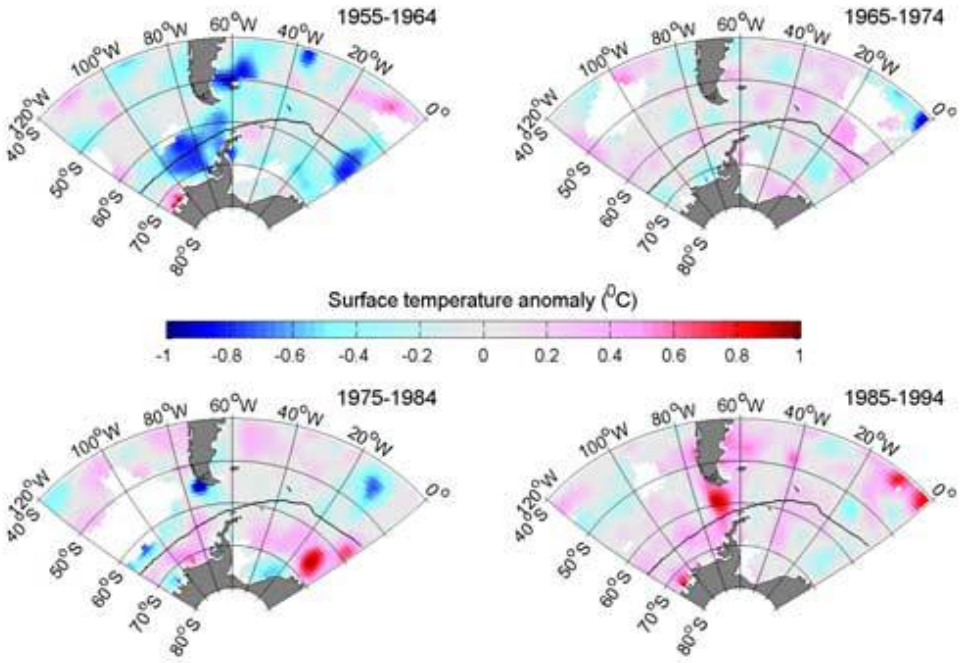

Figure 2.5. Decadal means of oceanic summer surface temperature anomalies between 1955 and 1994 illustrating the increasingly warming Southern Ocean, particularly to the west of the Antarctic Peninsula. Source: Meredith and King (2005).

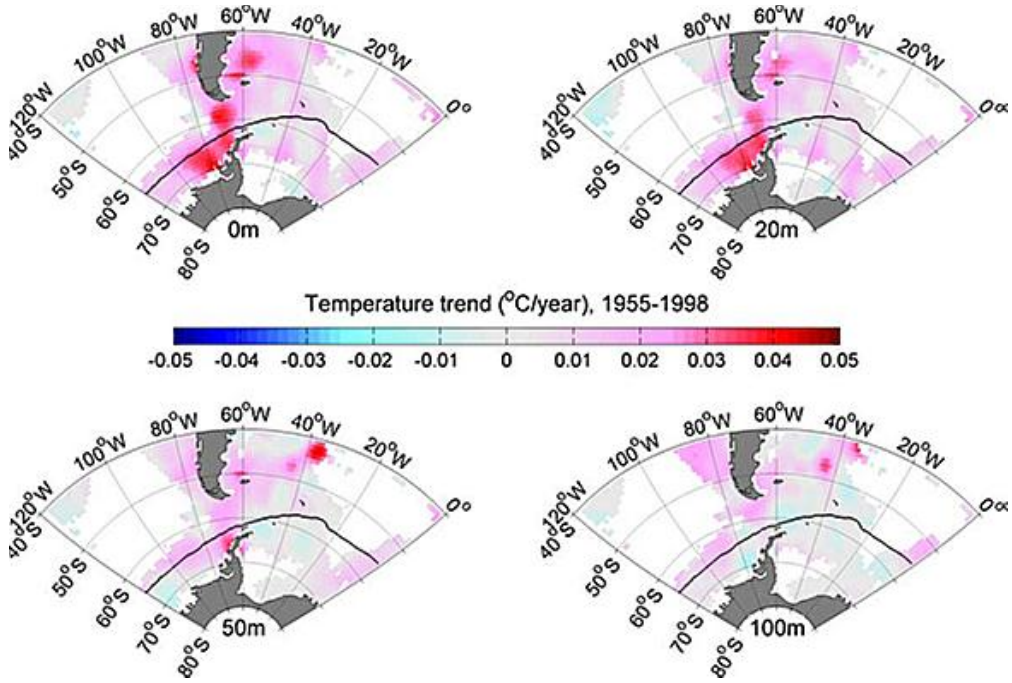

Figure 2.6. Trends in oceanic summer temperatures (1955-1998) at four different depth intervals. Note 1) the significant warming on the west Antarctic Peninsula between 0-20 m depth, slight warming at 50 m depth, but almost negligible warming at 100 m depth, and 2) oceanic warming at the northern extremities of the Antarctic Peninsula (east and west) even at 50 m depth that corresponds to some of the most dramatic ice-shelf collapse events in recent decades (e.g. Prince Gustav, Larsen A and Larsen B). Source: Meredith and King (2005).

2.2.2.2 Variation in sea-ice extent

Due to the oceanic and atmospheric circulation patterns of the Bellingshausen Sea and Weddell Sea, sea-ice extent in these two locations differs greatly. Routine satellite monitoring of sea ice around Antarctica began in 1973 (Jacobs and Comiso, 1997). Generally, in the Antarctic Peninsula, sea-ice extent since then has decreased in both winter and summer months (Zwally *et al.*, 1983; Jacobs and Comiso, 1993, 1997; Comiso, 2000; Stammerjohn *et al.*, 2008; Cavalieri and Parkinson, 2008; Parkinson and Cavalieri, 2012; Figure 2.7), strongly linked with surface air temperature increase (Morrison, 1990). In the Bellingshausen Sea, sea-ice data (Fetterer *et al.*, 2002, 2009) indicate a substantial decrease in summer sea-ice extent compared to the winter extent (Figure 2.7). The seasonal range of sea ice in the Bellingshausen Sea is the smallest in Antarctica, whereas significant retreat occurs in the eastern Weddell Sea region during the summer months (Zwally *et al.*, 1983; Gloersen *et al.*, 1992).

Over the past 30 years, sea-ice extent in the Bellingshausen Sea has retreated significantly during the winter months, but most noticeably in the summer (Yuan and Martinson, 2000; Comiso, 2000). Since 1989-1990, the north-western tip of the Antarctic Peninsula has been free of sea ice, even during the winter months. In the Weddell Sea region, sea-ice extent has increased significantly since 1979 spreading further east towards the South Atlantic and Indian Oceans.

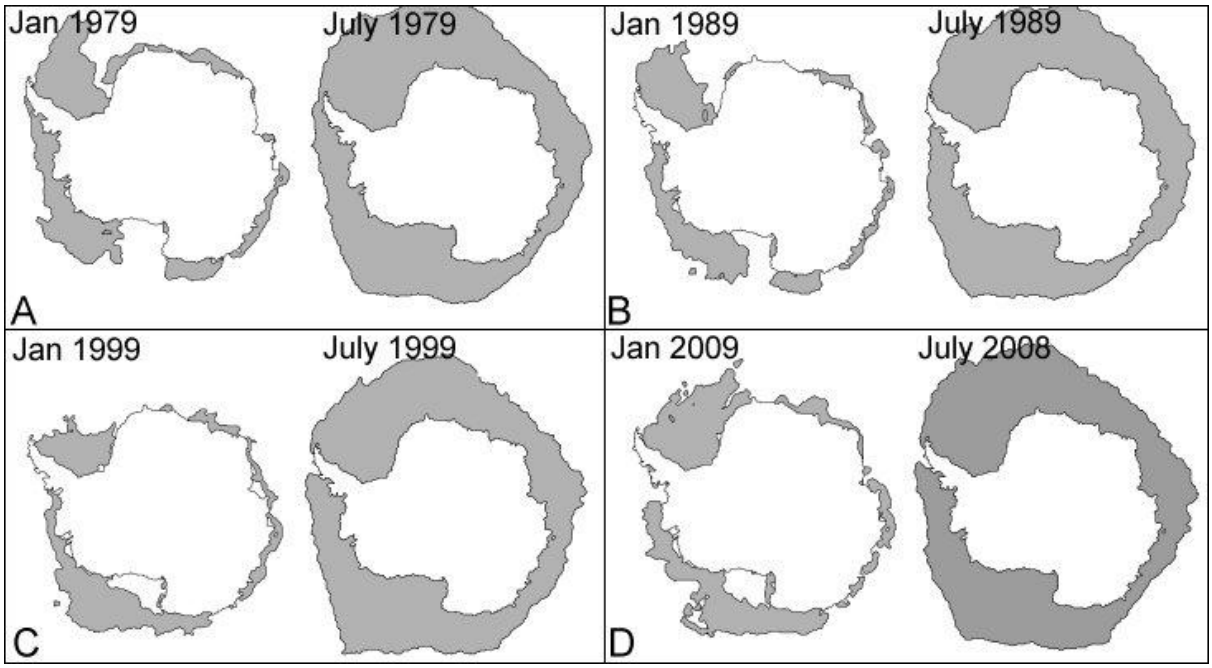

Figure 2.7. Summer and winter sea-ice extent (grey polygons) around Antarctica from 1979 to 2009 illustrating the general decrease in extent to the west of the Antarctic Peninsula. Source: Fetterer *et al.*, (2002; 2009) available at http://nsidc.org/data/seaice_index/

The significance of the lessening sea-ice concentrations extends beyond the Antarctic Continent. Sea-ice cover has the potential to influence global climate over a range of temporal scales (Fletcher, 1969; Walsh, 1983). Over a short timescales (hours to days), sea-ice extent can influence local winds and albedo (Grumbine, 1994), whereas over longer timescales (years to decades), Global Climate Models suggest that 37% of the annual average atmospheric warming is attributed to non-linear feedbacks driven by changes in sea ice (Rind *et al.*, 1995).

2.3 Ice-shelf retreat on the Antarctic Peninsula

Various investigations have produced coastal change and glaciological maps of Antarctica to determine the rate of change observed on the periphery of the continent (Williams *et al.*, 1995; Williams and Ferrigno, 1998). In particular, attempts have been made to illustrate the retreat of individual glaciers around the Antarctic Peninsula (Rau *et al.*, 2004; Cook *et al.*, 2005; Davies *et al.*, in press) and more recently, of the larger ice-shelf systems (Cook and Vaughan, 2010). Of 313 glaciers studied by Rau *et al.* (2004) in the northern Antarctic Peninsula region (< 70°N), 170 were found to be retreating with a total loss of 146.1 km^2, whilst only 40 glaciers advanced (+7.1 km^2) between ca. 1988 and 2001 (102 glaciers were found to be stationary). In a similar study by Cook *et al.* (2005) 212 of 244 glaciers were found to be retreating and only 32 glaciers in advance. This investigation extended the observation period from 1945 to 2004 and illustrated the ever-increasing retreat rate of Antarctic Peninsula glacier systems (Figure 2.8). An updated inventory (Davies *et al.*, in press) of northern-peninsula glaciers revealed 90% retreated between 1988 and 2001, and 79% retreated between 2001 and 2009.

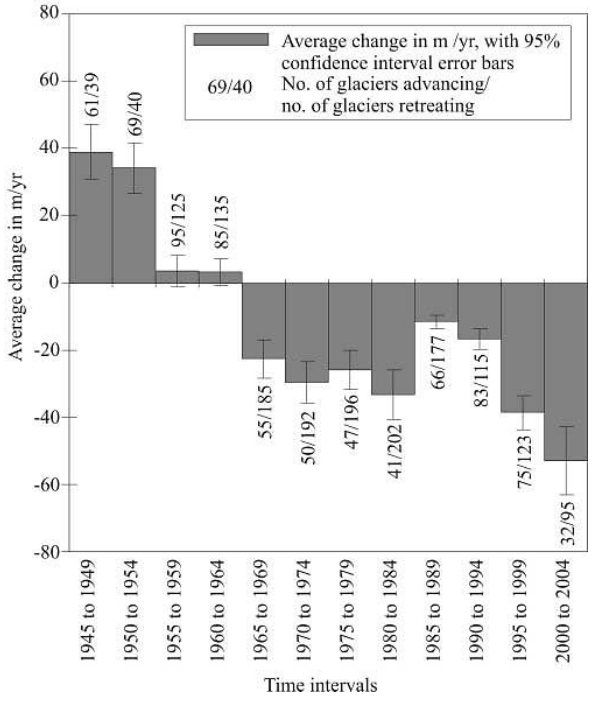

Figure 2.8. Average change of northern Antarctic Peninsula glaciers (<70°N) illustrating the general pattern of advance between 1945-1959, period of stability between 1959-1964 and increasing rate of retreat from 1964 to 2004. Source: Cook *et al.* (2005).

Recently, the changing frontal positions of Antarctic Peninsula Ice Shelves have been mapped (Cook and Vaughan, 2010), revealing ice loss on 11 of the 12 ice-shelf systems in the region. The following sections (2.3.1 to 2.3.7) introduce the key glaciological changes observed on the present day ice shelves of the Antarctic Peninsula.

2.3.1 Müller and Jones Ice Shelves

Müller Ice Shelf and Jones Ice Shelf (Figure 2.9A, C) are (and were) the two smallest ice shelves in the Antarctic Peninsula region measuring only 51 km^2 and 25 km^2 during 1947 respectively (Ward, 1995; Fox and Vaughan, 2005; Cook and Vaughan, 2010). Müller Ice Shelf initially underwent an advance between 1947 and 1957 before retreating into two narrow adjacent embayments fed by Bruckner and Antevs glaciers; both the eastern and western ice fronts currently display concave ice profiles yet appear relatively stable due to the geometry of the embayment and large pinning point of Humphreys Island (Swithinbank and Lucchitta, 1986) that limits the current rate of retreat (Cook and Vaughan, 2010).

Conversely, Jones Ice Shelf, despite being situated only 25 km south of Müller Ice Shelf (Fox and Vaughan, 2005), broke up entirely in several retreat phases between 1957 and 2003. This particular ice shelf sat in Jones Channel and had two opposing ice fronts separated by 10 km of floating shelf ice (Figure 2.9C). The western ice front was much larger but occupied a converging channel and was also impeded by a small ice rise, whereas the eastern ice front occupied a narrower but diverging channel. Hughes (1983) noted that the presence of ice rises within the ice shelf system or near the ice front act as stabilising points that limit retreat. As a result, the western ice front underwent a more progressive and steady retreat, whereas the eastern ice front endured one large retreat during the 1970s. During the late 1990s, Jones Ice Shelf broke into two separate systems, one flowing off Blaicklock Island and the other off Arrowsmith Peninsula.

The differing patterns of retreat between these two ice shelves, and even between the two ice fronts of Jones Ice Shelf, illustrated that atmospheric forcing was/ is not the sole governing factor of ice-shelf retreat. Fox and Vaughan (2005) and Swithinbank and Lucchitta (1986) both concluded that the ice front geometry, embayment geometry and the presence of islands near the ice fronts also govern the rate and patterns of retreat, principally by affecting the strain rates of the ice-shelf system.

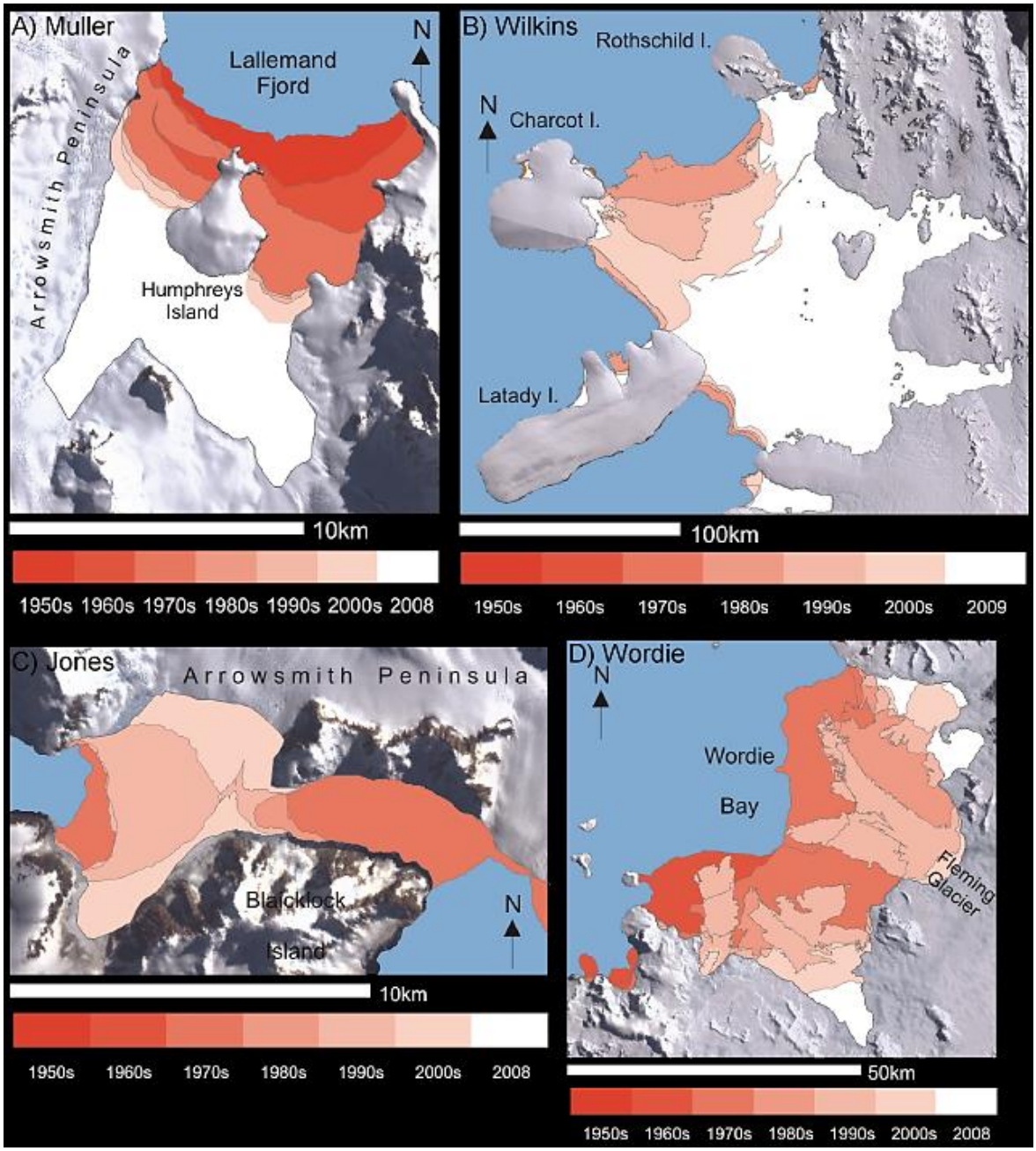

Figure 2.9. Patterns of retreat on western Antarctic Peninsula Ice Shelves as presented in Cook and Vaughan (2010), and discussed in the accompanying text. Note the different ice shelf and embayment geometries that may govern the rate of retreat of each of the ice shelves. See Figure 1.2 for ice shelf location. Source: Cook and Vaughan (2010).

2.3.2 Wordie Ice Shelf

Wordie Ice Shelf was the first major ice shelf to undergo dramatic retreat phases, with two punctuated events recorded in the 1970s and 1980s (Cook and Vaughan, 2010). By the early 1990s, the extent of the ice shelf resembled that of five individual marine-terminating

glacier tongues, and currently only four regions of shelf-ice exist in small embayments generally less than 8 km in width (Figure 2.9D).

Fleming (1940) commented on 'poor surface conditions' on the ice shelf during the British Graham Land Expedition (1934-1937) and suggested that the longevity of the ice shelf was limited. Structural analysis by Reynolds (1988) revealed several areas of heavily fractured and rifted ice, and later, Doake and Vaughan (1991) suggested that the breakup of the ice shelf was linked to increased surface meltwater infilling these surface fractures, reducing the fracture toughness. The pattern of retreat presented in Cook and Vaughan (2010) revealed weaknesses between the dominant flow units extending to the headlands and peninsulas in the zones of former glacier confluence. Furthermore, the presence of at least 10 ice rises or ice rumples (Fleming, 1940; Reynolds, 1988; Doake and Vaughan, 1991) caused fracturing of the ice shelf both upstream and as it flowed downstream that ultimately controlled the rate of retreat from the ice front. Cook and Vaughan (2010), however, commented that it is unclear whether this fracturing was as a result of, or a cause of the ensuing breakup phases.

2.3.3 Wilkins Ice Shelf

In recent years, interest in the stability of Wilkins Ice Shelf has increased, with several studies investigating its recent glaciological changes (e.g. Braun *et al.,* 2009; Humbert and Braun, 2008; Braun and Humbert, 2009; Scambos *et al.,* 2009; Padman *et al.,* 2012). Currently, it is the largest ice shelf on the Antarctic Peninsula actively undergoing significant breakup, with three notable events occurring in 1998 (Scambos *et al.,* 2000), 2008 (Scambos *et al.,* 2009; Braun and Humbert, 2009) and 2009 (Padman *et al.,* 2012), with regular, small scale calving events continually taking place.

It is widely reported that Wilkins Ice Shelf is unusual, with relatively stagnant ice flow rates (30-90 ma^{-1}), a large ice-shelf area compared to its glacier catchment area (Cook and Vaughan, 2010), and a topographic low in the centre of the ice shelf (Vaughan *et al.,* 1993). Abundant meltwater occupies a significant surface area during the austral summer, and the unusually thin ice shelf means that it may be brine-soaked to sea level (Vaughan *et al.,* 1993; Swithinbank and Lucchitta, 1986). As a result of the glaciological conditions, Lucchitta and Rosanova (1998) suggested that the ice shelf may be subject to rapid collapse, providing an alternative theory to Vaughan *et al.* (1993) who stated that Wilkins Ice Shelf would undergo steady calving until at least the ice shelf became decoupled from

its adjacent island (Figure 2.9B). During the more recent collapse events, this decoupling occurred, thus leaving Wilkins Ice Shelf more susceptible to future retreat.

Whilst meltwater is held responsible for some retreat events of the Wilkins Ice Shelf, the largest calving phases of 2008 and 2009 occurred in the austral autumn/ winter when surface meltwater was not present. Scambos *et al.* (2009) suggested that plate-bending at the ice front caused initial fracturing that led to retreat, with Braun *et al.* (2009) commenting that the stress regime changed after each major calving event that may have led to further calving events. Scambos *et al.* (2009) further suggested that brine infiltration into surface fractures during the autumn/ winter breakup events could have acted as a substitute for surface meltwater causing the rapid breakup events through hydro-fracture mechanisms, both of which are described in more detail in Section 2.5. Whether the processes of breakup suggested above are correct or not, the timing of the breakup events with respect to surface conditions, indicates that there is more than one governing factor that leads to rapid retreat.

2.3.4 Prince Gustav Ice Shelf

Prince Gustav was one of the first ice shelves that underwent significant ice loss, and indeed is the ice shelf with the longest historic accounts from field-campaign reports (c.f. Cooper, 1997). Historical evidence (Reece, 1949; Cooper, 1997) suggests that Prince Gustav Ice Shelf had been in retreat since at least 1843, and once was adjoined to the Larsen Ice Shelf to its east, disconnecting in the late 1940s (Francis, 1947). It finally collapsed in 1995 after regular breakup events during the 1970s and 1980s (Cook and Vaughan, 2010), leaving an open channel between Trinity Peninsula and James Ross Island. Interestingly, Pudsey and Evans (2001) demonstrated that during the Holocene, the extent of the Prince Gustav Ice Shelf fluctuated and may have been completely ice-free at some point, thus recent removal of this particular ice shelf cannot solely be linked to anthropogenic climate change.

Recent investigations (Glasser *et al.,* 2011; Davies *et al.,* in press) illustrate the continued recession of its former feeder glaciers both towards James Ross Island and Trinity Peninsula. At the time of collapse, abundant surface meltwater occupied the surface of Prince Gustav Ice Shelf (Glasser *et al.,* 2011).

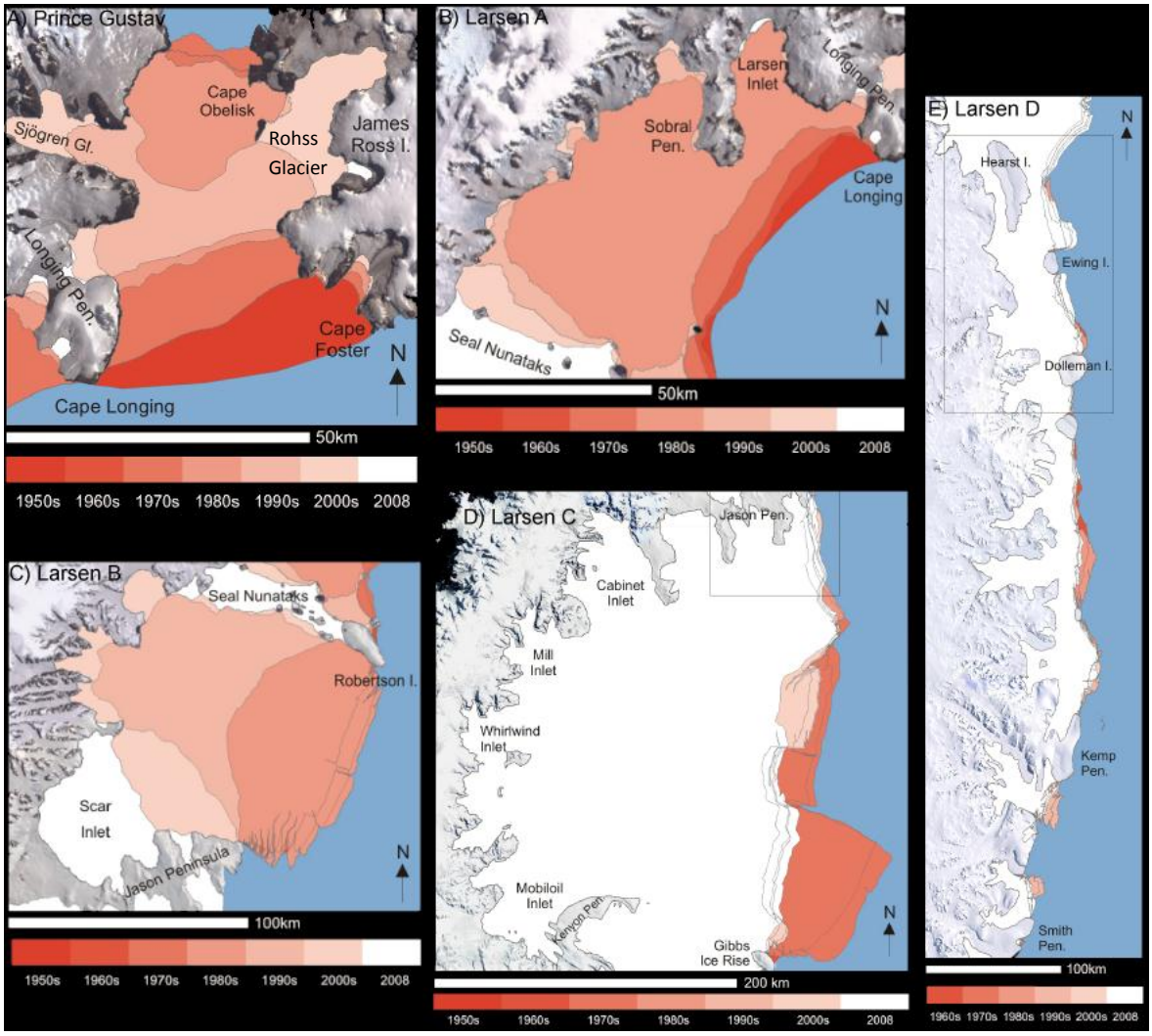

Figure 2.10. Patterns of retreat on eastern-Antarctic Peninsula Ice Shelves as presented in Cook and Vaughan (2010), and discussed in the accompanying text. Note the total removal of Prince Gustav and Larsen A Ice Shelves, the almost complete removal of Larsen B but relatively little retreat of Larsen C and Larsen D. See Figure 1.2 for ice shelf location. Source: Cook and Vaughan (2010).

The morphology of Prince Gustav Ice Shelf was unique; ice was fed to a northern and southern ice front from numerous eastern and western-flowing glaciers from Trinity Peninsula (Longing Peninsula) and James Ross Island (Figure 2.10A). The northern ice front was situated in a mostly-converging channel, whilst the southern ice front occupied a diverging channel, and was also comprised of a significant amount of stagnant shelf ice (Cooper, 1997; Cook and Vaughan, 2010). The two major flow units, Sjögren Glacier and Röhss Glacier merged in the centre of the Prince Gustav Channel, although a clear discontinuity between flow units was observed; flow of these two systems was never cohesive and played an important role in the final collapse event (Glasser *et al.*, 2011). Early retreat (1950s-1970s) occurred along smaller tributary glaciers and the flanks of the

main tributaries until the final collapse phase. Post-collapse, Röhss Glacier became pinned on Cape Obelisk until enhanced retreat between 2001 and present, coupled with dynamic thinning over the same time period (Glasser *et al.*, 2011). Recent analysis (Falcini *et al.*, in prep) of the frontal position of Sjögren Glacier reveals a similar retreat towards its grounding line.

2.3.5 Larsen A and Larsen B Ice Shelves

Larsen A and Larsen B Ice Shelves stretched from Cape Longing to Jason Peninsula on the north-eastern side of the Antarctic Peninsula, separated by Seal Nunataks and Robertson Island. Out of all of the ice shelves that have displayed major retreat phases on the Antarctic Peninsula, Larsen A and Larsen B are by far the most intensely studied. Subsequently these two ice shelves have provided the scientific community with a significant amount of information on ice-shelf-collapse processes.

The northern extent of the Larsen Ice Shelf had undergone steady retreat since at least the 1940s (Doake, 1982; Skvarca, 1993). During 1961, the Larsen A ice shelf measured ~4000 km^2 (Cook and Vaughan, 2010) before it gradually retreated along its whole ice-front edge until January/ February 1995 where it underwent rapid retreat over a few days losing almost 2000 km^2 of ice in the process (Figure 2.10B; Rott *et al.*, 1996, 1998; Doake *et al.*, 1998). Presently, only 397 km^2 of ice remains, although it is unclear whether this ice is floating or not (Cook and Vaughan, 2010).

After a steady advance of the Larsen B Ice Shelf between 1962 and 1995 (Skvarca *et al.*, 1999; Rack, 2000), 2320 km^2 of ice was removed from the ice front in a two week period during February 2002. In total, 1720 km^2 of this loss occurred through calving of a large, tabular iceberg, with the remaining 600 km^2 lost through smaller calving phases (Rack and Rott, 2004) along its entire ice front (Figure 2.10C). After these events, a similar pattern of gradual retreat, followed by a more dramatic collapse phase occurred on the Larsen B Ice Shelf, as observed on its northern neighbours. Of the 11500 km^2 are of ice that occupied the Larsen B embayment during 1963, only 2400 km^2 presently remains, most of this occupying Scar Inlet (Fricker and Padman, 2012).

The collapse of the Larsen A and Larsen B Ice Shelves appeared to be climatically driven (Rott *et al.*, 1998, 2002; Skvarca *et al.*, 1998, 2004; Scambos *et al.*, 2000; Vaughan *et al.*, 2001; Domack *et al.*, 2005), with an increase in surface melting and number of melt-days

(a^{-1}) recorded in the years preceding the eventual collapses, indicative of a warming atmosphere (Torinesi *et al.*, 2003; Vaughan *et al.*, 2003). From fieldwork and satellite observations carried out on Larsen A and Larsen B prior to their collapse (or investigated in its pre-collapse condition, post-1995/ 2002), various processes and mechanisms have been proposed to explain the atmospheric-cryospheric interactions:

Scambos *et al.* (2000, 2008), van den Broeke (2005) and van der Veen (2007) hypothesised that crevasse propagation via increased meltwater pressure was the main mechanism by which these ice shelves weakened, building on the theories of Weertman (1973), Hughes (1983) and van der Veen (1998). From this, MacAyeal *et al.* (2003, 2011) and Guttenberg *et al.* (2011) developed an ice-shelf-fragment-capsize theory, suggesting that a 'domino' effect took place once narrow icebergs calved at the ice front, thus explaining the dramatic disintegration phases observed. MacAyeal *et al.* (2003) subsequently commented that the susceptibility of an ice shelf to disintegration is mostly sensitive to the surface texture (glaciological structure) and ice-shelf thickness (i.e. those factors that govern iceberg geometry).

As well as surface melting, Shepherd *et al.* (2003) suggested that the Larsen B ice shelf became susceptible to enhanced fracturing through increased, progressive basal melting, thinning the ice shelf to a critical limit. More recently, Zwally *et al.* (2005) and Fricker and Padman (2012) suggested the average thinning rate of Larsen B prior to collapse was ~-0.2 ma^{-1}, with a similar rate of thinning (-0.19 ma^{-1}) currently occurring on the remaining Scar Inlet Ice Shelf. Currently, however, little is known about the oceanic-cryospheric interactions at the base of ice-shelf systems with respect to ice-shelf collapse.

Elsewhere, modelling studies of the changing stress regimes in the Larsen A Ice Shelf prior to collapse (Doake *et al.*, 1998) suggest that instabilities are governed by the geometry of the ice front. Briefly, Doake *et al.* (1998) illustrated that when the ice front bows outwards (convex) towards the centre of the ice shelf, uniaxial compression between the pinning points creates a stable geometry; Cook and Vaughan (2010) likened this to an arch of a stone bridge. When calving of the ice front removes this 'arch' and creates a linear or concave frontal profile, the compressive stresses are lost, permitting 'irreversible retreat' (Doake *et al.*, 1998; Rack *et al.*, 2000). This situation was subsequently observed after the initial stages of retreat of Larsen B.

Additionally, studies on the surface speeds of Larsen A and Larsen B prior to collapse revealed an increase in velocity. On Larsen A, flow speeds were determined through feature tracking of surface features at various intervals between 1975 and 1995, supplemented by field measurements, with increases of between 5% and 35% recorded over the 1984-1994 period compared to the previous decade (Bindschadler *et al.*, 1994). A further increase was reported prior to breakup in 1995 (Rack *et al.*, 2000). On Larsen B, stake measurements parallel with the ice front between 1984 and 1996 revealed a 10-20% increase in surface speeds between 1994 and 1996 compared to the previous decade (Rott *et al.*, 1998; Rack *et al.*, 2000), with further speed increases measured between 1997-1999 and 1999-2001 (Skvarca *et al.*, 2004). Using satellite interferometry (Rignot *et al.*, 2004) and numerical modelling (Vieli *et al.*, 2006, 2007) a surface velocity increase of almost 50% was revealed prior to the final collapse of the Larsen B Ice Shelf. These measurements of surface velocity increases are, to date, the only existing datasets that illustrate the response of ice-shelf systems prior to collapse phases. Furthermore, Khazendar *et al.* (2007) also illustrated the rheological changes of the ice shelf prior to collapse, and structural analysis by Glasser and Scambos (2008) highlighted discontinuities between flow units that weakened the mechanical strength of the ice shelf preceding breakup.

2.3.6 Larsen C and Larsen D Ice Shelves

Due to the collapse of Larsen A and Larsen B in response to atmospheric and oceanic temperature increases, the response of Larsen C Ice Shelf has naturally been of heightened interest over recent years (e.g. Glasser *et al.*, 2009; Jansen *et al.*, 2010; Haug *et al.*, 2010; Luckman *et al.*, 2012). It is by far the largest ice shelf on the Antarctic Peninsula, occupying an area of ~51,000 km^2, extending north to south from Jason Peninsula to Gipps Ice Rise (Figure 2.10D).

Skvarca (1994) highlighted the changing surface conditions and ice margins of Larsen C, observing an ice front advance near Jason Peninsula despite limited direct glacier input. South of this, major retreat phases occurred between 1975 and 1988, with two large icebergs (6520 km^2 and 1260 km^2) calving from the ice front. Since then, the ice front has slowly been advancing (Cook and Vaughan, 2010; Figure 2.10D), and few structural changes have been observed since 1963 (Glasser *et al.*, 2009). Indeed, Cook and Vaughan (2010) commented that these large calving events are likely to be part of the natural mass-

balance cycle rather than being climatically-induced. The current ice-shelf profile is largely convex, although less so than at previous times as documented in Cook and Vaughan (2010). However, Jansen *et al.* (2010), Glasser *et al.* (2009) and Khazendar *et al.* (2011) all comment that in its current configuration, Larsen C Ice Shelf is stable and shows little sign of weakening.

Currently, Larsen D is the only ice shelf exhibiting overall advance of its ice front (Cook and Vaughan, 2010; Figure 2.10E). It is composed of multiple narrow glacier tongues interspersed with thick fast-ice formed from sea ice and surface accumulation (Fricker and Padman, 2012). Its ice front is held in place by islands and ice rises that perhaps, along with the presence of fast-ice, limit the calving despite heavily fractured surface conditions. This is very much an atypical Antarctic Peninsula ice shelf in its present state.

2.3.7 Bach, George VI and Stange Ice Shelves

Bach, George VI and Stange Ice Shelves were similarly studied by Cook and Vaughan (2010). Their calculations illustrate that in total, 6% of Bach Ice Shelf and 7% of George VI Ice Shelf has been lost since 1947, whereas only 3% of Stange Ice Shelf has been lost since 1974 (Figure 2.11). All three ice shelves on the south-west Antarctic Peninsula have thus been considered stable (Scambos *et al.*, 2000; Cook and Vaughan, 2010), although Bentley *et al.* (2005; 2011), amongst others, show that George VI Ice Shelf has been absent at various times during the Late Pleistocene and mid-Holocene. Bach, George VI and Stange Ice Shelves are discussed in more detail in Chapter 4 by way of introducing the study sites.

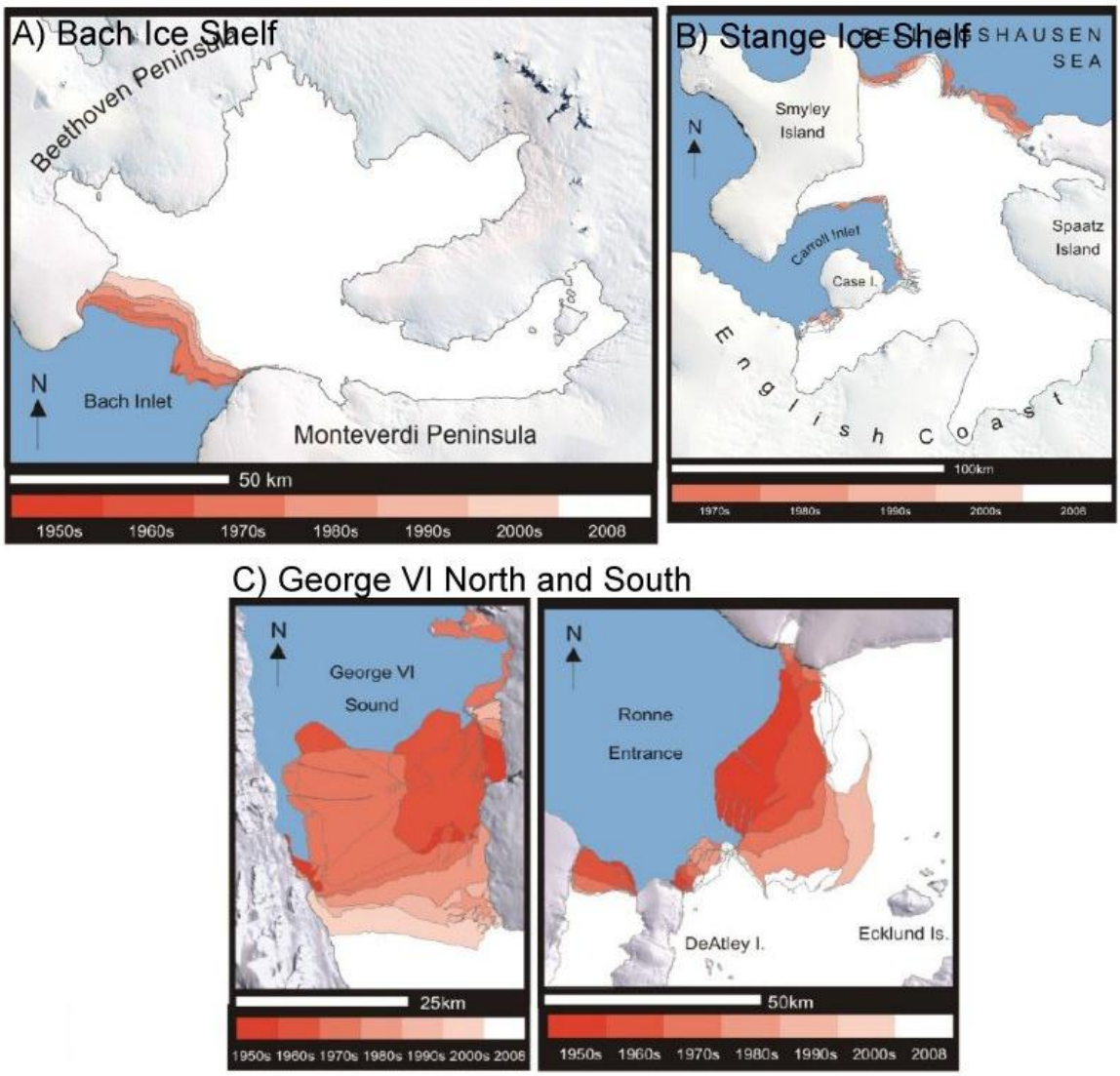

Figure 2.11. Patterns of retreat on Bach, Stange and George VI Ice Shelves as presented in Cook and Vaughan (2010), and discussed in the accompanying text. Note the comparatively small areal retreat of Bach and Stange Ice Shelves over time, and compared to that of neighbouring George VI Ice Shelf. See Figure 1.2 for ice shelf location. Source: Cook and Vaughan (2010).

2.4 Precursors to ice-shelf breakup, collapse and disintegration

Several key precursors to enhanced ice-loss have been identified in the literature and are summarised here. First, ice shelves that have undergone rapid retreat were preceded by periods of sustained ice-loss, typically resulting in an ice-front geometry that bows inwards towards the centre of the ice shelf from its lateral pinning points (Doake *et al.*, 1998). Second, ice-shelf systems that experienced rapid retreat had also undergone significant thinning in the years preceding eventual breakup/collapse/disintegration (Shepherd *et al.*,

2003; Fricker and Padman, 2012). Third, several authors commented on an increase in flow speed of the vulnerable ice shelf immediately prior to enhanced retreat (e.g. Rack *et al.*, 2000; Vieli *et al.*, 2007). Fourth, but not applicable to all breakup events, an increase in surface melting has been observed (e.g. Doake and Vaughan, 1991; Scambos *et al.*, 2004; Glasser *et al.*, 2011), attributed to atmospheric temperature increase. Fifth, enhanced fracturing and rifting, particularly between flow confluences, creates a mechanically weak ice shelf that is unable to resist further fracturing and rifting, and thus is prone to enhanced retreat. It is clear that other factors such as embayment geometry also have an effect on the stability of individual ice shelves.

2.5 Fracture controls and ice-shelf *'collapse'* mechanisms

A summary of the controls on ice-shelf fracture are presented in Table 2.4. Whilst not exhaustive, they represent the most documented controls in the published literature that have been attributed to ice-shelf retreat, breakup and collapse.

There are two leading mechanisms that have been proposed that explain ice-shelf collapse: 1) hydro-fracture (Scambos *et al.*, 2000; MacAyeal *et al.*, 2003), and 2) plate bending (Scambos *et al.*, 2009). For the hydro-fracture mechanism to initiate, the volume and distribution of meltwater upon the ice-shelf surface is fundamental (Scambos *et al.*, 2000; MacAyeal *et al.*, 2003; Vieli *et al.*, 2007). Penetration of surface meltwater into pre-existing crevasses warms and softens the ice via latent heat transportation deep into the ice shelf. Furthermore, surface meltwater that drains into surface crevasses influences the ice-shelf rheology via deepening of such features, potentially through the entire ice-shelf thickness, leading to rift propagation and local decoupling, resulting in a mechanically weakened and fragmented ice shelf (Figure 2.12; Scambos *et al.*, 2000; Vieli *et al.*, 2007).

Table 2.4. Key fracturing controls that have been proposed to cause or retard ice-shelf retreat, breakup and collapse.

Development and/or propagation mechanism	Description/ comments	Key References
Hydro-fracture	Increased volume of surface meltwater in pre-existing surface fractures further penetrates the ice-shelf surface and leads to possible rifting. Deemed an important process that eventually led to the disintegration of Larsen A and Larsen B, and may have played an decisive role in the breakup of Prince Gustav and Wordie Ice Shelves.	Scambos *et al.*, 2000, 2003. van der Veen, 1998
Ice-shelf-fragment-capsize	Initial fracturing causes pre-existing weaknesses that leads to iceberg calving. Where the iceberg width is less than the iceberg depth, capsizing is initiated that could lead to further fracturing, rifting and calving events through the ensuing wave action. Suggested as a key mechanism in explosive disintegration as observed on Larsen A and B.	MacAyeal *et al.*, 2003.
Plate-bending	Stress fields at the ice-front/ocean vertical interface causes the ice shelf to bend vertically, increasing tensile stresses on the surface. Fractures may further developed by other mechanisms. Thought responsible for initial fracturing of Wilkins Ice Shelf where surface meltwater was not present.	Scambos *et al.*, 2009.
Shearing	Discontinuity in flow leads to rupturing along unit boundary. Illustrates heterogeneous dynamics and mechanical strength of different ice-shelf tributary systems and held partially responsible for collapse of Larsen B as it permitted a significant alteration in dynamics.	Glasser and Scambos, 2008.
Micro-tsunami	Impulsive, frequent ocean surface waves generated by glacier calving, iceberg collision and/or ice-shelf rifting leads to enhanced flexure of intact ice-shelf, causing further fracturing. Theoretical mechanism developed from ice-shelf-fragment-capsize mechanism.	MacAyeal *et al.*, 2009.
Tsunami	Triggered by (1) capsize of calved icebergs or collapse of ice-shelf edge, or (2) earthquake-derived tsunami. Both instances create greater oceanic swell that increases tidal flexure of ice-shelves that triggers further fracturing or dislodgement of ice along pre-aligned fractured/rifts. Observed at the front of Sulzberger Ice Shelf following 2011 Honshu earthquake.	(1) MacAyeal *et al.*, 2011. Guttenberg *et al.*, 2011. (2) Brunt *et al.*, 2011.
Infragravity waves	Storm-forced oceanic swell causes higher-amplitude waves than normal tidal conditions. These waves are not dampened by the presence of sea-ice and thus impact on ice-shelf flexure throughout the year. Increased wave forcing induces fracturing. Theoretical model.	Bromirski *et al.*, 2010
Reduction in sea ice	Reduction in sea-ice in front of the ice shelf permits wave action to increase flexure of ice front leading to increased surface fracturing and iceberg calving. Theoretical, no direct observations made.	Massom (*in* Fricker and Padman, 2012)
Ice melange presence	Considered a controlling factor on the rate of rift propagation, but also thought to have influenced the partial collapse of the 2009 Wilkins breakup event. Thick ice melange between rifts stabilises rift propagation, acting as a restraining substance. Thinning or removal weakens rifts and permits further fracturing.	Bassis *et al.*, 2005; Fricker *et al.*, 2005; Humbert and Braun, 2008.
Geometric instability/ ice front profile	Regular small-scale calving causes the ice front to bow inwards at its centre, leading to a stress regime more favourable to large-scale retreat. Evidence of increased fracturing once the geometry has been reshaped, but required pre-existing fractures to drive the initial calving/retreat.	Doake *et al.*, 1998; Rack *et al.*, 2000.
Increasing flow speed	Fractures caused by increasing flow speed either as a result of frontal pulling or tributary-glacier pushing. Not fully understood to be a cause or consequence of fracturing. Theory developed after breakup of Larsen B.	Vieli *et al.*, 2006, 2007.
Ice-shelf thinning	Caused by a combination of surface melting, bottom melting or as a response to increased velocities. Reduces mechanical strength of ice shelf and leaves it prone to further fracture and/ or enhanced retreat. Considered significant in collapse of Larsen B.	Shepherd *et al.*, 2003, Fricker and Padman, 2012

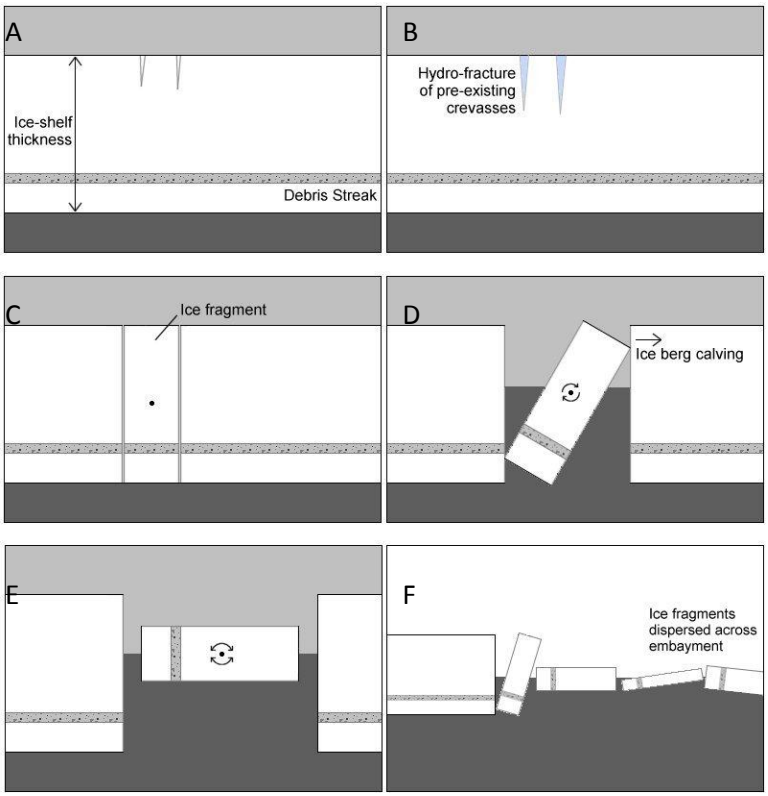

Figure 2.12. Hydro-fracture ice-shelf collapse mechanism. A) initial ice-shelf configuration with surface crevasses. Increase in surface meltwater increases the depth of these crevasses (B) as a result of increased pressure, until fractures penetrate the entire ice shelf (C). Iceberg calving is initiated (D), that may lead to the capsizing of thin ice-shelf fragments (E) where their longitudinal distance is less than the ice-shelf thickness. Capsizing continues to weaken the ice shelf and enhanced further iceberg calving, distributing ice-shelf fragments across the embayment (F). This method was proposed following the collapse of Larsen B. Source: MacAyeal *et al.* (2003).

Once hydro-fracturing has occurred, an associated iceberg-capsize mechanism disperses the ice fragments across the embayment, principally driven by gravitational potential energy released during iceberg capsizing from the ice front (Figure 2.12, MacAyeal *et al.*, 2003). The large spread of fragments during and after collapse, as seen in the Larsen A and Larsen B collapse-events, is attributed to narrow ice fragments 'rolling' on an axis that initiates further break-up through micro-tsunami events (MacAyeal *et al.*, 2003, 2009; Guttenberg *et al.*, 2011).

Whilst the hydro-fracture mechanism suitably explains the summer collapse events of Larsen A and Larsen B, it does not transfer to the winter breakup phases of Wilkins Ice shelf during May, June and July 2008 (Scambos *et al.*, 2009), and during June 2009 (Padman *et al.*, 2012). Both Braun *et al.* (2009) and Vaughan *et al.* (1993) infer that the Wilkins Ice Shelf has extensive brine infiltration, initiating at the ice front via lateral

wicking of seawater through porous firn at the waterline (Scambos *et al.*, 2009). It is possible that the brine content within the firn layer acted as a substitute for a proportion of the meltwater ponds that are absent in the winter breakup events, although the stresses required for rapid-disintegration are considered too great for brine-hydro-fracture alone.

Scambos *et al.* (2009) proposed an ice-shelf plate-bending process (Figure 2.13). In this theory, pressure differences between the ice-shelf plate and the surrounding ocean cause bending of the ice shelf, inducing a surface-extensional stress perpendicular to the margin, which is sufficient to initiate fracturing in the upper firn layer. Where water is present within the firn layer (brine/ saturated firn), it can infiltrate into these cracks increasing the net stress and causing further vertical fracturing. This, coupled with a change in glaciological stresses is enough to initiate major break-up events during winter months (Scambos *et al.*, 2009), and indeed the evolution of surface fractures during breakup events (e.g. Braun *et al.,* 2009) fit with this proposed mechanism.

The collapse mechanisms detailed above require a number of atmospheric, glaciological and oceanic influences that contribute towards ice-shelf breakup/collapse/disintegration. Rapid retreat is aided by the structural configuration of the ice shelf, surface meltwater occurrence, glacier or ice-shelf thinning and changes in velocity. It is likely that the stability of ice-shelf systems is governed by an environmental threshold where the interaction between atmospheric, oceanic and glaciological factors is crucial, and when exceeded, the associated pressures are sufficient to cause an irreversible decline by either one, or a combination of, the two collapse mechanisms.

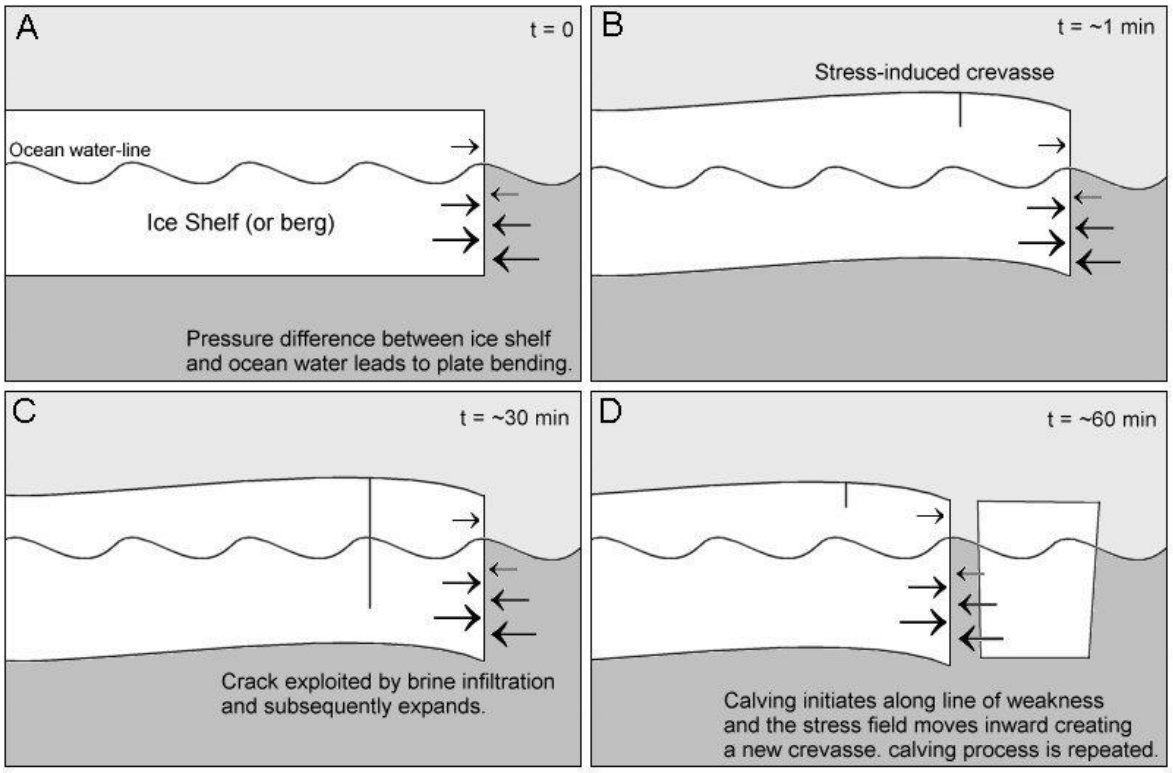

Figure 2.13 Plate-bending mechanism. A) Ice shelf at time = zero. Pressure difference between the ice shelf and the ocean (enhanced also by tidal amplitude) causes the entire ice-shelf plate to bend (B) that instigates surface crevassing. The crevasse continues to expand, and is aided by brine infiltration once the fracture is deep enough to allow lateral wicking of ocean water (C). Eventually an iceberg is formed (D) and the plate-bending mechanism begins once again. Source: Scambos *et al.* (2009).

2.6 Chapter summary

In Chapter 2, the past and present glaciological and climatic situations of the Antarctic Peninsula have been discussed, as well as the details of the oceanic circulation patterns and water masses that operate on a continental and regional scale. A review of the changes to other Antarctic Peninsula Ice Shelves has been presented, with the processes and mechanisms that govern ice-shelf instability also being detailed. In Chapter 3, a review of the key remote sensing datasets and techniques that have been used in ice-shelf investigations in Antarctica is given.

Chapter 3

Satellite Remote Sensing of Ice Shelves

3. Satellite remote sensing of ice shelves

Chapter 3 presents an overview of the principal satellite sensors used in the assessment of ice shelves in Antarctica. Section 3.1 concentrates on the available optical sensors and their key characteristics. In Section 3.2, satellite radar imagery is considered, and in Section 3.3 the non-imaging satellite sensors such as Radar Altimeters (RA) and Light Detection and Ranging sensors (LiDAR) are introduced. An overview of the principal applications is presented in Section 3.4, concentrating in particular on the use of remote sensing in spatial assessment, structural investigation, velocity-field derivation and thickness calculation of ice shelves. Those techniques implemented in this study are further described in Chapter 5.

3.1 Optical remote sensing

Optical sensors detect solar radiation reflected by the Earth's surface (passive systems) across the visible (VIS), near infrared (NIR, VNIR for visible-near infrared) and short-wave infrared (SWIR) electromagnetic spectrum, and also the radiation emitted by the Earth's surface in the thermal infrared (TIR) (Racoviteanu *et al.,* 2008. See Figure 3.1). It is most common to use a combination of the visible bands to create a 'true-colour' image of the area in question, although the inclusion of NIR, SWIR and TIR wavelengths in glacial assessment can be of particular value when identifying thermal structure through differing spectral characteristics between snow/firn/ice facies, for example (Hall *et al.,* 1987, 1988).

The use of optical remote sensing in glaciology has increased considerably over the past four decades for a number of reasons. First, the variety of sensors available has meant that there is near-global coverage at a range of areal scales from regional to local, permitting glacial assessments extending from ice sheets (e.g. Scambos *et al.,* 2007) to individual glaciers (e.g. Pritchard and Vaughan, 2007). Second, the spatial resolution at which satellite sensors operate ranges from coarse (> 500 m, Moderate Resolution Imaging Spectroradiometer, MODIS) to fine (< 0.5 m, IKONOS, QuickBird), with the most common sensors acquiring data between 80-10 m spatial resolution, allowing detailed assessments to be made of glacier and ice-sheet surfaces. Third, the relatively short time period between repeat image acquisition allows for regular monitoring of rapid glacial change (ice-shelf collapse, for example), and fourth, the availability of catalogued data permits long-term changes to be analysed. The most commonly-used optical sensors in

studying ice shelves are summarised in Table 3.1, with a range of their applications outlined in Section 3.4.

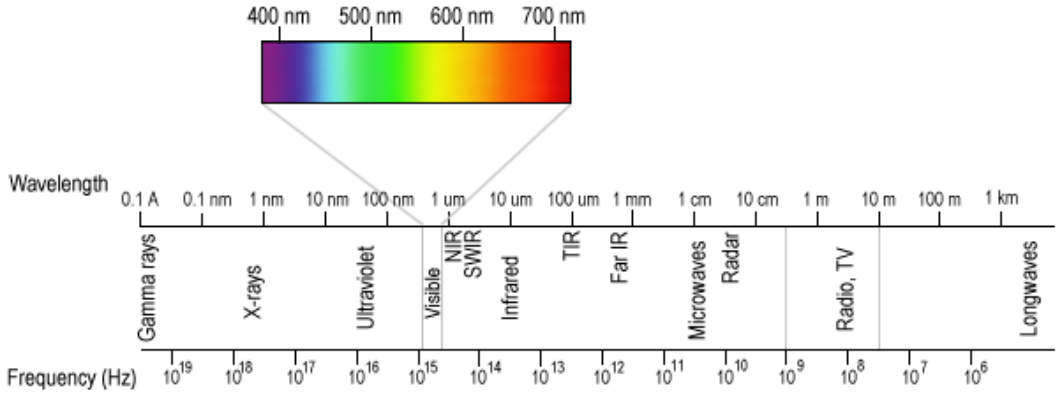

Figure 3.1. The **e**lectromagnetic spectrum illustrating the Visible, NIR, SWIR and TIR wavelengths as described in the text.

3.2 Radar imaging and Synthetic Aperture Radar

In contrast to passive optical imaging systems that require the Sun's illumination, radar imaging is an active system (Lillesand *et al.*, 2008), meaning that it can acquire data over any 24 hour period, irrespective of daylight or weather conditions. The radar beam is illuminated in a side-looking direction with respect to the platform course (Figure 3.2), with the radar image subsequently constructed based on the brightness (amplitude, *A*) of the return signal received back at the antenna (see Figure 3.2 for acquisition properties). The amplitude of this signal is dependent on the physical characteristics of each point on the Earth's surface.

Where a smooth surface such as still water or bare ground is detected, the angle of reflectance is approximately equal to the angle of incidence, thus the return signal at the antenna is negligible (Figure 3.3A). On rough surfaces or over rugged terrain, the radar beam can be scattered significantly, with the return signal dependant on the magnitude and morphology of the detected surface (Figure 3.3B). Over regions where loose sediment or snow pack is apparent, the radar beam is able to penetrate the uppermost layer; Figure 3.3D illustrates the refraction and scattering of a radar beam directed onto a glacier surface. Finally, it is possible that the return signal is approximately equal to the transmitted radar beam where double-bounce occurs (Figure 3.3C). This is conceivable where the initial

Table 3.1. Overview of key optical remote sensors used in ice-shelf investigation

Optical Sensor	Spatial Resolution	Spectral Resolution	Temporal Resolution	Swath	Archive Length	Comments
ASTER[1]	15 m (VNIR), 30 m (SWIR), 90 m (TIR)	VNIR 0.52-0.86 µm, SWIR 1.60-2.43 µm, TIR 8.13-11.65 µm	4-16 days	60 km	2000 to present (SWIR to 2008 due to equipment failure)	Stereo coverage available
Landsat MSS[2]	79 m (Landsat 1-3), 82 m (Landsat 4-5)	VNIR 0.5-1.1 µm	18 days	180 km	1972 to 1995 over five Landsat missions	
Landsat TM[3]	30 m (VNIR-SWIR), 120 m (TIR)	VNIR 0.45-0.9 µm, SWIR 1.55-1.75 µm, TIR 10.4-12.5 µm	18 days	185 km	1982 to present over two Landsat missions	Landsat 5 still acquiring TM data albeit intermittently.
Landsat ETM+[4]	15 m (Pan), 30 m (VNIR-SWIR), 60 m (TIR)	VNIR 0.45-0.9 µm, SWIR 1.55-2.35 µm, TIR 10.4-12.5 µm	16 days	185 km	1999 to present	Scenes acquired after 2003 are affected by failure of the Scan Line Correction instrument that causes data gaps towards the lateral image edges
SPOT V[5]	2.5-5 m (Pan), 10 m (VNIR), 20 m (SWIR)	VNIR 0.5-0.89 µm, SWIR 1.58-1.75 µm	2-3 days	60 km	2002 to present	Stereo coverage available
Quickbird	0.6 m (Pan), 2.4 m (VNIR)	VNIR 0.45-0.9 µm	1-3.5 days	16.5 km	2001 to present	Stereo coverage available
IKONOS	0.46 m (Pan) to 4 m (VNIR)	VNIR 0.53-0.85 µm	~3 days	11.3 km	1999 to present	Stereo coverage available
MODIS[6] **Terra**	250 m, 500 m and 1000 m	36 bands across 0.41-14.39 µm	1-2 days	2330 km	1999 to present	Course resolution suitable for regional scale assessment, but finer features and characteristics are overlooked
AVHRR[7]	1000 m – 2500 m	VNIR 0.58-1.64 µm, IR 3.55-3.93 µm, TIR 10.30-12.50 µm.		1000 km	1978 to present	On board the National Oceaic and Atmospheric Administration satellites.

[1]Advanced Spaceborne Thermal Emission and Reflection radiometer. [2]Multi-Spectral Scanner. [3]Thermatic Mapper. [4]Enhanced Thermatic Mapper Plus. [5]Système Pour l'Observation de la Terre. [6]Moderate Resolution Imaging Spectrotadiometer. [7]Advanced Very High Resolution Radiometer.

radar beam is reflected off a smooth horizontal surface (e.g. water), and then off a near-by vertical surface (e.g. ice front), directing the radar beam back towards the antenna.

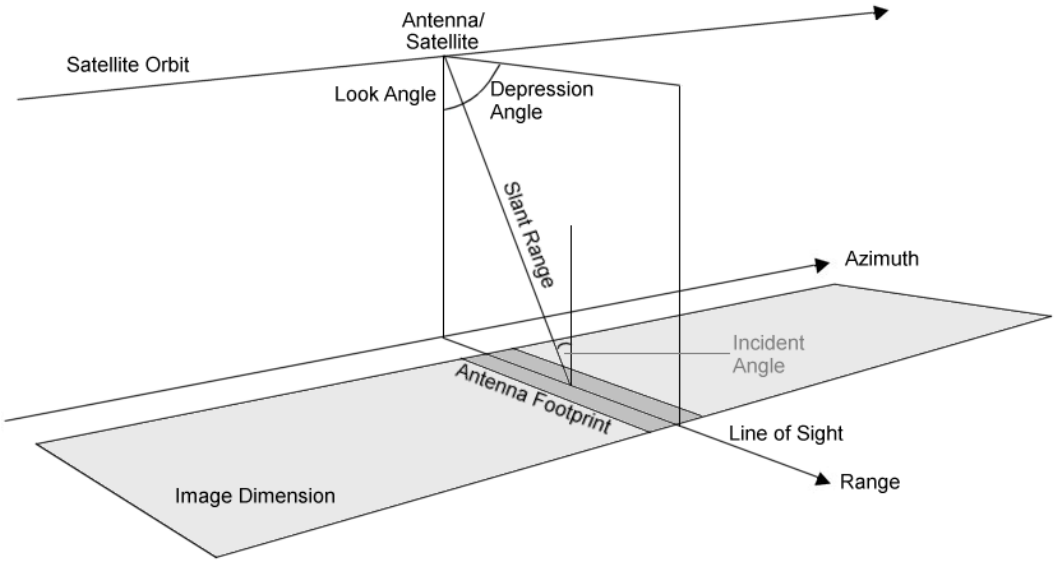

Figure 3.2. Acquisition properties and nomenclature of radar data.

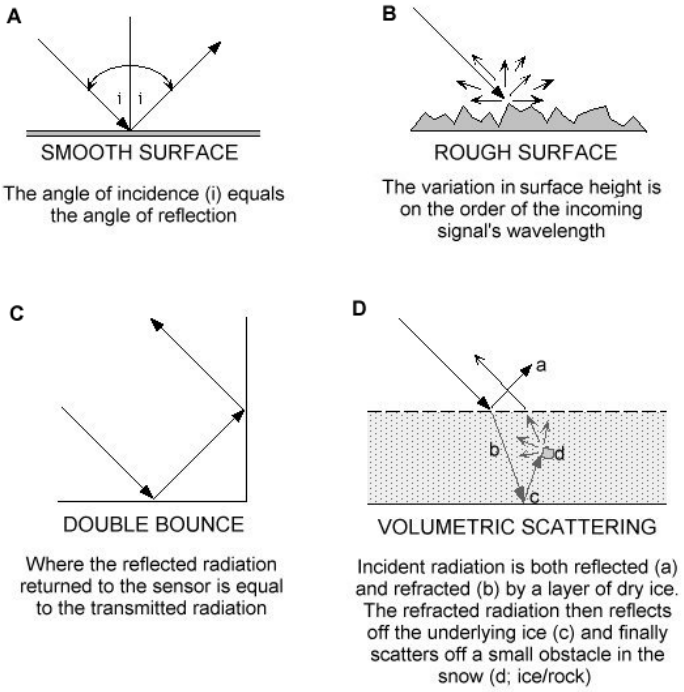

Figure 3.3. Scattering mechanisms based on the physical properties of the Earth's surface. Source: Jet Propulsion Laboratory (http://southport.jpl.nasa.gov/).

A radar image can be considered as a set of *A(x, y)* coordinates, where *x* represents the direction of the platform motion (azimuth) and *y* the look direction (range). The value of *x* is determined by the position of the platform and the radar beam width, whereas *y* is based on the arrival time of the echo and the timing precision of the radar (Lillesand *et al.*, 2008). Since beam width is inversely related to the antenna size, small antennas generate large footprints and thus result in poor-resolution imagery (Lillesand *et al.*, 2008). To overcome this, synthetic aperture radar (SAR) takes advantage of the Doppler history of the radar echo generated by the forward motion of the platform to synthesise a larger antenna, thus significantly improving the azimuth resolution in the image, despite a small physical antenna (Figure 3.4; Lillesand *et al.*, 2008). In SAR images, amplitude data from the returned signal and phase information of the radar echo is retained, although only amplitude is displayed in its image.

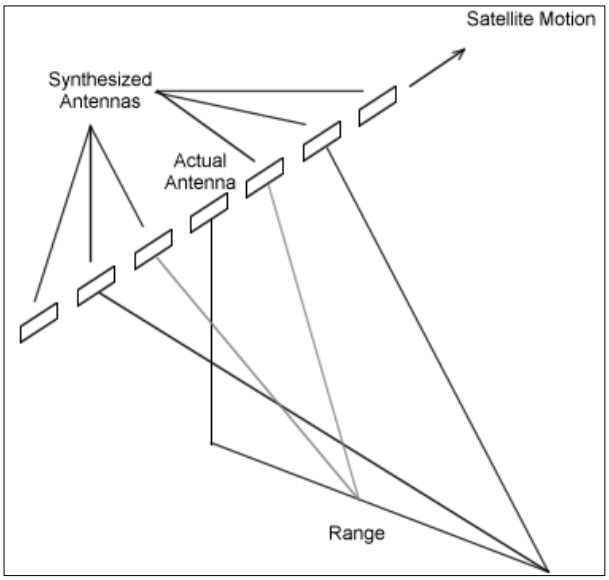

Figure 3.4. SAR image acquisition showing the position of the actual antenna, previous positions and projected positions generated by the satellite in motion. Range points nearer the actual antenna are viewed by fewer antenna elements than those at far-range, meaning that the synthetic antenna increases with distance, resulting in an almost constant azimuth resolution irrespective of range distance. Source: Lillesand *et al.*, (2008).

Table 3.2. Key radar sensors used in ice-shelf investigations

Microwave imaging	Spatial Resolution	Spectral Resolution	Polarisation*	Temporal Resolution	Swath	Archive Length	Active/ Passive	Comments
[1]**ERS-1/2 SAR**	~20-30 m	C-band (5.7cm)	VV	35 days	100 km	1991 to 2011 (combined archive)	Active	Satellites in tandem during 1995/96 permitting 1 day repeat pass
[2]**Envisat ASAR**	30-1000 m	C-band (5.7 cm)	HH/HV or VV/VH	35 days	100-400 km	2002 to 2012	Active	Specifications similar to ERS-1/2 for continued coverage in C-band. Communication lost early 2012.
TerraSAR-X	1-16 m	X-band (3.1 cm)	HH/HV or VV/VH	11 days	5 x 10 km to 100 x 150 km	2007 to present	Active	TanDEM-X satellite launched mid-2010 to permit 1 day repeat coverage for DEM generation.
RADARSAT-1/2	10-100 m	C-band (5.7 cm)	HH	25 days	45-500 km	1995 to present (combined archive)	Active	
[3]**JERS-1**	18 m	L-band (23.5 cm)	HH	44 days	75 km	1992-1998	Active	
[4]**ALOS PALSAR**	7-100 m	L-band (23.5 cm)	HH/HV or VV/VH	46 days	20-350 km	2006 to 2011	Active	Inaccurate data. Power lost during 2011.

*VV = Vertical transmission and Vertical reception. HH = Horizontal transmission and Horizontal reception, and so forth for HV and VH. [1]European Remote Sensing. [2]Enviromental Satellite. [3]Japanese Earth Recourses Satellite. [4]Advanced Land Observing Satellite.

The key benefits of using SAR imagery are as follows. First, the microwaves transmitted from the antenna and subsequently received back are able to penetrate cloud cover, and being active systems, to not require the Sun's illumination for image acquisition. As a result, SAR imagery at the poles can be collected intra-annually during the austral winter where daylight is at a minimum, whereas optical sensors only acquire data during the austral summer. Second, the variety of sensors (Table 3.2) permits data collection at a range of imaging wavelengths and polarisations, meaning that the type of backscatter received at the antenna differs from one sensor to another. As a result, the use of multiple sensors can aid the identification of surface and subsurface features (Hall *et al.*, 1995). Third, the repeat frequency of image acquisition varies from one sensor to another (Table 3.2), and therefore allows regular monitoring of rapid glacial events (e.g. ice-shelf collapse). The availability of a back-catalogue of data also permits historical assessment to be made, particularly the ERS-1/2 and Radarsat sensors. Fourth, the use of two independent SAR images with a short temporal baseline can be used to construct interferograms from the acquired phase data, thus permitting terrain and displacement measurements to be calculated over glacial regions at a scale comparable to the wavelength of the imaging sensors (Fatland and Lingle, 1998). The application of interferometry is discussed in more detail in Section 3.4.3.

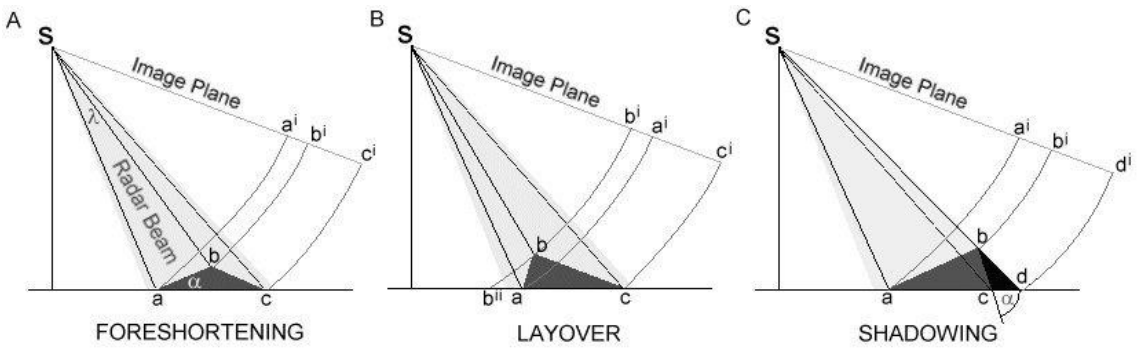

Figure 3.5. The three main limitations in SAR imagery. A) Foreshortening; the distance between *a* and *b* and *b* and *c* are equal, but because of the SAR look direction, the distance between a^i and b^i appears shorter than the distance between b^i and c^i in the image plane. B) Layover; due to the look direction of the satellite (S), point *b* is sensed before point *a*, and therefore in the image plane, point a^i is not detected. C) Shadowing; point *b* obscures point *c* in the SAR image, thus a shadow is created in the image plane. A similar situation exists if the geometry of the Earth remains the same, but the look angle of the SAR sensor significantly alters. Source: Lillesand *et al.*, (2008).

The limitations of SAR imagery are often due to acquisitional properties. In high-mountain regions, foreshortening, layover and shadowing within the imagery are the most common problems (Figure 3.5), with image quality a limiting factor on surface feature mapping.

However, for ice sheets and ice shelves, where low surface slope generally exists, and surface features are significantly greater than those on smaller valley glaciers, these limitations are not as problematic. Limitations specific to interferometry are discussed in Section 3.4.3.

3.3 Non-imaging Satellite Sensors

In addition to the imaging satellites described above, the Earth's surface can also be characterised by non-imaging sensors such as radar altimeters, and those that emit and receive laser pulses. The most useful non-imaging sensors within glaciology acquire surface-terrain data and can be used to construct moderate-to-fine scale Digital Elevation Models (DEMs), with repeat acquisitions used, for example, to assess the mass balance and vertical dynamics of glaciers and ice sheets.

3.3.1 Radar Altimetry (RA) Satellite Sensors

The principle of RA systems is based on time-of-flight theory; a radar wave is transmitted from the satellite sensor (in the nadir direction) and received back after a period of time. As the microwave pulse is constant, the difference between each wave received back at the sensor is a function of the time elapsed, which can be used to derive the surface height of the terrain below (Remy and Parouty, 2009). The key RA sensors are summarised in Table 3.3.

Table 3.3. Key Radar Altimetry systems for ice sheet study.

Satellite	RA frequency	Revisit period	Archive length
SeaSat	Ku-band (13.8 GHz)	N/A	1978 only (equipment failure)
ERS-1/2	Ku-band (13.8 GHz)	35 day	1991 to 2003 (combined archive)
Envisat	Ku-band (13.8 GHz) and S-band (3.2 GHz)	35 day	2002-2012
CryoSat-2	Ku-band (13.5 GHz)	369 days with 30 day sub-cycle	2010 to present

ERS-1 was the first polar-orbiting satellite with an altimeter on board, later followed by an improved sensor on ERS-2 (Remy and Paroutry, 2009). RA systems acquire data at a higher frequency (Ku-band, Table 3.3), but have the same benefits in terms of data collection and availability as the imaging sensors on board. A similar system was included in the Envisat mission to permit continued coverage of the Earth's surface, but also acquired data in the S-band (Table 3.3). The footprint of the RA system on both ERS-1/2 and Envisat satellites ranges from 3 to 20 km depending on acquisition mode, with a vertical accuracy of 2.5 cm over flat terrain (Bamber and Gomez-Dans, 2005). Each

footprint is approximately 3.5 km apart (Bamber and Gomez-Dans, 2005), thus by combining multiple RA tracks, broad surface DEMs have been produced (e.g. Bamber, 1994). The application of RA data in Antarctica is discussed in more detail in Section 3.4.4.

3.3.2 Light Detection and Ranging (LiDAR) Satellites

Similar to RA data acquisition, LiDAR systems record the time taken for a laser pulse to be transmitted to the Earth and reflected back to the sensor. The return time for each pulse is processed to calculate the distances between the sensor and the various surfaces present on (or above) the ground (Lillesand *et al.,* 2008). Being a laser pulse, LiDAR sensors are unable to penetrate through cloud cover, but do provide elevation measurements over a much finer spatial resolution than the RA alternatives; for example, the footprint of Ice, Cloud and Elevation Satellite's (ICESat) Geoscience Laser Altimetry System (GLAS) data is approximately 70 m, with a sub-centimetre accuracy over flat terrain (Schutz *et al.*, 2005), with successive data acquisitions occurring approximately every 170 m along the Earth's surface.

ICESat was launched by NASA in January 2003 to an approximate orbit of 600 km with the intention of providing a view of the Earth in 3-Dimension. The primary purpose of data collection was to determine both inter-annual and long-term changes in polar ice sheet volume and mass balance to permit an assessment on their impact upon global sea level (Zwally *et al.,* 2002). The elevation of a spot on the Earth's surface illuminated by the laser is established from the sum of two vectors; 1) the position of the laser instrument and, 2) the range vector. The resultant vector is the position of the laser footprint that can be transformed into longitude/latitude in conjunction with the elevation points for each location. ICESat GLAS has three lasers that were supposed to operate one-at-a-time; Laser 1 was commanded to start on February 20th 2003 and operated successfully for a short time before it failed on March 29th 2003. The operation plan was subsequently rescheduled to permit data acquisition in approximate 30-day periods, three times each year using Laser 2 and Laser 3 (Table 3.4). The operating lasers pulse at 40 Hz, with the return echo pulse captured by a 1 m diameter telescope, and redirected to an analogue detector that subsequently digitises the return signal into waveform data.

Table 3.4. ICESat operational campaigns

Campaign	Start date	End date	Days in operation
L1a	2003-02-20	2003-03-29	38
L2a	2003-09-25	2003-11-19	55
L2b	2004-02-17	2004-03-21	34
L2c	2004-05-18	2004-06-21	35
L3a	2004-10-03	2004-11-08	37
L3b	2005-02-17	2005-03-24	36
L3c	2005-05-20	2005-06-23	35
L3d	2005-10-21	2005-11-24	35
L3e	2006-02-22	2006-03-28	34
L3f	2006-05-24	2006-06-26	33
L3g	2006-10-25	2006-11-27	34
L3h	2007-03-12	2007-04-14	34
L3i	2007-10-02	2007-11-05	37
L3j	2008-02-17	2008-03-21	34
L3k	2008-10-04	2008-10-19	16
L2d	2008-11-25	2008-12-17	23

ICESat data have been used to study a variety of ice-shelf processes including grounding-line behaviour (Fricker and Padman, 2006; Brunt *et al.,* 2010), tidal flexure (Padman and Fricker, 2005), rift propagation (Bassis *et al.,* 2005) and ice-thickness changes (e.g. King *et al.,* 2009; Horgan *et al.,* 2011). The application of ICESat in determining ice-shelf surface elevation is discussed in more detail in Section 3.4.4.

3.4 Remote sensing application on ice shelves

Since the advent of satellite remote sensing, investigations into the extent, structure and dynamics of ice shelves have escalated, particularly those situated in the Antarctic Peninsula, those draining the West Antarctic Ice Sheet (e.g. Pine Island Glacier), and the largest ice shelves of Ross, Filchner-Ronne and Amery. The following section is a review of the application of remote sensing in ice-shelf studies.

3.4.1 Spatial extent

Changes to the areal extent of ice masses, from individual glaciers to whole ice sheets, are intrinsically linked to the regional climate (Williams *et al.,* 1995; Bindschadler, 1998; Gao and Liu, 2001). Variations in the cryosphere therefore act as a visual representation of the local climate through time. Studies on small glaciers in the European Alps, for example, have been on-going well before the advent of satellite remote sensing, as their relatively small size permits continuous monitoring from field-based measurements. For ice caps, ice sheets and their glacial components, the available records of their spatial extent are somewhat limited to inferences made from their geological imprint, and as a result the finer-detail of climate-change response is therefore overlooked. The development of satellite remote sensing in the 1970s permitted regular monitoring of regional-to-continental scale ice masses, and therefore an approximate 40-year catalogue of data exists from which their morphology can be assessed.

By far the most commonly used sensors in assessing ice-shelf extent are the Landsat MSS, TM and ETM+ series, owing to their lengthy archive (1972 to present), comparatively fine-scale spatial resolution (~ 80-15 m) and regular acquisition, particularly since the launch of the Landsat ETM+ sensor during 1999. Swithinbank *et al.* (1988) and Reynolds (1988) both used Landsat MSS imagery to map the extent of the Filchner-Ronne and Wordie ice shelves respectively as part of a larger structural analysis (discussed in Section 3.4.2) and since 1995, the Landsat MSS (missions 1-3) and TM (missions 4 and 5) have been incorporated into the USGS's Coastal Change and Glaciology Maps of Antarctica programme (Williams *et al.,* 1995; Williams and Ferrigno, 1998; Ferrigno *et al.,* 2009). The latter studies highlighted the dynamic fluctuations of ice shelves and glaciers around Antarctica, and the large-scale retreat of Pine Island Glacier and Thwaites Glacier on the West Antarctic Ice Sheet in particular. The USGS's study of ice-shelf extent presented a broad overview of the spatial changes, whilst more specific studies on individual ice shelves reinforced the apparent retreat of these systems and glacier tongues (Table 3.5).

Lucchitta and Rosanova (1998) complemented Landsat MSS imagery with ERS-1 radar data in order to assess the spatial changes at the northern ice front of George VI Ice Shelf and the Wilkins Ice Shelf between 1974 and 1995. Their study highlighted the continued retreat of the ice shelves on the Antarctic Peninsula which they attributed to the initial stages of large-scale disintegrations. More recently, Ferrigno *et al.* (2009) and Cook and Vaughan (2010) used a range of Landsat imagery and Envisat ASAR data to determine the

spatial change of ice shelves in the Antarctic Peninsula region (see Chapter 2), and Glasser *et al.* (2011) used Landsat TM, ETM+, ERS-1 SAR and ASTER data to track the ice front of the Röhss Glacier following the retreat of the Prince Gustav Ice Shelf. Furthermore, individual glaciers (e.g. Rau *et al.*, 2004; Davies *et al.*, 2011) have been assessed using a combination of Landsat TM, ETM+ and ASTER optical imagery.

Table 3.5. Summary of satellite imagery used in spatial assessment around the Antarctic Peninsula.

Ice Shelf	Satellites/ Sensors	Other data	References
Müller	Landsat MSS	Field data from Ronne Antarctic Research Expedition, vertical aerial imagery, oblique aerial imagery	Ward (1995)
Jones	Landsat MSS, TM	Oblique aerial photography, vertical aerial photography	Fox and Vaughan (2005)
Wordie	Landsat MSS, TM. SPOT. ERS-1 SAR.	N/A	Reynolds (1988), Doake and Vaughan (1991a), Vaughan (1993)
George VI	Landsat MSS, ERS-1 SAR.	Aerial photography. BAS field maps.	Luchitta and Rosanova (1998), Smith *et al.* (2007).
Wilkins	Landsat MSS, ERS-1. Landsat TM, ASTER, ERS-2 SAR, Envisat ASAR, MODIS	N/A	Luchitta and Rosanova (1998), Braun *et al.* (2009).
Prince Gustav	Landsat MSS, TM, ERS-1 SAR. ASTER.	Accounts (James Clark Ross; Swedish Antarctic Exploration; Andrew Taylor), field maps and aerial photography.	Cooper (1997), Glasser *et al.* (2011).
Larsen A	ERS-1 SAR	Field observations	Rott *et al.* (1996)
Larsen B	ERS-1/2 SAR, Landsat TM.	Field observations	Rott *et al.* (2002), Skvarca *et al.* (2004).
Larsen C	Landsat TM, MSS, ETM+, Envisat ASAR.	Kosmos-KATE aerial photography	Skvarca (1994), Cook and Vaughan (2010)
Larsen D	Landsat TM, ETM+, Envisat ASAR.	USGS Coastal Change Map	Cook and Vaughan (2010).

Datasets used in extent mapping have spatial resolutions ranging from ~80 m to 15 m, becoming finer over time. As a result, the positioning of the ice fronts has been delineated more accurately in recent years and due to the size of individual ice shelves, the error in defining their extent is comparatively small (up to 300 m, generally less than 60 m; Cook and Vaughan, 2010).

3.4.2 Ice-shelf structure and surface features

Satellite remote sensing is a proven medium from which the structure of glaciological systems can be investigated. Being able to assess the structures of glacier systems is of importance as the dynamic history of the ice mass is visually recorded. For example, longitudinal structures (also termed flow bands, flow stripes, streak lines), fractures, rifts and healed crevasses provide a detailed history of flow regime (Glasser and Gudmundsson, 2012) and rheological properties (Raup *et al.*, 2005). The identifiable structures are principally limited by the spatial resolution of each satellite sensor, so as expected, the detail in glaciological mapping has improved since early investigations.

Swithinbank *et al.* (1988), Reynolds (1988) and Reynolds and Hambrey (1988) used Landsat MSS imagery to detect surface features and structures on the Filchner-Ronne, Wordie and George VI ice shelves respectively, and provided interpretations of ice-shelf configuration and flow regime at 80 m pixel resolution. Elsewhere, Hambrey and Dowdeswell (1994) studied the structures of the Lambert-Amery system to assess its historical flow regime, dismissing suggestions of surge phases, whereas Wiute and Jezek (2009) illustrate past fluctuations of ice flow in the longitudinal structures of the Stancomb-Wills Ice Tongue through analysis of RADARSAT-1 imagery. More recently, Glasser and Scambos (2008), Glasser *et al.* (2009), Braun *et al.* (2009) and Glasser *et al.* (2011) used time-separated satellite imagery to assess both the long-term dynamic history, and the short-term changes in ice-shelf structure (see Table 3.6 for summary of satellite sensors used in structural assessments of ice shelves).

Detailed research has also been conducted on individual ice-shelf structure-types. Fricker *et al.* (2005) studied rift propagation at the ice front of the Amery Ice Shelf using a combination of MISR (Multi-angle Imaging SpectroRadiometer), Landsat ETM+, ERS-1 SAR and RADARSAT SAR data between 1996 and 2004. Their results highlighted a steady annual propagation rate, punctuated with seasonal expansion, linking the latter characteristic to a change in ice melange concentration and/or oceanic conditions. Elsewhere, Glasser and Gudmundsson (2012) provided an in-depth analysis on the formation and significance of longitudinal structures using 15 m Landsat ETM+ and ASTER optical imagery, and Raup *et al.* (2005) studied the same structure type using Advanced Land Imager (ALI) data.

Additionally, satellite remote sensing has enabled widespread analysis of surface meltwater patterns on ice shelves (e.g. Reynolds and Hambrey, 1988; Vaughan, 1993;

Sergienko and MacAyeal, 2004; Glasser and Scambos, 2008) that have been held responsible for the explosive nature of ice-shelf collapse. Other surface features and structures studied using satellite remote sensing include ice dolines (Landsat ETM+, IKONOS; Bindschadler *et al.,* 2002), pressure ridges (Landsat MSS; Reynolds and Hambrey, 1988), ice rumples, and ice rises (Landsat MSS; Reynolds, 1988; Swithinbank *et al.*, 1988).

Table 3.6. Summary of satellite imagery used for structural assessment of ice shelves around Antarctica.

Ice Shelf	Satellites/ Sensors	Comments/ Significance	Reference(s)
Larsen B	Landsat ETM+, ASTER	Assessed structural configuration before, during and after breakup phases in 2002. Breakup initiated along lines of weakness caused by rupturing of suture zones.	Glasser and Scambos (2008)
Larsen C	MODIS	No significant structural changes. Ice shelf remains stable.	Glasser *et al.* (2009)
Wilkins	Landsat ETM+, ERS-1/2.	Distinct breakup events along structural lines of weakness. Large-scale calving caused further fracturing that prompted enhanced retreat.	Braun *et al.* (2009)
Prince Gustav	Landsat TM, ERS-1, ASTER	Non-cohesive joint between two principal tributary glaciers preconditioned ice shelf for collapse. Heavily fractured prior to its initial breakup.	Glasser *et al.* (2011)
Wordie	Landsat MSS	Overview of key structures; longitudinal foliation present. Pre-existing fractures responsible for enhanced retreat caused by presence of ice rises.	Reynolds (1988)
George VI	Landsat MSS	Concentrated on northern section only. Illustrated dominant longitudinal structure and inferred flow type. Commented on ridge and groove structure of flowstripes and highlighted pressure ridges along Alexander Island. Largely compressive ice shelf.	Reynolds and Hambrey (1988)
Filchner-Ronne	Landsat MSS	Overview of surface features (flow bands, crevasses, rifts and ice rumples) and inferred dynamics. Detailed structural map presented.	Swithinbank *et al.* (1988)
Lambert Glacier/ Amery Ice shelf	Landsat TM	Used longitudinal foliation (longitudinal structures) to reject hypothesis of surge-type behaviour.	Hambrey and Dowdeswell (1994)

3.4.3 Ice-shelf flow regime

Whilst the analysis of ice-shelf structures and surface features enables a qualitative description of historical shelf dynamics, obtaining quantitative velocity data is vital to understanding the present-day ice-sheet dynamics. There are two main methods available for deriving velocity measurements from satellite imagery, 1) feature tracking, through the

use of manually tracked features or automated cross-correlation methods, and 2) interferometry. These are discussed below with respect to optical and radar data.

3.4.3.1 Optical image feature tracking

Measurement of ice-shelf motion from optical imagery was realised by Simmons and Rouse (1984) who manually measured the flow of the Brunt Ice Shelf using time separated Landsat MSS image pairs by tracking distinct surface features. Simmons (1986) later revised velocity measurements to include the whole Brunt Ice Shelf/ Stancombe-Wills Ice Stream system over an 11-year period, again by manually tracking distinct surface features and the ice front position. Whilst only providing a broad overview of the surface dynamics of the ice shelf, the work by Simmons and Rouse (1984) and Simmons (1986) acted as a reliable and accurate method for velocity-field derivation.

Bindschadler and Scambos (1991) and Scambos *et al.* (1992) furthered these feature tracking ideas by developing an automated cross-correlation method to detect and track distinct glacier surface features. Rather than training the programme to detect structure type, the cross-correlation method uses image matching of distinct image patterns, essentially a function of brightness caused by surface undulations, in their case, on Ice Stream E (MacAyeal Ice Stream). More sophisticated cross-correlation programmes (e.g. COSI-Corr) now assess the robustness of the feature tracking procedure based on a signal-to-noise ratio (SNR), which allows the user to reject poor velocity estimates, and therefore enhance the overall accuracy of surface displacement measurements.

Errors that arise through feature tracking methods are attributed to changes in feature pattern (i.e. too much distortion), geometric transformation of the imagery and errors caused by imprecise co-registration of the image pairs in the initial pre-processing stages (Luckman *et al.*, 2007; Quincey and Luckman, 2009). The amount of error in the calculated velocity fields generally reduces with an increased time delay between images, although the error in feature-matching increases as the pattern may have distorted beyond recognition over time. The major limitation of optical image feature tracking is the pixel resolution of the images used.

The value of optical image feature tracking has been realised in many studies of ice-shelf velocity and flow dynamics. Glasser and Scambos (2008) used feature tracking to highlight the discontinuity between flow units prior to the collapse of Larsen B, whereas Scambos *et al.* (2004) employed a cross-correlation algorithm to five time-separated Landsat ETM+

images on the former tributary glaciers of Larsen B, illustrating the increase in flow speed post-collapse. De Angelis and Skvarca (2003) tracked features between a Landsat ETM+ image and an ASTER image to show glacier surge after the removal of buttressing shelf ice, and Glasser *et al.* (2011) ran cross-correlation algorithms on a series of ASTER images to illustrate glacier acceleration of Röhss Glacier following the collapse of the Prince Gustav Ice Shelf.

3.4.3.2 SAR feature tracking (offset tracking)

The principles of SAR offset tracking are similar to those developed for automated optical-image feature tracking (Haung and Li, 2011) but rely on either the measurement of image speckle (speckle tracking, Joughin *et al.*, 2004) or image coherence (coherence tracking, Strozzi *et al.*, 2002). The former relies on speckle in the SAR images from constructive and destructive interference between multiple returns of the narrow bandwidth incident radiation, whilst the latter calculates displacement based on high coherence between two SAR images over small patches; areas with low coherence are rejected, and the displacement values are based on those with the maximum coherence (Strozzi *et al.*, 2002).

The application of both has been successful in deriving glacier surface velocities, although speckle tracking has been applied most commonly to ice-shelf and tributary glacier systems. Gray *et al.* (2001) used speckle tracking to the Filchner Ice Shelf based on RADARSAT SAR data and calculated glacier flux into the ice-shelf system. Similarly, Joughin *et al.* (2004) used RADARSAT SAR to calculate surface velocities for the Amery Ice Shelf using speckle tracking, and Rignot *et al.* (2002) employed a similar technique to show the acceleration of Pine Island and Thwaites glaciers in West Antarctica, using ERS-1 and ERS-2 SAR imagery. Rignot (2008) updated these velocity calculations by using speckle tracking on ALOS PALSAR data. The application of SAR speckle tracking has thus enabled more accurate estimates on ice flux, mass balance and ice-sheet response to atmospheric and oceanic warming.

3.4.3.3 Interferometric SAR (InSAR)

Interferometry takes advantage of the phase information preserved in SAR imagery, essentially calculating the difference between two received radar signals of the same point on the Earth's surface (Figure 3.6). InSAR methods within glaciology were developed by Goldstein *et al.* (1993), and detailed descriptions of InSAR methods have been made by Joughin *et al.* (1996), Michel and Rignot (1999), with an overview of its application in ice-sheet study provided by Quincey and Luckman (2009).

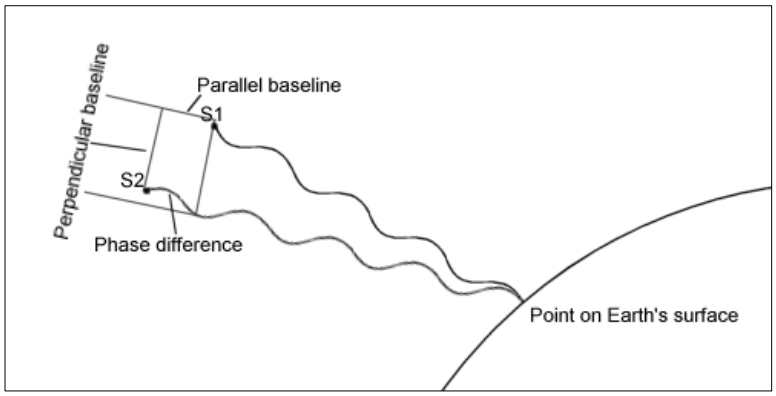

Figure 3.6. InSAR acquisition. S1 = first SAR image, S2 = second SAR image. The parallel baseline and perpendicular baseline are important components needed for calculation of the phase difference between image. The total phase difference is a combination of topographic relief, Earth curvature, image geometry and motion of the Earth's surface that can be separated with the use of a suitable DEM.

As radar data are acquired in a side looking direction, the resultant interferogram constructed from two SAR scenes is only sensitive to movement in that look direction (Rignot *et al.*, 2000) to an accuracy of a fraction of the wavelength. Line-of-sight (LOS) velocities can be converted to absolute velocities through the use of either a high-precision and fine resolution DEM (Joughin *et al.*, 1996) or from analysis of flow line features, for example (Joughin *et al.*, 1997). An alternative method of extracting velocity vector fields uses both ascending and descending SAR acquisitions (Figure 3.7), assuming that ice flow is horizontal to the glacier surface (Joughin *et al.*, 1998) and an independent DEM is available. This method is well-used within glaciology to derive surface velocity fields of individual glaciers (e.g. Rignot *et al.*, 1996; Luckman *et al.*, 2007; Huang and Li, 2011), ice caps (e.g. Palmer *et al.*, 2009), ice streams (e.g. Goldstein *et al.*, 1993; Joughin *et al.*, 1999), ice shelves (e.g. Rignot, 1998; Rignot *et al.*, 2000; Rott *et al.*, 2002; Larour *et al.*, 2004) and for the entire Antarctic Ice Sheet (e.g. Rignot *et al.*, 2011). An example of satellite sensors used in InSAR is given in Table 3.7.

The benefits of using InSAR for velocity derivation are as follows. First, the ability to detect subtle (< 1 cm) surface displacements over timescales ranging from 1 day to 46 days is of great value for assessing seasonal fluctuations in glacier dynamics, although this is more appreciated in study of valley glaciers rather than ice-sheet and ice-shelf dynamics that rarely display seasonal fluctuation. Second, velocity measurements are obtainable where distinct surface patterns and features are absent as InSAR is reliant on the phase information within the SAR data rather than the image construction as in feature, speckle and coherence tracking. Third, the availability of a range of satellite sensors that operate at different wavelengths (Table 3.7) permits velocity calculation at a variety of different temporal and spatial scales. Fourth, the back-catalogue of data available means that dynamic changes over time can be assessed.

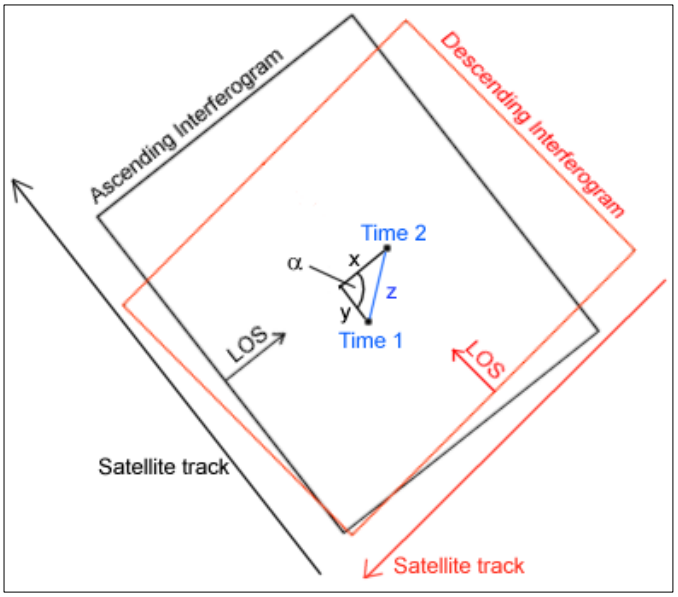

Figure 3.7. Four-pass InSAR construction. The ascending and descending interferograms are calculated using two time-separated SAR scenes each. The ascending interferograms is sensitive to ground movement along 'x', whereas the descending interferograms is sensitive to ground movement along 'y'. The true displacement 'z' can be calculated using trigonometric functions as long as the precise orbital parameters of both the ascending and descending passes are known.

InSAR techniques have also been used to detect grounding line positions (e.g. Fricker *et al.*, 2009) as the vertical motion of ice shelves and marine-terminating glaciers through tidal flexure is picked up in phase differencing. This is both a benefit and a drawback within glaciology, as whilst it is important to accurately detect grounding zone position for mass balance and ice flux studies, uncertainty in ice-shelf velocity is introduced. The vertical displacement phase can be removed if 1) the known tidal amplitude is available, 2) if it can be accurately modelled (DiCaprio and Simons, 2008), or 3) if horizontal

displacement can be averaged over longer time periods so that ice-shelf creep is greater than the tidal displacement. DiCaprio and Simons (2008) and Hetland *et al.* (2012) also implement InSAR Stacking to subdue the effect of tidal motion on horizontal motion detection through averaging the results of multiple interferograms. Other limitations are often linked to poor image coherence between SAR pairs, due to rapid surface change (high velocity, high melt rate, high accumulation rate) and poor quality DEMs, as is the case for large areas of Antarctica (Bamber and Gomez-Dans, 2005).

Table 3.7. SAR sensors used for glacier velocity derivation through InSAR techniques.

Sensor	Band	Repeat acquisition	Reference/s
ERS-1 SAR	C-Band	3 days (during 1992), 35 days otherwise	Goldstein *et al.* (1993)
ERS-1/2 SAR	C-Band	1 day tandem mission during 1995/96	Rignot *et al.* (2008).
RADARSAT	C-Band	25 days	Gray *et al.* (1998); Rignot *et al.* (2011)
ALOS PALSAR	L-Band	46 days	Yamanokuchi *et al.* (2011)
Envisat ASAR	C-Band	35 day	Rott *et al.* (2007)
TerraSAR-X (TSX)	X-Band	11 day	Rott *et al.* (2008); Rott *et al.* (2010)
TanDEM-X	X-Band	1 day (in tandem with TSX)	Eineder *et al.* (2011)

3.4.4 Ice-shelf surface elevation and thickness

Surface elevation measurements and thickness estimates of Antarctic ice shelves have been made available through RA and ICESat GLAS measurements. The most commonly used elevation dataset is the RADARSAT Antarctic Mapping Project (RAMP) DEM (Liu *et al.*, 2001) that offers a spatial resolution of roughly 200 m. The RAMP DEM was mostly constructed through RA datasets collected from the ERS-1 satellite, although aerial and ground-based radar echo sounding (RES), GPS surveys and geodetic maps were incorporated where RA data was incomplete. Elsewhere, the BEDMAP dataset (Lythe *et al.*, 2001; Steinhage *et al.*, 2001) contains estimates of ice thickness calculated using a hydrostatic assumption of surface elevation measurements from RA datasets (and RES surveys), with updated and more accurate DEMs developed through incorporating ICESat laser altimetry data (e.g. Bamber *et al.*, 2009; Griggs and Bamber, 2009a). The improved ICESat DEM has been converted to thickness estimates of Antarctic ice shelves (e.g. Griggs and Bamber, 2011) so that a more detailed overview of ice-sheet mass balance can be studied.

It has become apparent over recent decades that ice shelves respond vertically to oceanic and atmospheric warming (e.g. Shepherd *et al.*, 2003; Pritchard *et al.*, 2012), thus repeat

measurements of ice surfaces permit elevation and thickness-change estimates to be calculated. A nearly continuous 35-day interval time-series of elevation measurements exists from the back-catalogue of ERS-1/2 and Envisat RA data, from 1992 to 2012 (Fricker and Padman, 2012). Shepherd *et al.* (2003) used RA data from the ERS-1/2 satellites to obtain surface elevation trends of the Larsen B and Larsen C ice shelves from 1992 to 2001, and Zwally *et al.* (2005) conducted a similar study, but over both the Greenland and Antarctic ice sheets. More recently, Fricker and Padman (2012) used a combination of Seasat, ERS-1/2 and Envisat RA data to highlight the broad spatial pattern of time-averaged surface elevation changes of Antarctic Peninsula ice shelves. All three major studies illustrated a mostly negative surface-elevation change of ice shelves over decadal timescales, from which thinning was inferred.

Elsewhere, King *et al.* (2009), Pritchard *et al.* (2009, 2012), Joughin *et al.* (2010), Horgan *et al.* (2011) and Rott *et al.* (2011) used LiDAR data from the ICESat GLAS sensor to determine elevation changes on ice shelves and tributary glaciers around Antarctica from 2003 to ca. 2009. Of these, Pritchard *et al.* (2012) highlighted the most significant thinning of ice shelves located around Antarctica, and specifically at the periphery of the West Antarctic Ice Sheet, yet the study did not detail specific changes to each ice shelf on the Antarctic Peninsula.

3.5 Chapter Summary

In this chapter, satellite sensors, their data and commonly-applied techniques have been outlined with respect to ice-shelf systems. The review has demonstrated that the use of optical, radar and non-imaging satellite data can be used independently to assess individual ice shelves, or indeed, can be integrated to build a comprehensive understanding of ice-shelf size, structure and dynamics. The remainder of this thesis is devoted to applying the most suitable methods to the available datasets to obtain information on the structural and dynamic response of Antarctic Peninsula ice shelves to documented oceanic and atmospheric warming. Key methods briefly outlined in this chapter are described in more depth in Chapter 5.

Chapter 4

Study Sites

4. Study Sites

A significant amount of research at present is focussing on the structure of ice shelves, their stability, glaciological processes and the effects of their removal on the eastern side of the Antarctic Peninsula (e.g. Glasser *et al.,* 2009; Haug *et al.,* 2010; Hellmer *et al.,* 2011; Khazendar *et al.,* 2011; Rott *et al.,* 2011; Luckman *et al.,* 2012). This study, however, concentrates on the remaining ice shelves on the south west Antarctic Peninsula (Figure 4.1) that are currently considered stable, and that have had considerably less attention than their eastern peninsula counterparts. This in itself gives reason to study Bach, George VI and Stange ice shelves, as there is evidence that glaciological changes prior to a final breakup/collapse/disintegration phase, can be identified well in advance. Indeed, documented changes on Wilkins Ice Shelf (e.g. Braun *et al.,* 2009; Padman *et al.,* 2012) immediately north of Bach Ice Shelf and west of George VI Ice Shelf, suggest that changes on the west Antarctic Peninsula are occurring at present.

Whilst George VI Ice Shelf has been intensely studied in the past (e.g. Wager, 1972; Reynolds and Hambrey, 1988; Luchitta and Rosanova, 1998; Smith *et al.,* 2007), an ice-shelf wide investigation of its structural and dynamic regime is absent. Furthermore, Bach and Stange ice shelves have rarely been investigated, thus, there is a significant gap in our current understanding of the configuration of these ice shelves and indeed the principal responses to atmospheric and oceanic changes. For Bach and Stange ice shelves in particular, there is a further rationale behind their inclusion as the glaciological regimes on both ice shelves are poorly understood, and thus this study aims to fill those particular knowledge gaps. An overview of the present day glaciology, climate and oceanography has already been provided in Chapter 2 for the whole of the Antarctic Peninsula region. Therefore in Chapter 4, attention is given to each individual ice shelf considered in this study, by way of introducing the ice-shelf systems.

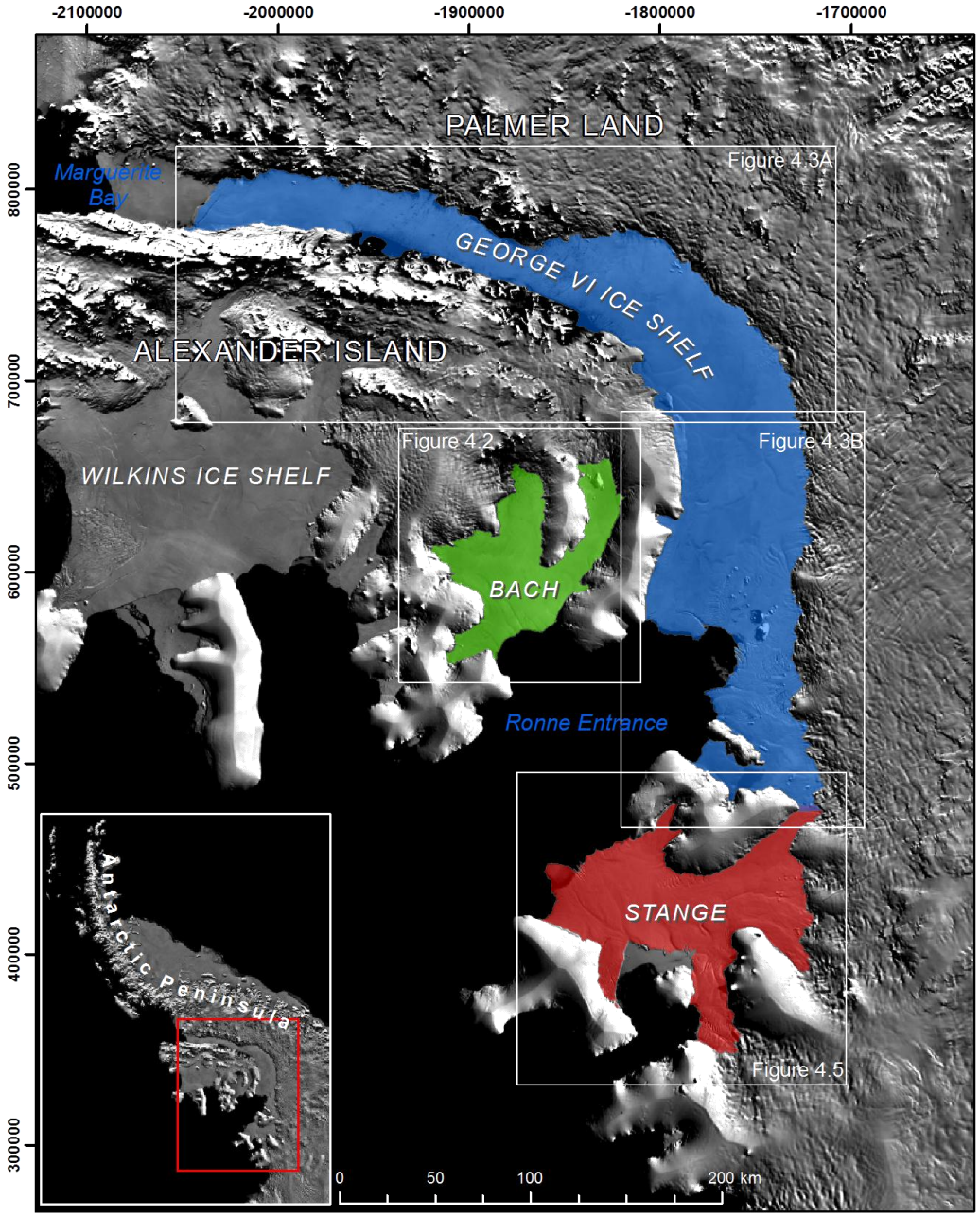

Figure 4.1. Location of Bach, George VI and Stange ice shelves on the south-west Antarctic Peninsula. Note also the proximity of Wilkins Ice Shelf that has undergone recent breakup phases as reported by Braun *et al.* (2009) and Padman *et al.* (2012). Separate figures are provided for each ice shelf in Section 4.1, Section 4.2 and Section 4.3 for Bach, George VI and Stange ice shelves respectively. Map in Polar Stereographic projection (metre unit).

4.1 Bach Ice Shelf

Bach Ice Shelf is fed by glaciers flowing entirely off Alexander Island (Figure 4.2). The island itself is mostly covered by an ice cap up to 1200 m thick (Graham and Smith, 2012) with only a few major nunataks towards its northern edge, and those adjacent to George VI

Ice Shelf (Johnson *et al.*, 2012). Bach Ice Shelf covers an area of approximately 4500 km^2, and is the smallest recognised ice shelf remaining on the south west Antarctic Peninsula. Four major ice domains exist, namely Weber, Boccherini, Williams and Stravinsky, which feed the central portion of Bach Ice Shelf (Figure 4.2). Large, ice-covered headlands exist between each of the four ice domains, giving the ice shelf its unique morphology.

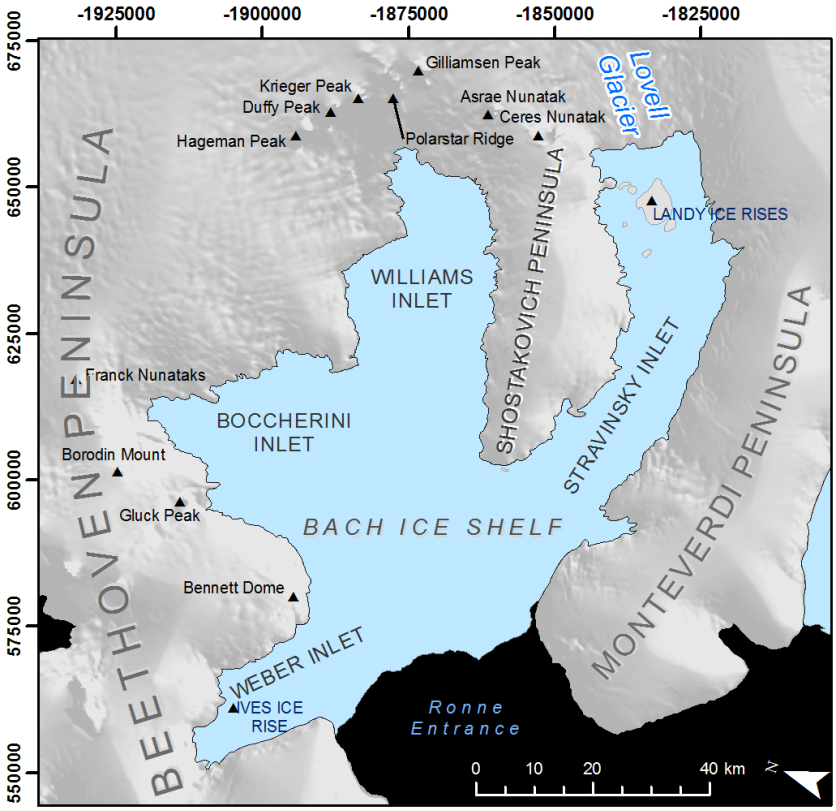

Figure 4.2. Bach Ice Shelf. Note the four smaller ice domains of Weber, Boccherini, Williams and Stravinsky that all feed into the centre of Bach Ice Shelf that flows towards the Ronne Entrance. The ice front is currently pinned between the tip of Beethoven Peninsula and Monteverdi Peninsula. Lovell Glacier is the only named tributary that feeds the ice shelf. Ice-shelf extent from January 2010, overlain on MODIS image Mosaic of Antarctica (MOA) (Haran *et al.*, 2006), place names obtained from the UK Antarctic Place-names Committee (www.antarctica.ac.uk/apc/namemap.html); 'APC' hereafter.

Weber Ice Domain is the smallest of the four units situated to the north-west of Bach Ice Shelf and is fed by ice off Beethoven Peninsula and Bennett Dome. Within Weber Inlet, a single ice rise is present (Ives Ice Rise) that causes flow to diverge upstream and converge again downstream. Boccherini and Williams ice domains form the bulk of Bach Ice Shelf. Ice flows into these inlets via several tributary glaciers off Beethoven Peninsula. Much of the ice entering Williams Inlet can be traced from a series of nunataks 10-20 km east of

Bach Ice Shelf. During the summer months, large surface melt ponds cover a large portion of these three ice domains. The southern-most ice domain, Stravinsky, is an 80 km long, 15 km wide channel fed by ice off Monteverdi Peninsula, Shostakovich Peninsula and from Lovell Glacier that stretches some 50 km further upstream. A series of ice rises exists towards the eastern regions of Stravinsky Ice Domain, the largest of which covers an area of ~29 km^2. These islands are formally known as the Landy Ice Rises and have an impact on the flow regime of Lovell Glacier. The ice front is located between the tip of Monteverdi Peninsula and Beethoven Peninsula.

Very few studies have been specifically carried out on Bach Ice Shelf and thus its glaciological regimes are poorly understood. Scambos *et al.* (2000) and Cook and Vaughan (2010) comment that whilst in retreat, the ice shelf is under no immediate threat of rapid disintegration, but largely base this analysis on the retreat patterns alone. Bach Ice Shelf is also investigated by Fricker and Padman (2012) who show of the ice shelf thinning from 1978 to 2008. However, their analysis is based only on three data points over the central portion of the ice shelf, and thus has poor spatial coverage. Elsewhere, Woodruff and Doake (1977) measure basal melt rates at 0.65 ma^{-1}, and more recently, Holland *et al.* (2010) model mean basal melt rates at 1.10 ma^{-1}. Overall, there is a significant absence of glaciological data for Bach Ice Shelf at present.

4.2 George VI Ice Shelf

George VI Ice Shelf (Figure 4.1, Figure 4.3) occupies George VI Sound that is situated between Alexander Island and Palmer Land. It covers an area of approximately 24,000 km^2 and is thus the largest ice shelf on the west Antarctic Peninsula (Humbert, 2007; Smith *et al.*, 2007) and second largest ice shelf remaining across the whole region after Larsen C. George VI Ice Shelf has two ice fronts; a northern ice front that calves into Marguerite Bay (Figure 4.3), and a southern ice front that terminates into the Ronne Entrance that is interrupted by a succession of ice rises (Eklund Islands and De Atley Island) (Figure 4.4). The distance between the two fronts is approximately 450 km along its centreline. The northern front sits in a channel ~20 km wide, with the southern margin measuring ~75 km from Monteverdi Peninsula to the English Coast (Roberts *et al.*, 2008). The ice shelf varies in thickness from 100 m at the northern ice front to 600 m in the central region, before thinning again towards the southern ice front (Talbot, 1988; Lucchitta and Rosanova, 1998; Smith *et al.*, 2007). Recent calculations have revealed that the whole of George VI Ice

Shelf has experienced sustained, but varying thinning rates since 1978 (Fricker and Padman, 2012; Pritchard *et al.*, 2012).

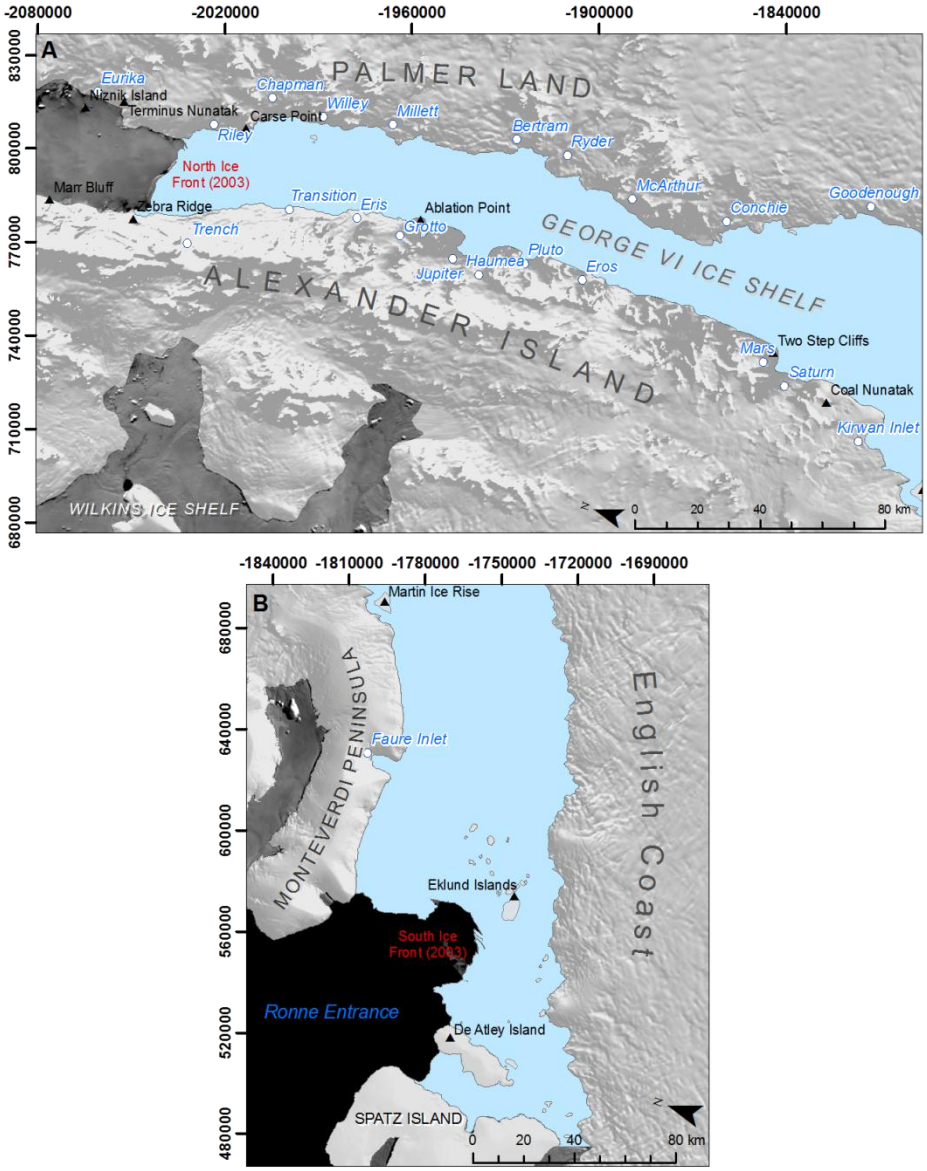

Figure 4.3. A) The northern region and, B) southern region of George VI Ice Shelf showing the key locations. Names taken from the APC. Known glaciers labeled in blue text.

The subglacial bathymetry (Figure 4.4) is characterised by steep-sided trench slopes and rough surface morphology with depths ranging from 400 m to 1000 m (Maslanyj, 1988; Smith *et al.*, 2007). In the north, two channels ~800 m in depth are separated by a ridge running from north to south (Crabtree *et al.*, 1985). The 'W-shape' morphology (Smith *et al.*, 2007) is not apparent for the entire length of the ice shelf, though where it is present, the western channel is more shallow and narrower than the eastern channel (Smith *et al.*, 2007). These channels are thought to have been modified by a larger ice sheet during the

LGM when grounded ice existed in the sound (Clapperton and Sugden, 1982). Beyond the southern margin, a seaward channel stretches beyond the present limit of George VI Ice Shelf, indicating a greater spatial extent during the Holocene (Figure 4.4, Smith *et al.*, 2007).

The ice shelf catchment covers much of Alexander Island and western Palmer Land with 12 km^3 and 46 km^3 of ice flowing into George VI Ice Shelf respectively each year (Reynolds and Hambrey, 1988). Ice from Alexander Island only extends, laterally, a few kilometres into the ice shelf system (Lucchitta and Rosanova, 1998) as tributary glaciers are generally small (between 54 km^2 and 144 km^2; Humbert, 2007). Glaciers flowing from Palmer Land are typically larger systems (e.g. Goodenough Glacier) and supply much of the ice to George VI Ice Shelf (Humbert, 2007). This domination of inflow from Palmer Land produces stagnation points along the ice shelf (flowing less than 30 ma^{-1}), created as ice flows towards the opposite grounding line but diverges prior to reaching this point (Reynolds and Hambrey, 1988). Flow speeds reach approximately 140 ma^{-1} and 380 ma^{-1} at the northern and southern ice front respectively (Humbert, 2007).

Wintertime snowfall on George VI Ice Shelf rarely lasts through the summer melt season due to high surface melt rates, particularly in the northern regions (Wager, 1972; Ridley, 1993). The ice shelf thus consists of largely consolidated glacier ice, fed from inland glacier systems (Humbert, 2007). During the melt season, an extensive area of meltwater ponds are observed in the northern section of George VI Ice Shelf, stretching from Coal Nunataks to Carse Point, with little surface melt visible south of this towards the southern margin.

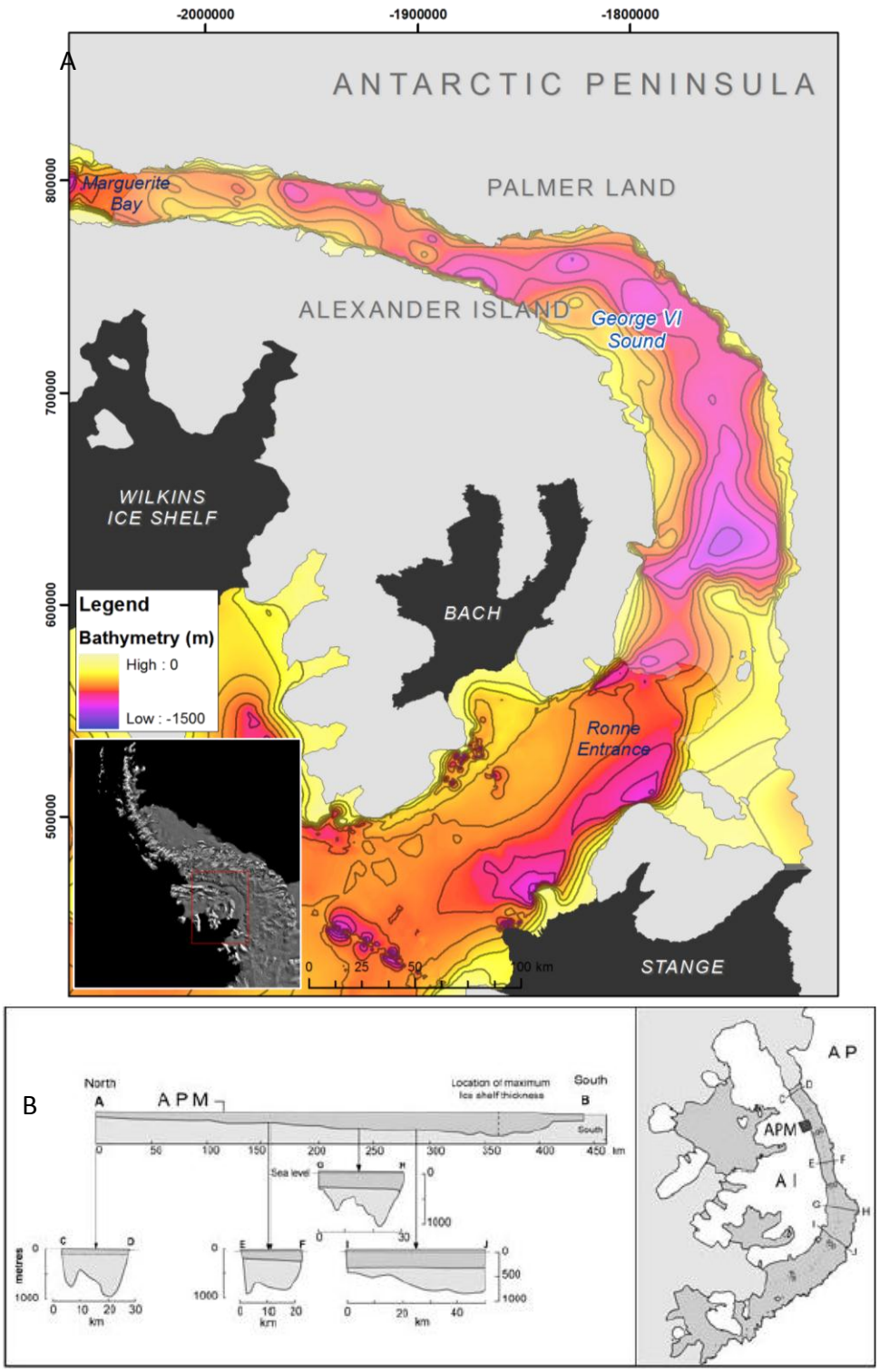

Figure 4.4. Bathymetry of Ronne Entrance and subglacial topography of George VI Ice Shelf A) Graham *et al.* (2011) calculated using previously acquired datasets, including those presented in B), taken from Smith *et al.* (2007) and originally from Maslanyj (1988). Subglacial bathymetry of Bach and Stange is unknown. Notice the deep troughd in George VI Sound that extend from Marguerite Bay to Ronne Entrance. APM refers to Ablation Point Massif, a location of interest in the orginal study by Maslanyj (1988).

Ablation occurs almost entirely as a result of seasonal-frontal calving and basal melting (Pearson and Rose, 1983; Reynolds and Hambrey, 1988; Lennon *et al.*, 1982). Potter and

Paren (1985) suggest that the ice margins of George VI Ice Shelf advance periodically before calving along natural rifts and fissures that penetrate the entire depth of the ice shelf. Mercer (1978) first noted the retreat of the northern margin of George VI Ice Shelf. More recently, Doake (1982), Lucchitta and Rosanova (1998) and Smith *et al.* (2007) use a combination of historical accounts and satellite imagery to document the fluctuation of ice shelf margins. Between 1947 and 2008, 1939 km^2 of ice was lost from the northern and southern ice fronts with no significant advance (Lucchitta and Rosanova, 1998; Smith *et al.*, 2007; Cook and Vaughan, 2010). However, it is thought that the southern ice front is more stable than the northern ice front as ice rises and the Eklund Islands in George VI Sound 'pin' the ice (Humbert, 2007). Despite these studies, there is little analysis of the spatial or temporal patterns of retreat over time.

Basal melting on George VI Ice Shelf has been calculated by various authors. Lennon *et al.* (1982) suggested that basal melting at the northern margin could exceed 10 m a^{-1}, Potter *et al.* (1984) estimated the spatially-averaged basal melt to be 2.1 ma^{-1}, Jenkins and Jacobs (2008) suggested rates of between 2.3 and 4.1 ma^{-1}, and Dinniman *et al.* (2012) calculated melt rates of up to 6 ma^{-1}. Significantly, although George VI Ice Shelf only equates to 1.5% of the total area of Antarctic ice shelves, if in equilibrium, it would supply 10% of the total melt (Jacobs *et al.*, 1992); thus there is a strong relationship between ice shelf basal melt and oceanic regime on this ice shelf.

Warm water intrusion (+ 2°C) from the Circumpolar Deep Water (CDW) current originating from the south east Pacific basin flows onto the continental shelf and extends underneath George VI Ice Shelf contributing significantly to basal melt (Potter *et al.*, 1984; Potter and Paren, 1985; Lucchitta and Rosanova, 1998; Holland *et al.*, 2010). This process is thought to be linked to the strength of the Antarctic Circumpolar Current (ACC) and a cross-current bathymetric low (Klinck and Smith, 1993). It has long been speculated that the stability of George VI Ice Shelf and other marine-terminating glaciers and ice shelves are the result of oceanographic induced melting (e.g. Talbot, 1988). Shepherd *et al.* (2003, 2004) and Payne *et al.* (2004) have linked the presence of the CDW to the rapid retreat of Larsen B and thinning of Amundsen Sea glaciers respectively, but limited quantitative datasets from basal locations prevents reliable evidence. Nevertheless, oceanographic observations have indicated that the influx of the CDW beneath George VI Ice Shelf increases both temperature and salinity from the ice shelf base to the sea floor (Smith *et al.*, 2007). The maximum observed temperature from within George VI Sound is +1.1°C, 3°C

warmer than the freezing point at the base of the ice (Talbot, 1988) and it is accepted that the CDW current flows beneath the entire length of George VI Ice Shelf.

Reynolds (1982) and Reynolds and Hambrey (1988) assessed the surface features and structures of the northern regions of George VI Ice Shelf, concentrating on meltwater ponds, longitudinal structures and crevasse patterns. Their analysis reveals a highly compressive flow regime fed by Palmer Land glaciers that was later emphasised by LaBarbera and MacAyeal (2011) through numerical modelling of structural development, and Humbert (2007) who modelled ice-shelf velocities. Despite these studies, there have been no structural investigations carried out along the northern ice front, or in the southern region of George VI Ice Shelf. Thus, there is no documented evidence of any structural changes or structural evolution. Likewise, velocity measurements are poorly constrained or do not take into account a broad temporal scale to assess change. There is subsequently an absence of ice-shelf-evolution data for George VI Ice Shelf despite it being one of the most intensely studies systems in the region.

4.3 Stange Ice Shelf

Stange Ice Shelf is situated south-west of George VI and likewise sits within the coastal regions of the Bellingshausen Sea (Figure 4.1, Figure 4.5). The two ice shelves are joined southeast of Spatz Island, but are linked only by a narrow 9 km wide channel. Tributary glaciers feed Stange from three grounded-ice locations, with the English Coast on the main Antarctic Peninsula accounting for the vast majority of the ice influx. A few smaller glaciers also feed the ice shelf from Smyley Island in the west and Spatz Island to the east, that are completely ice-covered.

These two islands, along with Case Island make for a unique ice-shelf morphology. In total, the ice shelf covers an area of approximately 8000 km^2 (Cook and Vaughan, 2010) and has three ice fronts. The largest (north ice front) terminates into Ronne Entrance, measures approximately 62 km in width and it is fed by glacier ice from all three grounded-ice locations. The mid ice front is made up of three smaller ice-front units and therefore has an atypical profile. The south-facing portion is made up from Smyley Island-derived ice, whereas the north facing portions are fed by different glacier systems originating from the English Coast. Multi-annual sea ice is present adjacent to the mid ice front. The third ice front sits between Case Island and Rydberg Peninsula and measures

only 17 km in width; this portion of Stange Ice Shelf is largely independent of the rest of the shelf.

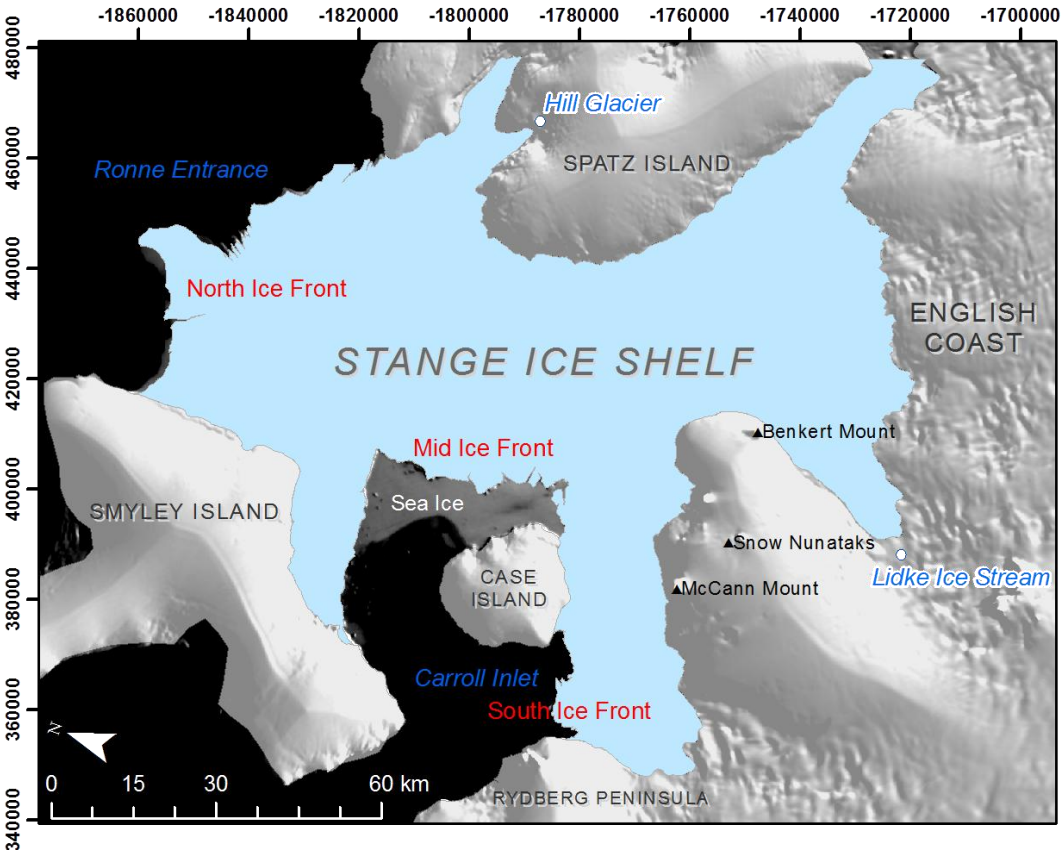

Figure 4.5. Stange Ice Shelf and its key locations. Note the influence of Spatz Island, Smyley Island and Case Island on its atypical morphology. Names taken from the APC.

As with Bach, very little investigation has been carried out of Stange Ice Shelf. Cook and Vaughan (2010) comment that only 3% of the ice shelf has been lost since the first available datasets that document its size in 1973, and Fricker and Padman (2012) show spatially averaged thinning rates of between 1 and 6 ma^{-1} since 1978. Holland *et al.* (2010) model mean basal melt rates of 0.32 ma^{-1}; no direct measurements have been published. Again, there is an absence of key glaciological data on Stange Ice Shelf that can be filled through structural and dynamic assessment.

Chapter 5

Data Sources and Methods

5. Chapter Overview

Chapter 5 is presented in two sections. In Section 5.1, the optical, radar and non-imaging data sources used in this study are outlined, with secondary datasets also detailed. In Section 5.2, the principal methods and processing techniques are provided in three subsections. In Section 5.2.1, the methods used in conducting spatial assessment and surface-feature mapping are presented, with processing techniques for velocity-field derivation outlined in Section 5.2.2. Consequently, the major processing steps for surface elevation-change measurements are provided in Section 5.2.3. All datasets were either acquired or converted to a Polar Stereographic projection using a WGS84 datum for further analysis.

5.1 Data sources

5.1.1 Landsat data series

In total, 87 Landsat scenes were acquired (Table 5.14) from the USGS Global Visualisation programme (http://glovis.usgs.gov), already georeferenced and processed to Level 1T (terrain corrected). The Landsat missions were identified as the best data source for spatial assessment and structural mapping due to the available back-catalogue of datasets from 1973 to present (Table 5.1). Landsat missions 1-3 acquired data in four spectral bands via a multi-spectral scanner (MSS) at approximately 80 m spatial resolution from 1972 until 1983 inclusive. The earlier missions also carried a Return-Beam Vidicom camera but image quality was poor, and the data have rarely been used. In addition to the MSS instrument, Landsat missions 4 and 5 also collected data via a Thermatic Mapper (TM) sensor (replacing the RBV), providing visible-near infrared and shortwave infrared data at 30 m spatial resolution. Landsat 4 remained active until 1993, but Landsat 5 still acquires data at present, albeit at irregular intervals and only via its TM sensor (the MSS sensor failed during 1995). Landsat 7, which was launched in 1999, carries an enhanced TM (ETM+) sensor on board that permits panchromatic data collection at a finer, 15 m resolution. Since 2003, Landsat ETM+ has been operating with reduced effectiveness as a result of equipment failure (the scan-line corrector) that caused a loss of data along both lateral parts of the images (Figure 5.1). Landsat 6 failed on launch and did not take to orbit. The Landsat series is summarised in Table 5.1, with sensor characteristics outlined in Table 5.2.

Figure 5.1. An example of scan-line corrector 'off' Landsat ETM+ imagery with increasingly larger data gaps towards the edges of the images. The scene shows the central portion of George VI Ice Shelf during January 2010.

Table 5.1. Overview of the sensors and archive length of the Landsat series of satellites. See Figure 5.2 for example image.

Landsat Mission	Sensors on board (Spatial resolution)	First data acquisition	Last data acquisition
Landsat 1	MSS, RBV Camera	1972	1978
Landsat 2	MSS, RBV Camera	1975	1982
Landsat 3	MSS, RBV Camera	1978	1983
Landsat 4	MSS, TM	1982	1993
Landsat 5	MSS, TM	1984	Still active
Landsat 7	ETM+	1999	Still active

Table 5.2. Key sensor characteristics flown on board the Landsat series of satellites, as outlined in Table 5.1.

Sensor	Band	Spectral Resolution		Spatial
		(µm)	(range)	Resolution (m)
MSS	Band 4	0.500-0.600	Green	79/82
	Band 5	0.600-0.700	Red	79/82
	Band 6	0..700-0.800	Near infrared	79/82
	Band 7	0.800-1.100	Near infrared	79/82
TM/ ETM+	Band 1	0.450-0.520	Blue	30
	Band 2	0.520-0.600	Green	30
	Band 3	0.630-0.690	Blue	30
	Band 4	0.760-0.900	Near infrared	30
	Band 5	1.550-1.750	Mid infrared	30
	Band 6	10.400-12.500	Thermal infrared	120
	Band 7	2.080-2.350	Mid infrared	30
	Band 8*	0.520-0.920	Panchromatic	15

**Flown only on Landsat 7 as part of the ETM+ sensor*

5.1.2 ASTER

The ASTER sensor was launched during 1999 on board the Terra Earth Observation Satellite (EOS), specifically designed for data collection over glacierised regions as part of the Global Land Ice Measurement from Space (GLIMS) project. The sensor carries two telescopes. Its nadir telescope collects data in 14 bands (Table 5.3) in visible-near infrared (VNIR, 15 m), shortwave infrared (SWIR, 30 m) and thermal infrared (TIF, 90 m), with its back-looking telescope (VNIR) collecting a single data band (near infrared, 15 m) that permits derivation of high-resolution DEMs through stereo photography. Equipment failure during 2008 meant that the SWIR sensor no longer acquired data, but the VNIR and TIR sensors are still functioning at present.

Although the Terra EOS has a 16 day repeat-track cycle, the ASTER instrument only operates in full-mode for eight minutes during daytime due to the volume of data that can be stored in the on board recorder (Yamaguchi et al., 1999). As a result, ASTER data are not temporally continuous over large areas, and are primarily used here to fill the gaps not covered by Landsat ETM+ imagery. A total of 5 ASTER images was downloaded via the Global Visualisation programme as an already orthorectified product (AST14) (see Figure 5.2E and Table 5.14).

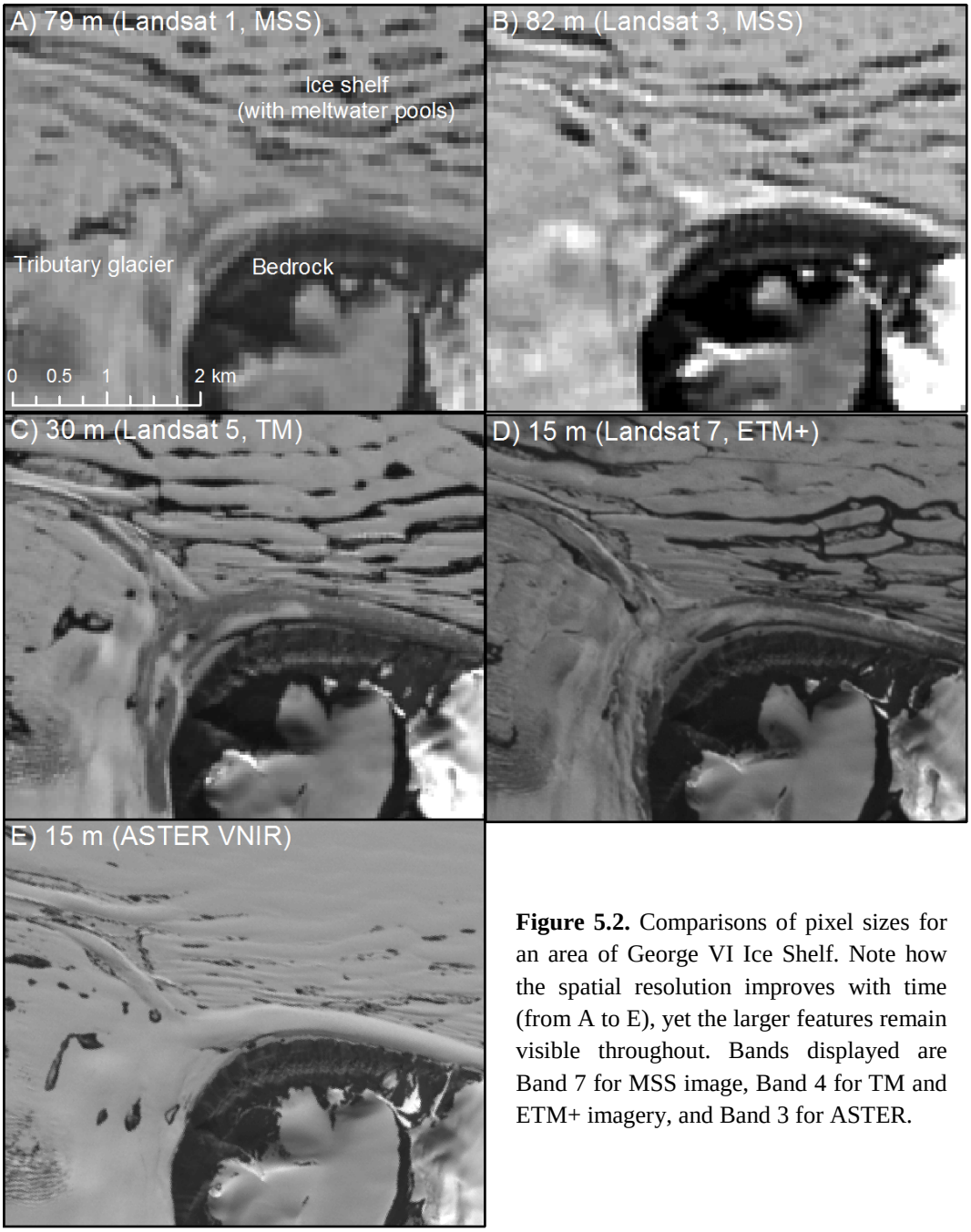

Figure 5.2. Comparisons of pixel sizes for an area of George VI Ice Shelf. Note how the spatial resolution improves with time (from A to E), yet the larger features remain visible throughout. Bands displayed are Band 7 for MSS image, Band 4 for TM and ETM+ imagery, and Band 3 for ASTER.

Table 5.3. ASTER sensors and characteristics

	Band	Spectral resolution (µm)	Spatial resolution (m)
VNIR	B1	0.520-0.600	15
	B2	0.630-0.690	15
	B3N*	0.760-0.860	15
	B3B**	0.760-0.860	15
SWIR	B4	1.600-1.700	30
	B5	2.145-2.185	30
	B6	2.185-2.225	30
	B7	2.235-2.285	30
	B8	2.295-2.365	30
	B9	2.360-2.430	30
TIR	B10	8.125-8.475	90
	B11	8.475-8.825	90
	B12	8.925-9.275	90
	B13	10.250-10.950	90
	B14	10.950-11.650	90

**Nadir Band, **Back-looking Band*

5.1.3 European Remote-sensing Satellite (ERS-1 and ERS-2) SAR imagery

Each ERS satellite carried a Radar Altimeter, an Along-track Scanning Radiometer, a Wind Scatterometer, a Microwave Radiometer and a Synthetic Aperture Radar (SAR), with additional Global Ozone Monitoring Experiment instruments and an upgraded Along-track Scanning Radiometer onboard ERS-2. The SAR systems operated at C-band (5.3 GHz, 5.6 cm wavelength), with vertical transmit and receive polarisation (VV) and an incident angle of between 19.5° and 26.5°. The satellites were positioned in a near-polar orbit at a mean altitude of 780 km. The swath of the ERS SAR imagery is ~100 km with a standoff of 250 km to the right of the satellite and an approximate spatial resolution of 4 m in the azimuth and 8 m in the range. Five times the data was acquired in the azimuth direction, thus raw single-look complex (SLC) images appear stretched along the satellite's track (Figure 5.3). Each global orbit was completed within 100 minutes, achieving 14.3 orbits each day. The ERS satellites had three orbital configurations for three-day, 35-day and 176-day repeat pass acquisitions. Between April 1995 and March 1996 ERS-1 and ERS-2 satellites were synchronised with a 24 hour separation permitting one-day repeat-pass acquisition. ERS-1 failed during March 2000, with ERS-2 suffering instrument failure

during 2001 and 2003 that limited its data quality and acquisition performance. Here, 10 ERS-1 and ERS-2 image pairs, separated by 24 hours, were used to calculate ice-shelf surface velocities (Table 5.15). An additional three images were used for spatial assessment to fill gaps left by optical imagery. A further 40 images were initially obtained but poor coherence between image pairs limited their value. All SAR images were acquired in single-look complex (SLC) format so that phase information was retained, and projected in a natural SAR slant-range/azimuth coordinate system for InSAR processing.

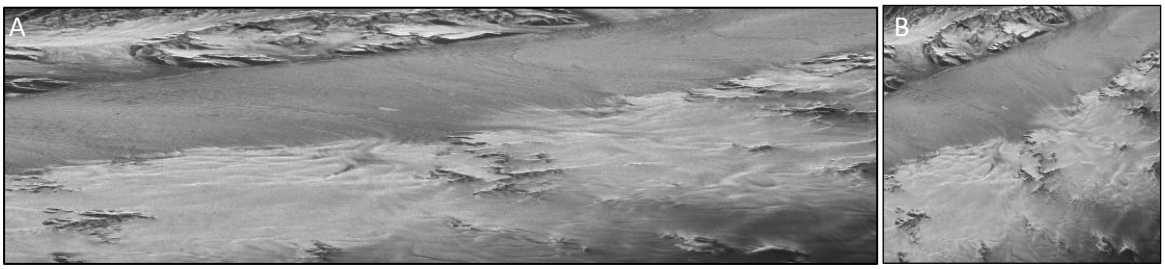

Figure 5.3. A) Single-look complex (SLC) image (ERS-2 1996) and B) its multi-looked complex (MLI) image equivalent illustrating the 'stretched' effect of the raw data compared to a true-look image over a section of George VI Ice Shelf.

5.1.4 European Environmental Satellite (Envisat)

Envisat was launched in March 2002 and similarly carried an array of instruments including an advanced SAR (ASAR) sensor. Envisat was put into orbit resembling that of ERS-2 shortly after launch to ensure a continuation of data products following the failure of other SAR sensors. During March 2012, Envisat lost communication with receiving stations on Earth, bringing the end to the SAR imaging capabilities of the satellite. The ASAR system operated at C-Band (5.6 cm) over a repeat cycle of 35 days, in either Image Mode or Wave Mode, with the latter designed for oceanographic study only. In total, 5 ASAR images were acquired for this study in Image Mode, with a VV polarisation to match the ERS-1 and ERS-2 specifications, although only one image was used in the final thesis for meltwater extent assessment of Bach Ice Shelf.

5.1.5 Ice, Cloud and Elevation Satellite (ICESat)

ICESat was launched in 2003 with the intention of collecting near-continuous, sub-decimetre elevation data over ice sheets and ice caps. ICESat carried three identical lasers on board the Geoscience Laser Altimeter System (GLAS), of which Laser 1 failed shortly after its initial commencement. Lasers 2 and 3 were put into a periodic acquisition mode as outlined in Chapter 3, Section 3.3.2. ICESat data was preferred over other elevation

sources as it offered the best spatial resolution along track, with a data point collected every ~170 m. Although the temporal resolution is limited, a longer time series of elevation-change has since been made available (e.g. Fricker and Padman, 2012).

ICESat GLAS data were acquired pre-processed via Helen Fricker and Matt Siegfried from Scripps Institution of Oceanography. Data used covered the time period from October 2003 to December 2008 (refer to Table 3.4). The pre-processing techniques implemented, and subsequent processing of ICESat GLAS data, are outlined in Section 5.2.3.

5.1.6 Auxiliary data sources

5.1.6.1 Radarsat Antarctic Mapping Project (RAMP) DEM

The RAMP v2 DEM provides coverage of the whole of Antarctica, combining topographic data from a wide range of sources, including topographic maps from the USGS and Australian Antarctic Division, elevation data from ERS-1 satellite radar altimetry, airborne radar echo sounding and station-based echo sounding (Liu *et al.,* 2001). The National Snow and Ice Data Center (NSIDC, http://nsidc.org/) provide RAMP v2 DEM in 1 km, 400 m and 200 m spatial resolution, whilst the real spatial resolutions vary from location to location (Liu *et al.,* 2001). For the Antarctic Peninsula and the Transantarctic Mountains, the true DEM spatial resolution is estimated at 200 m, whereas the spatial resolution for the interior of the Antarctic continent varies from 1 km to 5 km depending on the availability of airborne echo sounding (Liu *et al.,* 1999). The geolocation accuracy of RAMP v2 data is governed by the accuracy of the topographic data sources and is generally better than the horizontal resolution (Liu *et al.,* 1999). The vertical accuracy of the RAMP v2 DEM for different surfaces and locations is provided in Table 5.4.

Table 5.4. Vertical accuracy of RAMP v2 DEM (from Liu *et al.*, 1999, 2001).

Topography type/ region	Accuracy
Mountainous terrain	± 100 m
Steeply sloped coastal regions	± 15 m
Ice shelf surfaces	± 1 m
Gently sloped interior ice sheet	± 7.5 m
Rough and steeply-sloped ice-sheet perimeter	± 17.5 m
Latitudes south of 81.5°	± 50 m

In this study, the RAMP v2 200 m DEM was selected over other available elevation data because of its comparatively finer spatial resolution and spatial coverage. The ICESat

DEM also available from the NSIDC offers an improved vertical accuracy (DiMarzio *et al.*, 2007) over the ICESat portions, but a coarse spatial resolution of 500 m. Conversely, the ASTER Global-DEM offers a finer 30 m spatial resolution, but does not include elevation data over ice shelves. Furthermore, the ASTER Global-DEM has significant errors due to cloud cover in the original ASTER scenes (ERSDAC, 2009).

5.1.6.2 Ice-shelf thickness data

Ice-thickness data for Bach, George VI, and Stange Ice Shelves were provided by Griggs and Bamber (2011) during the latter stages of this thesis. Prior to the availability of their dataset, thickness estimates were often poorly constrained on Antarctic Peninsula Ice Shelves as a result of data interpolation across shelf and grounded ice, and in areas where the ice shelf was not in hydrostatic equilibrium. This effectively created a bias in the thickness estimates towards the grounding zone that meant ice flux into the ice shelves was both inaccurate and imprecise. The ice thickness datasets provided by Griggs and Bamber (2011) were calculated from ERS-1 RA and ICESat GLAS surface elevation data using the principles of hydrostatic equilibrium:

$$H_i = \frac{(e-\delta)\rho_w}{\rho_w - \rho_i} \qquad \text{Equation 5.1}$$

(Griggs and Bamber, 2011)

$$Z - \delta = \frac{(e-\delta)\rho_w}{\rho_w - \rho_i}$$

where H_i is the total ice-shelf thickness (if all ice were of meteoric origin ρ_i), Z is the actual ice thickness (including a layer of variable-density firn), e is the ice-shelf elevation about the mean sea level, ρ_w is the density of the water column under the ice shelf and δ is the firn density correction (Griggs and Bamber, 2011). The thickness data were used primarily in assessing the patterns of ice-shelf retreat, ice-shelf stability and calculating the consequences of ice-shelf removal in Chapter 9.

5.1.6.3 MEaSUREs InSAR-based velocity map

The MEaSUREs (Making Earth Science Data Records for Use in Research Environments) InSAR velocity maps (Rignot *et al.*, 2011) were similarly only made available towards the latter stages of the thesis, and were therefore not considered in the results or interpretation chapters of the individual ice shelves. The velocity map of Antarctica was developed through the integration of an array of InSAR-capable SAR sensors. For the Antarctic Peninsula, ALOS PALSAR imagery was used and surface velocities thus represent the

time period from 2006 to 2008 (Rignot *et al.*, 2011). The data were downloaded from the NSIDCs website and used to estimate ice-flux across the grounding zone in Chapter 9.

5.2 Major processing steps and method description

In this section, the methods used to derive ice-shelf spatial extent, structural maps, surface speeds and surface elevation changes are outlined. The following methods make use of the optical, radar and non-imaging satellite data described above, with a full list of satellite imagery used provided in Table 5.14 (optical) and Table 5.15 (radar).

5.2.1 Ice-shelf spatial assessment and surface feature mapping

5.2.1.1 Pre-processing

All optical datasets were acquired in a georeferenced, orthorectified format. Landsat imagery was terrain corrected to Level 1T using a RAMP DEM (200 m), with ASTER imagery orthorectified to its own DEM by the USGS. As a result, the only pre-processing procedure required on the optical imagery was co-registration, which was carried out in the Geographical Information System (GIS) software ArcMap 9.3, by manually adjusting the top left image coordinate (x and y) so that areas of bare ground (i.e. a nunatak) or distinct grounded-ice locations were to within 1 pixel, achieving accuracies of ~80 m, 30 m and 10 m for MSS, TM and ETM+/ASTER images respectively. Atmospheric correction was not applied as there was no requirement for time-series change detection in relation to spectral reflectance within the data, other than for meltwater classification where histogram matching was applied to the relevant images.

5.2.1.2 Ice-shelf mapping

Ice-shelf extent and surface features were mapped in ArcMap 9.3 using time-separated images for each of the study sites (Table 5.5), following similar procedures to Glasser and Scambos (2008) and Braun *et al.* (2009). Whilst maps of ice shelf spatial extent exist (e.g. Ferrigno *et al.*, 2009; Cook and Vaughan, 2010), the extents were independently digitised here to allow direct comparison to structural changes and evolution also investigated. Digitised features included the location of the ice front and ice-shelf grounding zone for spatial assessment, rifts, fractures, fracture traces, crevasses and crevassed zones (fields), longitudinal structures (elsewhere termed flow stripes, flow bands, foliation), transverse structures, pressure ridges, ice rises, ice rumples and ice dolines (see Table 5.6 and Figure 5.4 for a description and example of each feature). Meltwater pools were automatically

classified in Definiens Developer 7.0, and later added to their respective surface feature maps (see Section 5.2.1.3).

Table 5.5. Years when full structural maps were produced for each ice shelf. Smaller regions and/or individual features may have been mapped at more regular intervals and are detailed when necessary in the following chapers.

Location	Map 1	Map 2	Map 3	Map 4	Map 5	Map 6	Map 7
Bach	1973	1978	1989	1995*	2003	2005	2011
George VI North and Central	1974	1979	1989	1996*	2001	2010	N/A
George VI South	1973	1986	1991	1996*	2003	2010	N/A
Stange	1973	1986	1996*	2001	2005	2011	N/A

**Mapped from SAR imagery only.*

Structural and surface-feature mapping was performed using image bands that offered the best spatial and spectral resolution. For example, Landsat MSS Band 5 (0.6 – 0.7 µm, ~80 m), Landsat TM and ETM+ Band 4 (0.76 - 0.9 µm, 30 m), Landsat ETM+ Panchromatic Band 8 (0.52 – 0.9 µm, 15 m) and ASTER Band 3N (0.76 – 0.86 µm, 15 m) were used in mapping the surfaces of all three ice shelves for the time periods indicated in Table 5.5. Whilst this resulted in feature-mapping being conducted on grey-scale images, it greatly reduced the computational power required, and permitted multiple active images within a single GIS project without compromising processing speed. Standard image-enhancement stretches (e.g. Gaussian stretching, equalisation) were applied on an image-by-image basis to improve the appearance of surface features (Figure 5.5).

Table 5.6. Ice-shelf features, identifying criteria and significance. Adapted from Glasser and Scambos (2008) and Glasser *et al.* (2009).

Feature	Identification	Significance
Ice front (Figure 5.4A)	Sharp transition from ice shelf to open ocean (summer) or sea ice (winter, fast-ice). Often seen as a bright sunlit or dark shaded sub-linear feature. Sea ice or icebergs often visible close to the edge indicative of active calving.	Clear indicator of the maximum ice-shelf extent for a particular time period. Sequential images can track the fluctuation of the ice margin to develop an understanding of ice-front dynamics.
Fracture (Figure 5.4B)	A clear opening in the ice-shelf surface. Not possible to infer whether the fracture penetrates the entire thickness of the shelf. Observed as a distinct couplet of dark/light reflectance indicating the fracture walls.	Typically formed when the ice exceeds a temperature-dependant threshold. Fractures form perpendicular to the direction of maximum tension.
Rift (Figure 5.4C)	Ice-shelf surface fracture with a visible opening often perpendicular to the principal ice-flow direction. Large rifts can be filled with ice melange; a mixture of refrozen sea ice and angular calved ice blocks. A rift penetrates the entire depth of the ice shelf, inferred where melange or sea water is visible in its opening.	Typically formed when the ice exceeds a temperature-dependant threshold. Rifts form perpendicular to the direction of maximum tension.
Crevasses and crevasse fields (Figure 5.4D)	Surface fractures appearing as dark (open or water-filled) or bright (snow-covered) linear lines. Often form in distinct zones. In this study, the term crevasse is applied to fractures originating on grounded ice to differentiate them from ice-shelf fractures that form in floating ice.	Formed when the stresses within the ice exceed a given threshold. Form perpendicular to the direction of maximum tension. Open crevasses indicate extensional flow.
Fracture trace (Figure 5.4E)	Resembles a fracture or rift on the ice-shelf surface, but where no clear opening is observed. Naturally form down ice of fractures and rifts. Impossible to differentiate between fracture trace and rift trace without prior knowledge of its previous form, thus all such features are termed *fracture trace*.	Formed when ice is compressed perpendicularly (or approximately) to the orientation of the original fracture and/or rift.
Longitudinal surface structures (Figure 5.4F)	Long, linear structures aligned parallel with the principal flow direction. Typically <1 km in width but often exceeding tens-to-hundreds km in length. Observed as dark and light lines caused by shaded relief. Originate from the confluence of two flow units and in regions of positive relief, at bed protuberances or in regions of high basal friction.	Generally indicate regions of faster ice flow and depict suture zones of different flow units. Cumulative length is due to the slow decay timescale relative to the time required for ice to travel a long distance.
Transverse structures (Figure 5.4G)	Term given to sub-linear surface features where no clear method of formation exists. Appear as dark lines on the ice-shelf surface.	May indicate degraded surface fractures or surface undulations caused by ice-shelf buckling under compressive stresses. Significance discussed on a case-by-case basis.
Pressure ridges (Figure 5.4H)	Succession of dark and light linear bands appearing perpendicular to principal flow direction. Often located near bedrock or ice-rises or between coalescing flow units	Formed by ice straining vertically under longitudinal compressive stresses.
Grounding zone (Figure 5.4I)	Sudden break in surface slope or area of intense crevassing. Meltwater ponds tend to form at the grounding zone where there is a change of gradient.	Junction between grounded ice and floating ice. A dynamic zone often flexing with tidal amplitude.
Ice rises (Figure 5.4J)	Elevation of the ice-shelf surface with disturbance to ice flow indicated by pressure ridges on the stoss-side and/or crevasses in the lee of the ice rise.	Local bedrock high where the ice shelf is grounded.
Ice rumples (Figure 5.4K)	Elevation of the ice-shelf surface with disturbance to ice flow indicated by crevasses.	Local bedrock high where the ice shelf is partially grounded, but ice flow continues.
Surface meltwater (Figure 5.4L)	Dark, flat areas on ice-shelf surface either as open or closed systems. May or may not form along pre-existing structural discontinuities.	Indicates surface ablation and can suggest ice-shelf surface slope orientation where flow direction is apparent. Assessing time-series of surface meltwater can indicate increasing/ decreasing atmospheric temperatures.
Ice dolines (Figure 5.4M)	Large sub-rounded surface hollows often filled with meltwater during the height of the melt season.	May indicate a link between the ice-shelf surface and subsurface. Considered to be located in thin and weak ice. Formation linked to abundant surface meltwater.

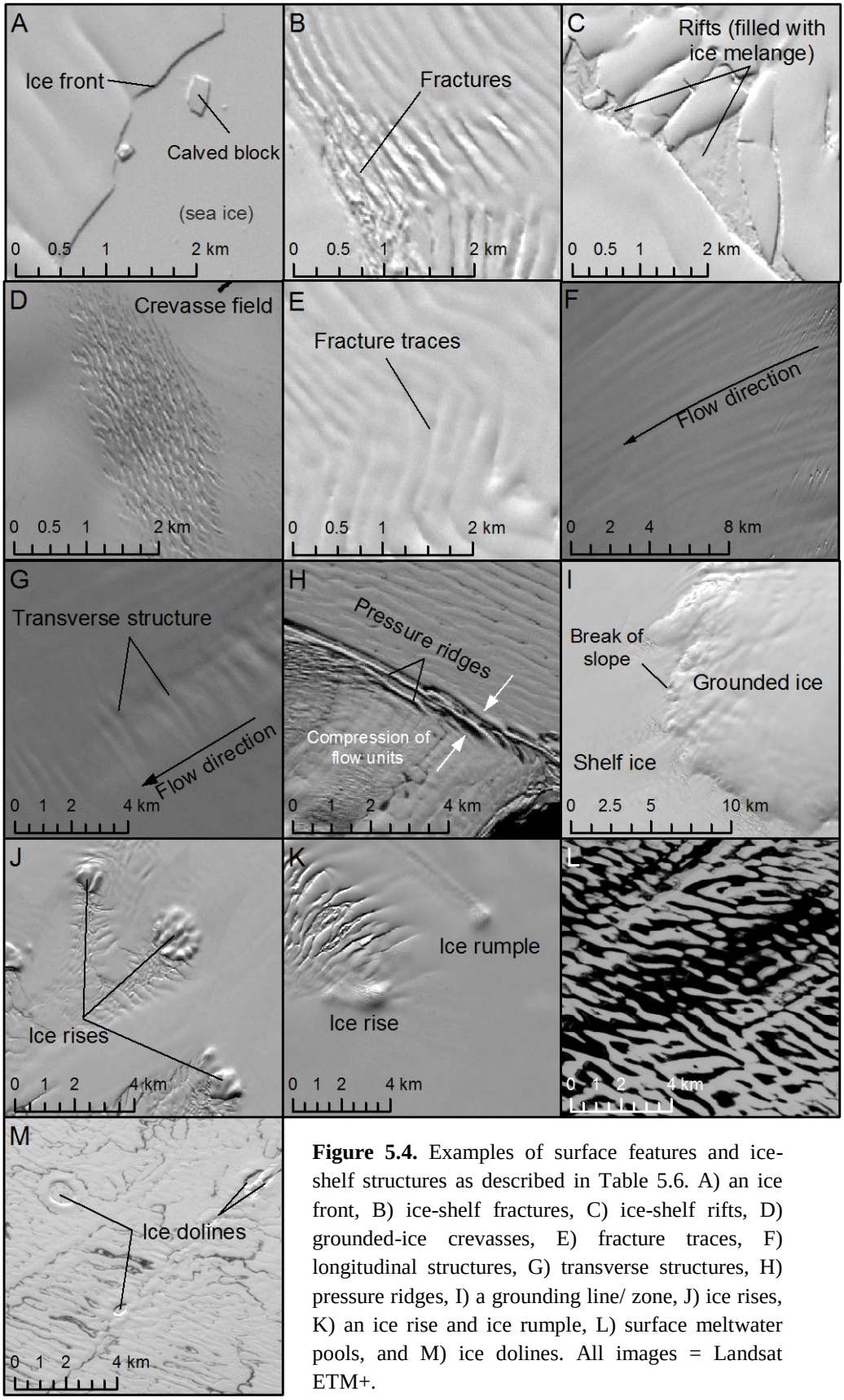

Figure 5.4. Examples of surface features and ice-shelf structures as described in Table 5.6. A) an ice front, B) ice-shelf fractures, C) ice-shelf rifts, D) grounded-ice crevasses, E) fracture traces, F) longitudinal structures, G) transverse structures, H) pressure ridges, I) a grounding line/ zone, J) ice rises, K) an ice rise and ice rumple, L) surface meltwater pools, and M) ice dolines. All images = Landsat ETM+.

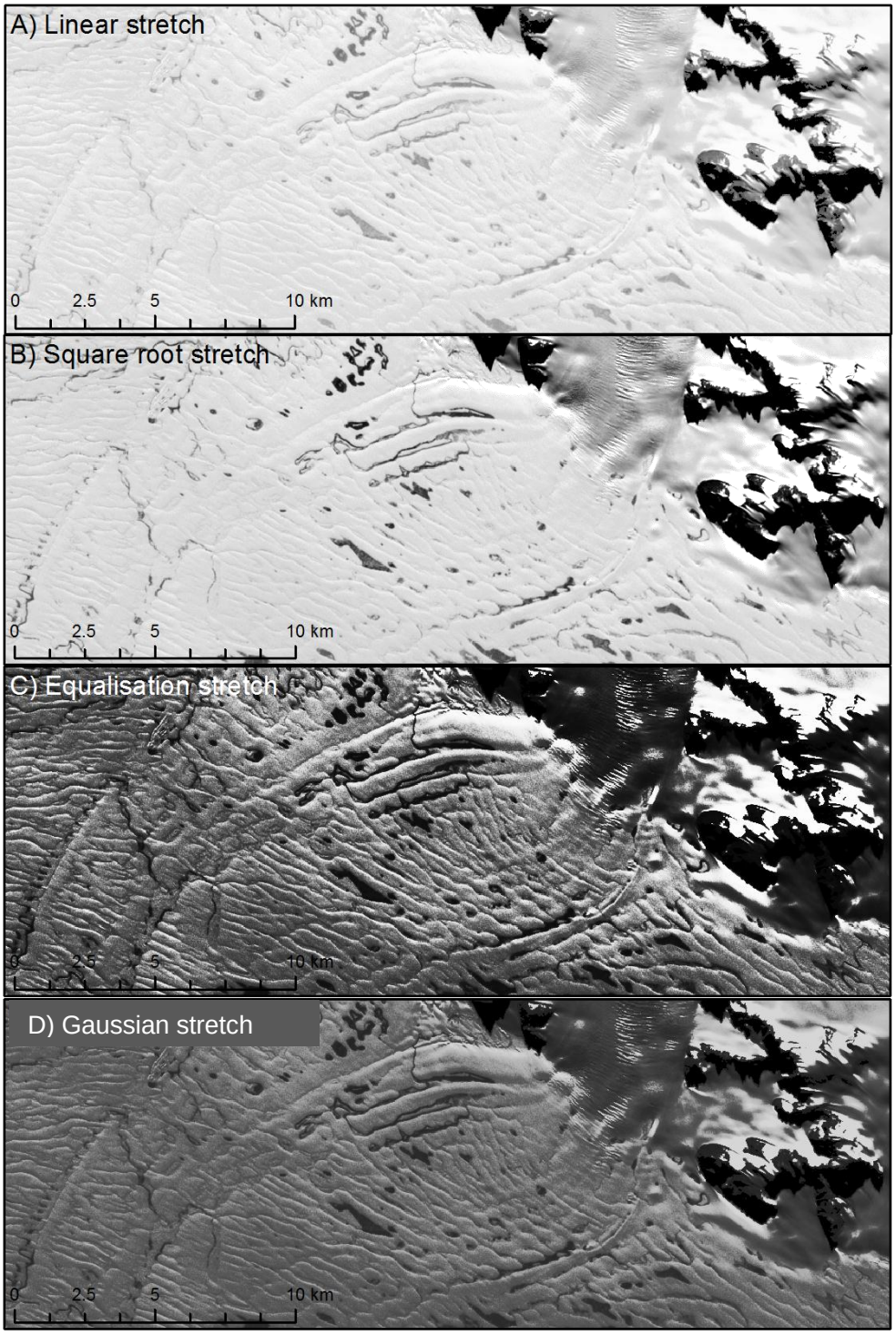

Figure 5.5. Image contrast stretches used to enhance surface features and ice-shelf structures during digitising. Example showing Landsat ETM+ imagery.

Digitising was carried out at three main scales for consistency across all three ice shelves and all time periods: 1) 1:100,000 was used for large surface features such as confluence zones and longitudinal structures, 2) 1:50,000 was used for fractures, rifts, the ice front and the grounding zone, and 3) 1:25,000 was used for crevasses, crevassed zones, transverse structures and pressure ridges. Other features, such as nunataks and ice rises, were mapped

at scales appropriate to their individual characteristics. By following the same procedure for each ice shelf, 25 full glaciological maps were produced over the southwest Antarctic Peninsula over a quasi-decadal scale. For areas where significant change was observed, further mapping was carried out to detail short-term changes at finer spatial resolutions.

Whilst this method for glaciological mapping is commonly used, some limitations exist. First, the horizontal resolution of the image limits the minimum size of features mapped. Thus, surface features that measure less than the horizontal resolution of the imagery are overlooked. As a result, the maps of glaciological surface features would naturally become more detailed over time, as the spatial resolution of satellite imagery becomes finer. However, major structures are often greater than the coarsest resolution used in this study. Second, unless there is a distinct spectral difference between surface features (i.e. surface meltwater, bare ice), structures on ice shelves are only identifiable by the reflectance value altered by the Sun's illumination/ shadow off surface undulations. Third, cloud cover cannot be penetrated by optical sensors, thus partial cloud cover or fine atmospheric haze can reduce the quality of the satellite image, prohibiting structural and surface feature mapping.

5.2.1.3 Post-processing of fracture, rift and fracture trace polylines

To assess the changes in distribution and extent of fractures, fracture traces and rifts, the corresponding polylines used to digitise the features were manipulated within ArcMap. First, the polylines were converted to point data at 250 m intervals, so that individual structures were represented as a succession of points rather than single polyline-features. Second, a 1 km polygon grid was created, with the centre point of each individual cell calculated. Third, the number of fracture, fracture trace and rift data points within each cell were counted, with the final value attributed to the cell-centre point. Fourth, the centre-point data were extracted to a separate shapefile, and subsequently interpolated using a nearest neighbour function, resulting in a visual representation of fracture-segment density. Comparing a time-series of these datasets permitted a semi-quantitative assessment on surface feature-change.

5.2.1.4 Meltwater classification

Mapping of surface meltwater features from Landsat MSS, TM, ETM+ and ASTER imagery was carried out in Definiens Developer 7.0 software (eCognition) using an object-orientated approach (Figure 5.6). This permitted all surface meltwater to be digitised without manually mapping each individual meltpool by taking advantage of the spectral difference between snow/ice and water. This classification method differs significantly from the conventional pixel-based classification procedures that can often result in a 'salt and pepper' appearance. Image objects are formed using a segmentation algorithm that detects local contrasts in the high-resolution satellite imagery (Definiens, 2005). Multi-resolution segmentation creates image objects starting from a single pixel and grows in subsequent steps to construct larger objects. The process is based on the weighted heterogeneity of the image objects and terminates when a user-define threshold is reached. The result is a segmentation of the satellite image into spectrally homogeneous objects that can be based on essential features (e.g. contrast), topological features (e.g. geometric relationship) and context features (e.g. 'a meltwater pond is 100% surrounded by ice'). As a result, the number of objects to be classified is significantly less using an image object approach than a pixel-based approach, whilst retaining high accuracy and precision of classified images.

Developer 7.0 uses a rule-based classification approach, centred on the user's knowledge of the environment under investigation. Spectral reflectance, along with the shape and texture of the image objects, can be used in the classification procedure. Statistical thresholds (e.g. $\alpha < 3$) and boundaries (e.g. $1 < \alpha < 3$) are set at the users discretion to distinguish certain image objects. Furthermore, Developer 7.0 implements fuzzy logic; instead of exact answers 'yes' (1) and 'no' (0), results are transformed to a continuum between 1 and 0 based upon a set of user-defined rules. Thus, an image object is assigned to a class to which it is most suited. Fuzzy logic implements instructions 'if', 'and', 'or' and 'then' to assign a specific object to a certain class. Thus in its simplest description, if a condition is met then an action takes place.

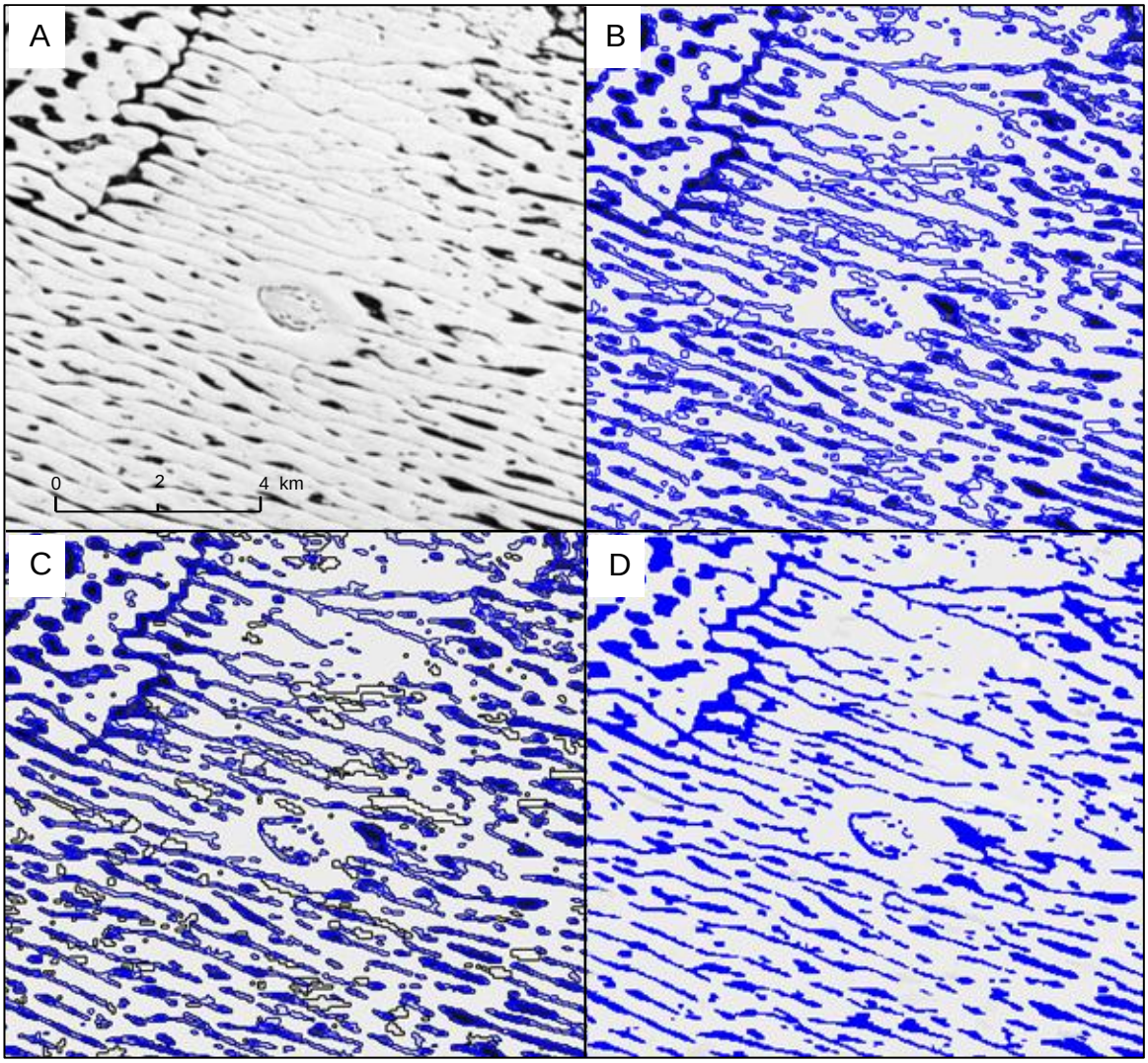

Figure 5.6. Meltwater classification procedure from image band (A), to segmented image based on spectral homogeneity (B), to classified image based on spectral thresholds (C, Table 5.7) to final exported shapefile of meltwater extent (D). Example based on an area of George VI Ice Shelf and a Landsat TM image from January 1991.

Here, image segmentation (Figure 5.6B) was carried out using the multi-resolution approach based solely on Landsat MSS Band 5, Landsat TM/ETM+ Band 4 and ASTER band 3N as these bands offered the greatest spectral contrast between snow/ice surfaces and meltwater. Due to the differences in spatial resolution between the sensors, different scale parameters were used to determine the object sizes (Table 5.7). The scale parameter controls the amount of spectral variation within image objects, and therefore their resultant size; the larger the scale parameter then the larger the resulting image objects. A shape factor (that determines the overall geometry of each segment) was set at 0.0 to ensure the spectral reflectance was the main determinate of the image objects, and a compactness value of 1.0 was used for all scenes to ensured that the segmentation was based solely upon

spectral properties. Image objects were thus shaped according to the contrast between surface meltwater and surrounding ice at a scale comparable to the imagery.

Table 5.7. Parameters and thresholds for automatic classification of meltwater features for the different sensors and spatial resolutions.

Sensor (Band)	Spatial resolution (m)	Scale (unitless)	Shape (unitless)	Compactness (unitless)	Spectral thresholds (unitless)
MSS (Band 7)	82/79	7	0.0	1.0	0-95
TM (Band 4)	30	15	0.0	1.0	0-93
ETM+/ASTER (Pan/Band 3N)	15	30	0.0	1.0	0-97

Classification of surface meltwater was based on a set of statistical rules in the form of thresholds and boundaries for 10 Landsat and 3 ASTER images, histogram matched for consistency between rule sets (Table 5.7). To avoid inaccurate classification of bare ground and/or shaded relief (that hold similar spectral properties to water), an image mask of the ice-shelf area, digitised in ArcMap during spatial assessment, was imported into the Developer project; only the image area with the image mask was considered during classification. A complete classification of surface meltwater was consequently achieved (Figure 5.6D) for the individual Landsat scenes, with classified regions merged and exported as smoothed polygons and imported into ArcMap GIS for extent and distribution analysis.

5.2.2 Ice-shelf velocity derivation

5.2.2.1 InSAR

InSAR was used to derive surface velocities (ca. 1996) for Bach Ice Shelf, and the northern and central regions of George VI Ice Shelf using a four-pass interferometry; one image pair was used to construct an ascending interferogram, with another pair of ERS-1/2 images used to construct a descending interferogram. The resulting interferograms were then used to calculate three-dimensional velocity fields of the ice-shelf surfaces via a trigonometric approach. Poor image coherence between ERS-1/2 image pairs over the southern regions of George VI Ice Shelf and Stange Ice Shelf prevented InSAR calculations in these regions.

InSAR measures surface displacement at the sub-centimetre scale using the phase information retained during image acquisition. Essentially, the phase change between two

radar signals on successive tracks over the same portion of the Earth's surface is measured (e.g. Fatland and Lingle, 1998; Figure 5.7). Interferometric phase of the surface can be resolved by Equation 5.2:

$$\delta\phi = \frac{4\pi}{\lambda}\,(S_1M - S_2M) \qquad \text{Equation 5.2}$$

where λ is the wavelength of the imaging radar, S_1M and S_2M are the optical paths from *M* (see Figure 5.7 for nomenclature) to the successive paths of the satellites (S_1 and S_2), and *B* is the interferometric baseline.

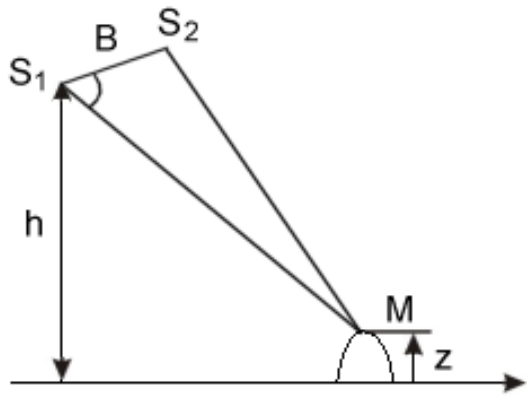

Figure 5.7. Radar imaging geometry for interferometric SAR processing. S_1 and S_2 are successive satellite acquisitions of the ground point *M*, at elevation *z*. *B* is the baseline (i.e. distance) between both satellite acquisitions resolved from precise orbiting information, and *h* is the true, perpendicular altitude of the satellites during acquisition. Source: Michel and Rignot (1999).

The phase recorded at the receiving antenna is dependent on the image geometry, length of baseline, surface topography and surface displacement (Equation 5.3). Thus, by removing the unwanted phase components (through precise orbital data records, and a DEM), the surface deformation component can be isolated and used to calculate surface velocities.

$$\psi_{total} = \psi_{geom} + \psi_{topo} + (\psi_{disV} + \psi_{disH}) \qquad \text{Equation 5.3}$$

where ψ_{geom} is the phase component caused by InSAR geometry, ψ_{topo} is the phase caused by topography, and ψ_{disV} and ψ_{disH} represent the vertical and horizontal surface displacement. For marine terminating glaciers and ice shelves, the surface displacement contains both a vertical (tidal flexure, pressure difference) and horizontal (ice-shelf motion) component, thus the best ice-flow assessments are made where ψ_{disV} can be separated from ψ_{disH} through the use of accurate tidal information, modelled tidal amplitude, applying an inverse barometer correction, or by averaging ice-shelf velocities

over a longer time period (stacking) to subdue the residual, short-term vertical dynamics. However, tidal amplitude records for ice-shelf surfaces are poorly distributed, and as a result, modelling tidal amplitude is challenging (King and Padman, 2005) over large ice-shelf areas. Furthermore, the effect of atmospheric pressure differences was considered negligible over a 24-hour period of acquisition and was thus not removed, but insufficient datasets were available for 'stacking' interferograms to average steady motion over longer time periods (e.g. McMillan *et al.,* 2012). As a result, InSAR velocity measurements presented contain a vertical displacement error as discussed in Step 8. InSAR processing was carried out in GAMMA Remote Sensing processing software (Werner *et al.,* 2001); the major processing steps are detailed below and in Figure 5.8. Steps 1-6 were carried out for an ascending and descending pair of ERS-1/2 images, with Step 7 bringing together these two independent interferograms.

1. Generation of image parameter files and retrieval of orbital information

Parameter files containing orbital data were generated for the ERS-1 and ERS-2 images using the information retained in their original files. They were improved using state vectors, inserted into the parameter files by downloading the associated Orbital Data Records (ODRs; http://www.deos.tudelft.nl/ers/precorbs/orbits). State vectors give the latitude and longitude of each satellite pass every 10^{th} of a second, to an accuracy of 5 cm (Scharroo and Visser, 1997), thus giving a precise location and permitting accurate determination of image baselines needed for the removal of the geometric phase in Step 4.

2. Intensity image co-registration

SLC images (intensity images) were co-registered based on data contained within their respective parameter files and user defined information. The ERS-2 image was used as the reference image, with the ERS-1 image selected as the slave; this hierarchy is respected throughout the processing procedure. A Cross Correlation of Intensity (CCI) algorithm was applied to co-register the images to within a fraction of a resolution cell (Fatland and Lingle, 1998). CCI generates offset estimates by correlating intensity patterns between images, based on image patches, the dimensions of which are user-defined and largely governed by the visual quality of SAR imagery. The CCI approach is more computationally efficient than other methods, and also permits images with no interferometric correlation to be co-registered. Confidence in offset estimation is measured by comparing the height of the correlation peak relative to the mean level of correlation function to yield a correlation signal-to-noise ratio (SNR). Here, image registration was

only accepted where the SNR values were greater than 7.0, implying a registration accuracy of better than one pixel.

3. Computation of an interferogram from registered intensity images

Interferograms were generated by subtracting the phases of the two SLC images on a pixel-by-pixel basis. During this processing step, the interferograms were multi-looked, with one look in the range direction, and five looks in the azimuth direction so that the resulting interferogram represented a true-look image (i.e. to compensate for the five azimuth data points for each range data point). The associated intensity images were also multi-looked for further processing.

4. Adaptive filtering, baseline estimation and interferogram flattening (geometric phase removal)

The resulting interferogram was filtered to remove phase noise using a two-step adaptive filtering approach. Adaptive filtering reduces the number of residues in an interferogram, effectively merging two residue cells into a single cell, reducing the phase noise of the interferogram. The first filtering step used a fast-Fourier transform (FFT) window size of 64, with the second step using a FFT window size of 32 to refine the filtering stage, thus ensuring that phase noise was at a minimum for further processing. For both filtering steps, an exponent of 0.25 was used so that the removal of tightly-packed interferometric fringes in regions of rapid acceleration or deceleration was avoided.

At this stage, the interferogram was made up of three components; topographic phase, geometric phase, and displacement phase (see Equation 5.3). Geometric phase is introduced into an interferogram as a result of the Earth's curvature, and must be systematically removed to leave the topographic and displacement phase only. The geometric phase is regular across an interferogram, and is near-linear (modulo 2π). Its dependence on the baseline means that it can be removed without altering the topographic and displacement phase components.

An initial baseline estimate was made using the orbital parameter files of the corresponding ERS-1/2 images. The simulated phase caused by the baseline was removed from the filtered interferogram to leave it 'flattened'. The initial baseline estimate was then refined by calculating the residual phase in the flattened interferogram using a FFT algorithm, based on the remaining interferometric fringe rate. The residual baseline phase

was then added to the original baseline estimate, which was then used to remove the total baseline-derived phase from the filtered interferogram, leaving only the topographic and displacement phase.

5. Removing topographic phase

To remove the topographic phase, the RAMP DEM was used. First, a DEM parameter file was created and used to generate a geocoding look-up table that enabled conversion from map coordinates (Polar Stereographic) to range-doppler coordinates (RDC; radar geometry), and vice-versa. Second, a simulated SAR image was produced from the DEM file that permitted offset estimation between this and actual SAR intensity files. The RAMP DEM was then geocoded to RDC to match that of the ERS-1/2 interferogram using a nearest neighbour 1/distance weighting function. The RAMP DEM was filtered to reduce the noise using a Gaussian weighting function with a 20-pixel window size, effectively smoothing the DEM. Third, a topographic phase simulation file was calculated using the geocoded DEM, the ERS-2 MLI (multi-looked image) parameter file and the refined baseline estimate. This was subsequently subtracted from the flattened interferogram leaving the displacement-phase component only. Finally, any topographic residual phase was removed by calculating the baseline of the displacement-only interferogram, using a FFT algorithm, based on interferometric fringe rate. This refined baseline value was subsequently added to the original baseline estimate, and then subtracted from the displacement-only interferogram in a similar way that removed residual geometric phase.

6. Phase unwrapping and displacement conversion

The displacement phase in the interferogram at this point was represented by an ambiguous 'fractional wavelength' that indicates only small radial distance changes at each resolution cell, relative to their neighbouring cells (Fatland and Lingle, 1998). The unwrapping stage essentially converted the radial distance to a horizontal or vertical measurement. By unwrapping from a stable point (e.g. rock outcrop) and setting this value at 0 m per day, small increments of phase variation between pixels were achieved, thus constructing a velocity field from the phase information in the interferogram in the line-of-sight (LOS) direction. Due to the nature of the Antarctic Peninsula, a stable rock outcrop was not always available to initiate unwrapping. Instead, regions where velocities were considered to be small in comparison to the flow of the ice shelf were chosen as the starting point for

phase unwrapping; this was often on ridges between flow basins where ice speeds were considered to be negligible.

7. Converting LOS velocities to directional velocities

The final step in the interferometric processing was to convert the LOS velocities to directional velocities. First, look vectors for both the ascending and descending interferograms were calculated using the DEM, and parameter files of the DEM and MLI intensity images. These look vectors, along with the two displacement interferograms and the ERS-2 MLI, were subsequently geocoded using the geocoding look-up table from RDC to map coordinates (generated in Step 5). Second, these files were interpolated using a bicubic spline method based on offsets manually calculated (through visual assessment) between the two geocoded MLI images. The displacement field was then calculated based on two motion components within each of the interferograms using a trigonometric approach, with the assumption that the displacement motion was in the horizontal surface plain. The final displacement map presented directional velocities in metres per day that were later extrapolated to metres per annum for direct comparison between feature-tracking-derived surface speeds.

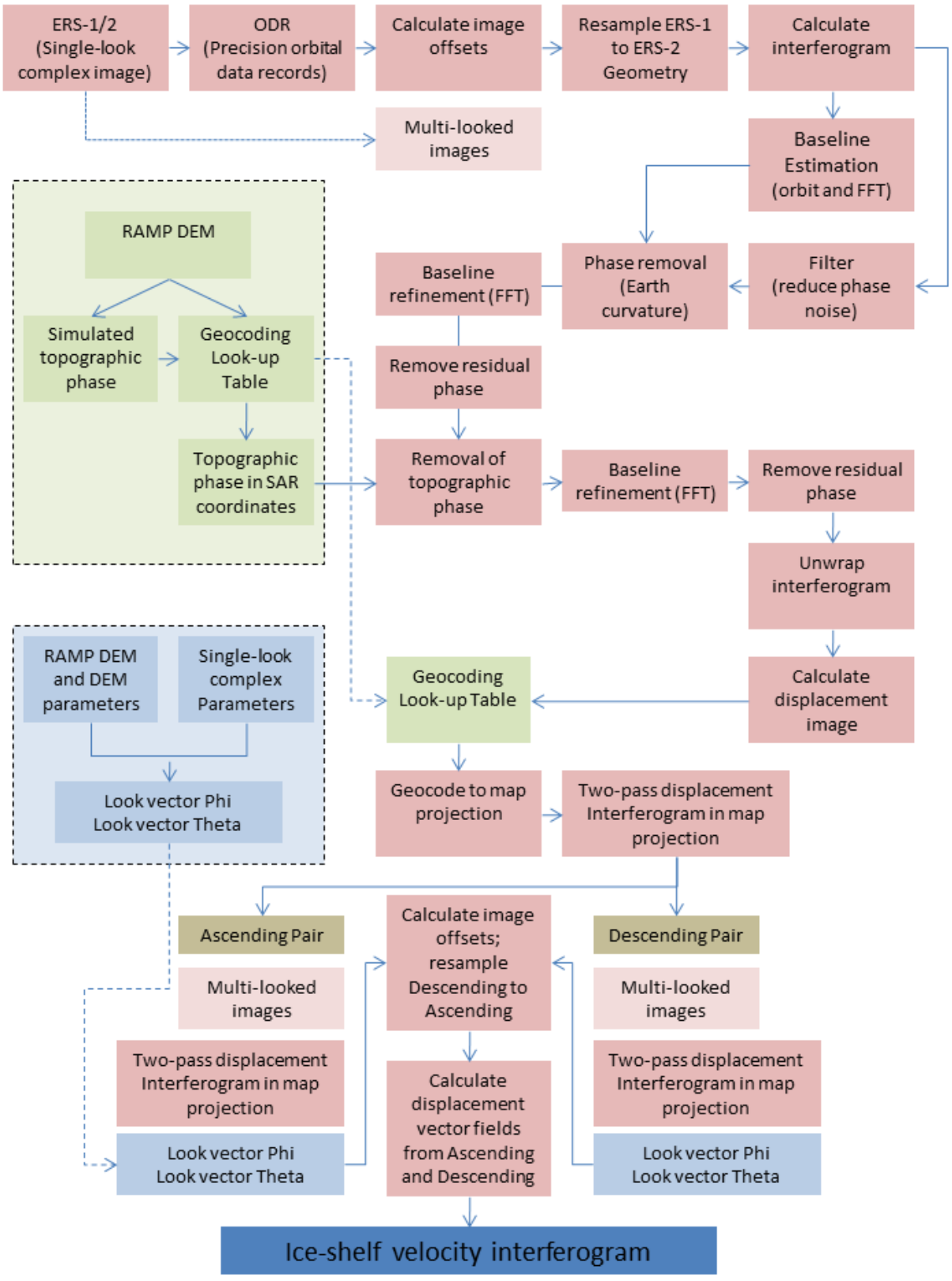

Figure 5.8. Processing steps developed for four-pass velocity-field displacement map generation.

8. Error assessment

Limitations in the available data sources (or poor coherence between image pairs) prevented a sufficient number of interferograms being produced to allow image stacking that would have reduced the errors in the InSAR velocity measurements (McMillan *et al.*, 2012). As a result, errors in the final displacement maps include those caused by tidal motion, as well as residual errors from image geometry and topographic removal. The latter two components were estimated by assessing those velocity measurements on surfaces where displacement should not occur (e.g. rock outcrop), or is likely to be negligible (i.e. an ice divide or ice ridge) (Table 5.8). The tidal error was estimated by visually assessing the interferometric fringe rate along the grounding zone of the ice shelf; one complete interferometric fringe (colour cycle) equates to 0.0028 m of vertical change. Thus by estimating the vertical tidal component in each ascending/ descending interferogram and obtaining incident angle data, the total horizontal error was estimated.

Table 5.8. Error estimation from areas of bedrock or ice divides

Ice Shelf (interferogram number)	**Maximum error (± ma^{-1})**
Bach	4.221
George VI (1)	6.214
George VI (2)	6.331
George VI (3)	5.889
George VI (4)	5.665

Each two-pass (either ascending or descending) displacement map was visually assessed for its vertical tidal component, with an estimation based on the appearance of the fringe rate around the grounding zone or around ice rises. The incidence angle from the ERS-2 scene was taken from the parameter file as the LOS displacement maps were based on the geometry of ERS-2 image. Both known parameters were thus entered into the trigonometric Equation 5.4:

$$\tan(\alpha).\, dis_V = dis_H \qquad \text{Equation 5.4}$$

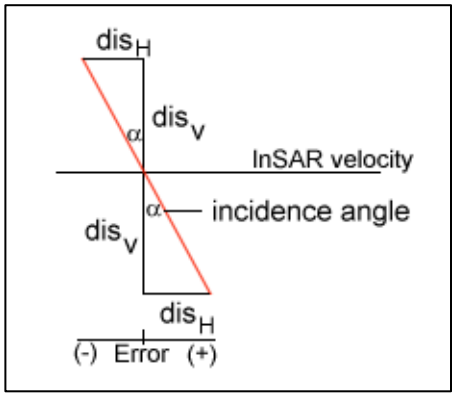

Figure 5.9. Error estimation for a single LOS interferogram. dis_V is the estimated vertical height, and α the incident angle of the ERS-2 image. dis_H was calculated (±) using Equation 5.3.

where α is the incidence angle of the ERS-2 image, dis_V is the known vertical displacement caused by tidal amplitude, estimated from the LOS displacement maps (Figure 5.9). Following the estimation of the horizontal error (±, as there is no indication whether the tide had raised or lowered), it was added to (and subtracted from) the original LOS displacement maps calculated in Step 6 (both ascending and descending). Step 7 was then repeated with the following combination of displacement maps to obtain an estimation of the maximum and minimum ice-shelf surface displacement:

1) Ascending positive error and descending positive error
2) Ascending negative error and descending negative error

The resulting tidally-induced errors for each interferogram are displayed in Table 5.9. This method of estimating horizontal error, however, relied on some assumptions to be made. First, it is assumed that the incidence angle is the same across the image. Here, the centre point incidence angle is used only, thus the error is skewed towards the edges of the interferograms; this, however, is considered to have a negligible impact on the final error estimation due to the height of the satellite's orbit in comparison to the ground swath of the image. Second, it is assumed that the tidal amplitude is linear across the ice-shelf surface, whereas in reality there may be spatial variation depending on the thickness and rheology of the ice shelf. As a result, it is assumed that the horizontal error is also linear across the surface. However, this method gives a good approximation as to the surface-velocity error calculated in the original surface-displacement maps. The maximum vector error was calculated by subtracting the original LOS displacement map from the two corrected displacement maps. The maximum tidal errors (Table 5.9) were then added to the

estimated errors caused by InSAR geometry and topographic removal and are displayed in Table 5.10.

Table 5.9. Estimation of horizontal error in InSAR derived velocity fields.

Ice shelf (interferogram number)	Ascending			Descending			Maximum vector error (± ma^{-1})
	Incidence angle (°)	Tidal motion (± m)	Horizontal error (± m)	Incidence angle (°)	Tidal motion (± m)	Horizontal error (± m)	
Bach	23.411	0.0140	0.1258	23.452	0.0070	0.1268	45.22
George VI (1)	23.386	0.0140	0.0787	23.431	0.0070	0.0512	40.68
George VI (2)	23.402	0.0140	0.0868	23.447	0.0070	0.0606	41.64
George VI (3)	23.389	0.0070	0.0401	23.435	0.0140	0.1097	42.26
George VI (4)	23.431	0.0070	0.0532	23.473	0.0070	0.0785	41.11

Table 5.10. Total error estimation of InSAR flow velocities.

Ice Shelf (interferogram number)	Maximum InSAR error (± ma^{-1})	Tidally induced error (± ma^{-1})	Total error (± m^{-1})
Bach	4.221	45.22	49.441
George VI (1)	6.214	40.68	46.894
George VI (2)	6.331	41.64	47.971
George VI (3)	5.889	42.26	48.149
George VI (4)	5.665	41.11	46.775
George VI mean	6.025	41.42	47.445

5.2.2.2 Manual feature tracking of optical imagery

Manual feature tracking was selected over automated alternatives for a number of reasons. First, automated systems perform best where there is some regularity between feature dimensions that permits the selection of effective and efficient window sizes. As the size and shape of surface features on an ice-shelf vary considerably, even within a small area, defining effective window sizes for velocity derivation was not achievable. Second, automated techniques are only capable of creating a displacement map based on two time-separated images. By conducting assessment manually, more than two images could be assessed within a given time frame over a given area, with measured displacements collated into a single displacement map. This was particularly beneficial where only partial coverage of the ice-shelf surface was available for analysis (e.g. due to cloud cover, or data gaps in Landsat ETM+ imagery caused by equipment failure). Third, automated feature tracking procedures rely on a cross-correlation of intensity (CCI) algorithm, thus where fine cloud or atmospheric haze is present, poor or no surface displacements would be derived. However, manually tracking features that are only partially visible is still achievable, at the user's discretion. Finally, whilst manually tracking surface features requires more user interaction, the computational power required is considerably less.

Optical datasets were used for feature tracking as the visual quality of the imagery is far superior to that of SAR imagery. Furthermore, by using Landsat data the temporal resolution was extended back to 1986, thus creating an approximate 25-year window to assess velocity change. In total 59 Landsat scenes were used in the feature tracking procedures, over time periods of no more than three years between image pairs. The major processing steps for manually deriving ice-shelf surface velocities, for any given time period, are described below.

1. Image coregistration

All images were acquired georeferenced and orthorectified as described in Section 5.2.1.1. Images were coregistered using the *shift* function in ArcMap 9.3, using bare ground or stable ice-covered areas as the reference point to assess accuracy. In all cases, Landsat imagery was coregistered to within 1 pixel accuracy. Mapping was carried out to an estimated accuracy of 1 pixel, thus resulting in a total inaccuracy of manual feature tracking of 2 pixels.

2. Feature selection and measurement of total displacement

Surface features were chosen based on 1) their distinctness between image pairs, and 2) their distribution across the image. Generally, fractures and rifts were tracked, although distinct pressure ridges were also used where they could be identified in both images. A polyline was drawn from the feature's starting point on image 1 to the same point on image 2. The total polyline length (i.e. distance moved) was calculated and added to the attribute table.

3. Conversion to point data, normalisation and interpolation

The centre point for each polyline was calculated and similarly added to the attribute table as *x* and *y* coordinates (in Polar Stereographic projection). The measured displacement values were subsequently exported as *x*, *y*, *z* data (where *z* contained the surface displacement between images in metres). They were then added to the GIS as a separate point data file. The displacement measurements were then converted from total displacement, to displacement in metres per annum by satisfying Equation 5.5. Normalising the measurements in this way permitted data collation between different image pairs, within the same general time period.

$$z = \frac{z_{total}}{d} . 365.25 \qquad \text{Equation 5.5}$$

where z_{total} is the measured displacement, d is the number of days between image 1 and image 2. Until this point, a separate shapefile was used for each image pair. Following normalisation of each point, they were merged into a single shapefile, representative of total displacement in ma^{-1}, for that particular time period. Next, for George VI and Stange ice shelves, the data points were interpolated using a Natural Neighbour algorithm. This was selected over other algorithms as it performs equally well with regularly and irregularly distributed data (Watson, 1992). For Bach Ice Shelf, this step was skipped, as the distribution of features tracked was poor, thus the interpolation of those points did not produce a representative output of the surface speeds. Finally, the resulting interpolated surface velocity files were clipped to the extent of the ice shelf for the respective years using the area shapefile produced for assessing the spatial extent of the individual ice shelves.

In total, nine surface-velocity files were produced, three each for the northern ice front of George VI, southern ice front of George VI and for Stange Ice Shelf. The surface speeds of Bach Ice Shelf were calculated at 12 points from 97 individual features, but not interpolated across the shelf. Table 5.11 shows the number of feature points used to interpolate surface velocities for the different time periods and locations, and Figure 5.10 illustrates these point locations.

Table 5.11. Feature tracking observation periods and number of features tracked for interpolation. Distribution shown in Figure 5.10.

Ice Shelf	Period 1 (points used)	Period 2 (points used)	Period 3 (points used)
Bach	Ca. 2007 (97)*	N/A	N/A
George VI North	Ca. 1989 (274)	Ca. 2002 (565)	Ca. 2007 (503)
George VI South	Ca. 1989 (470)	Ca. 2002 (960)	Ca. 2009 (621)
Stange	Ca. 1989 (324)	Ca. 2004 (502)	Ca. 2010 (572)

**Not interpolated; Average distance calculated at 12 cluster points.*

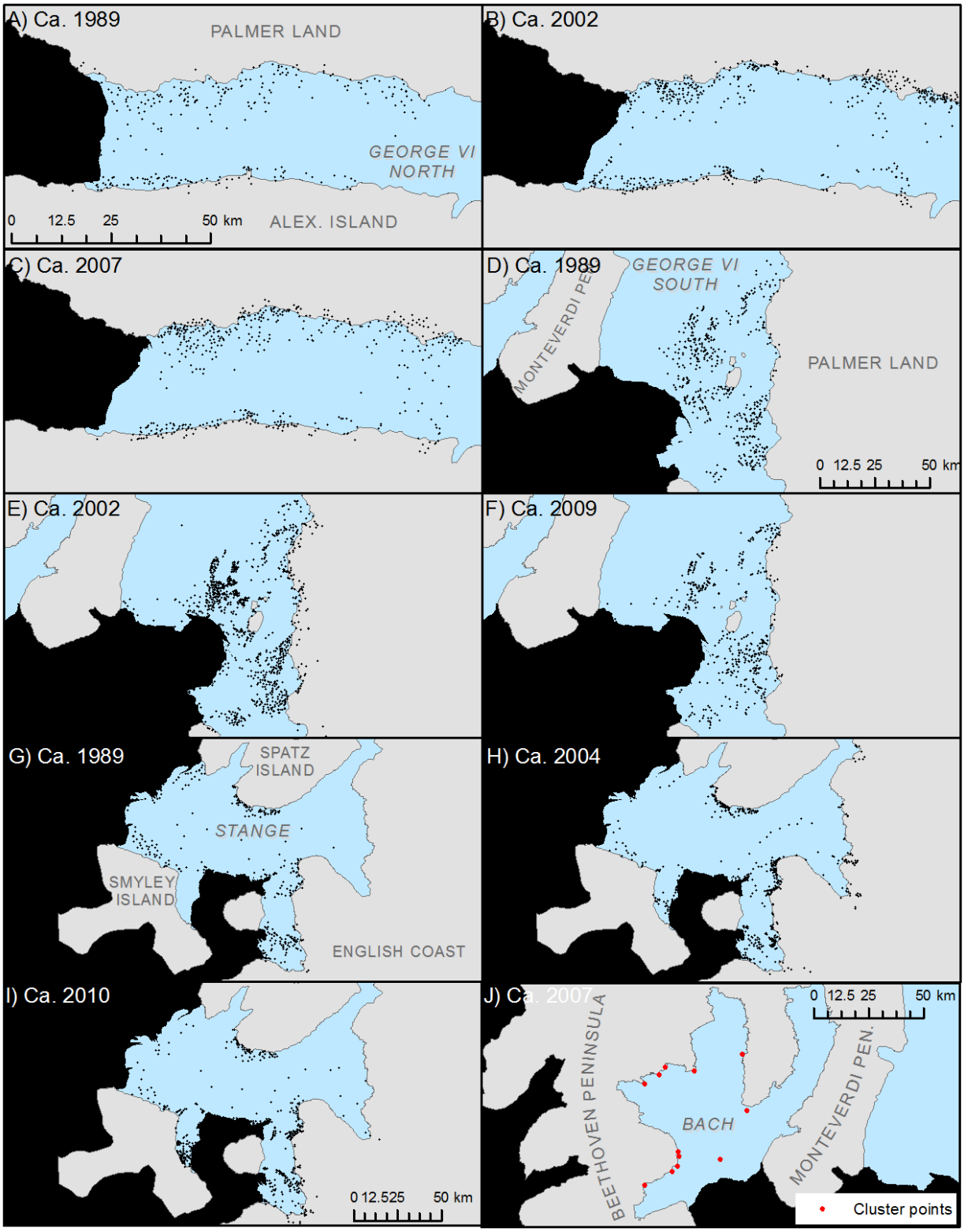

Figure 5.10. Location of tracked features for George VI North (A, B, C), George VI South (D, E, F), Stange (G, H, I) and Bach (J). Black dots (A-I) show centre point of each tracked feature used in interpolation. Red dots (J only) is the cluster point of tracked features used to assess changes in ice shelf dynamics. Also refer to Table 5.11.

Uncertainty in the resulting data is generally a function of image pixel size, coregistration accuracy, user accuracy and time delay between image pairs. Whilst InSAR errors are amplified by converting data from md^{-1} to ma^{-1}, feature tracking measurements are generally calculated over time periods of two years or more, thus the overall uncertainty (in ma^{-1}) is reduced. For each of the 10 feature tracking periods, uncertainty was calculated using Equation 5.6.

$$Uncertainty\ (ma^{-1}) = 2p.(\frac{365.25}{t2-t1}) \qquad \text{Equation 5.6}$$

where *p* is the pixel resolution and *t2-t1* is the time, in days, between image 1 and image 2. The maximum uncertainties calculated for each of the feature tracking time periods are presented in Table 5.12.

Table 5.12. Feature tracking uncertainties for each time period

Ice Shelf	Period 1 (uncertainty)	Period 2 (uncertainty)	Period 3 (uncertainty)
Bach	Ca. 2007 (± 15 m)	N/A	N/A
George VI North	Ca. 1989 (± 30 m)	Ca. 2002 (± 15 m)	Ca. 2007 (± 15 m)
George VI South	Ca. 1989 (± 30 m)	Ca. 2002 (± 15 m)	Ca. 2009 (± 15 m)
Stange	Ca. 1989 (± 30 m)	Ca. 2004 (± 15 m)	Ca. 2010 (± 15 m)

5.2.3 Ice-shelf elevation change

5.2.3.1 Overview of pre-processing methods

The ICESat GLAS data were provided in a pre-processed format by Helen Fricker and Matt Siegfried from Scripps Institution of Oceanography. Here, ICESat product GLAS12, Release 531, was acquired for Bach, George VI and Stange Ice Shelves for 28 separate tracks from October 2003 to December 2008, over 16 individual acquisition periods (see Table 3.4). Release 531 contains automatically removed tidal data from the GOT99.2 global-ocean tidal model (Fricker and Padman, 2006). Since the ice-shelf analysis required accurate, tide-corrected elevation measurements, the data were initially "retided". Essentially, the predicted tidal amplitudes were added back using the GOT99.2 model (Fricker and Padman 2006), then converted to a WGS84 ellipsoid. A more accurate tidal model was then used to remove the effects of vertical tidal motion (model CATS2008a), following the methods outlined in Padman *et al.* (2002) and King and Padman (2005). Data were also corrected for the inverse barometer effect (IBE, Brunt *et al.*, 2010) and inter-campaign biases (Siegfried *et al.*, 2011). After these steps, data from laser campaigns

affected by clouds were removed by inspecting gain and return energy values on a track-by-track basis. Finally the ICESat points were resampled from each individual track to an interpolated reference track (Brunt *et al*, 2010), which allowed for repeat-track analysis.

As the ICESat elevation measurements were only being assessed against other ICESat measurements, the absolute accuracy of the ICESat data is inconsequential. The precision of the data, however, was determined by examining crossover points on the ice-shelf surfaces. Using all available data and iteratively removing outliers (following the methods of Brenner *et al.*, 2007), a precision of 15.3 cm (1 standard deviation, n=30) was obtained. This value is slightly greater than the calculated precision of ICESat data from early campaigns (e.g. Shuman *et al.*, 2006), which is expected as the precision over ice shelves accounts for instrumental uncertainty as well as uncertainty in the IBE, tide, and inter-campaign bias corrections.

5.2.3.2 ICESat elevation assessment

Following the pre-processing of the ICESat data, each track was converted to a Polar Stereographic projection to match other datasets in this study, and then subset to the ice-shelf area in hydrostatic equilibrium using the extents calculated by Brunt *et al.* (2010). This was carried out to ensure that any surface elevation changes reflected changes in the ice-shelf thickness from either surface or basal accumulation/ablation. Next, ICESat data were further culled, removing any points potentially affected by the motion of ice-shelf surface undulations (i.e. fractures, rifts, pressure ridges, longitudinal structures) so that the resulting surface elevation changes reflected a true elevation change rather than a change in position of surface structure. This process was similarly undertaken by Horgan *et al.* (2011), although instead of manually removing data, here the structural maps for ca. 2003 and ca. 2010 were used to automatically select and remove the elevation points in ArcMap within 100 m of any distinct surface feature.

Finally, surface elevation changes were calculated between comparable campaigns (i.e. on 12-monthly timescales or multiples of) to avoid elevation changes caused by short-term ablation and/or accumulation. The campaigns that offered the best spatial and temporal resolution for each individual track were selected, and whilst inter-campaign elevations were not used in the final elevation-change assessments, a sub-decadal record of surface elevation changes was consequently obtained.

5.2.3.3 Thickness change estimation from ICESat data

To gain a better understanding of the vertical changes within each ice shelf, thickness changes were calculated along each ICESat GLAS track using the surface elevation change measurements. In order to calculate ice thickness, the terms of Equation 5.7 were satisfied following the procedures of Braun *et al.* (2009).

$$H = \frac{\rho_{sw}}{(\rho_{sw} - \bar{\rho}_{ice})} \times h \qquad \text{Equation 5.7}$$

where ρ_{sw} is the density of sea water through a vertical column, $\bar{\rho}_{ice}$ is the mean density of ice through a vertical column and *h* is the measured surface elevation. Because ice shelves are made up of both meteoric ice and marine ice that differ in thickness and distribution (Bentley *et al.*, 1979; Bamber and Bentley, 1994; Fricker *et al.*, 2001; Joughin and Vaughan, 2004), an approximation was made in order for the term $\bar{\rho}_{ice}$ to be satisfied. Elsewhere, this has been derived by averaging the density of measured marine ice with measured meteoric ice (Fricker *et al.*, 2001; Braun *et al.*, 2009), but due to the lack of empirical data for either ice densities on all three ice shelves considered here, estimations are made based on previous studies in the Antarctic Peninsula. Doake (1984) determined the ice density in areas of surface melt on George VI Ice Shelf to be 915 kg m^{-3} and 884 kg m^{-3} in areas without surface melt and Zotikov *et al.* (1980) found the density of marine ice to be 927 kg m^{-3}. Therefore, $\bar{\rho}_{ice}$ is assumed to have a mean density of 913.25 kg m^{-3} (Equation 5.8).

$$\bar{\rho}_{ice} = \frac{\left(\left(\frac{(\rho_{met1} + \rho_{met2})}{n}\right) + \rho_{mar}\right)}{n} \qquad \text{Equation 5.8}$$

where ρ_{met1} is and ρ_{met2} represent densities of ice under surface melting and non-surface melting conditions, and ρ_{mar} is the generalised density for marine ice. Under average conditions, the density of sea water is calculated as 1027 kg m^{-3} (Griggs and Bamber, 2011) but as temperature decreases, water density increases, and conversely, as salinity decreases, water density increases. Elsewhere, a density of 1024 kg m^{-3} has been measured under the Ross Ice Shelf (Bamber and Bentley, 1994), whereas Fricker *et al.*, (2001) use a density of 1029 kg m^{-3} under the Amery Ice Shelf. Because direct measurements are not available for Bach, George VI or Stange Ice Shelves, a ρ_{sw} value of 1027 kg m^{-3} was used following the guidance of Griggs and Bamber (2011). Furthermore, because surface-elevation change has already been calculated, thickness change (ΔH) was estimated by

substituting ice-shelf elevation (*h*; Equation 5.7) with surface-elevation change ($h_2 - h_1$; Equation 5.8).

$$\Delta H = \frac{\rho_{sw}}{(\rho_{sw} - \overline{\rho}_{ice})} \times (h_2 - h_1) \qquad \text{Equation 5.8}$$

where h_2 and h_1 represent the most recent and earliest surface elevation measurement respectively. Thickness change estimates are discussed in the interpretation sections of Chapter 6, 7 and 8 for Bach, George VI and Stange Ice Shelves respectively.

5.3 Chapter Summary

Table 5.13 summarises the datasets created in this study. In Chapter 6, Chapter 7 and Chapter 8, these are analysed and interpreted for Bach, George VI and Stange Ice Shelves respectively. Table 5.14 and Table 5.15 illustrate the imaging datasets used in this study, and provides an overview of their key uses.

Table 5.13. Datasets produced for each ice shelf as discussed in Chapter 6, Chapter 7 and Chapter 8.

Ice Shelf	Full/partial structural assessment.	Spatial assessment	Meltwater assessment	Surface velocities	Surface-elevation change
Bach	1973, 1978, 1986, 1997, 2003, 2004, 2005, 2009	1973, 1978, 1989, 1996, 2003, 2011	1978, 1997, 2007, 2009	Ca. 1995, ca. 2007	October 2003-October 2008
George VI North/ Central	1974, 1979, 1986, 1996, 2001, 2010	1974, 1979, 1989, 1996, 2001, 2010	1973, 1986, 2003, 2010	Ca. 1989, ca. 1995, ca. 2002, ca. 2007	October 2003-October 2008
George VI South	19763, 1986, 1991, 2003, 2010	1973, 1986, 1991, 1996, 2003, 2010	N/A	Ca. 1989, ca. 1995, ca. 2002, ca. 2009	October 2003-October 2008
Stange	1973, 1986, 2001, 2005, 2011	1973, 1986, 1996, 2001, 2005, 2011	N/A	Ca. 1989, Ca. 2002, Ca. 2009	May 2004 – October 2007

Table 5.14. List of optical satellite images and their key uses. F = Full glaciological mapping assessment, P = partial assessment, S = spatial assessment, M = meltwater assessment, V = visual assessment only, and T = used in surface feature tracking. See Figure 5.11 for path and row locations.

Ice shelf	Sensor	Scene ID	Date (dd/mm/yyy)	Path	Row	Scene centre (Lat/ Long (°))		F	P	S	M	V	T
Bach	MSS	LM1233111007302910	29/01/1973	233	111	-71.713	-72.037	✓		✓	✓		
	MSS	LM3233111007836310	29/12/1978	233	111	-71.850	-72.237	✓		✓			
	MSS	LM5219111_11119841206	06/12/1984	219	111	-73.098	-72.223					✓	
	TM	LT5220111_11119860218	18/02/1986	220	111	-74.373	-72.218		✓			✓	
	TM	LT4219111008933050	26/11/1989	219	111	-72.218	-73.019			✓			
	TM	L5219111_11119970209	09/02/1997	219	111	-73.325	-72.169		✓		✓		
	ETM+	L71219111_11120011229	29/12/2001	219	111	-73.156	-72.222					✓	
	ETM+	LE7218111000304250	11/02/2003	218	111	-72.195	-71.558	✓		✓			
	ETM+	L71218111_11120040317	17/03/2004	218	111	-72.145	-71.655		✓				
	ASTER	AST_05010813224305011806O9	08/01/2005	219	111	-71.817	-72.981		✓				✓
	ETM+	L71219111_11120050311	11/03/2005	219	111	-73.158	-72.222	✓		✓			✓
	ETM+	L71218111_11120071223	23/12/2007	218	111	-71.383	-72.193						✓
	ETM+	L71218111_11120091110	10/11/2009	218	111	-71.637	-72.215		✓		✓		✓
	ETM+	L71219111_11120110123	23/01/2011	219	111	-73.003	-72.244			✓			
George VI	MSS	LM1231110007300910	09/01/1973	231	110	-70.759	-67.369	✓		✓	✓		
	MSS	LM1231111007300910	09/01/1973	231	111	-72.017	-69.683	✓		✓	✓		
	MSS	LM1231112007300910	09/01/1973	231	112	-73.245	-72.311	✓		✓			
	MSS	LM12331091974006AAA04	06/01/1974	233	109	-69.381	-68.182	✓		✓			

	MSS	LM32331101979034AAA04	03/02/1979	233	110	-70.647	-70.199	✓		✓			
	MSS	LM52171101985057AAA03	26/02/1985	217	110	-70.953	-67.891				✓		
	MSS	LM52171121986076AAA03	17/03/1986	217	112	-73.516	-72.198		✓	✓			✓
	TM	L5217110_11019860128	28/01/1986	217	110	-67.696	-70.914						✓
	TM	L4219109_10919880225	25/02/1988	219	109	-69.140	-69.567						✓
	TM	LT42191121989010XXX02	10/01/1989	219	112	-73.475	-75.568						✓
	TM	L4218110_11019890220	20/02/1989	218	110	-69.393	-70.896						✓
	TM	LT42171121989060XXX02	01/03/1989	217	112	-73.488	-72.537						✓
	TM	LT42181091989083XXX02	24/03/1989	218	109	-69.650	-67.469	✓		✓			✓
	TM	L4219109_10919891126	26/11/1989	219	109	-69.019	-69.646						✓
	TM	L4217110_11019900115	15/01/1990	217	110	-67.693	-70.926						✓
	TM	LT42191091990029XXX01	29/01/1990	219	109	-69.657	-69.024						✓
	TM	LT52191091991024XXX02	24/01/1991	219	109	-69.588	-69.167						✓
	TM	LT52161101991035XXX03	04/02/1991	216	110	-70.927	-66.516				✓		
	TM	LT52161111991035XXX03	04/02/1991	216	111	-72.191	-68.582				✓		
	TM	LT52161121991035XXX03	04/02/1991	216	112	-73.473	-70.867	✓		✓			✓
	TM	L5218110_11019910218	18/02/1991	218	110	-69.457	-70.872						✓
	TM	LT42171121989060XXX02	01/03/1989	217	112	-73.488	-72.537						✓
	ETM+	L71217112_11220000228	28/02/2000	217	112	-72.317	-73.505						✓
	ETM+	L71218109_10920010104	04/01/2001	218	109	-67.424	-69.626	✓		✓			✓
	ETM+	L71217110_11020010214	14/02/2001	217	110	-67.800	-70.965						✓
	ETM+	L71217110_11020011129	29/11/2001	217	110	-67.895	-70.949						✓
	ETM+	L71218110_11020011206	06/12/2001	218	110	-69.453	-70.925						✓
	ETM+	L71218110_11020020107	07/01/2002	218	110	-74.034	-73.472						✓
	ETM+	L71218112_11220020107	07/01/2002	218	112	-73.974	-73.499						✓

	ETM+	L71217110_11020021202	02/12/2002	217	110	-67.834	-70.958						✓
	ETM+	L71218110_11020021225	25/12/2002	218	110	-69.357	-70.933						✓
	ETM+	L71217112_11220030103	03/01/2003	217	112	-72.544	-73.463						✓
	ETM+	L71218110_11020030110	10/01/2003	218	110	-72.554	-73.354						✓
	ETM+	LE72181122003042EDC00	11/02/2003	218	112	-73.488	-74.155		✓				
	ETM+	LE72161122003012EDC00	12/01/2003	216	112	-73.473	-70.867	✓		✓			
	ETM+	LE72161112003012EDC00	12/01/2003	216	111	-72.191	-68.582	✓			✓		
	ETM+	LE72161102003044EDC01	13/02/2003	216	110	-70.947	-66.287	✓		✓	✓		
	ASTER	AST030126133017030212079 9	26/01/2003	216	111	-71.154	-67.434				✓	✓	
	ASTER	AST030126133026030212080 0	26/01/2003	216	111	-71.641	-68.159				✓	✓	
	ASTER	AST030126133035030212080 1	26/01/2003	216	111	-72.126	-68.919				✓	✓	
	ETM+	L72218110_11020040317	17/03/2004	218	110	-70.958	-69.385						✓
	ETM+	L72218110_11020050115	15/01/2005	218	110	-70.828	-69.400						✓
	ETM+	L72218110_11020060118	18/01/2006	218	110	-70.859	-69.391						✓
	ETM+	L72218110_11020080108	08/01/2008	218	110	-70.888	-69.355						✓
	ETM+	L72219112_11220081114	14/11/2008	219	112	-73.405	-75.721						✓
	ETM+	L72218110_11020090211	11/02/2009	218	110	-70.946	-69.379						✓
	ETM+	L72218109_10920091110	10/11/2009	218	109	-69.639	-67.507						✓
	ETM+	L72217110_11220100106	06/01/2010	217	110	-67.938	-70.871		✓	✓			✓
	ETM+	L72217112_11220100106	06/01/2010	217	112	-73.462	-72.415		✓				✓
	ETM+	L71218111_11120100113	13/01/2010	218	111	-71.557	-72.174		✓				✓
	ETM+	L71216111_11120100115	15/01/2010	216	111	-72.191	-68.582	✓		✓	✓		
	ETM+	L72216112_11220100115	15/01/2010	216	112	-73.494	-71.060	✓		✓			✓
	ETM+	L72218109_10920100129	29/01/2010	218	109	-69.641	-67.488						✓
	ETM+	L72218110_11020100129	29/01/2010	218	110	-70.822	-69.485	✓		✓	✓		✓

	ETM+	L72218112_11220100129	29/01/2010	218	112	-73.488	-74.155	✓					✓
	ETM+	L72216112_11220101201	01/02/2010	216	112	-73.522	-71.101	✓		✓			✓
	ETM+	L72218112_11220120307	07/03/2012	218	112	-73.992	-73.445					✓	
Stange	MSS	L1233113_11319730129	29/01/1973	233	113	-77.847	-74.051	✓		✓			
	MSS	L1233112_11219730129	29/01/1973	233	112	-75.036	-72.85	✓		✓			
	TM	L5220112_11219860218	18/02/1986	220	112	-76.856	-73.461	✓		✓			✓
	TM	L5220111_11119860218	18/02/1986	220	111	-74.518	-72.233	✓		✓			✓
	TM	L5220112_11219860306	06/03/1986	220	112	-76.931	-73.470	✓		✓			✓
	TM	L4219112_11219890126	26/01/1989	219	112	-75.574	-73.441						✓
	TM	L4219112_11219891212	12/12/1989	219	112	-75.520	-73.455						✓
	ETM+	L72220112_11220010102	02/01/2001	220	112	-76.96	-73.383	✓		✓			✓
	ETM+	L72219112_11220011127	27/11/2001	219	112	-75.667	-73.454	✓		✓			✓
	ETM+	L72220112_11220011220	20/12/2001	220	112	-77.260	-73.450	✓		✓			✓
	ETM+	L72220112_11220040315	15/03/2004	220	112	-77.130	-73.430		✓				✓
	ETM+	L72221112_11220050205	05/02/2005	221	112	-77.122	-73.299	✓		✓			
	ETM+	L72219112_11220051208	08/12/2005	219	112	-75.667	-73.454	✓		✓			
Stange	ETM+	L72220112_11220060116	16/01/2006	220	112	-77.075	-73.421		✓				
	ETM+	L72220112_11220070103	03/01/2007	220	112	-76.961	-73.402		✓				
	ETM+	L72220112_11220080122	22/01/2008	220	112	-76.955	-73.344		✓				✓
	ETM+	L72220112_11220081207	07/12/2008	220	112	-76.877	-73.377		✓				✓
	ETM+	L72221112_11220091115	15/11/2009	221	112	-77.122	-73.299		✓				✓

	ETM+	L72220112_11220110114	14/01/2011	220	112	-76.967	-73.403	✓		✓			✓
	ETM+	L72219112_11220110208	08/02/2011	219	112	-77.075	-73.421	✓		✓			✓

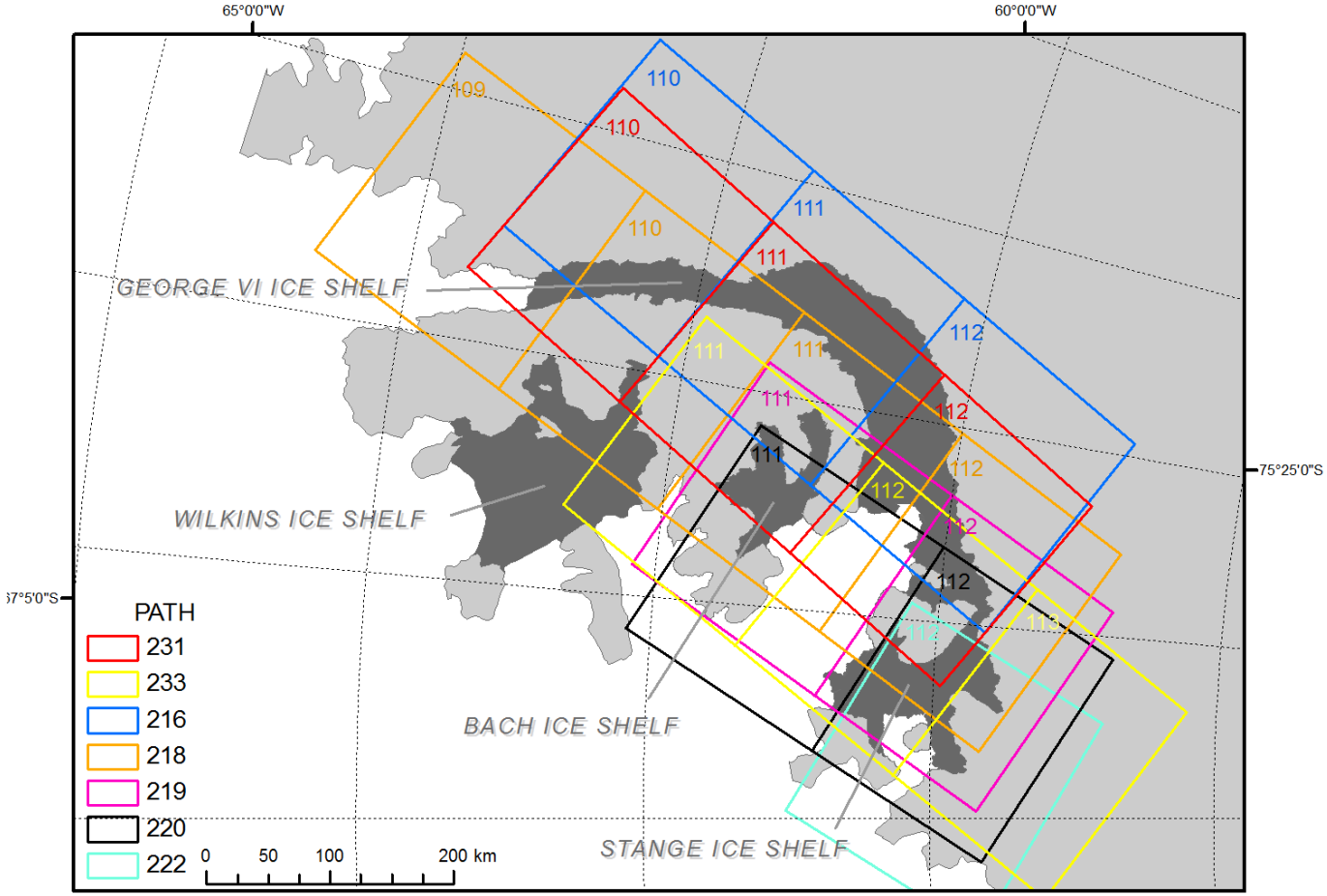

Figure 5.11. Position of each Landsat path and row number, as presented in Table 5.14.

Table 5.15. List of all SAR images used in this study. P = partial assessment, S = spatial assessment, V = visual assessment only, M = meltwater assessment and I = scenes used in InSAR processing. A/D = Ascending or Descending satellite pass. Image pairs, and four-pass interferogram files colour coded accordingly.

Ice shelf	Sensor	Orbit (A/D)	Frame	Date	Scene Centre (Lat Long (°))		P	S	V	M	I
Bach	ERS-1 SAR	24012 A	5677	17/02/1996	-72.165	287.602					✓
	ERS-2 SAR	04339 A	5677	18/02/1996	-72.131	287.505	✓	✓			✓
	ERS-1 SAR	22413 D	5114	28/10/1995	-71.983	287.268					✓
	ERS-2 SAR	02740 D	5114	29/10/1995	-71.987	287.260					✓
	Envisat ASAR	25986 D	9869	18/02/2007	-72.067	-72.748			✓	✓	
George VI	ERS-2 SAR	03924 A	5651	20/01/1996	-73.125	289.613	✓		✓		
	ERS-1 SAR	24155 A	5667	27/2/1996	-72.509	292.154					✓
	ERS-2 SAR	04482 A	5667	28/2/1996	-72.520	292.178					✓
	ERS-1 SAR	24245 D	5127	04/03/1996	-72.455	291.720					✓
	ERS-2 SAR	04572 D	5127	05/03/1996	-72.489	291.630					✓
	ERS-1 SAR	22337 A	5682	23/10/1995	-71.947	292.757					✓
	ERS-2 SAR	02664 A	5680	24/10/1995	-72.015	292.933					✓
	ERS-1 SAR	24245 D	5117	04/03/1996	-72.057	292.824					✓
	ERS-2 SAR	04572 D	5117	05/03/1996	-72.096	292.728					✓
	ERS-1 SAR	22523 A	5705	05/11/1995	-71.036	292.605					✓
	ERS-2 SAR	02850 A	5705	06/11/1995	-71.044	292.627					✓
	ERS-1 SAR	24102 D	5089	23/02/1996	-70.969	291.986					✓
	ERS-2 SAR	04429 D	5089	24/02/1996	-71.005	291.909					✓

Table 5.15. Continued. List of all SAR images used in this study. P = partial assessment, S = spatial assessment, V = visual assessment only, M = meltwater assessment and I = scenes used in InSAR processing. A/D = Ascending or Descending satellite pass. Image pairs, and four-pass interferogram files colour coded accordingly.

Ice shelf	Sensor	Orbit (A/D)	Frame	Date	Scene Centre (Lat Long (°))		P	S	V	M	I
	ERS-1 SAR	23983 A	5729	15/02/1996	-70.067	291.906					✓
	ERS-2 SAR	04310 A	5729	16/02/1996	-70.071	291.909	✓	✓			✓
	ERS-1 SAR	22413 D	5096	28/10/1995	-70.145	291.656					✓
	ERS-2 SAR	02740 D	5096	29/10/1995	-70.189	291.564					✓
	ERS-2 SAR	78033 D	5140	24/03/2010	-72.903	288.321	✓	✓			
Stange	ERS-2 SAR	04282 A	5655	14/02/1996	-72.955	283.462	✓	✓			

Chapter 6

Bach Ice Shelf

Chapter Overview

Chapter 6 comprises two sections. Section 6.1 presents the results derived through the spatial, structural and dynamic assessments of Bach Ice Shelf, focussing on the flow regimes, changes in ice-shelf extent, structural configuration and structural evolution. Ice-shelf surface elevation changes are also presented. Following this, Section 6.2 includes a detailed interpretation of the results presented in Section 6.1. An assessment of the spatial and structural changes is made, with thickness changes inferred using the surface-elevation measurements. These interpretations are specific to the glaciological regimes of Bach Ice Shelf, and are considered in a wider context in Chapter 9.

6.1 Bach Ice shelf Results

In this section, the dynamic regimes of Bach Ice Shelf are discussed, with a comparison made between InSAR surface velocities from 1995/96 (ca. 1996) and manual feature tracking surface velocities from 2005 to 2009 (ca. 2007). Furthermore, ice frontal recession and associated areal extents of the whole ice shelf are presented, followed by a detailed structural overview. Changes in surface structures, features and surface meltwater are then presented over various time periods from 1973 to 2011. Finally, ICESat GLAS elevation change measurements calculated from repeat-track data are presented and described. Figure 6.1 illustrates the general morphology of Bach Ice Shelf, its principal tributary glaciers and key locations as referred to in the following subsections.

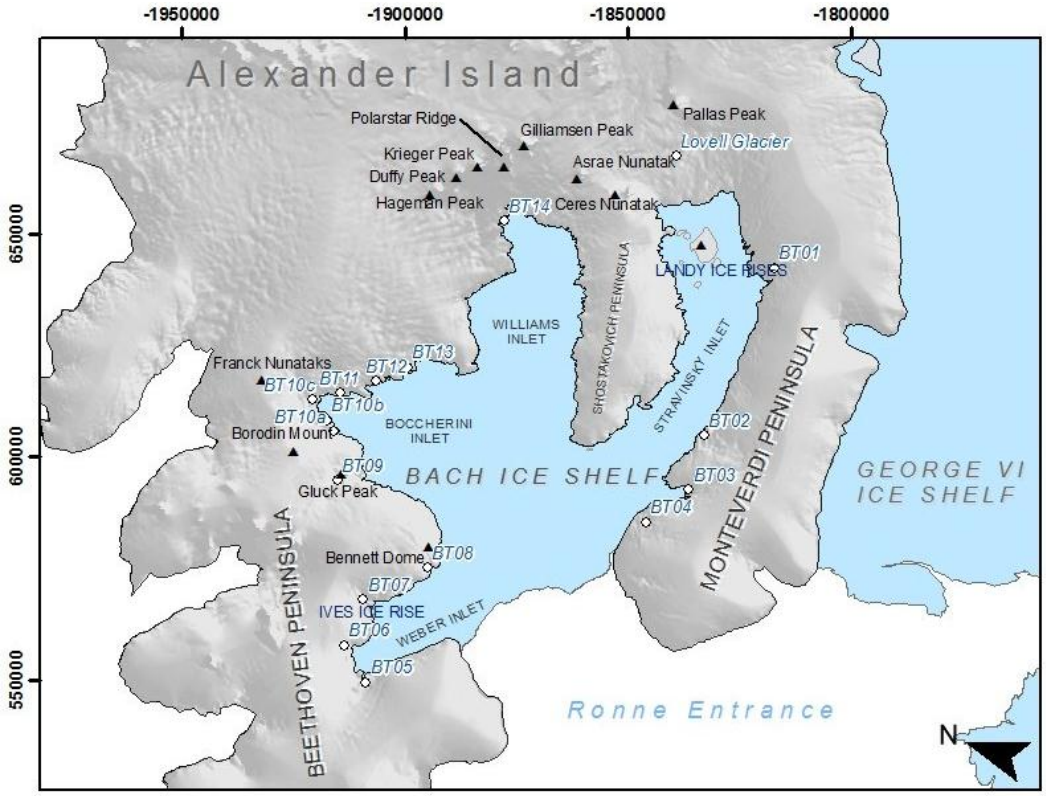

Figure 6.1 Bach Ice Shelf overview. Note the four ice domains (inlets) of Bach Ice Shelf that feed into a central zone towards the ice front, towards Ronne Entrance. Fifteen key tributary systems were observed from visual analysis of Landsat and ERS satellite imagery. Location names were obtained from the APC with the exception of unnamed tributary glaciers that were labelled sequentially from BT01 to BT14.

6.1.1 Surface Velocities

6.1.1.1 InSAR velocity fields and surface speeds

Surface speeds were calculated for Bach Ice Shelf using two pairs of ERS-1/2 24-hour separated SAR SLCs for 1995/96. One interferogram was calculated in the ascending-look direction, with a further interferogram calculated in the descending-look direction. The two interferograms were then used to construct a surface displacement map (Figure 6.2), as described in Chapter 5.

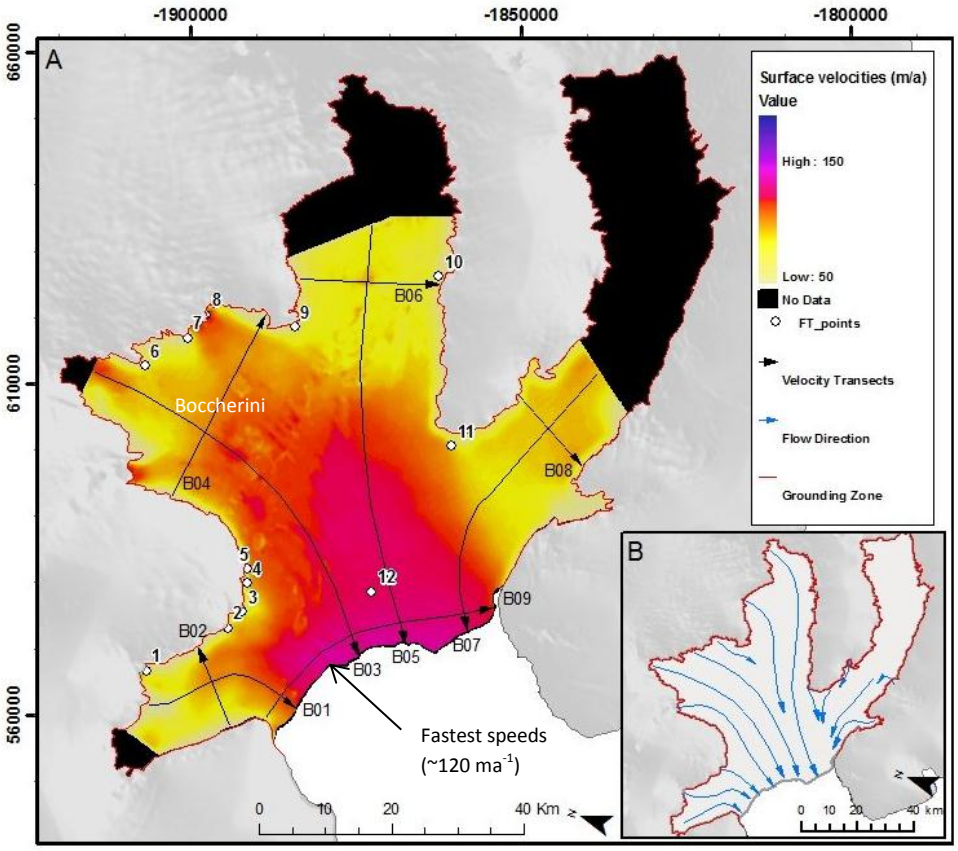

Figure 6.2. A) InSAR surface velocities (ma^{-1}) (ca. 1996) and feature tracking (FT_points) point locations calculated and displayed in Table 6.2. There is a clear increase in surface velocities from the grounding zone towards the ice front to a maximum approximately 120 ma^{-1}. Direction of transect arrow corresponds to X-axis direction in Figure 6.3. Insert (B) illustrates flow directions inferred from InSAR velocity fields.

Circa 1996, flow into Bach Ice Shelf occurred through 15 distinct tributary glaciers and through slow-moving sheet-flow along the length of the grounding zone (Figure 6.1). Greatest flow speeds were calculated in the central portions of the ice shelf, increasing towards the ice front. Ice flowing from the Boccherini Ice Domain is the most dominant on the overall flow dynamics of Bach Ice Shelf. The basic flow speed statistics described in the following section are presented in Table 6.1.

Table 6.1. Transect statistics for InSAR (ca. 1996) surface velocity calculations. Transect locations displayed in Figure 6.2 (L= Longitudinal, T= Transverse) and plots provided in Appendix 1a.

Transect	Locations	Minimum (ma^{-1})	Maximum (ma^{-1})	Mean (ma^{-1})
B01	Weber (L)	29.00	96.24	81.10
B02	Weber (T)	36.76	87.74	76.31
B03	Boccherini (L)	79.24	111.12	95.34
B04	Boccherini (T)	39.17	91.08	81.55
B05	Williams (L)	43.08	110.54	92.07
B06	Williams (T)	54.16	84.55	73.45
B07	Stravinsky (L)	75.40	106.72	87.15
B08	Stravinsky (T)	57.70	84.29	78.91
B09	Ice front (T)	71.88	112.33	104.49

The Weber Ice Domain was characterised by four principal flow units that crossed the grounding zone and merged into a single cohesive flow unit as ice migrated towards the ice front, at average speeds of 81.1 ma^{-1}. Flow speed increased with distance from the grounding zone, both longitudinally and transversely across Weber Ice Domain. The maximum velocities were calculated at the ice front (96.24 ma^{-1}).

Five main tributary glaciers fed the Boccherini Ice Domain (BT09-BT13). Flow speeds initially decrease from the grounding zone for up to 10 km, before gradually increasing through its centreline to the ice front, where a maximum speed of 111.12 ma^{-1} was recorded. There is a notable increase in surface velocities transversely across Boccherini Ice Domain, from ~30 ma^{-1} within 5 km at both grounding zones to speeds in excess of 90 ma^{-1} calculated over much of the ice domain (Figure 6.2).

The principal tributary glaciers feeding Williams Ice Domain enter Bach Ice Shelf east of the maximum extent of the interferogram thus transects and statistics are only representative of a portion of the area. Calculated flow speeds in the centre suggested cohesive flow dynamics, with an average of 92.05 ma^{-1} and a maximum speed at the ice front (110.54 ma^{-1}; Table 6.1). Speeds calculated transversely across the Williams Ice Domain indicated the maximum is along the centreline (84.55 ma^{-1}), decreasing to approximately 55 ma^{-1} towards both grounding zones.

Limitations in the available datasets prevented vector calculations from being made in the eastern-most parts of Stravinsky Ice Domain. Nevertheless, visual inspection of Landsat imagery, coupled with line-of-sight InSAR, suggests that Lovell Glacier is the principal contributor to the Stravinsky Ice Domain, but flow from this is forced around the Landy Ice Rises that limit its spatial impact. Absolute flow speeds calculated through InSAR towards the lower regions of Stravinsky Ice Domain gave average speeds of 87.15 ma^{-1}

along the centreline, before gradually increasing to a maximum of 106.72 ma^{-1} as it merged with ice from the Williams Ice Domain towards the ice front. Little variance in flow speeds is calculated across the narrow channel of Stravinsky Ice Domain. Along the ice front, flow speed increases from 71.88 ma^{-1} at the Beethoven Peninsula grounding zone to 102.14 ma^{-1} at Monteverdi Peninsula, with maximum speeds of 112.33 ma^{-1} recorded ~10 km along the transect.

6.1.1.2 Feature tracking surface velocities

To assess any changes in surface speeds over time, manual feature tracking was performed in 12 different locations across the surface of Bach Ice Shelf (Figure 6.2). In total, 97 individual features were tracked between 2005 and 2007, and 2007 and 2009 (ca. 2007). Measured surface displacements were averaged at each location and the respective centre point at each cluster of measurements was used as the location for comparison between ca. 2007 feature-tracking speed estimates to ca. 1996 InSAR velocities. Table 6.2 compares surface speeds calculated at the same geographic locations for InSAR and feature tracking.

Table 6.2. Surface velocity comparisons for InSAR (ca. 1996) and feature tracking (ca. 2007). Uncertainty given in brackets (as discussed in Chapter 5). All data extrapolated to metres per annum to allow direct comparison.

Point	InSAR ca. 1996 (ma^{-1})	Feature Tracking ca. 2007 (ma^{-1})	Change (ma^{-1})
1	68.12 (± 50)	72.52 (± 15)	4.40 (± 52.20)
2	50.25 (± 50)	56.12 (± 15)	5.87 (± 52.20)
3	63.30 (± 50)	75.65 (± 15)	12.35 (± 52.20)
4	69.06 (± 50)	63.25 (± 15)	-5.81 (± 52.20)
5	69.12 (± 50)	68.20 (± 15)	-0.92 (± 52.20)
6	68.34 (± 50)	69.78 (± 15)	1.44 (± 52.20)
7	50.89 (± 50)	62.36 (± 15)	11.47 (± 52.20)
8	96.25 (± 50)	85.69 (± 15)	-10.56 (± 52.20)
9	55.74 (± 50)	68.68 (± 15)	12.94 (± 52.20)
10	60.01 (± 50)	69.35 (± 15)	9.34 (± 52.20)
11	77.02 (± 50)	86.58 (± 15)	9.56 (± 52.20)
12	104.54 (± 50)	110.35 (± 15)	5.81 (± 52.20)

Although an increase in speed has been calculated at nine of the 12 feature tracking points, there are no changes in surface velocities that exceed the calculated uncertainty in the data, thus suggesting that there have been no significant velocity changes on Bach Ice Shelf between ca. 1996 and ca. 2007. The largest observed change occurred at Point 9 at the confluence between ice flow from Boccherini Ice Domain and Williams Ice Domain, with a similar increase observed at Point 3 at the confluence of Weber Ice Domain and Boccherini Ice Domain. The largest reduction of surface speed has been calculated at Point

8, at the input of BT13 into Bach Ice Shelf. Surface speeds in the centre of the ice shelf (Point 12, Figure 6.2) increased by 5.81 ma^{-1}.

6.1.2 Bach Ice Shelf spatial extent

The areal extent of Bach Ice Shelf has been calculated for seven individual years between 1973 and 2011 using Landsat and ERS-2 SAR imagery (Table 6.3, Figure 6.3, Table 6.4). Between 1973 and 2011, Bach Ice Shelf underwent a net change of -359.95 km^2 (-7.35% of the original 1973 extent) from its frontal position through regular calving events. The distinct shape of the ice front is mostly maintained, with ice continuing to protrude beyond its respective pinning points in the regions fed by Williams and Stravinsky ice domains (Figure 6.4). Conversely, the western portion of the ice front fed by Weber and Boccherini ice domains became increasingly concave as it retreated back upstream. Table 6.4 gives a detailed description of frontal change and ice shelf areal extent over the observation periods.

Table 6.3. Areal calculations and spatial changes of Bach Ice Shelf 1973-2011. Rate of loss calculated based on number of dates between images and extrapolated to $km^2 a^{-1}$. Data presented in Figure 6.3.

Year	Ice Shelf Area (km^2)	Retreat (km^2)	Advance (km^2)	Net change (km^2)	Rate of advance/ retreat (km^2a^{-1})	% Loss from 1973 extent	% Remaining of 1973 extent
1973	4896.63	N/A	N/A	N/A	N/A	0.00	100.00
1978	4823.89	72.74	0.00	-72.74	-12.30	1.49	98.51
1989	4765.05	58.84	0.28	-58.56	-5.91	2.69	97.31
1995	4688.78	76.27	0.00	-76.27	-12.84	4.24	95.76
2003	4585.78	103.00	0.00	-103.00	-14.17	6.35	93.65
2005	4568.84	19.17	2.23	-16.94	-8.15	6.69	93.31
2011	4536.68	33.06	0.90	-32.16	-5.48	7.35	92.65

The largest areal loss occurred between November 1995 and February 2003 with a total change of -103 km^2 measured, yet the rate of retreat remained relatively steady throughout the whole observation period. Only small advances were observed between December 1978 and November 1989, and March 2005 and January 2011, 0.28 km^2 and 0.9 km^2 of advance were measured respectively. The greatest advance occurred between March 2003 and March 2005, where an advance of 2.23 km^2 was observed along the eastern half of the ice front.

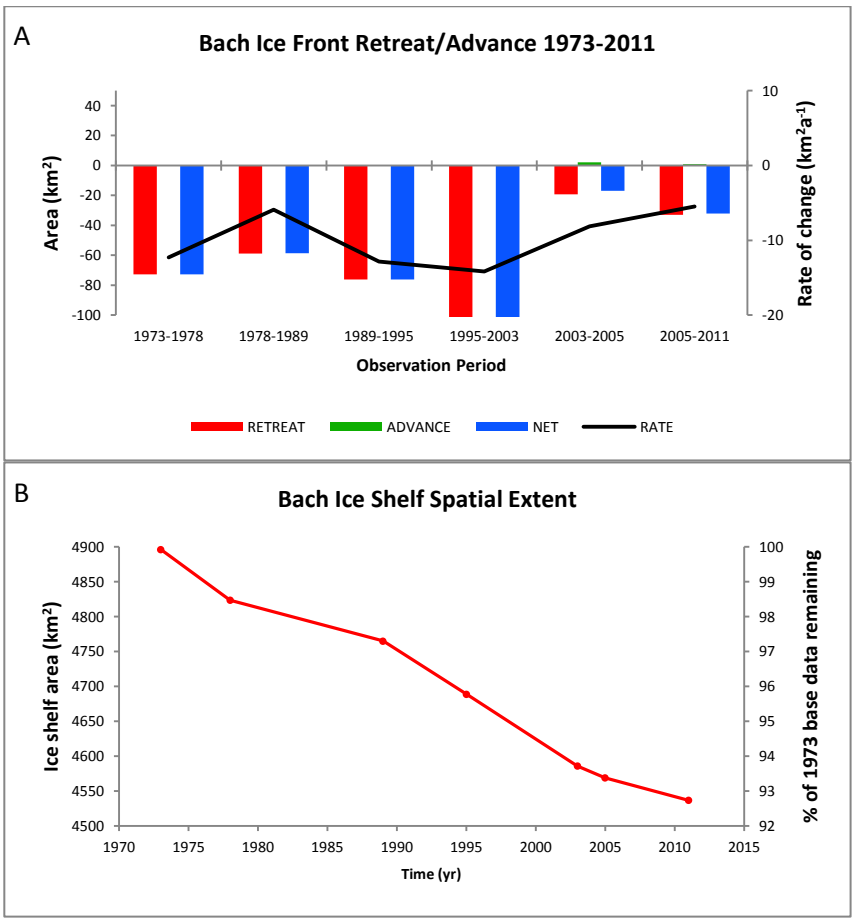

Figure 6.3 A) Areal changes of Bach Ice Shelf and rate of change throughout six observation periods from 1973 to 2011. B) Spatial and temporal loss of ice observed at the ice front. Note a steady rate of retreat throughout the total observation period with only a minimal advance recorded during 2003 to 2005.

The locations of the pinning points at Beethoven Peninsula and Monteverdi Peninsula also retreat upstream between 1973 and 2011 (Figure 6.4, Table 6.4). The western pinning point along Beethoven Peninsula retreated 11.79 km (linear) and was situated 3.88 km southwest of the eastern-most tip of Beethoven Peninsula during January 2011. On the eastern margin, the pinning point retreated 7.09 km (linear). Gradual decoupling of the ice front from the tip of Monteverdi Peninsula between 1978 and 1989 permitted a narrow channel of open water to penetrate upstream. From 1989 to 2011, this channel propagated from 0.31 km wide to 1.32 km at its widest point, with active calving observed during 2011 (Figure 6.4G). Here, the front of the ice shelf has essentially decoupled from its grounding zone.

Table 6.4. Description of ice front locations of Bach Ice Shelf. Descriptions correspond to images displayed in Figure 6.4.

Date	Beethoven Pen. (X/Y) (m)	Monteverdi Pen. (X/Y) (m)	Channel Width (km)	Ice-front Length (km)	Retreat (km^2)	Advance (km^2)	Net Change (km^2)	Comments
29 Jan 1973	-1880776.9/ 545304.1	-1852342.9/ 571373.4	38.10	60.07	N/A	N/A	N/A	Channel in front of BIS contains few, small icebergs measuring no larger than 0.5 km^2.
29 Dec 1978	-1881092.6/ 546233.8	-1852366.4/ 571936.2	38.45	51.68	-72.74	0	-72.74	No icebergs. Entrance was free of sea ice
26 Nov 1989	-1880872.1/ 546260.0	-1853327.1/ 577159.6	41.36	68.65	-58.84	0.28	-58.56	Narrow channel of open water developed adjacent to Monteverdi Peninsula. Entrance to Bach Inlet scattered with unconsolidated plates of sea ice and calved icebergs ranging in size from 0.2 km^2 to 22 km^2.
5 Nov 1995	-1880966.6/ 546307.3	-1853090.8/ 578529.8	42.61	57.04	-76.27	0	-76.27	Channel adjacent to Monteverdi Peninsula opened up further and retreated back upstream. Few, small icebergs no greater than 0.5 km^2 observed.
11 Feb 2003	-1883612.4/ 548433.4	-1852760.1/ 579333.0	43.67	56.89	-103.00	0	-103.00	Few, small icebergs no greater than 0.8 km^2 observed.
11 Mar 2005	-1885549.6/ 552402.2	-1852618.4/ 579427.5	42.55	55.49	-19.17	2.23	-16.94	Entrance to Bach Inlet scattered with unconsolidated and fractured plates of sea ice measuring no more than 5.5 km^2 in area.
23 Jan 2011	-1885502.3/ 552449.4	-1852807.4/ 579380.2	42.42	53.30	-33.06	0.9	-32.16	Icebergs located immediately adjacent to ice front with smaller icebergs scattered sparsely across Ronne Entrance.

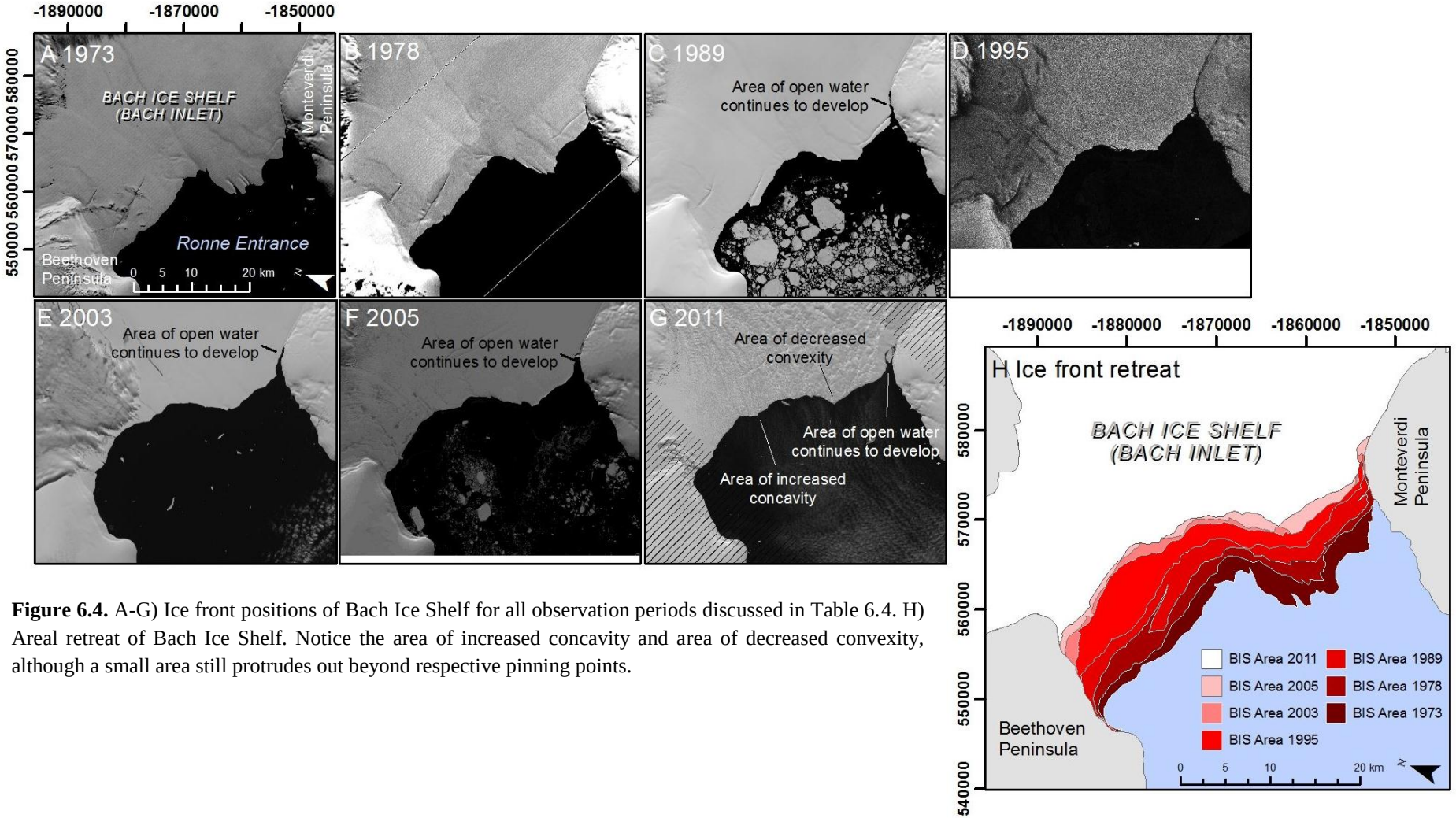

Figure 6.4. A-G) Ice front positions of Bach Ice Shelf for all observation periods discussed in Table 6.4. H) Areal retreat of Bach Ice Shelf. Notice the area of increased concavity and area of decreased convexity, although a small area still protrudes out beyond respective pinning points.

6.1.3 Bach Ice shelf Structural Overview

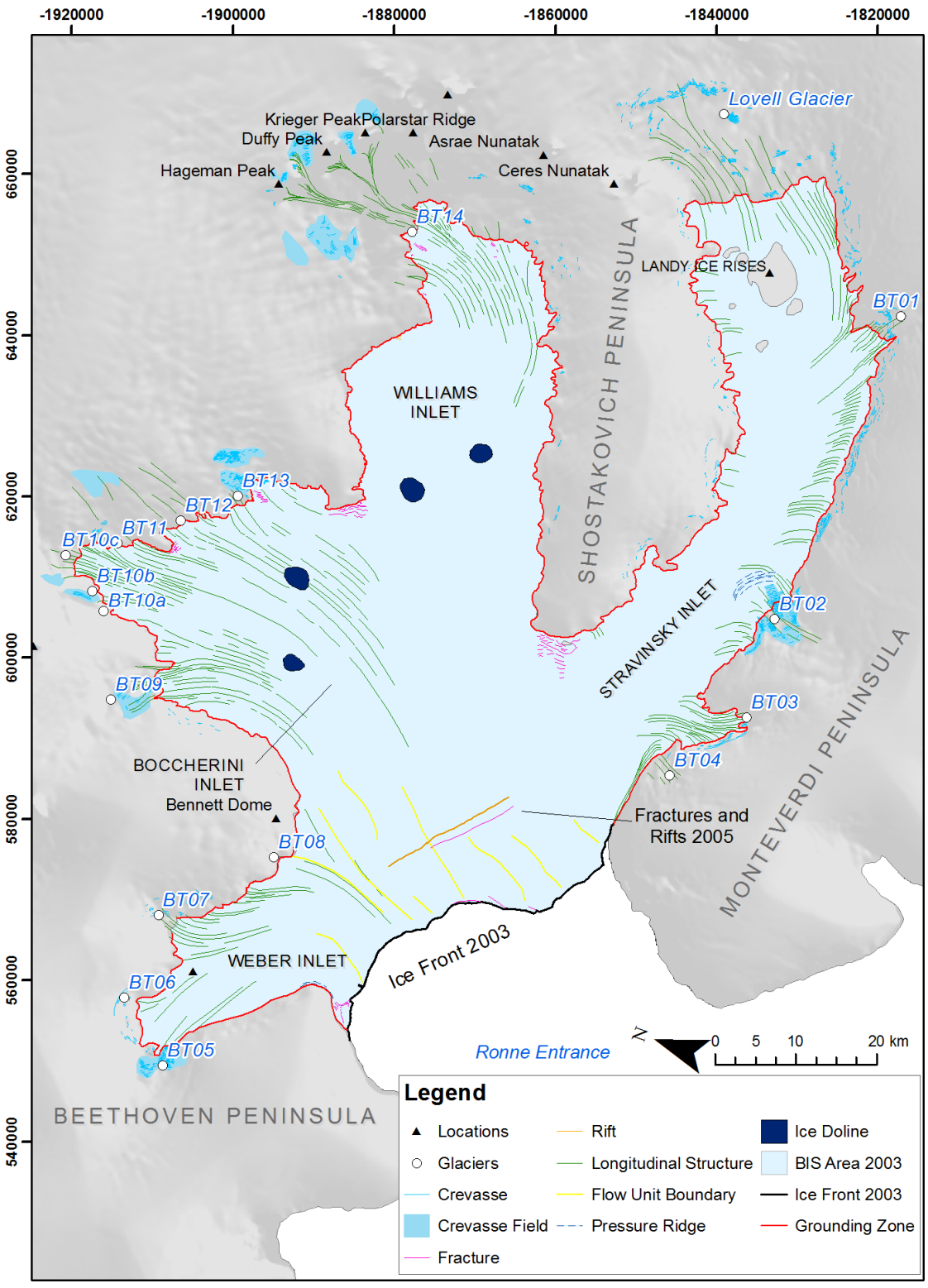

Figure 6.5. Composite structural overview of Bach Ice Shelf (2003-2005). Longitudinal surface features are the most dominant glaciological structure observed on Bach Ice Shelf. Surface meltwater from 2003 has been omitted and is displayed in Figure 6.8. The structural configuration is described in Section 6.1.3.

In the following section, the surface features and surface structures of Bach Ice Shelf are detailed. Initially an overview of the key structures and locations is presented using a composite map digitised from 2003 and 2005 Landsat ETM+ and ASTER imagery (Figure 6.5). Major structural changes and structural evolution are subsequently discussed, concentrating in particular on its ice front and surface meltwater extent.

6.1.3.1 Longitudinal Structures

Longitudinal structures are the most dominant surface feature on Bach Ice Shelf. During the austral summer, surface meltwater pools highlight the presence of these longitudinal structures and aid their identification in some instances. Where surface meltwater is absent, these structures are represented as couplets of dark and light linear bands associated with shadowing. They form parallel to the principal flow direction and originate in three distinct zones:

Type 1: At the confluence of two tributary glacier systems on grounded ice. These tend to be thin at their origin (≤0.1 km), cross the grounding zone into the ice shelf and flow down-ice for between 10-20 km. They retain their linearity and spacing down glacier but become increasingly indistinct from the surrounding ice.

Type 2: At the confluence of two tributary glacier systems at or near the grounded-ice/ice-shelf interface. These are typically 0.2-0.3 km in wavelength, flow down ice uninterrupted for 20-30 km, and similarly remain linear along their length. These are the most striking of longitudinal features, and near the ice front, these flow unit boundary zones can be seen emerging clearly on the ice-shelf surface.

Type 3: Within the main channel of tributary glaciers and flow units, typically at or near to the grounding zone, with only a few traceable back onto grounded ice. These features tend to be the widest type at their origin (up to 0.5 km), but can only be observed for 3-10 km down ice before becoming indistinct. Again, their linearity is maintained down ice.

Longitudinal structures exist in each of the four ice domains (Figure 6.5). In the Weber Ice Domain, they can be traced for between 2.5 and 12 km, with larger features (>12 km) stretching from the grounding zone to within 2.5 km of the ice front. The largest features are situated between the flow units of BT05, BT06, BT07 and BT08.

On Boccherini Ice Domain, longitudinal features typically originate at or near to the grounding zone, with only a few features observed flowing off the grounded ice of Alexander Island (BT09 and BT10c). The most prominent longitudinal features are again associated with flow-unit boundaries, with individual features traceable for up to 35 km from their origin (Type 2).

Longitudinal features observed on the surface of Williams Ice Domain exist predominantly in the eastern-most region. These features associated with flow unit BT14 can be traced from their origin where they begin abruptly (Type 1), are narrow and are grouped in sets of three or more. As distance from their origin increases, their appearance becomes less clear, with only the most prominent Type 1 and Type 2 longitudinal features crossing over the grounding zone onto the ice shelf surface.

Within the Stravinsky Ice Domain, short (1.5-6 km) longitudinal structures are observed flowing from Shostakovich Peninsula and Monteverdi Peninsula along much of the grounding zone, but these are rarely traced back onto grounded ice (Type 3). Longer features are observed at the input of Lovell Glacier, BT01, BT02 and BT03, although on the ice-shelf surface, these features become indistinct within 7-15 km and can rarely be observed beyond the Landy Ice Rises. On the surface of tributary glacier BT01, the longest longitudinal features measure ~13 km, and exist at the tributary glacier flanks as Type 2 features. Shorter (~7 km) features are observed in the centre of BT01 flow unit and can be traced back to the grounding zone (Type 3).

At BT02, longitudinal features originate at the grounding zone, and can be traced for ~8.5 km into the ice shelf. At -1832900 610400 m these features are cross-cut by pressure ridges that form transverse to the principal flow of BT02. Only two longitudinal features here can be traced upstream onto the grounded ice of Monteverdi Peninsula, for ~8 km, but their visibility on the ice-shelf surface is limited to <3 km. Finally, a cluster of longitudinal features originate abruptly at the grounding zone of BT03 and flows out into the main ice shelf. These features can be traced for up to 11 km. Longitudinal structures between BT03 and BT04 flow from the grounding zone towards the ice front along Monteverdi Peninsula.

6.1.3.2 Flow unit boundaries

At the ice front, faint, linear surface structures are visible in all cloud-free satellite images from 1973 to 2011 and can be linked to Type 2 longitudinal structures further upstream. These structures are perpendicular to the ice front (parallel to flow) and can be traced back upstream for at least 3 km before becoming indistinct from the surrounding ice. Only where surface meltwater is present in the austral summer can some of these features be followed back towards their origin at the grounding zone.

6.1.3.3 Pressure Ridges

Pressure ridges (also termed pressure rollers, Cook and Vaughan, 2010) on the surface of Bach Ice Shelf are located where glacier ice from BT02 enters the shelf, between 3 and 5 km from its grounding zone (-1835900 609500 m). The series of four distinct pressure ridges is arced convexly with the principal, localised flow direction and measure up to 7 km in length. At their easterly edge they cross-cut longitudinal features created by the tributary glacier BT02. Further pressure ridges are also located where ice from Weber Inlet impinges upon the tip of Beethoven Peninsula.

6.1.3.4 Crevasses, Fractures and Rifts

Numerous crevasse fields exist around the edges of Alexander Island, but few open crevasses migrate across the grounding zone onto the ice-shelf surface. The larger crevasse fields are associated with tributary glaciers that flow off Alexander Island into the main shelf. Crevasses within these regions are often <2 km in length and are generally no greater than 0.6 km in width. Typically, crevasse fields are comprised of regularly organised fractures running perpendicular to the local flow direction. Crevasses are also present along the steep-sided slopes of Shostakovich and Monteverdi peninsulas, with individual crevasses often stretching for over 4 km. These ice-slope crevasses are generally aligned parallel or sub-parallel to each other and rarely cross-cut other crevasses.

Ice-shelf surface fractures exist in two distinct zones, 1) between merging flow units around headlands or peninsulas, and 2) at or near to the ice front. Those existing between the confluences of two flow units initiate abruptly at the grounding zone and are observed as well-defined, linear, dark lines on the ice-shelf surface. As distance travelled from the grounding zone increases, these structures become less clear, often lighter in appearance and increasingly deformed, until these fracture traces eventually become indistinct from

the surrounding ice. On Bach Ice Shelf there are four such zones, each displaying comparable physical properties as described above, but on differing spatial scales.

Fractures that exist along Bach ice front cut back into the ice shelf. These fractures are rarely greater than 3 km in length and do not appear to follow a regular or standard pattern of development across the ice-front profile. Occasionally, these features initiate along flow-unit boundaries and propagate upstream, forming rifts perpendicular to the ice front (parallel to flow); these rifts are often short-lived as calving of adjacent ice is instigated and a retreat of the ice-front thus achieved.

Surface fractures also develop as ice flowing from Weber Inlet nears the margin, and diverts around the tip of Beethoven Peninsula. Within 2 km from their origin, these particular fractures appear to penetrate the entire depth of the ice shelf to form rifts, and consequently become in-filled with uniform, consolidated ice. Over time, these rifts are observed migrating towards the ice front with ice-shelf motion, and propagate lengthways to at least 10 km in length. These rifts eventually instigate iceberg calving at the ice front.

Finally, between March 2003 and March 2004, two large fracture features (~18 km in length) developed in the central region of Bach Ice Shelf, ~7-12 km from the ice-shelf front. During 2005, these features were linearly aligned sub-parallel to the ice front, and lay between up to 1.2 km apart from each other. The development of these particular features is described in more detail in Section 6.1.4.

6.1.3.5 Surface Meltwater

Meltwater develops on the surface of Bach Ice Shelf in mid-December near the grounding zone. Gradually, meltwater progresses across the ice-shelf surface throughout December and January before reaching a maximum during late-February to early-March. By mid-March, meltwater extent begins to reduce and is absent from much of the ice-shelf surface by the end of March.

Meltwater on the surface of Bach Ice Shelf appears as both individual melt ponds and elongated, interconnected pools. The former vary in size from <0.005 km^2 to 6 km^2 and develop in three situations. First, individual melt ponds form at the grounding zone where a break in slope is observed between the steep-sided grounded ice and the gentle slopes of the ice shelf. Second, melt ponds develop in surface fractures and fracture traces located within flow-unit boundary zones, and thus give a pock-marked appearance on the ice shelf

surface; this is evident at the confluence of Weber and Boccherini ice domains. Finally, melt ponds are distributed across the ice-shelf surface, interspersed between the elongated meltwater pools.

The interconnected pools are observed across much of the surface of Weber Ice Domain and Boccherini Ice Domain, the eastern regions of Williams Ice Domain and the far-eastern reaches of Stravinsky Ice Domain around the Landy Ice Rises. They are associated with the longitudinal structures and are principally aligned parallel with flow. The pools often cross-cut longitudinal features to create a complex network of surface meltwater pools that can be traced uninterrupted down ice for distances greater than 20 km. At the ice front, the northern reaches are characterised by large meltwater pools; there is also evidence of ice scoured by meltwater towards the ice front at -1872400 572000 m. At the western edge of the ice front, surface meltwater is not observed at any time between 1973 and 2011.

6.1.3.6 Ice Dolines

Ice dolines are unique ice-shelf features that form almost exclusively in regions where surface meltwater is abundant (Bindschadler *et al.*, 2001). Elsewhere, smaller ice dolines are termed ice blisters (Kovacs, 1992; Moore, 1993) and ice calderas (Stephenson and Fleming, 1940) which effectively describe both the appearance and form of such features; ice dolines on the surface of Bach Ice Shelf fit both of these descriptors. Surface meltwater during the austral summer highlights the presence of at least four ice dolines from 2003 to 2011, although fewer features are identified in earlier imagery and are discussed further in Section 6.1.5. In each of these identified features, meltwater forms a circular channel around its internal caldera which also partially fills with surface meltwater; the internal ‘caldera’ is best observed where meltwater is absent (Figure 6.6B) when shadowing of an external rim can clearly be observed. During 2003, two ice dolines are observed in both the Boccherini Ice Domain and Williams Ice Domain, they range in diameter from 2.7 to 3.5 km, and tend to elongate along the principal ice flow direction (Figure 6.6A). There is little indication in the satellite imagery as to what governs their location and/or development, other than a supply of surface meltwater.

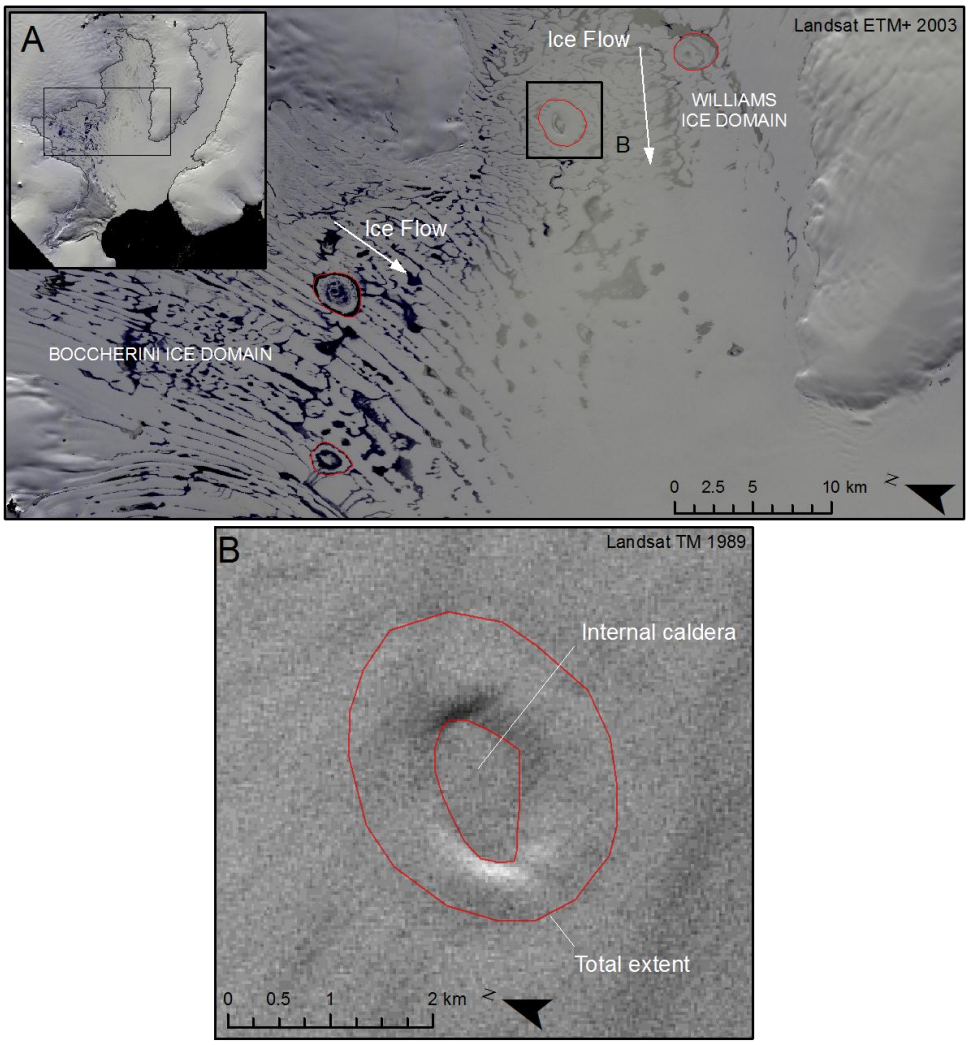

Figure 6.6. A) Location of identified ice dolines on the surface of Bach Ice Shelf (2003, Landsat ETM+). Faint cloud cover reduces clarity over Williams Ice Domain. Ice doline extent includes the external meltwater channels that form around an internal caldera. B) Close-up of meltwater-free ice doline (1989, Landsat TM) illustrating the shadowing produced by the rim of the ice caldera.

6.1.4 Major structural changes and structural evolution

In order to assess the glaciological changes of Bach Ice Shelf, the major structural developments are described here. Generally, structural changes are confined to fracture and rift development and their migration towards the ice front. Typically, such features form the basis for iceberg calving.

During 1973, two open rifts are observed at -1885800 558900 m and -1879200 557500 m towards the tip of Beethoven Peninsula in ice feeding in from Weber Ice Domain (Figure 6.7A). Rift A measured 3.5 km in length, with Rift B measuring 11.3 km. Both rifts were filled with brash ice, giving a speckled appearance. At approximately

-1860000 561000 m, three fractures measuring ~2.3 km in length, cut back longitudinally into the ice shelf. Further south, towards the Monteverdi Peninsula, a single fracture cut transversely across into ice shelf for ~4 km, also crossing a flow unit boundary.

By 1989, Rift A and Rift B had migrated towards the ice front with ice flow (Figure 6.7B). Rift A propagated both longitudinally and transversely, measuring 6.7 km in length and ~0.5 km in width at its widest point. During 1989, Rift B formed part of the frontal profile; the remaining section of Rift B measured 6.9 km in length and 0.5 km at its widest point. Both rifts were filled by consolidated, uniform ice. At -1883900 553800 m, 1.4 km from the ice front and 1.3 km from Beethoven Peninsula, new fractures are observed; they are non-aligned in their formation and distribution. Towards Monteverdi Peninsula, the fracture observed in 1973 extended to a length of 10.1 km and open water was observed in the fracture at its southern tip; it is thus considered to penetrate the ice-shelf depth. An area of open water began to open up back along Monteverdi Peninsula, creating a narrow channel between the ice front and the former pinning point.

During 1997 (Figure 6.7C), Rift A had propagated further across the shelf and measured 7.6 km in length whilst maintaining an approximate width of 0.5 km. Rift A was filled with small amounts of water, running parallel with the rift walls along the centre of the feature. At the ice front, adjacent to the tip of Beethoven Peninsula, iceberg calving was actively taking place; further iceberg calving was observed at -1875100 565000 m. From approximately -1872000 569000 m towards Monteverdi Peninsula, thick cloud cover prevented feature identification on the ice-shelf surface.

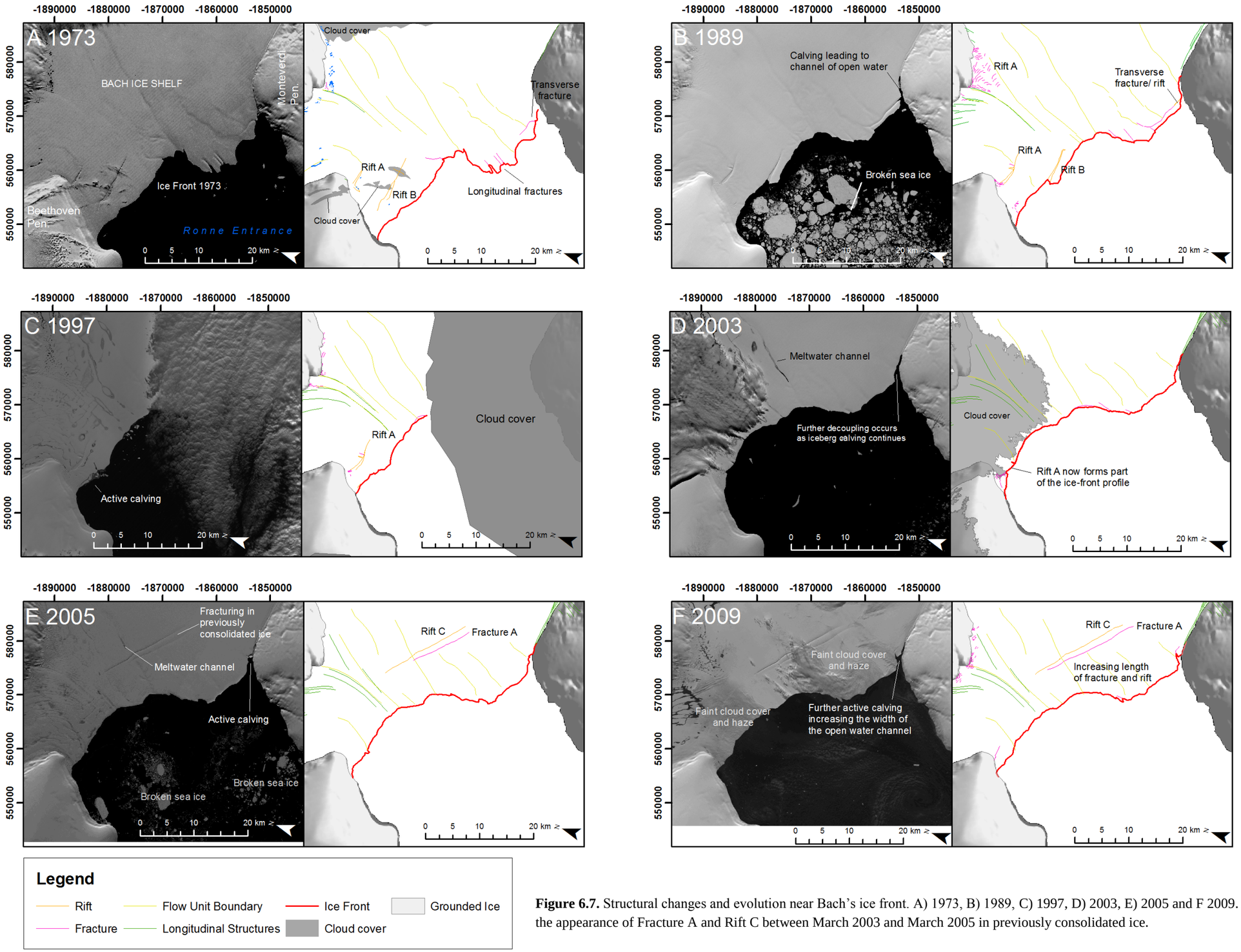

Figure 6.7. Structural changes and evolution near Bach's ice front. A) 1973, B) 1989, C) 1997, D) 2003, E) 2005 and F 2009. Note the appearance of Fracture A and Rift C between March 2003 and March 2005 in previously consolidated ice.

Rift A continued to migrate towards the ice front and between 1997 and 2003 facilitating iceberg calving; during 2003, the back wall of the former Rift A forms part of the ice-front profile. Faint surface fractures were observed along the ice front for the first time, measuring no more than 3.6 km (Figure 6.7D).

The greatest structural change occurred between March 2003 and March 2004 (Figure 6.7E); two large fractures opened up in the centre of Bach Ice Shelf in ice fed by the Boccherini Ice Domain in previously consolidated ice. By March 2005, Rift C measured 17.2 km in length and ~0.2 km in width. Fracture A measured 12.6 km in length, and was much fainter in appearance than Rift C. Furthermore, along the ice front several fractures developed and cut back into the ice shelf, but measured no more than 4 km in length. At the Monteverdi Peninsula pinning point, active iceberg calving was observed, widening the open-water channel between the protruding ice front and the grounded ice of Monteverdi Peninsula.

Between March 2005 and March 2009 (Figure 6.7F), Rift C increased in length to 18.9 km whilst maintaining an approximate 0.2 km-wide opening. Fracture A increased in size to 17.8 km, propagating at either end of the feature. The distance between Rift C and Fracture A ($\leq$ 1.3 km) was maintained along the stretch of both features. At the tip of Monteverdi Peninsula further fracturing was observed between the ice front and the grounded ice opening the open-water channel further, whilst at Beethoven Peninsula, a new surface fracture was observed at -1887000 559300 m.

6.1.5 Surface Meltwater

The distribution and spatial extent of surface meltwater was observed on 29 January 1973, 9 February 1997, 11 February 2003 and 18 February 2007. For each date, the meltwater limit was digitised by linking the outermost edges of meltwater features. There is a clear southward-migration of the meltwater limit on Bach Ice Shelf over the period 1973 to 2007 (Figure 6.8).

On 29 January 1973, 111.13 km^2 of meltwater was observed on the ice-shelf surface, mainly confined to the northern section of Weber Ice Domain and the eastern-most regions of Boccherini and Williams ice domains. No surface meltwater was observed on Stravinsky Ice Domain. By 9 February 1997, meltwater features had spread to cover much of the surface of Weber Ice Domain and Boccherini Ice Domain. The eastern portions of

Williams Ice Domain and all of Stravinsky Ice Domain were covered in cloud and thus meltwater calculations could not be made. Nevertheless, 353.59 km^2 of surface meltwater covered the visible portions of the ice shelf, an increase of at least 242.40 km^2 (318%) on 1973 measurements.

By 11 February 2003, the meltwater limit had migrated further south, particularly near the ice-shelf front. Surface meltwater was also observed in the eastern regions of Stravinsky Domain around the Landy Ice Rises. Cloud cover centred on the flow-unit boundary zone of Weber and Boccherini ice domains prevented a comprehensive analysis of surface meltwater. Over the visible portions of Bach Ice Shelf during 2003, a meltwater spatial extent of 403.40 km^2 is calculated, an increase of 292.27 km^2 (363%) on the initial 1973 calculation.

The southward migration of the meltwater limit continued between 2003 and 2007 as established through Envisat ASAR data. The total spatial extent of surface meltwater on 18 February 2007 is not made due to poor image quality of the SAR data and requirements of the classification procedure. Overall, a clear southward migration of the surface meltwater extent is observed, with a minimum increase of 363% on 1973 measurements (Figure 6.8).

Coupled with the southward migration of the meltwater limit is the appearance of ice dolines on the surface of Bach Ice Shelf. It has already been alluded to that from 2003 to 2011 four ice dolines existed. In 1973, 1978 and 1986 Landsat imagery only one ice doline was visible (ID1, Figure 6.9 A, B, C). Between 1986 and 1989, ID2 began to develop (Figure 6.9D), followed by ID3 and ID4 between 1989 and 1995 (Figure 6.9E). No further ice dolines formed on the surface between 1995 and 2003 (Figure 6.9F), or indeed to 2011.

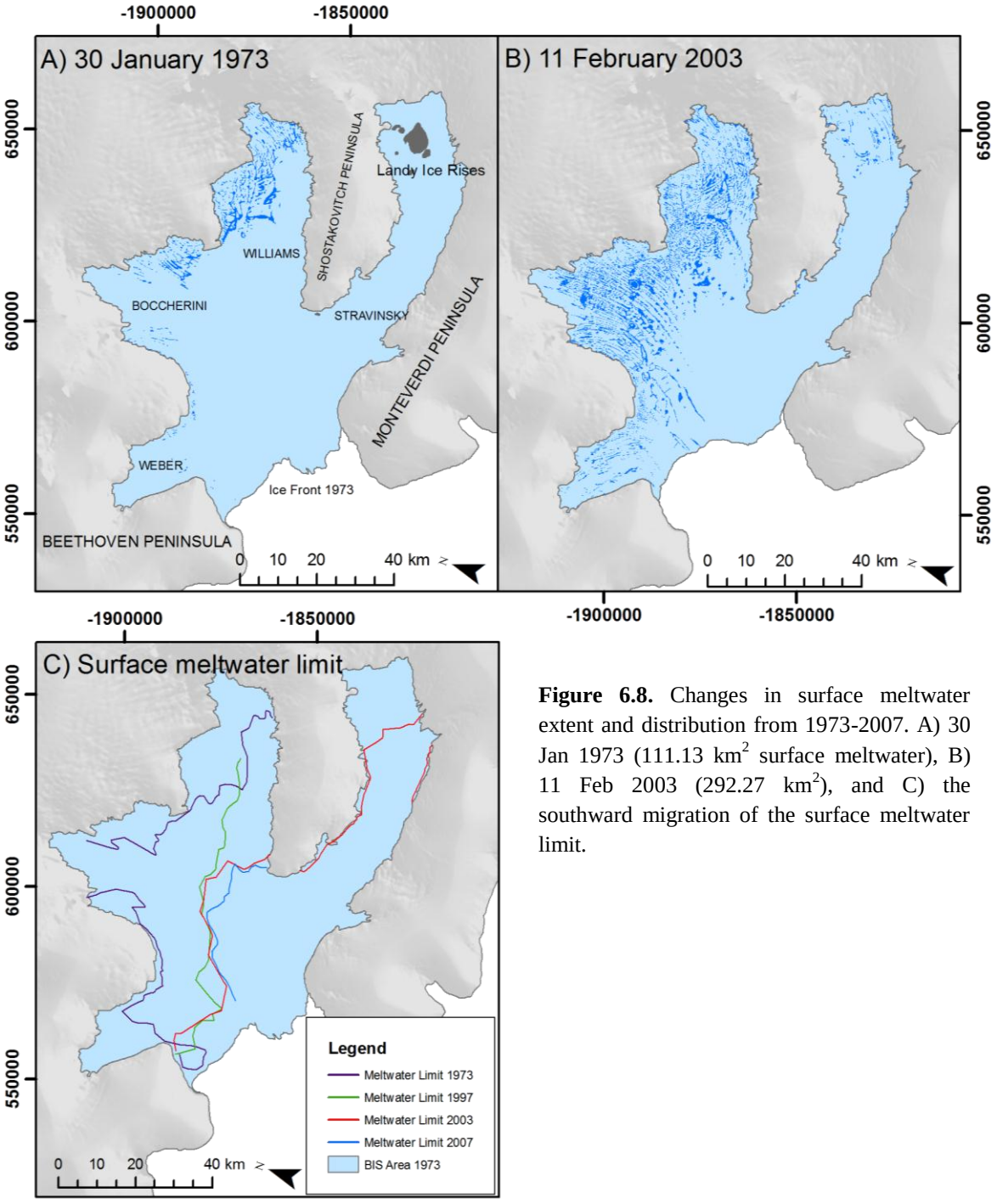

Figure 6.8. Changes in surface meltwater extent and distribution from 1973-2007. A) 30 Jan 1973 (111.13 km^2 surface meltwater), B) 11 Feb 2003 (292.27 km^2), and C) the southward migration of the surface meltwater limit.

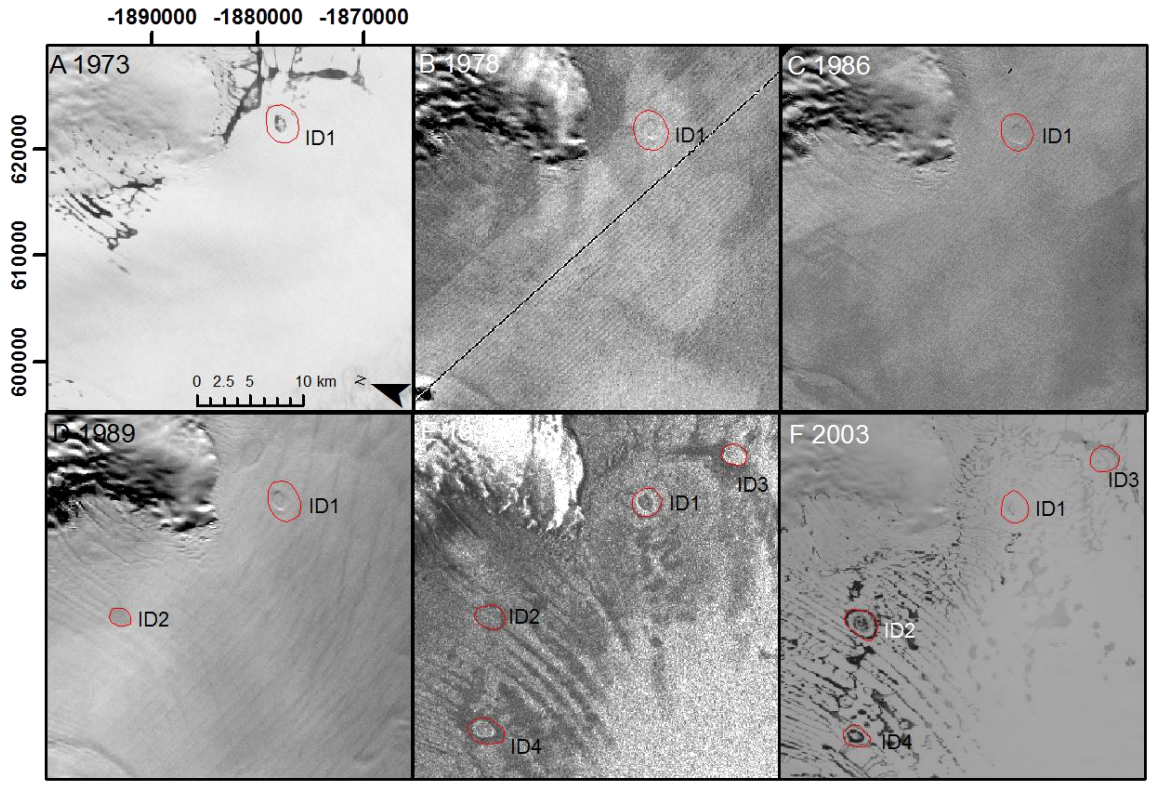

Figure 6.9. Ice doline development on the surface of Bach Ice Shelf following the southern migration of the meltwater limit as illustrated in Figure 6.8. Ice dolines highlighted in red and labelled according to sequential development.

6.1.6 Surface-elevation change

Changes in surface elevation across Bach Ice Shelf were calculated over seven ICESat GLAS tracks between October 2003 and December 2008 at 950 repeat measurement locations. The resultant filtered datasets (outlined in Chapter 5) were used to produce composite surface-elevation change estimates. Whilst this approach sacrifices short-term annual variations, it enhances a broad spatial assessment on a sub-decadal scale that subdues the effects of anomalous annual surface-elevation changes. Ultimately, the resulting surface elevation change calculations represent a mean surface-elevation change (ma^{-1}) calculated between October 2003 and December 2008.

The analysis of ICESat GLAS data illustrates widespread negative surface-elevation change, interspersed with localised pockets of increased surface elevation. Statistics for individual tracks and detailed descriptions are presented in Table 6.5 with plots available in Appendix 1b and spatial analysis presented in Figure 6.10 and Table 6.6.

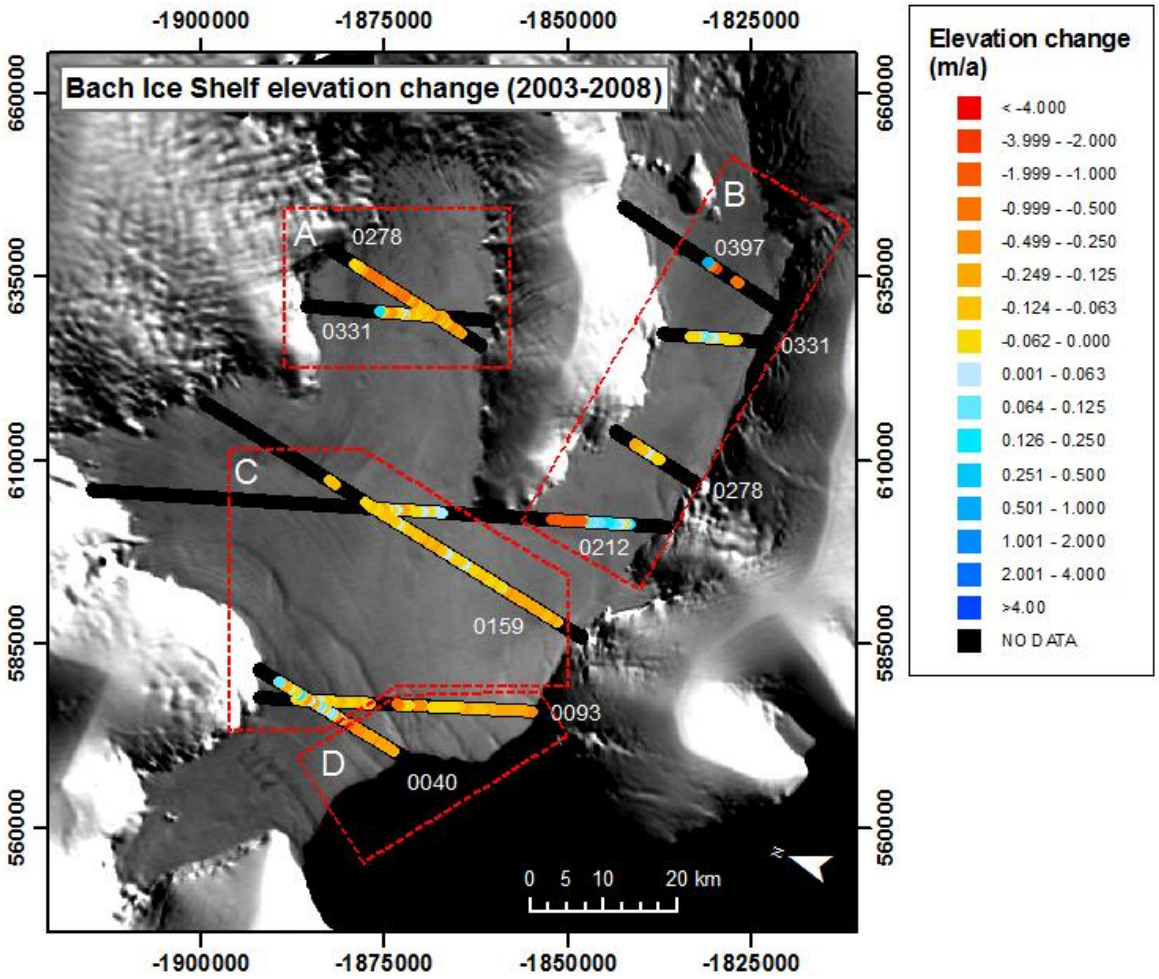

Figure 6.10. ICESat GLAS track locations, surface-elevation changes and Zones of spatial assessment for Bach Ice Shelf as discussed in the main text. Widespread surface lowering is evident across the majority of the ice shelf, with only localised pockets of increased surface elevations recorded, particularly towards the eastern extent of Zone B.

Table 6.5 Analysis of ICESat GLAS acquired surface elevation and calculated surface elevation changes. Refer to Figure 6.10 for track location and Appendix 1b for track plots.

Track	Laser campaign	Observation period	Max + change (m)	Max - change (m)	Mean change (m)	Max + annual change (ma^{-1})	Max - annual change (ma^{-1})	Mean annual change (ma^{-1})	Track Description
0040	2a-3k	24/10/03 – 12/10/08	0.725	-3.024	-0.779	0.146 (± 0.098)	-0.609 (± 0.098)	-0.107 (± 0.098)	Increase in surface elevation from the grounding zone to the ice-shelf front from ~7 m to 16 m. Sharp change in elevation recorded at 9.5 km along the transect. Clear negative surface elevation change between 0-9.5 km along the track at the ice-shelf front with fluctuating, indistinct elevation changes from 10.5 km to 20 km. Maximum positive and negative surface elevation changes recorded ~ 3 km from grounding zone.
0093	2a-3k	28/10/03 – 15/10/08	0.512	-2.691	-0.577	0.103 (± 0.098)	-0.541 (± 0.098)	-0.116 (± 0.098)	Surface elevation increases from ~7 m at the Bennett Dome grounding zone to ~28 m towards the ice-shelf front, before sharply decreasing to ~17 m at the Monteverdi Peninsula grounding zone. Sharp fluctuations in surface elevations between 20-18 km along GLAS track. Distinct negative surface elevation change from ice front to ~30 km along transect before fluctuating changes are recorded.
0159	3a-3i	20/10/04 – 18/10/07	0.143	-0.857	-0.265	0.048 (± 0.089)	-0.286 (± 0.089)	-0.089 (± 0.089)	Overall increase in elevation from centre of Bach Ice Shelf towards the ice front, with a sharp decrease recorded at the Monteverdi grounding zone. Pattern of negative surface elevation change dominates along the track; few significant regions of positive elevation change are recorded
0212	3c-3f	09/06/05 – 12/06/06	0.205	-1.604	-0.262	0.204 (± 0.089)	-1.590 (± 0.089)	-0.260 (± 0.089)	Track 0212 crosses the tip of Shostakovich Peninsula; a steady decrease in elevation is recorded from the centre of Bach Ice Shelf (39 km) towards the Shostakovich grounding zone, with an equally steady increase in elevation to the centre of the Stravinsky Ice Domain (8 km). Between 39-27 km surface elevation changes fluctuate between positive and negative with no clear pattern observed. Surface elevation changes between 16-0 km represent two different regimes, with large negative elevation changes recorded between 16-10 km and mostly positive changes recorded between 10-0 km.
0278	3e-3h	18/03/06 – 04/04/07	0.026	-0.872	-0.283	0.025 (± 0.097)	-0.832 (± 0.097)	-0.270 (± 0.097)	Track 0278 crosses both the Williams and Stravinsky Ice Domains. Over the former area, surface elevation increases from ~12 m to 25 m

									across the shelf, with negative surface elevation recorded (mean -0.33 ma^{-1}). In Stravinsky Ice Domain, surface elevation principally underwent negative change over the observation period, with little positive surface change recorded.
0331	2a-2d	13/11/03 – 11/12/08	0.771	-1.457	-0.310	0.151 (± 0.097)	-0.287 (± 0.097)	-0.062 (± 0.097)	Similarly, track 0331 crosses both the Williams and Stravinsky ice domains. Mainly negative surface elevation changes are observed over the former of these areas (mean -0.26 ma^{-1}), interspersed with peaks of positive surface change. The surface of Stravinsky Ice Domain across track 0331 underwent a combination of surface lowering and raising; a mean change of -0.07 ma^{-1} was calculated over this region. Surface elevations in Williams Ice Domain are ~ 5 m lower than that of Stravinsky Ice Domain
0397	3a-3d	04/11/04 – 21/11/05	0.696	-2.816	-1.085	0.664 (± 0.089)	-2.690 (± 0.089)	-1.036 (± 0.089)	The few data points over track 0397 reveal mainly negative surface elevation change. Surface elevations fluctuate between 28-43 m, with a large peak observed as the track crosses an ice rise associated with the Landy Ice Rises complex.

Following on from the individual analysis presented in Table 6.5, ICESat GLAS tracks were segmented into four spatial zones covering the Williams Ice Domain (A), Stravinsky Ice Domain (B), the central portions of Bach Ice Shelf (C) and an ~10 km zone at the ice front (D) (Figure 6.10) to gain a better understanding of spatial changes across the ice shelf. Table 6.6 displays statistical analysis of surface-elevation changes within each of these zones.

Over the central portions of Williams Ice Domain (Zone A), a negative surface elevation change is principally observed, with a mean annual change of -0.253 ma^{-1} calculated. Small, positive surface-elevation change is noted towards the northern limit of track 0331. Across the Stravinsky Ice Domain (Zone B), positive surface elevation change was observed along the centreline of the region, with the greatest positive change observed at the southern end of track 0212. North and south of the centreline, along Stravinsky Ice Domain, negative-surface elevation was observed, with the greatest amount of surface lowering observed along track 0397 and track 0212. A mean surface elevation change of -0.317 ma^{-1} is calculated within Zone B.

Table 6.6. Spatial analysis of ICESat GLAS surface elevations

Zone	Tracks (campaigns)	Max + annual change (ma^{-1})	Max - annual change (ma^{-1})	Mean annual change (ma^{-1})
A	0278 (3e-3h) 0331 (2a-2d)	0.152	-0.832	-0.253
B	0397 (3a-3d) 0331 (2a-2d) 0278 (3e-3h) 0212 (3c-3f)	0.664	-2.689	-0.317
C	0212 (3c-3f) 0159 (3a-3i) 0093 (2a-3k) 0040 (2a-3k)	0.146	-0.286	-0.067
D	0093 (2a-3k) 0040 (2a-3k)	N/A	-0.609	-0.169
TOTAL		0.664	-2.689	-0.167

In Zone C, in the central region of Bach Ice Shelf, a mean annual change of -0.067 ma^{-1} was observed. This is the smallest mean annual negative change out of each of the four zones, and is characterised by a maximum positive change of 0.146 ma^{-1} and a maximum negative change of -0.286 ma^{-1}. Within Zone D at the ice-shelf front, only negative surface elevation changes took place, the maximum of which (-0.609 ma^{-1}) was observed in the

Boccherini-fed region of track 0040. Within the ice-shelf frontal zone, a mean annual surface elevation change of -0.167 ma^{-1} is calculated between 2003-2008.

6.1.7 Section summary

In this section, the surface dynamics, structural configuration and evolution over time and surface elevation changes have been presented. The key findings are summarised below.

1) Bach Ice Shelf is characterised by ice flow that merges into four cohesive ice domains that eventually meet at the ice front. There is little variance in flow between individual tributary glaciers that cross the grounding zone. An increase in the speed of ice flow occurs with increased distance travelled from the respective grounding zones towards the centre of the ice domains and towards the ice front. There is no indication that there has been a change in the surface speed of the ice shelf between ca. 1996 and ca. 2007.
2) Between 1973 and 2011, Bach Ice Shelf underwent a net change of approximately -360 km^2 in regular calving events along the length of its ice front. The greatest loss was observed between 1995 and 2003. The ice-front profile became increasingly concave over time and particularly so since March 2003. The two pinning points at the ice front retreated back along Beethoven Peninsula (~12 km) and Monteverdi Peninsula (~7 km), with the latter seeing a channel of open water develop back upstream, adjacent to the peninsula, decoupling along its grounding zone.
3) Structurally, changes were observed principally along the ice front, with fractures and rifts continually developing and forming the basis for frontal calving. The most significant structural change was the appearance of fractures and rifts that ran sub-parallel to the ice front, ~10 km upstream between March 2003 and March 2004. These features crossed the flow-unit boundary and associated meltwater channel between the Boccherini and Williams Ice Domains, but exhibited little longitudinal and transverse propagation as they migrated towards the ice front.
4) An increase in the spatial extent and distribution of surface meltwater in a southward direction was observed between 1973 and 2007. Between 1973 and 2003, a 363% increase in the areal extent of surface meltwater was calculated between comparable dates, and ice doline distribution increased from north to south.

5) There were widespread, negative-elevation changes calculated over the surface of Bach Ice Shelf, with the most notable changes observed within 10 km of the ice front.

In the Section 6.2, these results are integrated to allow interpretations on the areal and vertical changes, the significance of surface structures and their evolution with respect to ice shelf dynamics and the significance of surface meltwater on Bach Ice Shelf. Interpretations are made based on information presented so far in this study. Further discussions are presented in Chapter 9 that compare Bach Ice Shelf to the other ice shelves in this study and previously published datasets.

6.2 Bach Ice Shelf Interpretations

Whilst interpretations of the surface structures and surface features have already been made to permit structural mapping, their significance for ice-shelf dynamics and glaciological configuration has not been discussed. In the following section, the structural and dynamic components of the study are integrated. First, both horizontal and vertical spatial changes are discussed before the relationship between glaciological surface structures, surface features, and ice-shelf dynamics are considered. Discussions on ice-shelf stability and future changes are made in Chapter 9 in a wider context.

6.2.1 Interpretation of ice-shelf retreat and spatial extent

Bach Ice Shelf lost ~360 km^2 of ice between January 1973 and January 2011, an overall change of approximately 7% of the 1973 baseline area used in this study. Various events captured in Landsat and ERS SAR imagery suggest that calved icebergs were often no greater than 3 km^2 in size and occurred along pre-conditioned fractures at the ice front. Since 1973, Bach Ice Shelf has been in a phase of sustained retreat that was slightly enhanced between 1995 and 2003.

The distinct ice-front profile observed in 1973 is generally maintained, although it became increasingly concave towards its western portion and decreasingly convex towards Monteverdi Peninsula. Analysis of ICESat GLAS tracks and a 200 m resolution RAMP DEM identifies greater surface elevations towards this eastern portion, from which it is inferred that thicker ice exists towards Monteverdi Peninsula, and thus explains its convex profile (Figure 6.11, Figure 6.12). It is proposed that thicker ice occurs here due to the dominance of Boccherini and Williams ice domains and the adjacent input of ice from Stravinsky Ice Domain. Importantly, spatial assessment of ice-front retreat illustrates that since 1973, this thicker ice is no more nor no less likely to undergo retreat than relatively thinner ice towards Beethoven Peninsula (Table 6.7, Figure 6.13). The overall shape of the ice front, however, is considered to give greater stability to the ice shelf, limiting the rate of retreat (Doake *et al.,* 1998).

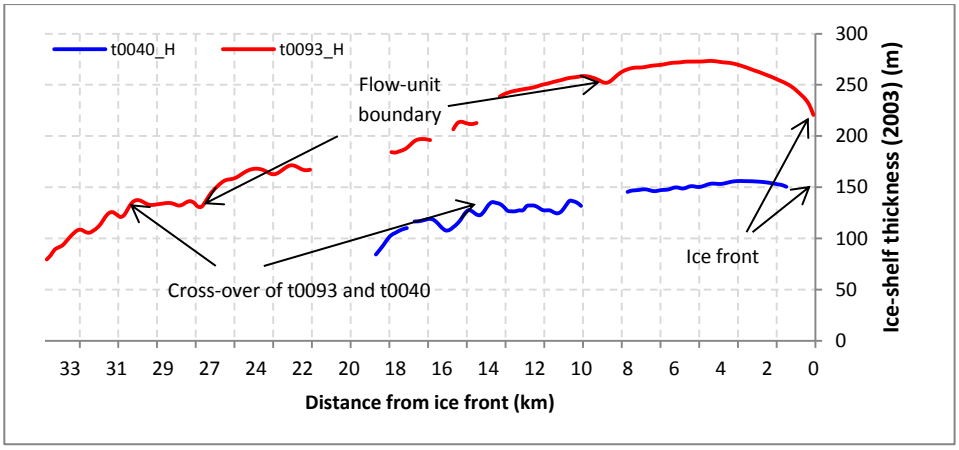

Figure 6.11. Ice-shelf thickness (H) calculated along ICESat GLAS tracks t0040 (blue) and t0093 (red) from 2003 illustrating the relative thickness at the ice front between the convex and concave portions of the ice shelf. Refer to Figure 6.12B for geographic location of annotated points and Equation 6.1.

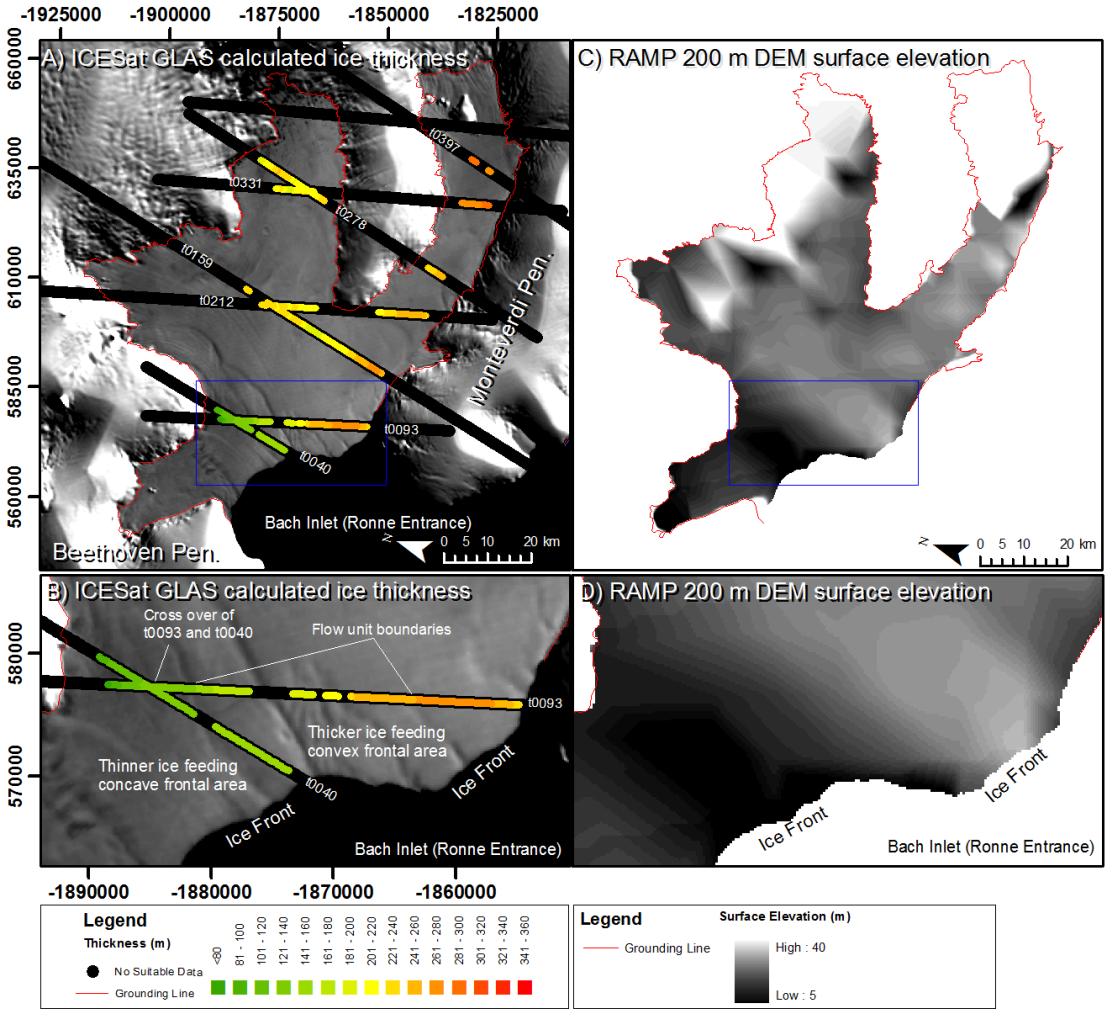

Figure 6.12. A) Calculated ice-shelf thicknesses from ICESat GLAS track data with overall pattern of increasing thicknesses towards ice sources, and B) close up of Bach ice front illustrating the concave portion associated with thinner ice and convex portion associated with thicker ice. C) and D) show surface elevation data from RAMP 200 m DEM illustrating greater surface elevations where thicker ice exists.

Table 6.7. Horizontal retreat data for five transects across Bach ice front (BIF) 1973-2011. Data displayed in Figure 6.13.

Time period	BIF01 Retreat (km)	BIF02 Retreat (km)	BIF03 Retreat (km)	BIF04 Retreat (km)	BIF05 Retreat (km)
1973-1978	0.87	1.78	1.31	3.86	3.16
1978-1989	2.11	0.68	1.63	1.82	0.73
1989-1995	1.32	3.46	1.94	1.97	2.10
1995-2003	3.77	4.95	2.27	1.80	0.47
2003-2005	0.67	0.75	0.42	0.28	0.00
2005-2011	0.46	0.63	0.52	1.84	0.93
Total retreat	9.20	12.25	8.09	11.57	7.39

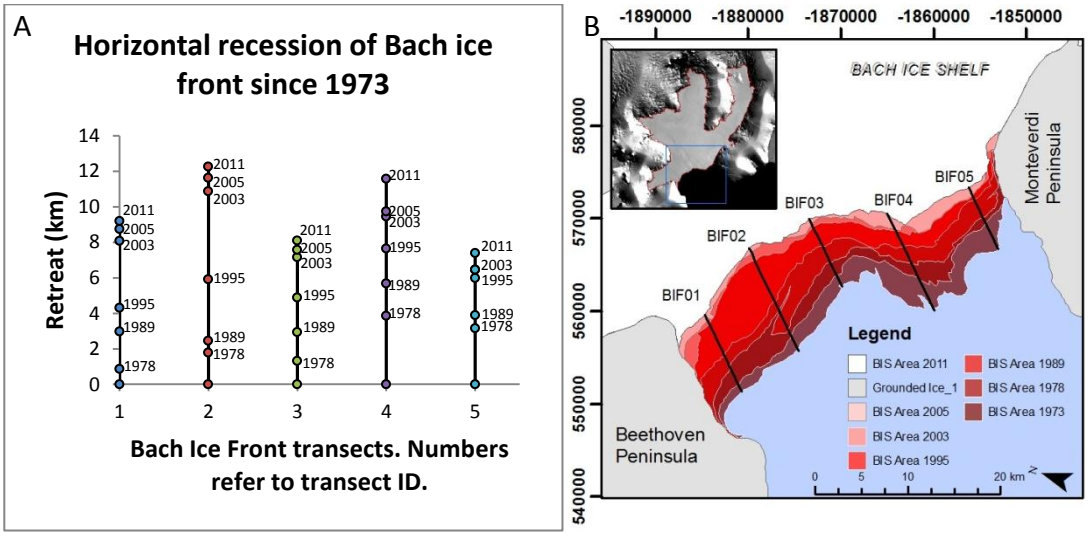

Figure 6.13. A) Transect data illustrating similar patterns of retreat in both thinner (BIF01, BIF02 and BIF03) and thicker ice (BIF04 and BIF05). B) Location of ice-front retreat transects displayed over areal retreat.

Progressive decoupling of the ice shelf from the tip of Monteverdi Peninsula occurred as the ice front retreated back upstream; this is significant for two reasons. First, the overall linear channel width that the ice front occupied increased by ~4 km between 1973 and 2011, and whilst the results illustrate that the actual ice-front length reduced over time, there is greater potential for it to increase from its current position through continued retreat. (The decrease in ice-front length between 1973 to 2011 is mainly attributed to a reduction in open rifts at the ice front that were included in the original profile-length calculations). An increase in ice-front length naturally increased the frontal-surface area subjected to tidal-induced stresses at the ice front. Secondly, ice from Stravinsky and Williams Ice Domains had previously impinged upon the tip of Monteverdi Peninsula as ice flow was diverted towards the ice front. It is inferred that high compressional stresses

would have been exerted at this point. Subsequent decoupling of the ice shelf from the grounding zone is likely to have reduced the compressive stress regimes and increased localised tensile stresses at the ice front. Continuing retreat of the ice front along the Beethoven Peninsula could see a similar decoupling from the northern-most pinning point, thus leading to a situation where tensile stresses dominate at the ice front, rather than compressive stresses as inferred until present.

6.2.2 Assessment of surface elevation changes and inferences on ice-shelf thickness

The removal of elevation data points in regions where distinct surface undulations exist and where hydrostatic equilibrium of the ice shelf is not reached reduces uncertainty in the change measurements by lessening the effects of both horizontal and vertical motion of the ice shelf. Furthermore, assessment was carried out over the maximum temporal scale for each ICESat GLAS track, therefore mostly subduing localised anomalies (prolonged snow cover, for example) and thus results in a broad spatial assessment of ice-shelf elevation changes.

Because a comparison is being made between repeat-track measurements of the ICESat GLAS data over (approximate) yearly timescales (or multiples of) and not between two separate instruments or at different periods in the mass-balance year, it is anticipated that calculations are representative of any real elevation changes, with uncertainties in the results caused mainly by pre-processing procedures to remove vertical tidal motion, corrections for the inverse barometer effect (IBE) and biases introduced by instrument characteristics as discussed in Chapter 5. However, one key assumption is made to enable surface elevation changes to be calculated; that the rate of elevation change has remained constant between October 2003 and December 2008, and by extrapolating the absolute data to rate-of-change measurements (ma^{-1}) to permit comparison between tracks (and ultimately ice shelves), results remain indicative of actual elevation and therefore thickness changes. Thickness change estimates were obtained by following the procedures outlined in Chapter 5, Section 5.2.3.3.

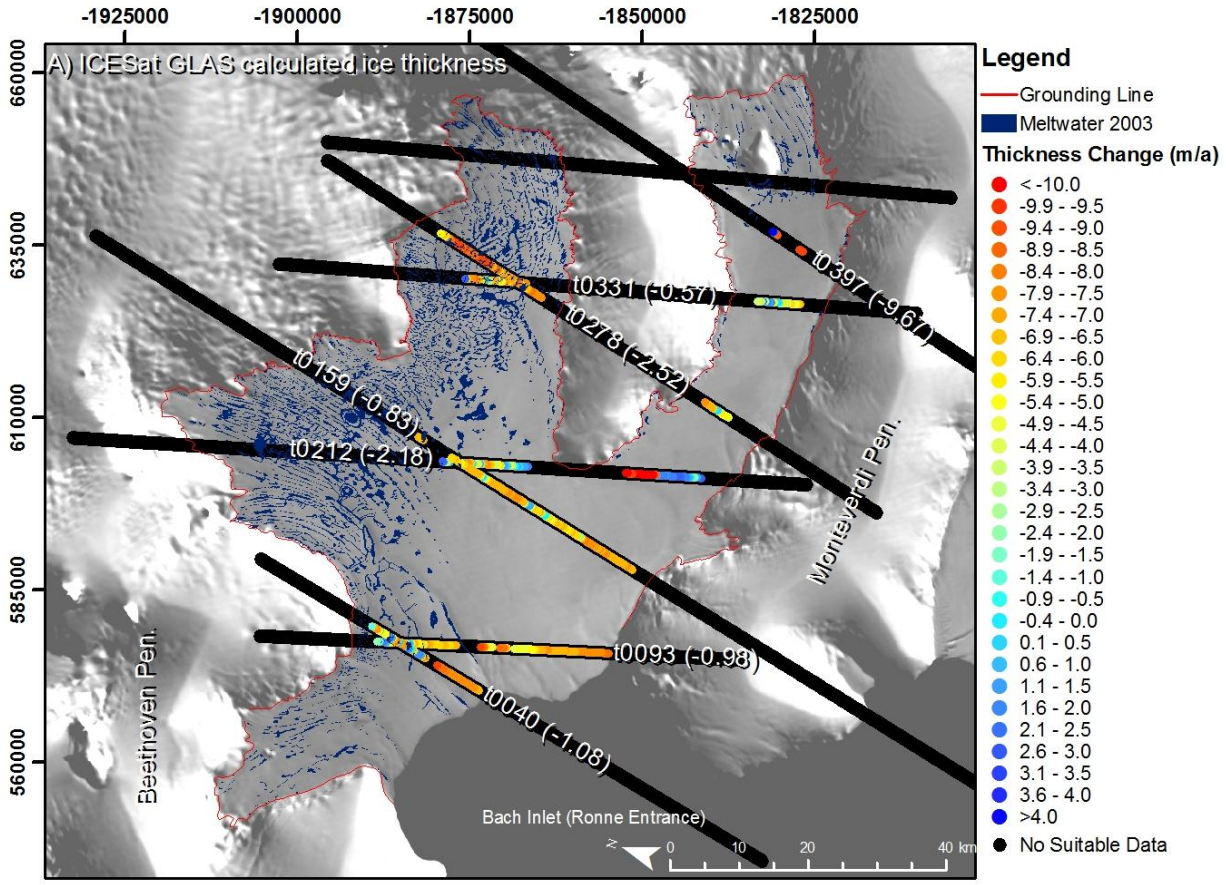

Figure 6.14. Calculated ice thickness changes from repeat track ICESat GLAS elevation data, extrapolated to ma^{-1} as described in Chapter 5. Meltwater extent during 2003 is included to highlight thinning both within and outside of this region that is subjected to surface melting. Numbers given in brackets represent the mean thickness changes for each respective track.

Whilst individual ICESat GLAS surface-elevation measurements only exist along narrow tracks, the use of multiple cross-cutting acquisitions develops a grid of data measurements that can be used to highlight the temporal and spatial changes to ice-shelf surface elevations. The widespread negative surface elevation change, and thus inferred thinning, observed across Bach Ice Shelf between October 2003 and December 2008 illustrates its response to documented atmospheric and oceanic changes (Vaughan *et al.*, 2003; Morris and Vaughan, 2003; Meredith and King, 2005). Only small pockets of positive elevation changes (thickening) are detected across Bach Ice Shelf (Figure 6.14). These could be considered as localised thickening anomalies rather than being representative any significant changes to the ice-shelf system, caused by short-term ablation/accumulation of surface snow with respect to the timing of data acquisition, or, most likely, horizontal motion of undetected (thus unfiltered) surface undulations or protuberances. Alternatively, positive changes may reflect actually thickening due to surface or basal accumulation. Along the southern-most points of track t0212, large positive surface elevation changes

(thickening) are also calculated. This region is located between the influx of glacier ice from BT02 and BT03 and thus the changes observed here may be influenced by short-term, localised dynamics of these tributary systems and associated surface structure.

Despite widespread thinning, there is no observed retreat of the grounding zone between 1973 and 2011. Typically, a retreating grounding line is the only observational parameter of a thinning ice shelf, as indicated elsewhere (e.g. Thomas *et al.*, 1988; Rignot, 1998; Shepherd *et al.*, 2001). Ultimately, the positioning of the grounding zone is determined by the thickness of the grounded ice, thickness of the ice shelf, and the gradient of the underlying topography. The surface slopes of the surrounding grounded ice along Bach Ice Shelf mostly display high gradients (Figure 6.15), and in the absence of bathymetric data beneath Bach Ice Shelf, it is assumed that the steep topography continues to the sea bed, thus limiting the potential of horizontal movement of the grounding zone despite high thinning rates. Furthermore, the spatial resolution of Landsat imagery (80-15 m) may be too coarse to observe any grounding line retreat on Bach Ice Shelf, as horizontal retreat would have to be greater than this resolution.

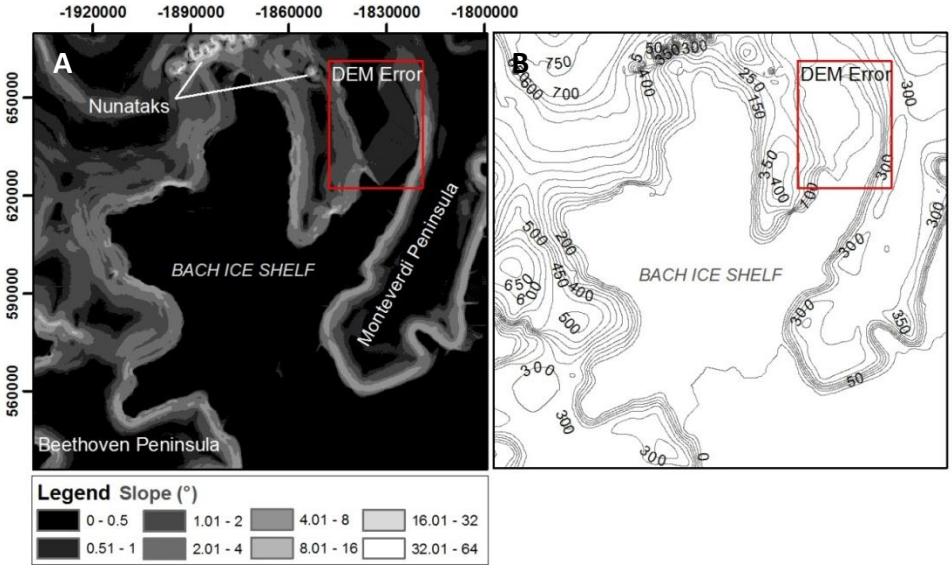

Figure 6.15. Calculated surface slope (A) in degrees and elevation contour lines (B) for the grounded portion of ice surrounding Bach Ice Shelf illustrating the steep-sided topography and high-degree surface slopes of feeder glaciers.

6.2.3 Interpretation of structures and their significance on ice-shelf dynamics

Surface features not only illustrate current glaciological processes, but also hold key information into past processes and dynamics of an ice shelf system. In the following section, the present-day structural configuration of Bach Ice Shelf is discussed in terms of current and historical contexts.

6.2.3.1 Flow-related surface structures

The most dominant flow-related features on Bach Ice Shelf are longitudinal surface structures. Despite their frequency and regularity on ice-shelf systems, the formation of longitudinal structures in such systems is still not fully understood. Several key concepts have been proposed, linking internal stratigraphy and ice-flow dynamics, yet data insufficiency prevents a definitive, transferable method of origin from being established. Where a three-dimensional relationship can be demonstrated, these longitudinal structures are interpreted as foliation (Hambrey and Dowdeswell, 1994; Hambrey and Glasser, 2003), formed by progressive deformation (Hambrey, 1977) under laterally-compressive dynamic conditions; their presence down-ice is maintained through longitudinal extension in the principal ice-flow direction. Ice-penetrating radar profiles across longitudinal surface structures on fast-flowing ice streams reveal isochronous internal reflectors illustrating the englacial pattern of foliation within the ice, associated with the longitudinal surface structures (e.g. Jacobel *et al.*, 1993; Ng and Conway, 2004; Rippin *et al.*, 2006). However, Campbell *et al.*, (2008) revealed inconsistencies in linking longitudinal surface structures and internal layering on the Kamb Ice Stream, but proposed that surficial-processes down-ice change the visible portion of longitudinal structures whilst the internal stratigraphy remains unaffected.

Alternatively, results from ice-flow modelling suggest that longitudinal surface structures can develop as a result of high velocities at the ice/bed interface compared to shearing through the ice thickness. As a result, undulations at the bed are transmitted through the ice to the surface (Gudmundsson *et al.*, 1998, Raup *et al.*, 2005). Furthermore, Merry and Whillans (1993) proposed that such features arise due to localised high shear-stresses initiated at the onset of ice streams, and Hulbe and Whillans (1997) argued that they form due to the nature of aligned crystal fabric within the ice. These processes of formation are further discussed in Chapter 9.

On Bach Ice Shelf, longitudinal surface structures develop in three principal locations; Type 1 at the confluence of tributary glaciers on grounded ice, Type 2 at the confluence of two ice-shelf flow units, and Type 3 within the channel of individual flow units, often, but not exclusively, near to the grounding zone. It is not possible to quantitatively infer longitudinal-structure development from datasets utilised in this study because a three-dimensional representation is not available. However, a qualitative assessment is offered based on their form and associated dynamics.

Type 1 and Type 2 structures are similar in their formation, but Type 2 are more distinct in their appearance and suggest greater surface relief and amplitude, and can be traced down ice for greater distances. Both Type 1 and Type 2 features form abruptly at the confluence of two separate flow units that consequently govern the spacing between individual features. Type 1 features can be traced down-ice for several tens of kilometres but tend to become indistinct from surrounding ice due to the development of new longitudinal features as progressive coalescence of tributary glaciers takes place. The characteristics of both Type 1 and Type 2 longitudinal structures suggest that their formation is directly linked to the lateral compression and merging of ice along flow unit boundaries, with their physical appearance most likely to be representative of the mass, dynamics and mechanical properties of the individual, coalescing flow units.

The similarity of Type 3 longitudinal features to foliation structures on temperate valley glaciers leads to the inference that they are formed by visco-plastic deformation of ice under transverse compression, and transmitted down-ice with flow through secondary longitudinal extension (Hambrey, 1977; Hooke and Hudleston, 1978; Glasser *et al.,* 2009). Flow dynamics calculated through InSAR support this proposition. It is possible that other factors such as bed perturbations in regions of fast-flowing ice result in surface deformation, yet formation of longitudinal structures at the grounding zone of Bach Ice Shelf even where flow speeds are comparatively low suggests otherwise.

Despite uncertainty surrounding their origin and development, two prominent attributes of longitudinal features on Bach Ice Shelf are their persistence down-ice and their apparent resistance to lateral-spreading. Elsewhere, the endurance of longitudinal features down-ice is associated with ‘fast-flowing’ or ‘active’ ice (Campbell *et al.,* 2008; Figure 6.16). The longevity of longitudinal structures on Bach Ice Shelf is principally attributed to an increase of surface speeds within active flow units.

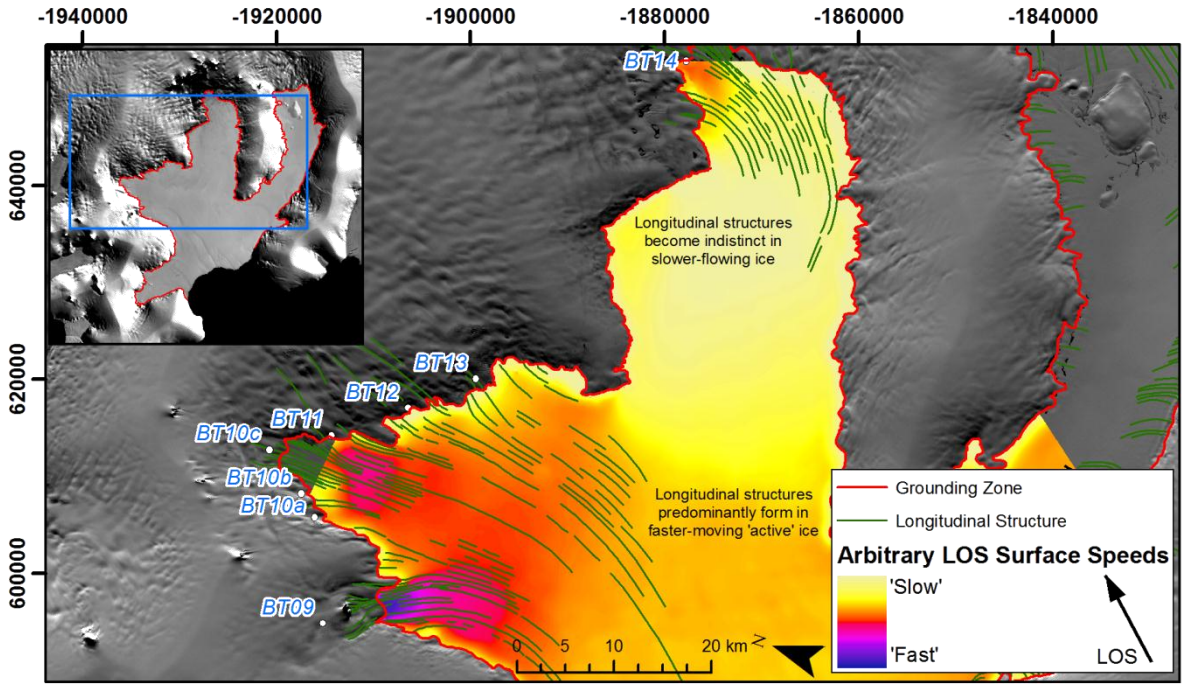

Figure 6.16. InSAR line-of-sight (LOS) surface speeds calculated from two ascending SAR scenes illustrating the preferential development and endurance of longitudinal features in more active ice. InSAR is most sensitive to movement to and from the sensor, along the line-of-sight as indicated in the Legend.

The most distinct longitudinal structures on Bach Ice Shelf develop in the Boccherini Ice Domain. Only occasionally can these features be traced upstream over the grounding zone, thus it is proposed that these structures are principally Type 2 or Type 3 features. Their existence down-ice is highlighted in the austral summer due to surface meltwater that preferentially fills surface furrows created during longitudinal feature development (it is also likely that meltwater further develops surface furrows by incising into the ice-shelf surface) (Figure 6.17). In the Williams Ice Domain, longitudinal structures exist in the most eastern portion but cannot be traced down-ice for more than 15 km. Surface meltwater pools during the austral summer are less homogeneous over Williams Ice Domain suggesting that there are fewer preferential linear channels to accommodate, thus highlighting the absence of longitudinal structures. Many longitudinal features observed on the surface of Williams Ice Domain can be traced back to their origin over the grounding zone to a succession of flow confluences around a series of nunataks at approximately -1883400 664000 m, and explain their less-distinct characteristics on the ice-shelf surface (Type 1). Absence of InSAR velocity calculations in this region prevents detailed structural/dynamic assessment from being made, although line-of-sight speeds calculated from the descending ERS-1/2 image pair display active flow where longitudinal structures exist and less-active flow where they become indistinct (Figure 6.16).

The short but regular longitudinal structures observed along the grounding zone of the Stravinsky Ice Domain, and in particular off Monteverdi Peninsula, illustrate the limited effect of tributary glaciers and sheet flow on ice dynamics in this region. Differential InSAR measurements are also absent over the eastern reaches of this domain, but ascending line-of-sight interferograms illustrate the active flow of tributary glacier BT02 where longitudinal structures are more distinct. Additionally, the line-of-sight interferograms show a decrease in surface velocities associated with BT02 into the main flow channel of Stravinsky Ice Domain; this corresponds to observed pressure ridges in Landsat and ERS SAR imagery, formed where the ice shelf buckles under compressive flow stresses (Figure 6.18). These are further discussed below.

A common characteristic of longitudinal structures on Bach Ice Shelf is their linearity down-ice, independent of their length, spacing and amplitude. This emphasises the compressional and cohesive regime of Bach Ice Shelf caused by the overall morphology of the ice shelf and its associated inlets and peninsulas that consequently retard lateral spreading. This cohesive regime is also reflected in the surface dynamics, with no enduring flow discontinuities observed between tributary glaciers. Their linear characteristics down-ice also suggest that there have been no recent alterations in the configuration and flow dynamics of Bach Ice Shelf.

At the ice front, distinct longitudinal structures are apparent. Termed flow-unit boundaries in the structural maps, they are linked to longitudinal structures developed at the major confluences upstream, and are likely to reappear at the ice front due to increased ablation of surface layers. Indeed, two of these flow unit boundaries coordinate well with Type 2 longitudinal structures flowing from BT09, whereas other flow unit boundary features cannot be traced to their origin. These features may represent internal layering linked to longitudinal structure development upstream. Where they emerge, they exist mainly as longitudinal surface depressions rather than surface ridges, and also appear to have been subjected to a certain degree of deformation; they are neither as linear nor regular as their surface counterparts and may have undergone surface and/or subsurface degradation through time (Campbell *et al.*, 2008).

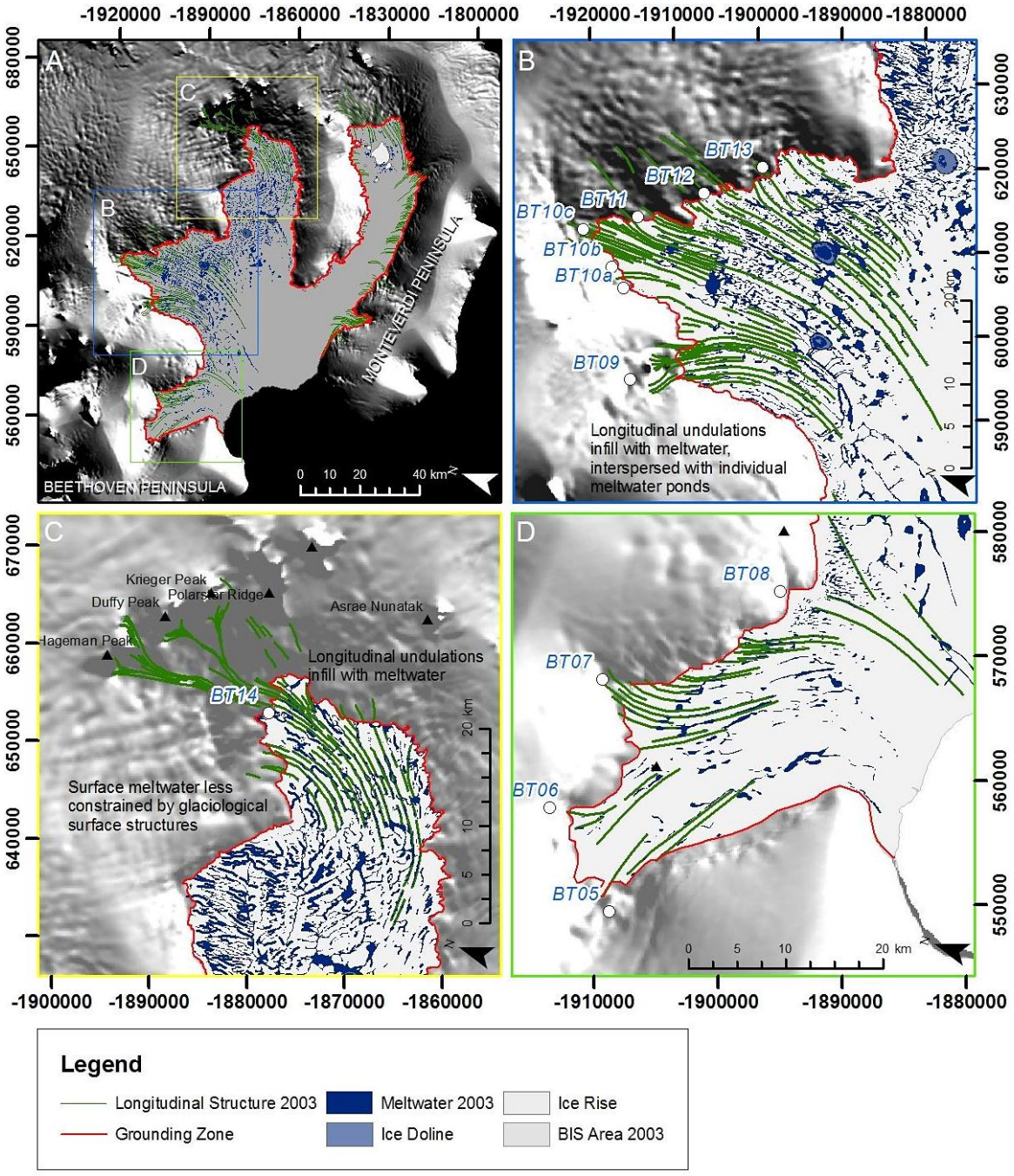

Figure 6.17. Surface meltwater and longitudinal structure interaction for February 2003 in, (B) Boccherini Ice Domain, (C) Williams Ice Domain, and (D) Weber Ice Domain. Meltwater pools predominantly follow longitudinal structures but also interlink, and are interspersed with individual meltwater ponds.

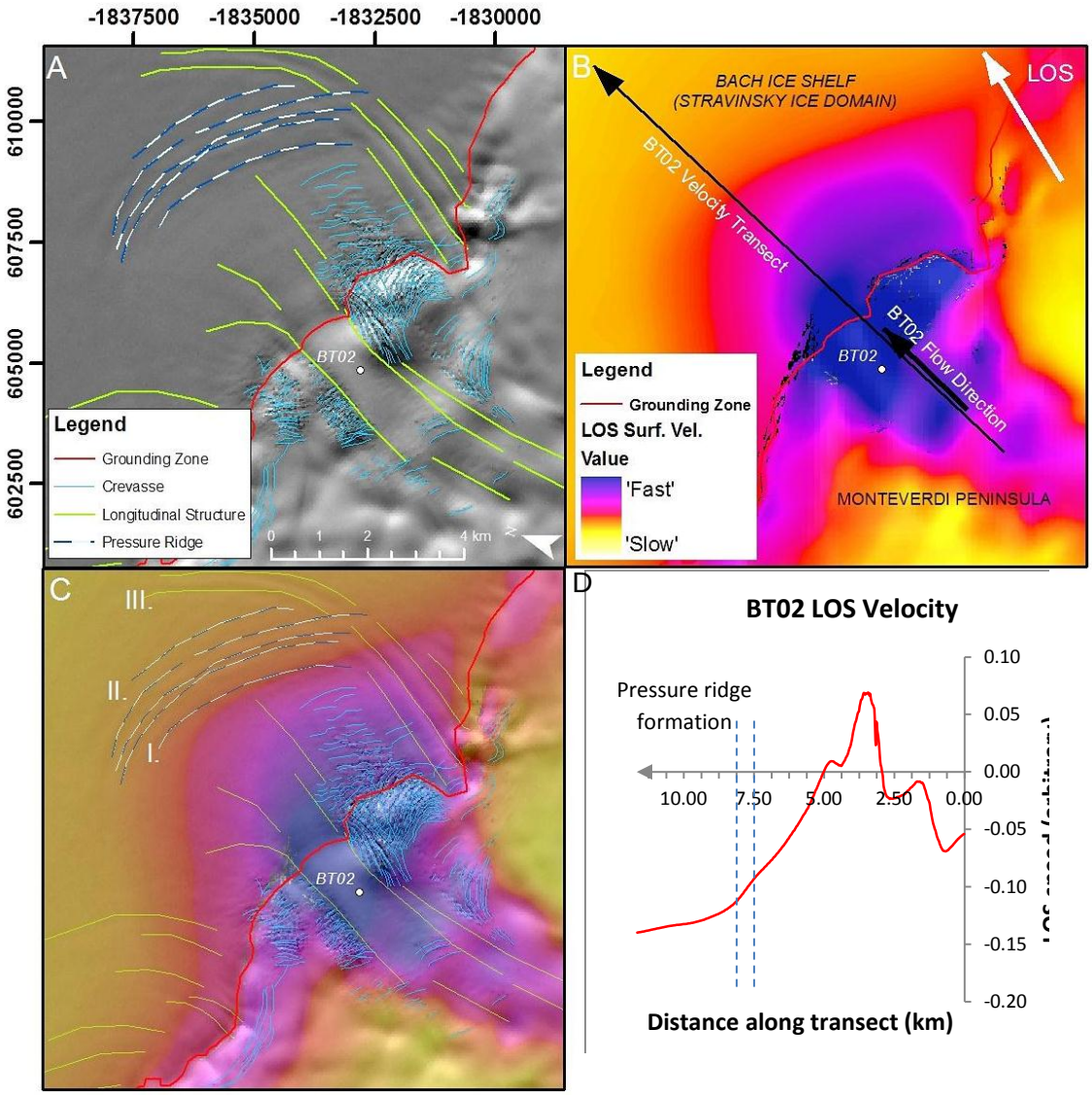

Figure 6.18. A) Major surface structures associated with tributary glacier BT02 and (B) calculated line-of-sight (LOS) surface velocities illustrating decreasing speeds along transect (BT02). Values represent unidirectional movement of ice from the sensors position. C) Displays surface structures overlaid on top of LOS velocities that emphasize the development of pressure ridges as surface speeds reduce (I). Pressure ridges migrate down-ice with the motion of BT02 (II). (III) Deflection of longitudinal surface structure as the dominant flow of the Stravinsky Ice Domain encourages ice north-easterly. D) Surface velocities extracted along transect BT02 that illustrate the decreasing velocities as ice enters the ice shelf. Pressure ridges are initially formed at 8 km along the transect.

Pressure ridges referred to above form in regions where ice is under high compressive-longitudinal stresses caused by faster flowing ice rapidly decelerating against a more resilient object. Elsewhere, these features are termed pressure rollers (Kehle, 1964; Smith *et al.*, 2007; Cook and Vaughan, 2010), and consist of linear hummocks that are elevated above the surrounding ice (Hayes, 1928). The locations of pressure ridges on Bach Ice Shelf thus indicate zones where further compressional-stresses are exerted on the ice and also show areas where horizontal ice dynamics become rapidly inactive. They are most

evident at the input of BT02 (Figure 6.18), and at the tip of Beethoven Peninsula where ice from Weber Ice Domain diverts to the ice front; fracturing down ice immediately after ice has rounded the headland illustrates the rapid shift from compressive to tensile stresses, and is discussed in more detail below.

6.2.3.2 Crevasses, fractures and rifts

Fracturing of ice occurs when tensile stresses exceed some threshold, allowing suitably-orientated pre-aligned cracks to deform (Vaughan, 1993; Rist *et al.,* 2002). The evidence of few surface crevasses, fractures and rifts on Bach Ice Shelf suggest that this threshold is not reached, except for in three principal zones; 1) in tributary glacier systems prior to entering the ice shelf; 2) at or near the ice-shelf front; and 3) on the lee side of headlands and peninsulas, as two flow units converge. Crevasses are also evident along the steep slopes of feeder glaciers, but rarely transmit across the grounding zone into the ice shelf, thus illustrating initial tensile stresses on grounded ice followed by increasingly compressive stresses at the grounding zone.

At the ice front, fractures form both transversely and longitudinally to the principal ice-flow direction. Transverse fractures in ice-shelf fontal zones most likely develop due to enhanced longitudinal extension through accelerated horizontal motion, high-tensile stresses caused by plate-bending of the ice front, and due to tidal flexure of the ice shelf (Rist *et al.,* 2002; Larour *et al.,* 2004; Scambos *et al.,* 2009). On Bach Ice Shelf, transverse fractures propagate at the western and eastern pinning points of the ice front as ice migrates around Beethoven Peninsula and Monteverdi Peninsula from Weber and Stravinsky/Williams ice domains respectively. Typically, these fractures propagate the entire depth of the ice front to form rifts which influence the dimensions of iceberg calving at the front, and consequently the spatial and temporal regimes of calving events (Weiss, 2004; Joughin and MacAyeal, 2005).

At the tip of Beethoven Peninsula in particular, a switch from compressive stresses to tensile stresses is inferred. As alluded to in section 6.2.3.1, pressure ridges are observed where the ice shelf has buckled under compressive stress; as ice migrates beyond this pinning point, fracturing takes place that eventually penetrates the entire depth of the ice shelf and propagates/migrates towards the ice front. A flow-speed transect (Figure 6.19) taken across this zone during 1995 illustrates the differences in surface speeds across this particular rift. It has been demonstrated through multi-annual surface analysis that these

rifts form the basis for iceberg calving along the ice front. It is likely that a similar process occurred at the opposite side of the ice front along Monteverdi Peninsula prior to the ice-shelf decoupling from its pinning point, and gives reason for transverse fracturing that also lead to iceberg calving.

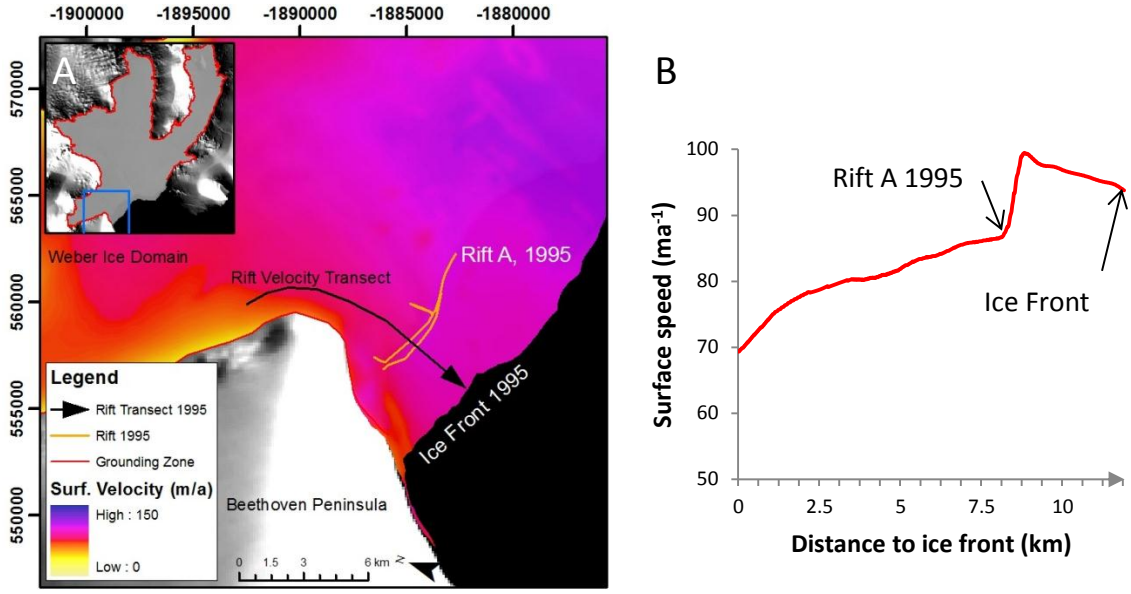

Figure 6.19. A) InSAR surface velocities from Weber Ice Domain towards the ice front illustrating (B) the sharp increase in speeds associated with rifting.

Longitudinal fractures at the ice front are typically no greater than 3 km in length and follow no apparent spatial pattern of development. Occasionally, these do cut back along former-flow unit boundaries but are most likely caused by localised, short-term changes in stress fields as a result of ice-shelf flexure, horizontal motion and/or increased tensile stresses following backstress-release from previous iceberg-calving events (Rist *et al.*, 2002; Larour *et al.*, 2004; Dupont and Alley, 2005; MacAyeal *et al.*, 2009; Guttenberg *et al.*, 2011). These flow unit boundaries are perhaps naturally weaker (Glasser and Scambos, 2008), being less cohesive, thinner (Vieli *et al.*, 2007), and with a greater concentration of marine derived ice (Fricker *et al.*, 2001; Khazendar, 2003). This concept is discussed further in Chapter 9.

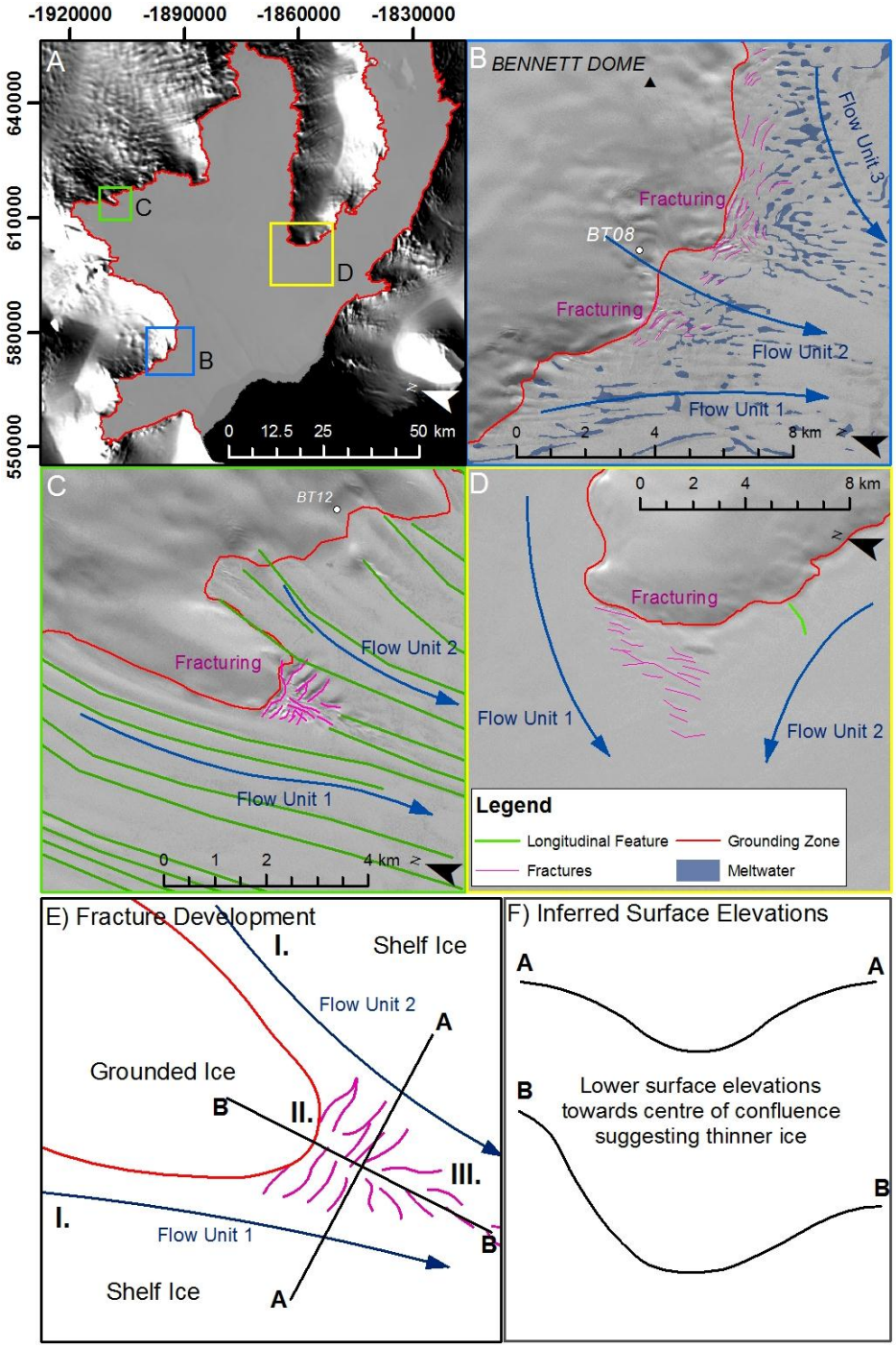

Figure 6.20. Fracture development in areas of flow-unit coalescence. A) Overview of Bach Ice Shelf, B) Complex fracturing between Flow Unit 1 (Weber), Flow Unit 2 (BT08) and Flow Unit 3 (Boccherini) around Bennett Dome. C) Fracturing between BT11 and BT12 and D) fracturing between Williams and Stravinsky ice domains. E) Schematic of fracturing illustrating the two flow units (I.), intermediary fracturing as ice is stretched away from the grounded ice (II.) and deformation of fractures down-ice (III.). F) Inferred surface elevations transversely (A-A) and longitudinally (B-B) in the coalesce zone.

Fractures and rifts also develop in zones between merging flow units on the ice shelf. Fracturing takes place at relatively slow speeds as ice is stretched longitudinally from the

grounding zone along the boundary of confluence, influenced by the faster flow units at either flank (Figure 6.20). Brash ice is also apparent in some instances, and illustrates the high-tensile stresses initially exerted on these regions. It is possible that these fractures also incorporate marine ice into the ice shelf through basal cavities that is consequently concentrated along flow unit boundaries (Khazendar, 2003). As distance from the grounding line increases, tensile stresses within these fracture zones reduce, whilst transverse loading increases, forcing fractures to deform and eventually reseal down ice (Figure 6.20F (III.)). Analysis of ICESat GLAS tracks over these zones illustrates a surface depression in the region of confluence. It is inferred from analysis of the RAMP DEM that ice in these fracture zones is thinner than that within the main flow channels, and combined with surface fracturing and incorporation of marine ice, is weak compared to the surrounding, consolidated ice.

The development of new, large fractures and rifts between March 2003 and March 2004, approximately 10 km from the ice front, illustrates a change in recent glaciological regimes in Bach Ice Shelf. Prior to 2003, there was no evidence of surface (optical datasets) or sub-surface (radar datasets) fracturing in this zone, thus the appearance of these new fractures/rifts is particularly striking. These features are mostly linear and stretch for ~18 km, sub-parallel to the ice front, cutting across several former flow-unit boundaries associated with tributary glaciers feeding the Boccherini Ice Domain, and at least one major meltwater channel. At their eastern tips, the fractures also cross the inferred boundary between Boccherini and Williams ice domains. Analysis of Landsat and Envisat ASAR imagery leads to the inference that these features formed simultaneously 'in-situ' rather than having been formed in different places or at different times, and having been transmitted down ice.

ICESat GLAS elevation measurements illustrate that this zone has undergone significant negative surface elevation changes (up to -0.61 ma^{-1}) from which thinning is inferred, but there is no suggestion that there has been an increase in surface velocities between ca. 1996 and ca. 2007 in the vicinity of fracture development. Thus it is unlikely that their formation is velocity driven.

The fractures exist in ice principally fed by the Boccherini and Williams ice domains, and has thus been in the floating portion of the ice-shelf system for between a minimum of 561 years and 625 years respectively (Table 6.8). This emphasises their recent, rapid creation

'in-situ' near the ice-shelf front rather than progressive development through the ice shelf. It also shows the cohesive nature of ice along flow unit boundaries further upstream that permit the fractures to propagate across the confluences.

Table 6.8. Calculation of the minimum time in which the newly-fractured ice has been in its respective ice domains.

Ice Domain (transect)	Mean velocity along transect ($\bar{v}$) (km a^{-1})	Total distance of transect (d) (km)	Minimum time of ice in transit (d/$\bar{v}$)
Boccherini (B03)	0.093	52.13	560.54*
Williams (B05)	0.090	56.25	625.00*

*Due to data insufficiency, velocity transects are not extended back to the grounding zone, thus these are minimum timescales only. It is expected that mean velocities would decrease over an increased distance if these transects were fully extendable to the grounding zone.

In consideration of this, the development of the fractures can be mostly attributed to plate bending at the ice front. Rist *et al.,* (2002), Larour *et al.,* (2004) and Scambos *et al.* (2009) all reference bending of the ice-shelf front due to the effect of buoyancy stresses exerted on the ice shelf as described by Reeh (1968). Essentially, differences in stress fields between tidal motion and wave propagation against the ice-shelf front, and the forward motion of the ice shelf cause upwardly convex profile that induces surface fracturing (Scambos *et al.,* 2009). Over time, these fractures deepen with increased stress either with or without the presence of surface meltwater. In the case of Bach Ice Shelf, meltwater is observed draining into Rift C, but not Fracture A; this supplementary hydro-fracture mechanism (Scambos *et al.,* 2002) may explain the difference between these two structures after initial fracturing. However, it is this initial fracturing that is most striking; another threshold must have been satisfied to permit fracturing between 2003 and 2004.

Continued recession of Bach Ice Shelf has seen the ice front retreat into a wider channel of Bach Inlet, and consequently led to an increase in the surface area exposed to these tidal forcings and the forward motion of the ice shelf. Together with the decoupling of the ice front from the tip of Monteverdi Peninsula during the late 1980s, and subsequent removal of a key pinning point, the conditions for plate-bending may have been satisfied by March 2003, not only explaining their development, but also their prior absence with a more stable ice front. Furthermore, it has been observed that the ice front has become increasingly concave through continued retreat, and the recent fracturing may have been a response to these changes through changing stress fields and a shift to an increasingly instable geometric setup.

Any one of these processes, or indeed a combination of two or more, provides possible conditions that explain recent fracturing near the ice front.

6.2.4 Significance of surface meltwater and associated features.

Reference has already been made to the preferential filling of meltwater into surface undulations associated with longitudinal surface structures to create a network of elongated meltwater pools. At the ice-shelf grounding zone, individual meltwater ponds are also observed throughout the austral summer, occupying surface depressions interpreted as the local minimum of the grounding zone, caused by continuous tidal flexure (Brunt *et al.*, 2010).

At the onset of the melt season, surface meltwater begins to form as individual ponds at the grounding zone but soon develops in the centre of the ice shelf from north to south. This highlights the southward migration of the annual thermal boundaries during the austral summer that initiates the gradual increase in surface meltwater across the ice shelf each season. The existence of individual meltwater ponds across the surface illustrates widespread melting of the ice-shelf surface rather than localised melting in the north and subsequent redistribution of meltwater across its surface in supra-glacial meltwater channels.

Because of the largely compressive flow regime over much of the ice shelf, few surface fractures exist, thus meltwater drainage through the shelf is largely prevented. This is significant for two reasons; first, meltwater features on Bach Ice Shelf are present for much longer than is normal (Cook and Vaughan, 2010), illustrating that the presence of surface meltwater alone is not enough to govern widespread fracturing of an ice-shelf system. Second, it is inferred that at the end of the melt season, surface melt ponds refreeze on the ice shelf, thus creating an impermeable stratum through which subsequent surface melting is unable to penetrate (Wager, 1972), and therefore giving reason to the remarkably similar pattern of surface meltwater features in successive melt-events.

In the few locations where surface meltwater coincides with surface fractures, there has been no detectable expansion in the dimensions of these fractures in the satellite imagery. This occurs almost exclusively in flow-unit boundary zones where initial tensile stresses at the grounding line switch to a compressive regime at the confluence of adjacent flow units. This suggests that either the force of meltwater within the surface fractures does not reach

the necessary threshold to further expand the fractures, or expansion is superseded by fracture healing.

One important alteration to the meltwater regime, however, is associated with the appearance of the large fracture/rift system near to the ice front. Prior to their existence, surface meltwater was evident flowing from the Boccherini Ice Domain towards the ice front (although never reaching it), yet after their formation, surface meltwater seemingly drains from the surface through the aforementioned rift, thus providing a viable route for surface drainage. Indeed, the draining of surface meltwater through rifts and crevasses has been ascribed as one of the possible mechanical processes of ice-shelf collapse (Scambos *et al.,* 2002). However, here this is not considered important on Bach Ice Shelf due to the already large opening and limited surface meltwater entering the rift, although it may have been an important factor in initial rift propagation; from the data presented here it cannot be confirmed or refuted.

There is a clear increase in the spatial extent of surface meltwater between January 1973 and February 2003. Further analysis of meltwater extent depicted in a series of Landsat and Envisat ASAR imagery also indicates a southward migration of meltwater limit between January 1973, February 1997, February 2003 and February 2007, and illustrates the proposed southward migration of warmer thermal boundaries associated with regional climate change since the 1950s (King, 1994; Morris and Vaughan, 2003).

During the austral summer, meltwater occupies distinct ice dolines on the surface of Bach Ice Shelf. At least four, large dolines are identified and display sizes of up to 3.5 km. On Larsen B, these features are rounded, hollowed depressions tens of metres deep, and are considered weaken the surrounding ice shelf (Bindschadler *et al.,* 2002). These features are also visible on Bach Ice Shelf in imagery absent of surface meltwater from which it is possible to infer steep-sided walls and smooth, consolidated floors. Elsewhere it has been shown that their formation requires abundant surface meltwater that actively encourages development through the creation of sub-surface voids that eventually collapse (Bindschadler *et al.,* 2002). These authors suggest that the presence of meltwater acts as a weight on the ice-shelf surface and induces unequilibrated stresses that have the potential to cause localised fracturing in the underlying impermeable layers. Draining of the surface meltwater into underlying firn initiates further melting that consequently drains through the ice shelf to the ocean below thus finally allowing the roof of the void to collapse

(Bindschadler *et al.,* 2002). On Bach Ice Shelf these features form exclusively in regions where substantial meltwater is evident thus satisfying the basic theoretical prerequisites for formation.

Bindschadler *et al.* (2002) also show that ice dolines can form quickly (months) but remain on the ice-shelf surface for much longer. The sequence in which the ice dolines on Bach Ice Shelf form fits with the progressive southward migration of the meltwater limit, but due to data limitations, it is impossible to further pinpoint ice doline formation.

Although suggested to create weak points (Bindschadler *et al.,* 2002), the presence of ice dolines on Bach Ice Shelf is not considered to present any immediate widespread instabilities due to their positioning within the ice-shelf system. Indeed, to date, there has been no indication the ice dolines have affected the stability of any collapsed or partially disintegrated ice shelf, and thus the effects of any weaknesses are only considered to be localised.

6.2.5 Section summary

In this section key interpretations made from integrating the empirical data presented in Section 6.1 have been presented. Below is a brief summary of these interpretations.

1. The analysis of glaciological surface structures and features in consideration of ice-shelf velocities has illustrated the largely compressive dynamic regime of Bach Ice Shelf, limiting the creation and development of fractures and rifts to flow-unit boundary zones around distinct headlands, and at the ice-shelf edge. In the latter of these zones, changes to the glaciological stress regimes attributed to a retreating ice front, have been contemporaneous with the appearance of new fractures/rifts in ice previously considered cohesive.
2. The gradual expansion of surface meltwater from 1973 to 2007 is considered to be a response to the southward migration of warmer thermal boundaries caused by regional atmospheric-temperature increase (Morris and Vaughan, 2003). However, it has been further emphasised that an expansive surface meltwater distribution is not enough to solely govern widespread fracturing of ice-shelf surfaces, although localised fracturing of impermeable layers in the ice has seen the development of ice dolines on the surface of Bach Ice Shelf.

3. Widespread ice-shelf thinning is inferred from ICESat GLAS-derived surface elevation changes using a standard method of conversion and by applying generalised densities for meteoric and marine ice, and sea water. It is proposed that a combination of enhanced surface melting and basal melting is the cause of the widespread thinning. These are discussed further in Chapter 9.

Chapter 7

George VI Ice Shelf

Chapter Overview

This chapter is split into two sections. Section 7.1 presents the results for George VI Ice Shelf, focussing on the spatial, structural and dynamic changes in the northern and southern regions. Section 7.2 presents an interpretation of these results, largely concentrating on those changes observed at the two ice fronts and their tributary glaciers. Where similar interpretations are made (structural development, for example) the reader is referred back to Chapter 6 to avoid repetition. The results and interpretations presented here are further discussed in Chapter 9.

7.1 George VI Ice Shelf Results

In this section, the dynamic regimes and surface velocities of George VI Ice Shelf are described, concentrating in particular on its northern and southern ice fronts. Secondly, the change in ice-shelf extent from ca. 1973 to 2010 is assessed, looking at its spatial and temporal response over several observation periods. Thirdly, a detailed structural overview is presented for the whole ice shelf, with subsequent analysis of the major structural changes analysed for both the north and south ice fronts. Finally, the calculated changes in surface elevations are presented, with particular emphasis again on the northern and southern ice fronts to complement the dynamic and structural components as outlined above. Figure 7.1 illustrates the general morphology, main tributary systems and key locations on and around George VI Ice Shelf as referred to in the following subsections, and also illustrates the velocity fields of George VI Ice Shelf as discussed in Section 7.1.1.1.

7.1.1 Ice-shelf dynamics

Four, four-pass interferograms were calculated over the northern sections of George VI Ice Shelf between October 1995 and March 1996 (ca. 1995). Additionally, manual feature tracking of surface structures was undertaken at the north and south ice fronts using Landsat imagery during observation periods outlined in Table 7.1.

Table 7.1 Feature tracking time periods and alias

Location	Observation period	Alias
George VI Ice Shelf North	1986 – 1991	ca. 1989
George VI Ice Shelf North	2001 – 2003	ca. 2002
George VI Ice Shelf North	2004 – 2010	ca. 2007
George VI Ice Shelf South	1986 – 1991	ca. 1989
George VI Ice Shelf South	2000 – 2003	ca. 2002
George VI Ice Shelf South	2008 - 2010	ca. 2009

**Plus InSAR ca. 1995 for George VI Ice Shelf North*

7.1.1.1 George VI Ice Shelf dynamic configuration

The dynamics of George VI Ice Shelf (Figure 7.1) in its northern section are principally controlled by the input of ice off Palmer Land, in particular from Riley, Chapman, Millett, Bertram, Ryder and Goodenough Glaciers. Smaller tributary glaciers (e.g. Naess, Willey,

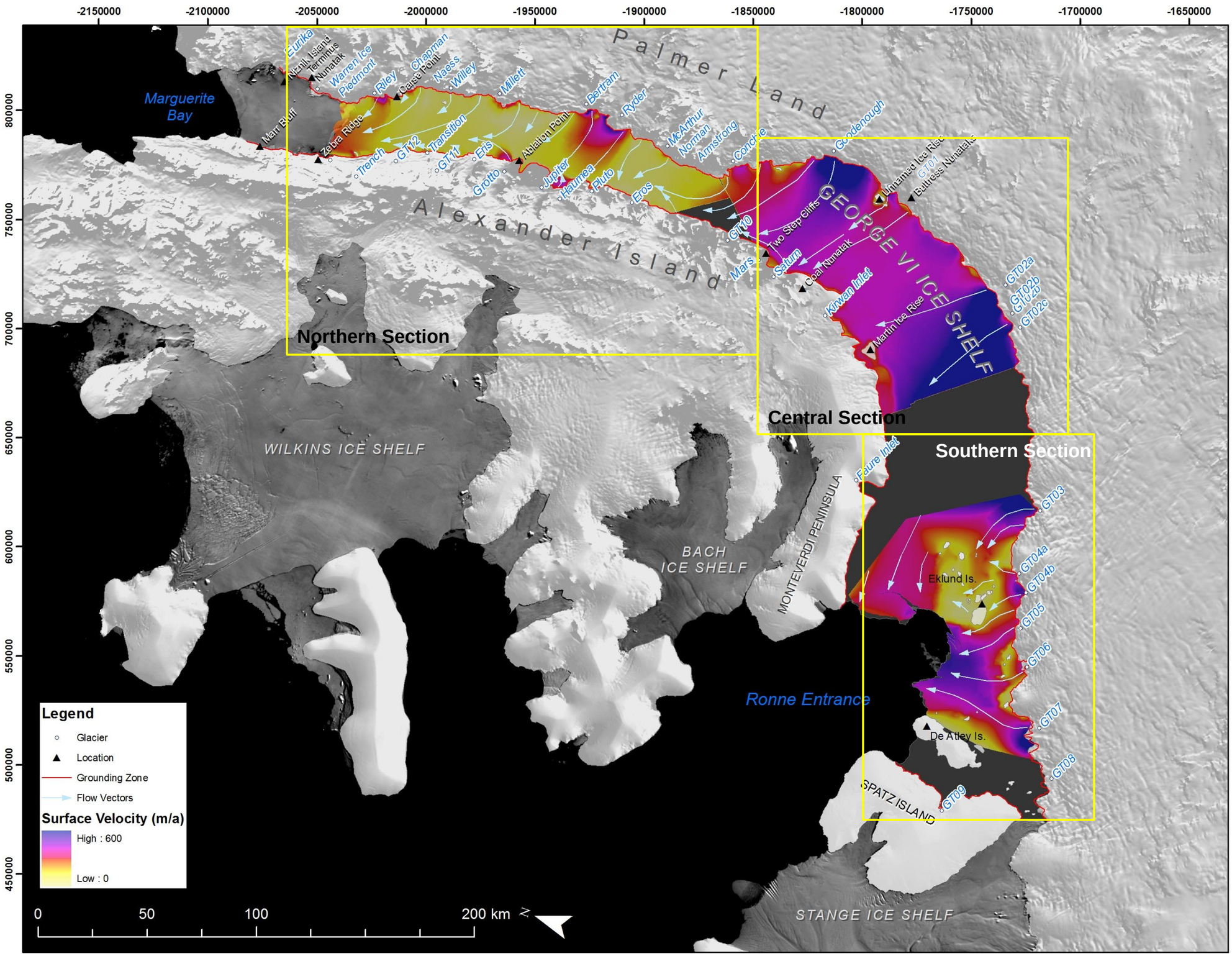

Figure 7.1. Overview of George VI Ice Shelf with location names, major/ key tributary glaciers, surface velocities and inferred flow direction. Displayed surface velocities in the northern and central sections calculated by InSAR (ca. 1995) with surface velocities in the southern section calculated by feature tracking (ca. 2009). Both velocity datasets displayed in ma^{-1} and are included here to illustrate the velocity fields and flow dynamics only. Absolute velocities are discussed in greater detail in Section 7.1.1.2. Place names taken from the APC. Background image = MOA 2003 (Haran *et al.*, 2006)

McArthur, Norman, Armstrong and Conchie) contribute to the overall mass of George VI Ice Shelf but their input does not impact greatly upon its dynamic regime. Near the northern ice front, ice flow is controlled by the input of glacier ice fed from Riley glacier that gradually increases in speed towards the ice front, diverting from a westerly to northerly flow towards the centre of the ice front. The speeds at the northern ice front are thus greatly influenced by the flow of ice from Riley Glacier (March 2010).

Along the western (Alexander Island) margin of George VI Ice Shelf, numerous, small tributary glaciers are observed flowing out from the mountain chain of Alexander Island (Figure 7.2). With the exception of Grotto Glacier, these tributaries have little impact on the overall flow dynamics of the ice shelf; Grotto Glacier is by far the greatest contributor of ice flow at the western margin. The remaining Alexander Island tributary glaciers are largely prevented from entering the centreline of George VI Sound by the steady, westward-to-northerly flow of glaciers from Palmer Land. These smaller flow units off Alexander Island are consequently forced to flow towards the northern ice front along the ice margin.

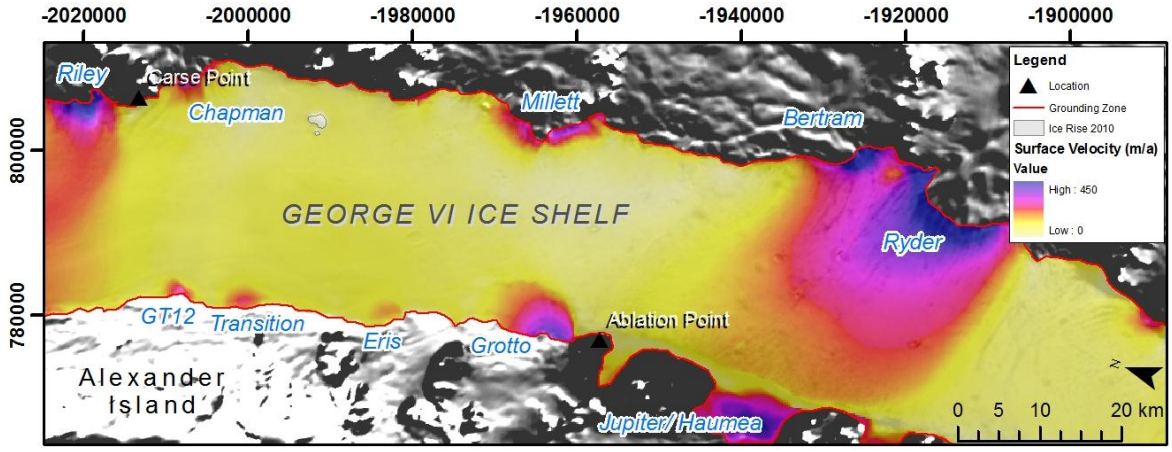

Figure 7.2. Flow velocities in the northern portion of George VI Ice Shelf highlighting the limited input of Alexander Island glaciers and dominance of Ryder Glacier across George VI Sound.

Further south along Palmer Land, input of ice from Millett Glacier and Bertram Glacier flows in a westward direction across George VI Sound. Flow velocities of Millett Glacier quickly reduce as ice crosses the grounding zone, becoming indistinct from the surrounding flow patterns. Bertram Glacier enters the shelf in a south-westerly direction and quickly impinges against the dominant flow of Ryder Glacier (Figure 7.2). As a result, there is a rapid reduction in the flow speeds associated with Bertram Glacier as it moves

over the grounding zone onto the shelf. Interferograms in the northern section of George VI Ice shelf illustrate the dominance of Ryder Glacier on the flow regime within the narrow channel of the Sound. Ice from Ryder Glacier flows directly across the shelf in a westward direction and only migrates northwards as it nears Alexander Island (Figure 7.1). The northward flow of the ice shelf south of Ryder Glacier is restricted across the entire width of the Sound by the input of glacier ice in this region, and ice flowing from Jupiter/ Haumea Glaciers is prevented from entering the centreline of the ice shelf as they flow directly towards Ryder Glacier.

As George VI Sound begins to widen, Armstrong and Conchie Glaciers enter the ice shelf at -1856650 774000 m and -1844000 774400 m respectively, yet it is Goodenough Glacier ~20 km south of this that dominates the flow within this region. Goodenough Glacier measures ~19 km across its grounding zone width and is one of the largest individual tributary glaciers that feeds into George VI Ice Shelf. Flow enters the shelf in two separate channels which merge together ~4 km into the shelf from the grounding zone into one flow unit. Flow patterns created by Goodenough Glacier can be traced across the 50 km-wide channel to the west margin where the ice shelf impinges against Alexander Island, reducing in speed and diverting to a northerly flow. Again, glaciers flowing from Alexander Island into George VI Sound are unable to penetrate into the main ice shelf and are instead pinned at, or near to, their respective grounding zones because of the dominant flow of Palmer Land glaciers.

Approximately 15 km south of Goodenough Glacier, a small unnamed glacier (GT01) enters the ice shelf. Its flow is diverted over a series of ice rumples before merging with the main ice-shelf. West of GT01, flow is controlled by the input of an unnamed glacier (GT02a) that enters the shelf at approximately -1742000 712200 m and diverges to the north and south margins. Flow towards the southern ice front is thus initiated at the input of glacier GT02a, as well as smaller tributary glaciers immediately south of this (GT02b, GT02c). The ice flows across George VI Sound towards Martin Ice Rise gradually diverting to a westerly flow. The speed of glacier ice from GT02a reduces as it crosses the grounding zone. At approximately -1755800 683000 m, the speed of GT02 begins to increase again as it enters the central region of George VI Ice Shelf. Westward from GT02c, sheet-flow is observed from the coast of Palmer Land with few distinct individual tributary glaciers observed. There is negligible input of ice from Monteverdi Peninsula in the southern regions of Alexander Island into George VI Ice Shelf.

Towards the southern region of the ice shelf flow from GT03 (-17242500 616700 m) is diverted westwards towards the Eklund Islands and does not flow across the width of the ice shelf as observed elsewhere. As it crosses the grounding zone, flow speeds reduce quickly over a distance of <10 km. As this flow unit approaches the eastern side of the Eklund Islands, speeds reduce further and divert around the ice rises and ice rumples creating complex velocity fields.

Glaciers GT04a and GT04b enter the ice shelf from the English Coast and flow directly towards the largest of the Eklund Islands causing GT04a to divert towards the main flow channel of GT03, where flow speeds are quickly reduced. Conversely, ice from GT04b is diverted in a westward direction, where it encounters GT05 (-1728200 566100 m). The dominance of GT05 at this point squeezes the flow of GT04b against the largest Eklund Island and as a result, the speed of the ice shelf is further reduced.

Ice flowing from GT05 splits into two channels as it approaches small ice rises and ice rumples of the Eklund Islands. These islands impact on the speed and velocity fields of George VI Ice Shelf at the southern front, reducing lee-side velocities considerably. Further west, tributary glaciers GT06 and GT07 enter George VI Ice Shelf from the English coast and supply ice directly to the southern ice front between the Eklund Islands and De Atley Islands, with ice velocities increasing towards the ice front. Finally, GT08 enters George VI Ice Shelf and is the dominant supplier of ice between De Atley Island and Spatz Island, eventually merging with GT09; flow between these two islands is confined to a narrow (~15 km) channel and largely independent of the main ice shelf.

7.1.1.2 George VI Ice Shelf flow speeds and dynamic changes

Ice-shelf velocities calculated at the northern ice front, and associated velocity transects, are illustrated in Figure 7.3 and Appendix 2a respectively. Furthermore, statistics for each transect are presented in Table 7.2. Velocities for the southern ice front are similarly displayed in Figure 7.4 and Appendix 2b, with transect statistics presented in Table 7.3. Surface speeds are displayed as metres per annum (ma^{-1}) to allow a direct comparison between InSAR-derived and feature tracking-derived results.

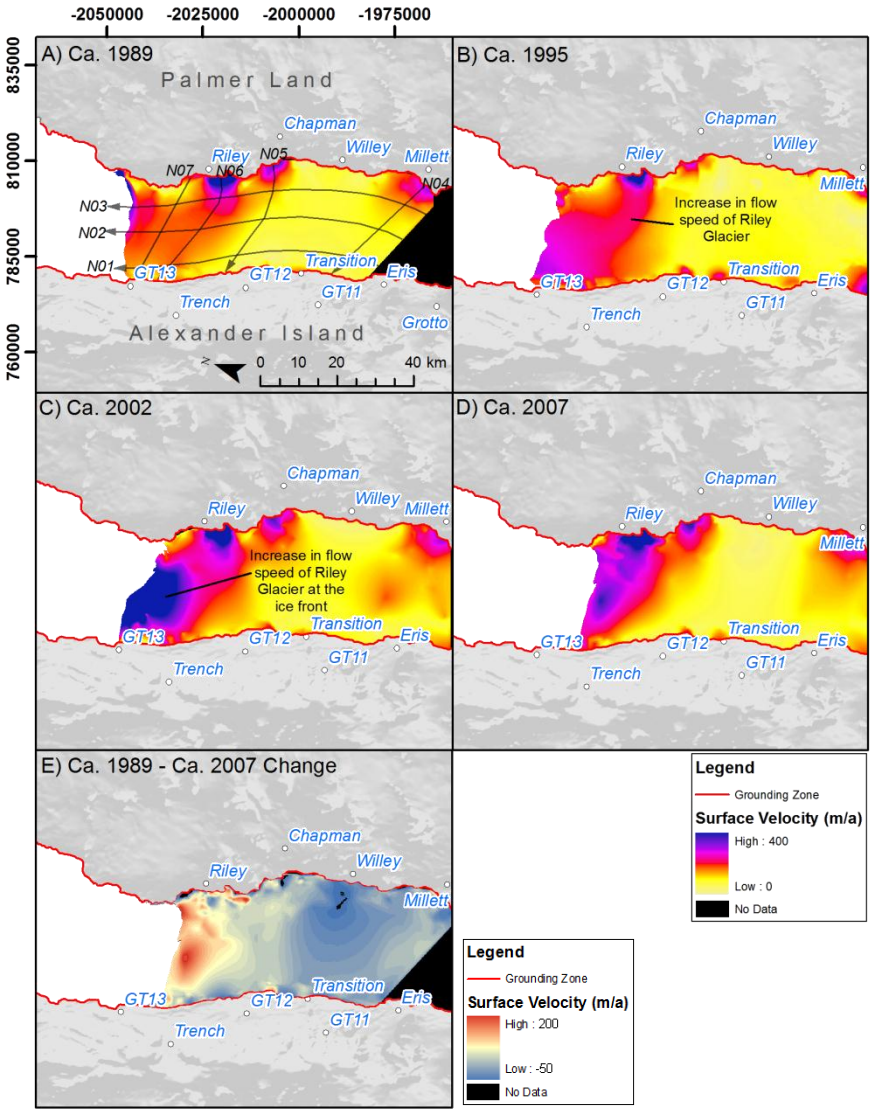

Figure 7.3 Surface velocity measurements for ca. 1989 (A), ca. 1995 (B), ca. 2002 (C), and ca. 2007 (D) at the northern ice front, and overall velocity change (E) from ca. 1989 to ca. 2007. A, C and D were calculated through manual feature tracking whereas B was calculated by InSAR. All velocities are displayed as ma^{-1}. Note the dominant flow associated with Riley Glacier at the northern ice front and its apparent speedup between A, B and C as the ice front retreats. Transect location given in A.

Table 7.2. Velocity-transect statistics for north George VI Ice Shelf. Plots available in Appendix 2a.

	Minimum (ma^{-1})				Maximum (ma^{-1})				Mean (ma^{-1})			
Transect	**Ca. 1989**	**Ca. 1995**	**Ca. 2002**	**Ca. 2007**	**Ca. 1989**	**Ca. 1995**	**Ca. 2002**	**Ca. 2007**	**Ca. 1989**	**Ca. 1995**	**Ca. 2002**	**Ca. 2007**
N01	43	77	68	63	175	283	374	246	97	151	149	109
N02	77	72	95	54	307	264	637	347	135	140	208	144
N03	69	20	73	26	439	226	319	327	162	108	165	155
N04	48	46	87	60	286	259	310	314	119	93	150	131
N05	75	84	67	62	371	307	359	378	122	122	159	157
N06	126	25	99	116	526	507	542	598	214	243	304	328
N07	82	14	77	78	218	288	666	256	149	207	376	159

The velocity measurements illustrate the dominance of flow off Palmer Land, decreasing in speed towards the centre of the ice shelf, with a slight increase in speed towards Alexander Island at the input of smaller tributary glaciers. There are no notable increases or decreases in surface velocities calculated over N04 or N05 over time (Table 7.2, Appendix 2a), and only a slight increase in flow speed recorded along N06. It is evident that an increase in surface velocity has occurred towards the northern ice front over time (Figure 7.3E), and is particularly noticeable from 40 km to 75 km along transect N02 between ca. 1989 and ca. 2002 (Table 7.2).

At the south ice front (Figure 7.4, Table 7.3, Appendix 2b), transects SG01, SG02, SG03, SG04, SG05 and SG06 all illustrate an increase in surface velocities between ca. 1989 to ca. 2009 (Figure 7.4D). Between the Eklund Islands and De Atley Islands, feature tracking velocities show an increase stemming from the grounding zone, related to the increased influx of tributary glacier GT07, and along the ice front. Around the Eklund Islands much slower velocities are illustrated and show no distinct increases or decreases in surface speeds over time. Similarly, flow velocities show little alteration between the Eklund Islands and Monteverdi Peninsula from ca. 1989 to ca. 2009 (Figure 7.4D).

Table 7.3. Velocity transects statistics for south George VI Ice Shelf. Plots available in Appendix 2b.

	Minimum (ma^{-1})			Maximum (ma^{-1})			Mean (ma^{-1})		
Transect	**Ca. 1989**	**Ca. 2002**	**Ca. 2009**	**Ca. 1989**	**Ca. 2002**	**Ca. 2009**	**Ca. 1989**	**Ca. 2002**	**Ca. 2009**
SG01	172	217	209	288	688	756	222	348	407
SG02	252	339	449	389	472	635	319	421	525
SG03	222	233	224	463	540	682	343	422	534
SG04	234	169	323	473	566	809	370	410	531
SG05	244	110	367	444	471	749	361	417	520
SG06	135	221	233	259	456	489	195	281	286
SG07	40	24	75	412	557	582	154	169	240
SG08	52	73	139	557	601	690	286	308	382
SG09	226	281	306	365	395	478	325	346	364

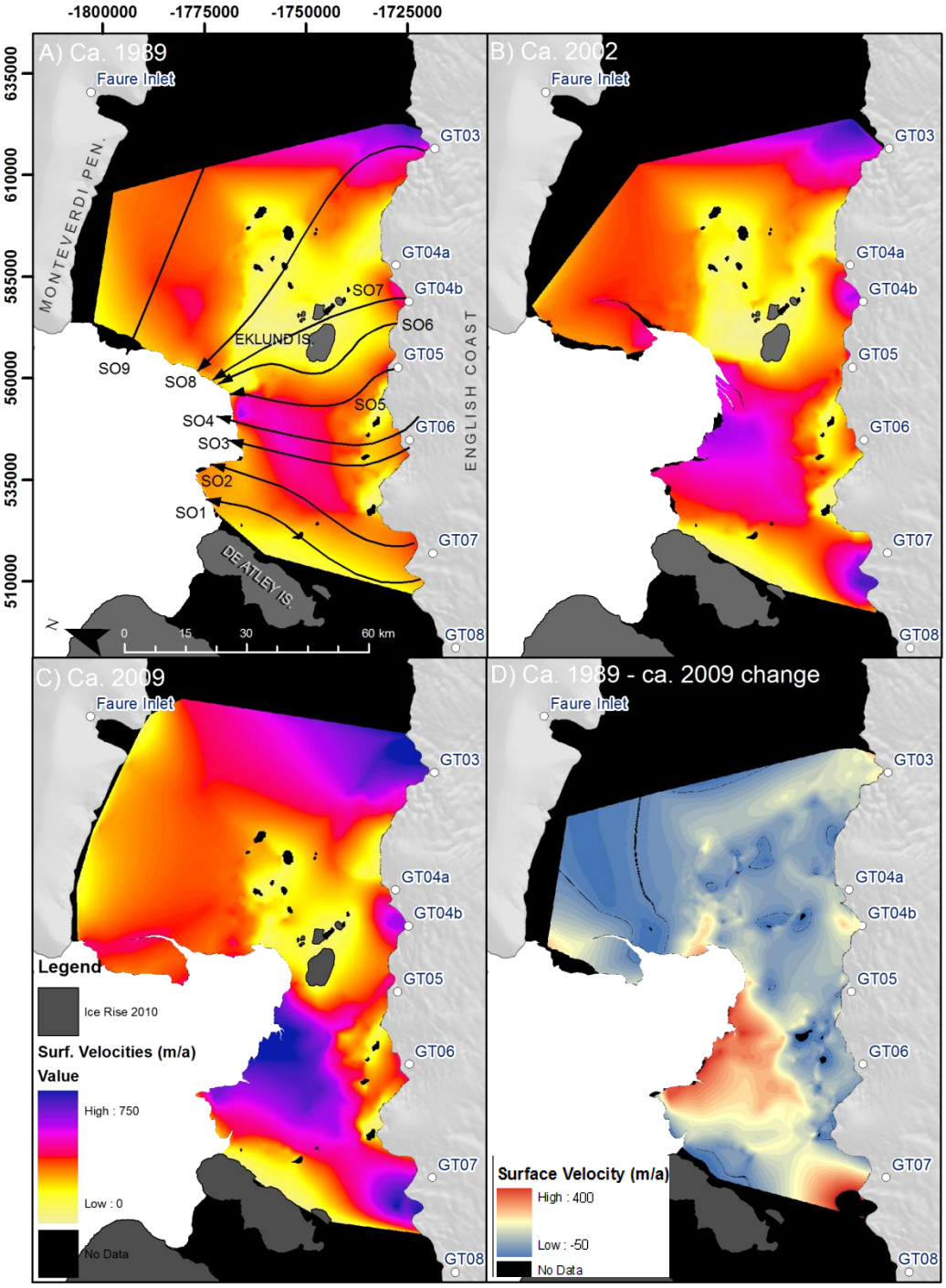

Figure 7.4. Surface velocity calculations for the southern ice front of George VI Ice Shelf for A) ca. 1989, B) ca. 2002 and C) ca. 2009, with velocity changes from ca. 1989 to ca.2009 (D). All velocities calculated through manual feature tracking. A clear increase in velocity is measured on the ice-shelf surface between the Eklund Islands and De Atley Island, and also in flow associated with GT07 off the English Coast. Flow in the centre of the ice shelf is retarded by the presence of the Eklund Islands, with flow towards Monteverdi Peninsula stemming from tributary glaciers further upstream showing little change over time.

7.1.2 George VI Ice Shelf spatial extent

The total spatial extent of George VI Ice Shelf has been calculated using Landsat and ERS satellite data from January 1973 to January 2010 at five intervals (Figure 7.5, Table 7.4). Due to limitations of the satellite data, three assumptions have been made in order to assess the total spatial extent of the ice shelf.

1) Extensive cloud cover over the northern ice front during 1973 prohibited the identification of the northern extent during this year, thus the first spatial extent calculations are made using the northern ice front extent on 6 Jan 1974, and the southern extent on 9 Jan 1973. It is assumed with some confidence, due to the presence of sea ice in the pro-ice shelf area in the austral summer in both 1973 and 1974 that the northern margin had not greatly advanced or retreated between these two dates.
2) Data limitations also prevented the identification of the 1991 northern ice front. Spatial extent calculations are thus made for the 1989/1991 (ca. 1990) period using the northern extent from 24 Mar 1989 and the southern extent from 4 Feb 1991. A second image from 27 Feb 1991 was used to map the southern ice front between De Atley Island and Spatz Island. Again, it is thus assumed that there is no significant change in the ice-shelf northern margin between 1989 and 1991.
3) Similarly, excessive cloud cover in successive images during 2003 prevented the northern margin from being digitised. Instead, the northern ice frontal position from 2001 is used to calculate the spatial extent for 2003; there is little change in the western edge of the north ice front between 2001 and the visible portion in 2003. It is thus assumed that the eastern edge of the northern ice front has also not undergone significant change.

Table 7.4. Areal calculations and spatial changes of George VI Ice Shelf based on composite imagery from 1973 to 2010. Approximated rate of loss calculated is based on the number of years between images and extrapolated to $km^2 a^{-1}$. Data presented in Figure 7.5 and further analysed for the northern and southern ice fronts in Table 7.5 and Table 7.7 respectively.

Year	Approx. Ice Shelf Area (km^2)	Approx. Net change (km^2)	Approx. rate of change ($km^2 a^{-1}$)	% Loss from ca. 1973	% Remaining of ca. 1973
Ca. 1973	25366.54	N/A	N/A	0.00	100.00
Ca. 1990	24190.21	-1176.33	-71.29	4.64	95.36
Ca. 1996	23931.45	-258.76	-47.05	5.66	94.34
Ca. 2001	23678.46	-252.99	-38.92	6.65	93.35
2010	23370.94	-307.52	-38.44	7.87	92.13

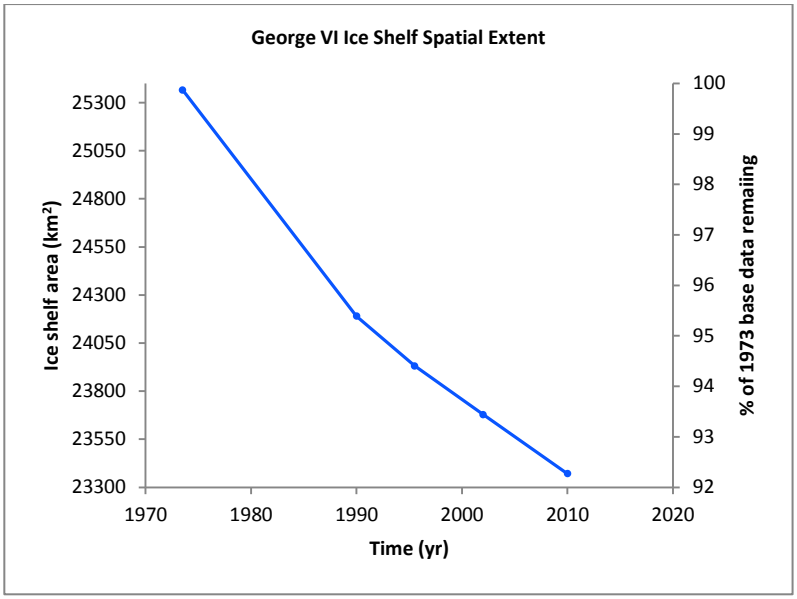

Figure 7.5 Rate of retreat for the whole of George VI Ice Shelf from ca. 1973 to 2010 calculated over four observation periods. Note the initial large-scale retreat between 1974 and 1986, but relatively steady retreat since.

Between ca. 1973 and 2010, George VI Ice Shelf lost 1995.6 km² of ice from its north and south margins combined, equating to 7.87% of the original spatial measurements calculated in ca. 1973. Of this, 4.64% of the retreat occurred within the approximate 17-year period from ca. 1973 to ca. 1990, with the remaining 3.23% occurring from ca. 1990 and January 2010. The large calving event observed during January 1973 at the southern margin is not included in the calculation as it had already detached from the shelf. In order to develop a better understanding of the ice-shelf system, the northern and southern ice fronts are hereafter considered individually.

7.1.2.1 George VI Ice Shelf north ice front

Table 7.5. Spatial changes at the north ice front from 1974 to 2010. Rate of loss based on number of days between images and extrapolated to $km^2 a^{-1}$. Data presented in Figure 7.6.

Year	Areal retreat (km^2)	Advance (km^2)	Net (km^2)	Rate of advance/ retreat (km^2a^{-1})	% of Total North Ice Front Loss
1974	N/A	N/A	N/A	N/A	0.00
1979	-820.44	0.00	-820.44	-161.63	65.39
1989	-90.30	0.00	-90.30	-8.91	7.20
1996	-92.05	0.68	-91.37	-13.24	7.34
2001	-53.75	0.90	-52.85	-10.82	4.28
2010	-198.09	0.00	-198.09	-21.88	15.79

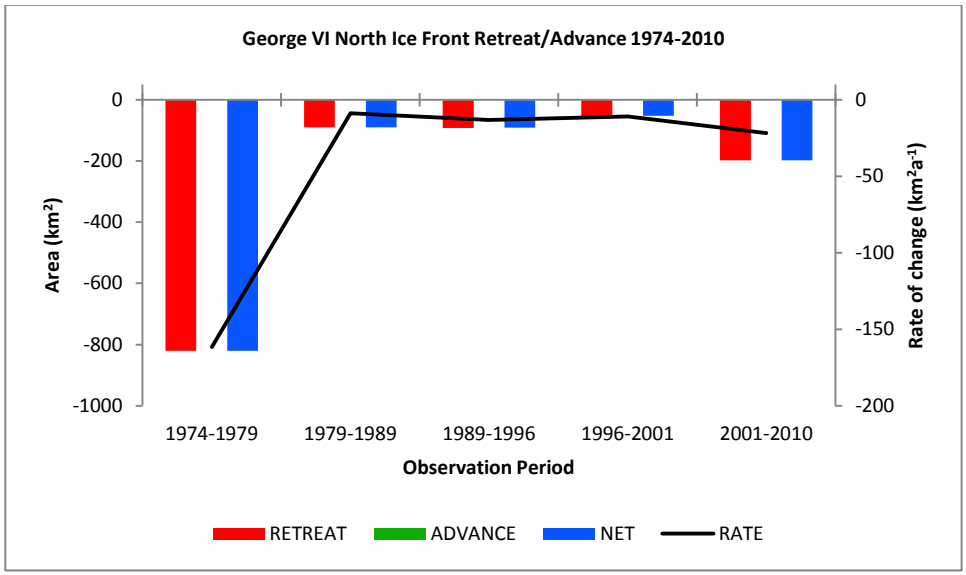

Figure 7.6 Spatial and temporal retreat of George VI Ice Shelf north ice front illustrating the initial large-scale retreat between 1974 and 1974, followed by regular retreat between 1979 and 2010.

Detailed descriptions of the north ice front of George VI Ice Shelf and its changes over time are given in Table 7.5. Between 1974 and 1979, approximately 820 km^2 of ice was lost off the north ice front (Figure 7.6, Figure 7.7). Further retreat was recorded along the Palmer Land grounding zone between 1979 and 1989, 1989 and 1996, and from 1996 to 2001, whilst the Alexander Island pinning point remained relatively stable (adjacent to Zebra Ridge) until retreating between 2001 and 2010. In total, 1255 km^2 of ice was lost from the northern ice front between 1974 and 2010, with the centre of the ice front retreating 40.63 km into a narrower channel of George VI Sound. Over each of the time periods, a slight concave profile was observed.

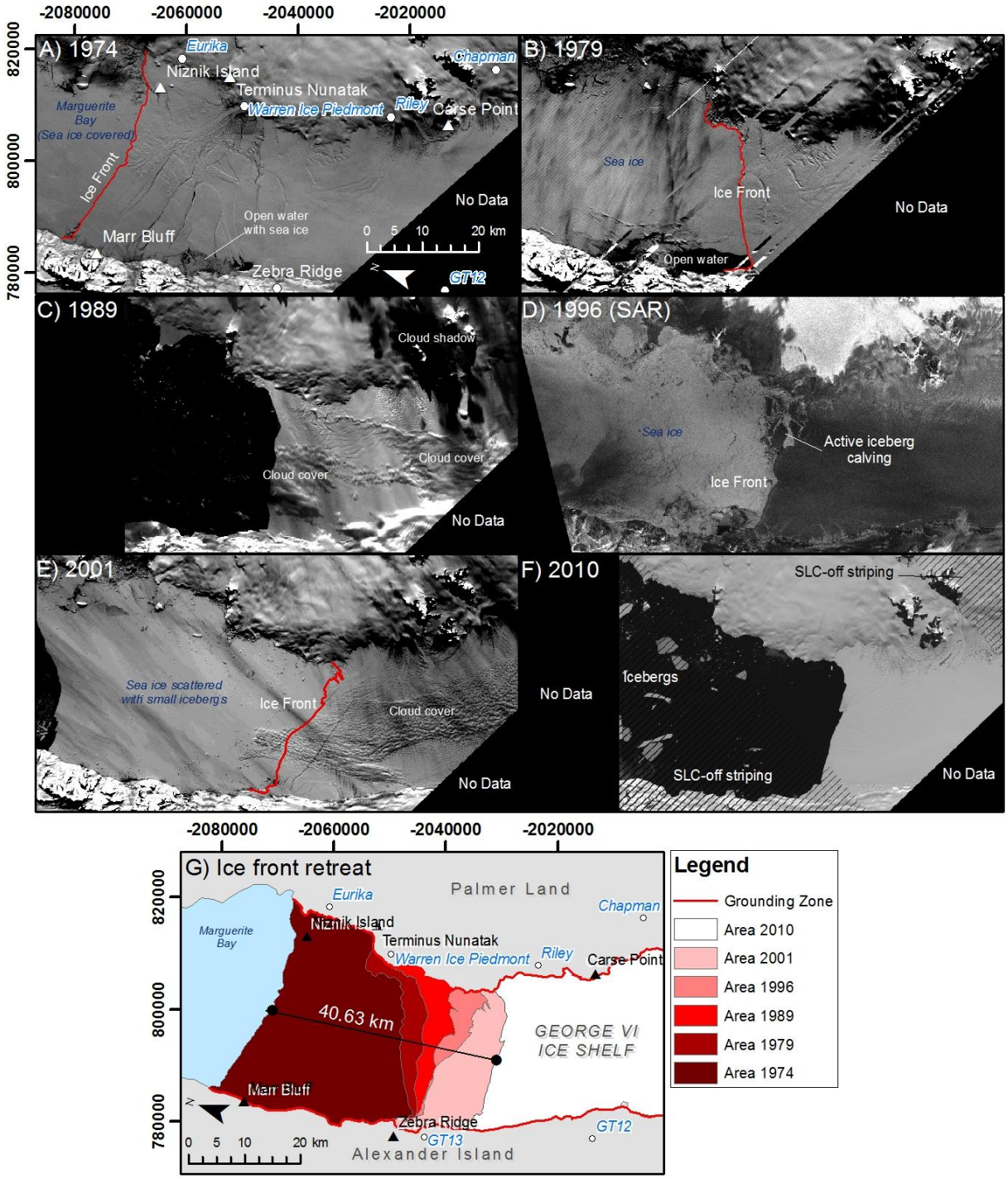

Figure 7.7. North ice front positions for George VI Ice shelf (A-F) as discussed in Table 7.6. G) illustrates the spatial retreat of the ice front between 1974 and 2010. Notice the slight concavity in the ice-front profile in all time periods, and pinning point adjacent to Zebra Ridge between 1979 and 2001.

Table 7.6. Detailed description of George VI Ice Shelf north ice front between 1974 and 2010. Imagery of ice front displayed in Figure 7.7

Date	Alex. Is. (X/Y) (m)	Palmer Land (X/Y) (m)	Channel Width (km)	Profile Length (km)	Loss (km^2)	Gain (km^2)	Net (km^2)	Comments
6 Jan 1974	-2082193.1/ 786006.2	-2067365.6/ 819729.5	36.83	41.74	N/A	N/A	N/A	Small icebergs scattered across GVI Sound held in-situ by consolidated sea ice. Open water and fractured sea ice at -2067831 818069 m and -20802110 787208 m in front of the ice shelf, and behind the ice front profile between Marr Bluff and Zebra Ridge; the ice shelf at this point has decoupled along its grounding zone.
3 Feb 1979	-2051066.1/ 780198.4	-2053193.8/ 810428.8	30.23	42.93	-820.44	0.00	-820.44	Linear recession of ~25 km. Area in front of northern margin is covered with extensive and consolidated sea ice.
24 Mar 1989	-2049299.6/ 780278.7	-2049982.1/ 808060.2	27.75	36.91	-90.30	0.00	-90.30	Retreat skewed Palmer Land grounding zone. Open water dominates area in front of the northern ice front with few icebergs scattered across George VI Sound.
16 Feb 1996	-2049299.6/ 780278.7	-2038821.3/ 803403.1	25.39	33.80	-92.05	0.68	-91.37	Retreat skewed towards Palmer Land grounding zone. George VI Sound occupied by extensive but fractured sea ice, with open water observed adjacent to Zebra Ridge.
4 Jan 2001	-2049299.6/ 780198.4	-2034043.9/ 803082.0	27.46	40.73	-53.75	0.90	-52.85	Retreat skewed towards Palmer Land grounding zone. Calved icebergs held in-situ by extensive sea ice. Icebergs also scattered across the Sound, generally measuring <1 km^2.
29 Jan 2010	-2038125.0/ 778662.0	-2031437.7/ 803388.0	25.49	33.80	-198.09	0.00	-198.09	Pinning point along Alexander Island retreated over a linear distance of 11.47 km. Small icebergs (<2 km^2) observed in front of the northern margin with larger icebergs (up to 8 km^2) observed further downstream of the ice margin; larger icebergs displayed faint surface features similar to those observed on the surface of GVIIS.

7.1.2.1 George VI Ice Shelf south ice front

Table 7.7. Spatial changes at the southern ice front from 1973 to 2010. Rate of loss based on number of days between images and extrapolated to $km^2 a^{-1}$. Data presented in Figure 7.8.

Year	Areal retreat (km^2)	Advance (km^2)	Net (km^2)	Rate of advance/ retreat (km^2a^{-1})	% of Total South Ice Front Loss
1973	N/A	N/A	N/A	N/A	0.00
1986	-221.99	39.34	182.65	-13.86	24.01
1991	-118.97	36.03	82.94	-16.76	12.87
1996	-181.59	14.20	167.39	-34.19	19.64
2003	-222.51	22.37	200.14	-28.04	24.07
2010	-179.50	70.07	109.43	-15.89	19.41

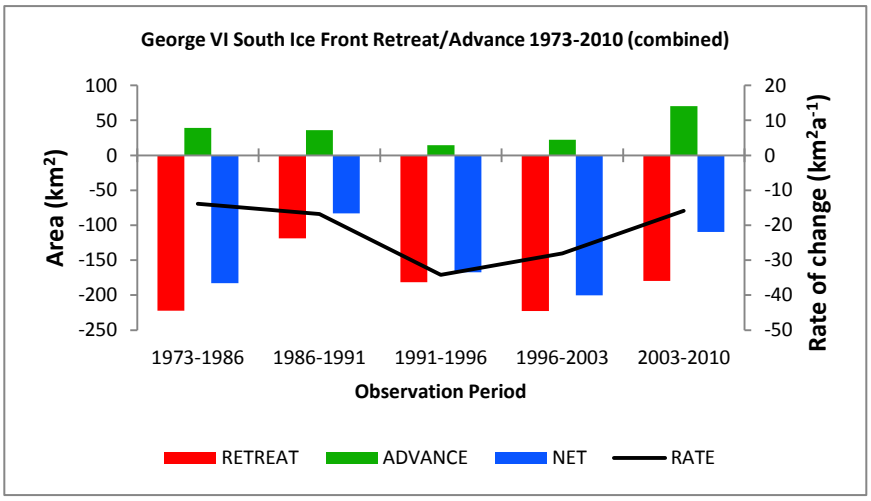

Figure 7.8 Spatial and temporal fluctuation of George VI Ice Shelf south ice front illustrating the total retreat, limited advance and net change. Notice slight increase in the rate of retreat between 1991 and 1996.

Detailed descriptions of the south ice fronts of George VI Ice Shelf are given in Table 7.7, Table 7.8 and illustrated in Figure 7.8 and Figure 7.10. In total, ~925 km^2 of ice was lost from the south ice front, with 182 km^2 of ice advancing. A net loss of 743 km^2 was thus recorded between January 1973 and January 2010. Furthermore, between 1991 and 1996 there is an increase in the rate of retreat at the southern ice front to a maximum of -28.04 km^2a^{-1}, almost twice the rate in the previous (-16.75 km^2a^{-1}) and proceeding time periods (-15.89 km^2a^{-1}).

The retreat was concentrated in the central portions of the southern ice front, northwest of the Eklund Islands, with only limited retreat observed at the ice-front pinning points along

Monteverdi Peninsula, De Atley Island and Spatz Island. Along the centreline of this central portion, the ice shelf retreated up to 28.03 km between January 1973 and January 2010. Smaller regions of retreat were also observed northeast of De Atley Island, between De Atley Island and Spatz Island, and immediately adjacent to Monteverdi Peninsula. Advance of the ice front was principally recorded near to its Monteverdi Peninsula grounding zone in successive observation periods from January 1973 to January 2010.

Visual analysis of March 2010 ERS-2 SAR data reveals further retreat in the central section but is not included in the analysis here because the imagery does not cover the full extent of the south ice front. The continued retreat in the central section subsequently splits the main south ice front into two independent sections, South Ice Front 1 from Monteverdi Peninsula to IR18 (Eklund Islands, Figure 7.9), and South Ice Front 2 from IR18 to De Atley Island. A smaller, third ice front between De Atley Island and Spatz Island is always independent over the timescales investigated here, and is discussed in Table 7.9.

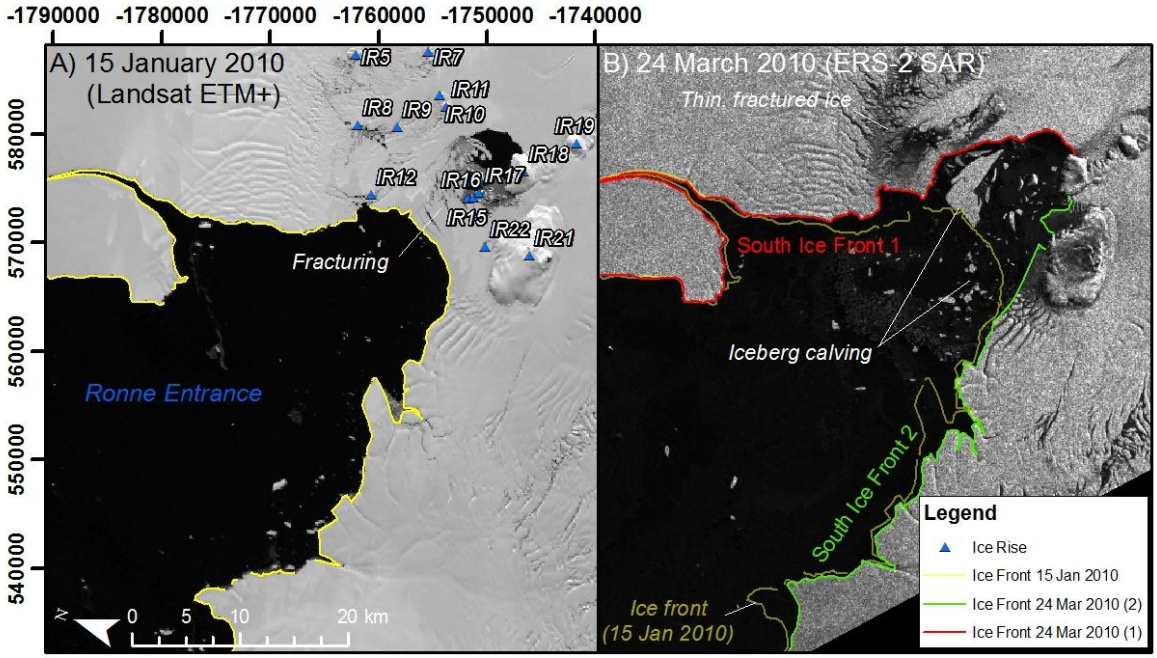

Figure 7.9. Ice-front retreat between A) 15th January 2010, and B) 24th March 2010 highlighting the creation of two independent ice fronts at the southern margin of George VI Ice Shelf.

It is clear from the visual analysis that the south ice front became increasingly concave between January 1973 and January 2010, although the further retreat between 15th January 2010 and 24th March 2010 subsequently created two slightly-convex ice fronts. The smaller ice front between De Atley Island and Spatz Island similarly became increasingly concave over time.

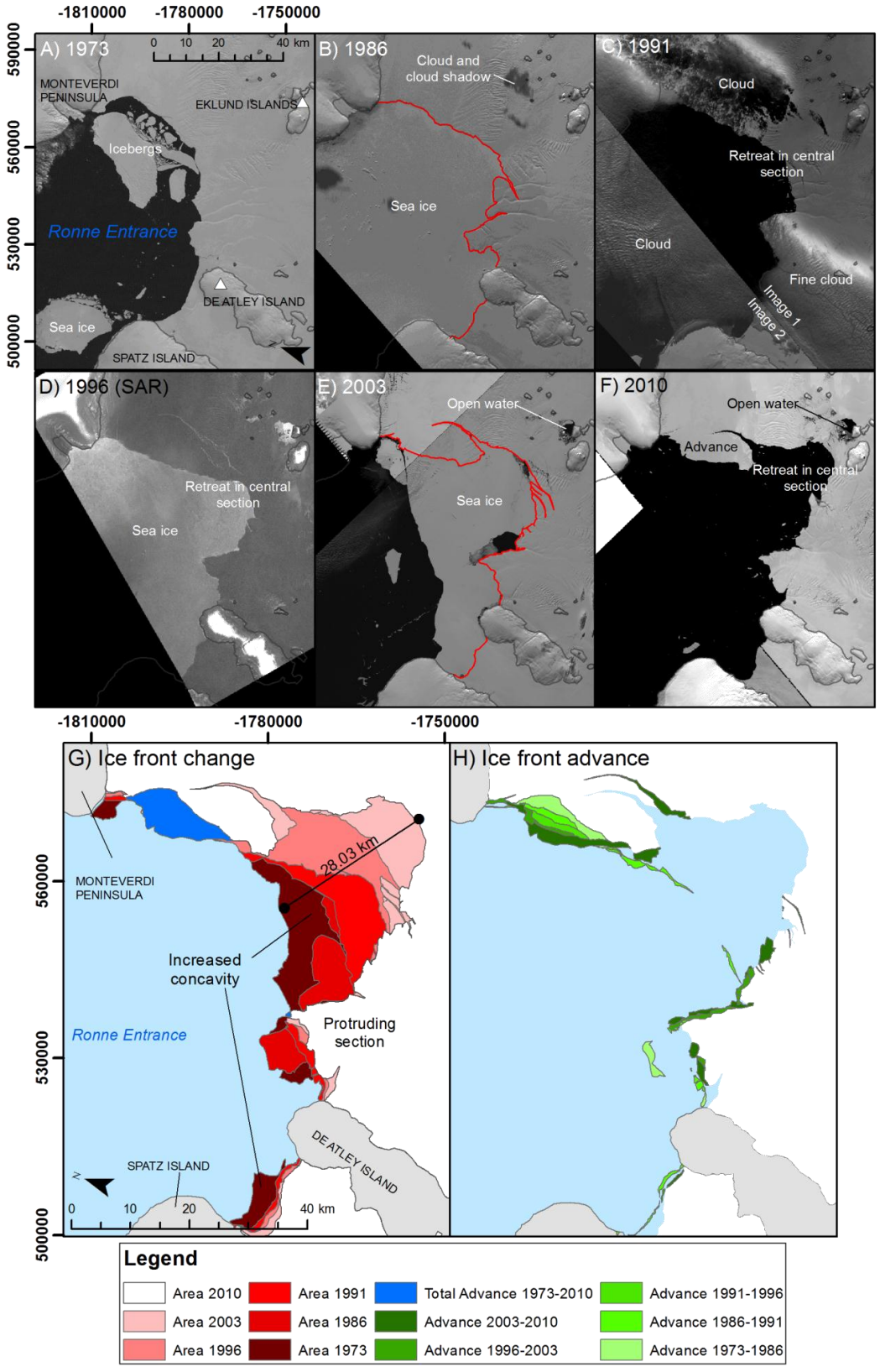

Figure 7.10. Ice front positions of George VI Ice Shelf, southern margin for each year discussed in Table 7.8 (A-F). G) Areal extent of the southern ice front during each of the time periods with associated ice retreat and advance. Note the concentration of retreat in the central portions of the main ice front and advance towards Monteverdi Peninsula. H) Advance of the southern ice front during each of the observation periods.

Table 7.8. Detailed description of George VI Ice Shelf south ice front between Monteverdi Peninsula and De Atley Island, 1973 to 2010. Imagery of ice front displayed in Figure 7.10

Date	Monteverdi Pen. (X/Y) (m)	De Atley (X/Y) (m)	Channel Width (km)	Profile Length (km)	Loss (km^2)	Gain (km^2)	Net (km^2)	Comments
9 Jan 1973	-1810103.8/ 571162.4	-1771227.0/ 522864.6	61.93	95.15	N/A	N/A	N/A	Large tabular icebergs occupied open water immediately adjacent to Monteverdi Peninsula, the largest of which measured 328 km^2. A further 196 km^2 of calved bergs were present. Smaller icebergs scattered non-uniformly across Ronne Entrance; large pallets of sea ice were also visible adjacent to De Atley Island and Spatz Island.
17 Mar 1986	-1808219.6/ 573953.0	-1771632.5/ 523031.6	62.75	131.70	-183.29	39.34	-143.95	Ronne Entrance covered with consolidated sea ice with few icebergs held in-situ. Little change in the position of both pinning points but retreat in the central section of the ice front.
27 Feb 1991	-1808219.6/ 573953.0	-1771417.8/ 523460.9	62.54	101.45	-118.84	27.90	-90.94	Ronne Entrance largely free of sea ice and calved blocks, although faint cloud cover prevents detailed observation towards the Monteverdi Peninsula margin. Little change in the position of both pinning points but similar concentration of retreat in central portion.
20 Jan 1996	-1807861.8/ 574215.3	-1771083.9/ 522816.9	63.20	120.41	-171.54	14.20	-157.34	Little change in the position of pinning points. Ronne Entrance covered with extensive sea ice with few observed icebergs.
11 Mar 2003	-1808004.9/ 574620.8	-1770535.4/ 522840.8	63.90	235.77	-214.68	21.85	-192.83	Retreat observed largely in the central regions of the ice front. Development of rift that cuts back towards the Monteverdi Peninsula. Sea ice occupied large areas of the Ronne Entrance immediately adjacent to the ice front, with areas of open water observed at -1763016 545337 m and -1772178 540582 m.
29 Jan 2010	-1807146.3/ 575169.4	-1770487.7/ 522745.4	63.97	205.12	-168.48	68.75	-99.70	Further retreat concentrated northwest of the Eklund Islands. Rifts containing open water observed immediately behind the ice front. Little change in the location of the pinning points along the margins.

Table 7.9. Detailed description of George VI Ice Shelf south ice front between De Atley Island and Spatz Island, 1973 to 2010. Imagery of ice front displayed in Figure 7.10.

Date	De Atley (X/Y) (m)	Spatz Is. (X/Y) (m)	Channel Width (km)	Profile Length (km)	Loss (km^2)	Gain (km^2)	Net (km^2)	Comments
9 Jan 1973	-1774748.8/ 513111.5	-1786531.0/ 502307.1	15.86	22.23	N/A	N/A	N/A	Ice front protruded out beyond its pinning points in the central region. Sea ice connected to the ice front and adjacent De Atley Island and Spatz Island.
17 Mar 1986	-1774510.2/ 512896.8	-1785767.8/ 501090.8	16.33	19.32	-38.70	0.00	-38.70	Ice front protruded beyond its pinning points to the east of the shelf-section but a concave profile was displayed towards the west. Retreat of Spatz Island pinning point. Extensive and consolidated sea ice occupied Ronne Entrance.
27 Feb 1991	-1774748.8/ 513135.4	-1787151.2/ 502474.1	16.42	20.48	-0.13	4.15	4.02	Little change in location of the ice front was observed; advance of 4.15 km^2 towards the eastern portion, whilst a retreat of 0.13 km^2 occurred towards the west. Little change in location of pinning points. Evidence of pallets of unconsolidated sea ice; cloud cover prevented detailed observation.
20 Jan 1996	-1774557.9/ 512729.9	-1784813.8/ 501567.7	15.24	18.51	-10.05	0.00	-10.05	Small retreat of pinning points back upstream observed. Ronne Entrance occupied by extensive sea ice.
11 Mar 2003	-1774701.1/ 513111.5	-1784813.8/ 501543.9	15.29	19.09	-7.83	0.52	-7.31	Pinning points remained stable; retreat occurred within the central portion of the ice front. Sea ice connected to the ice front was largely consolidated.
29 Jan 2010	-1774295.6/ 512753.7	-1785481.6/ 501472.3	15.87	21.51	-11.08	1.33	-9.75	Ice front continued to protrude beyond its pinning points along the eastern-most region of the shelf-section, with a concave profile exhibited towards the west. Skewed retreat of ice front towards Spatz Island. Ronne Entrance free of sea ice, but contained non-uniformly scattered icebergs, generally < 1.5 km^2.

7.1.3 George VI Ice Shelf structural overview

Surface structures and surface features of George VI Ice Shelf were digitised at various time intervals between 1973 and January 2010 (Table 7.10) using the methods outlined in Chapter 5. Firstly, the surface structures and features for the whole ice shelf are summarised using the composite structural interpretation of 2010 (Figure 7.11), focussing on the key characteristics. Subsequently, the structural interpretations and major structural changes at the north and south ice fronts are detailed individually. The spatial extent and distribution of surface meltwater ponds and associated features are also discussed.

Table 7.10. Dates of structural analysis for George VI Ice Shelf

Section	Date
North	January 1974
	February 1979
	March 1989
	February 1996
	January 2001
	January 2010
Central and South	January 1973
	March 1986
	February 1991
	March 2003
	January 2010
	March 2010*

*Visual analysis only – no structural mapping

7.1.3.1 Longitudinal structures

Longitudinal structures observed on George VI Ice Shelf almost exclusively form as a result of ice flow off Palmer Land into George VI Sound, with few exceptions noted in distinct locations off Alexander Island. The largest can be traced for up to 60 km in the central portions of the ice shelf where George VI Sound is at its widest, although elsewhere their length is limited to <25 km due to the narrow channel in the northern section into which the ice flows. Here, longitudinal features stretch across the ice shelf towards Alexander Island and are aligned parallel to the principal flow direction. During the austral summer, longitudinal features are visually enhanced by the presence of surface meltwater towards the northern extents of George VI Ice Shelf. Towards the mid and southern regions of George VI Ice Shelf, longitudinal features are observed as couplets of dark and light linear bands flowing off Palmer Land. At the southern margin, longitudinal structures diverge around the ice rises and ice rumples of the Eklund Islands, but can rarely

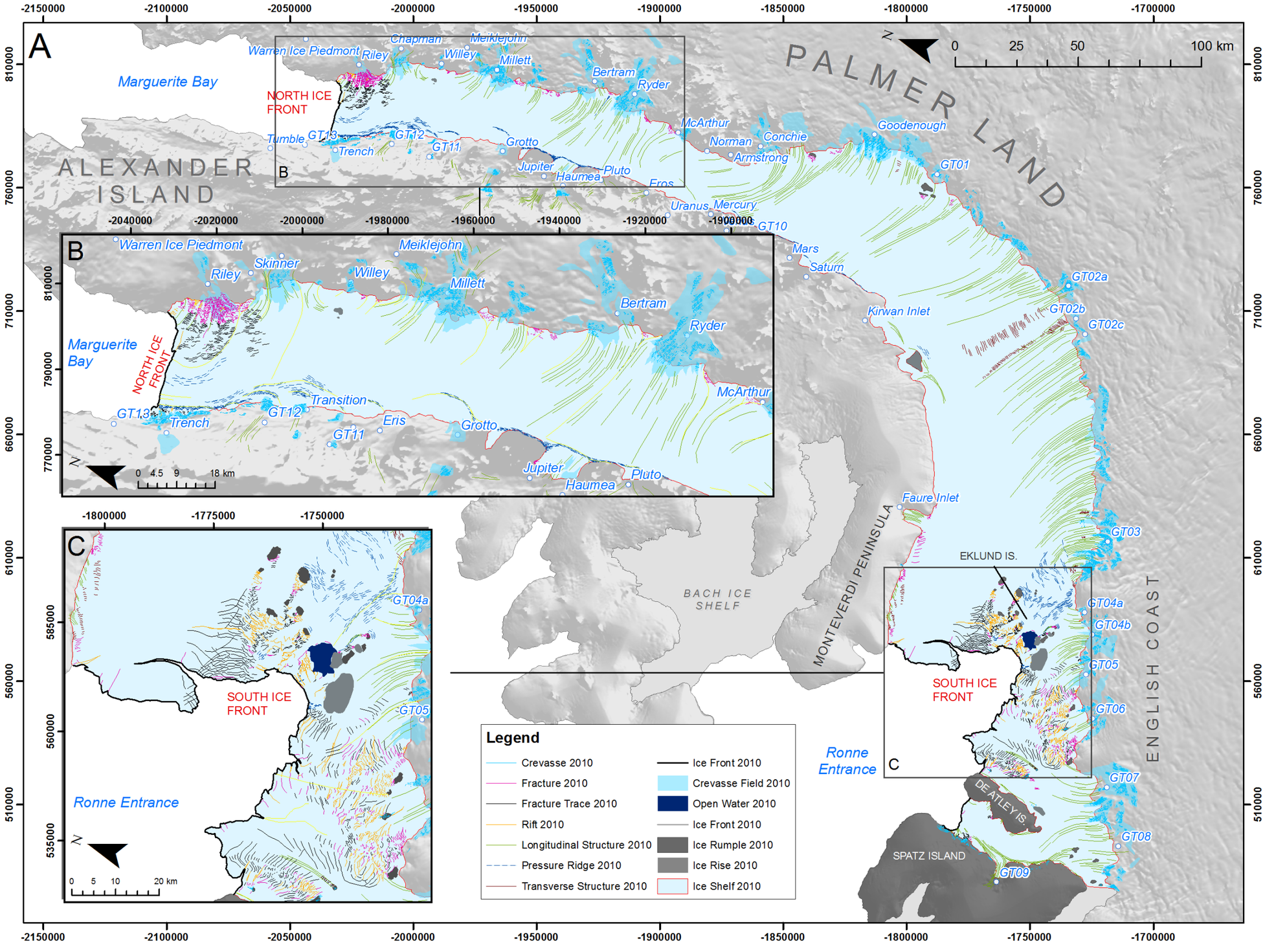

Figure 7.11. A) Structural overview of George VI Ice Shelf from 2010. Longitudinal structures are the most dominant ice-shelf wide flow-related feature and illustrate the localised flow directions of tributary glaciers.B) Surface structures in the northern extent highlighting crevasses along the slopes of tributary glaciers and limited fracturing of the ice shelf. C) Surface structures in the southern region of George VI Ice Shelf highlighting the excessive fracturing of ice between the Eklund Islands and De Atley Island.

be traced to the ice margin due to extensive fracturing and rifting. Longitudinal structures from Alexander Island glaciers are limited to certain locations around Kirwan Inlet, Martin Ice Rise, Faure Inlet and off Monteverdi Peninsula, 30 km from the south ice front. These can be traced for up to 16 km before becoming indistinct from the surrounding ice, but generally measure no more than 5 km in length.

Longitudinal structures within the George VI Ice Shelf system form in comparable circumstances to those observed on Bach Ice Shelf as discussed in Section 6.1; 1) at the confluence of two flow units on grounded ice, 2) at the confluence of two flow units within the ice shelf, and 3) at or near the grounding line within the main channel of tributary glaciers. Those forming at the confluence of flow units at or near to the grounding line (Type 2) tend to be more distinct than those formed on grounded ice and in the centre of flow units. Only at the entrances of Ryder Glacier (Figure 7.12), Millett Glacier and Chapman Glacier do the longitudinal structures flow radially; elsewhere their linear, uniform pattern is maintained down ice.

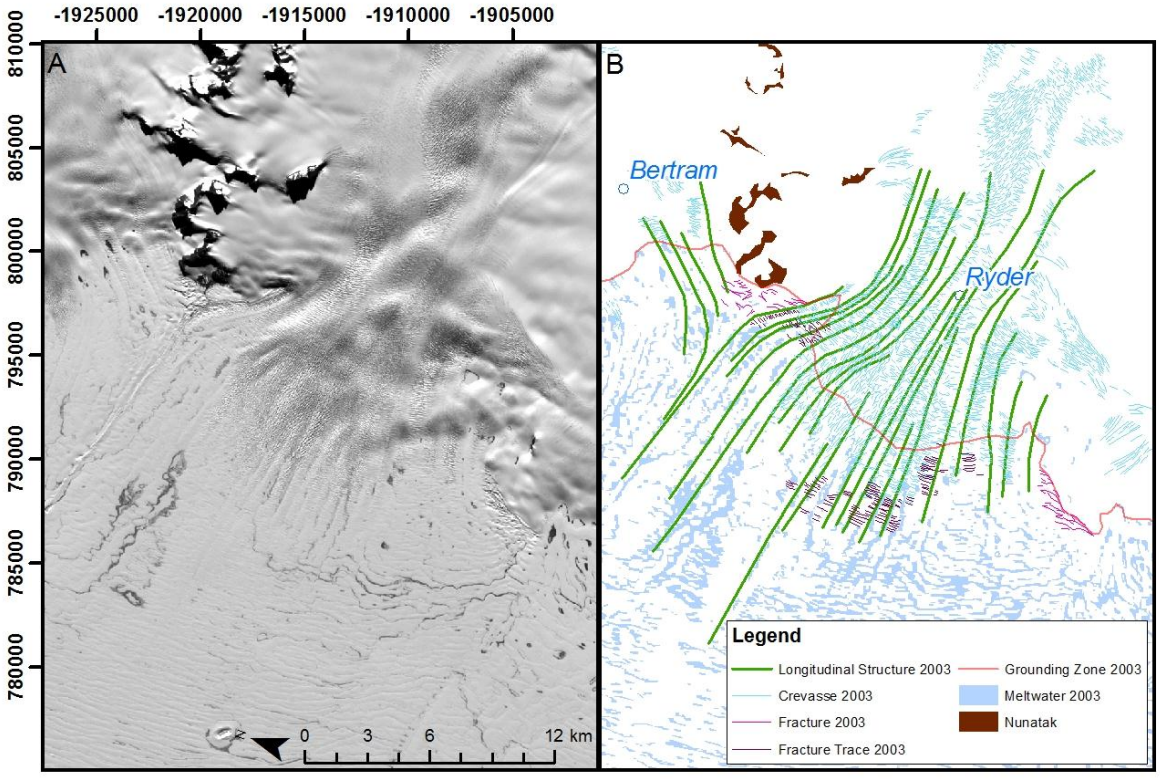

Figure 7.12. A) Landsat ETM+ 2003 and B) interpreted surface structures and features. Note splaying longitudinal structures at the grounding zone of Ryder Glacier, becoming increasingly linear further west as the ice migrates across the ice shelf.

7.1.3.2 Pressure Ridges

Pressure ridges have been identified in distinct regions across George VI Ice Shelf. In its northern extent, they are situated along the Alexander Island grounding zone, appearing as elongated ridges that have undergone a certain degree of deformation. They form perpendicular to the ice front and main flow direction. Further downstream pressure ridges are observed at flow-unit boundaries where individual tributary glaciers flowing from Alexander Island enter the main ice shelf and impinge on the dominant flow off Palmer Land. Such features are particularly evident at GT12 (Figure 7.13B), Transition Glacier, Eris Glacier and Grotto Glacier where a succession of ridges forms. These can often be traced for several kilometres down-ice and are occasionally enhanced by elongated meltwater lakes during the austral summer. Immediately south of Grotto Glacier, pressure ridges forms at the grounding zone and can be traced for ~50 km towards Eros Glacier, and also form at the boundary of tributary glaciers and the ice shelf (Figure 7.13A). Further south still, pressure ridges are seen intermittently from Mercury Glacier to Kirwan Inlet. On the eastern margin, at the confluence of Bertram Glacier and Ryder Glacier, pressure ridges have also been identified at the flow unit boundary for up to 10 km, forming parallel to ice flow.

At the southern ice front, pressure ridges are identified in three distinct regions. First, ~10 km from the grounding line of GT03, perpendicular to ice flow, ridges can be observed from here towards the Eklund Islands as distinct couplets of dark and light bands (Figure 7.13D). As distance from their origin increases the pressure ridges become increasingly distorted, particularly where they impinge upon the Eklund Islands. A second set of pressure ridges form at the flow unit boundary of GT03 and GT04a (Figure 7.13D). Finally, another series of pressure ridges is observed immediately west of the Eklund Islands. Pressure ridges in this region are formed at, or near to, the boundaries of different flow units deflected around the ice rises and ice rumples. Here, they are less distinct than those previously mentioned, yet display similar characteristics, forming in linearly-arranged groups either parallel or perpendicular to flow.

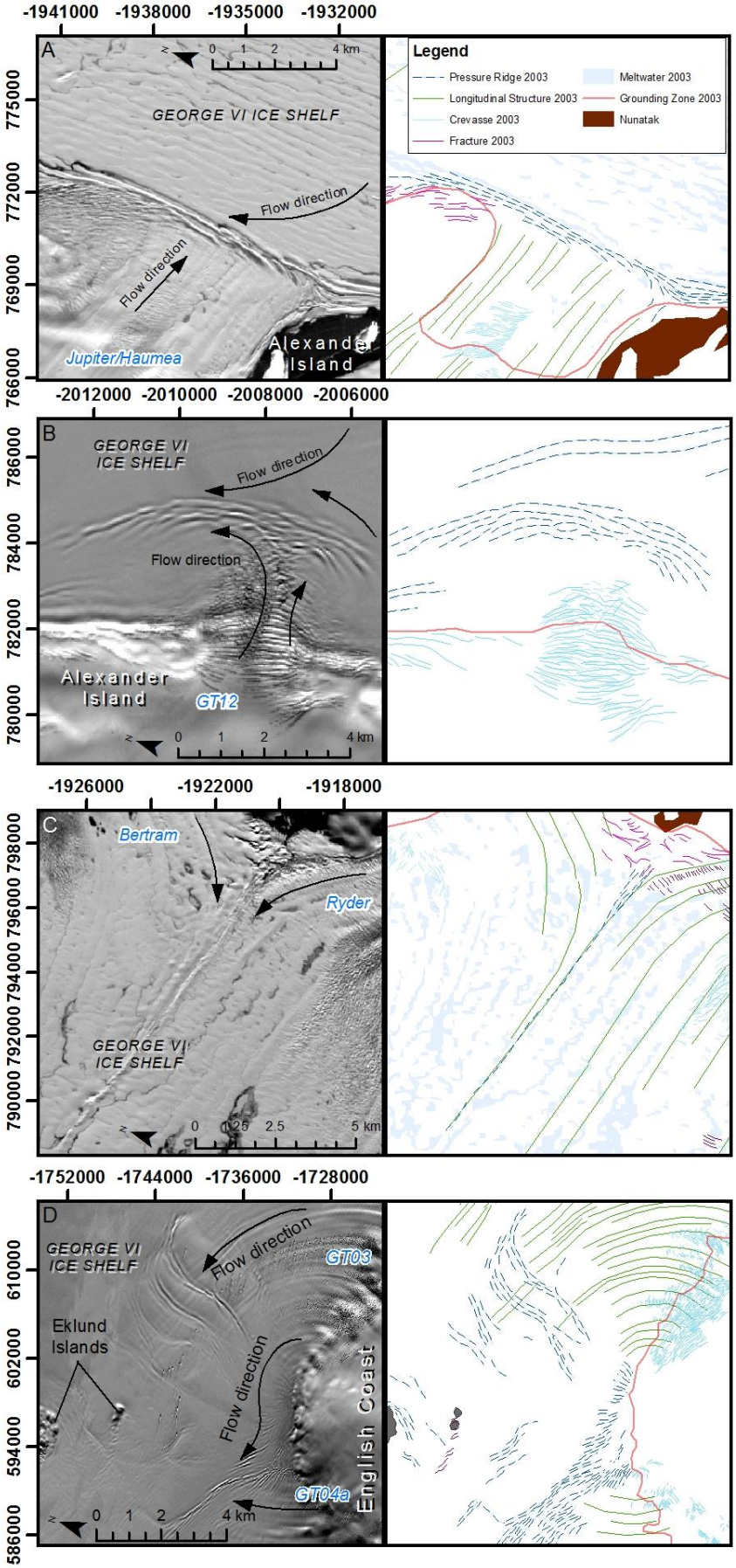

Figure 7.13. Examples of pressure ridge structures on George VI Ice Shelf. A) At the confluence of Jupiter/Haumea glaciers with the main channel of George VI Ice Shelf that limits the influx of tributary ice, B), as GT12 enters the ice shelf near to the northern ice front, C) at the confluence of Bertram and Ryder glaciers and D) as ice from GT03 enters the ice shelf, and as it flows against ice from GT04a. All pressure ridge structures are similar in appearance despite their formation under different

7.1.3.3 Crevasses, Fractures and Rifts

Significant crevassing occurs along the entire stretch of the Palmer Land tributary systems, with the largest crevasse fields (up to 200 km²) associated with Millett, Bertram, Ryder, Conchie and Goodenough Glaciers, and those entering the shelf in the southern regions (GT01-GT07) (Figure 7.11). On Alexander Island, crevassing is limited to tributary glaciers flowing from the northern reaches of its mountain chain towards the ice shelf. Occasionally, crevasses form in regular, uniform patterns, however, in general, crevasse fields consist of irregular, complex and chaotic fractures, often cross-cutting one another. Open crevasses associated with larger tributary glaciers flowing from Palmer Land are able to cross the grounding zone into the ice shelf for up to 5 km. The majority of crevasses that cross the grounding zone close at this point and only appear on the ice-shelf surface as faintly speckled regions of ice that eventually become indistinct from the surrounding ice.

Open fractures on the ice-shelf surface develop in three distinct zones, 1) at the northern ice front, 2) towards the southern ice front, and 3) between the confluence of individual flow units adjacent to headlands or peninsulas, or lee-side of ice rises and ice rumples. At the northern ice front, fractures cut back into the ice shelf along which calving is initiated. Surface fractures and fracture traces also flow towards the northern ice front in Riley, Skinner and Chapman Glaciers from the Palmer Land grounding zone, and from Alexander Island tributary glaciers GT13 and Trench. Occasionally, fractures at the northern ice front penetrate the entire thickness of the shelf to form rifts; brash ice and occasional calved blocks are apparent with open water also visible.

At the southern ice front, extensive fracturing and rifting is observed as ice flow is diverted around the ice rises and ice rumples of the Eklund Islands (e.g. (Figure 7.14)). Fractures form immediately downstream of IR2 and penetrate the depth of the ice shelf to form irregular and disordered rifts. These rifts are occasionally filled with brash ice that gives a rough surface appearance, but have a tendency to close down ice to form a distinct pattern of fracture traces that splay towards the ice front. Similar fracturing is observed in front of IR3 and lee side of the cluster of ice rises IR5 to IR12. Significant areas of brash-ice-filled rifts are observed within this area of ice rises, consisting of unconsolidated glacier ice, sea ice and occasionally, open water. As shelf-ice flows away from the ice rises towards the ice front, these rifts and fractures also heal, but the fracture-trace patterns do not splay as readily as those forming downstream of IR2, and are generally compressed to a point.

Occasionally, as these fracture traces near the ice front, they reopen to form fractures and/or rifts that act as a precursor for localised iceberg calving. During 2010, this is apparent across the south ice front, particularly in ice towards Monteverdi Peninsula where a large rift forms part of the ice-front profile. Extensive 'refracturing' is also evident in front of IR12 to IR17 in the ice bridge between IR12 and IR21 (Figure 7.14).

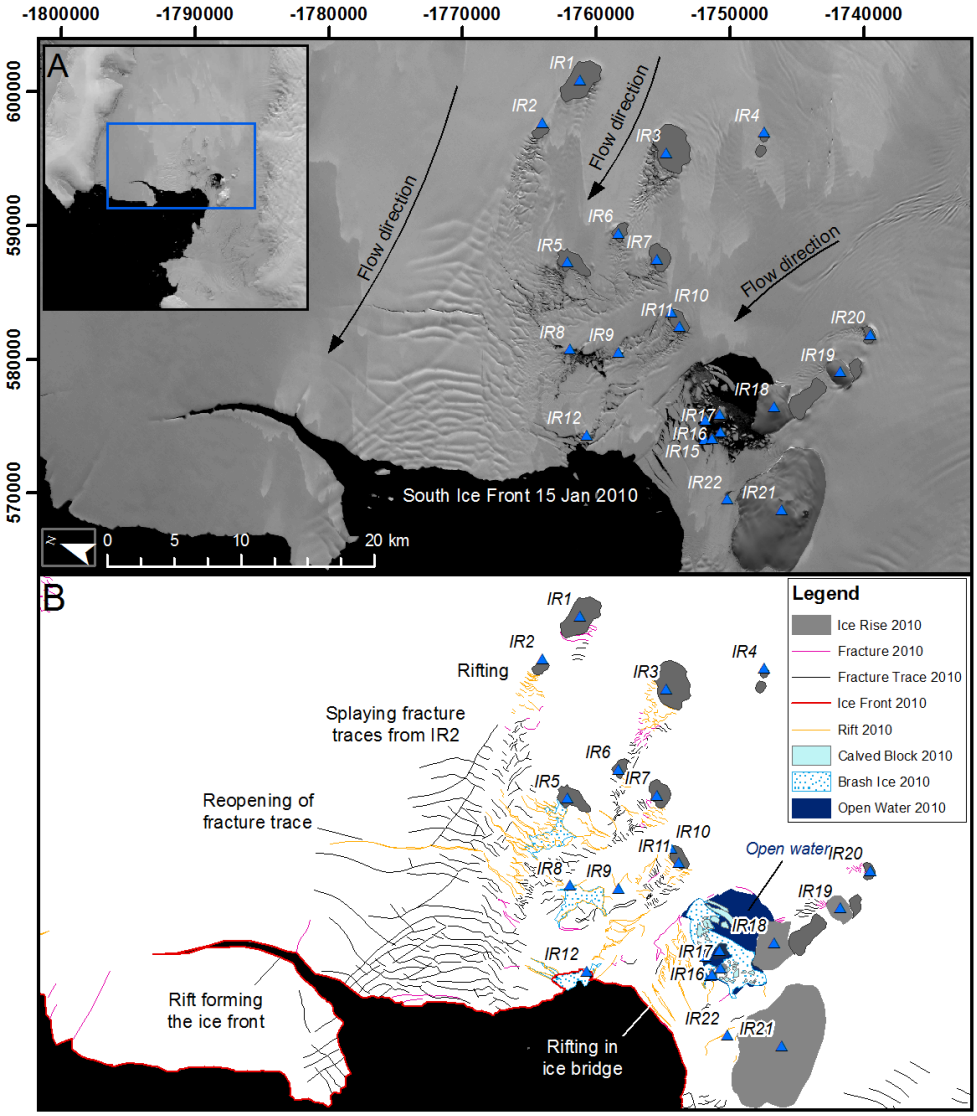

Figure 7.14. Fracturing and rifting at the southern ice front during January 2010 emanating from lee-side of the Eklund Island ice rises and ice rumples. Fracture traces splay towards the ice front from IR2, occasionally refracturing. Brash ice and calved blocks evident in rifts down-ice of IR5, IR7, IR8, IR9 and IR10 with open water clearly visible in rifts located in the ice bridge between IR12 and IR21.

Furthermore, fracture traces can be followed intermittently to the south ice front from the grounding zone at the English Coast in ice originating from GT04b. Further west, large areas of fracturing and rifting are observed, forming transversely to the predominant ice

flow direction in GT05, GT06 and GT07. Fractures and rifts initiate at or near to the grounding zone and downstream of IR23-IR26 that interrupt the flow of GT06 and GT07 (Figure 7.15). The largest of these structures contain a mixture of calved blocks and brash ice that gives a rough-surface appearance; open water is also apparent in some of these structures. As ice migrates towards the ice front, fractures and rifts tend to narrow, leaving a distinct impression of fractures and fracture traces on the ice-shelf surface. Along the southern ice front profile between the Eklund Islands and De Atley Island, several fractures, fracture traces and rifts cut back both transversely and longitudinally into the ice shelf.

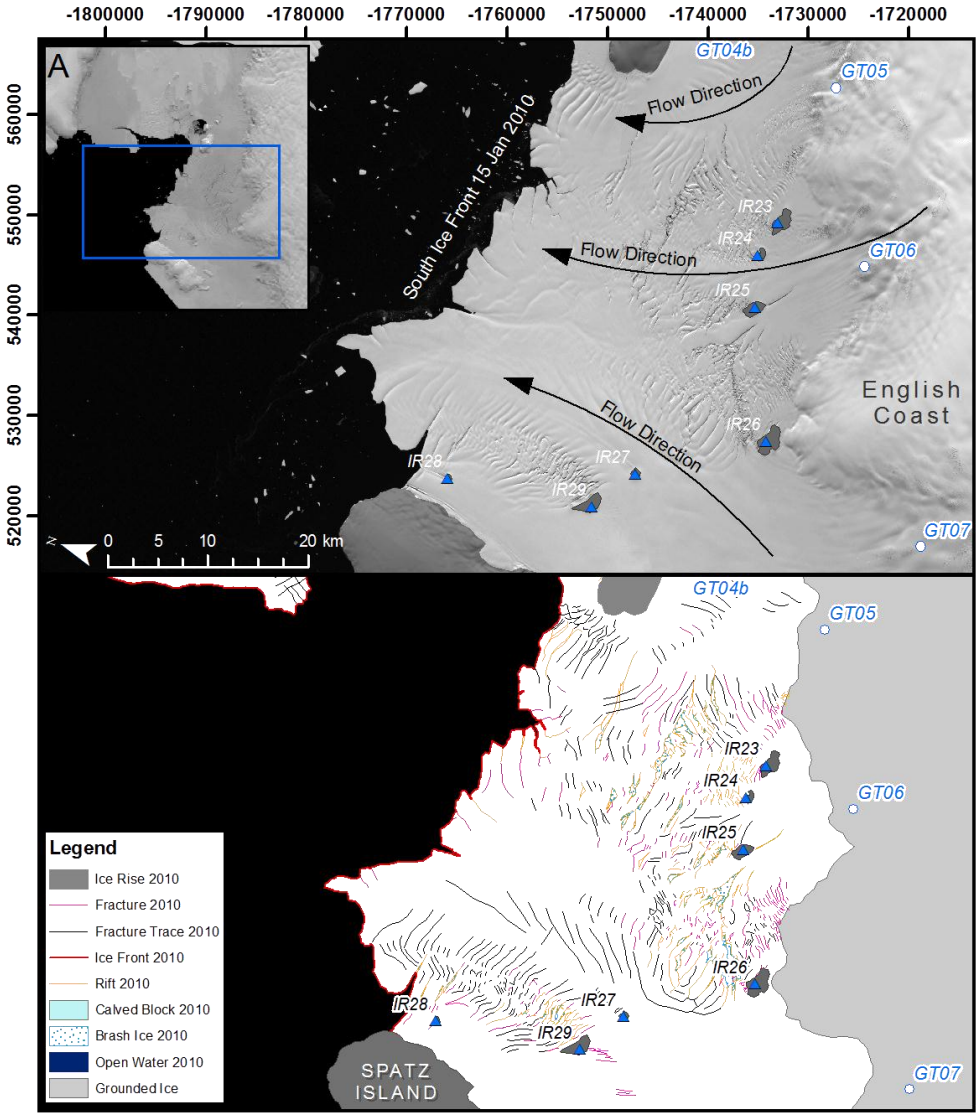

Figure 7.15. Fracturing and rifting between the Eklund Islands and Spatz Island during January 2010. Significant rifting particularly lee-side of the ice rises along the English Coast and east of Spatz Island that narrow as they migrate towards the south ice front.

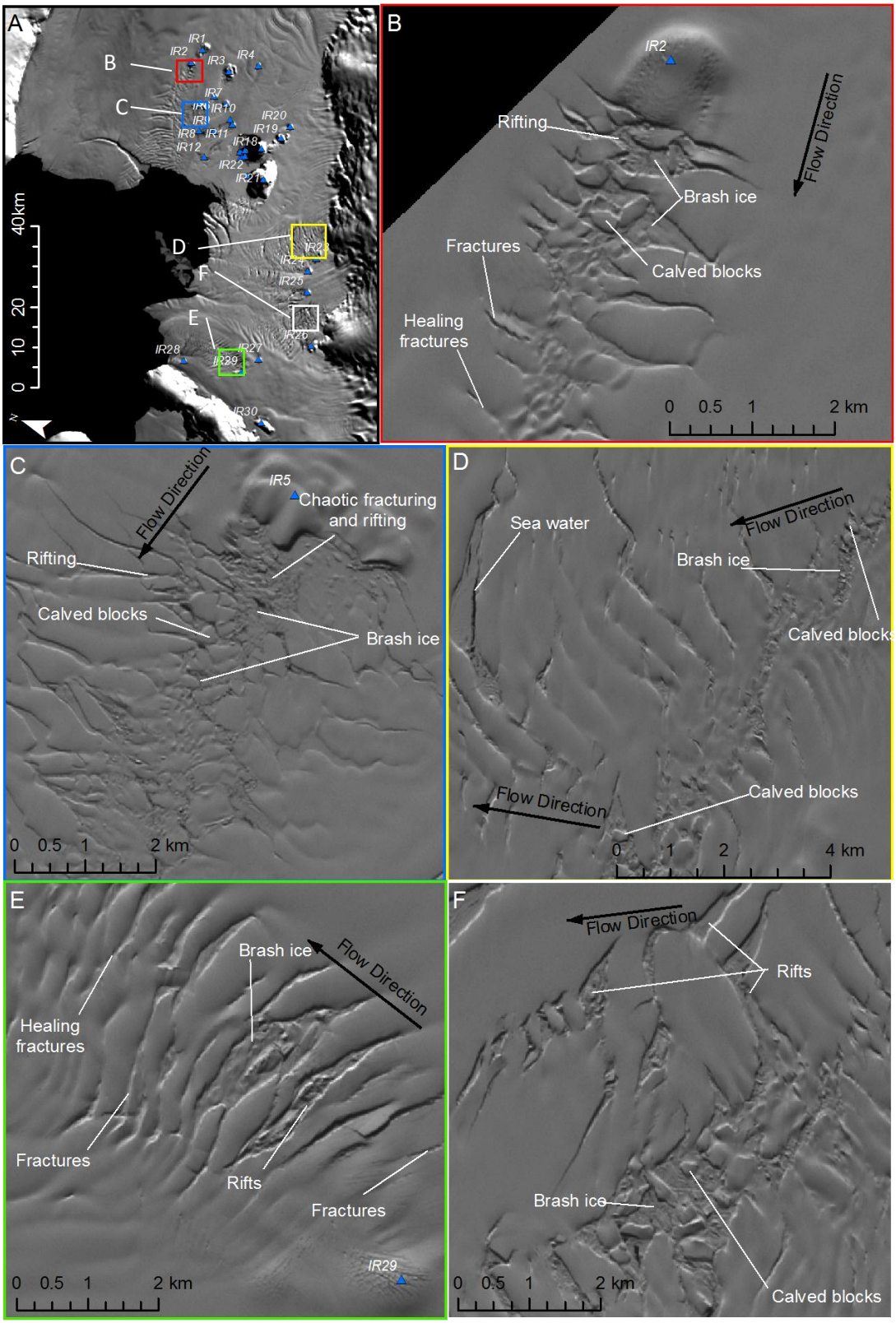

Figure 7.16. Fracturing lee-side of ice rises and ice rumples of the Eklund Island and the English Coast. A) MOA overview map with locations of B-F. B) Rifting at IR2 and eventual healing down-ice. Rifts filled with a mixture of brash ice and calved blocks. C) Chaotic rifting and fracturing lee-side of IR5 containing numerous, small calved blocks and brash ice. D) Fracturing and rifting north-west of IR23. Evidence of calved ice and brash ice, and open sea water in larger rifts. E) Fracturing, rifting and eventual healing of fractures lee-side of IR29; rifts filled with brash ice. F) Rifting and fracturing between IR25 and IR26 with chaotic brash ice and calved blocks visible in large rifts. Evidence of small pools of sea water in rifted areas.

Along the whole length of the Palmer Land grounding zone, small-to-medium scale fracturing also occurs at the confluence of flow units around headlands and peninsulas (Figure 7.17). A similar situation is observed on Bach Ice Shelf and has been discussed previously in Chapter 6. At the grounding zone, fractures form perpendicular to the main flow direction, but soon become distorted and compressed to a point with increased distance from the grounding zone. There are no clear circumstances in which these flow-unit confluence fractures occur along the Alexander Island grounding zone.

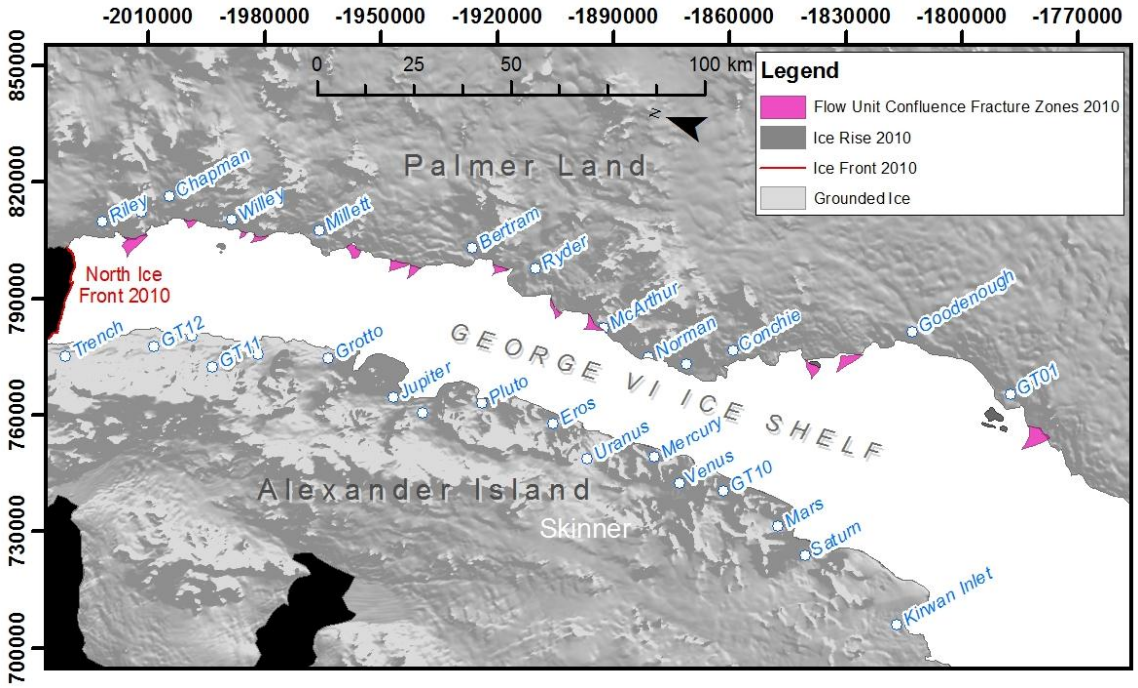

Figure 7.17. Flow unit confluence fracture zones along Palmer Land. Fractures form parallel to the local grounding zone but become increasingly distorted with distance travelled. Fractures eventually heal and are compressed to a point.

7.1.3.4 Transverse structures

Following on from the feature descriptions outlined in Chapter 5, transverse structures are those whose origin is not clear from structural analysis alone; i.e. aligned perpendicularly to flow, do not exhibit a distinct surface opening, nor are formed as a result of a surface fracture closing such as a fracture trace. Transverse structures are distinct in two closely linked locations on the surface of George VI Ice Shelf, originating at the grounding zone south of GT02a and north of GT02b (Figure 7.18). These features flow across the shelf for at least 41 km before becoming indistinguishable from the surrounding ice. Transverse structures traced back to GT02a appear more irregularly across the ice shelf in terms of

their width and their distance between each individual structure, where as those associated with GT02b are more orderly.

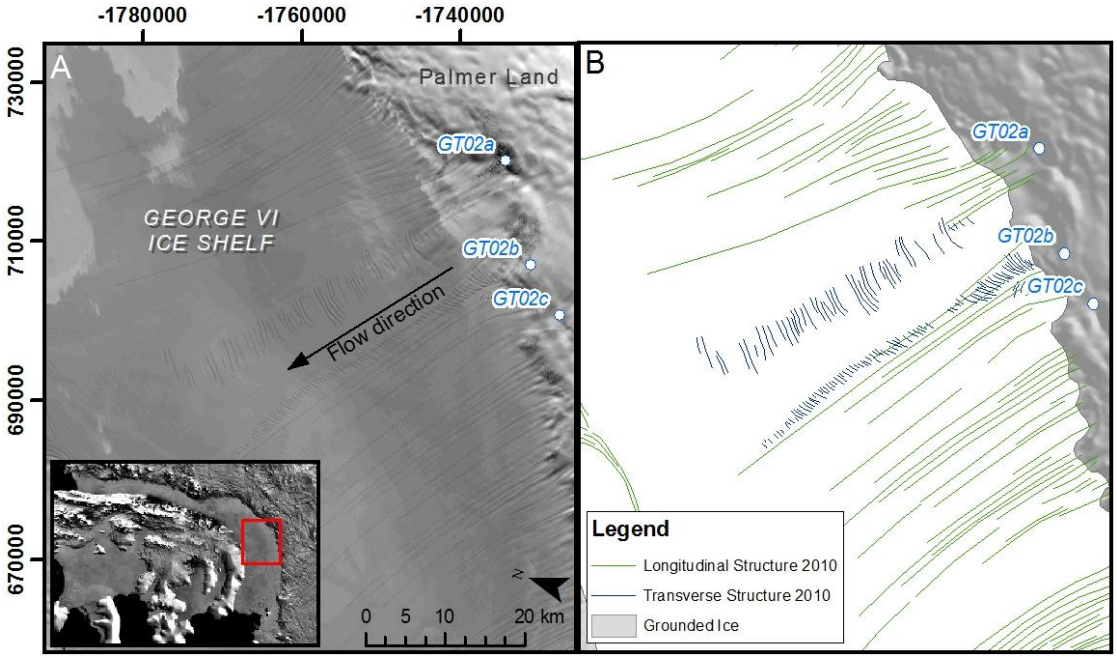

Figure 7.18. Transverse and longitudinal structures in the central section of George VI Ice Shelf flowing from Palmer Land. Transverse structures originate at the grounding zone, whereas some longitudinal structures can be traced back onto the grounded ice, particularly at GT02a. Transverse structures measure between 0.8 km and 5.8 km and can be traced for up to 43.8 km from the grounding zone into the ice shelf at almost regular intervals (0.52 km).

7.1.3.5 Surface Meltwater

Meltwater on the surface of George VI Ice Shelf is largely confined to the northern channel of the George VI Sound, covering an ice-shelf surface area of ~5900 km² (Figure 7.19). Regions of meltwater are also identified along the Monteverdi Peninsula margin towards the southern ice front. Surface meltwater develops in mid-to-late December at the western extremities of the ice-shelf along Alexander Island, spreading rapidly during January to mid-February before reducing in size and extent throughout March, towards the end of the melt season. By the end of March, surface meltwater on George VI Ice Shelf is non-existent.

During the peak of the melt season, primary and secondary pools can be identified on the surface of George VI Ice Shelf. Primary meltwater pools stretch across the ice shelf with the principal flow direction and are unequivocally linked to the structural glaciology created by longitudinal features referred to above (Section 7.1.3.1). Secondary pools cross-cut and subsequently link the primary pools, largely flowing perpendicularly to them.

Primary meltwater pools exhibit greater widths (up to 1.5 km) than secondary pools (<0.5 km), and are spaced at greater distances along the shelf. The overall length of the primary pools is limited to ~50 km due to the nature of ice shelf and George VI Sound, whereas secondary pools can be traced for far greater distances, possibly along the entire stretch of ice-shelf surface that is subjected to surface melting. Where primary and secondary pools cross, melt-ponding occurs. Individual, non-aligned meltwater ponds are also are widely scattered across the northern section of George VI Ice Shelf. Larger individual meltwater ponds are located along the grounding zone where there is a clear break in surface slope.

7.1.3.6 Ice dolines

At least 46 individual ice dolines existed across George VI Ice Shelf (January 2003), varying in their distribution, shape and size (Figure 7.20). Further potential ice dolines have been identified, but it is not possible to interpret these features as definite ice dolines, proto-dolines or active/remnant surface meltwater ponds, due to the spatial resolution and quality of the imagery.

Ice dolines in George VI Ice Shelf exist in three distinct zones, 1) in ice previously crevassed (Figure 7.20B), 2) where an abundant supply of surface meltwater is available (Figure 7.20D), and 3) in clusters at or near to flow unit boundaries (Figure 7.20E). Indeed, all ice dolines only occur in areas where some meltwater is present. All but three ice dolines are located in ice that originates from Palmer Land; ID18 is located in ice fed by GT11 off Alexander Island, whereas ID41 and ID42 exist in ice fed into George VI Ice Shelf from Eros Glacier (Figure 7.20A).

Whilst some ice dolines elongate with flow direction, others elongate transversely, whilst others tend not to show any preference. The largest observed doline is located at -1979400 789500 m (ID16, Figure 7.20C) and measured 2.5 km in length and 1.2 km in width. Generally, ice dolines on George VI Ice Shelf measure no more than 1 km in length and less than 0.8 km in width. Visual inspection of shadowing individual ice dolines suggests steep-sided cliffs around an internal crater as also observed on Bach Ice Shelf (Figure 7.20C).

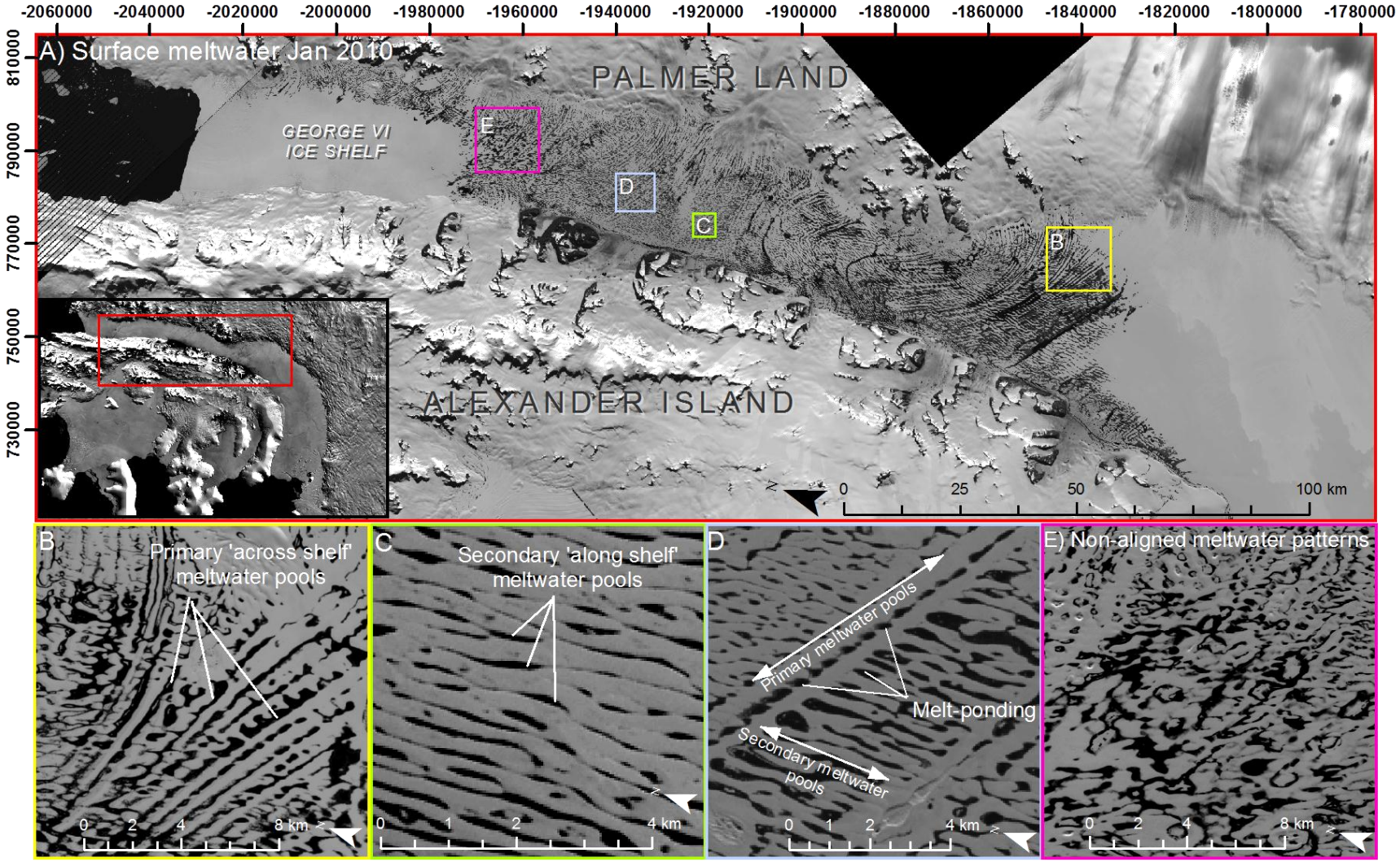

Figure 7.19 A) Surface meltwater distribution in the northern section of George VI Ice Shelf (January 2010) illustrating B) primary, across-shelf meltwater pools linked to longitudinal structures, C) secondary, along-shelf meltwater pools that are more narrow than primary pools, D) the ponding of meltwater associated with the interaction of primary and secondary pools, and E) largely non-aligned meltwater patterns evident in the northern section of George VI Ice Shelf. In total, surface meltwater occupies an approximate area of 5900 km^2.

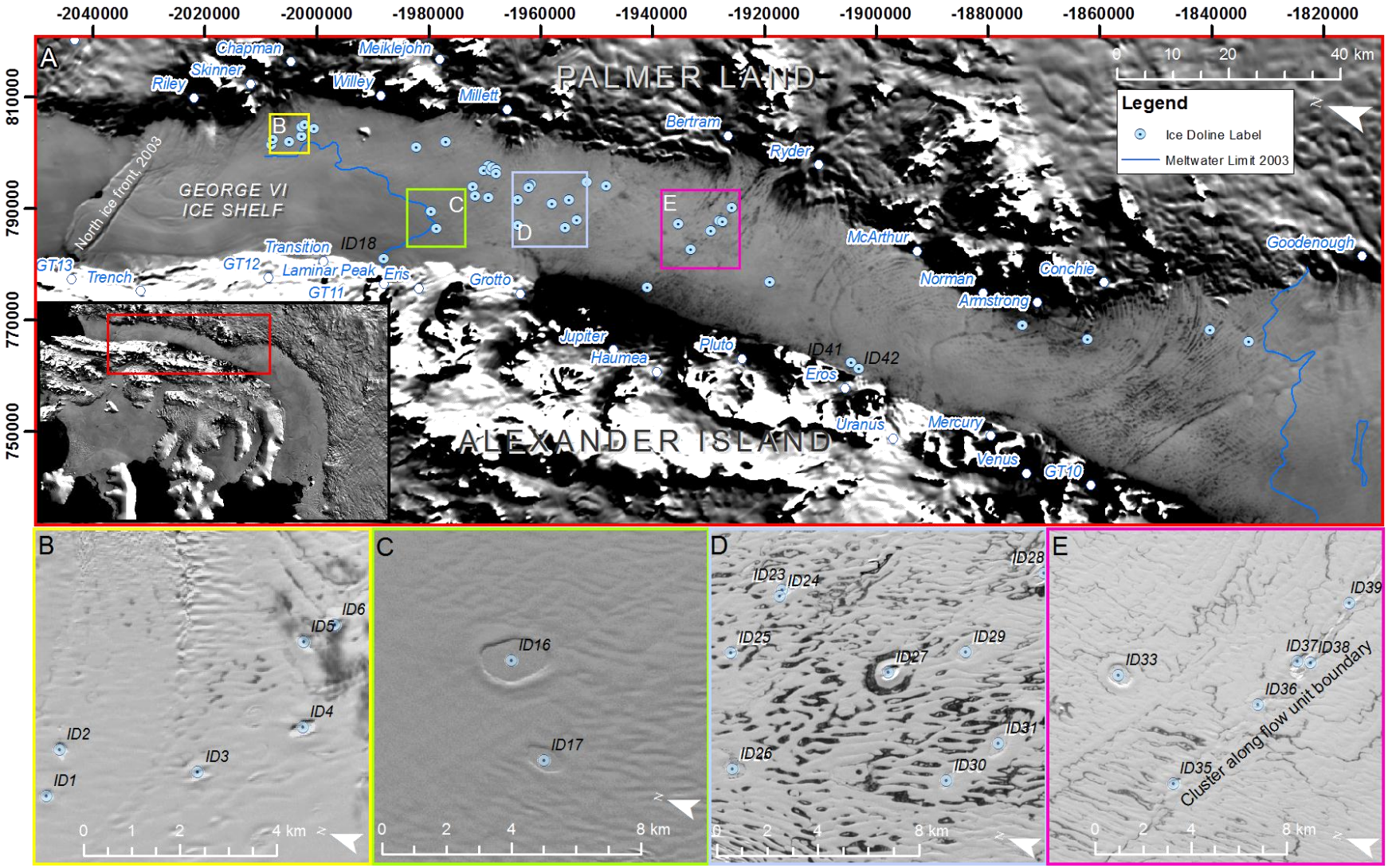

Figure 7.20. Location of identified ice dolines on George VI Ice shelf for 2003, and 2003 meltwater limit (A). Notice the clustering of ice doline structures in previously crevassed ice flowing from Skinner and Chapman glaciers (B), the largest identified ice doline and clear internal crater (C), clustering in locations of abundant surface meltwater (D), and clustering along distinct flow-unit boundaries, in particular between Bertram and Ryder glaciers (E).

7.1.4 Major structural and surface feature changes

The greatest structural changes occured at the northern and southern ice fronts of George VI Ice Shelf and are discussed below, whereas few surface-structural changes are observed in the central section. Furthermore, observed changes in surface meltwater extent in the northern portions of the ice shelf, and the apparent retreat of the English Coast grounding line, are presented.

7.1.4.1 Structural changes and evolution at the north ice front (Figure 7.21)

During 1974, the eastern portion of the north ice front was characterised by widespread, non-aligned fracturing and rifting. Ice flowing from Warren Ice Piedmont into the ice shelf was heavily fractured, transverse to flow, and could be traced to the north ice front, becoming increasingly chaotic (Figure 7.21B). To the north and south of this, brash ice, containing many small-to-medium sized blocks of ice, was observed; this pattern of ice heterogeneity continued along the Palmer Land grounding line. In the central portions of the north ice front, large rifts filled with smooth, uniform ice existed, although rifts nearer to the ice front had visible streaks of open water running along their length (Figure 7.21A). These rifts could be traced back towards the northern boundary of Riley Glacier. Between Marr Bluff and Zebra Ridge along the western margin, a region of heavily fractured brash ice and open water was observed, scattered with calved blocks and sea ice (Figure 7.21A, B).

During 1979, complex fracturing and rifting existed along eastern margin. Rifts filled with smooth, uniform ice originated at -2031000 803500 m, north of Riley Glacier and could be traced for ~15 km towards the ice front. The largest of these rifts stretched for at least 13 km perpendicular to the main flow direction of the shelf, and was similarly filled with smooth, consolidated ice; it was situated ~4.6 km south of the ice front. Poor data availability prevents feature identification along the western margin.

By 1989, the floating tongue of Warren Ice Piedmont had all but disappeared from the ice front, with only a 2 km-wide portion remaining (Figure 7.21F). Further along the Palmer Land margin, crevasses that had migrated over the grounding zone formed ice-shelf fractures perpendicular to the ice front. Rifts opened perpendicularly to these crevasses, and were filled with brash ice. Rifts continued to form north of Riley Glacier and could be traced down ice for ~11 km to the ice front. New rifts that had developed in this area

exhibited a more complex formation, fracturing both transversely and perpendicularly to the local flow direction. Fine cloud cover prevented detailed feature identification towards the centre of the ice front and Alexander Island.

An ERS-2 SAR image from 1996 (Figure 7.21G) captured large-scale calving at the eastern edge of the ice front, the largest fragment of which measured ~10 km². At the Alexander Island margin, open rifts were observed for the first time in ice originating from Transition Glacier (Figure 7.21H). These fractures measured up to 3 km in length, were spaced between 1.3 km and 3.1 km apart, and flowed towards the ice front, diverting easterly around the entrance of GT11. By 2001 (Figure 7.21I, J), the largest of these fractures had propagated across the central portions of the ice shelf for ~20 km. Smaller rifts propagated towards the ice front to the north of Riley Glacier where active calving was again observed. Along Palmer Land, fracture traces became increasingly visible, emanating from complex fractures and rift patterns at the input of Riley Glacier.

Between 6 Jan 2010 and 29 Jan 2010, large-scale calving from the northern ice front took place. This calving was captured in Landsat ETM+ imagery, but detailed observation is limited due to poor data quality (Figure 7.22). Few fractures were observed along northern ice front, with the exception of some small rifts at each of the grounding zones, and a 4.5 km fracture originating in the central portions of the ice front (Figure 7.22).

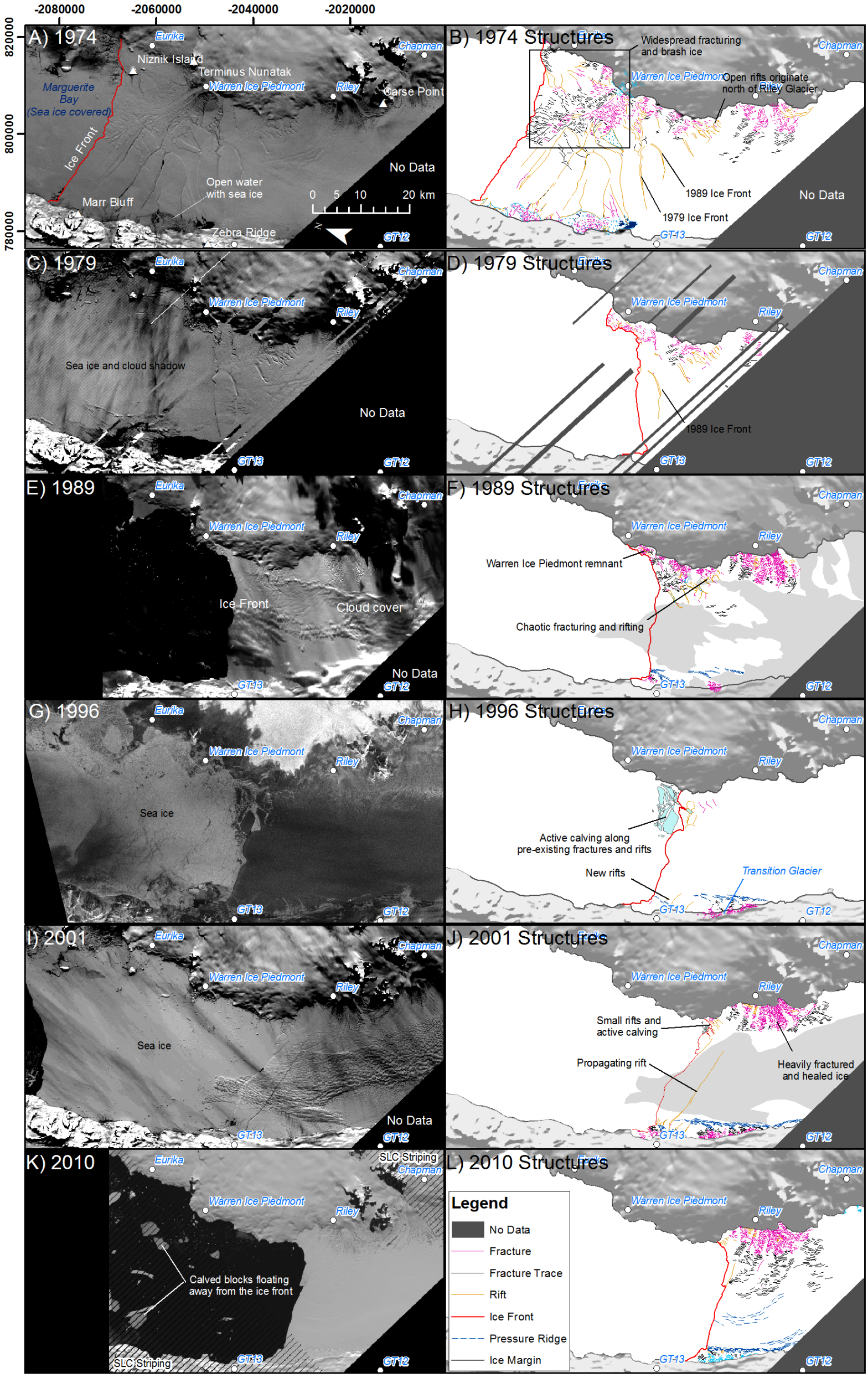

Figure 7.21. Structural evolution at the northern ice front for 1974 (A, B), 1979 (C, D), 1989 (E, F), 1996 (G, H), 2001 (I, J) and 2010 (K, L) illustrating the key changes at the northern ice front. Overall, there is a reduction in the number and distribution of ice-shelf wide fractures and rifts that were so evident in 1974 and 1979. Indeed, the northern ice front during 2010 is largely absent of significant fractures and rifts with the exception of those linked with the input of Riley Glacier. Scale bar and north arrow in A applicable for each subset. Legend displayed in L also applies to all structural maps.

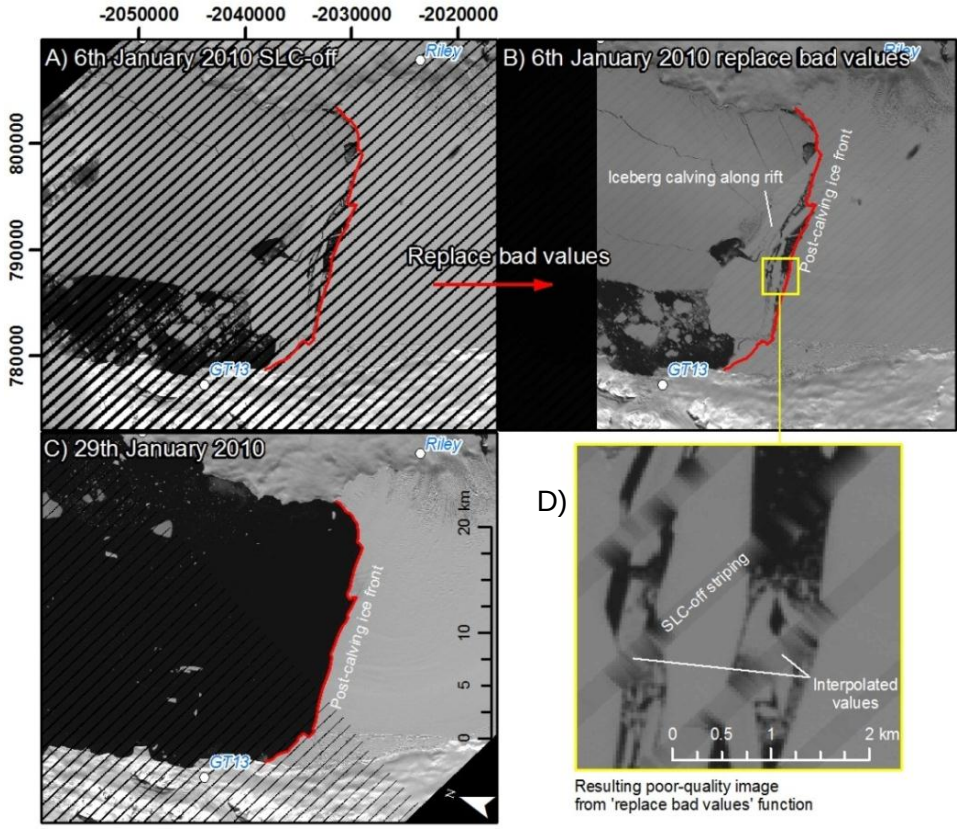

Figure 7.22. Iceberg calving between 6th and 29th January 2010 at the northern ice front of George VI Ice Shelf. A) Striping as a result of the Scan-line corrector instrument failure, B) interpolated 'bad' data using the replace bad values function in ENVI 4.6 (and insert (D)). C) Resulting ice front view, post-calving event.

7.1.4.2 Structural changes and structural evolution at the southern ice front: Monteverdi Peninsula to the Eklund Islands

The ice-shelf surface between Monteverdi Peninsula and the Eklund Islands during 1973 was dominated by cross-cutting fractures, fracture traces and rifts, particularly those that splayed laterally from IR2 towards the ice front (Figure 7.23A, B). Lee-side of IR2, ice appeared brash, with chaotic rifts containing a number of calved blocks. Similar rifts were observed down-ice of IR3 and IR5, with smaller open fractures observed lee-side of IR6 to IR11. Between IR13 and IR21, small pools of open water and broken ice were observed. West of this towards the ice front, the ice surface became smoother, only disturbed by faint surface pressure ridges linked to ice flow from the west of IR21. Along Monteverdi Peninsula, surface fractures were observed in ice that migrated towards the ice front. These fractures measured no more than 2 km in length and could be traced back upstream for ~13 km to their point of origin and were filled partially with surface meltwater.

By 1986, several of the larger fractures and rifts observed in 1973 had propagated further. At the Monteverdi Peninsula grounding line, fractures continued to migrate towards the ice front but remained similar in their dimensions. Between 1986 and 1991, a greater number of rifts was observed on the lee-side of IR2, IR3 and IR5, containing a mixture of calved blocks and brash ice. An area of open water north of IR15 had grown and stretched to IR10-15; icebergs were also visible within this region measuring up to 0.4 km² in size. Cloud cover prevented structural observation towards Monteverdi Peninsula during 1991.

Large-scale rifting across the south margin between Monteverdi Peninsula and the Eklund Islands was observed in ERS-1/2 imagery during 1996 (Figure 7.24). The fractured area measured ~35 km in length and consisted of several rifts orientated sub-parallel to the ice front. Approximately 4 km down ice from this larger rift system, a second cluster of rifts was observed. Newly-formed fractures and rifts were observed on the lee-side of IR2, IR3 and IR5, with smaller areas of brash ice observed in front of IR07, IR08 and between IR10 and IR11. An annotated image of the ERS-2 SAR image is provided in Figure 7.24 and not included in Figure 7.23 due to poor image quality that hindered detailed structural mapping.

By 2003, the large rift system described above formed the profile of the ice front following retreat. The area of open water in front of IR15 had increased and was occupied by several icebergs and calved blocks of ice, the largest of which measured 2.8 km². Northwest of IR21, rifts had opened up behind the ice front profile, the largest of which also contained calved blocks of ice. At the Monteverdi Peninsula grounding line, a succession of fractures propagating towards the ice front opened up to form rifts measuring up to 4.6 km in length and 0.2 km in width.

Rifts and fractures continued to propagate on the lee-side of the Eklund Islands between 2003 and 2010. Further downstream, a large rift had propagated in previously fractured ice stemming from IR2, measuring ~16 km from tip to tip, and 0.3 km at its widest point. The area of open water to the north of IR15 had further increased in size, and occupied an area of ~33 km² during January 2010. This region was scattered with brash ice, with several larger calved blocks visible. The subsequent ice bridge between the area of open water and the main embayment of Ronne Entrance is heavily rifted on 15th January 2010. By 24th March 2010 this barrier had broken away thus forming South Ice Front 1 and South Ice Front 2 as discussed previously in Section 7.1.2.1.

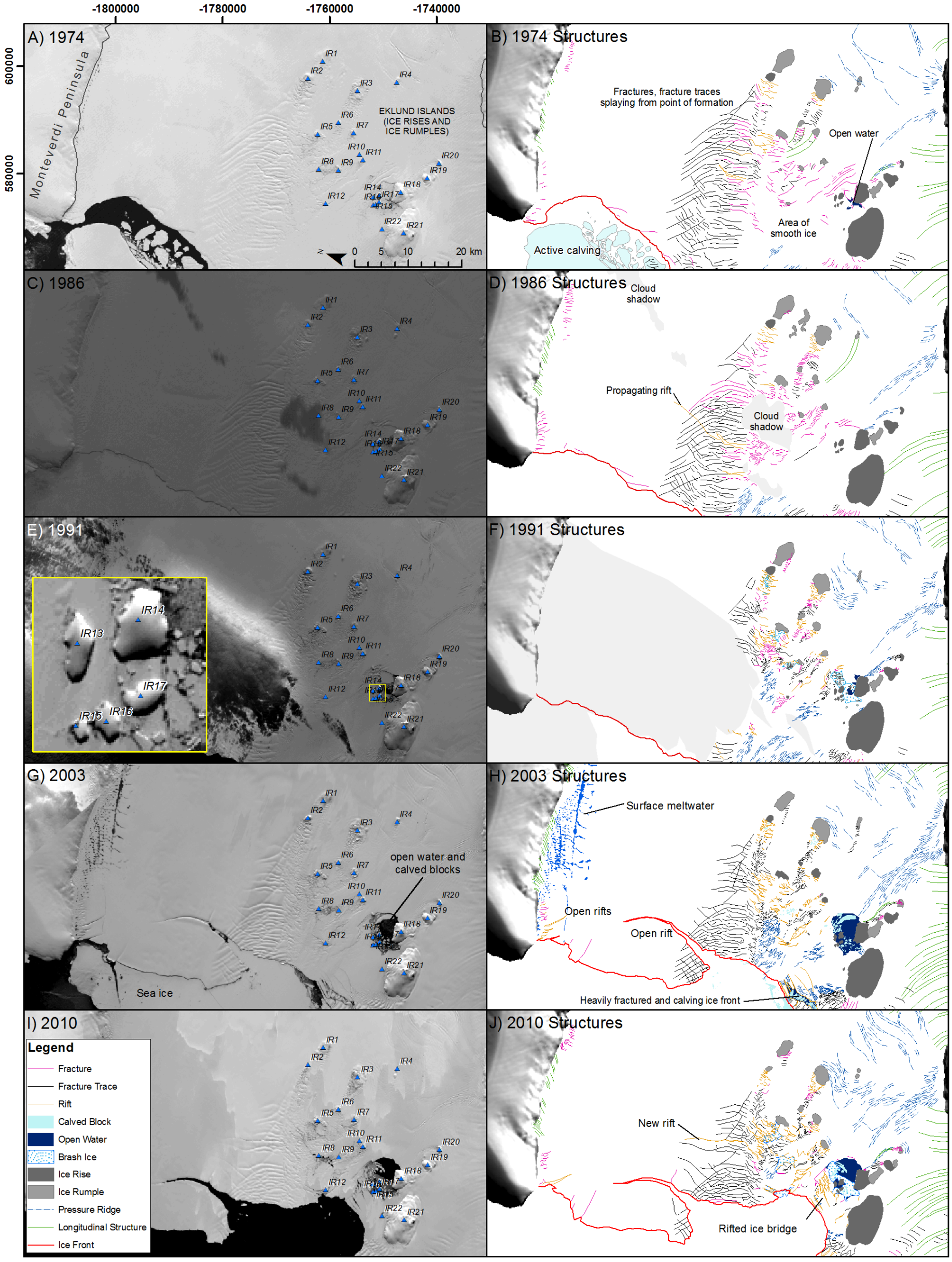

Figure 7.23. Structural evolution at the southern ice front for 1973 (A, B), 1986 (C, D), 1991 (E, F), 2003 (G, H) and 2010 (I, J) illustrating the key changes at the southern ice front between Monteverdi Peninsula and the Eklund Islands. The insert (E) illustrates cluster of ice rises. Major structural changes are associated with fractures and rifts emanating from IR2 as they propagate towards the ice front. Major changes also observed north of IR21 that result in the removal of the ice bridge between 15th January and 24th March 2010 (Figure 7.9). Annotated 1996 ERS-2 SAR image presented separately in Figure 7.2.

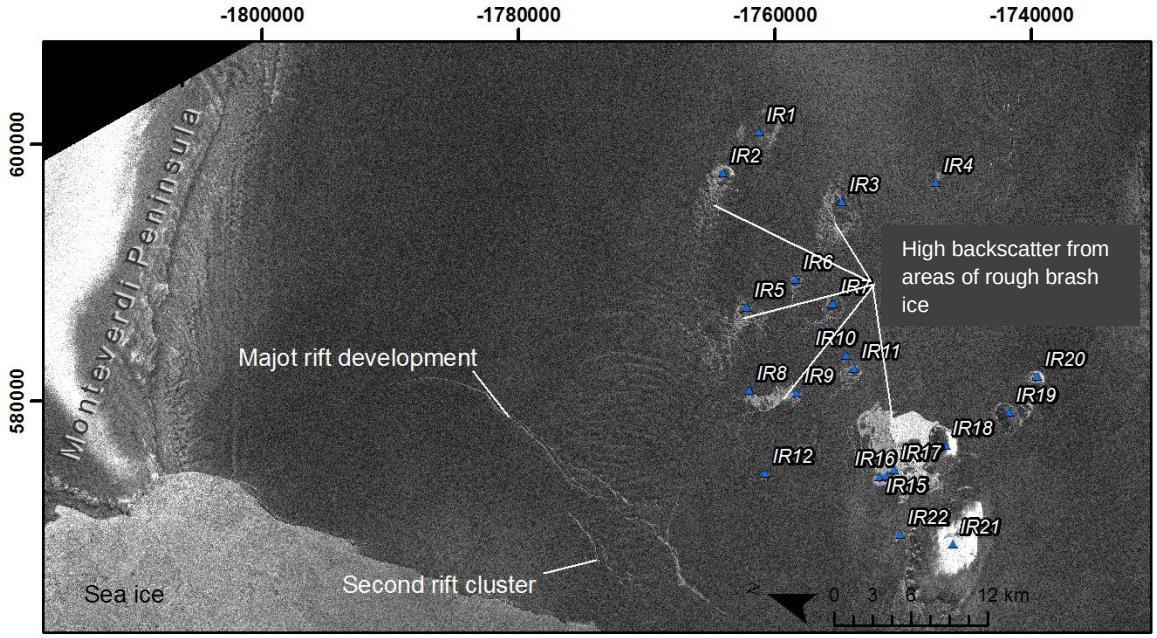

Figure 7.24. Rift development in previously fractured ice during January 1996. The major rift later forms part of the profile of the ice front (2003-present) due to calving of ice between it and the second cluster of rifts. Also notice the high back-scatter regions lee-side of the Eklund Islands that indicate brash ice and/or fracturing.

7.1.4.3 Structural changes and structural evolution at the southern ice front: Eklund Islands to De Atley Island.

During 1973, the area situated between the Eklund Islands and De Atley Island exhibited surface fractures and fracture traces originating northwest and southwest of IR21. These structures spread towards the ice front where their presence became less evident (Figure 7.25B). Fracturing also took place in front of headlands and ice rises along the English Coast grounding zone. Dispersed within these fractures were occasional rifts, particularly on the lee-side of IR26, IR 25 and IR29. The area between these fractures and the ice front is smooth in appearance. Clear flow-unit boundary structures could be traced back from the ice front towards their respective flow units (Figure 7.25B).

By 1986, some fractures flowing to the west of IR21 opened to form rifts near the ice front that were filled with smooth, uniform ice; the ice front lay parallel with these rifts. Fractures and rifts continued to develop along the English Coast ice rumples, although older features had healed to form fracture traces as they migrated into the main shelf area (Figure 7.25C). A similar situation was observed in front of IR29, and new fractures were observed on the lee-side of IR28, ~5.4 km from the ice front. Surface fractures were

irregularly distributed along the ice front, cutting back into the ice shelf both transversely and longitudinally to the local flow direction (Figure 7.25D).

During 1991, rifts at the ice front northwest of IR21 no longer exhibited a smooth ice filling, but instead consisted of a mixture of brash ice and open water. The largest of these rifts measured 14 km in length and cut across a flow unit boundary. Brash-ice filled rifts were also located in front of all of the visible ice rises along the English Coast for the first time (Figure 7.25F). There are few fractures and rifts located along the ice front, although small-to-medium icebergs were observed in Ronne Entrance (Figure 7.25E).

High-radar backscatter in 1996 ERS-2 scenes along the English Coast indicates further fracturing and rifting of the ice shelf adjacent to the English Coast (Figure 7.26). During 2003, a succession of open fractures and rifts ~0.8 km apart dominated the ice front northwest of IR21. The rifts were filled with a mixture of open water and unconsolidated ice, and stretched for up to 12 km across two flow unit boundaries (Figure 7.25H). Smaller fractures and rifts was observed along the distance of the ice front and cut back into the ice shelf. Excessive fracturing and rifting continued to take place on the lee-side of the ice rises along the English Coast. The largest rifts were filled with brash ice with angular,

calved blocks of ice visible in Landsat imagery. Fractures and fracture traces could be tracked to the ice front in previously smooth, consolidated ice. Further fracturing and rifting of the ice shelf was observed in front of IR28 and IR29, with several of these structures clearly filled with brash, unconsolidated ice. Fracture traces from here could be tracked to the ice-shelf front (Figure 7.25H).

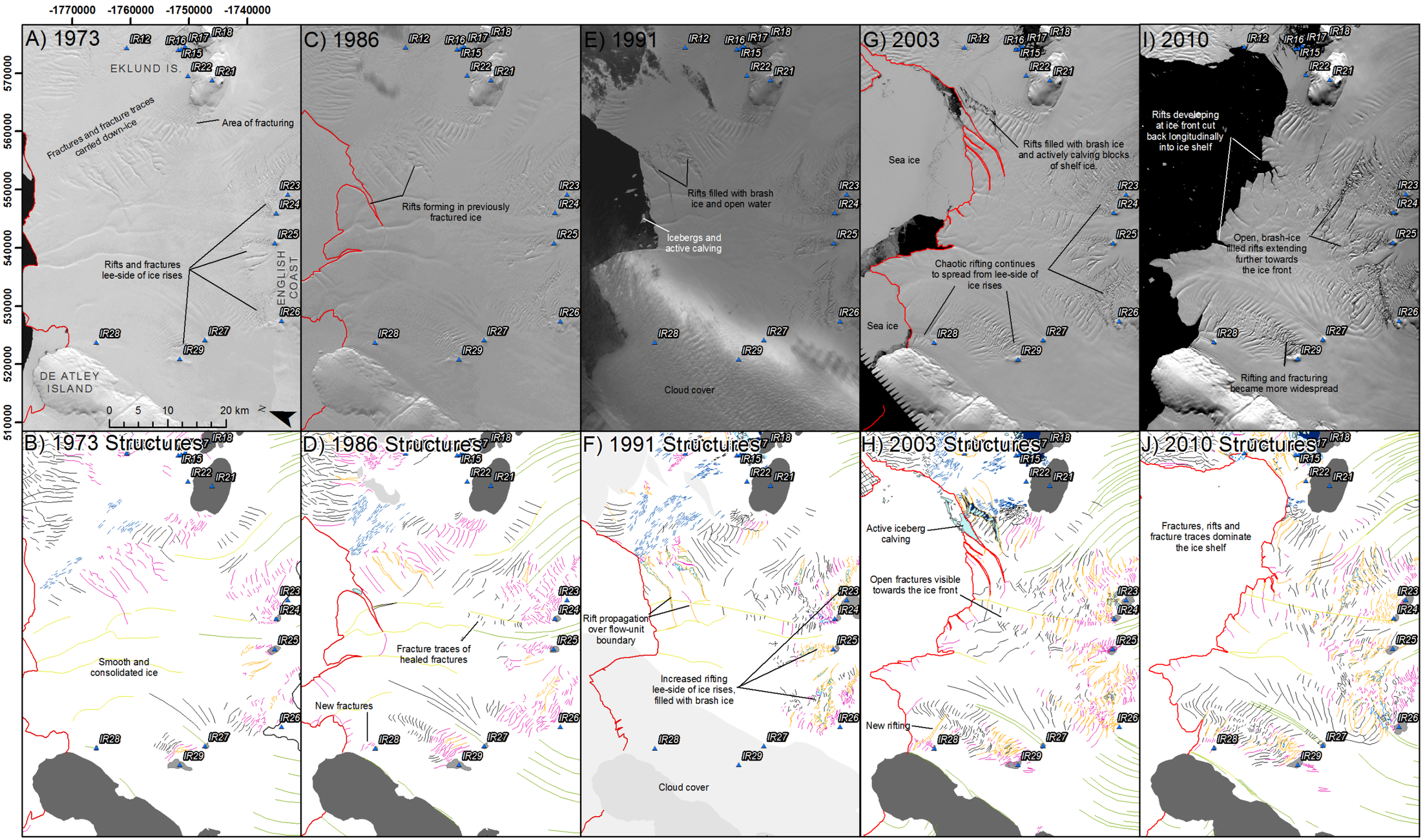

Figure 7.25. Structural evolution at the southern ice front for 1973 (A, B), 1986 (C, D), 1991 (E, F), 2003 (G, H) and 2010 (I, J) illustrating the key changes at the southern ice front between the Eklund Islands and De Atley Island. Fracturing and rifting clearly increases in this region, stemming from the grounding zone, lee-side if IR23-IR26. Iceberg calving continues along pre-existing fractures and fracture traces along the ice front. Annotated 1996 ERS-2 SAR image presented separately in Figure 7.25.

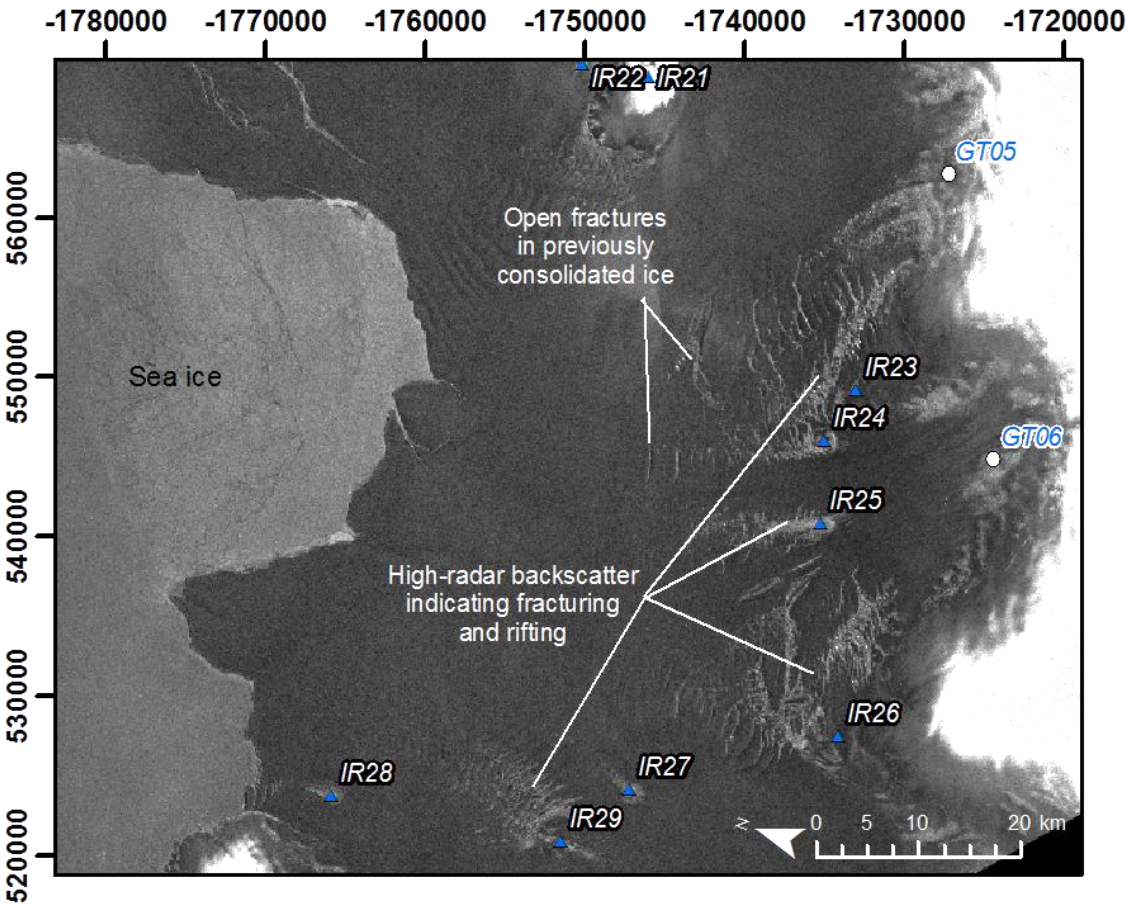

Figure 7.26. ERS-2 SAR image (1996) illustrating the continued fracturing down-ice of the succession of ice rises along the English Coast and propagation of these fractures towards ice front. High back-scatter values also indicative of brash ice.

The ice front northwest of IR21 during 2010 became heavily fractured, transverse to flow (Figure 7.25I, J). These fractures opened up to form rifts at the front, but were filled with smooth, uniform ice. Further west, a large fracture had propagated and cut across a flow unit boundary and fracture traces. Widespread rifting continued northeast of IR23 and IR24; these rifts were clearly filled with a mixture of brash ice and open water, with few large angular blocks of ice also visible. Immediately north of IR24, IR25 and IR26, smaller, chaotic fracturing and rifting had taken place. Open rifts could be traced further down-ice, and were often filled with brash ice. On the upstream-side of IR25, a new rift developed parallel with the localised flow direction; there was no evidence of a surface fracturing in this region in previous imagery. On the lee-side of IR28 small fractures and fracture traces were observed perpendicular to flow, but the fracturing extending from the lee-side of IR29 dominated this region having become increasingly fractured and rifted over time.

7.1.4.4 Surface meltwater extent and distribution

To assess surface meltwater extent over George VI Ice Shelf, the northern-most and southern-most meltwater limits have been mapped using the maximum-observed boundary of active or remnant surface meltwater features (e.g. scoured channels and dry meltwater ponds) for 1973, 1986, 1991, 2003 and 2010 (Figure 7.27). The northern ice limit had migrated northward between 1973 and 1986, and again between 1986 and 2003/2010; there has been little observed change between the northern limits during 2003 and 2010, although the meltwater limit had extended further west from the eastern margin over the same time periods. The southern limit of surface meltwater fluctuated between 1973 and 2010, thus no distinct pattern of advance/retreat can be inferred; the greatest extent of the southern meltwater limit was observed during 1991.

Quantifying the actual spatial extent of surface meltwater over these exact time periods was prevented due to 1) poor data coverage over the entire meltwater extent as a result of persistent cloud cover image quality, and 2) incomparable acquisition dates between observation periods. However, during January 1973 approximately 1444 km^2 of surface meltwater was classified, and in January 2010, approximately 1424 km^2 of surface meltwater was observed, covering an ice-shelf area of ~5900 km^2.

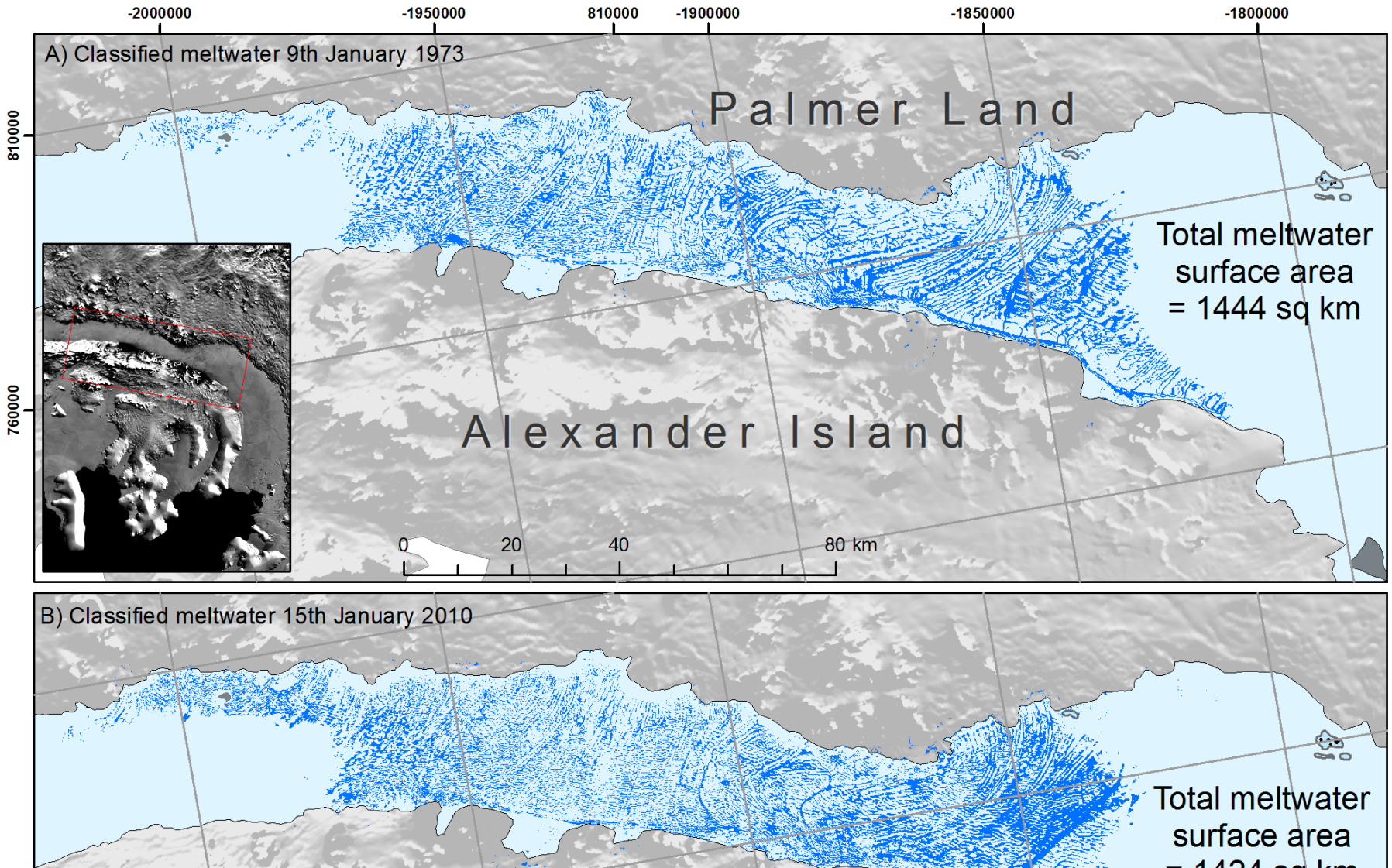

Figure 7.27. Classified surface meltwater extent on George VI Ice Shelf in A) January 1973 (1444 km^2) and B) January 2010 (1424 km^2). Surface meltwater highlights structural configuration across the northern section. C) Illustrates the northward migration of the surface meltwater limit digitised in 1973, 1986, 1991, 2003 and 2010 and the fluctuating meltwater limit at its southern extent in 1973, 1991, 2003 and 2010.

Visual inspection of Landsat imagery over George VI Ice Shelf in successive years highlights remarkably similar patterns of surface meltwater features. Distinct primary pools associated with longitudinal structures and flow unit boundaries are most prominent, with secondary pools and meltwater ponds moving across the shelf towards Alexander Island with shelf flow. Figure 7.28 highlights this similar organisation of meltwater features on George VI Ice Shelf from 1973 to 2010.

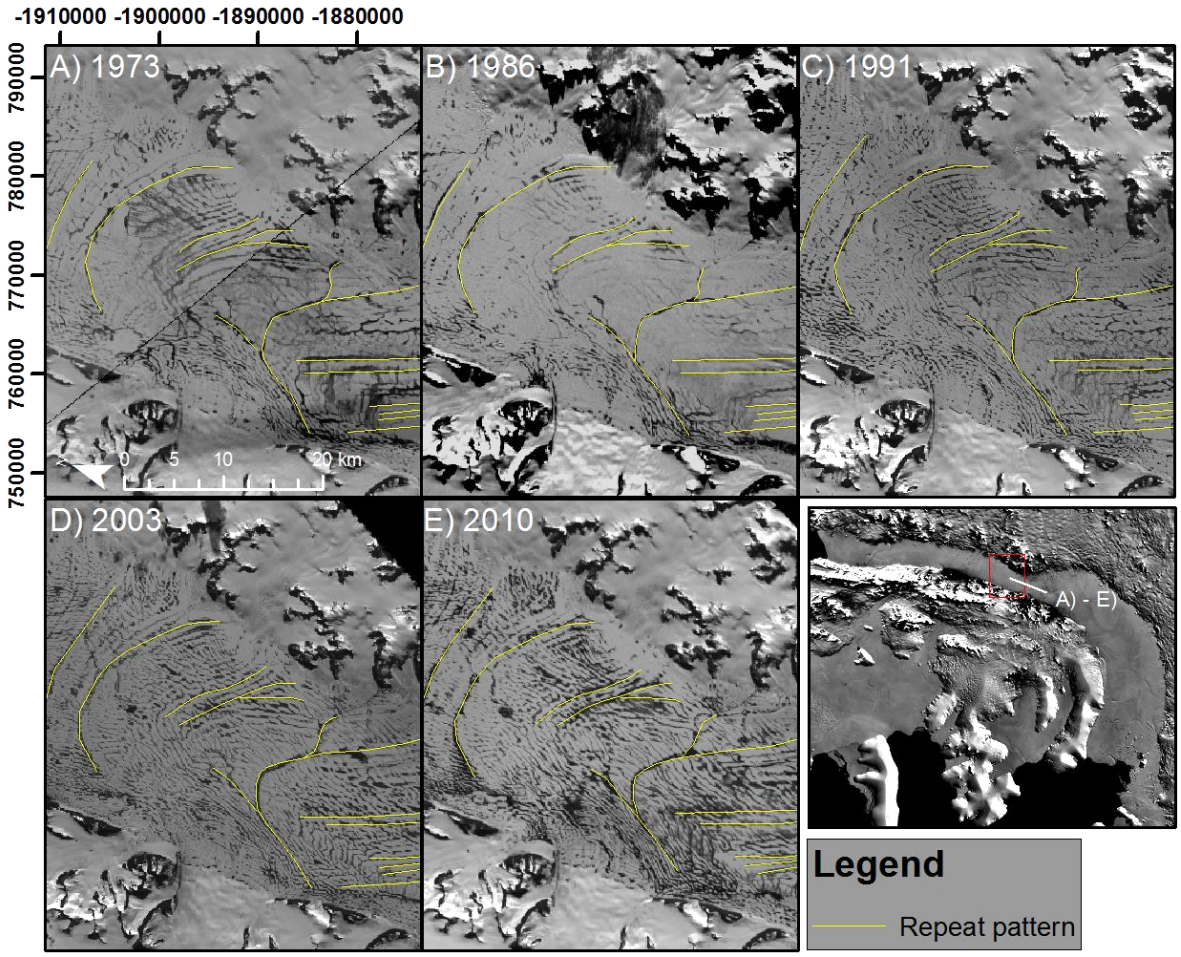

Figure 7.28. Repeat meltwater patterns on the surface of George VI Ice Shelf for A) 1973, B) 1986, C) 1991, D) 2003 and E) 2010. Digitised features are the most prominent and generally follow longitudinal profiles across the ice shelf. Repetitive nature of secondary-channel structures and meltwater ponds also visible at finer spatial scales but are more dynamic across the shelf, moving with the general flow of George VI Ice Shelf.

7.1.4.5 Grounding zone retreat

The grounding zone was mapped as the break of slope/ local minimum, identified in optical imagery by changing surface texture from undulating grounded ice to smooth shelf-ice. The true grounding line is likely to be further upstream, and the point of hydrostatic equilibrium further downstream (Smith, 1991; Vaughan, 1994; Fricker *et al.*, 2009). There is a gradual retreat of the grounding zone between 1973 and 2010, concentrated towards the southern extent of George VI Ice Shelf along the English Coast of Palmer Land (Figure 7.29). In total, 172.23 km^2 of ice shelf area was affected by the retreating grounding zone over a 90 km stretch, between the eastern extent of GT04a and the western boundary of GT07 (Figure 7.29). There is no evidence of grounding zone retreat elsewhere along either Palmer Land or Monteverdi Peninsula, although the reducing surface impression of IR2 also suggests a localised retreating grounding zone (Figure 7.30).

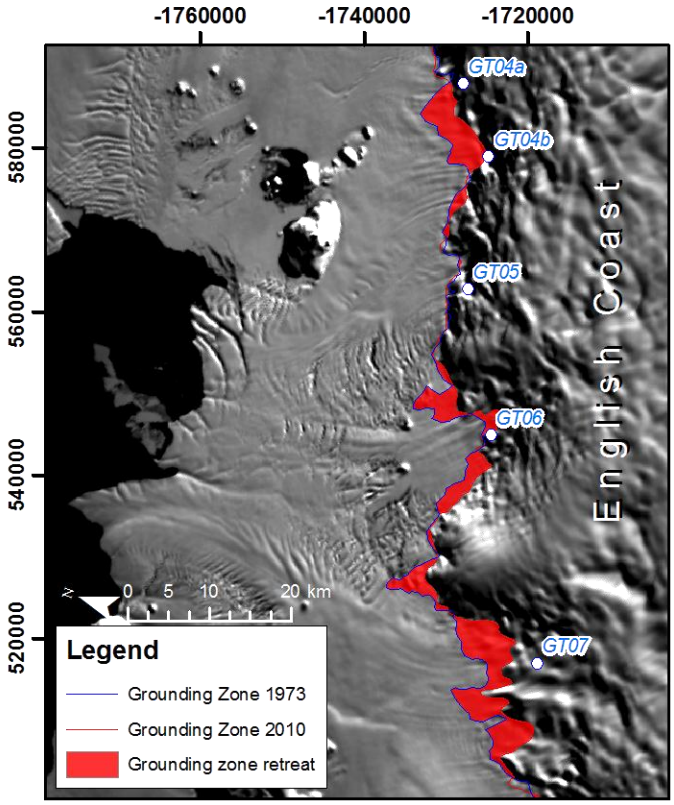

Figure 7.29. Grounding zone retreat between GT04a and the southern extent of GT07 off the English Coast. Retreat is principally in the main flow-unit channels, with the exception of GT05. The greatest areal change is identified at GT07 where the grounding zone retreated up to 7.6 km from its 1973 position.

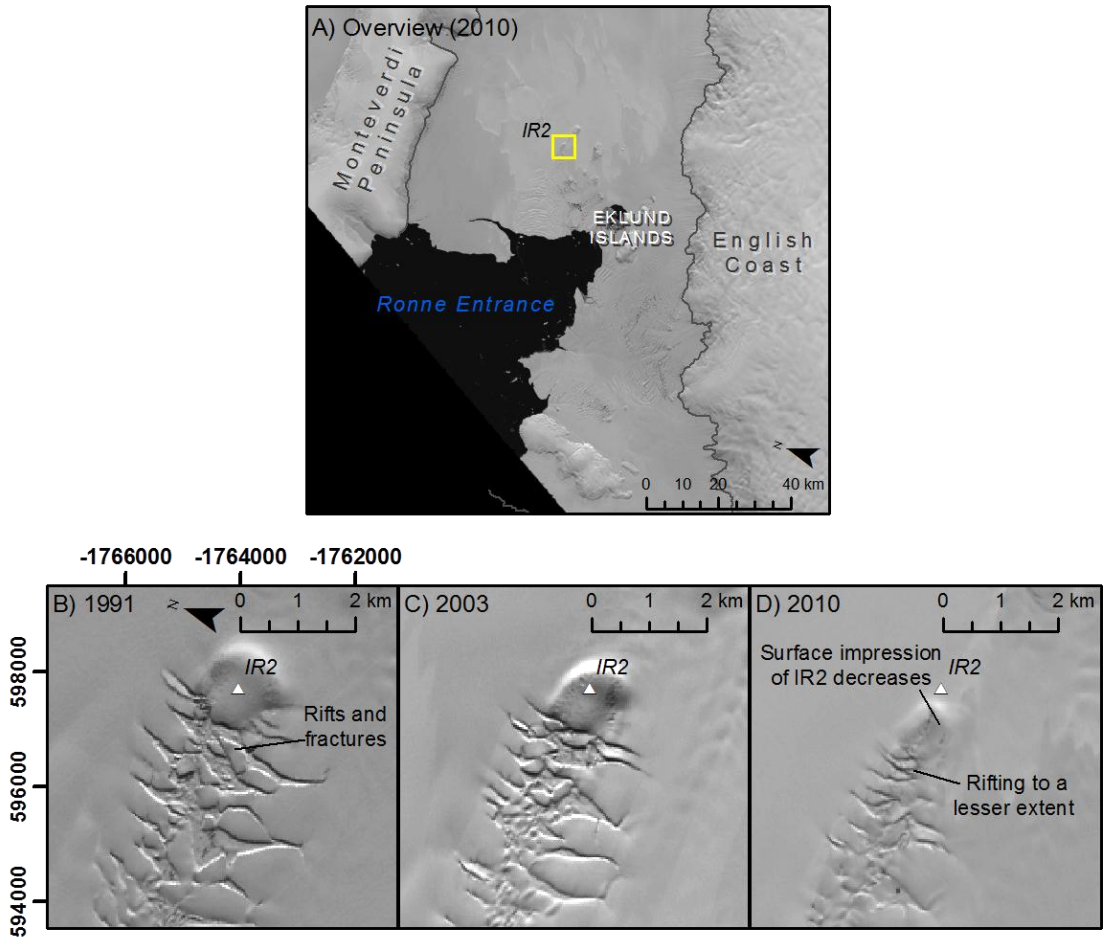

Figure 7.30. Decreasing surface impression of IR2 of the Eklund Islands and associated decreasing extent of rifting and fracturing on its lee-side in B) 1991, C) 2003 and D) 2010. Decreasing areal extent of IR2 due to localised grounding zone retreat.

7.1.5 Surface elevation and surface-elevation changes

Change in the surface elevation on George VI Ice Shelf was calculated over 16 tracks between October 2003 and March 2008 following the same methods outlined in Chapter 5 and Chapter 6. Statistics and a description of each track are given in Table 7.11. Furthermore, surface-elevation changes are analysed spatially for the northern, central and southern extents (Figure 7.31) and are outlined below.

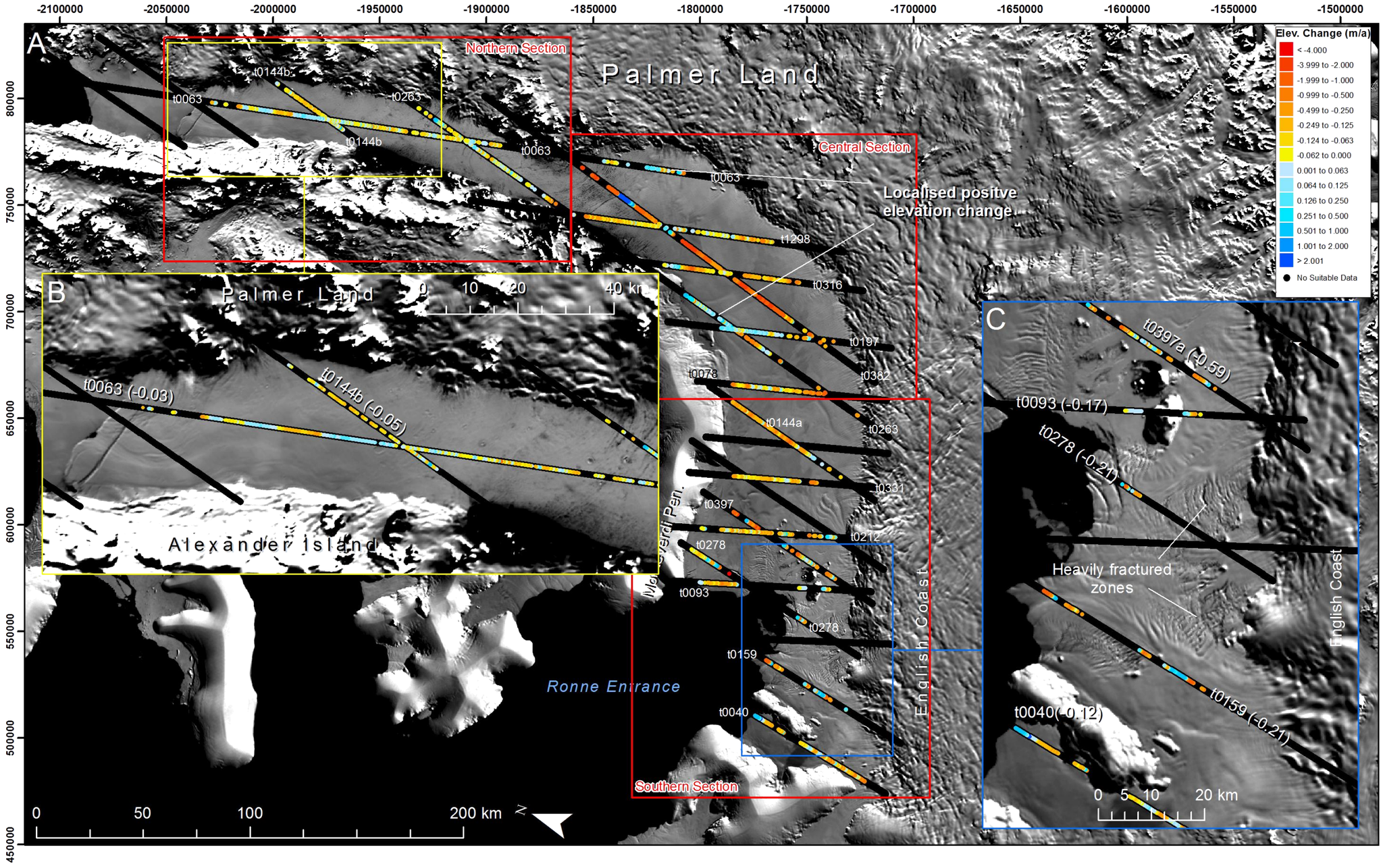

Figure 7.31. ICESat GLAS surface elevation change calculations displayed as ma^{-1}. Note widespread negative surface elevation changes interspersed with localised, positive surface elevation changes. Insert B illustrates non-significant surface elevation changes towards the northern ice front (mean transect elevation changes in brackets) and Insert C illustrates significant negative elevation changes towards the southern ice front, although repeat measurements have been heavily filtered due to surface fracturing and rifting as discussed previously (mean transect elevation changes in brackets). Table 7.11 details transect statistics and descriptions, Appendix 2c illustrates transect measurements and surface elevation changes for each track. ICESat GLAS further analysed below by considering elevation changes in the northern, central and southern sections as defined by the red polygons.

Table 7.11. Detailed description of surface elevation measurements and surface elevation change calculations from ICESat GLAS repeat measurements.

Track	Laser campaign period	Observation period	Max + change (m)	Max - change (m)	Mean change (m)	Max + annual change (ma^{-1})	Max - annual change (ma^{-1})	Mean annual change (ma^{-1})	Description of elevation and elevation change
t0063	2a-3k	25/10/03 – 13/10/08	1.470	-7.946	-0.164	0.296 (± 0.045)	-1.600 (± 0.045)	-0.033 (± 0.045)	Gradual increase in surface elevation from north ice front (219 km) to central ice-shelf region (0 km). No distinct pattern of negative or positive elevation change, with weak, non-significant negative change calculated over the whole transect. (Appendix 2cA).
t0144b	3d-3i	04/11/05 – 17/10/07	1.520	-0.646	-0.098	0.781 (± 0.038)	-0.332 (± 0.038)	-0.050 (± 0.038)	Surface elevation greater in the centre of the ice shelf (centre of transect), decreasing gradually to each grounding line (63 km, 0 km). General pattern of negative surface elevation change recorded, with localised increase in surface elevation observed towards the Alexander Island (AI) grounding line (80 km). (Appendix 2cB).
t0382	3a-3d	03/11/04 – 20/11/05	7.935	-15.11	-2.223	7.577 (± 0.167)	-14.435 (± 0.167)	-2.123 (± 0.167)	Transect stretches over the central portion of the central section of GVIIS. There is an increase in surface elevation across the transect from 170 km to 0 km. Calculated widespread and significant negative surface elevation changes, with limited and discreet pockets of positive surface elevation change. (Appendix 2cC).
t1298	3c-3f	21/05/05 – 25/05/06	0.249	-0.735	-0.128	0.234 (± 0.167)	-0.728 (± 0.167)	-0.127 (± 0.167)	General, stepped increase in elevation from AI grounding zone (115 km) towards Palmer Land (PL) grounding zone with fluctuating surface elevation changes between positive and negative. Mean annual change is non-significant. (Appendix 2cD).
t0316	3a-3i	30/10/04 – 28/10/07	0.903	-4.610	-0.738	0.302 (± 0.089)	-1.540 (± 0.089)	-0.246 (± 0.089)	Increasing surface elevation cross GVIIS from Alexander Island (AI; 85 km) to PL (0 km). Negative surface elevation change calculated over much of the transect, with only a few distinct pockets of positive elevation changes calculated. (Appendix 2cE).
t0197	2a-3i	03/11/03 –	0.937	-1.127	0.194	0.237	-0.285	0.0490	Increase in surface elevation from AI (73 km) to PL (0 km). Positive

		20/10/07				(± 0.089)	(± 0.089)	(± 0.089)	surface elevation changes recorded over much of the transect with only distinct negative surface elevation changes observed at 54 km, 40 km and 30 km. (Appendix 2cF).
t0263	3a-3i	26/10/04 – 25/10/07	3.970	-5.624	-0.021	1.326 (± 0.045)	-1.879 (± 0.045)	-0.007 (± 0.045)	No distinct pattern of positive or negative surface elevation changes in the northern or southern reaches of the transect, reflected in very weak, non-significant mean annual elevation change (-0.007). (Appendix 2cG, H).
t0078	2a-3k	26/10/03 – 14/10/08	3.263	-6.736	-0.958	0.657 (± 0.089)	-1.356 (± 0.089)	-0.193 (± 0.089)	Steady surface elevation (~45 m) across the ice shelf from AI (68 km) to PL (0 km). Clear negative surface elevation change across the ice shelf, interspersed with five distinct peaks of positive change at 53 km, 48 km, 44 km, 39 km and 21 km. (Appendix 2cI).
t0144a	2a-3i	30/10/03 – 17/10/07	0.466	-4.151	-1.137	0.118 (± 0.038)	-1.048 (± 0.038)	-0.287 (± 0.038)	Even surface elevation stretching from AI (84 km) to PL (0 km), with a distinct pattern of negative surface elevation changes recorded across the ice shelf. Limited increase in surface elevation over time recorded at four distinct points, but is not widespread. (Appendix 2cJ).
t0331	2b-3e	18/03/04 – 24/03/06	0.795	-1.817	-0.255	0.395 (± 0.097)	-0.901 (± 0.097)	-0.127 (± 0.097)	Negative surface elevation changes across the ice shelf are prominent, with pockets of elevation increases also measured. Distinct surface profile from AI (79 km) to PL (0 km), but generally greater surface elevations towards the latter. (Appendix 2cK).
t0212	3c-3f	08/06/05 – 12/06/06	0.670	-0.721	-0.116	0.664 (± 0.089)	-0.715 (± 0.089)	-0.115 (± 0.089)	Large fluctuations in surface elevation across the transect as a product of the EI ice rises, with statistically significant negative surface elevation changes calculated across the whole track (-0.115 ma^{-1}). (Appendix 2cL).
t0397	3a-3d	04/11/04 – 21/11/05	0.592	-4.084	-0.615	0.565 (± 0.089)	-3.900 (± 0.089)	-0.587 (± 0.089)	Transect cuts across the Eklund Islands (EI), associated with lower surface elevations between ~47 km and 12 km. Negative surface elevation changes towards Monteverdi Peninsula (MP), with distinct pockets of positive changes in and around the EI. Strong negative

									surface elevation changes calculated over the whole track (-0.587 ma^{-1}). (Appendix 2cM).
t0093	2a-3k	27/10/03 – 15/10/08	1.234	-7.209	-1.236	0.249 (± 0.098)	-1.451 (± 0.098)	-0.249 (± 0.098)	Track stretched across southern ice front from MP (49 km) to PL (0 km), cutting across main EI ice rise (~15 km). Surface elevation from MP to EI generally lower than surface elevation from EI to PL. Negative surface elevation change recorded across track, with few localised pockets of positive elevation observed towards MP grounding line. (Appendix 2cN).
t0278	3d-3i	13/11/05 – 26/10/07	2.558	-5.581	-0.238	0.854 (± 0.097)	-1.864 (± 0.097)	-0.079 (± 0.097)	Large fluctuations in surface elevations across track 0278 as it stretches over open water at the ice front and a heavily fractured ice-shelf surface. Weak but non-significant negative surface elevation changes recorded over few spatial measurements. (Appendix 2cO).
t0159	3a-3i	19/10/04 – 18/10/07	2.427	-4.375	-0.645	0.811 (± 0.089)	-1.461 (± 0.089)	-0.215 (± 0.089)	Gradual increase in surface elevation from the ice front (59 km) to PL grounding line (0 km). Distinct pockets of positive surface elevation changes, but widespread negative surface elevation changes recorded, significant over of the whole transect (-0.215 ma^{-1}). (Appendix 2cP).
t0040	2a-3k	23/10/03 – 11/10/08	1.219	-6.844	-1.327	0.245 (± 0.098)	-1.378 (± 0.098)	-0.267 (± 0.098)	Gradual increase in surface elevation from the ice front (60 km) to PL grounding line (0 km). Localised areas of positive surface elevation changes, but widespread negative surface elevation changes recorded along most of the transect. (Appendix 2cQ).

Surface elevations and surface elevation changes in the northern section of George VI Ice Shelf are calculated over three tracks with a total of 1017 repeat-measurements. Generally, there is a steady decrease in surface elevations along the centreline of the northern section towards the north ice front, with greater surface elevations recorded towards Palmer Land, reducing across the ice shelf to Alexander Island. Surface elevation measurements across t0144b, however, suggest greater surface elevations along the centreline, decreasing towards each grounding zone. Consequently, the northern section of George VI Ice Shelf displays complex surface morphology across and along its channel.

Track t0063 stretches from the input of McArthur Glacier to the northern ice front, whereas t0144b and t0263 cut across George VI Ice Shelf from Palmer Land to Alexander Island. Mean surface elevation measurements observed over the northern sections illustrate a weak, non-significant, negative change, and there are few distinct spatial patterns within this region.

In the central section, six ICESat GLAS tracks cut across George VI Ice Shelf, with 1657 repeat track measurements analysed. Surface elevations are always greater towards Palmer Land, decreasing across the ice shelf to Alexander Island. This central section illustrates a complex pattern of surface elevation changes, with positive changes observed at the input of Goodenough Glacier (t0063) and towards the northern extents of t0197 and t0263, near the input of Kirwen Inlet. Significant negative elevation changes are recorded along t0382 that cuts across the centreline of the central region of George VI Ice Shelf. Tracks t1298 and t0316 both illustrate ice-shelf wide negative surface elevation changes from Alexander Island to Palmer Land.

Towards the southern extent of George VI Ice Shelf, a widespread negative surface elevation change has been calculated over 1649 repeat measurements, interspersed with localised pockets of positive elevation changes. Due to ice-shelf fracturing and rifting towards the southern ice front, the ICESat GLAS dataset was heavily filtered, and therefore direct measurements of surface elevation changes are incomplete towards the English Coast and around the Eklund Islands.

7.1.6 Section Summary

George VI Ice Shelf is a complex and unique ice-shelf system exhibiting two diverse ice fronts. The north ice front is confined to an approximate 20 km-wide channel between Palmer Land and Alexander Island, with the south ice front positioned in a wider, approximate 75 km-wide channel interrupted by the cluster of ice rises and ice rumples of the Eklund Islands. The key findings from Section 7.1 are as follows:

1. The northern ice front is predominantly supplied by ice flowing off Palmer Land, with Riley Glacier currently being the most influential on the dynamics of the ice front. Larger tributary glaciers such as Millett, Bertram and Ryder Glaciers enter the ice shelf further upstream and flow across the ice shelf towards Alexander Island, diverting to a northwardly flow as ice approaches the opposing grounding zone. Because of the dynamic configuration, little ice is inputted into the ice shelf from Alexander Island, and George VI Ice Shelf exhibits regions of both fast and slow flow regimes within distinct and often confined channels.
2. In total, George VI Ice Shelf lost ~1995 km^2 from its areal extent at its north and southern fronts. Between 1974 and 2010, the north ice front underwent continuous retreat over a total distance of ~40 km, with over half of this occurring between 1974 and 1979. Spatially, 1255 km^2 of ice was lost from the north ice front, calving along pre-conditioned fractures and/ or rifts in regular events. Since 1979, the retreat at the northern ice front has been steady (~25 km^2a^{-1}). When viewed from above, the north ice front always displayed slight concavity towards the centre point.
3. At the southern ice front, retreat was concentrated in a central section towards the Eklund Islands. In this area, a linear retreat of ~28 km was recorded between January 1973 and January 2010. Retreat continued beyond January 2010 and subsequently split the south ice front into two independent fronts, one stretching from Monteverdi Peninsula to the Eklund Islands, and the other from the Eklund Islands to De Atley Island. A third, smaller ice front was always present between De Atley Island and Spatz Island, and also underwent continued retreat. Overall, the retreat rate doubled during the period 1991 to 1996, before steadily decreasing to ~18 km^2a^{-1} between 2003 and 2010.
4. Dynamically, the southern ice front is complex. The presence of the Eklund Islands acts as a buttress to otherwise more dynamic flow to their north and west. Ice is

delivered to South Ice Front 1 from tributary glaciers up to 160 km back upstream (GT02), whereas ice at South Ice Front 2 is provided by five individual tributary glaciers that flow directly out towards the ice front, converging in the area between the Eklund Islands and De Atley Island. Over time, flow velocities in this region increase from the grounding zone to the ice front, whereas little change was observed in ice supplying South Ice Front 1.

5. Structurally, George VI Ice Shelf is dominated by flow-related longitudinal features stretching from Palmer Land into the shelf. Fracturing is limited on the ice shelf to both of the ice fronts and in distinct flow-unit confluence zones along Palmer Land. At the northern ice front, fracturing decreases over time due to continuous iceberg calving along these structural weaknesses. Currently, there are no ice-shelf wide fractures or rifts in this zone. Conversely, at the southern ice fronts, fractures and rifts are dominant and increase in size, distribution and extent over time.
6. Surface meltwater was observed in the northern and central sections in all observation periods from 1973 to 2010, covering an approximate ice shelf area of 5900 km^2. The total extent of meltwater has not varied greatly over time (1444 km^2 in January 1973 and 1424 km^2 in January 2010), yet the northern extent migrated northward. The southern extent of the meltwater did not show a southern migration and instead fluctuated between each observation period.
7. Between 2003 and 2008, ICESat GLAS repeat measurements reveal widespread, negative surface elevation changes over much of the southern and central sections, interspersed with distinct pockets of positive surface-elevation changes. In the northern section, however, there is little evidence of significant positive or negative elevation changes. Furthermore, in the southern section, a retreat of the grounding zone has been identified along the English Coast, with the greatest linear retreat measuring ~7.6 km.

Section 7.2 presents an interpretation of these observations with respect to spatial changes at the north and southern ice fronts, the significance of ice-shelf dynamics and inferences on structural changes.

7.2 George VI Ice Shelf interpretation

In Section 7.1, the spatial changes of George VI Ice Shelf, its structural glaciology and structural evolution from ca. 1973 to 2010, its surface dynamics and velocity changes over the last two decades, and changes to its surface elevation from 2003 to 2008, were described. Here, these four components are integrated to allow interpretations of the glaciological changes to be made. Due to its size and complexity, the following sub-chapter considers George VI Ice Shelf in three spatial sections (north, central and south as detailed in Section 7.1) and presents an interpretation of; 1) the patterns of spatial changes; 2) surface structures, surface features and their inference on ice-shelf configuration, dynamics and ice-shelf heterogeneity; and 3) surface elevation changes and significance for ice-shelf thickness estimates.

7.2.1 Interpretation of spatial changes

George VI Ice Shelf is unique; its two ice fronts are situated ~450 km apart and exist in two different environments. The north ice front is confined to a narrow, 20-25 km-wide channel between Alexander Island and Palmer Land, and is fed predominantly by ice flowing from the latter of these grounded regions, entering the ice shelf almost parallel to the ice-front. The southern ice front is similarly fed by ice flowing almost entirely from the main Antarctic Peninsula, but the principal flow direction is approximately perpendicular to the ice-front shape. Thus, the ice-shelf dynamics at the northern ice front are very much dependent on one tributary glacier (Riley Glacier during 2010), whilst the dynamics at the southern ice front are influenced by multiple tributary glaciers each flowing towards the ice front. These two very different dynamic regimes result in equally different ice-loss regimes between ca. 1973 and 2010.

7.2.1.1 North Ice Front

The greatest recorded ice loss at the northern ice front occurred between 1974 and 1979, with ~820 km^2 calving into Marguerite Bay. It is unclear from the temporal resolution of the observation period whether this loss occurred in a single retreat event or several calving events over successive years. The northern ice front during 1974 was heavily fractured and rifted across almost the entire channel width between Alexander Island and Palmer Land, extending back upstream for ~40 km to the northern boundary of Riley Glacier. Rifts developed in this region and propagated across the ice shelf at regular (~4 km) longitudinal intervals, increasing in length with distance from the grounding zone. The regularity of

fractures and rifts in this zone of relatively slow-moving ice suggests that these features had been gradually developed for some considerable time, forming at the grounding zone through 1) flow-induced longitudinal extension and/or 2) bending stresses caused by vertical tidal motion, before propagating across the ice shelf towards the north-ice front. Further rifting across the north-ice front between 1996 and 2001 eventually led to a large calving event during January 2010, although rift development this time stemmed from the western margin near Alexander Island rather than from Palmer Land. Most of the retreat at the northern ice front was thus governed by pre-conditioned and longstanding active rifts developed well in advance of actual calving (Figure 7.32), although small (up to 2 km^2) icebergs were also observed throughout the observation period in Marguerite Bay. Indeed, the 1979 and 1989 ice-front profiles were observed as rifts in 1974 Landsat MSS imagery, thus emphasising the long-term development of retreat patterns at the northern ice front. As of March 2010, no ice-shelf-wide rifts existed in this region, thus no further immediate large-scale calving is anticipated based on historical patterns.

Spatial changes at the northern ice front between 1974 and 2010 occurred in an area relatively absent of direct glacier input along the adjacent grounding zones of Alexander Island and Palmer Land, and thus present a viable explanation for continued fracture and rift propagation and the consequent pattern of retreat (Figure 7.32). Zones of fractured ice are observed along the grounding zone of George VI Ice Shelf between coalescing flow units; these areas tend to exhibit longitudinal extension at the grounding zone causing initial fracturing, with stress regimes becoming more and more compressive with increased distance from the ice-shelf margin, due to the coalescing of ice-flow units. Thus the switch from an initial tensile regime to a compressive stress regime within a limited spatial extent restricts fracture and rift propagation, and indeed prompts the sealing of fractures. North of Riley Glacier, coalescence with a second tributary glacier does not occur, thus ice does not undergo a compressive stress regime. It is proposed that as a result of this dynamic configuration, fractures emanating from the north boundary of Riley Glacier at the grounding zone are able to spread transversely across the ice shelf as it flows towards the northern ice front with little or no resistance.

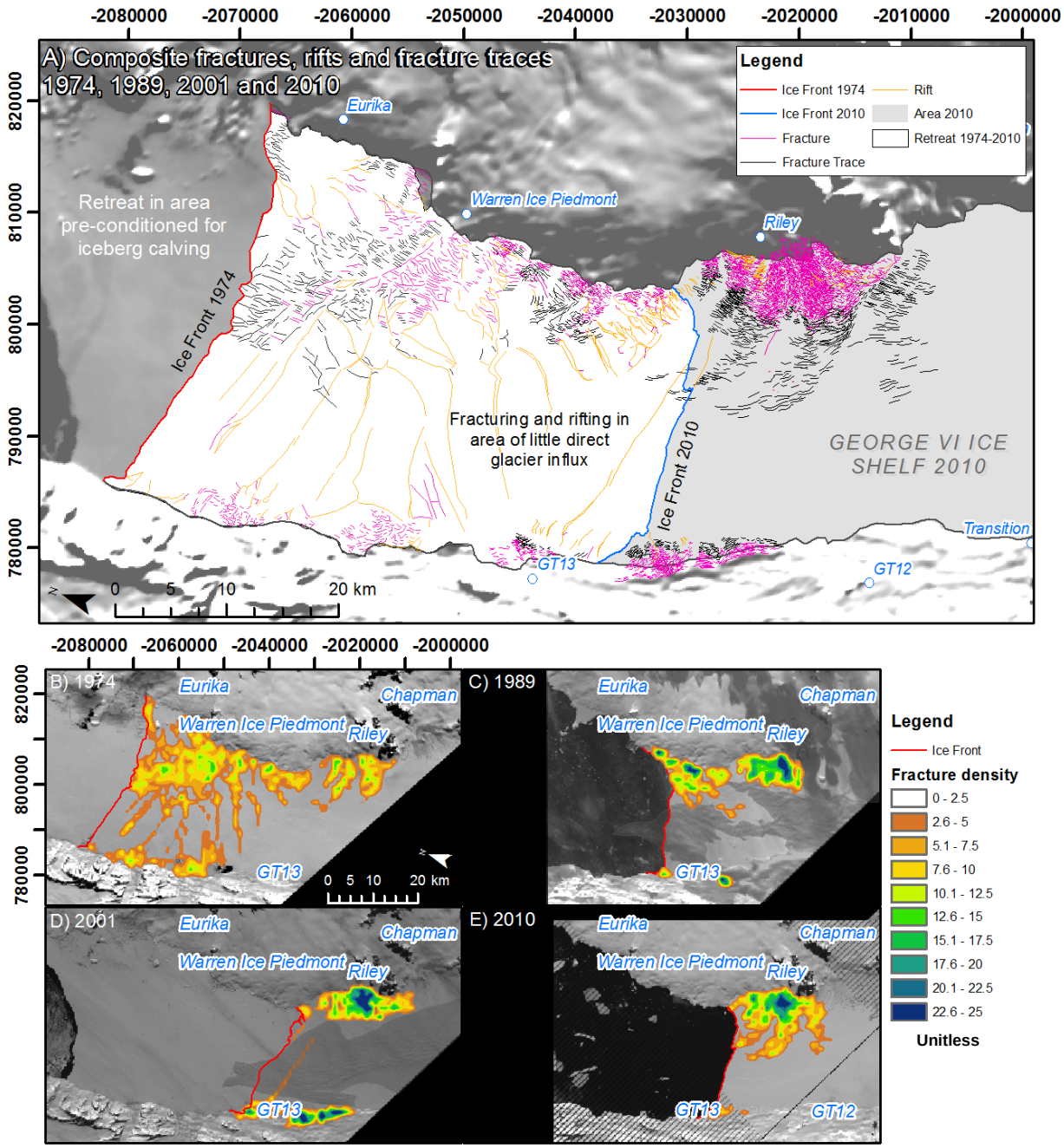

Figure 7.32. A) Composite fracture, rift and fracture trace structural maps from 1974, 1989, 2001 and 2010 illustrating the preferential calving of fractured ice between 1974 and 2010. It is inferred that longitudinal compression is limited in this region due to limited influx of ice between Riley Glacier and the north ice front that may otherwise act as a buttress to up-stream ice. B-E) Illustrate the fracture densities (arbitrary scale) interpolated from digitised maps for 1974, 1989, 2001 and 2010. Note the general reduction in ice-shelf wide fractures as the ice front retreats but increasing density of fractures, rifts and fracture densities associated with Riley Glacier.

The resultant north ice front during January 2010 displayed a slight concave geometry, bowing inwards from its pinning points to the centre of the ice front, when viewed from above. Doake *et al.* (1998) suggested that this frontal characteristic creates a geometrically

unstable ice front that could lead to further ice loss. This pattern of slight-concavity is also portrayed in each of the time periods and thus suggests that George VI Ice Shelf has been geometrically configured for continued retreat since at least 1974, at its northern ice front.

As a result of ice-front recession, the northern region of George VI Ice Shelf became increasingly dominated by the dynamics of Riley Glacier. Interpolated feature tracking measurements from ca. 1989, ca. 2002 and ca. 2007, coupled with InSAR velocity estimates from ca. 1995 clearly illustrate the increase in flow speeds of Riley Glacier over time. Elsewhere on the Antarctic Peninsula it has been demonstrated that the removal of an ice-shelf system results in an increase in velocity of former tributary glaciers (De Angelis and Skvarca, 2003; Dupont and Alley, 2005; Pritchard and Vaughan, 2007), and whilst Riley Glacier still contributes to the mass of George VI Ice Shelf, the continued retreat of the northern ice front has effectively removed a buttress, reducing back-stresses and consequently permitted an increase in surface velocity at the north margin. A measured increase in flow speed at the northern ice front between ca. 1995 and ca. 2002, and subsequent decrease between ca. 2002 and ca. 2007 is attributed to active rifting of the ice front between 2001 and 2003 and consequent iceberg calving. Further upstream, flow velocities of Skinner and Chapman Glaciers on Palmer Land and GT12, Transition Glaciers on Alexander Island do not show a significant increase or decrease over time, and thus further illustrate the dominance and controlling nature of Riley Glacier on the dynamics of the north ice front.

7.2.1.2 South Ice Front

Between 1973 and 2010, the south ice front underwent a net change of -742 km^2. The vast majority of this retreat occurred within the central portion of the main south ice front, northwest of the Eklund Islands. It is inferred from visual assessment of Landsat imagery (Figure 7.33) and coarse 200 m RAMP DEM data (Figure 7.34) that this region has lower ice-shelf surface elevations on the down-ice-side of these ice rises and it is thus inferred to be an area of thinner ice, surrounded by heavily fractured shelf-ice (Figure 7.33).

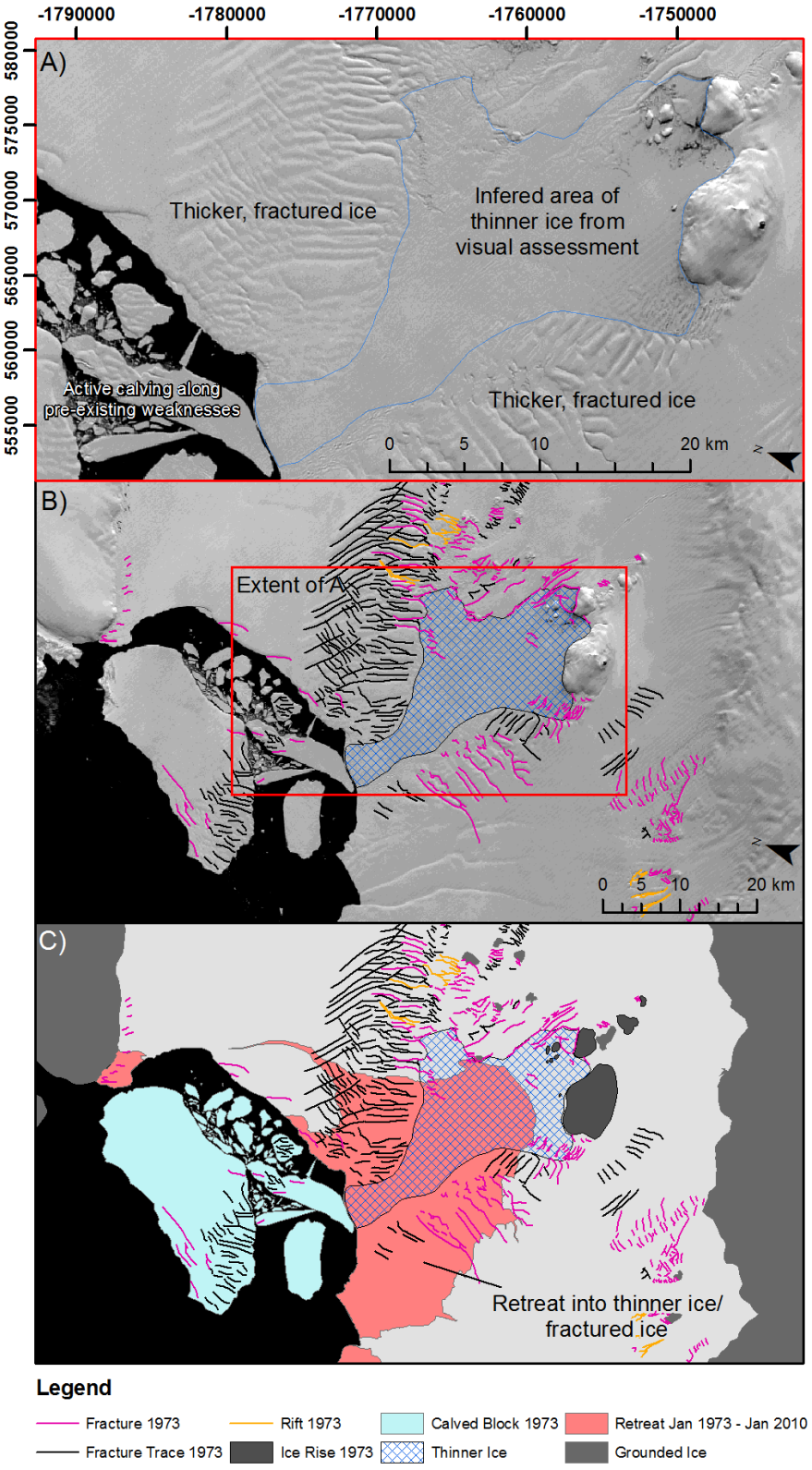

Figure 7.33. A) 1973 extent of inferred thinner ice from visual assessment of Landsat imagery. B) Area of thinner ice and fractures/rifts superimposed on 1973 Landsat MSS image, and C) structural interpretation illustrating the concentrated retreat of thinner and fractured ice between 1973 and 2010.

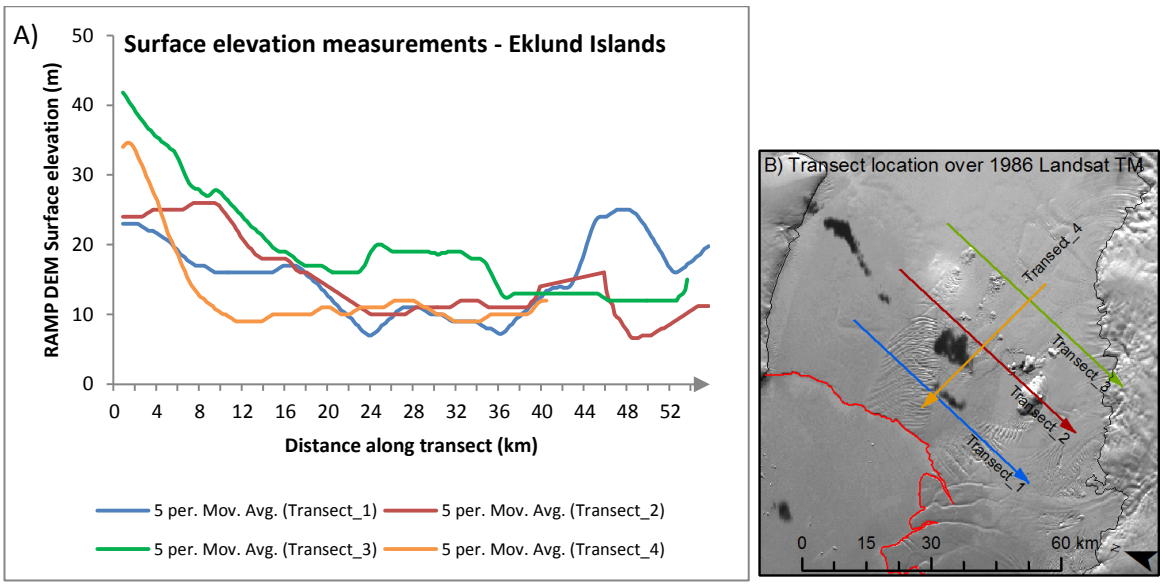

Figure 7.34. RAMP DEM surface elevation transects down-flow (Transect_1, Transect_2), up-ice (Transect_3) and longitudinally across (Transect_4) of the Eklund Islands illustrating lower surface elevations lee-side of the ice rises and ice rumples from which thinner ice is inferred. B) Location of transects superimposed over 1986 Landsat TM imagery. Transect direction indicated by arrow on transect and X-axis in A.

The presence of ice rises and ice rumples at the south front is important to the retreat characteristics of George VI Ice Shelf for three reasons. First, their presence causes regular fracturing and rifting of the ice shelf as it flows around (or over) such features, due to a shift from high-compressional stresses upstream to tensile stresses downstream. Second, the composition of shelf-ice, lee-side of ice rises and ice rumples has elsewhere been shown to have a higher concentration of warmer, marine-derived ice, accreted in basal cavities and incorporated into the ice shelf through the resealing of fractures down-flow (Fricker *et al.*, 2001; Khazendar, 2003). Whilst considered to be less brittle than meteoric ice (Lui and Miller, 1979), the warmer (Vieli *et al.*, 2007), marine-derived ice is more susceptible to oceanographic variations (Fricker *et al.*, 2001). Third, these obstructions also have a profound effect on regional surface velocities and thus the supply of ice to this region. Feature tracking measurements from each of the observation periods reveals substantially slower flow speeds down-ice of the Eklund Islands than those observed outside of this region; the Eklund Islands essentially acting as a buttress to flow.

Furthermore, during 1973, the southern ice front arguably satisfied Doake *et al.'s* (1998) criteria for irreversible retreat, displaying a largely concave profile. A combination of these factors made large portions of the south ice front pre-conditioned for iceberg calving and continued retreat as observed between 1973 and January 2010.

Visual examination of Envisat ASAR imagery from March 2010 shows continued retreat in this region, with the small ice bridge between Ronne Entrance and the area of open water breaking apart between January and March 2010. The significance of this is that the southern portion of George VI Ice Shelf is now characterised by three totally independent ice fronts; 1) running from Monteverdi Peninsula to the north-side of the largest of the Eklund Islands, 2) from the east-side of this ice rise to De Atley Island, and 3) from De Atley Island to Spatz Island. The separation of South Ice Front 1 from South Ice Front 2 occurred gradually from 1973 to present, although enhanced retreat was observed between 1991 and 2003.

South Ice Front 1 comprises two distinct zones (as of March 2010), 1) the region of heavily fractured ice lee- side of the Eklund Islands, and 2) a largely consolidated region of ice towards Monteverdi Peninsula. This area of consolidated ice advances into Ronne Entrance at ~350 ma^{-1} and is the major contributor to ice advance at the southern ice front. This area is characterised by a large rift that cuts back transversely into the ice-shelf towards Alexander Island. The rift increased in width and length over time since its formation in ca. 1986, and is likely to form the dimensions for large-scale iceberg calving in the future. Interestingly, the positioning and dimensions of this rift create an area at the ice-front that is similar to the large calving event captured in 1973 Landsat MSS imagery (Figure 7.35), thus suggesting an approximate 40-year cyclical advance/calving regime in this region (assuming imminent calving).

The initial rifting occurred in pre-fractured ice as a result of ice-shelf motion over IR2 and consequent flow towards the south margin; fractures initially sealed, but reopened further down ice creating favourable conditions for rift propagation along pre-conditioned structural weaknesses. Visual analysis of 2010 Landsat ETM+ imagery reveals similar 're-fracturing' at -1771500 583500 m and may represent the next stage of ice-shelf rifting and eventual iceberg calving at the south ice front. This is discussed in more detail in Section 7.2.2.3. This portion of South Ice Front 1 is driven by ice flowing from both Palmer Land, up to 160 km upstream, and the adjacent Monteverdi Peninsula. Overtime, the pinning point of the south ice front along Alexander Island retreats only 4.8 km, thus illustrating greater stability of ice outside of the ice rise and ice rumple fracturing zone.

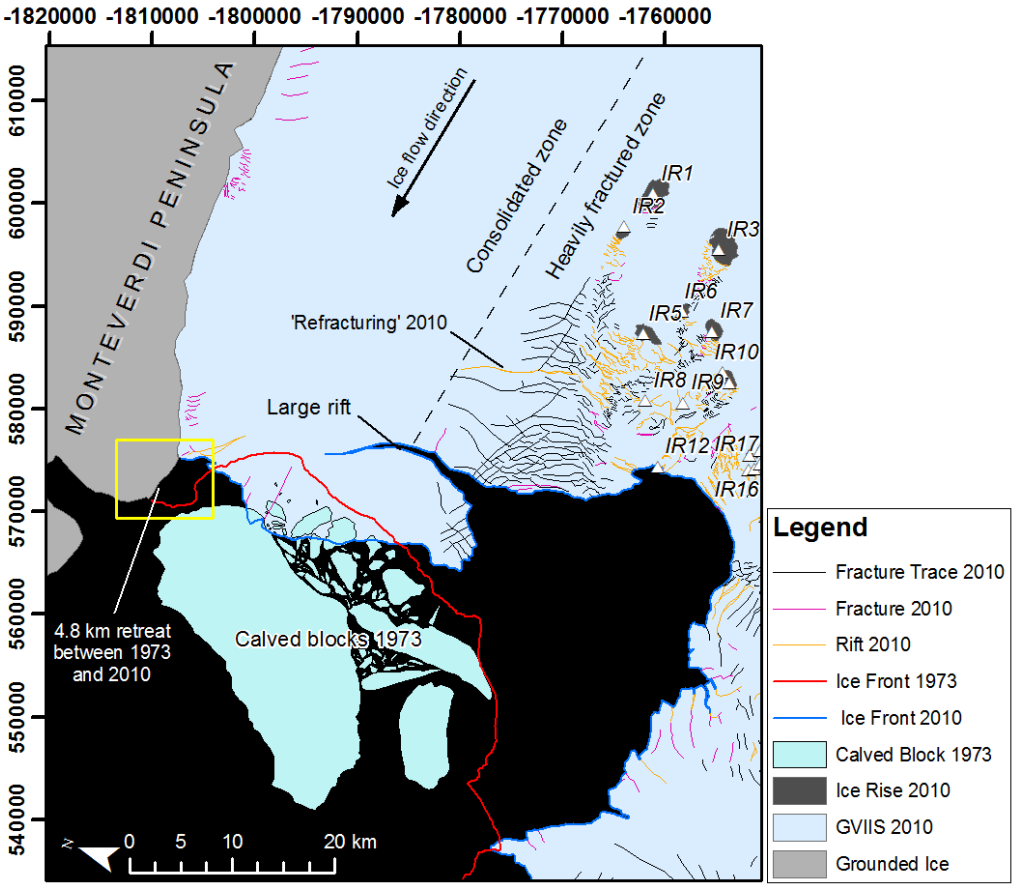

Figure 7.35. The two distinct zones between Monteverdi Peninsula and the Eklund Island ice rises. Towards Monteverdi Peninsula, a largely consolidated region of ice exists, whereas the presence of the ice rises causes fracturing of the ice shelf towards the ice front. Occasionally, a large fracture or rift extends and propagates into the consolidated zone making ideal conditions for large iceberg calving as observed in 1973. Note the similar location and shape of the current ice front and the icebergs from 1973 calving events.

South Ice Front 2 stretches from the Eklund Islands to De Atley Island and is fed by ice flowing entirely from Palmer Land tributary glaciers GT04b to GT07 inclusive. The ice front during January 2010 is generally convex-shaped, with several areas jutting out into Ronne Entrance (most notably at -1770000 53500 m Figure 7.36), and thus it should be considered stable in its current geometry (Doake *et al.*, 1998). Fracturing occurs along the ice front both longitudinally and transversely. Preferential, longitudinal fracturing and rifting back upstream along flow-unit boundaries provides a visual representation of ice-shelf heterogeneity, with weaknesses exploited between different flow units at the ice front. Transverse fractures are likely to be formed as a result of tidal flexure (Larour *et al.*, 2004) and re-fracturing of ice along pre-existing weaknesses as they reach the ice front. Fracturing and rifting in ice feeding South Ice Front 2 are discussed in more detail in

Section 7.2.2.3. The western pinning point of South Ice Front 2, along De Atley Island also underwent little retreat between 1973 and 2010 despite the amount of ice loss observed in the southern region; the proximity of IR28 to the ice front and De Atley Island may provide additional pinning-point stability in this region (Figure 7.36) (Hughes, 1983; Humbert, 2007; Jansen *et al.*, 2011).

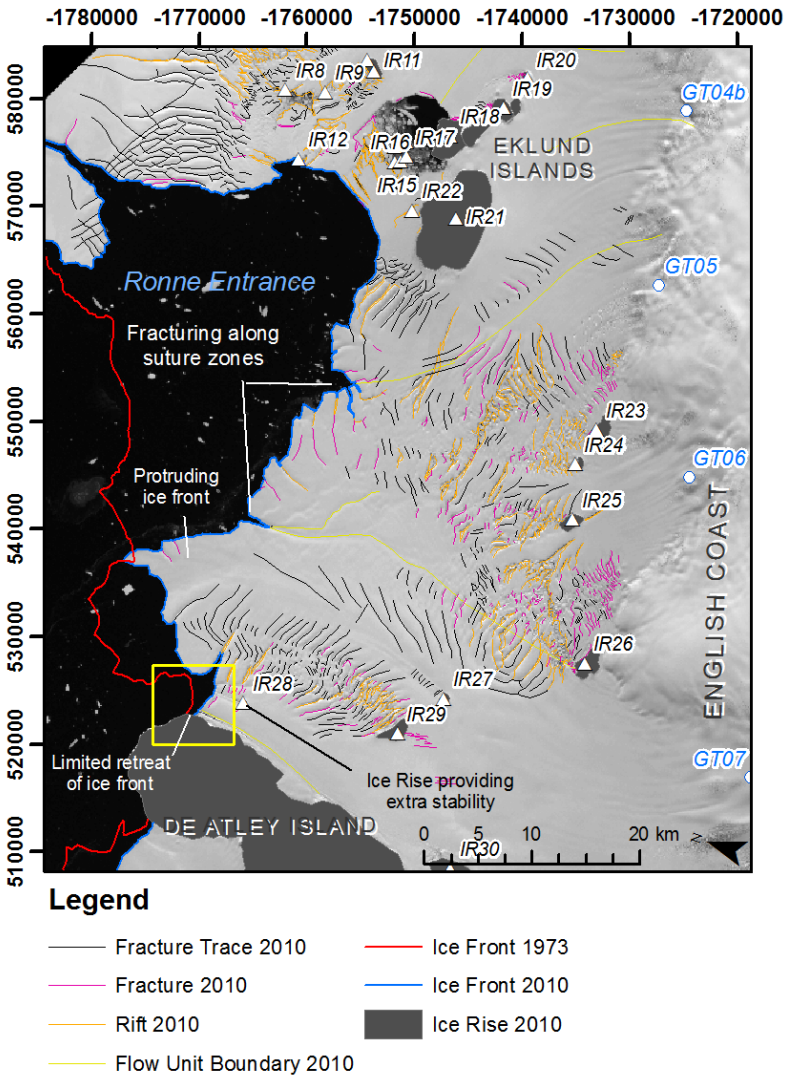

Figure 7.36. Structural glaciological map superimposed on Landsat ETM+ image from January 2010 between the Eklund Islands and De Atley Island. Note the general convex profile of the ice front and protruding sections. Little retreat is recorded along De Atley Island due to the presence of IR28 acting as a stabilising pinning point. Fracturing along the ice front occurs longitudinally along suture zones/ flow unit boundaries, that illustrates the weaknesses inherent in these structures. Transverse fracturing at the ice front is also apparent and is discussed further in Section 7.2.2.3.

South Ice Front 3 has been separate from the main southern ice front of George VI Ice Shelf between 1973 and 2011. Its ice front is fed by GT08 flowing off the main Antarctic Peninsula, and a smaller unit, GT09, flowing out of Spatz Island. This portion of the southern region of George VI Ice Shelf is confined to a narrow channel, approximately 16 km in length. Its original frontal profile generally protruded out beyond its pinning points at De Atley Island and Spatz Island, but became increasingly concave towards its western margin through regular calving events (Figure 7.37). As of January 2010, most of the retreat at South Ice Front 3 was concentrated towards Spatz Island; analysis of the RAMP DEM suggests lower surface elevations in the region where enhanced retreat has been recorded. It is thus inferred that this ice is thinner, and thus more susceptible to retreat than thicker ice to the east (Figure 7.37).

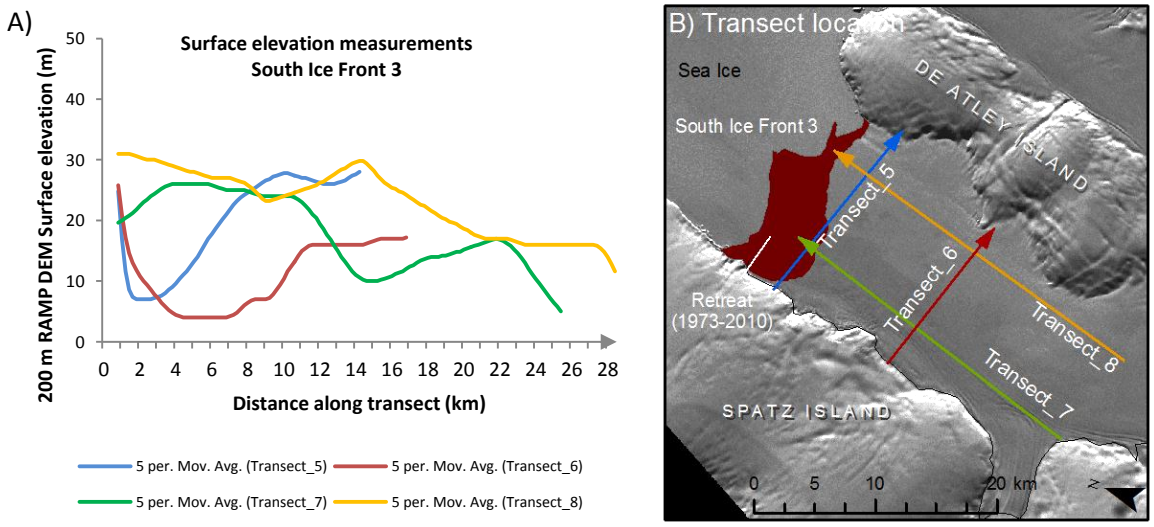

Figure 7.37. RAMP DEM surface elevation transects across channel (Transect_5, Transect_6), and along channel (Transect_7, Transect_8) illustrating lower surface elevations in area of increased ice-front concavity, from which thinner ice is inferred. B) Location of transects superimposed over 1986 Landsat TM imagery. Transect direction indicated by arrow on transect and X-axis in A.

7.2.2 Interpretation of surface structures, surface features and their significance for ice-shelf configuration and dynamics

7.2.2.1 Northern section

Longitudinal surface structures and pressure ridges are the most dominant and widespread flow-related features within the northern extent of George VI Ice Shelf. Each of these has previously been discussed in Section 6.2 for Bach Ice Shelf, and are considered here in terms of their inference on the dynamics and configuration of George VI Ice Shelf. It has

already been stated that the formation of longitudinal surface structures is not well understood, yet their resemblance to foliation structures on temperate valley glaciers suggests that they form due to visco-plastic deformation; initially ice is compressed transversely, before being stretched longitudinally downstream (Hambrey, 1977). They may also form where ice rapidly flows over bedrock perturbations that deform the ice through its vertical column (Gudmundsson *et al.*, 1998).

Longitudinal surface structures are principally formed in ice flowing from Palmer Land at 1) the confluence of grounded-ice tributary glaciers, 2) at the confluence of ice-shelf tributary systems and 3) within the main channel of flow in grounded-ice tributary glaciers; Type 1 and Type 3 are transmitted across the grounding line into the ice shelf where they can be traced for up to 50 km. Type 2 longitudinal features are more distinct and represent the boundary and shear zone between two ice-shelf units. The orientation of longitudinal surface structures is inextricably linked to the regionalised flow direction of ice-shelf units, with their distribution and extent highlighted by the presence of surface meltwater during the austral summer. On Alexander Island, longitudinal features are observed in grounded ice tributary glaciers, but only occasionally flow into the ice shelf due to the dominance of Palmer Land flow units on the overall dynamics.

Longitudinal structures associated with Ryder, Millet and Chapman Glaciers initially splay laterally as they cross the grounding zone into the ice shelf, whereas longitudinal features associated with other tributary glaciers appear to resist lateral spreading, and maintain regular transverse spacing along their flow units, down-ice. The three aforementioned glaciers that undergo lateral spreading near the grounding zone are dominant tributary glaciers in their respective locations and supply a significant amount of ice into otherwise less-active regions of George VI Ice Shelf and are thus not initially constrained to a distinct channel. Chaotic fracture patterns at the entrance of Ryder, Millet and Chapman Glaciers that cross cut one another illustrate the biaxial tensile stresses caused by splaying tributary glaciers, often associated with longitudinal and transverse extension. Open crevasses can no longer be observed where active lateral splaying ceases; these areas are thus proposed to be affected by longitudinal and transverse compressive stresses as a result of reducing ice speeds as they enter the main channel of George VI Sound (Figure 7.38); fracture traces and water-filled fracture traces give the surface a pock-marked appearance which elsewhere indicates fracture healing down ice (e.g. Glasser and Scambos, 2008).

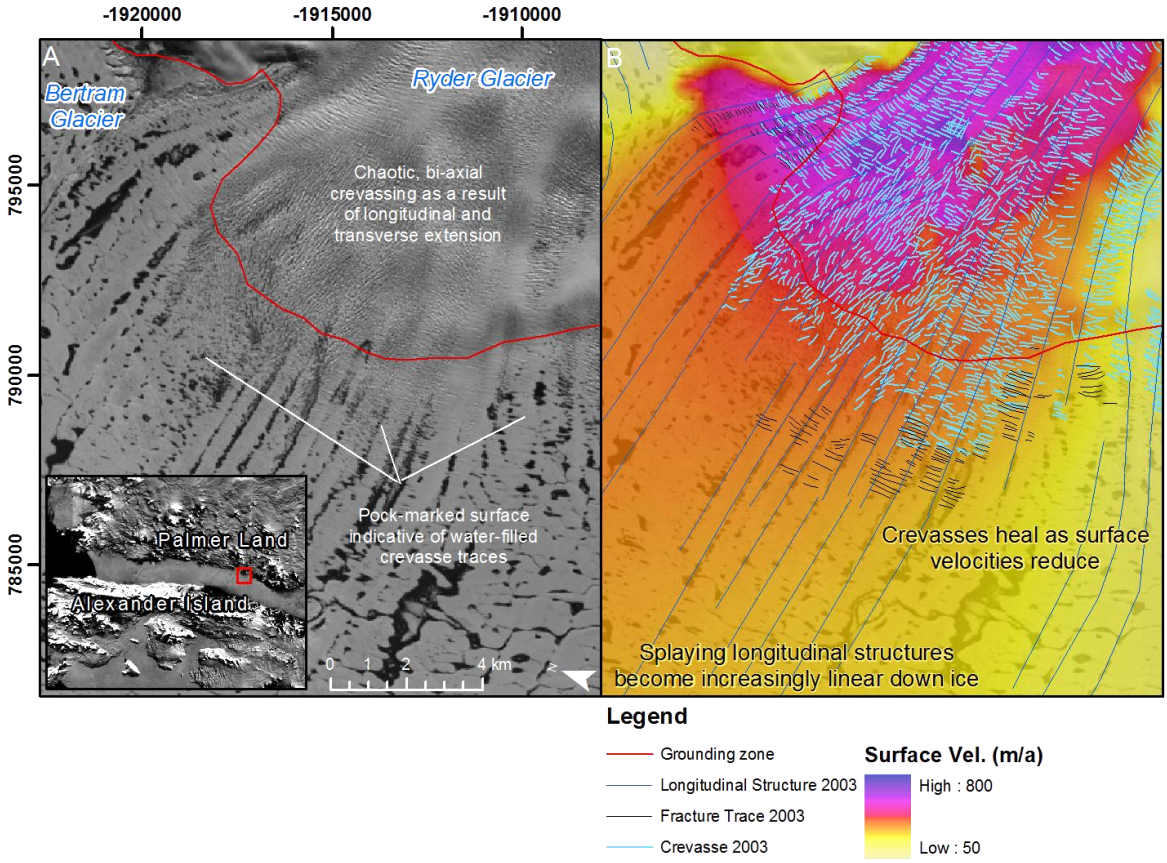

Figure 7.38. Chaotic crevassing observed behind the grounding line of Ryder Glacier soon heals as surface velocities reduce, caused by compressive stresses in the ice as it flows into the confined channel of George VI Sound. Open fractures are observed in areas where lateral spreading of longitudinal structures is apparent, and as these longitudinal features becoming increasing linear down ice, fractures heal. Often, fracture traces exhibit pock-marked surface characteristics as summer meltwater preferentially fills the surface undulations of the fracture traces.

In terms of the longitudinal structures, their ability to be traced down-ice even in areas of reducing surface velocities poses a problem for the visco-plastic deformation hypothesis that requires a down-ice extension in order to elongate the original lateral compression (Hambrey, 1977; Hambrey and Dowdeswell, 1994). However, within the northern section of George VI Ice Shelf, few longitudinal structures are formed at or near the grounding line, but are instead formed at the confluence of grounded tributary glacier systems and transmitted across the grounding line from further upstream, or in the main channel of fast-ice flow. Those forming at flow-unit boundaries are much more clearly defined across the ice shelf and can be traced back to their point of formation, whereas those transmitted across the grounding line are in general, only visible due to preferential filling of surface undulations by meltwater in the austral summer. It is thus proposed that, despite longitudinal compression when entering the ice-shelf system (Figure 7.38), the form of existing longitudinal structures is conveyed down-ice off Palmer Land towards Alexander

Island. It is therefore apparent that the longevity of longitudinal structures down-ice is governed by something other than, or in addition to, being situated in regions of 'active' or 'fast-flowing' ice (Campbell *et al.,* 2008). Furthermore, their disappearance down-ice in certain situations is thus governed by something other than being situated in regions of 'less active' or 'slow-flowing' ice and may be linked to localised surface accumulation or ablation (Glasser and Gudmundsson, 2012).

Pressure-ridge formation along the western grounding zone has elsewhere been linked to the direct flow of ice across George VI Sound, compressing glacier ice and surface pond-ice (refrozen, surface-meltwater) against the cliffs of Alexander Island (e.g. Reynolds and Hambrey, 1988; Reynolds *pers. comm*. 2012). Ice flowing from Palmer Land glaciers impinges upon the resistant Alexander Island bedrock causing a buckling-effect of the ice shelf that results in the formation of linearly arranged ice-shelf hummocks (see also Smith *et al.,* 2007, Cook and Vaughan, 2010; termed pressure rollers). During the austral summer, the troughs associated with pressure ridges fill with meltwater and create linear or pear-shaped lakes on the ice-shelf surface that are governed by the east-to-west flow dynamics of the ice shelf (Reynolds and Hambrey, 1988; MacAyeal, 2011, *pers. comm;* LaBarbara and MacAyeal, 2011).

Pressure ridges also form where ice flowing from Palmer Land meets Alexander Island derived ice, flowing in the opposite direction. The flow unit boundaries can be clearly defined as a series of surface deformations, particularly at the confluence of Venus, Uranus, Eros, Jupiter, Grotto (Figure 7.39) and Eris Glaciers with the main ice-shelf channel. Flow from Alexander Island tributary glaciers is diverted from an easterly flow, to a northerly flow direction, indicated by the associated arc of pressure ridges at their respective confluences. It is proposed that high compressive stresses in the ice at the point of confluence cause initial transverse deformation (similar to the buckling seen along the grounding line), with shear stresses subsequently straining the pressure ridges down-ice in a northerly direction along the confluence zone of two flow units.

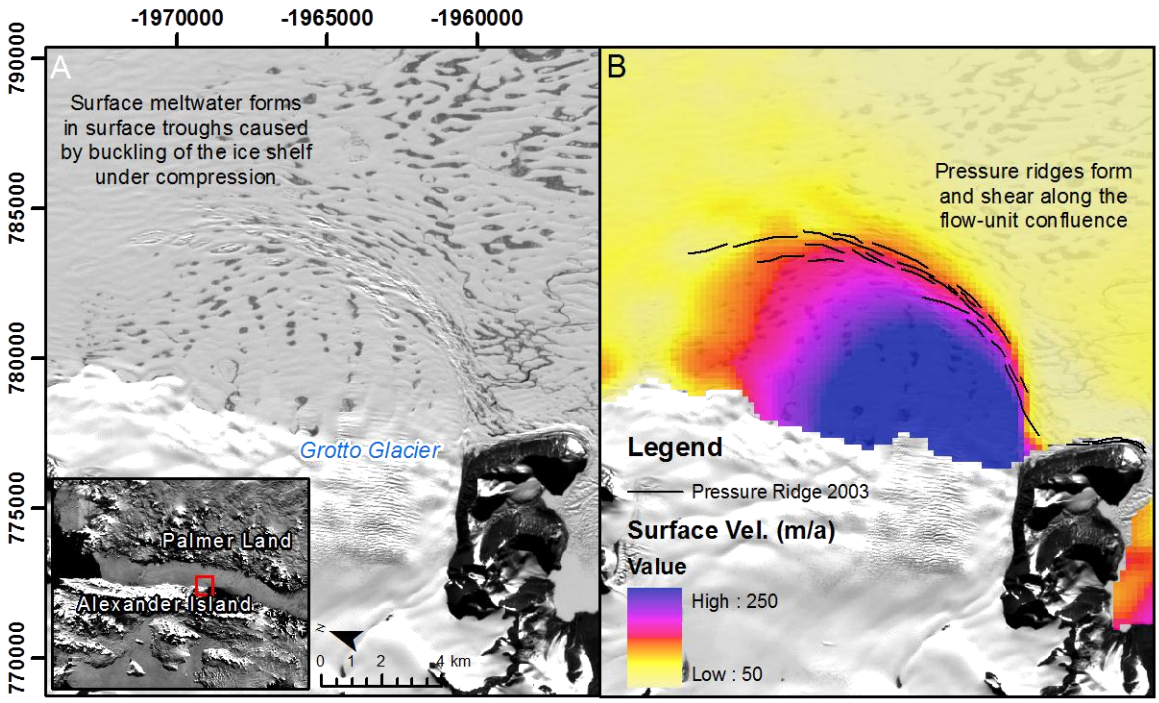

Figure 7.39. Pressure ridges forming at the confluence of Grotto Glacier from Alexander Island with the main flow channel of George VI Ice Shelf. Despite the much faster velocities of Grotto Glacier compared to the surrounding ice, flow is unable to penetrate greater than 6km into the ice shelf before it is deflected to a northward flow. Pressure ridges become increasingly deformed along the shear zone down ice with the general flow pattern of George VI Ice Shelf.

The almost unbroken distribution of pressure ridges along the Alexander Island grounding zone and glacier confluences clearly illustrates the highly compressive flow regime in the northern section of George VI Ice Shelf. Consequently, fracture propagation is largely prevented and limited to three distinct zones; 1) on the surface of tributary glaciers flowing from Palmer Land into the ice shelf, 2) the onset zone of glacier confluence in the shadows of headlands and peninsulas, and 3) at the northern ice front. Fracturing in each of these zones has previously been discussed in Section 7.1.

The significance of fracture limitation is emphasised by the presence of abundant surface meltwater from mid-December through to early-March. Elsewhere on the Antarctic Peninsula, ice-shelf surface fractures have provided a drainage route for surface meltwater and been considered as controlling factors in final ice-shelf breakup (Scambos *et al.*, 2000; 2003; 2004), yet on George VI Ice Shelf, the interaction of surface meltwater with ice-shelf fractures is limited to distinct regions near the Palmer Land grounding zone and at the entrance of Grotto Glacier on Alexander Island, where surface meltwater preferentially fills surface undulations of fracture traces. Thus, drainage of surface meltwater through the

ice shelf is considered largely absent and gives reason to the widespread distribution and extent of surface melt-pools and melt-ponds throughout the melt season.

Meltwater forms in a particularly distinct area with abrupt northern and southern limits, with roughly 1420 km^2 of meltwater occupying a 5900 km^2 ice-shelf area each year. The northern meltwater limit gradually extended northwards from 1973 to 2010, but no pattern of southward expansion was observed at the southern limit. It is therefore proposed that the extension of the northern limit is perhaps a response to increased atmospheric temperatures observed in the region (King, 1994; Morris and Vaughan, 2003), whilst the fluctuating pattern of the southern limit may be explained by the following reasons;

1) The fluctuation represents the differences in image-acquisition dates between the corresponding years used in this study, rather than changes in meltwater distribution.
2) The gradient of the ice-shelf surface elevation at its southern extent encourages drainage of surface meltwater down-ice, and therefore spatial fluctuations in the southern limit may represent changing meltwater drainage routes on the ice-shelf surface, enhanced by localised topographical characteristics.
3) Surface meltwater extent represents inter-annual changes in surface-air temperatures rather than long-term climatic trends.
4) Ice-shelf surface melting is controlled by other factors rather than regional climate and weather patterns.

Dates for image acquisitions from which the southern meltwater limit was obtained are displayed in Table 7.12, along with a numerical identifier for the most southern meltwater limit along the centre line of the ice shelf. There is no correlation between acquisition date (Julian date of corresponding year), and the most-southern meltwater limit, and acquisition date seemingly has no inferences on the expansion of the northward limit either. Thus option (1) can be regarded as an unsatisfactory explanation.

Table 7.12. Timing of maximum southern meltwater extent. Rank of southern extent (1 = most extensive meltwater cover, 4 = least extensive cover)

Rank of southern meltwater extent	Image date	Julian date
1	12 January 2003	12
2	4 February 1991	35
3	9 January 1973	9
4	15 January 2010	15

Both ICESat GLAS elevation measurements and the RAMP DEM do illustrate a slight negative gradient of the ice-shelf surface from Goodenough Glacier to Alexander Island, and thus may define the regional positioning of the southern meltwater limit. Furthermore, ICESat GLAS repeat-track measurements illustrate a significant surface lowering between Alexander Island and the centre line of this central zone, but conversely illustrate an increase in surface elevations at the influx of Goodenough Glacier. Consequently, between 2003 and 2008, the surface gradient would have become increasingly steep, thus creating a localised environment for preferential downslope meltwater drainage. However, there are no clear visual changes to the distribution of flow channels or drainage routes between January 2003 and January 2010. It is not possible using the datasets in this study to verify or refute options 3) and 4), thus these options are discussed in more detail in Chapter 9.

The preferential filling of surface undulations creates a complex meltwater network on George VI Ice Shelf consisting of: 1) across-shelf primary meltwater pools linked to longitudinal structures: 2) transverse (along-shelf) pools: and 3) individual melt-ponds distributed across the whole meltwater area. The pattern of surface meltwater can be further divided into three spatial zones that are seemingly controlled by the dynamic regimes of George VI Ice Shelf (Figure 7.40). Zone 1 largely exhibits a mixture of meltwater features both limited to distinct surface undulations and those seemingly less confined, that pool with no alignment. Zone 1 also contains a high number of ice dolines that persuade meltwater into a 'bull's-eye' appearance around their central cavity. The ice shelf in this zone are largely slow moving, with distinct flow structures (longitudinal, transverse) only observed along the grounding zones where tributary glaciers enter the shelf.

Zone 2 is mostly covered with narrow, transverse meltwater pools running from south to north, with wider, longitudinal meltwater pools (often non-continuous) interlinking and thus draining into the transverse pools; where they cross, ponding is often observed. Flow in this region is dominated by the input of Ryder Glacier that stretches across George VI

Sound forming both longitudinal structures as described above (Section 7.2.2.1) and transverse compressional structures as discussed below. In Zone 3, both longitudinal and transverse meltwater pools display greater dimensions, increased complexity and irregularity than those observed further downstream in Zone 1 and Zone 2. Interestingly, the larger meltwater pools in Zone 3 are situated in a region of faster-flowing ice (Figure 7.40), where longitudinal structures should, in theory, be more prominent (e.g. Campbell *et al.*, 2008).

From the configuration and distribution of surface meltwater it is thus possible to infer the surface structure and stress regimes of George VI Ice Shelf. Transverse meltwater pools tend to be narrower than longitudinal pools, and also interlink more readily along the ice shelf; longitudinal pools are often non-continuous, and in some regions are depicted only as a series of linearly arranged melt-ponds running from Palmer Land to Alexander Island. Furthermore, the distance between transverse meltwater pools is less than the spacing between longitudinal pools. Consequently, it is inferred that transverse structures on the ice shelf tend to have a shorter wavelength but greater amplitude than longitudinal structures. Meltwater thus preferentially fills the deeper undulations of transverse structures (Figure 7.41), whilst having a greater surface area in longitudinal depressions.

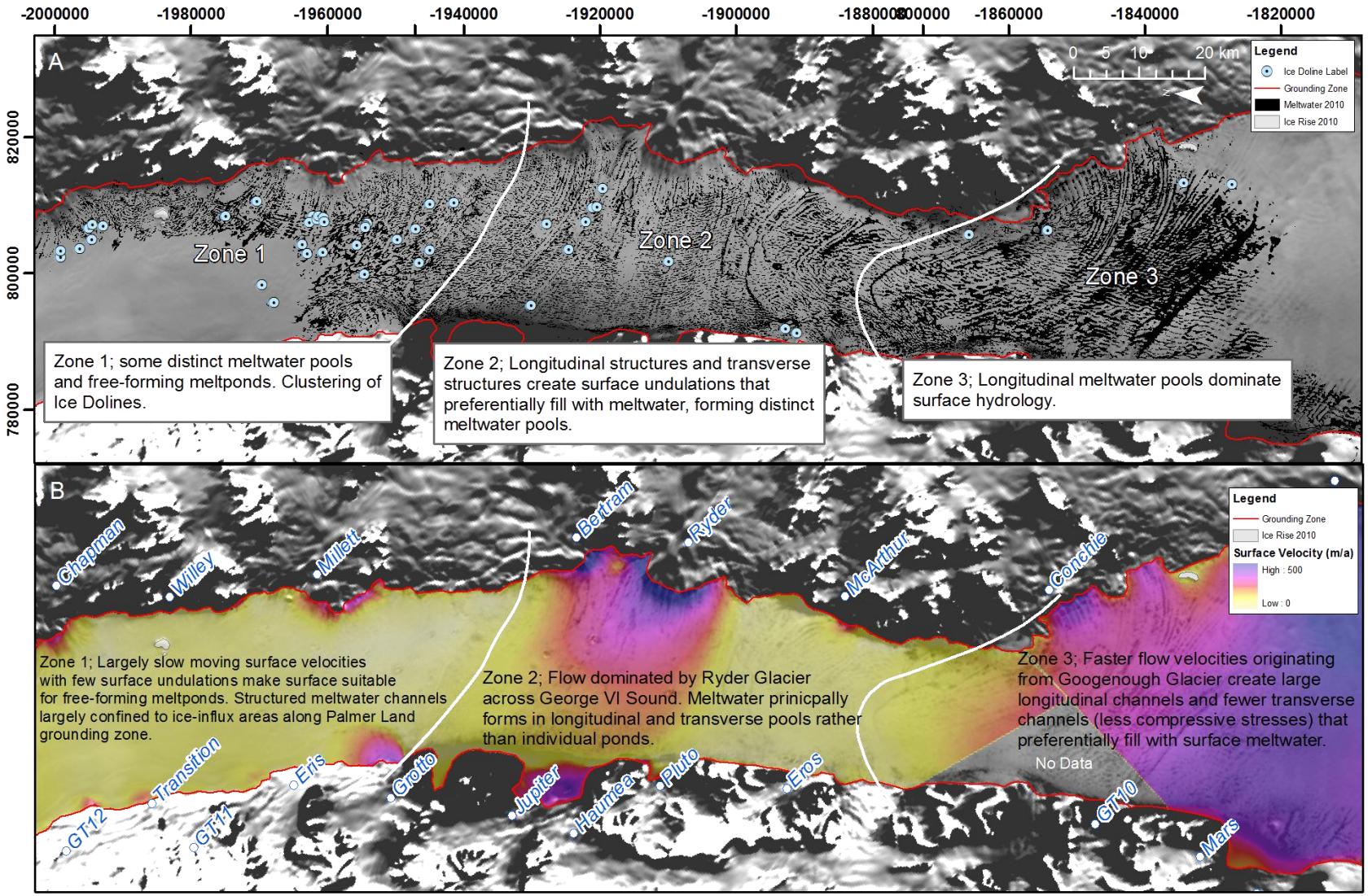

Figure 7.40. A) Surface meltwater patterns and their association with surface velocities (B) and consequent surface structures. See annotated sections for further information.

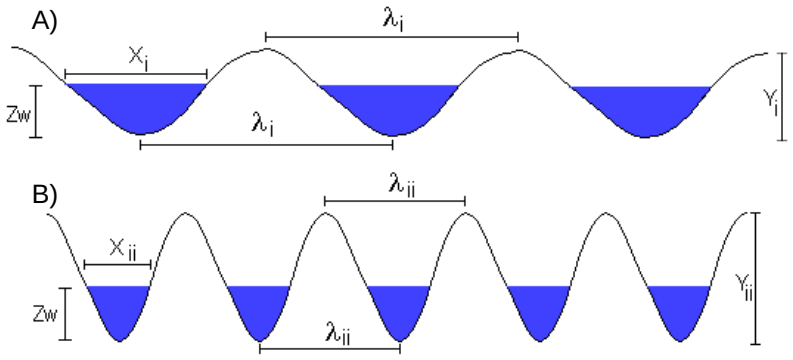

Figure 7.41. Theoretical **s**chematic of inferred longitudinal (A) and transverse (B) structure morphology where Z_w is the meltwater height and is equal in both (A) and (B), $X_i > X_{ii}$, and denotes meltwater surface cross-sectional distance, $\lambda_i > \lambda_{ii}$, and denotes structure wavelength and $Y_i < Y_{ii}$, and denotes structure amplitude. When viewed from above, transverse meltwater appears in narrower channels, more regularly across the ice shelf than their longitudinal counterparts.

By analysing this relationship over George VI Ice Shelf (Figure 7.42), it is inferred that longitudinal features are the primary, older structures, whereas the transverse features are the younger, secondary structures. Melt-ponding along longitudinal features occurs where the trough of a transverse feature cross-cuts that of a longitudinal structure; meltwater accumulates here until the water height reaches the minimum trough height of the interlinking, downstream channel (longitudinal or transverse), and consequently drains from the melt-pond. The formation of longitudinal (across-shelf) and transverse (along-shelf) meltwater pools is proposed to be a result of the following sequence:

1) Grounded tributary glaciers are constrained by topography and consequently undergo lateral compression through glacial valleys.
2) Increasing glacier velocities down-ice result in longitudinal extension, forming parallel ridges and grooves (longitudinal structures).
3) Upon reaching the grounding zone, these features (or at least their surface expression) are carried into the ice-shelf system. Occasionally, these features splay laterally, but are generally confined to linear channels.
4) The narrow channel of George VI Sound forces tributary glaciers to quickly reduce in speed, thus compressional stress regimes dominate at or near to the grounding zone. 'Buckling' occurs within the ice-shelf and creates transverse-to-flow surface undulations.
5) Where surface undulations of both longitudinal and transverse structures interact, localised, enhanced surface humps and depressions are created.

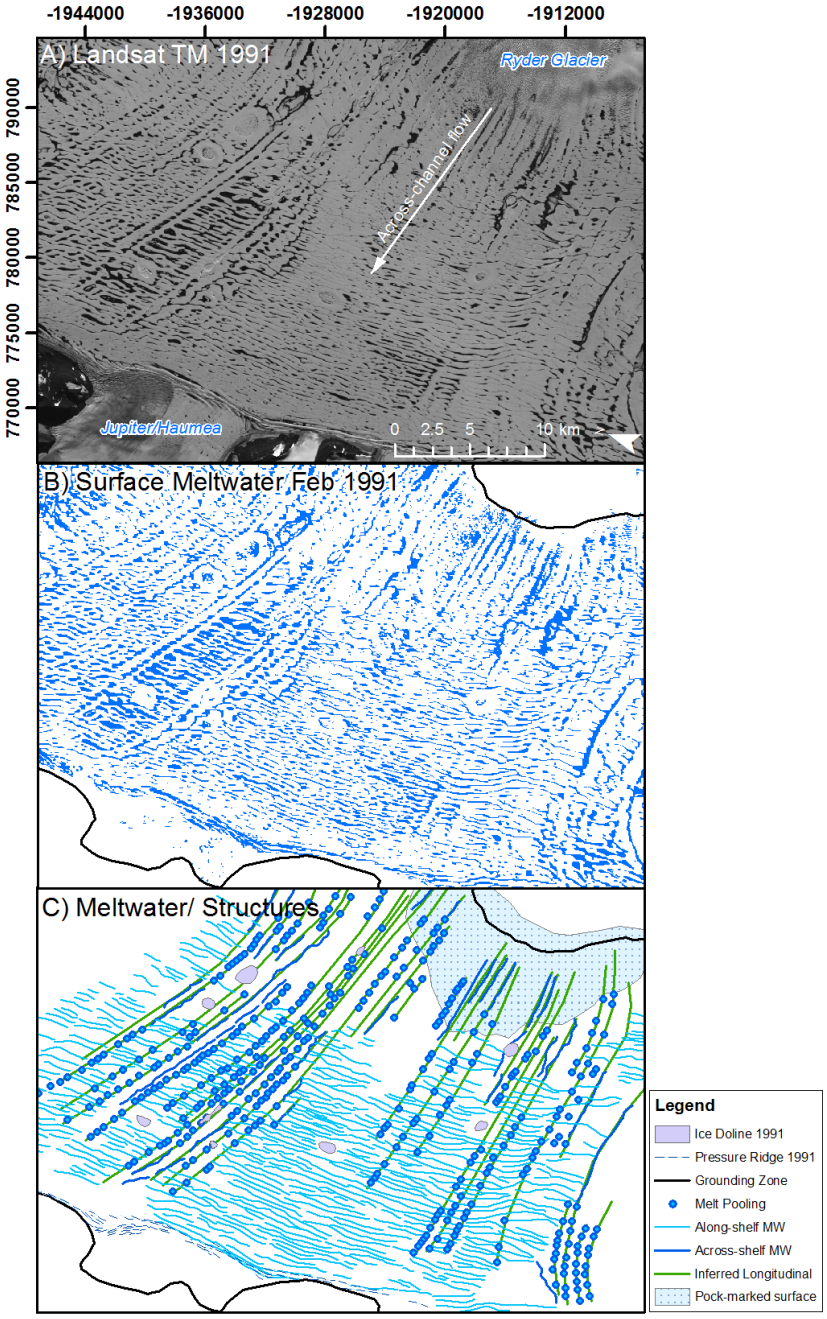

Figure 7.42. A) Landsat TM image of George VI Ice Shelf, 4th February 1991, in its northern section, and classification of surface meltwater (B). C) Whilst more prominent in the satellite imagery, longitudinal channels (across-shelf MW (meltwater)) are typically identified as successions of melt-pools. The melt-pooling is associated with longitudinal structures that flow off Ryder Glacier across the shelf, in this instance, to Jupiter/ Haumea Glaciers. The along-shelf, transverse meltwater pools are less distinct but more regular across the ice shelf, often forming interlinking and well-structured meltwater pools. Melt-ponding is observed where along-shelf and across-shelf meltwater pools join.

Assuming that the pattern of transverse meltwater channels approximates the distribution and extent of transverse features, it is inferred that the majority of the northern section of George VI Ice Shelf exhibits high longitudinal compressive stresses that resultantly limits the surface draining of meltwater from George VI Ice Shelf to distinct ice dolines that form

where surface meltwater interacts with weaker ice (pre-fractured or shear zones, for example).

7.2.2.2 Central section

The central section of George VI Ice Shelf is largely absent of widespread surface features, and indeed there are no significant changes observed to the structural composition between 1973 and 2010. Longitudinal structures are observed across the channel from Palmer Land to Alexander Island; they originate in similar situations as described above, but also form at, or near to, the grounding zone where ice-shelf velocities initially increase as ice transmits into George VI Sound. Within the wider channel of George VI Ice Shelf, longitudinal features can be followed for up to 50 km, generally maintaining their transverse spacing down-ice and thus illustrating the transverse compressional regime of the ice shelf. Additionally, the few surface fractures that transmit across the grounding line at the entrance of Goodenough Glacier are promptly sealed within a distance of 5 km and thus illustrate a further longitudinal compression as discussed for the northern region. Elsewhere along the steep-sided slopes of Palmer Land and in other tributary systems (GT01, GT02) surface fractures do not cross the grounding line into the ice-shelf system, yet longitudinal structures are maintained.

The links between longitudinal structures and ice-shelf flow orientation have already been made; here they provide further evidence of across-ice shelf flow, as observed in the northern section. Figure 7.43 illustrates the subtle changes in their orientation in the central section, which is used to identify the flow divergence zone between ice that flows towards the northern section of George VI Ice Shelf, and that which flows towards the south.

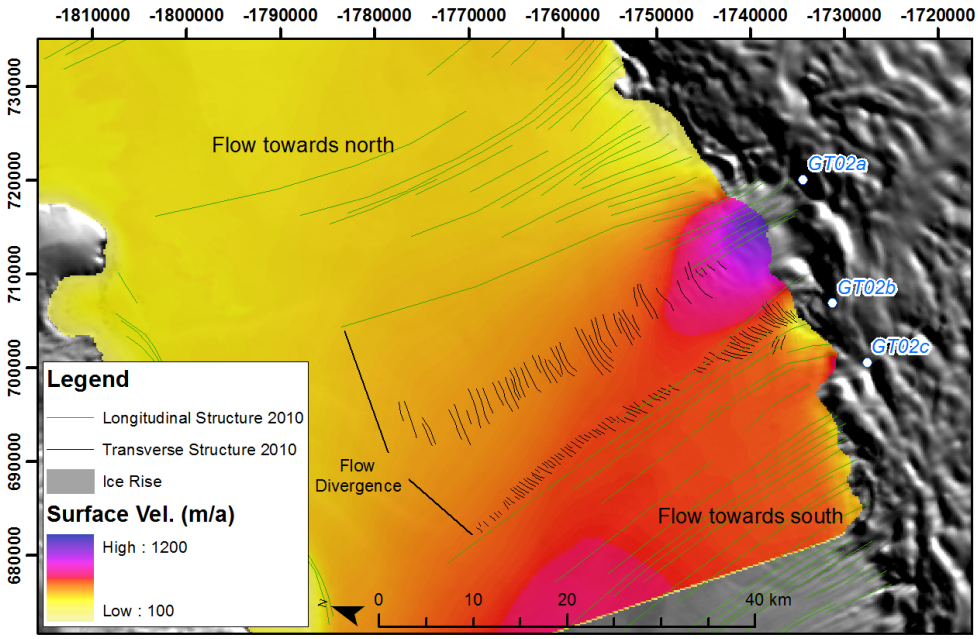

Figure 7.43. Flow divergence at the input of GT02a, GT02b and GT02c inferred through structural analysis of longitudinal features and flow dynamics. Transverse structures also highlighted originating in areas of reducing flow-velocities from GT02. Their regularity and linearity down ice suggests a steady flow history in the central section of George VI Ice Shelf, and suggest that this region is also under high compressive longitudinal stresses.

Transverse features emanating from the grounding zone of the GT02 tributary systems can be traced almost regularly (approximately every 600 m) down-ice for up to 44 km (Figure 7.43). These features remain almost linear down ice, and are thus used to illustrate 1) the prevailing across-channel flow of George VI Ice Shelf, 2) the stability of current and historical flow direction and 3) the stability of current and historical flow velocity in this region. Indeed, assuming that flow velocities have not altered overtime, it is inferred that the dynamic configuration in the central region has remained stable for at least the last 74 years (approx.), based on an across-shelf average velocity of 600 ma^{-1} obtained from InSAR velocity measurements. These transverse structures closely resemble transverse pressure ridges created by rapidly reducing flow velocities and consequent 'buckling' of the ice-shelf surface (Figure 7.44), and indeed InSAR reveals reducing velocities where the pressure ridges form.

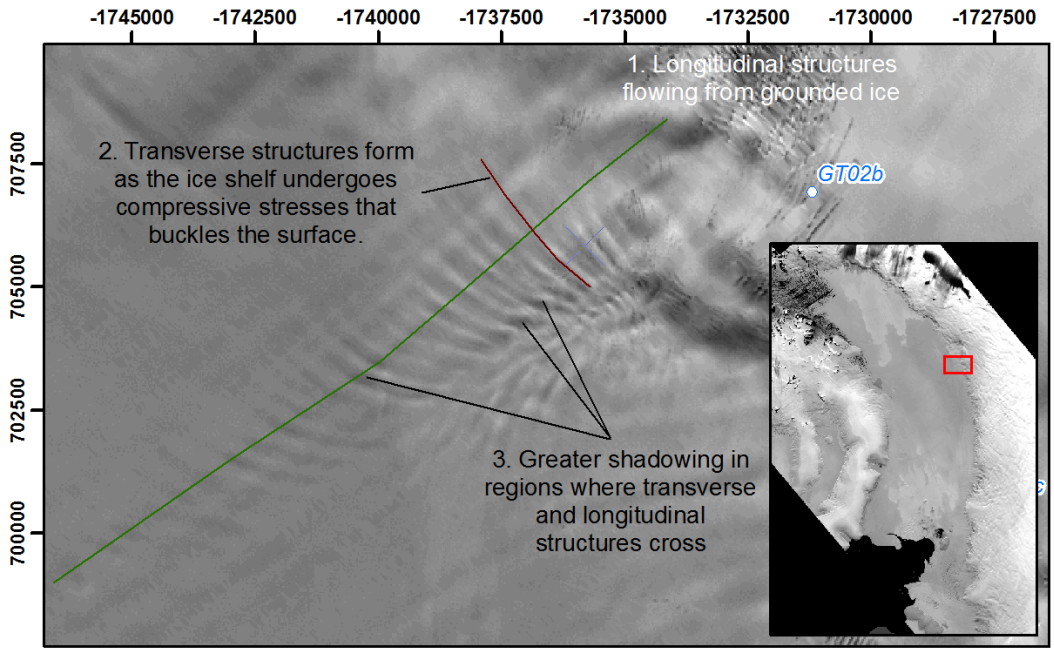

Figure 7.44. Interaction of primary longitudinal structures with secondary transverse structures illustrating the initial longitudinal extension and consequent longitudinal compression as ice from GT02 enters the ice shelf and reduces in velocity (see Figure 7.44). Where the two structures cross-cut, greater surface shadowing is inferred to illustrate greater surface undulations at the point of interaction, and also illustrates the same mechanism that creates an environment suitable to meltwater-pooling in the northern regions of George VI Ice Shelf.

The interaction of longitudinal structures and transverse structures in this zone is also clearly evident. Longitudinal structures flowing off Palmer Land are carried over the grounding line; ice is therefore compressed longitudinally creating transverse buckles. Where surface troughs associated with both longitudinal and transverse structures link, greater surface depressions are inferred, observed as larger, darker areas caused by shadowing on the surface. These features neatly illustrate the same formational processes linked to the complex meltwater network in the northern section of George VI Ice Shelf.

7.2.2.3 Southern section

Structurally, the southern extent of George VI Ice Shelf is complex; significant changes were observed between 1973 and 2010. The principal cause of this structural complexity is the existence and distribution of the ice rises and ice rumples towards the south ice front and along the English Coast grounding zone. In total, 34 individual ice rises, including ice rumples, have been identified within the southern extent of George VI Ice Shelf.

Heavily crevassed ice associated with GT03 enters the shelf at speeds of over 800 ma^{-1}. Whilst most surface fractures heal within 6 km of entering the ice shelf, and appear as faint fracture traces, a few fracture-remnants remain open and can be traced for up to 24 km down ice from the grounding zone; these, however, are rare occurrences (Figure 7.45, point 1). At approximately 13 km from the grounding zone, distinct transverse-to-flow pressure ridges exist, stretching up to 16 km in length across the GT03 flow unit. These pressure ridges are indicative of compressional stresses in the longitudinal flow direction, and initiate in a region where flow velocities rapidly reduce from ~425 ma^{-1} to ~350 ma^{-1} over a distance of only ~1.5 km. The surface appearance of these pressure ridges is transmitted down ice with flow and become increasingly convex (when viewed from above), linking well with observed faster flow velocities in the centre of the flow unit (Figure 7.45, point 2). A succession of these pressure ridges can be traced from their origin down ice, with the most distinct sets of undulations observed roughly every 2 km in the longitudinal direction, with only faint pressure ridges observed between them. From this structural configuration it is inferred that the pressure ridges are formed as a result of longitudinal compression as ice flow velocities rapidly reduce due to the influence of the Eklund Islands further down ice. It is also inferred that the regular formation of larger sets of pressure ridges is perhaps linked to cyclical changes in the glaciological stress regime within the ice; these distinct sets of pressure ridges form approximately every 2 km, thus equating to a temporal range of between four and five years, using a typical surface velocity for this region of ~400 ma^{-1}. This formation may be as a result of a gradual, multi-annual build-up and release of internal glaciological stresses, perhaps linked with intermittent velocity fluctuations specifically within GT03.

On the upstream side of IR3, regular pressure ridges develop as ice is compressed directly against this obstacle (Figure 7.45, point 3). Velocity measurements illustrate the influence of the Eklund Islands on the dynamics at the southern ice front, with a large velocity gradient observed both longitudinally down ice and transversely across the ice shelf from Palmer Land to Alexander Island; the Eklund Islands essentially act as a buttress to ice flow, and influence upstream and downstream velocities well beyond their absolute location.

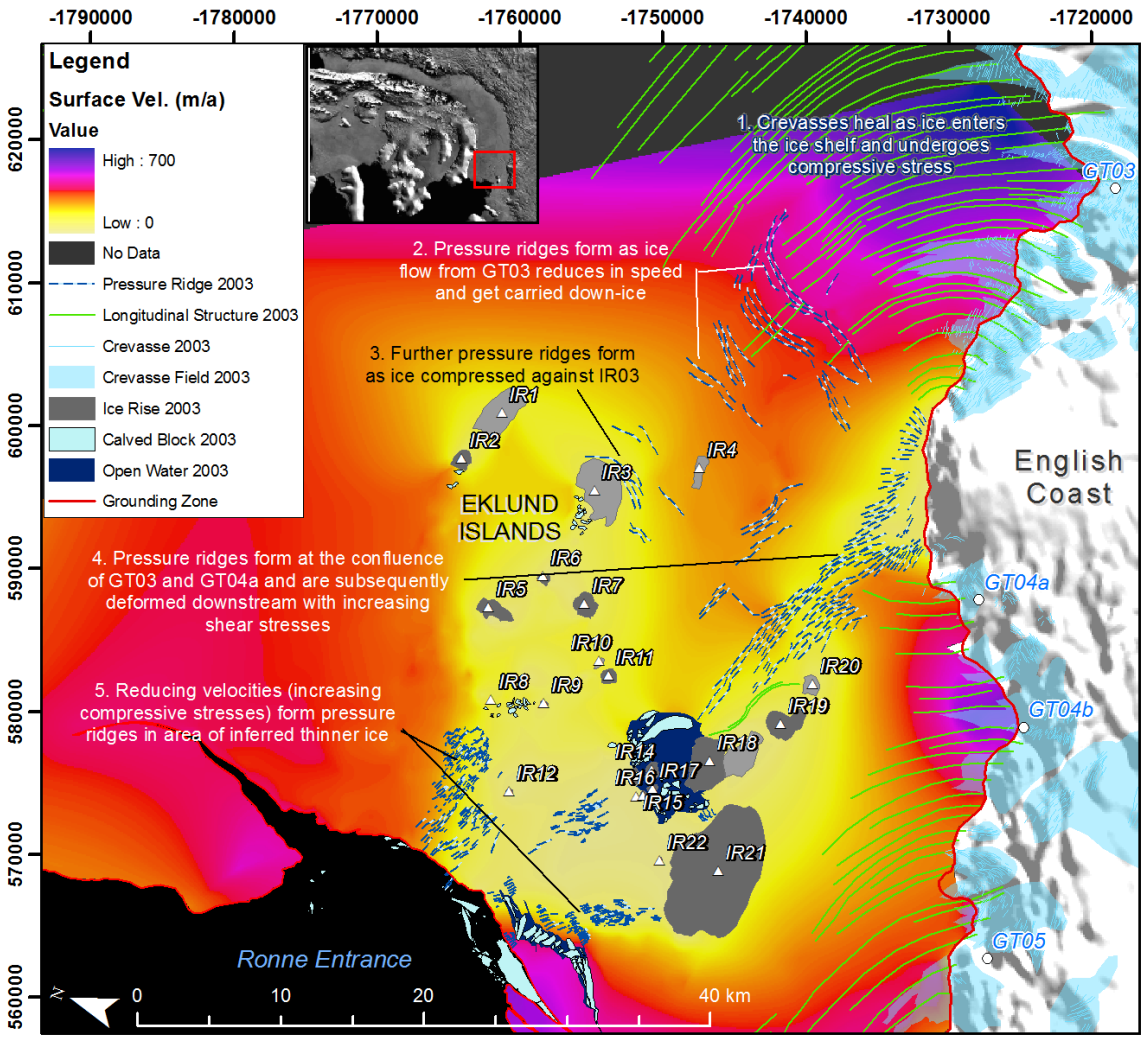

Figure 7.45. Flow-related features (January 2003) and surface velocities (ca. 2002) illustrating the compressive nature of flow around the Eklund Islands. Longitudinal surface structures represent flow direction and pressure ridges indicate regions of high longitudinal stresses.

Longitudinal structures from GT04a and GT04b divert eastwards and westwards respectively, with flow associated with the former of these domains subsequently merging with GT03. Further pressure ridges are formed at this confluence and illustrate the high compressional stresses between these coalescing flow units. These pressure ridges are consequently stretched longitudinally down ice and can be traced to the area of open water adjacent to IR18 (Figure 7.45, point 4).

The combined flow from GT04b and GT05 is diverted around the largest of the Eklund Islands (IR21), and consequently influenced northwards by the presence of GT06 to the west. Consequently, flow from these two tributary glaciers is forced directly into the area

of ‘thinner ice’, prior to its complete removal between January 2003 and March 2010. Structural assessments preceding 2010 revealed a succession of sub-linearly arranged pressure ridges in the area northwest of the Eklund Islands and illustrate both the dominant flow of GT04b/GT05 domains into this region, and the compressional stresses to which the area of thinner ice was exposed (Figure 7.45, point 5).

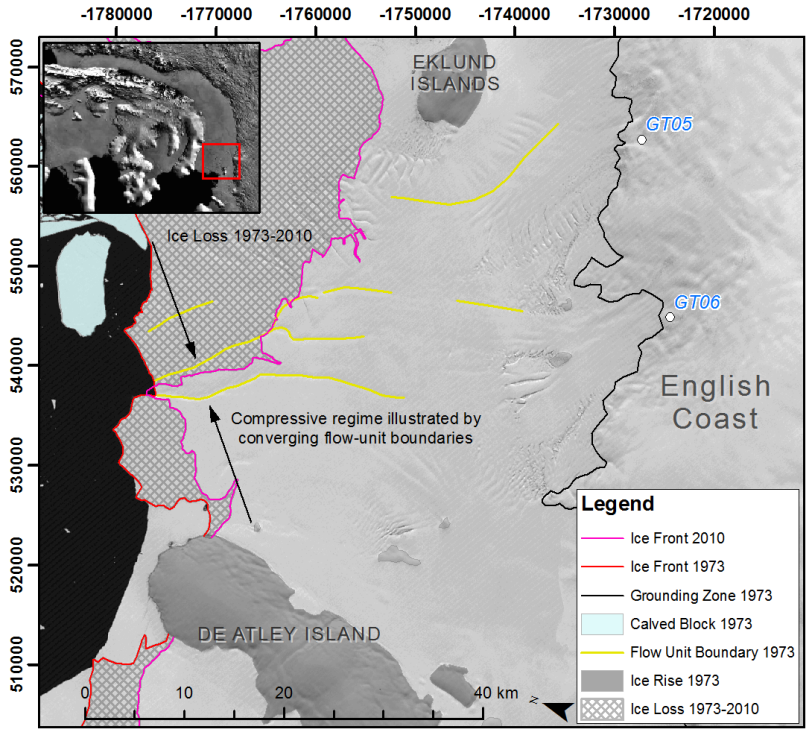

Figure 7.46. Converging flow unit boundaries towards the ice front during January 1973, illustrating compressive stresses transverse-to-flow. As the ice front retreated, the compressive nature of flow in this point was lost.

Visual assessment of Landsat MSS imagery from 1973 illustrates the transverse compression between individual flow units from the Eklund Islands to De Atley Island (Figure 7.46). This transverse compression is illustrated by the decreasing distance between distinct flow unit boundaries towards the ice front. As a result of the pattern of ice-shelf retreat, it is postulated that flow units supplying the ice front became subjected to less transverse compression over time, and indeed the removal of buttressing ice between 1973 and 2010 led to increased longitudinal extension through the reduction of back-stresses within the ice shelf. This is clearly reflected in feature tracking measurements between ca. 1989, ca. 2002 and ca. 2009, with increasing surface velocities between the Eklund Islands and De Atley Island over time. Indeed, between the Eklund Island and De

Atley Island, localised flow velocities had almost doubled from ~380 ma^{-1} to ~780 ma^{-1}. These increases appear to be driven by two different regimes, 1) linked to an increase in extensional pulling from the ice front and, 2) driven by an increase in GT07 velocities from its grounding zone.

There is a clear link between surface velocity changes over time and increasing distribution and extent of surface fractures, rifts and fracture traces (Figure 7.47). These changes and inferences on ice-shelf glaciological regimes are considered further below in three spatial locations, Zone A, Zone B and Zone C (Figure 7.48). These zones represent three different fracture regimes at the southern margin of George VI Ice Shelf, although the glaciological variations caused by fracturing is not fixed to these specific locations.

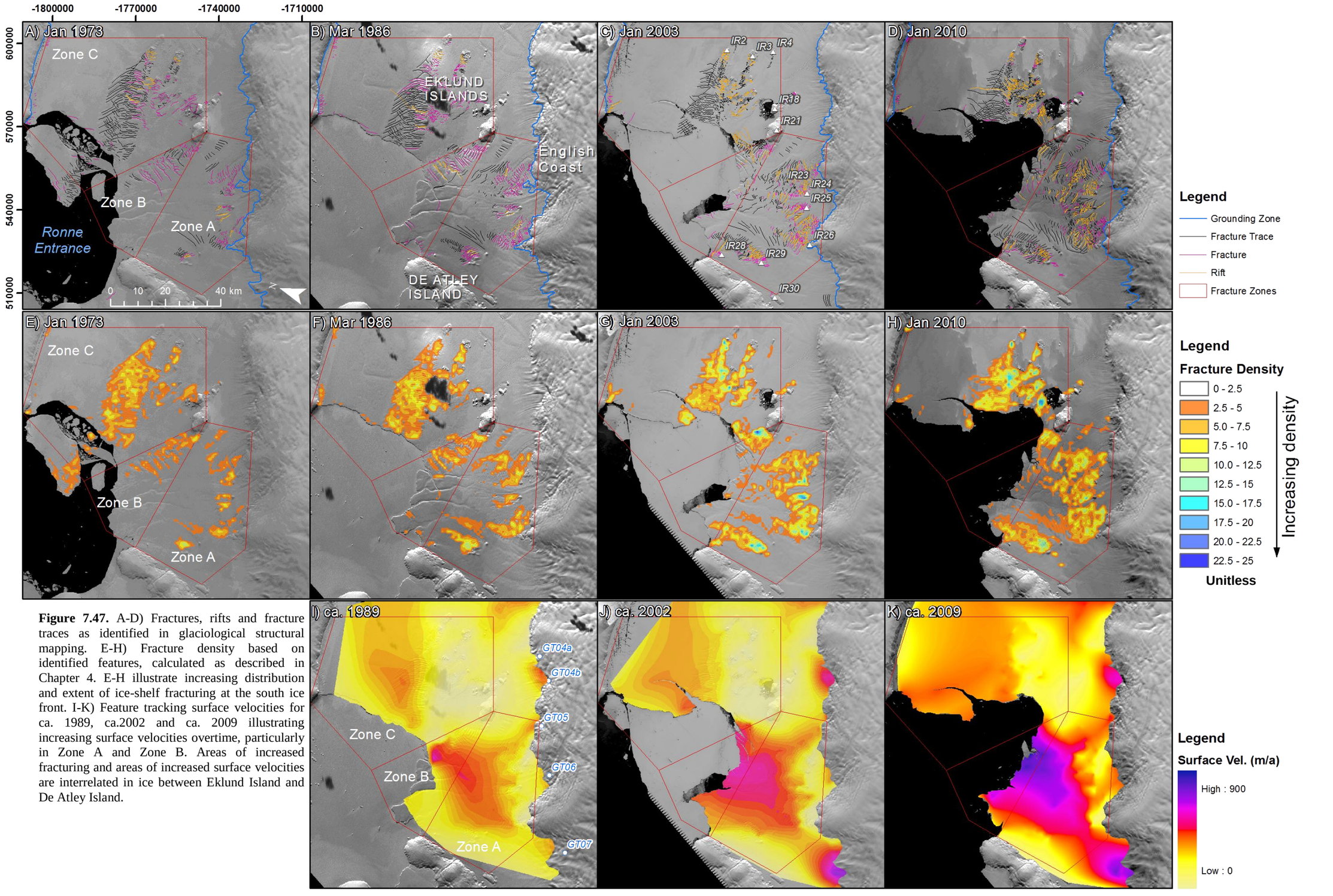

Figure 7.47. A-D) Fractures, rifts and fracture traces as identified in glaciological structural mapping. E-H) Fracture density based on identified features, calculated as described in Chapter 4. E-H illustrate increasing distribution and extent of ice-shelf fracturing at the south ice front. I-K) Feature tracking surface velocities for ca. 1989, ca.2002 and ca. 2009 illustrating increasing surface velocities overtime, particularly in Zone A and Zone B. Areas of increased fracturing and areas of increased surface velocities are interrelated in ice between Eklund Island and De Atley Island.

7.2.2.3.1 Interpretation of fractures, rifts and fracture traces – Zone A

Sub-decadal structural analysis within Zone A between 1973 and 2010 revealed a gradual increase in the distribution and concentration of surface fractures and rifts, developing and propagating from the grounding zone along the English Coast and from the lee-side of ice rises IR23, IR24, IR25 and IR26 (Figure 7.48 A-D, E-H). Landsat MSS imagery in 1973 captured large, open fractures emanating from the succession of these ice rises along the English Coast, for up to 10 km downstream. However, there were few fractures or indeed fracture traces observed further down-ice of these that leads to the proposition that fracturing in this particular region of George VI Ice Shelf is a relatively recent process occurring for at least 38 years.

By March 1986, fractures and rifts in Zone A became more widespread, particularly in ice fed by GT05, and in ice immediately downstream of IR23, IR24, IR26 and IR29. Open fractures and rifts observed in 1973 can occasionally be identified as fracture traces or fractures with a less-distinct opening further down-ice. The increased spatial distribution of fractures, rifts and fracture traces is therefore predominantly linked to the forward motion of existing structures with ice flow, and continual development and propagation of new fractures and rifts associated with the ice rises along the English Coast. A similar situation is inferred between March 1986 and February 1991. However, new fractures also began to develop in previously consolidated ice within the main flow channel of GT06 in 1991, and were limited to this area; fracture propagation was halted at its eastern and western confluence boundaries.

These new fractures are important for two reasons. First, their development in an area of previously un-fractured ice highlights the initial changes in glaciological conditions within this particular zone. Second, their spatial limitation within a distinct channel width illustrates ice-shelf heterogeneity between the main flow channel of GT06 and the heavily fractured ice to its east and west (downstream of IR24 and IR25 respectively) (Figure 7.48).

Velocity calculations from ca. 1989, ca. 2002 and ca. 2009 each illustrate an initial shear margin between the faster-flowing main channel of GT06 and the slower-moving fractured ice in front of IR24 and IR25 (Figure 7.48). In particular, this suggests that the process of fracturing and healing of ice lee-side of the English Coast ice rises caused by velocity differences reorganises the ice shelf into a more resistant configuration, and illustrates the

consequent disjointed nature of ice between these coalescing boundaries that prevents the fracture from propagating transversely. Despite being restricted laterally, these fractures widen as they transmit down ice and illustrate the dominant longitudinal extensional flow in this region. Indeed, by 2010, it is evident that the initial fractures have been longitudinally extended down-ice, but compressed transversely (Figure 7.48E).

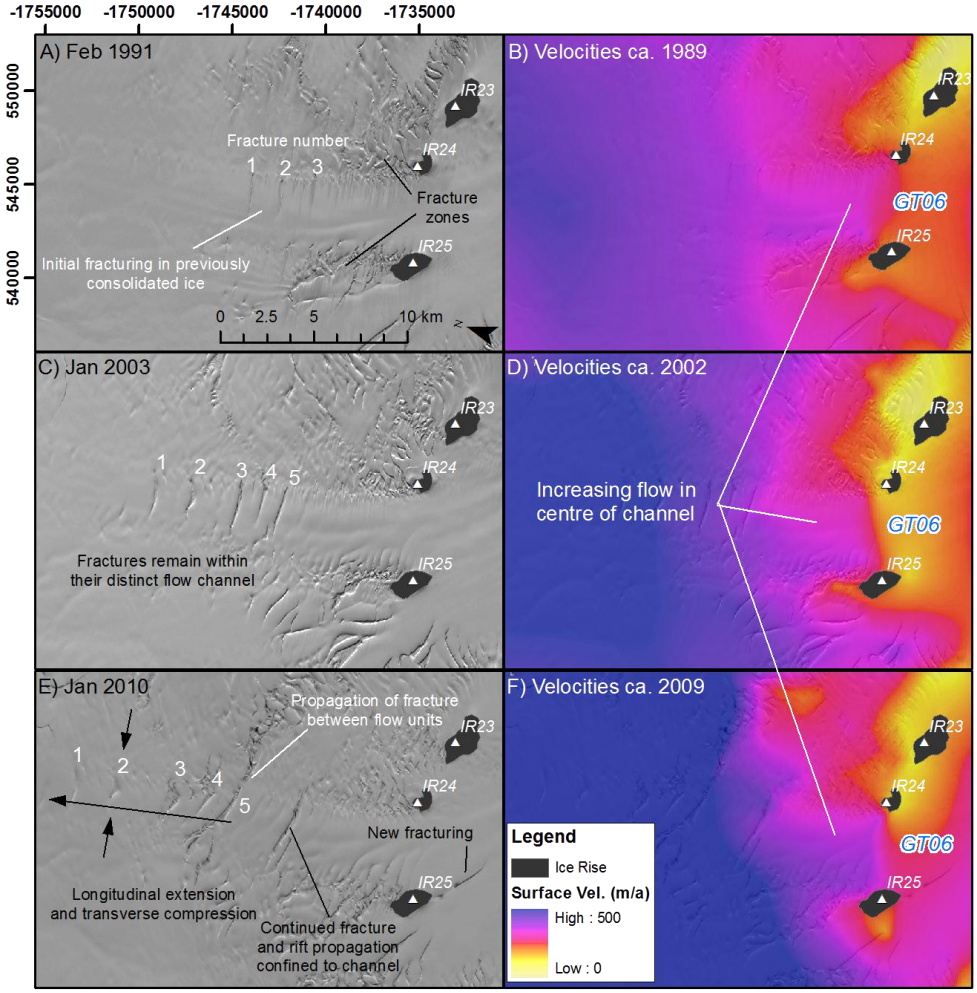

Figure 7.48. A) Initial fracturing (1, 2 and 3) confined to the main channel of GT06 that is unable to propagate over the flow-unit boundaries to the east and west. C) Continued fracture development (4, 5) still confined to the main channel of GT06. The spacing between fractures 1, 2 and 3 increases longitudinally, with each fracture also widening down ice. E) Similar longitudinal extension observed, with fractures 1, 2 and 3 undergoing compressive stresses transverse-to-flow. Fracture 5 merges with other fractures to the east and west thus cutting across the flow-unit boundary. B, D and F) Surface velocities calculated though feature tracking that illustrate the initial shear zone between the main channel of flow and slower moving regions of ice lee-side of IR24 and IR25 and the ever-increasing velocities down ice that emphasises the longitudinal extension of fractures as they migrate down ice.

However, Landsat ETM+ imagery from early 2010 illustrated that some of the larger open rifts and fractures had joined with neighbouring rifts and fractures thus propagating beyond these boundaries that had previously limited their dimensions (Figure 7.48). Furthermore, development of a large fracture was apparent, parallel with flow on the up-glacier side of IR25 for the first time.

Critically, these observations illustrate two distinct regimes within Zone A at the southern ice front of George VI Ice Shelf. First, a situation is developed where fracture traces within the ice migrate towards the ice front. Previously, these have remained sealed for some considerable distances down-ice; this has been occurring since at least 1973. During 2010, there is clear evidence that these fracture traces reopened to form either fractures or rifts down-ice, the latter of these are inferred by the presence of water within their surface openings that can only be sea water due to the absence of surface meltwater observed at any time in this specific location. These particular features develop along pre-conditioned weakness within the ice and reveal the varying stress regimes exerted over time. Secondly, the development of new fractures and rifts in previously consolidated ice is perhaps more important as the tensile stresses required to cause this specific fracturing are assumed to be larger than the force required to cause the re-fracturing of shelf ice. Thus the development of new fractures within Zone A of the ice shelf illustrates the increases in longitudinal tensile stresses over time within this region, directly linked with the increasing surface velocities towards the ice front.

7.2.2.3.2 Interpretation of fractures, rifts and fracture traces – Zone B

Zone B encompasses the area from the south ice front (-1782000 594400 m) to the boundary of Zone A, between IR21 and De Atley Island. During 1973, fracturing in this region could be further divided into two regimes, 1) those originating in ice flowing from the northwest of the Eklund Islands, and 2) those forming at the ice front within this study's observation periods. Fracturing and rifting within Zone B has thus had substantial control and influence on iceberg calving mechanisms at the south ice front and as of March 2010, the separate South Ice Front 2.

Considering the first of these regimes, during 1973 the majority of fractures and fracture traces originated in a distinct location at approximately -1754900 557950 m. Here, two sets of fractures were observed in each of the time periods in this study until January 2010 when the ice front had retreated beyond the point of fracture development for Fracture Set

2 (Figure 7.49). The first set of fractures developed adjacent to IR21; the regularity of these features and persistence down-ice for up to 12 km is evidence for long-term development within this particular zone. These fractures exhibited a primary transverse-to-flow orientation, with smaller fracture tips emanating irregularly along their distance, generally at 45° eastwards to flow. These fractures develop when ice from GT04b flows around IR21; it is thus proposed that an initial change from a compressive stress regime to longitudinal extension as ice rounds the ice rise causes its regular fracturing, and is indicative of the gradual build-up of back-stress and release. These features are consequently migrated down ice with flow into the region of inferred 'thinner ice' (Section 7.2.1.2) and gradually become less distinct through surface degradation; their dimensions do not appear to increase or decrease notably down-ice, further suggesting steady flow dynamics in this zone over time.

A second set of fractures, rifts and fracture traces develops in close proximity to Fracture Set 1 but is orientated to the northwest, and illustrates a localised point of flow divergence in the ice shelf. The irregular form of individual fractures and uneven transverse distances suggests a less ordered formation than Fracture Set 1. Fracture traces are observed towards the ice front (in January 1973) approximately 24 km from their formation point that similarly confirms the long-term process of fracturing within this zone. Over time, fractures and rifts belonging to this second set form the basis for large-scale iceberg calving at the south ice front, with active calving observed in February 1991 and January 2003.

The largest rifts are able to cut across two distinct flow unit boundaries, but do not penetrate through a third boundary. (Sequential Landsat imagery from 1973 to 2010 illustrates that this 'third' flow unit boundary is never penetrated by adjacent fractures or rifts). It has already been established that fractures in Zone A were unable to propagate beyond these flow unit boundaries prior to 2010, and thus the ability of these particular fractures and rifts to do so as early as 1973 suggests that either;

1) The forces exerted at the ice-shelf front are great enough to permit fracture tip penetration through the flow unit boundaries, caused by:
    a. Increased susceptibility to tidal bending, and/or,
    b. Greater longitudinal extension towards the ice front.

2) Flow-unit boundaries at the ice front are less resistant to fracture propagation across them because previously there has not been fracturing and resealing of adjacent ice, and thus the ice-shelf is much more homogeneous in its configuration. (Structural interpretations of early Landsat MSS imagery suggest that shelf-ice at the southern ice front was previously consolidated and fracturing lee-side of the English Coast ice rises was a relatively contemporary process).

Indeed, a combination of each of these is possible, and coupled with the instable geometric ice-front configuration throughout the observation periods, the second set of fractures created an environment pre-conditioned for ice-shelf retreat.

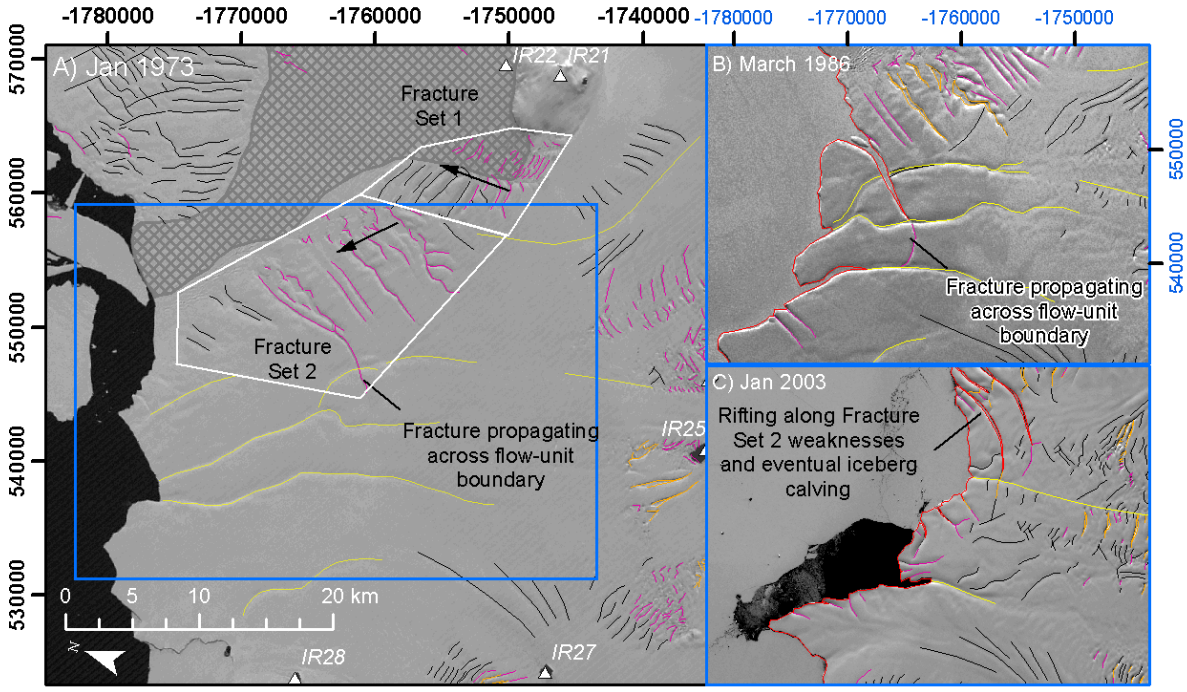

Figure 7.49. Fracturing within Zone B at the southern ice front of George VI Ice Shelf illustrating, A) the divergence of fractures west of IR21, B) ability of Fracture Set 2 to propagate across flow unit boundaries and C) ice-shelf retreat along pre-conditioned weaknesses in the ice shelf.

Fractures that formed at the ice front (rather than those carried towards the ice front) were relatively sparse prior to January 2003. However, by 2003, small, irregular fractures and rifts were observed along the ice front, cutting back into the ice shelf. By January 2010, further rift propagation and fracture development had created an ice front largely pre-conditioned for regular iceberg calving at a small scale. The largest rifts cut back along flow unit boundaries and permit a visual assessment of ice-shelf heterogeneity and inherent weaknesses in these confluence zones caused by fracturing and healing further upstream (Figure 7.50). ICESat GLAS elevation measurements across individual flow unit

boundaries and visual interpretation of multiple Landsat scenes illustrate a surface undulation linked with these flow unit boundaries; it is thus likely that these zones are also thinner, have basal cavities (Fricker *et al.*, 2001) and are thus inherently more susceptible to fracturing and rifting.

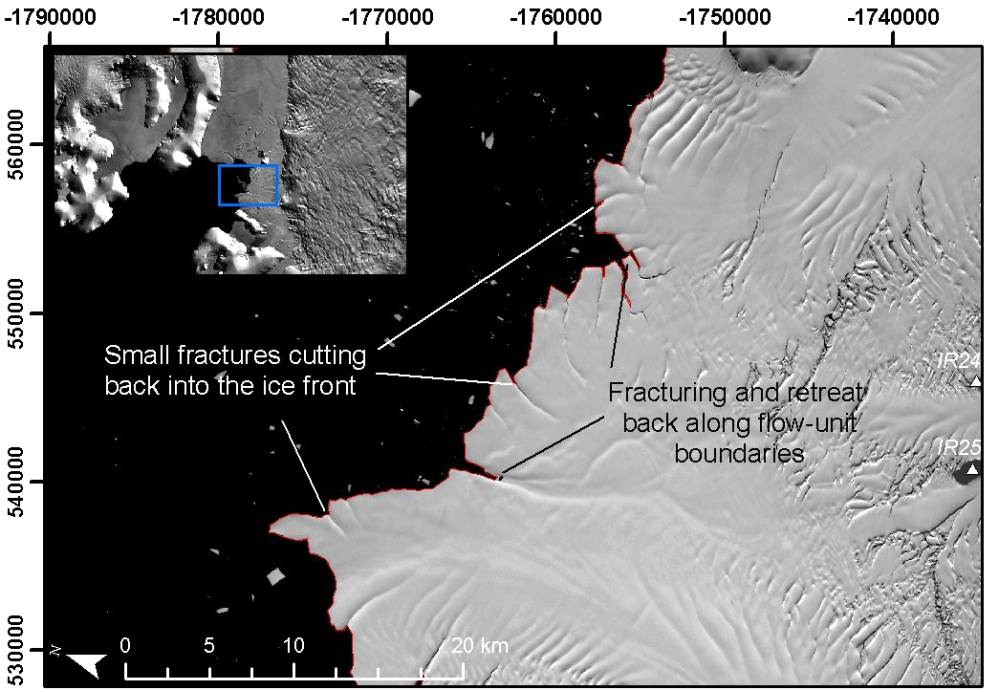

Figure 7.50. Preferential fracturing along flow unit boundaries at George VI South Ice Front 2 during January 2010. Ice in these confluence zones is inferred to be thinner than surrounding ice in the main flow channels and thus mechanically weaker.

7.2.2.3.3 Interpretation of fractures, rifts and fracture traces – Zone C

Zone C covers the area from the boundary of Zone B to the Monteverdi Peninsula, and includes the heavily fractured regions associated with the Eklund Islands' ice rises and ice rumples. The most distinct set of fractures, fracture traces and rifts emanates in ice downstream of IR2 and propagates transversely towards the ice front. This particular region consists of cross-cutting fractures likely to originate through a combination of initial chaotic fracturing and rifting adjacent to the ice rises, additional bending stresses from vertical tidal motion and the consequent influence on the flow dynamics of IR5 downstream. Over time, however, the magnitude of the fractures and rifts created down-ice of IR2 decreases, and the surface impression of IR2 on the ice shelf also lessens. This latter point is discussed in more detail in Section 7.2.4.

These fractures and fracture traces have two distinct boundaries; one to their north with largely consolidated ice originating from up to 150 km back upstream, and a second boundary to their southwest that marks the point where fractured ice meets the inferred 'thinner ice' downstream of the Eklund Islands. Feature tracking velocity measurements reveal a marked difference of ice-shelf speeds at the southern boundary that is evident throughout all of the observation periods.

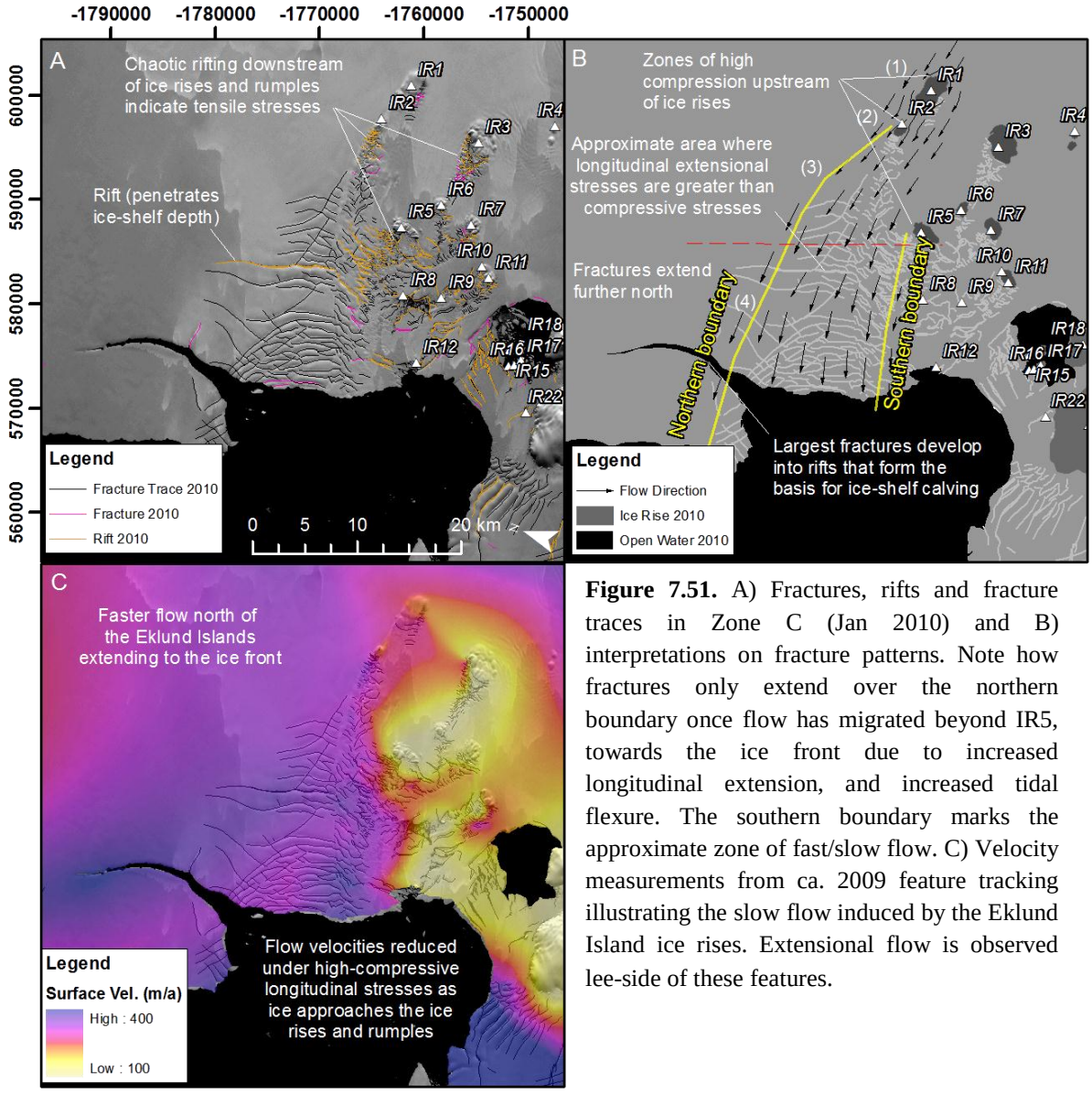

Figure 7.51. A) Fractures, rifts and fracture traces in Zone C (Jan 2010) and B) interpretations on fracture patterns. Note how fractures only extend over the northern boundary once flow has migrated beyond IR5, towards the ice front due to increased longitudinal extension, and increased tidal flexure. The southern boundary marks the approximate zone of fast/slow flow. C) Velocity measurements from ca. 2009 feature tracking illustrating the slow flow induced by the Eklund Island ice rises. Extensional flow is observed lee-side of these features.

Propagation beyond the northern fracture boundary is only occasionally achieved, first observed in 1986 and 2010 Landsat imagery as secondary fractures; i.e. healed ice that reopened along the same line of weakness. The 1986 rift later formed the distinct protruding ice front observed in 2003 and 2010. (The link between this cyclical fracture/rift propagation and large-scale iceberg calving has already been alluded to in Section 7.2.1.2).

These secondary fractures only develop (redevelop) once the ice in which it is situated is carried beyond IR5, in both 1986 and 2010, and thus the following sequence of events is proposed for rifting this particular location (see also Figure 7.51);

1) Ice is forced to flow around IR1, yet the immediate presence of IR2 down-ice prevents any significant fracturing due to high compressive stresses.
2) Ice is then subjected to IR2 where it is forced to flow around the obstacle. This process causes significant fracturing of ice that it likely to penetrate the entire thickness of the shelf. Elsewhere, it has been demonstrated that this process also leads to a high concentration of marine-derived ice being incorporated into the ice-shelf system (Thyssen *et al.,* 1993; Blindow, 1994; Fricker *et al.,* 2001).
3) The fractures remain open for approximately 3 km down-ice before healing, leaving a distinct imprint on the surface. It is proposed that this 'healing' process occurs because of the presence of IR5 that increases the compressive stresses in this locality.
4) Once ice flows beyond this point, longitudinal extension increases, permitting ice to re-fracture along a structural line of weakness (healed fracture, fracture trace) generated upstream. Re-fracturing only takes place when the extensional 'pull' of the ice further downstream rises above a critical threshold, and hence explains why not every fracture trace is subjected to secondary fracturing.

Fracturing of the ice shelf is also observed around IR3, IR5, IR6, IR7, IR8, IR9, IR11 and IR12 but on a much smaller scale. Indeed, the fracture-trace imprint on the ice-shelf surface is less obvious than those created down-ice of IR2, and may result from the continual compressive nature of the ice due to the clustering of the Eklund Islands in the region. Furthermore, ice-shelf surface velocities are much slower in this region than to the north of IR2, and west of IR21, thus fractures and fracture traces are not carried down ice with as much speed; essentially they form and reseal over a shorter distance as a by-product of localised ice-shelf velocity. Nevertheless, rifting and fracturing of the ice shelf surrounding these smaller Eklund Islands is still chaotic. In sequential Landsat imagery between 1991 and 2010, the amount of rifting increases on the lee-side of these ice rises and ice rumples, particularly IR3, IR5, IR8 and IR12; indeed by January 2011, the ice-shelf front had retreated back beyond IR12 (attached by a small ice-bridge) to run between IR8, IR9, IR10/11 to IR 18.

Observations downstream of ice rises and ice rumples and at the margin of different flow units (flow unit boundaries) have illustrated a higher concentration of marine-derived ice than elsewhere within an ice-shelf system (Thyssen *et al.*, 1993; Fricker *et al.*, 2001). It is therefore proposed that shelf ice immediately downstream of the Eklund Islands is largely marine-derived ice, accreted on to the base of meteoric-derived ice that is forced to flow over, or around the islands. Furthermore, it is postulated that due to ice-rise-derived rifting, marine ice is squeezed into basal cavities during healing of the ice-shelf rifts. These propositions, coupled with the inference of thinner ice, have a significant impact on the heterogeneity of the ice mass at the southern margins of George VI Ice Shelf, and thus the mechanical strength of the ice shelf, and its susceptibility to oceanographic variations.

7.2.3 Surface elevation change, grounding-line retreat and inferences on ice-shelf thickness

In Section 7.1, ICESat GLAS data was used to quantitatively calculate surface elevation changes over the maximum temporal extent for each track. Furthermore, surface elevation measurements were used to qualitatively infer relative ice-shelf thicknesses between different ice-shelf flow units, considering areas with lower surface elevation to be thinner. Here, surface elevation measurements and elevations changes calculated over time are used to estimate ice-shelf thicknesses and thickness changes as outlined in Chapter 5.

A few limited inferences on ice-shelf surface elevation changes and ice-shelf thicknesses have already been made. In the following subsection, ICESat GLAS repeat track measurements are considered in much greater detail, utilising the 4323 data points across George VI Ice Shelf, further divided into a northern, central and southern section as previously discussed.

7.2.3.1 Northern section

The northern section of George VI Ice Shelf displayed an average non-significant surface elevation change of -0.025 ma^{-1}, thus equating to -0.230 ma^{-1} thickness change between March 2003 and October 2008 (Figure 7.52). Only three ICESat GLAS tracks cross this section, and thus the 1017 data points are dispersed over a large ice-shelf surface area (approximately 4400 km^2). In Section 7.2.2.1 further evidence is presented for an ice-shelf surface structure consisting of both longitudinal and transverse surface features that were only partially considered in initial structural interpretation. It has been demonstrated through the analysis of surface meltwater channels, and visual assessment of Landsat imagery that these structures create an undulating surface morphology, thus the effect of these surface structures migrating across ICESat GLAS tracks remained in the filtered dataset from which the surface elevation change calculations were based.

The northern section of George VI Ice shelf also undergoes significant surface melting in the austral summer. However, it is not thought that the presence of surface meltwater has an effect on surface elevation measurements due to the timing of ICESat GLAS data acquisition between March and October when surface meltwater is negligible. The indirect effect of meltwater refreezing on the surface at different levels each year is also refuted as it is demonstrated in Section 7.1.4.4 that there is little change in the distribution and extent of surface meltwater between 2003 and 2010 other than that linked to the structural motion as mentioned above.

It is thus viable that measured surface elevation changes and calculated thickness changes are a result of either 1) amplification/ dampening of absolute elevation changes between 2003 and 2008 through the motion of surface structures across and along the shelf that were not culled during pre-processing, or 2) measurements represent minimal absolute elevation and thickness changes. Additionally, there are few distinct spatial patterns of surface-elevation change and thus it is inferred that the ice shelf within this northern region has not undergone significant thickness changes between 2003 and 2008. This is further supported by no clear indication of grounding line retreat along either ice-shelf flank, although this may also be controlled by the steep topography in the sound.

7.2.3.2 Central Section

The central section of George VI Ice Shelf illustrates a complex spatial pattern of surface elevation changes, and consequently thickness changes between 2003 and 2008 (Figure 7.52). The 1657 filtered data points suggest modest ice-shelf thinning towards Palmer Land, substantial thinning along the centreline of the central section, and slight thickening towards Alexander Island. An average surface elevation change of -0.38 ma^{-1} was recorded in the central section, thus equating to a mean thickness change of -3.36 ma^{-1}. The temporal scale (2003-2008) is too short to assume the patterns of thickness change observed are due to a redistribution of ice-shelf mass towards Alexander Island with the dominant south-to-north flow of the ice shelf. Furthermore, this particular region is outside that of abundant ice-shelf surface melting, as indicated by meltwater features limited to the northern periphery along Alexander Island. Thus a thinning of the ice shelf, particularly along its central zone is likely to be as a result of either short-term surface conditions (enhanced ablation) or enhanced basal melting, with surface elevation changes reflecting a vertical response through hydrostatic rebalancing.

The ICESat GLAS measurements indicate greater surface elevations within this central zone than towards the north and south, from which greater thicknesses are inferred; the 200 m RAMP DEM also confirms greater surface elevations in this zone over a larger spatial extent than the ICESat tracks permit. As a result, the base of George VI Ice Shelf in this central zone reaches much greater depths within George VI Sound than at any other point in the ice-shelf system, and thus may be subjected to warmer waters that tend to exist closer to the sea bed (Jenkins and Jacobs, 2008; Holland *et al.*, 2010). Thus, the thickest parts of George VI Ice Shelf are subjected to high rates of basal melt and lower rates of basal accretion that results in a net loss of ice through a vertical column; this idea is explored in more detail in Chapter 9.

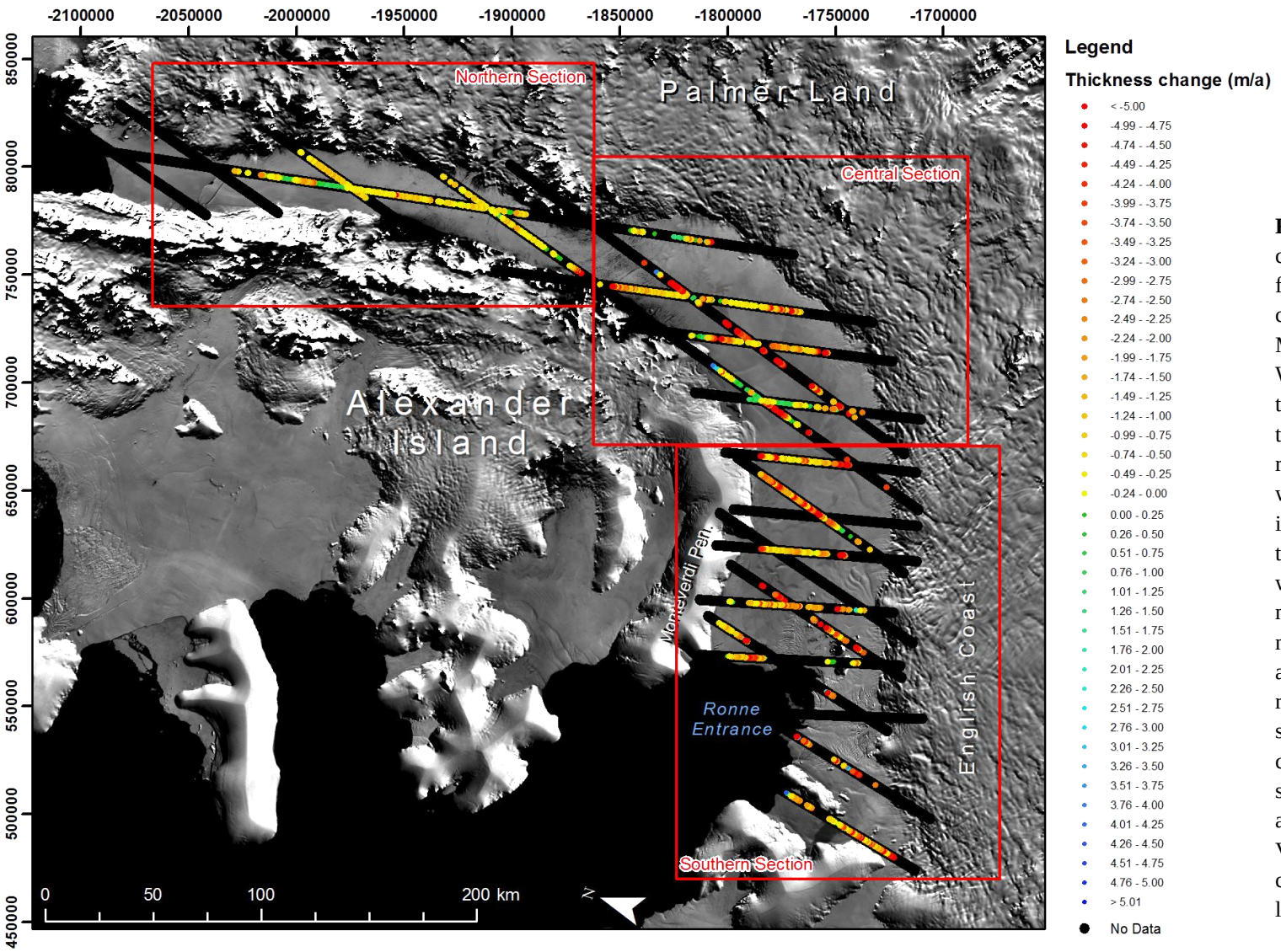

Figure 7.52. Calculated thickness changes in George VI Ice Shelf from ICESat GLAS elevation-change data, displayed as ma^{-1} from March 2003 to October 2008. Widespread but non-significant thickness changes are calculated in the northern region where the flow regime is largely dominated by westward-flowing tributary glaciers into George VI Sound. It is inferred that this dynamic regime coupled with the morphology of the Sound makes this section of the ice shelf more stable. Furthermore, elevation and thickness calculations may represent motion of surface structures rather than absolute changes. The central and southern sections display more widespread and significant thinning of George VI Ice Shelf across and along the channel with only a few pockets of localised ice-shelf thickening.

7.2.3.3 Southern Section

Due to substantial fracturing across much of the southern region of George VI Ice Shelf, ICESat GLAS tracks t0159 and t0278 in particular have been heavily filtered to subdue the effects of structural motion towards the southern ice front observed in initial structural mapping. Other tracks have been filtered for the topographic effects of longitudinal surface structures and because of the location of ice rises and ice rumples. Nevertheless, 1649 repeat measurements were acquired in total over eight ICESat GLAS tracks and illustrate widespread and significant thinning between 2003 and 2008, with only localised pockets of thickening observed sparsely over the southern region (Figure 7.52). In total, a mean elevation change of -0.21 ma^{-1} was calculated, equating to a thickness change of -2.02 ma^{-1}, between 2003 and 2008.

Whilst repeat-track measurements are largely absent from ice flowing from Palmer Land to South Ice Front 2, sequential Landsat imagery and resultant structural/ glaciological interpretations, reveal a marked retreat of the break of slope along the Palmer Land grounding zone from -1728400 589600 m to -1715600 485500 m, with a maximum linear retreat of ~7 km recorded from 1973 to 2010. Whilst the break of slope between grounded and floating ice does not reflect the true grounding line position, the retreat of the break of slope is undoubtedly linked to a retreat of the grounding zone. Elsewhere, Thomas *et al.* (1988), Conway *et al.* (1999) and Rignot (2002), for example, have illustrated a clear link between ice-shelf thinning and the migration of its grounding line further upstream, and coupled with the widespread thinning calculated from repeat ICESat GLAS acquisitions, there is no evidence to contest against a thinning ice shelf in this region. Whilst the horizontal movement of the grounding zone is indicative of ice-shelf thinning, poor knowledge of the subglacial bed topography prevents a quantitative thinning measurement from being calculated.

There is no evidence, however, of a retreating grounding line along Monteverdi Peninsula on Alexander Island. In Chapter 6, a similar situation is alluded to: The horizontal motion of the grounding line is essentially controlled by two main factors, 1) the thickness of the overlying ice, and 2) the gradient of the underlying bed topography. Where the gradient is ‘steep’, a greater amount of vertical change must occur in the ice shelf for the grounding line to respond horizontally, whereas if a ‘shallow’ bed topography exists, less vertical change is required to achieve a larger horizontal movement. Heuristically, the surface

topography of grounded ice can be used as a measure of the subglacial topography where it is above sea level, and thus the subglacial bed topography of the English Coast is believed to be more gentle than that of Monteverdi Peninsula (Figure 7.53). Furthermore, it is no coincidence that the greatest retreat of the grounding line is observed where tributary glacier systems enter the ice shelf along the English Coast, where subglacial-bed gradients are likely to be more gentle than the gradients associated with the headlands between flow units, due to greater basal erosion rates. As for the submarine topography of Monteverdi Peninsula, it is thus suggested that it has a steep gradient that inhibits the horizontal movement of the grounding line, and indeed no significant tributary glaciers flow off this peninsula.

In Section 7.2.3 the lessening surface expression of IR2 and the changing dimensions of ice-shelf rifts and fractures developed in this region were briefly reported. This response is also evident in IR1 and IR3, but not in other ice rises of the Eklund Islands. Possible reasons for this response are illustrated in Figure 7.54. For ice rumples, it is postulated that a thinning ice shelf would begin to decouple from the subglacial islands because of its state of hydrostatic equilibrium, thus reducing the contact area between the ice-shelf base and the submarine topography. The surface expression would thus lessen until the ice-shelf decouples from it completely. For an ice rise, a thinning ice shelf would not greatly affect the surface expression because a portion of its bedrock may be at, or above sea level, thus a thinning ice shelf would not necessarily lead to a thinning of the grounded-ice portion on the ice rise, and the surface expression would remain largely unchanged. Importantly, an ice-shelf system such as George VI that is experiencing widespread thinning, could possibly detach from such ‘pinning points’ that controls its dynamics, stress regimes and ultimately its localised stability.

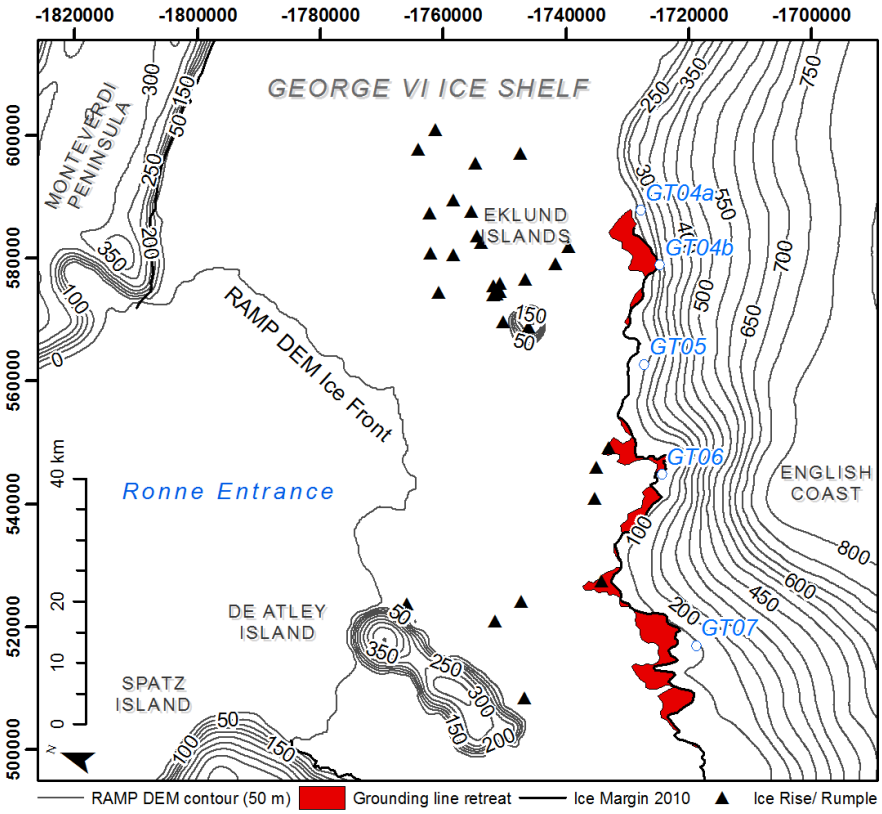

Figure 7.53. RAMP DEM 50 m contours illustrating the more gentle surface gradient of the English Coast than Monteverdi Peninsula along which the grounding line is inferred to have retreated between 1973 and 2010. Note also the general alignment of grounding line retreat with the tributary glacier systems along the English Coast; it is inferred that the subglacial bed topography of these tributary glaciers is more gentle than that of the headlands between flow units along which a greater grounding line retreat is facilitated.

In the southern section of George VI Ice Shelf repeat-track elevation measurements from ICESat, a retreating grounding line and a reducing surface expression of ice rumples all suggest a thinning ice shelf from 1973 to 2010. Such observations are critical in understanding the structural and velocity changes observed in the southern section over the same time period.

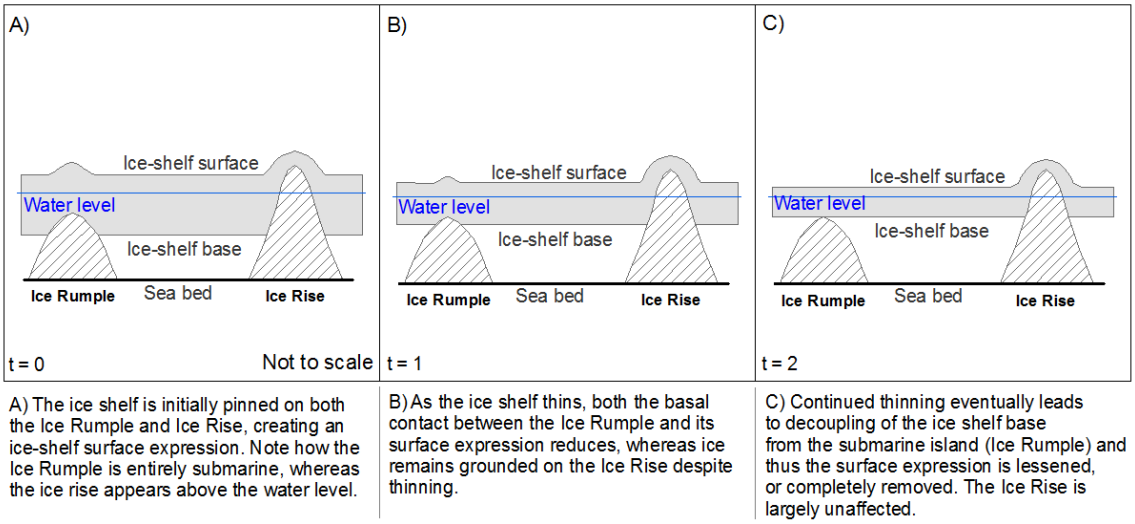

Figure 7.54. Schematic of ice rumple and ice rise response to ice-shelf thinning. Note how the surface expression of the ice rumple reduces as the ice shelf thins due to hydrostatic equilibrium whereas the surface expression of the ice rise remains approximately the equal throughout. 'Water level' refers to the sea level.

7.2.4 Summary of key observations and interpretations

Due to the large surface area of George VI Ice Shelf, its complexity and the wealth of data discussed in the previous sections, a brief account of the key interpretations is presented here for the north, central and southern sections as described above.

7.2.4.1 Key interpretations of the northern section

1. Short-term (decadal) ice loss observed at the northern ice front is linked to local dynamic configurations in response to the continued retreat of the ice shelf. Limited input from Palmer Land, north of Riley Glacier, enabled extensional stresses to dominate, and is reflected by large, cross-shelf fractures and rifts that are evident in all satellite imagery until January 2010.
2. Ice loss occurred predominantly along pre-existing, long-standing fractures and rifts that develop at least 10 years prior to actual calving, based on evidence presented in this study. Evidence is also presented for small-scale calving (< 2 km^2) at more regular periods throughout the observation period.
3. The north ice front illustrates a slight concavity in each of the observation periods suggesting that it is in a state of irreversible decline (Doake *et al.*, 1998).
4. Velocity increases calculated at the northern ice front through feature tracking and InSAR are linked to continued recession. It is proposed that the removal of slow-moving, buffering ice reduced the back-stresses associated with Riley Glacier that

enabled an increase in velocity between ca. 1989 and ca. 2007. Riley Glacier is thus the dominant tributary system at the northern ice front that will ultimately control future glaciological changes.

5. Analysis of surface meltwater patterns reveals a complex history of ice dynamics and current processes. It is proposed that longitudinal foliation structures within the ice are carried over the grounding line within tributary glaciers and undergo further transverse buckling as ice is compressed into the narrow channel of George VI Sound. An integrated pattern of primary and secondary meltwater channels preferentially fill surface furrows and hollows created by both longitudinal and transverse folding that can be seen across the ice shelf towards Alexander Island.
    a. The consistency in these patterns across the ice shelf, highlighted by meltwater presence, illustrates a steady dynamic regime.
    b. From the analysis of these meltwater patterns, a largely compressive stress regime is inferred, thus fracture development is retarded that consequently prevents the free-draining of surface meltwater through the ice-shelf system. This is perhaps only accomplished where there is evidence of ice dolines on the ice-shelf surface. Meltwater therefore persists on the surface of George VI Ice Shelf for longer than other ice-shelf systems on the Antarctic Peninsula (Cook and Vaughan, 2010).
6. The northward-migration of the northern meltwater limit from 1973 to 2010 is likely to be as a result of an increase in melt days per year (Torinesi *et al.*, 2003), and possibly increasing surface air temperatures over the last four decades (Morris and Vaughan, 2003). The southern meltwater limit fluctuates, and does not show any expansion and the reasons are further considered in Chapter 9.
7. Minimal, non-significant surface elevation changes, and thus thickness changes, are calculated from 2003 to 2008 over George VI Ice Shelf northern section.

7.2.4.1 Key interpretations of the central section

1. This section is dominated by flow-derived structures including;
    a. Longitudinal structures that originate from grounded ice positions and transmit across the grounding line into the ice shelf. These features define the ice-shelf ice divide between the northern and southern ice fronts.
    b. Transverse structures, inferred as pressure ridges and pressure buckles that form where ice flowing from Palmer Land is compressed in George VI

Sound with decreasing flow velocities. The interaction of longitudinal and transverse features resembles the ice-shelf surface pattern that is filled by meltwater in the northern section.

2. Surface fractures are limited to the grounding zones of tributary glaciers as ice flows down steep-sided slopes into the shelf. These crevasses are soon sealed by a compressive flow regime that also limits fracture development elsewhere in the central section of the ice shelf.
3. Few structural changes are observed, and although no repeat-velocity measurements are made, the consistent appearance of transverse and longitudinal features across the Sound illustrates steady dynamics for at least the last 74 years.
4. A complex pattern of ice-shelf thickness changes is calculated, with the centre of the ice shelf illustrating strong, significant thinning. This is attributed to the thickest parts of the ice shelf being subjected to warmer oceanic temperatures deeper in the underlying water column; this idea is further discussed in Chapter 9.

7.2.4.3 Key interpretations of the southern section

1. The glaciological complexity of the southern ice front(s) exists due to the presence of the Eklund Islands that influence the dynamics, structures and thickness of the surrounding ice shelf, and consequently its heterogeneity.
2. A region of thinner ice is inferred from ICESat GLAS and RAMP DEM elevations, down-ice of the Eklund Islands. It is within this area of thinner ice that much of the retreat of the southern ice front was concentrated that consequently impacted on the glaciological regimes across the region. Within this area a greater concentration of marine derived ice is also expected (e.g. Fricker *et al.*, 2001), and thus it is more susceptible to oceanic variation.
3. Continued retreat separated the south ice front into two main units north (South Ice Front 1) and south (South Ice Front 2) of the Eklund Islands respectively, with a third unit always present between De Atley Island and Spatz Island.
4. South Ice Front 1 exhibits cyclical advance/calving regimes. It is suggested that these cycles operate approximately every 40 years, with pre-existing structural weaknesses that emanate from IR2, being exploited to facilitate iceberg calving. There are no significant changes in the flow velocity associated with South Ice Front 1, and thus it is proposed that this section of the southern ice front is driven by stable gravitational flow originating up to 150 km upstream. Furthermore, South

Ice Front 1 is pinned within a narrow channel between the succession of ice rises and ice rumples and Monteverdi Peninsula that provides extra stability.

5. The area between the Eklund Islands and De Atley Island (South Ice Front 2) becomes increasingly fractured from 1973 to 2010, developing predominantly on the leeside of IR23, IR24, IR25, IR26 and IR29 and migrating down ice towards the ice front with the motion of the ice shelf. Fractures also develop and propagate along the ice front. These significant structural changes are linked to an increase in ice shelf velocities calculated by manual feature tracking for ca. 1989, ca. 2002 and ca. 2009.
6. Measured velocity increase is attributed to the removal of buttressing ice that consequently reduces the back-stresses along South Ice Front 2, allowing the longitudinal extension of ice fed by tributary glaciers off the English Coast.
7. Significant thinning is calculated across the southern region, both by repeat-track ICESat GLAS elevation measurements and inferred by grounding line retreat along the English Coast and around the ice rumples of the Eklund Islands.

Chapter 8

Stange Ice Shelf

Chapter Overview

This chapter is presented in two sections detailing the results (Section 8.1) and the interpretations of those results (Section 8.2) for Stange Ice Shelf. Similarly, the spatial, structural and dynamic components of the ice shelf are initially considered with the three elements later integrated. Following on from Chapter 6 and Chapter 7, this chapter refers the reader back to previous sections where appropriate to avoid repetition. The results and interpretations of Stange Ice Shelf are discussed in a wider context in Chapter 9.

8.1 Stange Ice Shelf Results

In the following section, the dynamic regime of Stange Ice Shelf is detailed, describing its configuration and assessing surface velocity changes between ca. 1989, ca. 2004 and ca. 2010. Second, ice-shelf spatial extent is assessed between 1973 and 2011 (inclusive) over 6 observation periods, illustrating the advance/retreat of its three ice fronts. Glaciological surface structures are then presented, with major changes between 1973 and 2011 detailed. Particular emphasis is given to observed changes in surface fractures and rifts between observation periods. Finally, changes in surface elevations between May 2004 and October 2007 are examined. Surface-elevation changes are calculated over the longest suitable time scale as outlined in Chapter 5, but are extrapolated to rate of change in meters per annum for direct comparison between different ICESat GLAS tracks. Figure 8.1 gives an overview of the tributary glaciers of Stange Ice Shelf, its morphology and key locations as referred to in the following sub-sections.

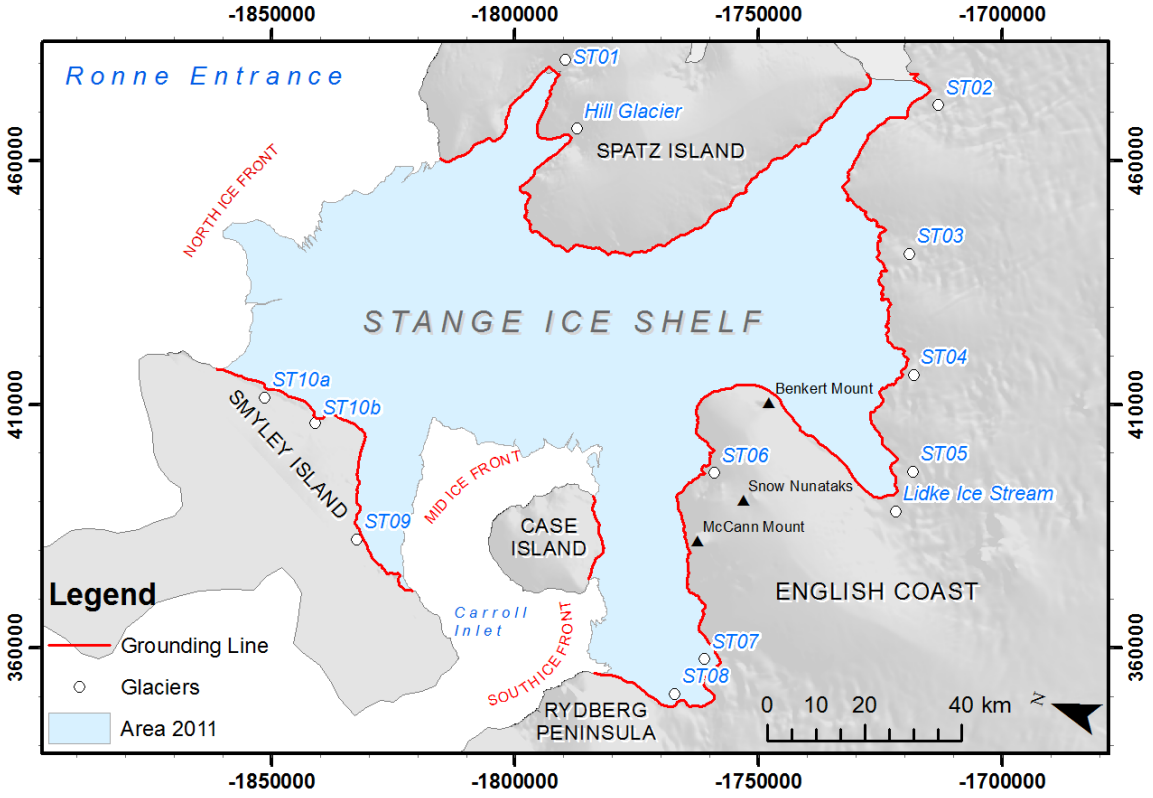

Figure 8.1 Stange Ice Shelf, its three ice fronts, 13 flow units and relevant locations as discussed in the text below. Previously unnamed tributary glaciers are termed ST##, with ST referring to 'Stange Tributary', all other names were obtained from the APC. Ice-shelf area (light blue) is representative of the 2011 extent.

8.1.1 Ice-shelf dynamics

Surface velocities have been calculated for Stange Ice Shelf using manual feature tracking and subsequent interpolation for three observation periods (1986-1989, 2001-2004 and 2008-2011) with mean annual surface velocities (ma^{-1}) extrapolated for each of the time intervals. First, the dynamic configuration of Stange Ice Shelf is discussed, before surface velocity changes between each time period are analysed.

Table 8.1. Feature tracking time periods and alias as referred to hereafter.

Observation period	Alias
1986 – 1989	ca. 1989
2001 – 2004	ca. 2004
2008 – 2011	ca. 2010

8.1.1.1 Stange Ice Shelf dynamic configuration

Ice is fed into Stange Ice Shelf from three grounded-ice locations, making for a dynamically complex ice-shelf system (Figure 8.2). From Spatz Island, two principal tributary glaciers, ST01 and Hill Glacier, flow into Stange Ice Shelf from a narrow channel (~15-20 km wide), and divert northwards towards the northern ice front when they merge with the main ice shelf flow that originates further upstream.

From the English Coast, eight tributary glaciers enter Stange Ice Shelf and deliver ice to each of the three ice fronts. Glacier ST02 enters the shelf near the boundary with George VI Ice Shelf to the east, at approximately -1715000 474000 m, and flows towards Spatz Island where it is forced through a narrow 8 km-wide channel and consequently influenced westwards. Eventually, ST02 merges with ST03 and flows for ~150 km to the northern ice front. Southwest of ST03, three larger tributary units, ST04, ST05 and Lidke Ice Stream, enter the shelf southeast of Benkert Mount. Their respective flow directions are diverted north-westerly as it enters the 35 km-wide channel between the tip of Benkert Mount and Spatz Island, impinging upon flow from ST02 and ST03 at the centre of this channel. Ice from ST04, ST05 and Lidke Ice Stream merges promptly as it enters the ice shelf, and flows collectively into the centre of the ice shelf as a single unit. As it rounds the headland of Benkert Mount, the ice mass flows towards the mid ice front and eventually converges with ice from Smyley Island. Ice fed into Stange Ice Shelf from these three flow units can be traced downstream for up to 108 km from their respective grounding zones.

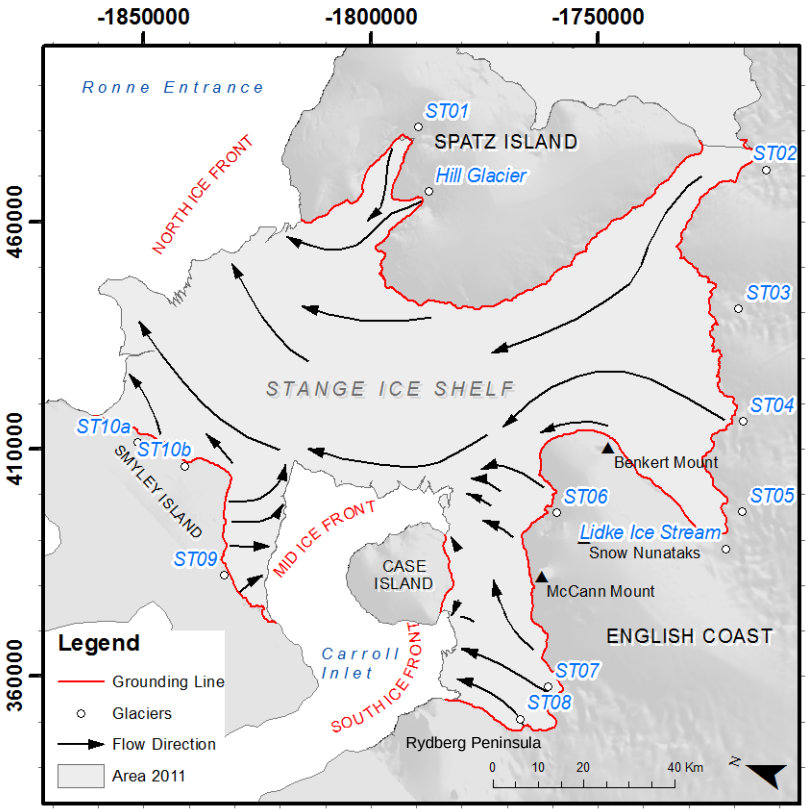

Figure 8.2. Surface flow directions of Stange Ice Shelf inferred from composite surface feature tracking calculations. Notice the dominant northward flow of tributary glaciers from the English Coast to the south, mid and north ice fronts.

North of Snow Nunataks, smaller tributary systems enter the ice shelf from the English Coast, but their advance is prohibited by Case Island. Flow is principally diverted northeast from ST06 where ice pushes against the main channel of flow from Lidke Ice Stream. Southwest of Case Island, two glacier systems enter Stange Ice Shelf simultaneously, one fed by ice flowing off Rydberg Peninsula and the other originating from the English Coast. These glaciers merge at the grounding line and flow predominantly towards the south ice front in Carroll Inlet, situated between Rydberg Peninsula and Case Island. Glacier ice from ST07 also influences the north-eastern flow of shelf ice between Case Island and McCann Mount.

Finally, two units flow off Smyley Island and distribute ice to the mid and north ice fronts. ST09 is a wide flow unit (~25 km) covering much of the south-eastern coast of Smyley Island, but only extends out between 4-11 km to the mid ice front. At -1832000 393900 m, flow from ST09 diverts easterly and impinges upon ice originating from Lidke Ice Stream, and is consequently forced north by the larger flow unit. ST10a and ST10b also enter Stange Ice Shelf off Smyley Island. Flow from these tributary glaciers enters the shelf in an

easterly direction, but is soon directed towards the northern ice front along a zone of confluence between the main shelf ice and that off Smyley Island.

8.1.1.2 Surface velocities and surface velocity changes, 1986-2011

The 12 tributary glaciers of Stange Ice Shelf contribute to a dynamic regime that can be divided into four distinct zones (Figure 8.3A). Circa 1989, Zone 1 displayed surface velocities of between 50-200 ma^{-1}, with the highest speeds calculated in the central portions of the northern ice front, and the lowest typically along the grounding lines and as flow unit ST09 merges with ice in the main shelf. In Zone 2, flow speeds range from ~180 to 275 ma^{-1} in ice that was fed by the tributary glaciers from the English Coast. The fastest recorded speeds are associated with ice that flowed out from the Lidke Ice Stream (275 ma^{-1}). Zone 3 is made up of slow-moving ice fed principally by ST06 and steady sheet flow off the adjacent headland. Surface speeds average ~80 ma^{-1} in this zone, with the highest observed at the confluence of ST06 and Lidke Ice Stream (Zone 2/ Zone 3). There is a sharp transition between Zone 3 and Zone 4, with surface speeds in the latter measured at >1000 ma^{-1}. At -1782500 368100 m along the south ice front, flow speeds reached ~1150 ma^{-1} in ice fed by ST07.

A similar situation was also observed ca. 2004 (Figure 8.3B). Flow speeds in Zone 1 were fastest in the central regions of the northern ice front, with a maximum speed of ~200 ma^{-1} recorded. Zone 2 likewise was a faster zone of ice flow. Between 2001 and 2004, flow calculations from the grounding zone reveal the dominant flow of each of the tributary glaciers from the English Coast, in particular the Lidke Ice Stream where the fastest velocities were recorded in this zone (511 ma^{-1}). Along the confluence of ST02 and ST03, there was a clear difference in flow speeds that could be followed for ~60 km before flow appeared to stabilise (Figure 8.3B). There are few observed differences in the flow regimes of Zone 3 and Zone 4 over time.

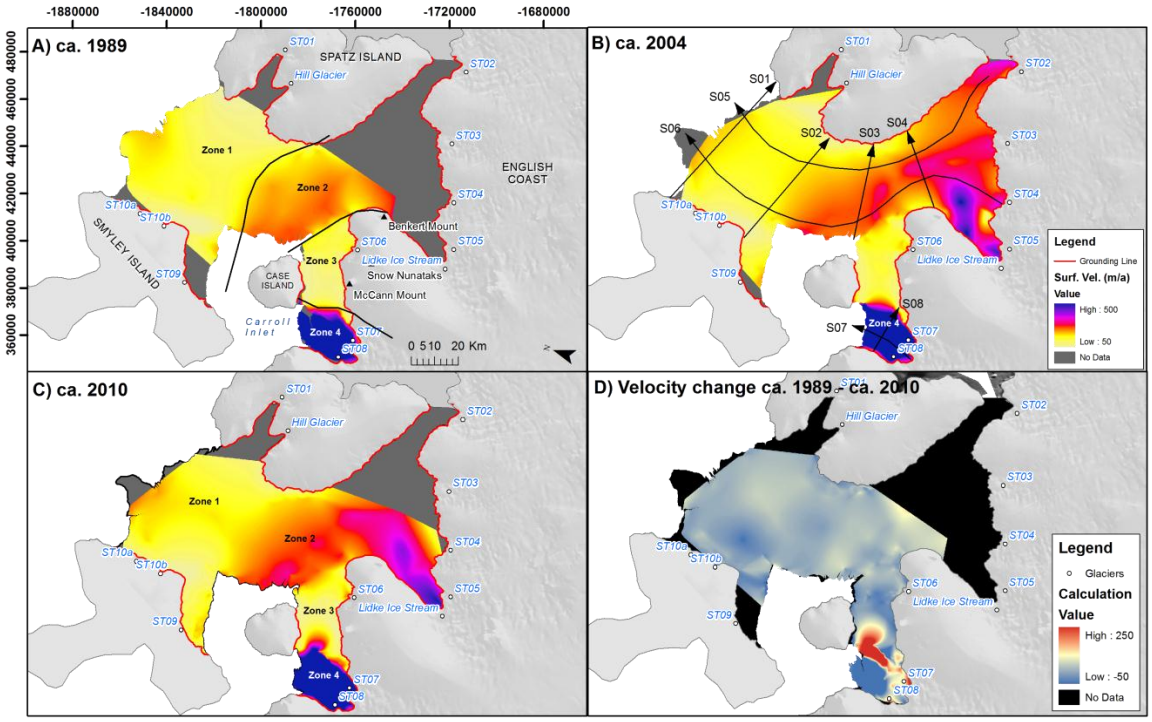

Figure 8.3. Feature tracking surface velocities calculated for A) ca. 1989, B) ca. 2004 and C) ca. 2010. Overall change from ca. 1989 and ca. 2010 is shown in (D). Note the dominance of Lidke Ice Stream, ST07 and ST08 on the overall dynamic regime of Stange Ice Shelf. Annotated zones (in A) refer to distinct dynamic regimes of Stange Ice Shelf and are discussed in the main text. Transect statistics are displayed in Table 8.2 with plots available in Appendix 3a.

Ca. 2010, the four dynamic zones are still distinguishable, with flow speeds in Zone 1 ranging from 50-230 ma^{-1}, increasing at the northern ice front by ~30 ma^{-1}. Zone 2 is again characterised by the Lidke Ice Stream, with a clearly defined flow unit, reaching speeds of ~500 ma^{-1} in the centre of the respective ice stream. Speeds at the mid ice front reach a maximum of 275 ma^{-1}. The fast-flowing ice in Zone 4 is maintained, and is beginning to encroach into the western edge of Zone 3. Changes in surface velocities between ca. 1988, ca. 2004 and ca. 2010 are analysed further along eight transects across Stange Ice Shelf (Figure 8.3B and Table 8.2).

Table 8.2. Summary statistics for Stange Ice Shelf surface-speed transects. Statistics refer to transects illustrated in Figures 8.3B and data presented in Appendix 3a.

Transect	Minimum (ma^{-1})			Maximum (ma^{-1})			Mean (ma^{-1})		
	Ca. 1989	Ca. 2004	Ca. 2010	Ca. 1989	Ca. 2004	Ca. 2010	Ca. 1989	Ca. 2004	Ca. 2010
S01	81	109	136	178	190	210	147	175	181
S02	15	39	51	145	176	170	109	137	124
S03	86	74	133	249	255	275	210	220	239
S04	221	171	208	232	310	324	226	234	279
S05	103	152	141	197	297	262	144	208	187
S06	116	126	106	252	375	336	190	233	226
S07	386	356	385	1024	875	903	828	766	774
S08	88	86	125	979	830	819	665	640	622

Transects S01, S02, S03 and S04 (see Figure 8.3, Table 8.2, Appendix 3a) are taken from the central regions of Stange Ice Shelf from ice fed predominantly from the English Coast and Spatz Island tributary glaciers. Along each of these transects, speeds calculated ca. 1989 are generally lower than those calculated ca. 2004 and ca. 2010, although (with the exception of S04) the increase is within the calculated uncertainties. Similarly, along transects S01, S03 and S04, surface speeds ca. 2004 are generally lower than those calculated between 2008 and 2011, but again are considered non-significant with respect to the uncertainties. Only along transect S03 are surface speeds ca. 2004 greater than ca. 2010. Along transect S01 across the northern ice front, flow velocities increase with distance towards the centre of the ice shelf from both grounding zones.

Data extracted along transect S02 reveal a similar pattern across the shelf (Table 8.2), with speeds at the Smyley Island grounding zone reducing from between 50-90 ma^{-1} to 10-50 ma^{-1} at the confluence of ST09 with ice in the central portions of the ice shelf. Flow speeds increase towards the centre of Stange Ice Shelf, before rapidly reducing to ~50-70 ma^{-1} at the Spatz Island grounding zone. There is a clear increase in surface speed between ca. 1989 and ca. 2010 (Table 8.2). Between ca. 2004 and ca. 2010, a slight decrease in surface speed was recorded along much of the transect, but generally remaining higher than those during ca. 1989 with the exception of a ~5 km stretch between 11 and 16 km along the transect.

Along transect S03, flow speeds gradually decrease from the mid ice front towards Spatz Island in all three observation periods, with the lowest speeds always recorded at the grounding line. With the exception of a 5 km stretch at either end of the transect, where velocities between time periods fluctuate, there is a general increase in surface speeds from ca. 1989 to ca. 2004 and again to ca. 2010 (Table 8.2). Along transect S04, surface speeds during ca.1989 flow at ~220 ma^{-1} along the first 13 km of the transect before a poor distribution of data points inhibits interpolation. In this same 13 km stretch, surface speeds between ca. 2004 and ca. 2010 differ greatly, with a linear increase in velocity observed from the English Coast grounding line to ~18 km in the former time period, and a steady flow regime observed in the latter. From 18 km along the transect towards the Smyley Island grounding line, flow patterns and speeds between both time periods are very similar, peaking at ~ 250 ma^{-1} before gradually decreasing.

Transects S05 and S06 (see Figure 8.3, Table 8.2, Appendix 3a) are taken longitudinally along Stange Ice Shelf from Stange tributaries ST02 and ST04 respectively. Ca. 2004, flow

speeds were calculated at 300 ma^{-1} from the English Coast grounding zone, decreasing steadily to ~250 ma^{-1} at 50 km along the transect. From here to the northern ice front, speeds decreased to ~200 ma^{-1}. A similar pattern is observed along the same transects from 50 km to the ice front ca. 2010, with a similar pattern also observed ca. 1989, but with lower surface velocities extracted along the whole transect. For transects S05 and S06, any changes are considered non-significant as they fall within the calculated uncertainty.

Surface speeds extracted from S06 fluctuate along the transect as ice flows from glacier ST04 into the centre of the ice shelf, although the overall surface speed decreases from ~350 ma^{-1} near the input of ST04 to ~100 ma^{-1} in the centre of the ice shelf, increasing to ~200 ma^{-1} at the northern ice front. There is little difference in the surface speeds calculated for all three time periods along most of the S06 velocity transect.

Transects S07 and S08 (Table 8.2) are extracted from the south ice front, with S07 along flow, and S08 transverse to flow from Rydberg Peninsula grounding zone to the main English Coast grounding zone. Flow speeds along S07 increase rapidly along the transect from ~400 ma^{-1} at the grounding line to >850 ma^{-1} within 10 km. From here, a slight decrease in surface speed was observed between all three time periods (Table 8.2) that is greater than the calculated uncertainty. Changes along transect S07 differ from previous transects; the fastest speeds (~1024 ma^{-1}) were observed ca. 1989, decreasing overtime to ca. 2004 and ca. 2010 (Table 8.2), with the greatest difference between ca. 1989 and ca. 2010 observed at 19 km along the transect.

Across the southern regions of Stange Ice Shelf, surface speeds rapidly increase from the Rydberg Peninsula towards the central part of the flow unit before reducing again towards the English Coast grounding line. Similar results between time periods are also observed here, with the fastest speeds extracted from the ca. 1989 data. One key difference illustrated by transect S08 is the width of the fast-flowing ice observed over time. Ca. 1989 and ca. 2004, the fastest speeds are generally confined to a 10 km channel, but ca. 2010, the channel width of fast-flowing ice is measured at ~15 km, despite a lower maximum surface speed.

8.1.2 Stange Ice Shelf spatial extent

The areal extent of Stange Ice Shelf has been calculated over five individual periods between 1973 and 2011 using a combination of Landsat and ERS-2 SAR imagery (Figure 8.4, Figure 8.5, Table 8.3). First, an overview of the spatial changes is discussed for the whole of Stange Ice Shelf, before each ice front is detailed individually.

Table 8.3. Spatial extent, net change, rate of change, percent loss and percent remaining for each of the observation periods.

Year	Area (km^2)	Net (km^2)	Rate (km^2a^{-1})	% Loss	% Remaining
1973	8256.36	N/A	N/A	0.00	100.00
1986	8102.47	-153.89	-11.78	1.86	98.14
1996	8008.39	-94.08	-9.41	3.00	97.00
2001	7899.66	-108.73	-18.78	4.32	95.68
2005	7889.07	-10.59	-2.63	4.45	95.55
2011	7918.40	29.33	5.75	4.09	95.91

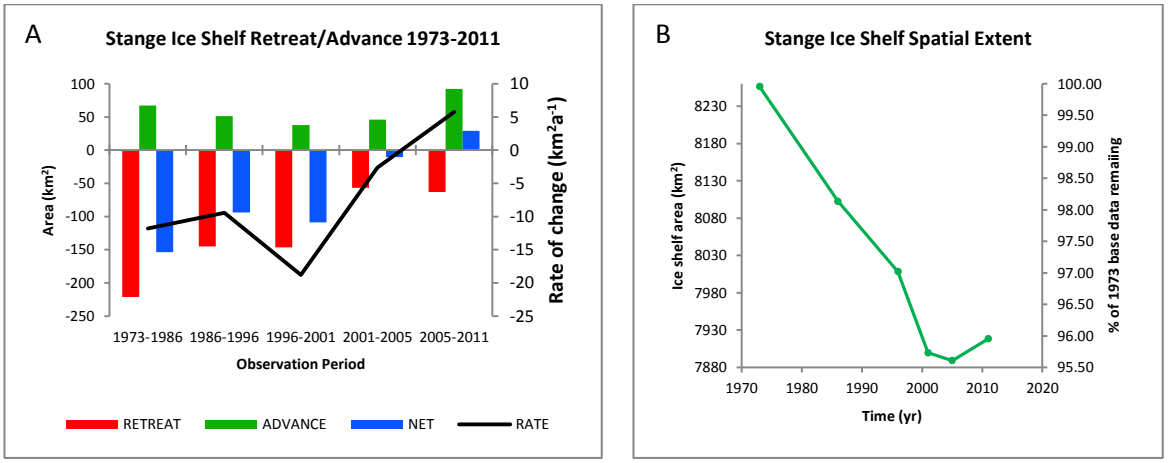

Figure 8.4. A) Areal changes calculated for the whole of Stange Ice Shelf from 1973 to 2011. B) Note the steady decrease in size between 1973 and 2001, followed by positive net changes between 2005 and 2011.

Between 1973 and 2011, Stange Ice Shelf underwent a net change of -337.96 km^2 (-4.09 %) from its three ice fronts, with the largest negative change recorded between 1973 and 1986 (-153.89 km^2) (Figure 8.4). An advance of the ice shelf was recorded in each of the observation periods, with the largest advance (92.34 km^2) occurring between 2005 and 2011, leading to a positive net change within that time period. During January 2011, ~96 % of the 1973 extent remained.

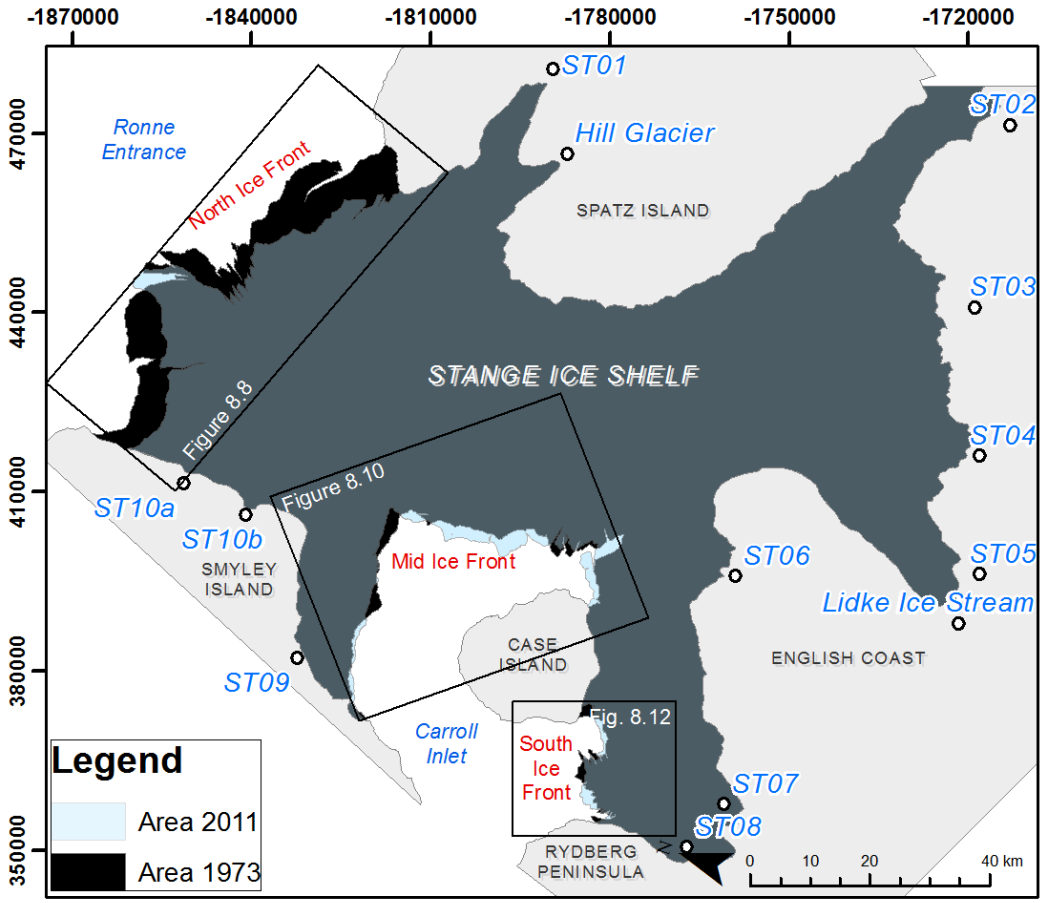

Figure 8.5. Stange Ice Shelf area for 1973 and 2011 illustrating that the majority of the retreat occurred at the northern ice front. The mid and south ice fronts underwent periods of advance and retreat with limited overall change. Rectangles illustrate positioning of Figure 8.7, Figure 8.9 and Figure 8.11 that detail the individual ice fronts in greater detail below.

8.1.2.1 North ice front

The northern ice front is fed by ice from Spatz Island, the English Coast and Smyley Island, making for a complex configuration that is reflected in the surface profile over time. The northern ice front always protrudes beyond its respective pinning points at Spatz Island and Smyley Island from 1973 to 2011. Towards Spatz Island, the ice front is often characterised by transverse fractures and rifts that form the basis for iceberg calving. The pinning point at Spatz Island retreated downstream by 8.15 km (linear) between 1973 and 2011, with it now positioned on the western tip of Spatz Island.

At -1842300 445900 m, the ice front is typified by a succession of at least eight longitudinal fractures/rifts that cut back into the ice shelf in each of the observation periods. Throughout time, the length of these fractures reduces as calving is initiated along the lines of weakness. Immediately adjacent of this, a section of ice shelf protrudes out into

the Ronne Entrance. This feature is maintained over time, whilst the area which it covers reduces. At Smyley Island, the grounding line retreated 6.65 km (linear).

The amount of ice lost at the northern ice front generally reduces over time, although a slight increase was noted between 1996 and 2001; a minimal amount (up to 19.94 km^2) of advance was recorded in each period (Table 8.4). With this retreat, the channel width in which the ice front was situated reduced from 69.51 to 63.18 km, whilst the length of the profile reduced from 160.97 km to 144.32 km. The shortest profile length was observed in February 1996 (110.96 km).

Table 8.4. Spatial changes of Stange Ice Shelf north ice front 1973-2011. Rate of loss calculated based on number of dates between images and extrapolated to km^2a^{-1}. Data presented in Figure 8.6 and Figure 8.7.

Year	Areal retreat (km^2)	Advance (km^2)	Net (km^2)	Rate of advance/ retreat (km^2a^{-1})
1973	N/A	N/A	N/A	N/A
1986	-184.21	10.10	-174.11	-13.34
1996	-70.25	19.94	-50.31	-5.04
2001	-89.96	5.70	-84.26	-14.57
2005	-44.82	6.97	-37.85	-9.39
2011	-52.36	14.92	-37.44	-7.34

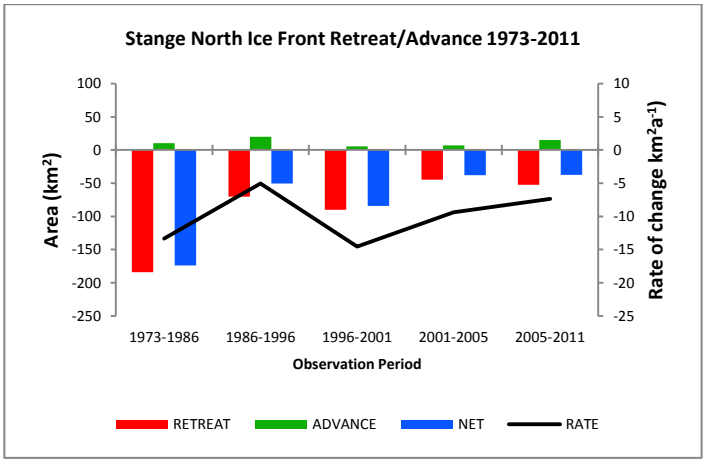

Figure 8.6. Retreat and advance observed at the northern ice front between 1973-86 and 2005-11, with rate of change calculated for 1973-2011. The north ice front consistently shows net loss, with limited advance of the ice front between each of the observation periods.

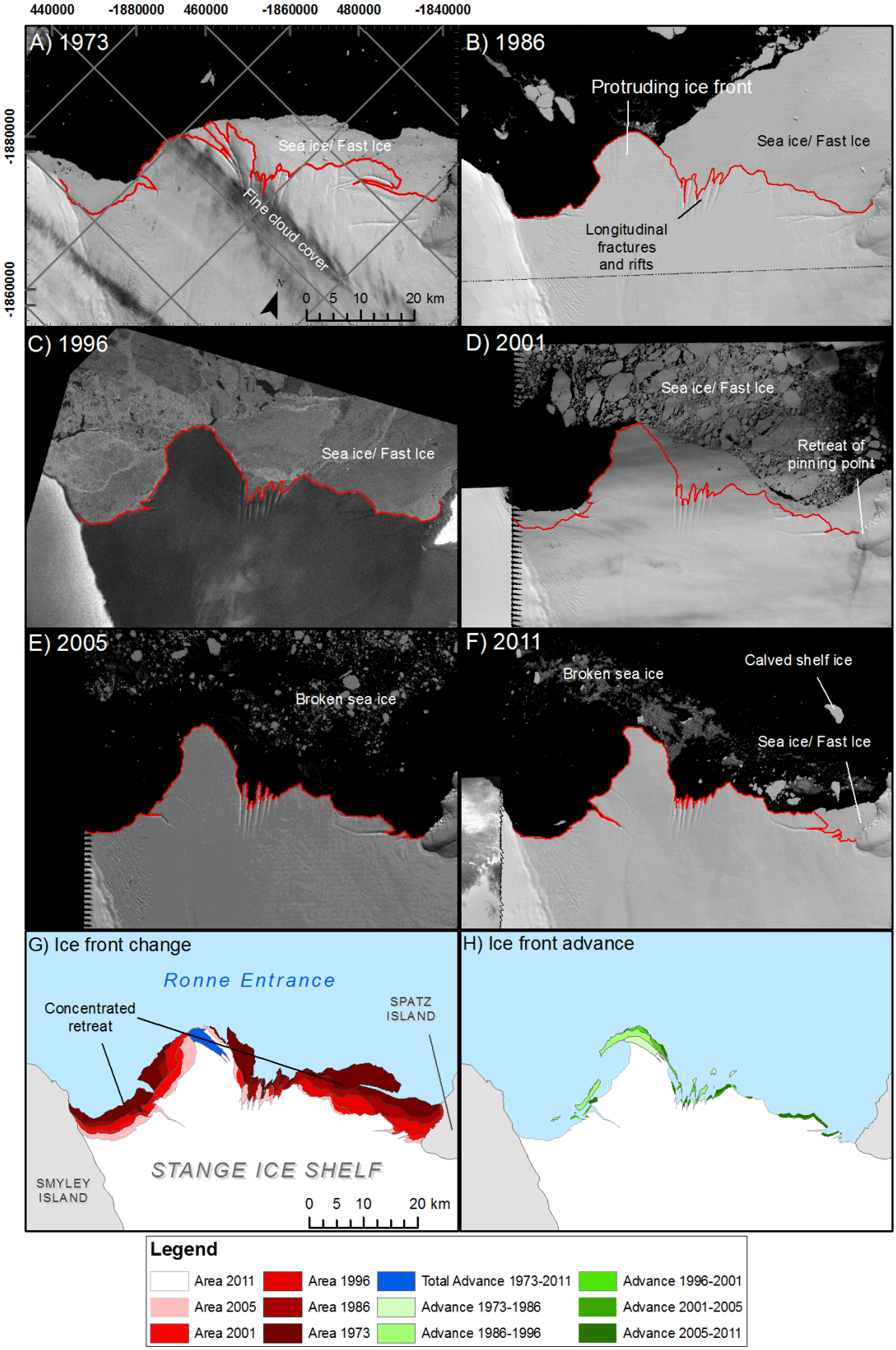

Figure 8.7. Stange Ice Shelf north ice front positions from 1973 to 2011 (A-F) as discussed in Table 8.4. G) Changes in ice front positions highlighting the predominant retreat of ice with limited advance. H) Advance recorded in individual observation periods. Note some of this advance was removed by subsequent retreat in the following years.

Table 8.5. Detailed description of Stange Ice Shelf north ice front from 1973 to 2011 corresponding to Figure 8.6.

Date	Spatz Is. (X/Y) (m)	Smyley Is. (X/Y) (m)	Channel Width (km)	Profile Length (km)	Loss (km^2)	Gain (km^2)	Net (km^2)	Comments
29 Jan 1973	-1818278.5/ 467431.8	-1869937.1/ 420816.4	69.51	160.97	N/A	N/A	N/A	Rifts and fractures cut back into the ice shelf along the northern margin. Generally, the ice-front profile protruded beyond its pinning points at the margins. Sea ice was connected to the ice front along the profile, with calved blocks held in-situ along its length. Ronne Entrance was largely free of sea ice.
18 Feb 1986	-1817685.0/ 467396.9	-1863653.5/ 418922.0	66.77	118.42	-184.21	10.10	-174.11	Ice-front profile protruded beyond its pinning points at the margins. Sea ice was connected to the ice front towards the eastern portions of the ice front.
14 Feb 1996	-1817789.8/ 467868.1	-1863072.0/ 418715.6	66.80	110.96	-70.25	19.94	-50.31	Ice front continued to protrude beyond its pinning points. Fracturing sea ice occupied Ronne Entrance along the northern ice front.
27 Nov 2001	-1815608.0/ 461724.4	-1862771.9/ 418640.6	63.87	126.49	-89.96	5.70	-84.26	Retreat of Spatz Island pinning point 7.5 km along the coast; Smyley Island pinning point remained stable. Despite net retreat, the ice front profile remained similar. Ronne Entrance filled with heavily fractures and unconsolidated pallets of sea ice.
8 Dec 2005	-1815468.4/ 461427.6	-1860427.1/ 417984.1	62.64	130.88	-44.82	6.97	-37.85	Sea ice connected to the ice front along the length of its profile. Ronne Entrance filled with heavily fractured and unconsolidated pallets of sea ice.
14 Jan 2011	-1815241.5/ 460607.3	-1861383.8/ 417402.6	63.18	144.32	-52.36	14.92	-37.44	Ice front protruded beyond its pinning points. Fractured, non-uniform pallets of sea ice scattered across Ronne Entrance. Fractures and rifts continued to develop along the ice front.

8.1.2.2 Mid ice front

The mid ice front is of complex formation and consists of ice fed from tributary glaciers off Smyley Island and the English Coast that merge at -1815000 406300 m. There is also a distinct confluence between ice that flows out of Lidke Ice Stream and ST06. Altogether, these systems produce three parts to the mid ice front that flow into the northern-most section of Carroll Inlet.

Extensive and largely consolidated sea ice was present in each of the observation periods in front of the mid ice front. During February 1996, the whole of Carroll Inlet was covered in sea ice containing few angular, tabular icebergs. This was the greatest observed extent of sea ice observed over time, with the least observed during December 2005, where active fracturing of this ice was captured in Landsat TM imagery. During January 2011, a more extensive area of open water was observed at -1795500 395500 m, although smaller regions are also observed in February 1986 and November 2001.

The pinning point along Smyley Island fluctuated overtime, but retreated in total by only 0.96 km between 1973 and 2011 whilst the Case Island pinning point advanced only 0.54 km over the same time period. Only during 1986 to 1996 was a negative change along the mid ice front calculated (-39.12 km^2), with net positive changes observed elsewhere. Advance and retreat occurred across the whole mid ice front, with greater advances recorded along the Lidke Ice Stream-fed region.

Table 8.6. Spatial changes of Stange Ice Shelf mid ice front 1973-2011. Rate of loss calculated based on number of dates between images and extrapolated to km^2a^{-1}. Data presented in Figure 8.8 and Figure 8.9.

Year	Areal retreat (km^2)	Advance (km^2)	Net (km^2)	Rate of advance/ retreat (km^2a^{-1})
1973	N/A	N/A	N/A	N/A
1986	-19.22	44.94	25.72	1.97
1996	-59.53	20.41	-39.12	-3.92
2001	-8.91	29.08	20.17	3.49
2005	-6.66	21.43	14.77	3.66
2011	-9.42	33.10	23.68	4.64

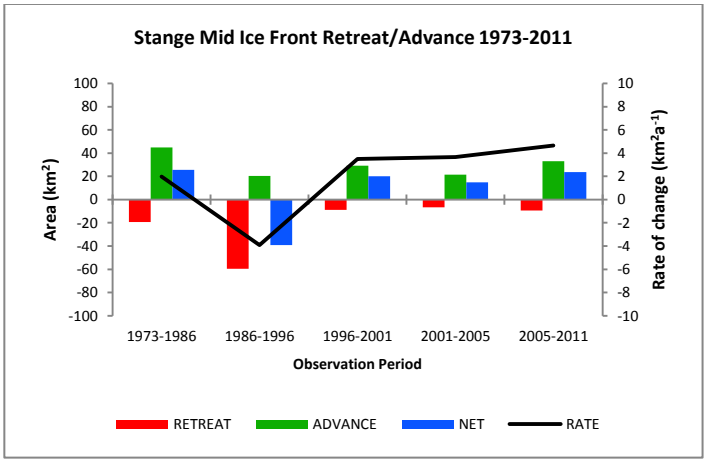

Figure 8.8. Retreat and advance observed at the mid ice front between 1973/86 and 2005/11. The mid ice front experiences net advance in four of the five observation periods, with a net loss recorded between 1986-1996. The rate of change thus represents the mostly-positive change at the mid ice front.

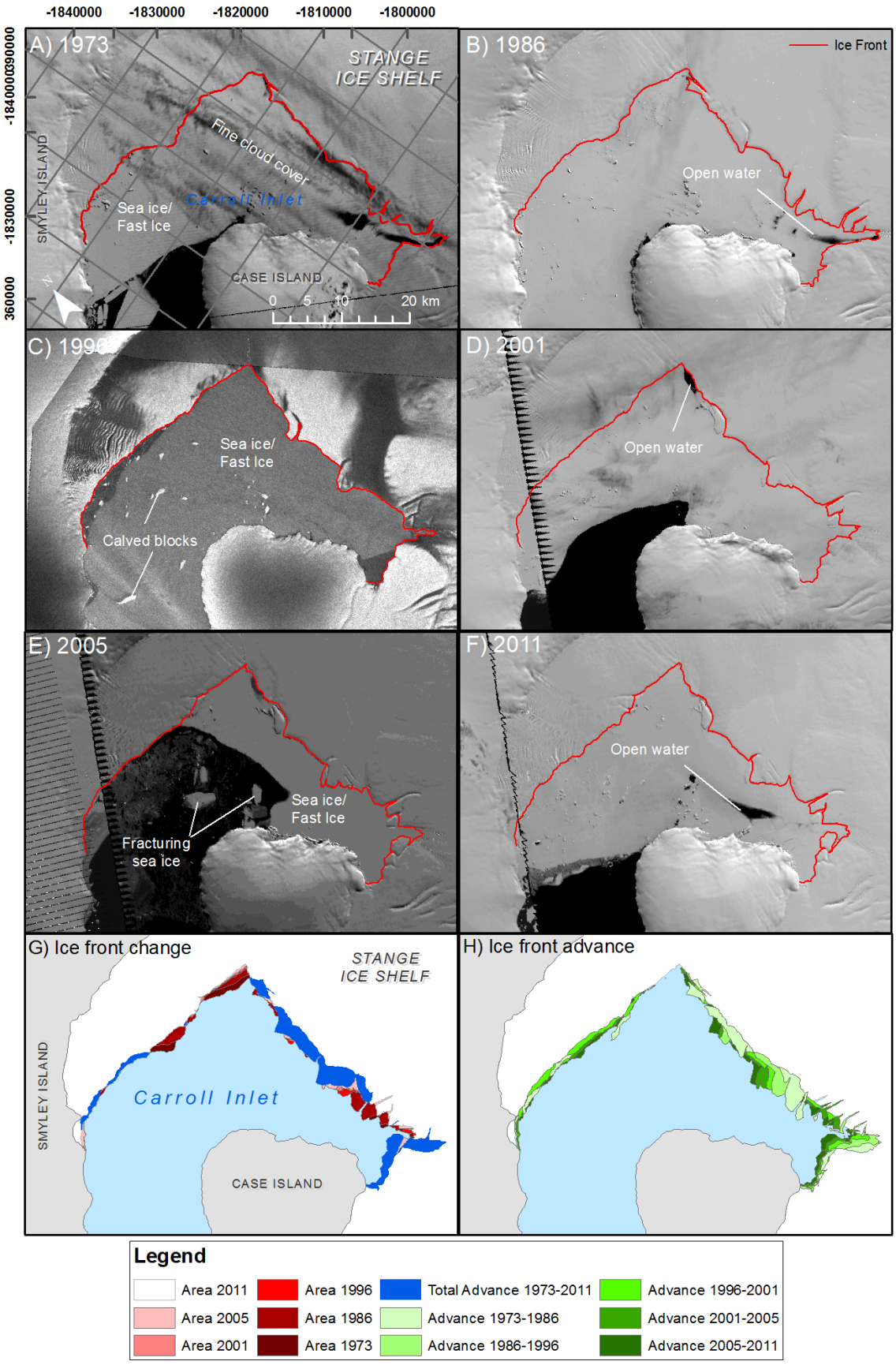

Figure 8.9. Stange Ice Shelf mid ice front positions from 1973 to 2011 (A-F) as discussed in Table 8.5. G) Changes in ice front positions highlighting the limited net change. H) Advance recorded in individual observation periods. Note some of this advance was removed by subsequent retreat in the following years.

Table 8.7. Detailed description of Stange Ice Shelf mid ice front from 1973 to 2011 corresponding to Figure 8.8.

Date	Smyley Is. (X/Y) (m)	Case Is. (X/Y) (m)	Channel Width (km)	Profile Length (km)	Loss (km^2)	Gain (km^2)	Net (km^2)	Comments
29 Jan 1973	-1820780.8/ 371780.3	-1783470.8/ 390927.8	41.87	119.27	N/A	N/A	N/A	Little observed changes in the location of pinning points along Smyley Island or Case Island. Fractures and rifts along the frontal profile permit regular, small-scale calving, but indistinct patterns of advance/retreat. Uniform and largely consolidated sea ice is observed in all observation periods between Smyley Island and Case Island. Calved blocks held in-situ within the sea ice rarely occupied an area > 1 km^2.
18 Feb 1986	-1821447.8/ 373069.7	-1783480.6/ 390776.1	41.83	139.36	-19.22	44.94	25.72	
14 Feb 1996	-1820025.0/ 371513.5	-1783695.0/ 391053.1	41.24	105.42	-59.53	20.41	-39.12	
27 Nov 2001	-1820336.2/ 371646.9	-1783925.9/ 391158.6	41.33	107.93	-8.91	29.08	20.17	
8 Dec 2005	-1819758.2/ 371157.8	-1783906.1/ 391185.0	41.12	111.01	-6.66	21.43	14.77	
14 Jan 2011	-1820869.8/ 371780.3	-1783906.1/ 391171.8	41.77	120.14	-9.42	33.10	23.68	

8.1.2.3 South ice front

The south ice front of Stange Ice Shelf occupies a narrow channel between Case Island and Rydberg Peninsula and terminates in Carroll Inlet. This region is the most dynamic region of the ice shelf, and is characterised by a rapidly changing ice front overtime. The south ice front undergoes cycles of advance and retreat, with dynamically driven advance offset by periodic large-scale calving, observed between 1996 and 2001.

Table 8.8. Spatial changes of Stange Ice Shelf south ice front 1973-2011. Rate of loss calculated based on number of dates between images and extrapolated to km^2a^{-1}. Data presented in Figure 8.10 and Figure 8.11.

Year	Areal retreat (km^2)	Advance (km^2)	Net (km^2)	Rate of advance/ retreat (km^2a^{-1})
1973	N/A	N/A	N/A	N/A
1986	-17.74	12.24	-5.50	-0.42
1996	-15.45	10.8	-4.65	-0.47
2001	-47.48	2.84	-44.64	-7.72
2005	-5.18	17.67	12.49	3.10
2011	-1.23	44.32	43.09	8.45

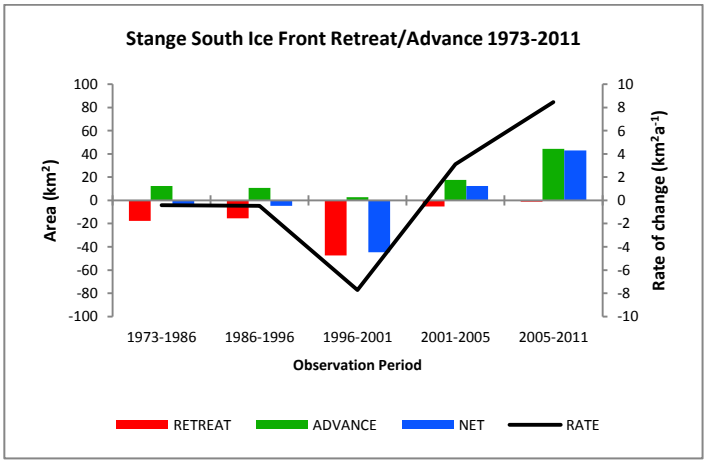

Figure 8.10. Retreat and advance observed at the south ice front between 1973/86 and 2005/11. Minimal net loss was observed from 1973 to 1986 and 1986 to 1996, with the greatest loss recorded between 1996 and 2003. Positive net change observed between 2001 and 2005, and 2005 to 2011. Since 2001, the south ice front has experienced net gain.

Between 1973 and 2011, a net change of only 0.79 km^2 was observed at the southern ice front. The greatest net loss was calculated for the period 1996 to 2001 (-44.64 km^2), with the greatest net gain observed between 2005 and 2011 (43.09 km^2). Between 1973-86, 1986-96 and 2001-05, little change was observed in the spatial extent of the southern ice

front. There was little change in the location of the Rydberg Peninsula (English Coast) grounding line, whilst the Case Island pinning point retreated 2.25 km (linear). Overall, the occupied channel width increased from 16.69 km to 18.95 km, whilst the profile length of the ice front fluctuated between 52.48 km (Jan 1973) and 31 km (Nov 2001).

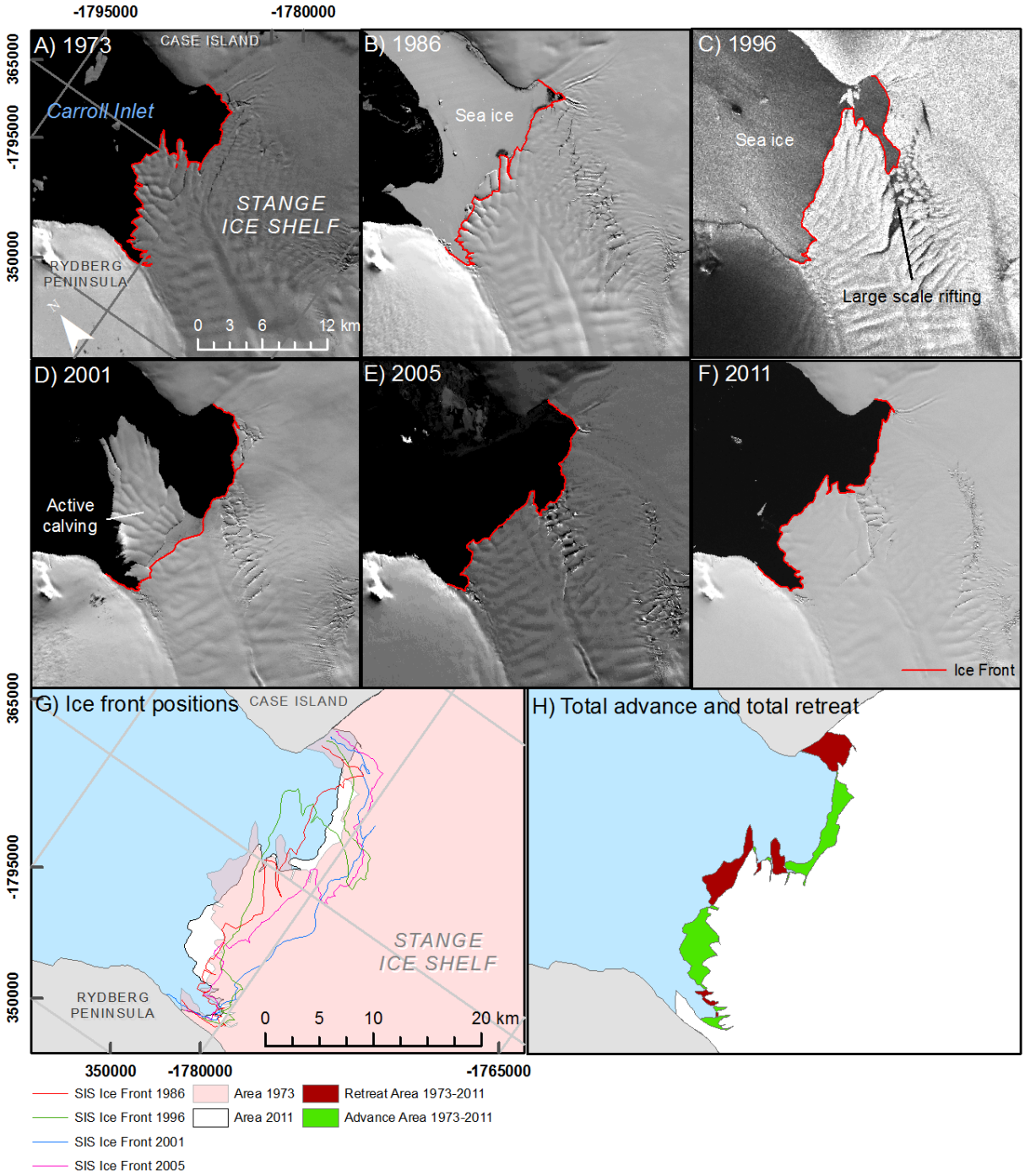

Figure 8.11. Stange Ice Shelf south ice front positions from 1973 to 2011 (A-F) as discussed in Table 8.9. G) Changes in ice front positions highlighting the fluctuating ice front over time. H) Total advance and retreat recorded in individual observation periods.

Table 8.9. Detailed description of Stange Ice Shelf south ice front from 1973 to 2011 corresponding to Figure 8.11.

Date	Case Is. (X/Y) (m)	English Coast (X/Y) (m)	Channel Width (km)	Profile Length (km)	Loss (km^2)	Gain (km^2)	Net (km^2)	Comments
29 Jan 1973	-1784494.3/ 372476.7	-1783293.7/ 355840.8	16.69	52.48	N/A	N/A	N/A	Eastern portion of southern ice front concave in appearance; western portion protruded beyond pinning points. Fractures and rifts visible along frontal profile. Calved blocks observed in front of ice shelf <3 km^2 in size in Carroll Inlet.
18 Feb 1986	-1784694.4/ 372819.7	-1782807.8/ 355183.34	17.70	39.08	-17.74	12.24	-5.50	Pinning point locations retreated 0.9 km and 1.5 km at Case Island and Rydberg Peninsula. Carroll Inlet occupied by consolidated sea ice with few small icebergs observed.
14 Feb 1996	-1784608.6/ 373219.9	-1781121.3/ 355011.8	18.57	41.56	-15.45	10.80	-4.65	Heavy fracturing and rifting of ice front observed. Calved blocks located behind the ice front surrounded by open water. Carroll Inlet occupied by extensive sea ice with few calved icebergs observed.
27 Nov 2001	-1784551.4/ 373562.9	-1783722.5/ 354926.1	18.71	31.98	-47.48	2.84	-44.64	Ice front occupies a concave profile along its length. Large tabular iceberg observed calving from the ice front into the ice-free Carroll Inlet. Fracturing and rifting observed along the ice front. Little change in the location of the pinning points since previous observation.
2 Feb 2005	-1784437.1/ 374048.8	-1782207.5/ 354783.2	19.34	34.67	-5.18	17.67	12.49	Advance of the western portion of the southern ice front despite both pinning points remaining stable. Rifting observed along flow-unit boundary where advance is located. Carroll Inlet free of sea ice and contained few icebergs.
14 Jan 2011	-1784808.7/ 374048.8	-1784751.5/ 355126.2	18.95	40.91	-1.23	44.32	43.09	Continued advance across the whole ice-front profile. Pinning points remained stable. Carroll Inlet free of sea ice.

8.1.3 Stange Ice Shelf structural overview

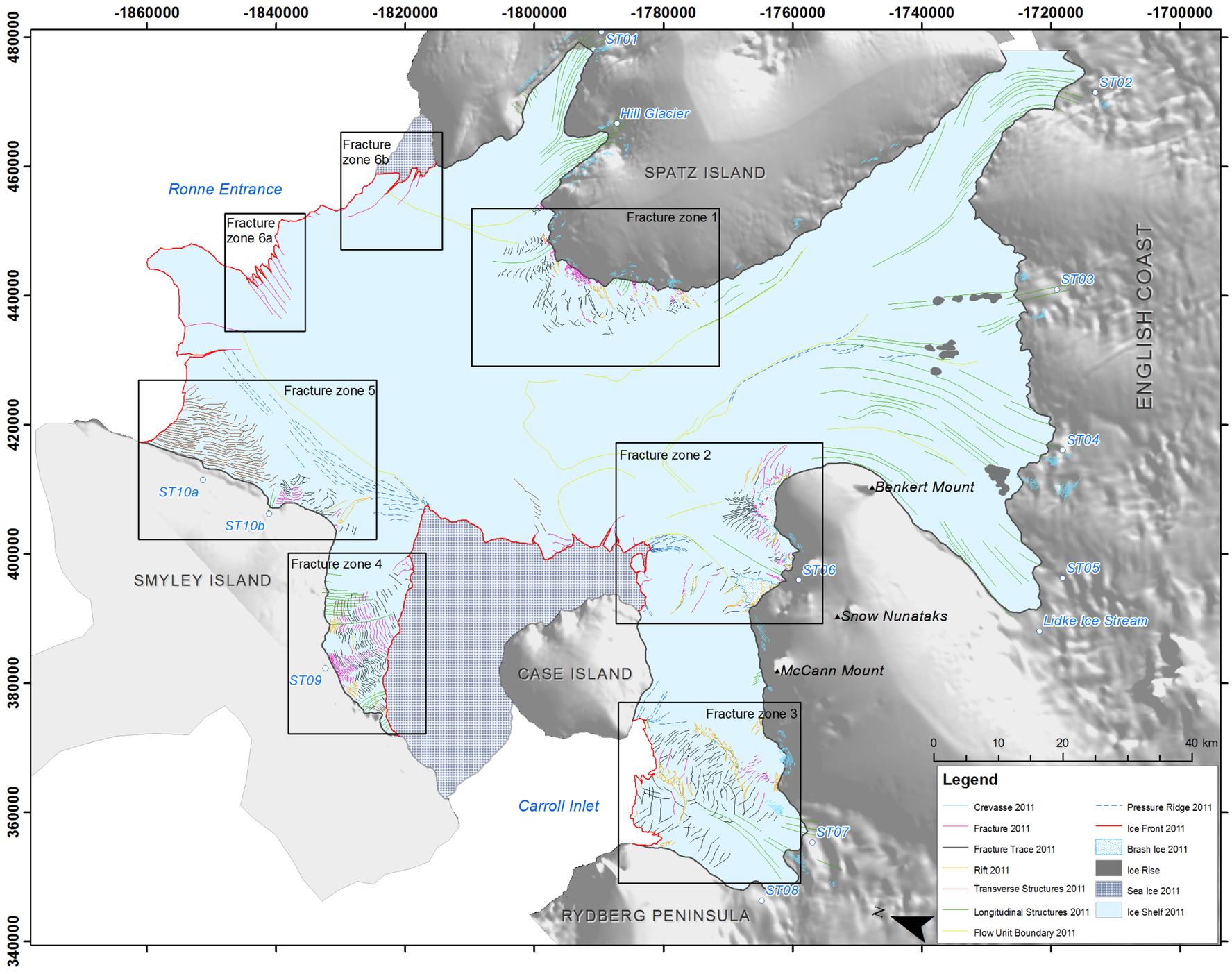

Figure 8.12. Structural overview of Stange Ice Shelf from 2011. Fractures, rifts and fracture traces exist in six main fracture zones across the ice shelf (discussed in Section 8.1.3.3). Generally, only longitudinal features, pressure ridges and flow-unit boundary-related features are observed outside of these zones.

Surface structures and surface features of Stange Ice Shelf have been mapped using Landsat satellite imagery from 1973, 1986, 2001, 2005 and 2011. A detailed overview of these structures and features is first presented with respect to those observed during January 2011 (Figure 8.12). Consequently, major changes in surface structures and surface features are detailed.

8.1.3.1 Longitudinal Structures

Longitudinal structures principally form in ice flowing from the English Coast tributary glaciers, and run parallel with the main flow direction. They originate at the confluence of ice shelf tributary glacier systems, but they are more apparent at the grounding line of ST02, ST03, ST04, ST05 and the Lidke Ice Stream. Thus, based on previous discussions (Chapter 6.1, Chapter 7.1), the longitudinal features on Stange Ice Shelf are principally Type 2 and Type 3 structures, with no distinct Type 1 (formed at the confluence of grounded features) recognised. Furthermore, there is no evidence for splaying of these longitudinal structures on the ice shelf and as a result they maintain their linear appearance down ice. The clearest longitudinal features flowing from the English Coast can be traced down ice for up to 25 km before becoming indistinct from the surrounding ice.

Well defined, but shorter (~15 km), groups of longitudinal structures are also observed in ice that flows out from ST01 and Hill Glacier. These longitudinal structures originate on grounded ice and are transmitted over the grounding line onto the ice shelf surface. Similar features measuring no more than 8 km are visible in ice flowing off Smyley Island, but their clarity is hindered by excessive surface fracturing in this region. Finally, longitudinal structures are also observed flowing towards the southern ice front from ST07 and ST08. Such features display no splaying characteristics as they enter the ice shelf or are transmitted down ice.

8.1.3.2 Flow Unit Boundaries

Distinct flow unit boundaries have been identified at nine locations on Stange Ice Shelf. The clearest of these features is observed either end of the main flow channel of ST02 and at the confluence of the larger flow units from the English Coast. Of particular interest are the three deformed features observed in the centre of the shelf in ice forming at the northern boundaries of ST02 and in ice at the confluence of ST03 and ST04 in two locations (-1795700 406100 m and -1778500 412700 m) (Figure 8.13); the fold hinges deform ~ 90° compared to present flow directions.

Flow unit boundaries are also observed between flow units ST07 and ST08 and the main channel of flow and Hill Glacier flowing off Spatz Island. Furthermore, there is a distinct feature along the confluence of ice flowing from Smyley Island and that of the main shelf that can be traced for up to 40 km parallel to the principal flow direction.

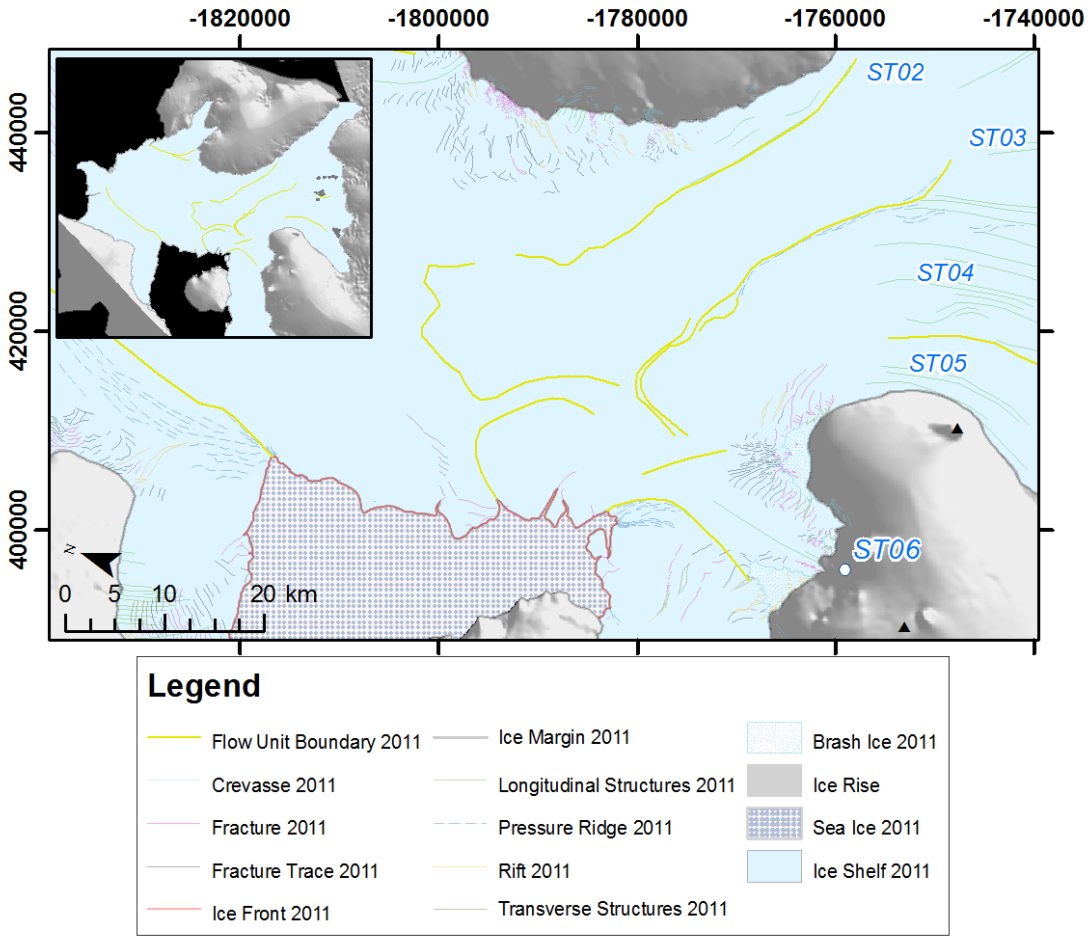

Figure 8.13. Deformed flow unit boundaries in the centre of Stange Ice Shelf forming at the boundaries of ST02/ST03 with ice to the north (-1801400 419200 m) and at the confluence of ST03 and ST04 in two locations towards the mid ice front (-1795700 406100 m and -1778500 412700 m). Other distinct boundaries are observed between ST04 and ST05, ST05 with ST06 and between ST06 and ice to its west.

8.1.3.4 Pressure Ridges

Distinct surface pressure ridges form in four locations on the surface of Stange Ice Shelf. First, pressure ridges exist along the flow unit boundary between ST03 and ST04, 2 km down ice from a series of ice rumples. These pressure ridges are visible down ice for up to 35 km. Two smaller regions of pressure ridges exist at the confluence of ST06 and Lidke Ice Stream at the mid ice front, and as ice from ST07 impinges upon Case Island. In both of these situations, pressure ridges form transversely to the flow of ice in which they are

situated, and can be traced for up to 6.3 km. An elongated zone of pressure ridges also exists between Smyley Island-fed ice and that of the main channel, following the pattern of the associated flow unit boundary.

8.1.3.3 Crevasses, fractures and rifts

Crevassing along the steep-sided slopes of Smyley Island and the English Coast is common, with numerous crevasse fields displaying complex, cross-cutting features. These are often, but not exclusively, linked to the large tributary glaciers. Open crevasses rarely cross the grounding zone, yet evidence of their existence is displayed as fracture traces on the ice-shelf surface.

Ice-shelf surface fractures and rifts exist in six distinct regions across Stange Ice Shelf. First, fractures and rifts develop along the grounding line of Spatz Island at -1787000 442500 m (Fracture zone 1, Figure 8.12) ranging from 1.5 km to 5.5 km in length. Their linearity becomes more apparent with increased distance travelled from their origin, and open rifts close to form fractures or fracture traces. Fractures and rifts also develop adjacent to flow unit ST06 (Fracture zone 2, Figure 8.12). Here, ice is heavily fractured, with rifts filled with unconsolidated, brash ice also apparent near to the grounding zone. These rifts generally seal with increased distance from the grounding line, but occasionally reopen as they approach the mid ice front (eg. -1776100 394000 m). Fractures created by the flow of ST06 are rarely greater than 5 km in length, and develop at regular 0.7 km intervals, particularly to the east of ST06.

At the south ice front (Fracture zone 3, Figure 8.12), the ice-shelf surface is dominated by complex formations of rifts, fractures and fracture traces. Transverse-to-flow features originate near to the grounding line and migrate with flow towards the south ice front where they become increasingly disorientated. During 2011, two clear zones of heavily rifted ice existed either side of ST07. To the east of ST07, rifts formed along the flow unit boundary and displayed a chaotic, non-uniform formation. Rifts are often filled with angular, calved blocks and brash ice giving a speckled and mixed appearance. A similar situation also exists within 8 km of the ice front between flow units ST07 and ST08. These rifts are again filled with chaotically fractured and calved ice blocks.

Ice that enters Stange Ice Shelf from Smyley Island is heavily fractured along much of its length in two zones displaying similar characteristics (Fracture zone 4 and Fracture zone 5, Figure 8.12). At the grounding line of ST09, fractures and/or rifts develop immediately at

regular, 0.3 km intervals transverse-to-flow. These features tend to deform and become more sinuous in appearance as they approach the mid ice front, particularly to the southern extent of ST09. Further north-west along ST09, fractures tend to remain linear in appearance but the distance between sequential features increases to a maximum of 0.65 km. At -1818800 398000 m, along the mid ice front, fractures form perpendicular to flow and cut back into the ice shelf. Overtime, calving is initiated at this point. Along the north-eastern facing coast of Smyley Island, excessive fracturing of the ice-shelf surface is also observed (Fracture zone 5), again forming at regular intervals, transverse to flow, with those fractures closest to the main channel of flow becoming increasingly deformed as ice nears the north ice front.

Finally, large surface fractures and rifts are observed along the north ice front in ice fed from the English Coast and Spatz Island (Fracture zone 6a and Fracture zone 6b, Figure 8.12). At -1842000 444800 m, eight fractures measuring no more than 8 km in length cut back longitudinally into the ice shelf at regular intervals over a 7.4 km section of ice front. To the east of these, transverse fractures characterise the north ice front near to Spatz Island.

8.1.4 Structural changes and structural evolution on Stange Ice Shelf

Five structural maps have been compiled for the whole of Stange Ice Shelf for January 1973, February 1986, November 2001, December 2005 and January 2011, to assess the long-term evolution of surface structures, with further maps produced for the south ice front for March 2004, January 2006, December 2006 and December 2010 to analyse the localised short term structural changes. Few surface structural changes are observed over much of the ice shelf between 1973 and 2011, thus the below sections concentrate solely on the northern and mid ice fronts and the southern section of Stange Ice Shelf.

8.1.4.1 Structural changes and structural evolution at the north ice front

The structural evolution at the north ice front is gradual (Figure 8.14), with few major changes observed between 1973 and 2011, other than the ice-front recession discussed in Section 8.1.2 (Figure 8.7). Transverse fractures continue to develop near the Spatz Island grounding line that form the basis for ice-shelf calving in this location. In the centre of the north ice front, eight regularly spaced longitudinal fractures cut back into the ice shelf. These features continue to propagate upstream as calving is initiated at their northern extremity, and are visible as open fractures for up to 8 km. Approximately 15 km west of this fracture zone at the confluence of the main shelf and Smyley Island ice, a further fracture is visible at the ice front. Over time, this fracture propagates back upstream by a further 4 km. Transverse fracturing of the surface continues to take place at the Smyley Island grounding zone.

8.1.4.2 Structural changes and structural evolution at the mid ice front

Similarly, structural changes near the mid ice front are steady (Figure 8.15), with changes mostly as a result of the forward motion of tributary glaciers towards, or adjacent to, the ice front itself. At -1828600 377700 m and -1831200 388500 m along the Smyley Island grounding line, fractures observed during 1973 appear to open up to form rifts during 2011, with other fractures remaining open for greater distances towards the ice front. These generally seal to form fracture traces but reopen at the ice front as either fractures of rifts with a clear brash ice filling. A greater number of fractures is identified in the 2011 Landsat imagery in this location.

In ice adjacent to ST06, fractures and rifts become increasingly chaotic from 1973, with these zones developing an increasing amount of brash ice by January 2011. At the tip of Benkert Mount, new fractures develop in previously consolidated ice. These features measure up to 8 km in length and open up to form rifts as they migrate down ice. Rifts west of ST06 (centre point -1770500 393500 m, 1973) migrate northwards with ice flow to (centre point) -1775800 393600 m in 2011, partially closing along their length to the eastern tips of these features. Between the English Coast and Case Island there is no change in surface structure.

8.1.4.3 Structural changes and structural evolution at the south ice front

The greatest changes in surface structures occur between the English Coast and Carroll Inlet in ice fed by ST07 and ST08 (Figure 8.16). This region of Stange Ice Shelf is the most dynamic and is reflected in both the long-term and short-term structural changes. Ice that supplies the south front is heavily fractured across much of its surface during 1973, with rifts, fractures and fracture traces becoming increasingly disordered towards the ice front. Open rifts exist near to the grounding zone at the confluence of ST07 and ice between the English Coast and Case Island. These rifts are typically <2 km in length and form in close association with similar-sized fractures running transverse-to-flow. Both rifts and fractures in this zone seal in the centre of the flow units yet remain visible as fracture traces. Along the south ice front during 1973, rifts form both transverse and parallel to flow, and display no regular pattern of formation. They often cut across fractures or fracture traces and form the basis for iceberg calving.

By 1986, a large section of open rifts had developed longitudinally along the east boundary of ST07, ~12 km from the grounding line, for ~17 km to the ice front. Rifts closer to the grounding zone were more linear, and measured no more than 4 km in length and 0.7 km in width. As rifts migrated towards the ice front they became increasing deformed, rotating northward, and developed a filling resembling brash ice. These rifts cross-cut fractures and fracture traces observed on the surface. Along the ice front, fractures and rifts continued to propagate back into the ice shelf forming a heavily fractured ice-front profile.

During 2001, a large calving event was observed (58 km^2) along the western portion of the south ice front in ice fed by ST08. Rifts continued propagate towards the ice front in ice fed by ST07, yet development of these rifts further upstream had ceased. Within these rifts, brash ice existed, with a few calved blocks apparent behind the ice front (-1777500 366000 m). The major change in surface structures between 1986 and 2001 is the development of a new region of large, filled rifts between ST07 and the slower moving ice between the English Coast and Case Island. These rifts form at the grounding zone and are transmitted down ice, appearing to open up further and becoming increasingly complex in their formation. Several rifts also exist at -1780250 372600 m where ice from ST07 begins to impinge upon Case Island.

These rifts develop further downstream between 2001 and 2005, with small (~1 km in length) rifts marking the eastern flow unit boundary of ST07. Rifts between ST07 and ST08 continue to migrate towards the ice front, but do not display any further deformation

characteristics. A new cluster of fractures and rifts developed at the Rydberg Peninsula grounding zone and are typically non-aligned in their appearance.

By January 2011, the area of rifted ice at the eastern margin of ST07 had increased considerably, stretching for over 15 km in length. Within this zone, rifts towards the centre of the flow unit displayed greater lengths (up to 4 km), but were generally narrower (<0.4 km). As the rifts migrated down ice towards the south ice front they become increasingly distorted, much shorter in length but larger in width. Calved angular blocks of ice were located within these rifts, which also contained large amounts of brash ice. Between flow units ST07 and ST08, the rifts that developed between 1973 and 1986 continued to migrate down ice. The most southern of these rifts had propagated westward and cut across the central region of flow unit ST08. This set of rifts also displayed an increased amount of ice melange and brash ice, with angular calved blocks also visible in the Landsat imagery.

Of particular interest is the rapid development of fractures and rifts along the eastern flow unit boundary of ST07 between November 2001 and January 2011. These rifts develop in previously consolidated ice, are chaotic in appearance and become increasingly filled with calved blocks and brash ice through time. The development of these features is illustrated in Figure 8.17 and Figure 8.18.

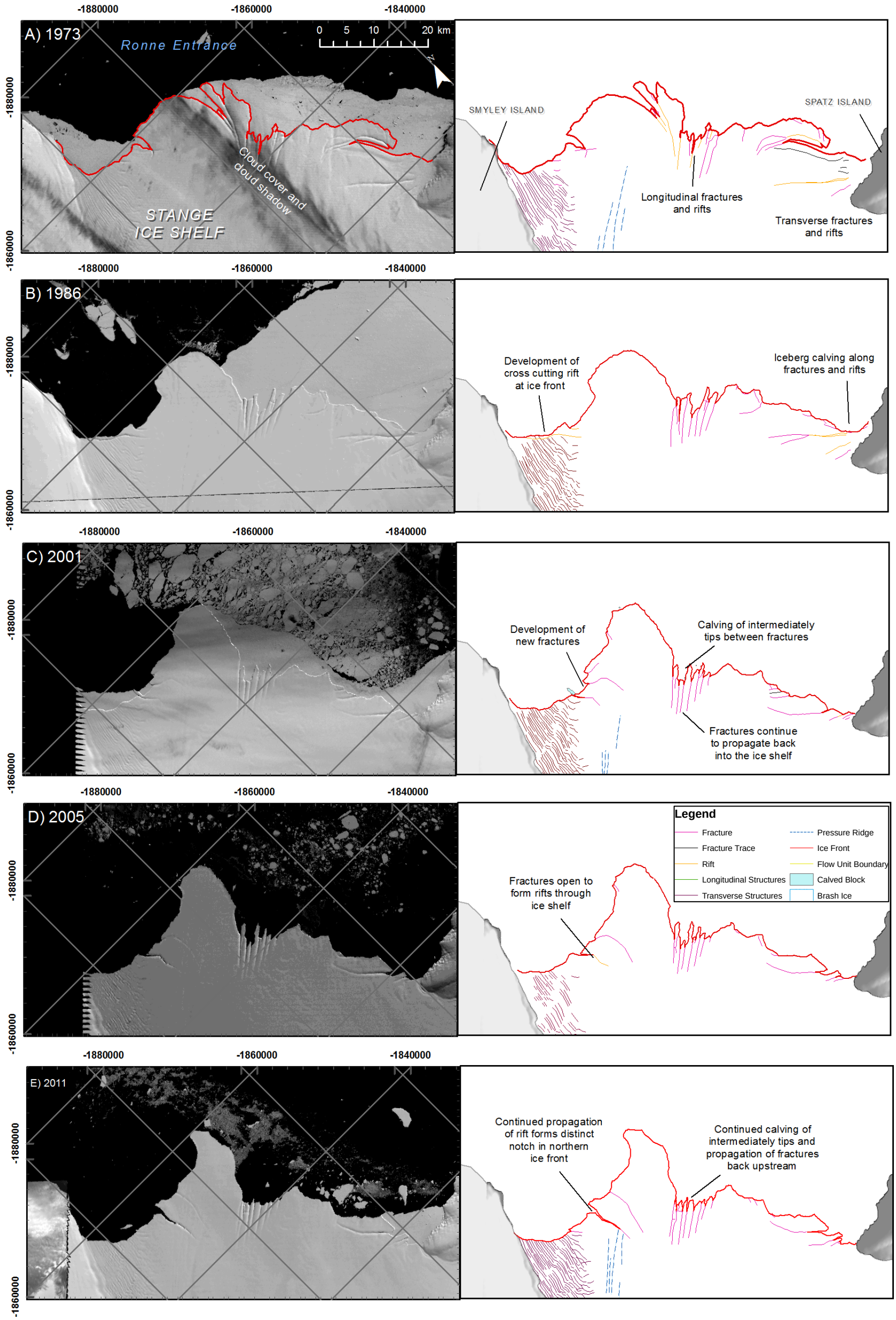

Figure 8.14. Structural changes at the northern ice front of Stange Ice Shelf between A) 1973, B) 1986, C) 2001 D) 2005 and E) 2011 illustrating that the general pattern of retreat is linked to pre-existing fractures and rifts. Longitudinal fractures in the centre of the ice front continue to propagate back upstream despite regular calving of their intermediately tips.

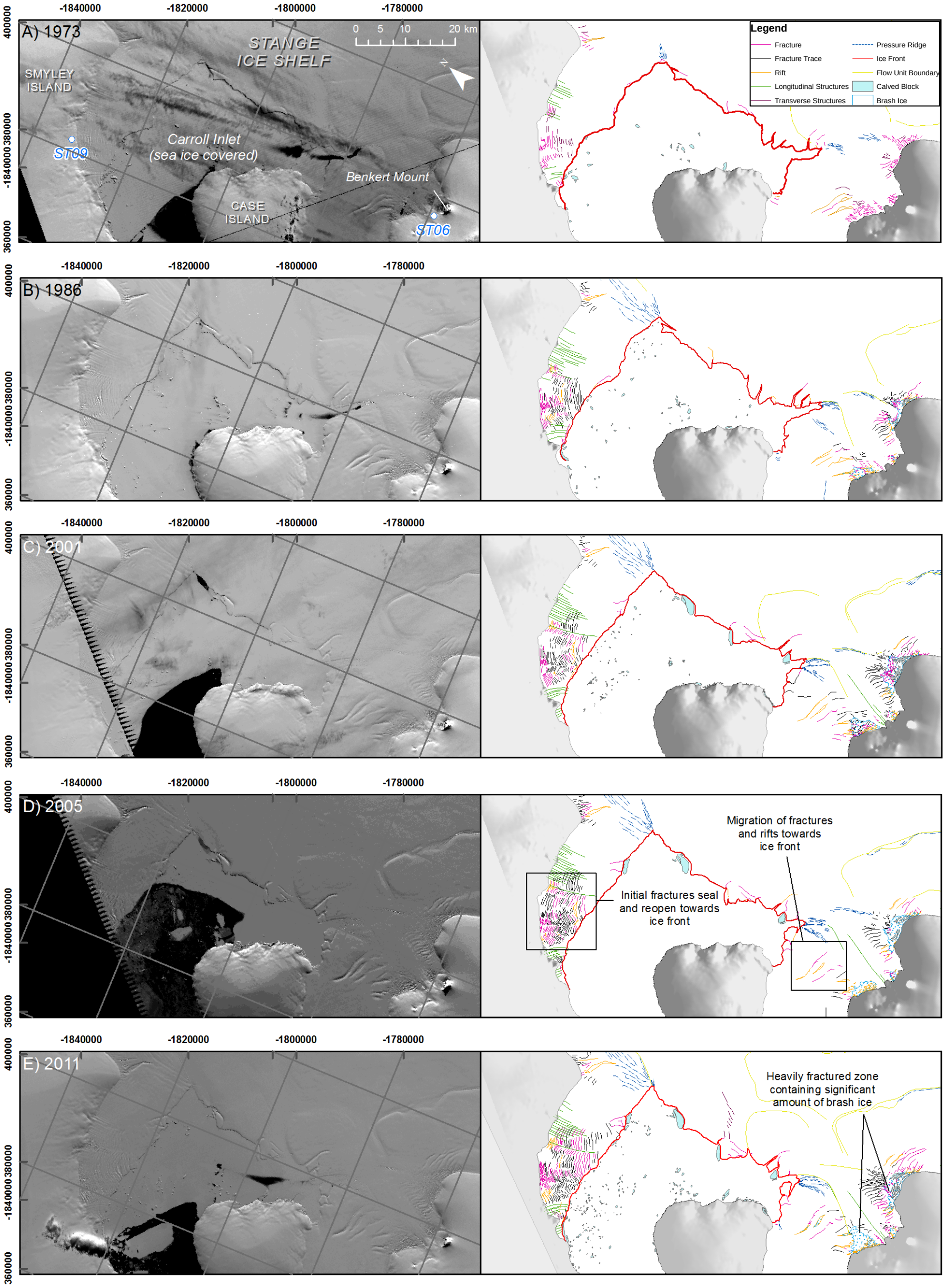

Figure 8.15. Structural changes at the mid ice front of Stange Ice Shelf between A) 1973, B) 1986, C) 2001 D) 2005 and E) 2011 illustrating the increased fracturing from the Smyley Island grounding zone and adjacent to ST06 where chaotic fracturing and brash ice becomes more widespread. Elsewhere, there are little structural changes.

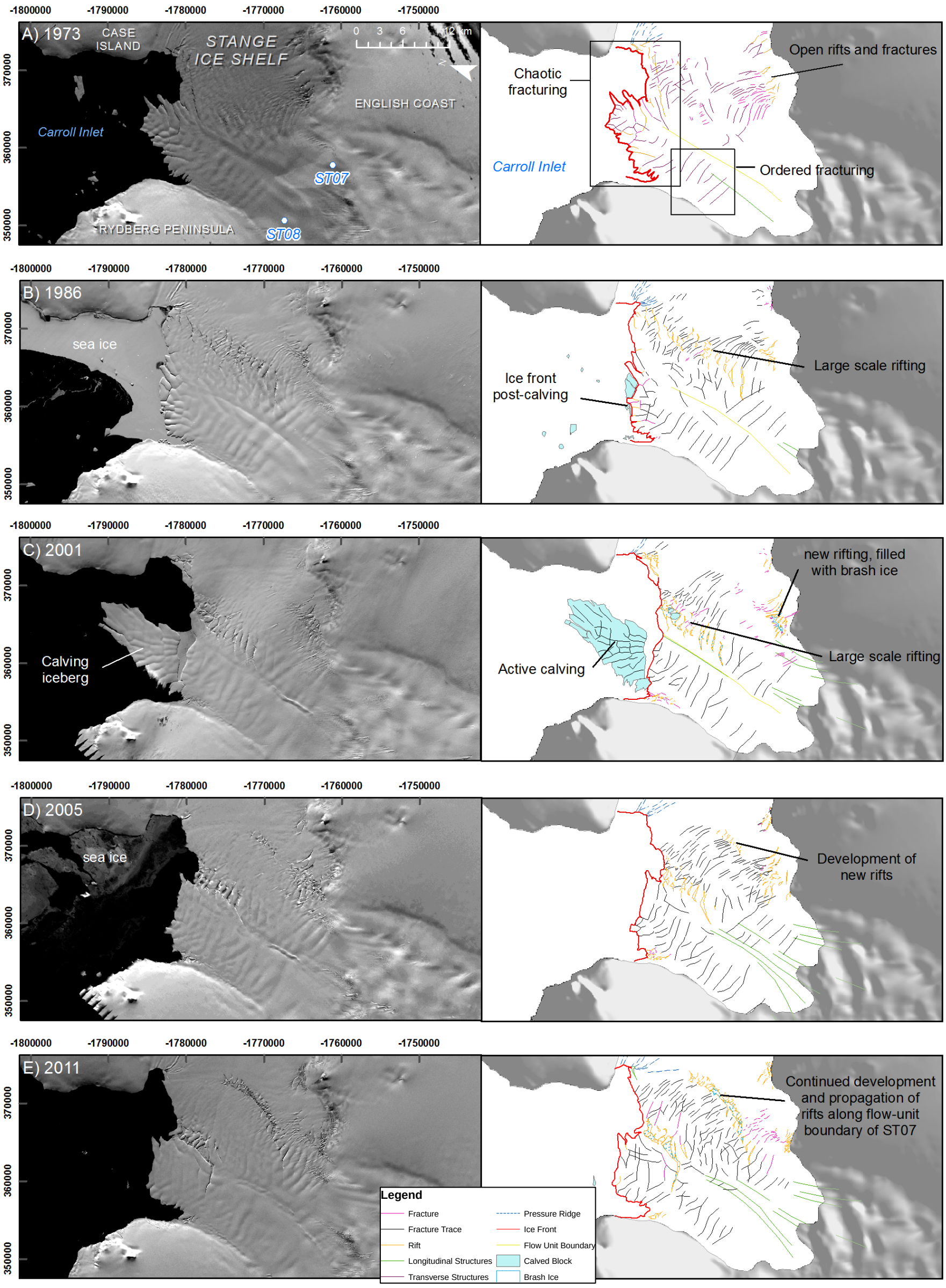

Figure 8.16. Structural changes at the south ice front of Stange Ice Shelf between A) 1973, B) 1986, C) 2001 D) 2005 and E) 2011 illustrating chaotic fracturing towards the ice front in ice fed by ST07 and ST08. Between 2001 and 2011, new rifts develop at the eastern boundary of ST07 and migrate towards the ice front with ice flow. Regular calving occurs at the ice front in ice fed by ST07, with more periodic calving events occurring in ice fed by ST08. In both cases, calving initiates along pre-existing fractures at the ice front.

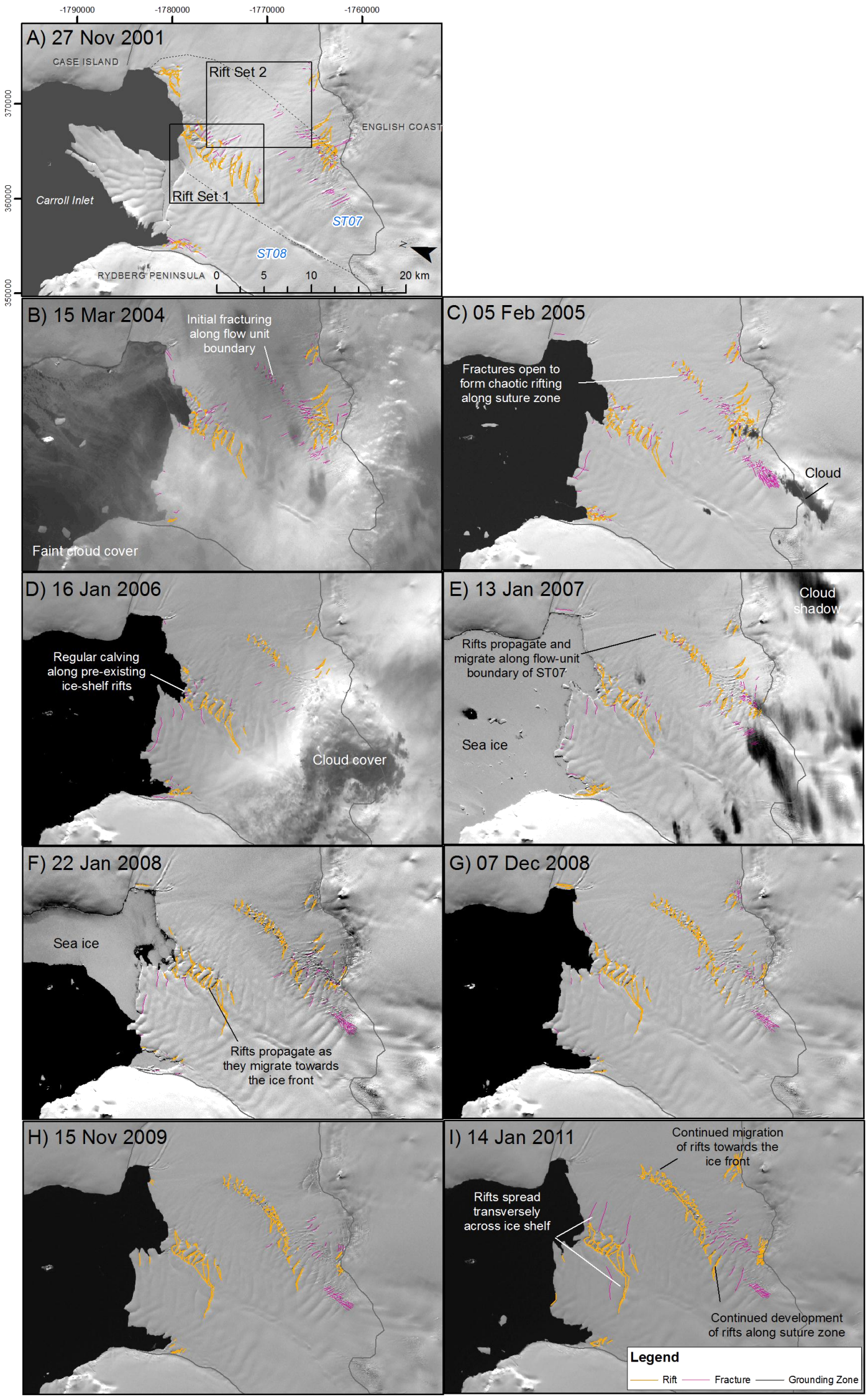

Figure 8.17. Rapid fracturing and rifting along the eastern flow unit boundary of ST07 with ice between the English Coast and Case Island (Rift Set 2) between November 2001 and January 2011. Rifts (Set 2) develop near to the English Coast grounding zone and migrate along the suture zone towards the ice front with ice flow. These become more chaotic over time and contain an increasing quantity of calved blocks and brash ice. New fractures cease to develop in Rift Set 1, but those already existent propagate transversely across the ice shelf over time and form the basis for iceberg calving at the ice front. Only fractures and rifts are illustrated to highlight the key structural changes.

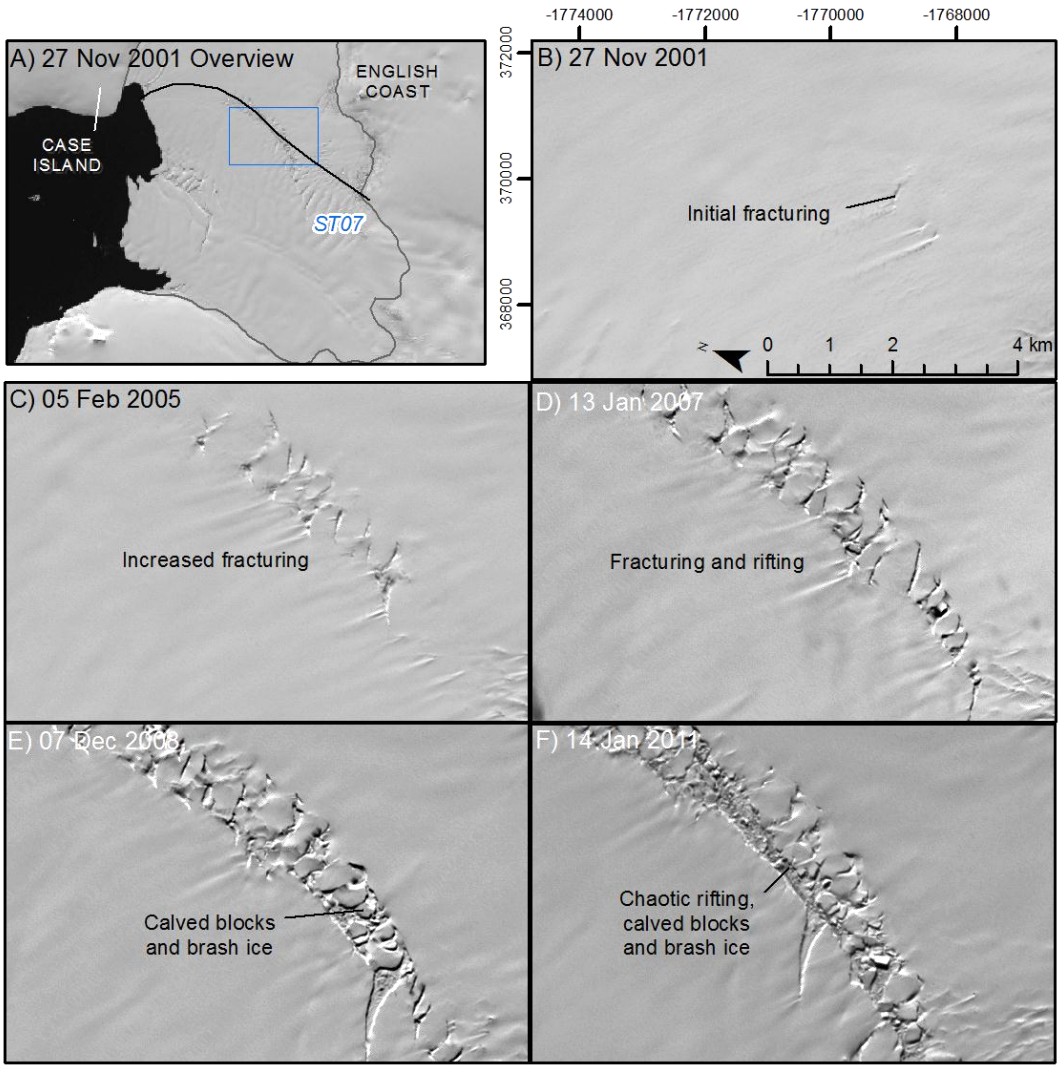

Figure 8.18. Fracturing and rifting along the ST07 flow-unit boundary zone with slower-moving ice between the English Coast and Case Island from November 2001 to January 2011. Note how initial fractures become increasingly chaotic and eventually open to form rifts. Calved blocks and brash ice become more apparent through time. During January 2011, the rifts are filled with a melange of calved blocks and brash ice. ST07 is almost separated from its adjacent ice along the confluence zone.

8.1.5 Surface elevation changes

Changes in surface elevation for Stange Ice Shelf were calculated over five ICESat GLAS tracks between May 2004 and October 2007 (Figure 8.19). In total, repeat measurements were made at 1056 data points across the surface of the ice shelf. Figures 8.21 and Appendix 3b illustrate the surface elevations and surface elevation-change of each track, which are further detailed in Table 8.10.

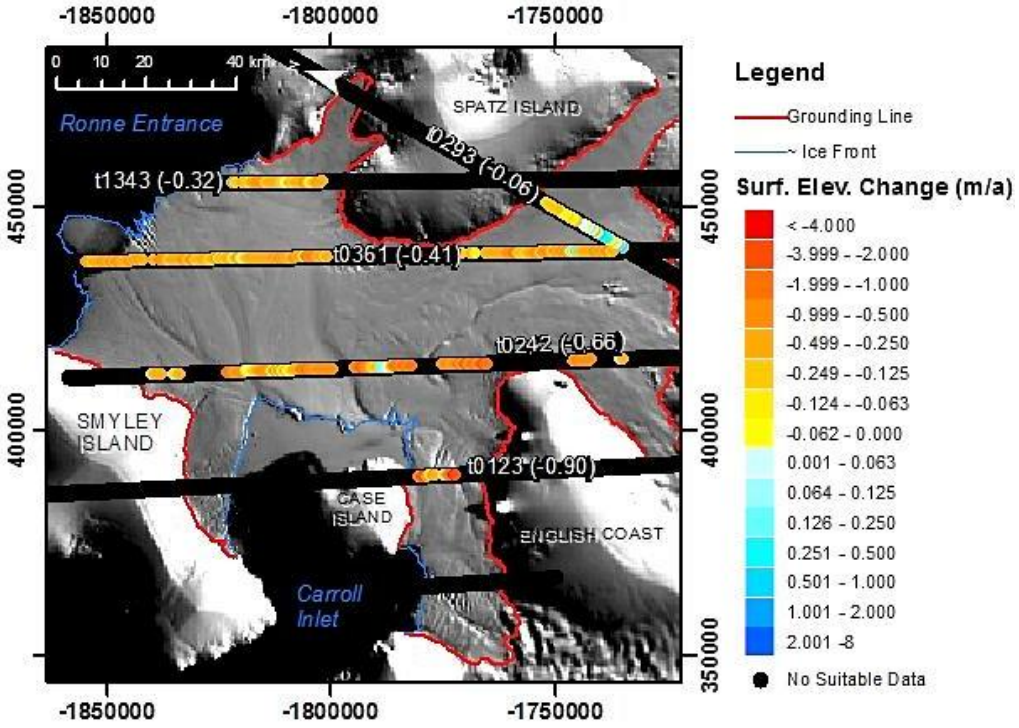

Figure 8.19. ICESat GLAS elevation changes for Stange Ice Shelf between May 2004 and October 2007, extrapolated to ma^{-1} (absolute dates for each track presented in Table 8.10). A strong significant negative surface elevation change is calculated over much of the surface with only localised, discrete areas of positive surface elevation change. Numbers given in brackets are the mean surface elevation change for each track. Data displayed over MODIS image mosaic of Antarctica (Haran *et al.*, 2006).

Repeat ICESat GLAS measurements over Stange Ice Shelf reveal a strong and significant negative surface elevation change over four of the five tracks, with track t0293 displaying weak and non-significant thinning and distinct areas of positive surface elevation change, towards the centre of the track (Figure 8.19, Table 8.10). Across tracks t1343, t0361, t0242 and t0123 a progressive increase in negative surface elevation change was observed from east to west across the ice shelf. Each track is subsequently described in detail in Table 8.10 and Figure 8.19.

Table 8.10. Analysis of ICESat GLAS acquired surface elevation and calculated surface elevation changes. Refer to Figure 8.19 for track location and Appendix 3b.

Track	Laser campaign	Observation period	Max + change (m)	Max - change (m)	Mean change (m)	Max + annual change (ma^{-1})	Max - annual change (ma^{-1})	Mean annual change (ma^{-1})	Comments
1343	2c-3c	22/05/04 – 24/05/05	0.314	-0.682	-0.325	0.312 (± 0.089)	-0.678 (± 0.089)	-0.323 (± 0.089)	A shallow negative surface elevation gradient from the ice front to the grounding line (increased distance along track), with sharp negative spike at ~7 km. General negative surface elevation change observed with three distinct points of positive change at ~7.5, ~21 and ~25 km along track. Significant mean annual surface elevation change calculated at -0.323.
0293	3a-3g	28/10/04 – 18/11/06	1.372	-1.375	-0.120	0.667 (± 0.089)	-0.669 (± 0.089)	-0.059 (± 0.089)	Surface elevations at the grounding zones (0-2 km and 33-35 km) generally greater than the central portions of ice shelf. Negative surface elevation change observed along the track, but positive surface elevation change calculated between ~11.5 and 23 km, interspersed with localised negative change. Between 23 and 29 km along track, negative surface elevation was observed. Weak and non-significant mean annual change of -0.059 ma^{-1} was recorded.
0361	3g-3i	23/11/06 – 31/10/07	0.313	-1.079	-0.384	0.333 (± 0.089)	-1.742 (± 0.089)	-0.410 (± 0.089)	Surface elevations along t0361 illustrate a large trough between 35 – 90 km, located in a zone close to the grounding line. Surface elevation between 0 and 35 km are at ~ 30 m, with greater surface elevations recorded between 90 and 122 km, peaking at ~43 m at the English Coast grounding line. A strong negative surface elevation change is observed across the track, with greatest change recorded at ~52 km and 100 km. Two distinct peaks of

									positive change recorded at ~35 km (-1.746 ma^{-1}) and ~100 km (-1.742 ma^{-1}).
0242	3g-3i	15/11/06 – 23/10/07	0.700	-2.444	-0.621	0.744 (± 0.089)	-2.540 (± 0.089)	-0.662 (± 0.089)	Surface elevations along track t0242 decrease from their respective grounding line (0 km, 122 km) into the centre of the ice shelf, although elevations at the Smyley Island grounding line in much less (~28 m) than the English Coast grounding line (~53 m). A strong and significant negative surface elevation change is observed across much of the track, with only five distinct peaks of positive surface elevation change observed. Mean annual surface elevation across the track is calculated as -0.662 ma^{-1}.
0123	3e-3h	07/03/06 – 24/03/07	0.334	-4.776	-0.942	0.919 (± 0.089)	-4.561 (± 0.089)	-0.900 (± 0.089)	A sharp increase in surface elevation is recorded at 11 km along the transect, with an equally sharp decrease observed at 20 km. Surface elevations at the Case Island grounding line are recorded at ~10 m, with elevations at the English Coast grounding line only at 2 m. Surface elevation change has only been calculated in the central portion of the track and shows strong negative change, interspersed with a distinct zone of positive elevation change of up to 0.919 ma^{-1}. Greatest negative surface elevation change recorded as -4.561 ma^{-1} at ~20 km.

8.1.6 Section Summary

In this section, the dynamic and structural regimes of Stange Ice Shelf have been described. The key results are summarised below:

1. Stange Ice Shelf has a complex dynamic regime with 13 flow units entering the ice-shelf system from three grounded-ice locations, feeding three individual ice fronts. The dominant flow originates from the English Coast on the most southern part of the Antarctic Peninsula. The Lidke Ice Stream in particular offers the most influential flow regime, feeding ice to both the north and mid ice fronts with speeds of up to 500 ma^{-1} observed.
2. Fastest surface velocities were detected in tributary glaciers ST07 and ST08, with speeds of almost 1000 ma^{-1} calculated. Conversely, slowest surface velocities (~40 ma^{-1}) were calculated in ice near to the grounding zone of Smyley Island.
3. The majority of ice-shelf retreat occurred through regular iceberg calving at the north ice front. In total, a net change of -384 km^2 is calculated at the north front between 1973 and 2011. At the mid ice front, a general advance is observed, with net-ice loss only calculated between 1986 and 1996. At the south ice front, a net change of only -0.79 km^2 is calculated. The south ice front offers two different scenarios, with a general retreat of the south ice front between 1973 and 1996, followed by an advance between 1996 and 2011. Overall, a net loss of 338 km^2 was recorded between 1973 and 2011.
4. Changes in the structural regime were concentrated near the southern ice front at the suture between the fast-flowing system of ST07 and slower moving ice to the east and involved the rapid development of a narrow, heavily fractured/ rifted zone between 2001 and 2011. Conversely, fracture development halted between flow units ST07 and ST08 in the same period.
5. ICESat GLAS repeat measurements revealed widespread and significant lowering of the ice-shelf surface between May 2004 and October 2007, with only small, localised areas of positive elevation change observed, mainly towards the English Coast grounding line.

These key observations are interpreted further in the following section, bringing together the structural and dynamic regimes and associated changes of Stange Ice Shelf.

8.2 Stange Ice Shelf interpretation

In Section 8.1, the structural and dynamic results of Stange Ice Shelf were presented, highlighting its complex configuration, spatial and structural particularities and surface elevation changes. These results are subsequently integrated here to interpret these changes, first through assessing its horizontal and vertical changes before contemplating the structural and dynamic relationships in response to documented climate change. The following chapter uses information and theories also presented in earlier chapters, and to avoid repetition, the reader is directed back to previous sections where necessary.

8.2.1 Interpretation of spatial fluctuations

8.2.1.1 North ice front

Stange Ice Shelf lost 338 km^2 of ice (~4%) between January 1973 and January 2011 that occurred almost entirely at its northern ice front (Figure 8.20). Ice is fed here from all three grounded-ice locations and is thus heterogeneous by nature, reflected in its most recent ice-front profile and structural composition. Largely, the northern margin continues to exhibit a convex profile despite the measured retreat, thus providing geometric stability (Doake *et al*., 1998), although the western section does display concave characteristics. At its eastern pinning point, calving along pre-conditioned fractures and rifts led to a linear retreat of ~8 km; spatial and structural analysis in this location revealed a succession of transverse-to-flow fractures and rifts developing at regular (~3 km) intervals as ice flows around the tip of Spatz Island. It is likely that longitudinal extension increases as ice rounds the adjacent headland thus influencing fracturing and consequent iceberg calving. Bending stresses caused by tidal motion and tidal forces at the ice front are also expected to play a role in fracture development in this zone (Rist *et al.,* 2002; Larour *et al.,* 2004; Scambos *et al.,* 2009), and thus fractures and rifts are expected to continue to develop and propagate at the ice front.

At -1842000 444800 m, eight longitudinal fractures cut back upstream into the north ice front. Despite the forward motion of the ice shelf and the observed southward retreat, these fractures continue to propagate following transverse calving of their intermediary tips. This cyclical pattern of calving and propagation suggests continued transverse-tensile stresses in this region and illustrates localised splaying of the ice front as flow diverges. To the west of these fractures, the north ice front juts out sharply into Ronne Entrance; this ice-profile characteristic is present throughout the observation period of this study but becomes

increasingly distinct throughout due to iceberg calving to the east and west. ICESat GLAS measurements and RAMP DEM data along the north ice front do not reveal any significant increases or decreases in surface elevation in this area so it is assumed that the protruding ice is no thicker or no thinner than that surrounding it, thus the extra 'stability' of this section is caused by something other than ice thickness.

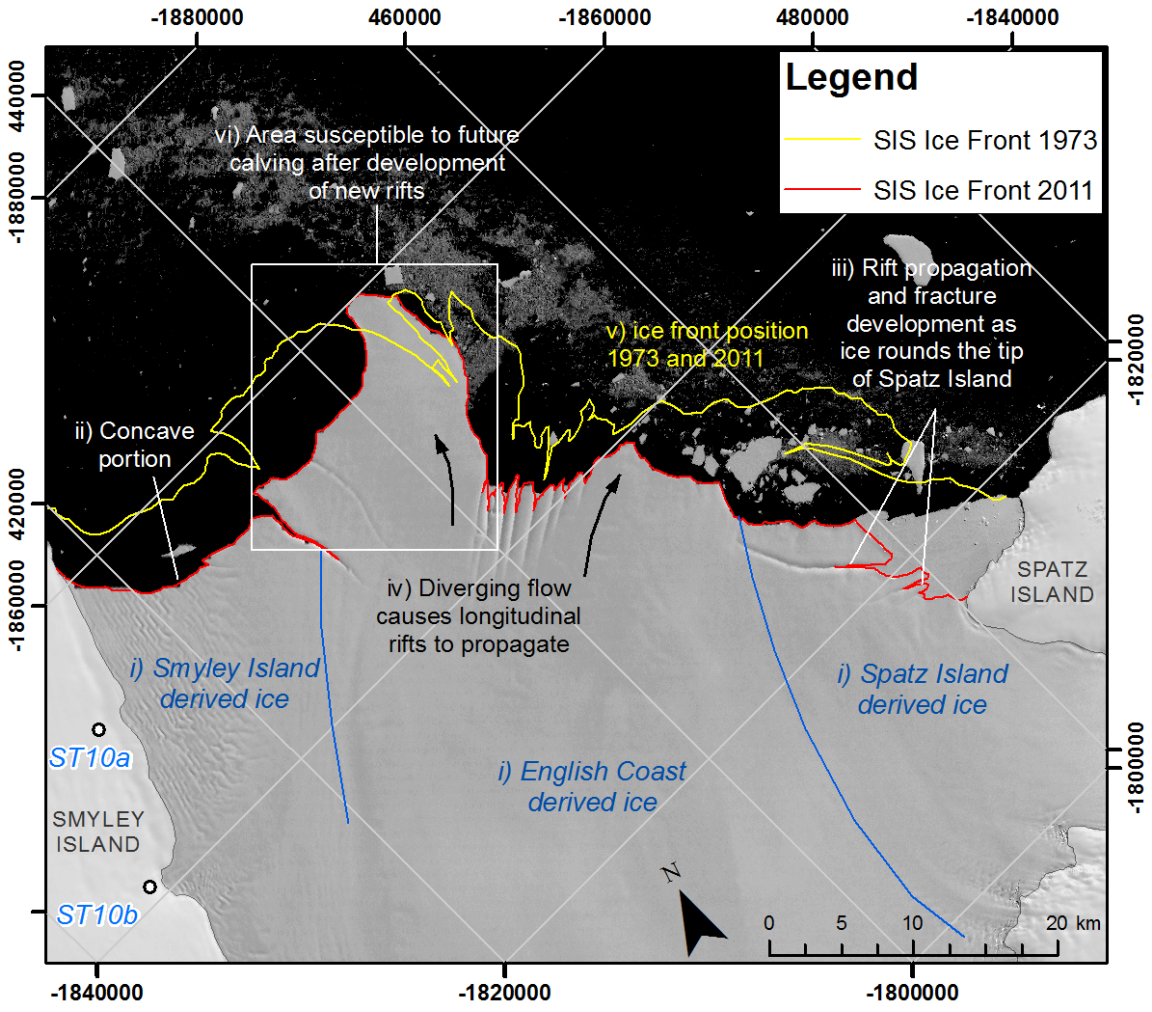

Figure 8.20. Interpretation of changes and structures at the north ice front illustrations i) the flow dynamics from the three grounded ice locations, ii) the profile of the ice front and in particular the concave shape towards it western edge, iii) calving along preconditioned fractures and rifts, iv) longitudinal fractures as ice flow diverges at the ice front, v) the spatial pattern of ice loss at the north ice front and vi) new fractures that suggest future calving at the ice front.

During January 2011, two further fractures are detected on the western side of the protruding ice front, thus suggesting that this area is gradually drawing away from the rest of the ice shelf. It is also proposed that the extended portion of ice is subject to heightened bending stresses caused by tidal motion (Rist *et al.*, 2002; Larour *et al.*, 2004) that exploits inherent ice-shelf weaknesses from its complex formation further upstream. Indeed, the existing fractures illustrate an ice front that is becoming increasingly susceptible to future

calving along pre-existing and recently developed fractures and rifts, that has the potential to significantly alter the profile and stability of the north ice front.

8.2.1.2 Mid ice front

The morphology of the mid ice front is unique, formed by ice flow off Smyley Island in its south-facing portion, north-westerly flow from the Lidke Ice Stream at its west-facing margin and northerly flow at its north-facing edge originating from west of ST06. Between these three dynamic regimes, large compressive stresses produce linear surface hummocks, interpreted as pressure ridges, suggesting that whilst complex, it is also compositionally stable. This is further reflected in the limited amount of retreat and advance observed across the mid ice front over the whole observation period, with any changes largely attributed to the atypical motion of the irregularly-shaped ice front rather than changes induced by iceberg calving (although some limited calving does take place) (Figure 8.21). Furthermore, retreat of the mid ice-front is controlled by the multi-annual presence of sea ice in Carroll Inlet between Smyley Island and Case Island, thus potentially limiting the amount of calving (Lucchitta and Rosanova, 1998; Cook and Vaughan, 2010).

The sea ice is present in all observation periods in this study. Elsewhere (e.g. Jacobs and Comiso, 1993; Folland *et al.,* 2001; Zwally *et al.,* 2002) it has been strongly suggested that sea ice extent in the western Antarctic Peninsula region is lessening as a result of both atmospheric (Vaughan *et al.,* 2003; Massom *et al.,* 2008; Yuan and Li, 2008) and oceanic temperature increases (Gille, 2002; Jacobs, 2006). Generally, the form of the sea ice coverage in Carroll Inlet is that of a consolidated pack that persists on multi-annual timescales. However, small pockets of sea water (polynia) occasionally develop within the fast ice, most notably during 2011, although the smallest areal measurement of sea ice was observed in 2005. The temporal resolution used in this study is too coarse to suggest that local sea ice extent is lessening; however, with increasing oceanic temperatures a likely consequence of climate change (IPCC, 2007), reducing sea-ice extent in this location is a realistic prospect. A lessening sea-ice pack adjacent to the ice front is significant because its removal could permit transoceanic waves to propagate to the ice front, thus causing localised destabilisation of the ice shelf (Glasser and Scambos, 2008), and thus enhanced calving rates. The role of oceanic temperature variations in relation to ice-shelf stability is discussed further in Chapter 9 in relation to the present and future stability of all ice shelves discussed in this study.

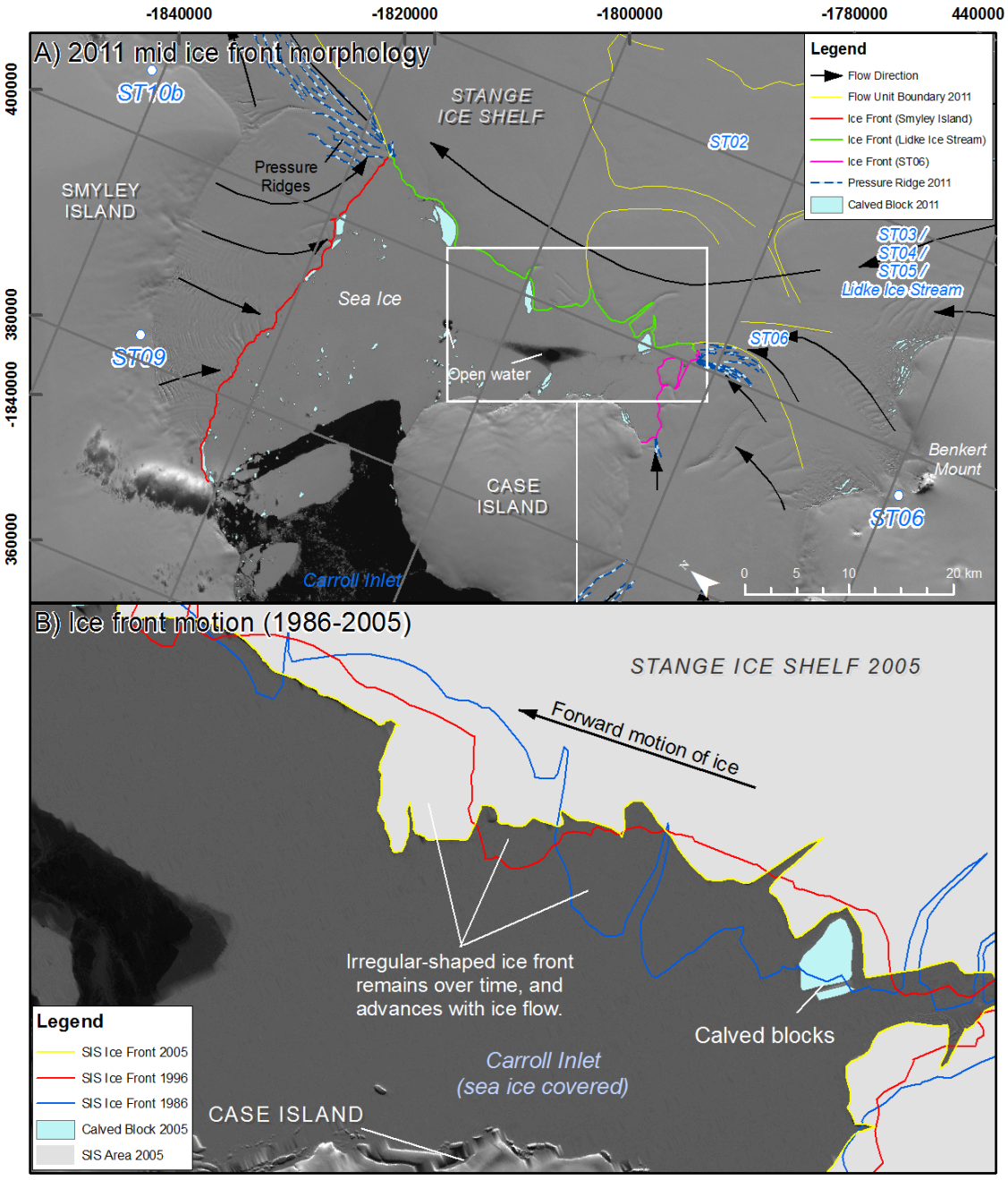

Figure 8.21. A) Flow dynamics and mid ice front morphology during 2011 illustrating its complex formation. Pressure ridges that form at the main confluences highlight compressive stresses at these locations that suggest stability of the ice front in these regions. There is limited iceberg calving along the north-facing and south-facing ice fronts, with larger blocks observed calving off the west-facing ice front fed by the Lidke Ice Stream. B) Recorded ice loss/ advance amplified due to forward motion of ice adjacent to the ice front.

8.2.1.3 South ice front

The south ice front is largely independent of the main ice shelf mass, connected by only a narrow channel of slow-moving ice between Case Island and McCann Mount, thus having little influence on the overall dynamic regime of Stange Ice Shelf. It is fed by fast-flowing glaciers ST07 and ST08, and displays cyclical patterns of frontal advance followed by large-scale calving of individual icebergs up to 60 km^2 in size. Indeed the spatial fluctuations observed at the southern ice front are very much controlled by the development of fractures and rifts, induced by the dynamic regimes of ST07 and ST08. The size of icebergs is partly determined by this regular fracturing and rifting that can be traced from the ice front back upstream towards the grounding zone. These surface fractures and fracture traces are regularly spaced longitudinally (1-1.5 km) and are developed as a result of tidal motion at the grounding zone (A. Humbert, *pers. comm.*). Their persistence down ice is aided by the longitudinal tensile stresses under fast-flowing conditions. However, not every fracture or fracture trace initiates iceberg calving; fracture traces are evident on the surface of the larger icebergs after such calving events and thus a secondary longitudinal tensile stress dictates the dimensions of frontal calving and hence amount of retreat.

Fractures and fracture traces that originate at the grounding zone develop cross-cutting fractures towards the south margin. It is thus inferred that these fractures are younger in age and emphasise a secondary fracturing process at the ice front as a result of increased tensile stresses through tidal forcing or longitudinal extension linked with flow dynamics (Rist *et al.,* 2002; Larour *et al.,* 2004; Weiss, 2004; Scambos *et al.,* 2009). It is the development of these ice-front fractures, and the propagation of existing rifts towards the ice front that controls calving rates at the southern ice front. Consequently, the form of the southern ice-front profile changes rapidly overtime and thus illustrates a healthy pattern of advance and retreat.

8.2.2 Spatial analysis of surface elevation changes and inferences on ice-shelf thickness

Widespread and mostly significant negative surface-elevation change is portrayed across Stange Ice Shelf through 1056 repeat-track ICESat GLAS measurements. The widespread thinning of the ice shelf over time illustrates perhaps a surprising response to documented atmospheric changes (Vaughan *et al.,* 2003; Morris and Vaughan, 2003) as it sits so far

south of the proposed atmospheric thermal limit of viability. The lack of significant surface melting on Stange Ice Shelf is evident through the absence of meltwater features in a succession of Landsat and ERS-1/2 imagery, thus it is proposed that thinning occurs principally as a result of basal melting, and surface elevation changes are recorded due to a vertical response through hydrostatic (re)balancing.

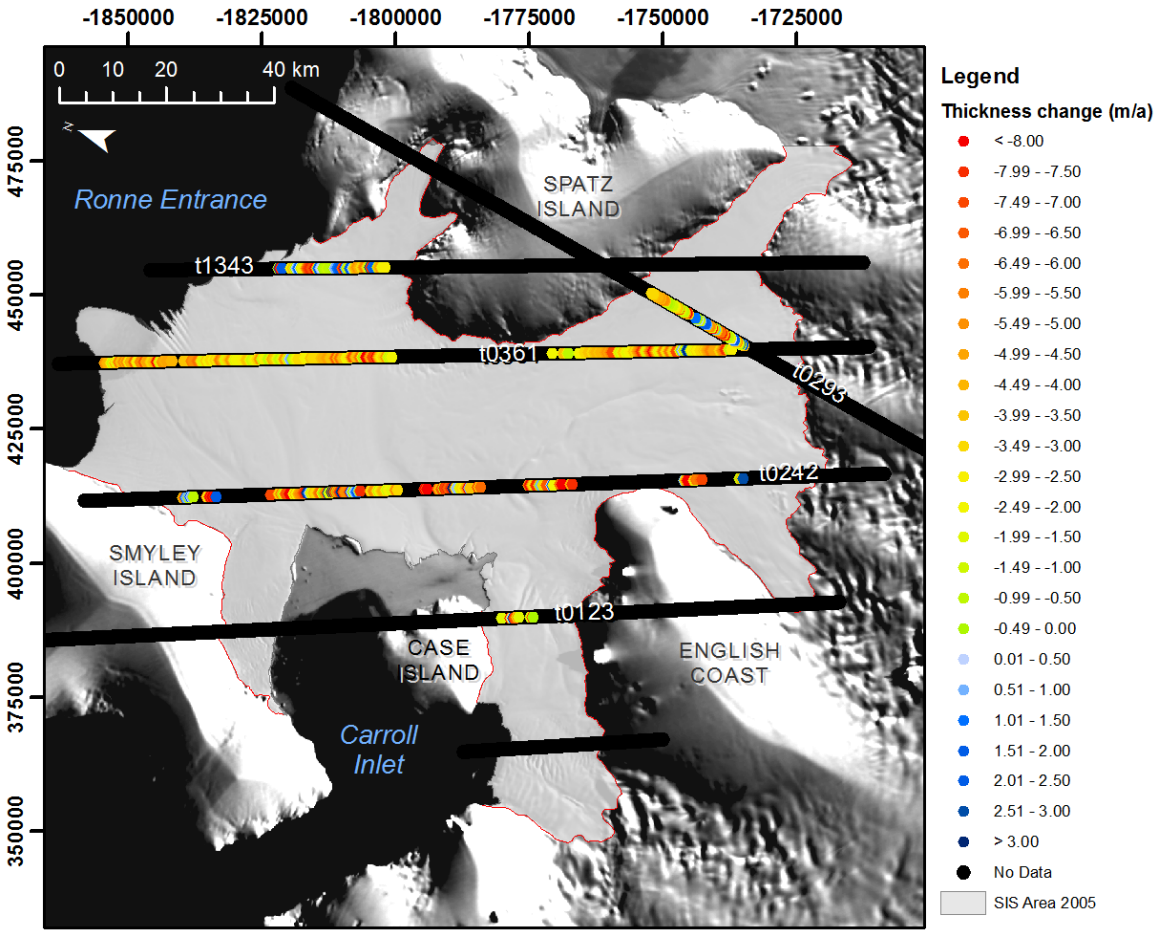

Figure 8.22. Calculated thickness changes in Stange Ice Shelf from ICESat GLAS elevation data, displayed as ma^{-1} from May 2004 and October 2007. Widespread thinning is observed, particularly in the central sections of the ice shelf and towards the north ice front. Data is likely to represent basal melting from the ice shelf as significant surface melting is absent (lack of surface meltwater ponds in a largely compressive ice shelf system).

ICESat GLAS measurements on Stange Ice Shelf are principally obtained through ascending-satellite passes, and whilst this does not affect the results obtained (Shuman *et al.*, 2006), it limits the spatial analysis of surface-elevation changes and subsequent inferred ice-shelf thickness. Nevertheless, there is a broadly consistent pattern of ice-shelf thinning across all tracks between May 2004 and October 2007.

Conversely, there is no detected migration of the grounding zone of Stange Ice Shelf that has elsewhere been used to infer ice-shelf thinning (e.g. Thomas *et al.*, 1988; Rignot, 1998; Shepherd *et al.*, 2001), or indeed no changing surface impression on the ice rises/ ice rumples located along the English Coast as observed in the southern region of George VI Ice Shelf.

Three reasons are offered to explain the absence of a retreating grounding zone. First, a grounding line would only respond to thickening/thinning of an ice-shelf system when the amount of vertical motion is large enough to influence horizontal retreat/advance. If this threshold is not met, then the grounding zone would remain relatively static. This is generally the case where the grounding zone sits on steep-sided topography where even significant thinning has little impact on the horizontal positioning of the grounded/floating ice interface. This is perhaps the reason why there is no detected change in grounding zone location between 1973 and 2011 on Spatz Island, Smyley Island, Case Island and the English Coast, south of the Lidke Ice Stream. Indeed analysis of the RAMP DEM and ICESat GLAS data illustrates the steep gradients of these grounded-ice locations that may also represent steep sub-glacial topography.

Secondly, in reference to Stange Ice Shelf in particular, a retreat of the grounding zone from the Lidke Ice Stream to ST02 is perhaps absent because of slight and insignificant thinning in the zone directly adjacent to the grounding line (see t0293, Figure 8.22), thus not subjecting the grounding zone to a horizontal retreat. Finally, any horizontal movement as a result of ice-shelf thinning is less than the spatial resolution of the imagery used to map the grounding zone/ break of slope position.

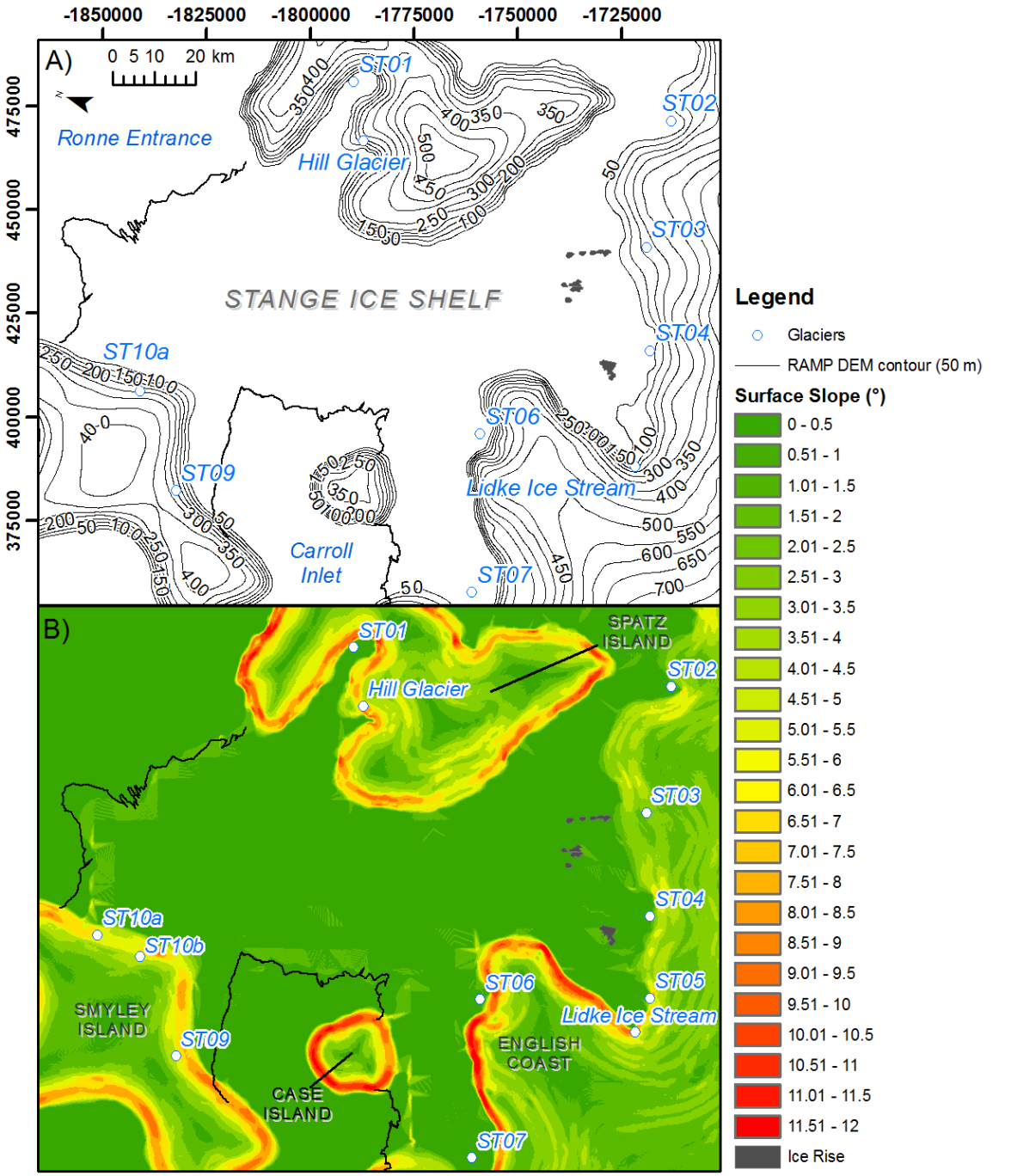

Figure 8.23. A) RAMP DEM 50 m contour and B) RAMP DEM surface slope. Notice the steep gradients along the margin of Stange Ice Shelf, in particular around Spatz Island, Smyley Island, Case Island and between ST07 and the Lidke Ice Stream. More gentle surface slopes are observed between Lidke Ice Stream and ST02 where the faster-flowing, and largest tributary glaciers enter the shelf. Note also the location of the ice rises along the English Coast that may stabilise the ice shelf in this region.

8.2.3 Interpretation of structures and their significance for ice-shelf dynamics and mechanical heterogeneity

Longitudinal structures, flow-unit boundaries and pressure ridges are the most distinctive flow-related features on Stange Ice Shelf and all illustrate its current and historical dynamic flow regime. Each of these have previously been discussed in detail in sections 6.2 and 7.2, and thus are only deliberated here in terms of their inference on Stange Ice Shelf dynamics and configuration.

8.2.3.1 Longitudinal structures

Longitudinal structures form principally at, or near to, the grounding zone (Type 2 or Type 3) or in the main channels of the principal tributary glaciers that flow off the English Coast, thus suggesting they form as a result of initial transverse compression followed by longitudinal extension. The evenness of all of these features down-ice illustrates the stability of the most-recent flow dynamics of the ice shelf (Glasser *et al.,* 2009). Only down-stream of the English Coast ice rises (approx. -1732200 421600 m, Figure 8.24, A) are deformations of longitudinal features observed, and are likely to represent historical, localised flow divergence around the associated ice rises that have been transmitted down-ice with horizontal motion. The deformed longitudinal structures can be tracked in Landsat imagery between 1986 and 2011 without further distortion, and no further surface deformations area developed in this region. As a result, it is also suggested that there had been a localised variation in its dynamic regime in its recent history that caused the ice to deform.

The resistance of all longitudinal structures to lateral spreading also represents a largely compressive flow regime (Glasser *et al.,* 2009) of Stange Ice Shelf, particularly at the confluence of ST01 and Hill Glacier from Spatz Island, and between ST03, ST04, ST05 and the Lidke Ice Stream flowing from the English Coast. Here ice is fed through a 35 kilometre-wide channel between Benkert Mount and Spatz Island, thus limiting lateral spreading, and indeed promoting further transverse compression (Figure 8.24). Longitudinal structures can rarely be traced past this point, but surface velocities interpolated from feature tracking illustrate the general pattern of converging flow across the ice-shelf surface towards the north ice front.

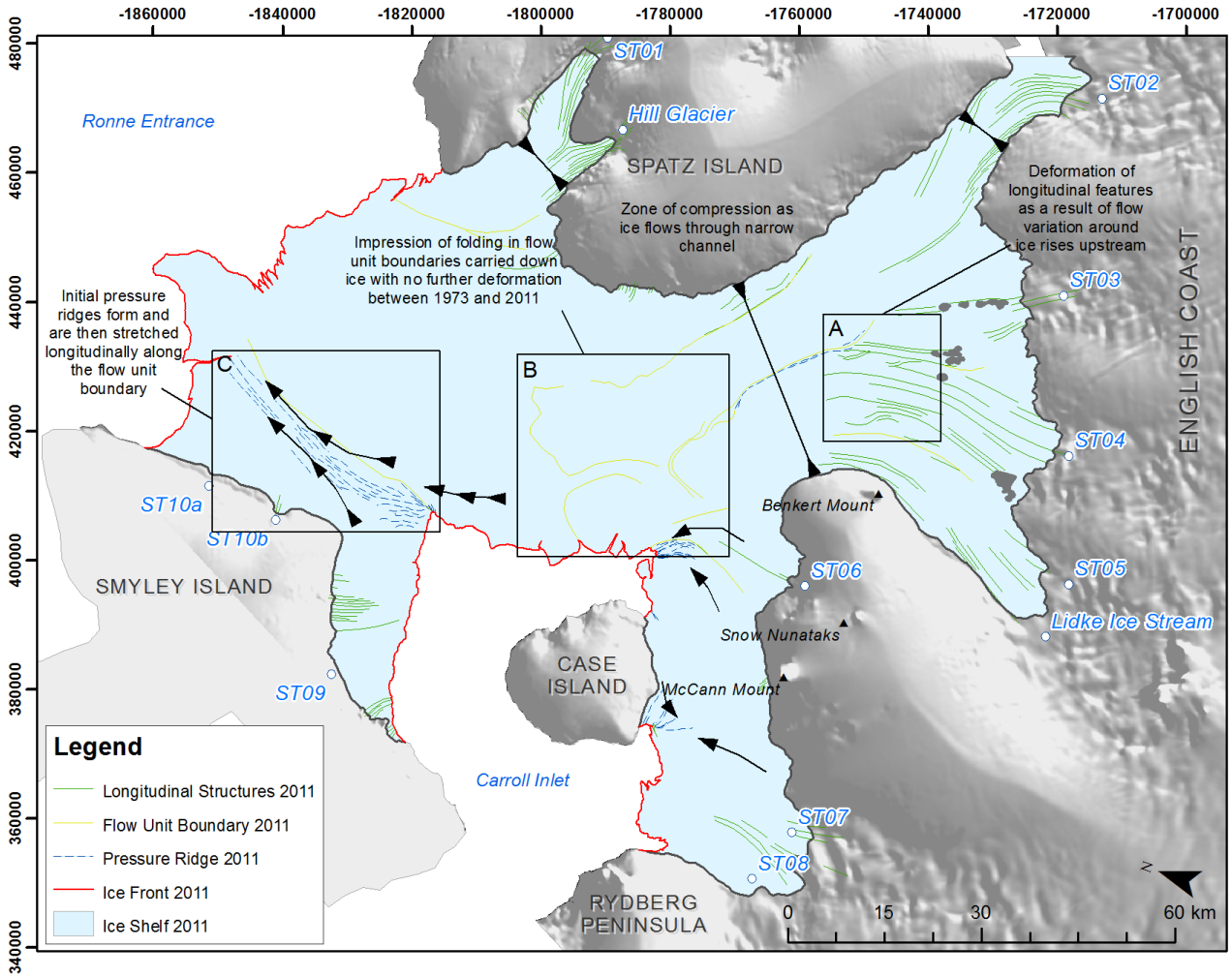

Figure 8.24. Longitudinal structures, flow-unit boundaries and pressure ridges on Stange Ice Shelf (2011) that indicate the compressive regime of the ice shelf (black arrows indicate inferred zones of compression). Of note are zones A, B and C as discussed in the text in 8.2.3.1, 8.2.3.2 and 8.2.3.3 respectively.

8.2.3.2 Flow-unit boundaries

The most pervasive longitudinal features are linked to flow-unit boundaries of ST02/ST03 and consequently ST02/ST03 with ST04. Their longevity down ice (some 77 km) illustrates the dominance of flow from these 'active' tributary glaciers (Figure 8.24, B). In the centre of Stange Ice Shelf, these flow unit boundary features can be traced into an arcuate shape and can be tracked down-ice from 1973 to 2011 without undergoing further deformation. Two of these folds are associated with ST04, ST05 and Lidke Ice Stream, with one related to ST02/ST03. Their infrequency, but spatial proximity on the surface of Stange Ice Shelf suggests formation under atypical or varying flow regimes, and may represent a point in history where the impetus of glacier ice from the English Coast increased and became progressively dominant on the overall dynamics, thus causing deformation of the ice shelf.

A paucity of historical datasets (pre 1973) from which structural analysis can be undertaken prevents a definite explanation for their formation from being proposed. However, by considering a stable dynamic regime since their formation and taking a mean velocity of approximately 252 ma^{-1} from the grounding zone to their current locations, it is proposed that these features were formed in the ice-shelf system between 225 and 350 years ago, thus it proposed that Stange Ice Shelf has remained in its current state for at least this amount of time.

8.2.3.3 Pressure ridges

Pressure ridges are most evident at the confluence of Smyley Island-derived ice and that of the main ice shelf and can be traced along this boundary from the mid ice front to the north ice front (Figure 8.24, C). This demonstrates the clear compressive nature of Stange Ice Shelf in this zone. Ice from the eastern-most, south-facing slopes of Smyley Island appears to be influenced by the northerly flow of the main ice-shelf channel, illustrated by vector data obtained through feature-tracking measurements. Here, surface velocities are extremely slow, (minimum ~30 ma^{-1}) and lack distinct longitudinal structures. On the eastern-facing slopes of Smyley Island, ice feeds into the shelf perpendicular to the grounding zone but is soon subjected to northward deflection by the main ice-shelf flow. It is within this zone of coalescence that pressure ridges are formed, and then consequently stretched down ice with the predominant flow. Whilst they demonstrate regional compressive stresses, the presence of these ridges also illustrates the relative strength of

Smyley Island-derived ice compared to the much larger mass of the main ice-shelf, and the consequent unified flow regime towards the north ice front; structural and dynamic analysis reveal no evidence of lateral shearing in this zone.

8.2.3.4 Crevasses, fractures and rifts

Crevasses, fractures and rifts are interpreted according to descriptions given in Chapter 5 (and discussed in Section 6.2 and Section 7.2). Crevasses are located around the steep-sided margins of Stange Ice Shelf and within grounded tributary systems, and illustrate regions of increased tensile stresses; however, these features can rarely be traced across the grounding zone. On the ice-shelf surface, fractures, fracture traces and rifts form in three distinct regions; 1) at each of the ice fronts, 2) along the grounding zone where longitudinal extension is dominant, and 3) between coalescing ice-shelf flow units around headlands or peninsulas (Figure 8.25). Absence of fractures in the central portions of Stange Ice Shelf demonstrates a largely compressive regime away from the ice shelf margins as discussed above.

At the north-ice front, the development of fractures has already been discussed in Section 8.2.1. Fractures and fracture traces migrating to the north-ice front from ST10a stem from the grounding zone of Smyley Island and are likely to be caused by vertical tidal motion at the grounding zone and maintained down ice with increasing flow velocities (Humbert, *pers. comm.*) (Figure 8.26A). A similar situation is observed in ice originating from ST09, ST08 and ST07, with their regular, transverse spacing influenced by respective velocities of individual flow units (Figure 8.26B, C). Greater spacing between fractures and fracture traces is observed at the southern ice-front due to greater surface velocities depicted in feature-tracking measurements.

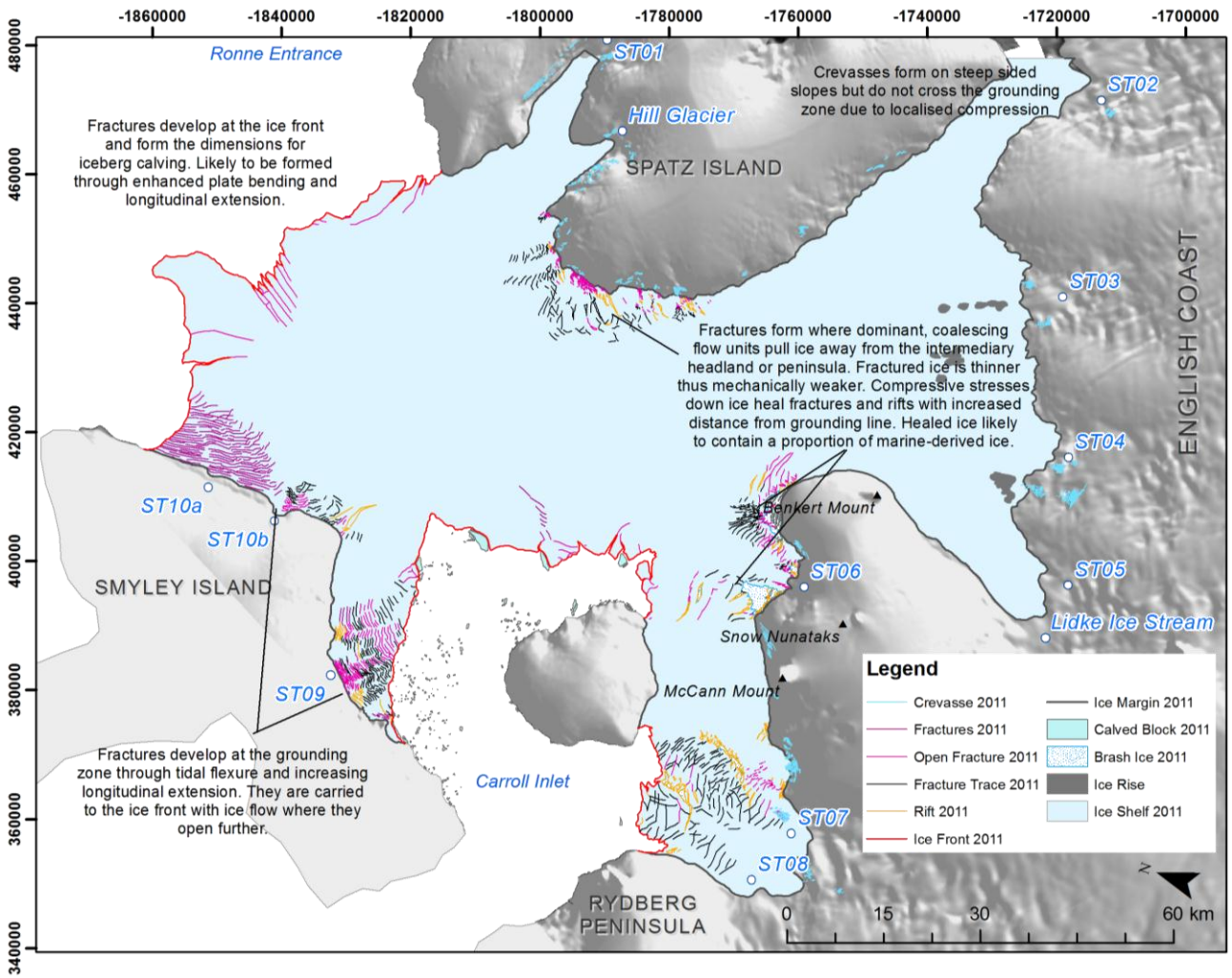

Figure 8.25. Fractures, fracture traces and rifts on Stange Ice Shelf (2011) illustrating regions of extensive flow as discussed in the text. Most of the fracturing takes place in three distinct zones, 1) at each of the ice fronts, 2) at the grounding zone and 3) between flow units around headlands or peninsulas.

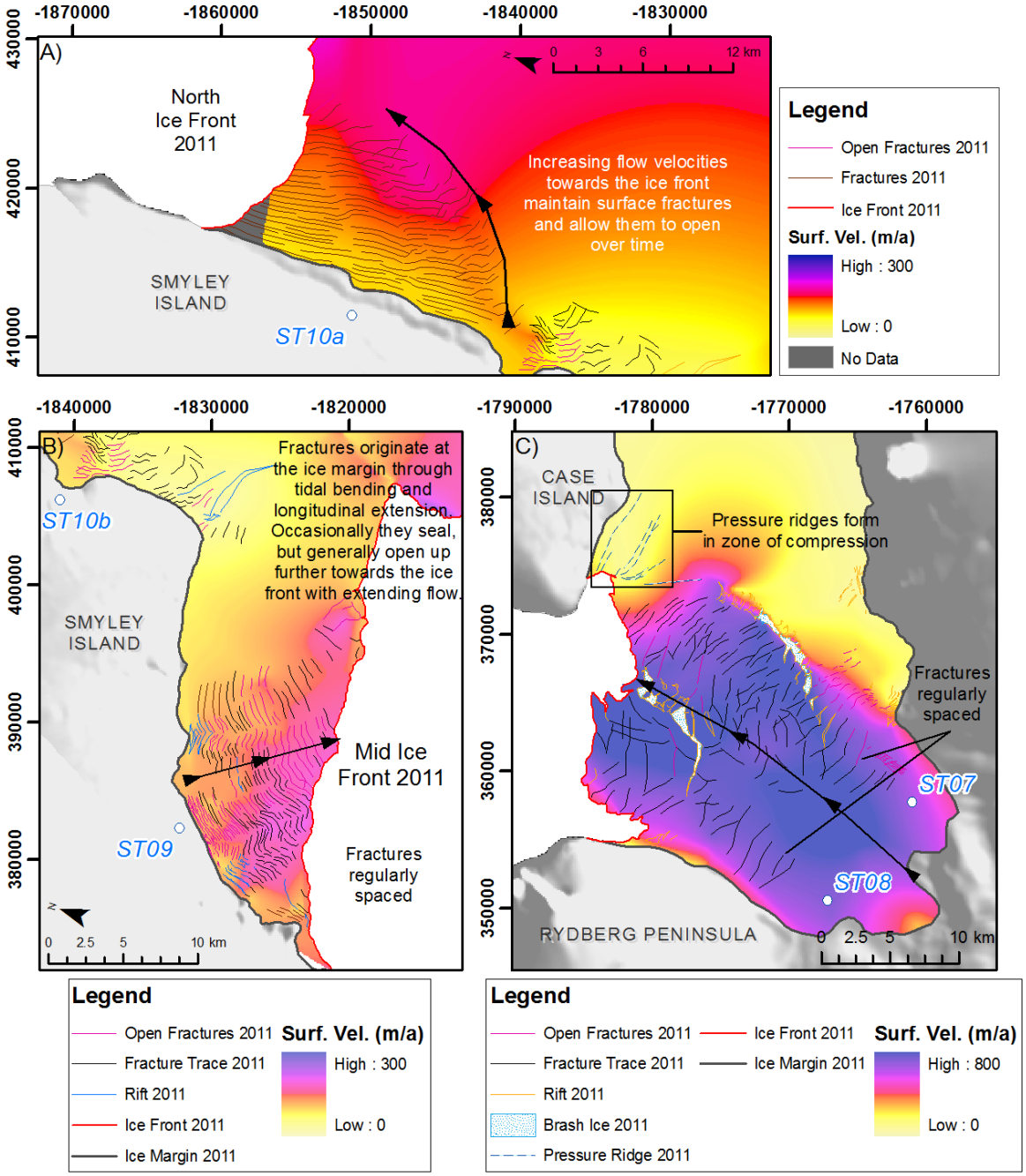

Figure 8.26. Surface fracturing and ice-shelf rifting in distinct regions on Stange Ice Shelf. A) The development of surface fractures along the grounding zone and consequent migration to the north ice front. B) Similar fracturing and rifting at the grounding zone of Smyley Island in ice fed by ST09. Longitudinal extension away from the ice margin towards the ice front permits fractures to remain open, and open further. Calving is observed along these fractures, and thus the rate of calving is governed predominantly by this, and the presence of sea ice in Carroll Inlet as discussed in Section 8.2.1.2. C) Fractures stemming from the grounding zone, and developing near the south ice front. Fractures and rifts propagate further with increasing flow velocities towards the ice front. Note also the excessive and chaotic rifting along the boundary between ST07 and slower moving ice to its east that form through shearing of two flow units.

Extensive regions of fracturing and rifting between flow units are observed between 1) ST02 and flow off of Spatz Island, 2) Lidke Ice Stream and ST06, and 3) ST06 and slower-moving ice to its west. Fracturing is particularly chaotic in these zones, with rifts containing a mixture of brash ice and calved blocks interpreted as ice melange (Figure 8.25). It is likely that these rifts also contain a significant amount of marine ice (Khazendar, 2003; Bassis *et al.*, 2005) that is consequently warmer and more resistant to further fracturing. These fracture zones initially display longitudinal extension away from the grounding zone, whilst their relatively short persistence down-ice as rifts, open fractures and fracture traces illustrates the eventual compressive nature of the ice shelf. Where fracturing of this nature takes place, ice is inferred to be much thinner (Glasser and Gudmundsson, 2012) and thus weaker in its mechanical strength. This is further demonstrated by lower surface elevations in these coalescent regions from which thinner ice is inferred. Furthermore, marine ice is likely to be incorporated into the shelf-ice during fracture healing, thus changing the physical glaciological properties of ice.

Further chaotic fracturing and rifting occurs between ST07 and ice units to its east and west (ST08) throughout the observation period and reflects the changing dynamic regime in this region. The development of distinct fracture zones is of particular interest as they are indicative of shearing between adjacent flow units rather than tensile stresses as observed elsewhere (Figure 8.26C). Observations in the satellite imagery suggest the following sequence of events;

1. Between ST07 and its eastern flow unit, fracturing and rifting takes place at some time from 1973 to 1986 (Rift Set 1, Figure 8.27), and illustrates the coalescent and dominant flow of ST07 and ST08.
2. Between 1986 and 2001, Rift Set 1 skews northwest across the ice shelf towards the ice front, potentially caused by an increased impetus of ice from ST07 relative to ST08. At the same time, development of new fractures in Rift Set 1 ceases, but they continue to propagate as they are transmitted towards the ice front and form the basis for small-scale calving in the eastern portion of the south ice front, and larger calving events in the western portion.
3. Between 2001 and 2011, fractures and rifts in Rift Set 1 continue this migration towards the ice front without new fractures developing (Figure 8.27). However, the most striking development between 2001 and 2011 is the appearance of the large zone of heavily fractured and rifted ice (Rift Set 2) between ST07 and its eastern

flow unit; a clear shearing motion in this coalescent zone is depicted in a series of Landsat images visible through clockwise rotation of calved blocks within the ice melange.

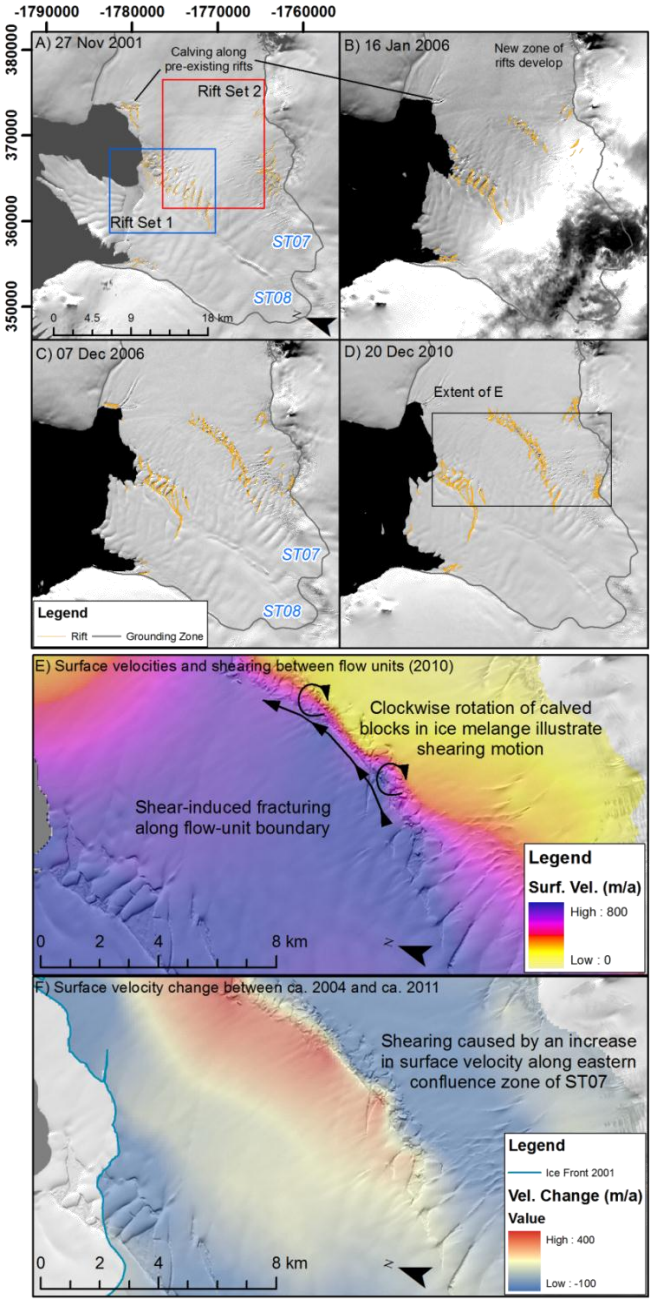

Figure 8.27. Development of fractures adjacent to ST07 between 2001 and 2011. A-D illustrate the progressive sequence of fracture propagation. E) Velocity difference across flow-unit boundary, and F) change in velocity along Rift Set 2 between ca. 2004 and ca. 2011 illustrating shear-induced fracturing.

Shear-induced fracturing between ST07 and slower moving ice to its east is emphasised further in the changing dynamics identified in measured surface speeds (Figure 8.27). Whilst actual glacier speeds in fact decrease over time over much of ST07 and ST08, the spatial extent of faster-flowing ice increases, extending into the previously slow-moving

zone between the English Coast and Case Island, thus creating a zone of increased surface velocities along this boundary (Figure 8.27). Fracturing and rifting on this scale produce a clear weakness in the ice-shelf surface and have been considered responsible for the initial breakup events of Larsen B during 2002 (Glasser and Scambos, 2008). This is also significant as it illustrates both a long-term and a short-term dynamic change of Antarctic Peninsula tributary glaciers outside of the theoretical limit of ice-shelf viability as proposed by Morris and Vaughan (2003).

Elsewhere on Stange Ice Shelf, little change to the glaciological structures is observed other than natural propagation of pre-existing fractures and development of new fractures in expected regions (at the ice shelf edge, for example). Furthermore there are no major changes in the dynamic regimes and indeed associated surface velocities over large spatial areas.

8.2.4 Surface structures and inferences on ice-shelf dynamic configuration

Thirteen flow units have been observed feeding the main bulk of ice into Stange Ice Shelf from three grounded-ice locations, thus making a dynamically complex ice-shelf system. Dominant flow is clearly delivered from the English Coast and in particular from ST04, ST05 and the Lidke Ice Stream. ST07 and ST08 are the fastest-moving tributary glaciers of the whole ice shelf but their influence on the main dynamics is spatially limited to the south ice front.

The cohesion of individual flow units on Stange Ice Shelf is anticipated to be strong, with the exception of ST07 and slower-moving ice to its east where active lateral shearing is observed, as discussed above. Even between the fast-flowing Lidke Ice Stream and adjacent flow units no structural evidence of shearing is visible, despite transverse-to-flow-discontinuities across the ice shelf. It has already been demonstrated through structural analysis that the ice shelf in the central portions is under lateral compression as ice flows between Benkert Mount and the tip of Spatz Island. However, areas where a clear flow-unit boundary can be demonstrated are often characterised by sub-ice shelf cavities that run parallel to the surface impressions left by the flow dynamics (Fricker *et al.,* 2001, Humbert, 2006).

Elsewhere, radio-echo sounding across Fimbul Ice Shelf reveals a coherent pattern between surface fractures and fracture traces, and cavities at the base of the ice shelf (Humbert and Steinhage, 2011). Thus, the pattern of surface structures is also reflected in

the sub-ice shelf configuration. For Stange Ice Shelf this is significant because of its complex configuration and many flow-unit boundary zones that are spatially spread out across the ice shelf, with heavily fractured/rifted areas concentrated along the margins and ice-fronts. It is therefore assumed that Stange Ice Shelf is comprised of many sub-ice shelf cavities in similar locations to those visible on the surface.

8.2.5 Section Summary

Section 8.2 has presented an interpretation of the results obtained through structural and dynamic analysis of Stange Ice Shelf, presented in Section 8.1. The key interpretations to carry forward are as such:

1. Most of the recorded ice loss of Stange Ice Shelf from 1973 to 2011 occurred at its northern ice front that flows into Ronne Entrance. The retreat occurs through calving of blocks along pre-conditioned fractures and rifts. The continued development and propagation of such weaknesses during 2011 Landsat imagery suggests that calving is likely to continue in this region.
2. Ice at the northern ice front is heterogeneous by nature, being fed from three distinct grounded ice locations. Currently, the north ice front displays stable characteristics, but recent fracturing along its central portions is likely to instigate further retreat, particularly in the area that juts out into Ronne Entrance.
3. Changes at the mid ice front are largely due to its complex morphology and associated flow dynamics. Calving on any significant scale is rare, and it is proposed that the presence of multi-annual sea ice in Carroll Inlet stabilises the ice front by dampening transoceanic wave propagation. Removal of this sea ice could potentially cause an increase in localised calving rates.
4. The south ice front is independent of the rest of Stange Ice Shelf, joined only by a narrow, slow-moving ice mass between Case Island and McCann Mount. The structural and dynamic assessment illustrates both long-term and short-term dynamic changes in ice feeding the south ice front, with active shearing between ST07 and the slower moving ice evident between 2001 and 2011; this is significant as it illustrates a dynamic response to a change in glaciological conditions outside of the thermal-viability-limit of ice shelves in the region (Morris and Vaughan, 2003).

5. Elsewhere, Stange Ice Shelf displays largely cohesive properties, with compressive flow in the centre of the ice shelf illustrated by the linearity and evenness of longitudinal flow structures and distribution/quantity of pressure ridges.
6. Large-scale thinning across Stange Ice Shelf is calculated from repeat ICESat GLAS measurements. It is inferred that, due to the lack of significant surface melting (lack of surface meltwater channels in a largely-compressive ice-shelf system), the majority of the thinning occurs through basal melting.

In Chapter 9, these data and interpretations are combined with those of Bach Ice Shelf and George VI Ice Shelf to analyse the regional change in these three systems. Their current stability is considered and used to make inferences on predicted future responses using data in this study and published elsewhere on Antarctic Peninsula ice shelves.

Chapter 9

Discussion

9. Discussion outline

Specific details of Bach, George VI and Stange Ice Shelves were discussed in Chapter 6, Chapter 7 and Chapter 8 respectively, concentrating on their spatial, structural and dynamic changes. In this chapter the key results and interpretations are discussed with reference to glaciological characteristics observed elsewhere on the Antarctic Peninsula prior to retreat, breakup and collapse of various ice shelves.

Chapter 9 comprises two sections. In Section 9.1 the empirical results obtained in this study are discussed in relation to previous work. Comparisons are made between the patterns and characteristics of ice-shelf retreat observed on other Antarctic Peninsula Ice Shelves and marine-terminating glaciers (e.g. Rau *et al.,* 2004; Cook *et al.,* 2005; Cook and Vaughan, 2010; see Figure 1.2 for locations), taking into account the retreat history, embayment and ice front geometry, ice shelf thickness changes, dynamic variation and structural configurations. This first section therefore gives an overview of glaciological precursors to collapse on Bach, George VI and Stange Ice Shelves, and an assessment of their immediate stability.

In Section 9.2 the empirical datasets and following discussions made in Section 9.1 are used to produce a semi-quantitative assessment on the future stability of Bach, George VI and Stange Ice Shelves. A heuristic approach is implemented based on the historical patterns observed in this study, and assessments of other ice shelves in the region.

9.1 Identifying precursors to breakup, disintegration and collapse

Several key patterns and characteristics have been identified in the literature (see Chapter 2) that are common in retreat, breakup or collapse phases of other Antarctic Peninsula Ice Shelves. They are summarised below:

- The gradual retreat of Antarctic Peninsula Ice Shelves is an on-going process, and in some instances has been occurring since the 1840s (Cooper, 1997). However, there appears to be an increase in the rate of retreat in more recent decades (Cook and Vaughan, 2010).
- The complete removal of some Antarctic Peninsula Ice Shelves (George VI, Prince Gustav) also occurred during the early-to-mid Holocene (Pudsey and Evans, 2001; Bentley *et al.,* 2005; Roberts *et al.,* 2008), illustrating the cyclical response of these systems to climate dynamics.

- Patterns of ice-shelf retreat are not solely governed by geographic location. The proximity of Müller and Jones Ice Shelves to one another, but their disparity in retreat rate and characteristics, suggests something other than a simple geographic forcing. It must be recognised, however, that the progressive removal of ice shelves further south over time (Morris and Vaughan, 2003) makes geographic location a long-term factor rather than short-term cause.
- Channel and embayment geometry is a controlling factor on response times and characteristics of retreat. In the case of Jones Ice Shelf (Fox and Vaughan, 2005), it was shown that ice flowing into a converging channel was stable for longer than ice flowing into a diverging channel, despite being subjected to the same atmospheric and oceanic regimes. A similar situation was found to have occurred during the initial stages of retreat of the Prince Gustav Ice Shelf.
- The presence of ice rises and ice rumples within the ice-shelf system or close to the ice front, acts as a stabilising point and thus limits retreat (Hughes, 1983). This was observed during the retreat of the western ice front of Jones Ice Shelf (Fox and Vaughan, 2005), during the retreat of Röhss Glacier (Cooper, 1997) and following the retreat of Müller Ice Shelf into two separate portions (Swithinbank and Lucchitta, 1986). The position of Rothschild, Charcot and Latady islands surrounding Wilkins Ice Shelf may have lengthened the stability of the ice shelf (Vaughan *et al.,* 1993). Furthermore, the current impingement of Larsen C on Bawden Ice Rise (Jansen *et al.,* 2011), the interaction of Larsen D ice shelf tributaries with a succession of ice rises, and the long-term survival of shelf ice between Seal Nunataks (Cook and Vaughan, 2010) following the collapse of Larsen A and Larsen B further demonstrate the stabilising effects of ice rises on floating ice.
- Conversely, the ice rises and ice rumples identified in Wordie Ice Shelf led to heavily fractured and rifted zones of ice (Reynolds, 1988) that consequently weakened the ice-shelf system to a point where retreat was inevitable (Doake and Vaughan, 1991). Furthermore, decoupling from ice rises increases the likelihood of retreat due to the reduction of drag along the base of the ice shelf.
- Rapid retreat and/or collapse of ice shelves are often linked to increasing atmospheric temperatures and the consequent increase in surface meltwater (e.g. Scambos *et al.,* 2000; Vaughan *et al.,* 2003; Morris and Vaughan, 2003). Where abundant meltwater interacts with surface fractures, the increased pressure may

cause surface fractures to propagate through the entire depth of the ice shelf (van den Broeke, 2005; van der Veen, 2007), thus weakening the ice and preconditioning it for further retreat. The presence of meltwater at greater depths in the ice shelf is also likely to have a profound effect of the temperature, and thus the rheology of the ice shelf, that may also weaken the mechanical strength (Vieli *et al.*, 2007).

- Basal melting (Shepherd *et al.*, 2003; Fricker and Padman, 2012) may also play a critical role in preconditioning ice shelves for enhanced retreat, although direct observations are limited. Furthermore, reduced basal accretion of marine ice and frazil ice due to increased oceanic temperature may reduce the overall mass of the ice shelf and similarly lead to a thinner system.
- Alternatively, a combination of brine-infiltration and plate bending of the ice shelf may lead to enhanced fracture propagation and consequent retreat and breakup events, particularly where surface meltwater is not present (i.e. winter breakup events of the Wilkins Ice Shelf; Scambos *et al.*, 2009).
- The structural configuration of Antarctic Peninsula Ice Shelves and their mechanical strength governs the retreat and breakup processes, especially along flow discontinuities and suture zones (Glasser and Scambos, 2008).
- Acceleration of the ice shelf prior to enhanced retreat may be either a result of previous retreat or a precursor of future retreat (Vieli *et al.*, 2007).
- Ice-front geometry is a controlling factor on the stability of an ice-shelf system, with a convex profile between pinning points enhancing compressive stresses and thus limiting the rate of retreat; a switch to a more linear or concave ice front is likely to lead to an irreversible retreat of the ice front, possibly in rapid collapse phases (Doake *et al.*, 1998) as observed on Larsen A and Larsen B.
- The presence of sea ice (or multi-annual fast ice) can limit iceberg calving from an ice-shelf system by stabilising the ice front and dampening oceanic surface waves that may otherwise cause further instabilities (Reynolds, 1988; Massom, *in* Fricker and Padman, 2012).

Subsequently, Bach, George VI and Stange Ice Shelves are discussed in relation to the following criteria up to their most recent observations as presented in this study, to highlight their current stability and identify any precursors to breakup. The following parameters are considered:

- Recent retreat history.
- Regional patterns/ disparity of change.
- Channel and embayment geometry.
- Ice front geometry.
- Ice-shelf thickness and thickness changes.
- Ice-shelf dynamics and velocity change.
- Structures, significance and controls on ice-shelf retreat.
- Ice shelf composition; meteoric vs marine ice.
- Atmospheric or oceanic driven changes?

9.1.3 Recent retreat history

Understanding the pattern of ice-front retreat is critical in assessing the overall stability of Antarctic Peninsula Ice Shelves. Whilst a thorough analysis of ice-shelf extent has been achieved over an approximate 40-year timescale (Figure 9.1), it is still a relatively short time period on which to base assessments on the overall stability of ice-shelf systems. Cook and Vaughan (2010) mapped the ice front location of Bach Ice Shelf in 1947 and 1968, estimating the total ice extent to be 4798 km^2 and 4721 km^2 respectively. During 1973, Bach Ice Shelf occupied an area of 4896 km^2 (calculated in this study) and thus prior to 1973 it is suggested that the ice front underwent episodes of frontal retreat followed by advance, leading Scambos *et al.* (2000) and Cook and Vaughan (2010) to label the ice shelf as stable. It is apparent, however, that during the time period investigated here, Bach Ice Shelf shows signs of retreat across its whole ice front, albeit on a small-scale compared to other ice shelves on the Antarctic Peninsula. In total ~360 km^2 of ice was lost from its ice front between 1973 and 2010. It is thus inferred that since 1973, Bach Ice Shelf has entered a period of sustained retreat similar to the early response of other ice shelves in the region that ultimately underwent major changes.

For Stange Ice Shelf, despite being the second largest remaining ice shelf on the west Antarctic Peninsula, there are no documented extents prior to 1973. Observations presented here (see Chapter 8) illustrate that the three ice fronts responded differently over time. Thus, despite being so closely related geographically, the retreat patterns of the three ice fronts of Stange Ice Shelf have varied considerably since 1973, and without prior knowledge, it is difficult to make sound conclusions about the current health of each ice front. It is likely, however, that the mid and south ice fronts have remained relatively stable

for some considerable time, with the northern ice front most likely to have seen the greatest changes.

Indeed, the latter point is made with some knowledge of the former ice-shelf extent within the Ronne Entrance region in which all three ice shelves terminate. Whilst data for Bach and Stange are sparse, there is a wealth of data available for George VI Ice Shelf that lies between them. Smith *et al.* (2007), Roberts *et al.* (2008) and Bentley *et al.* (2011) presented evidence for the dynamic Holocene history of George VI Ice Shelf, commenting that on at least two occasions (> 120000 BP, (Sugden and Clapperton, 1982) and ca. 9600-7945 BP (Bentley *et al.*, 2005; Roberts *et al.*, 2008; Smith *et al.*, 2007) George VI Sound was free of shelf ice, and during the mid-to-late Holocene, the ice shelf extended beyond the limits seen today (Sugden and Clapperton, 1980; Clapperton and Sugden, 1982).

Smith *et al.* (2007) further demonstrated the more recent retreat of the southern extent of George VI Ice Shelf, extending the observation period back to 1947 and ca. 1967. Their results indicate a continued retreat since 1947, with significant ice loss between ca. 1967 and 1973. From observations in this study, only a small portion of the southern ice front (adjacent to Monteverdi Peninsula) was found to be advancing, yet even this area appears to show periodic advance/calving regimes (over ~40 years), with large-scale calving anticipated in the near future. The overwhelming pattern of the southern ice front is that of steady retreat, concentrated in the centre of the ice front.

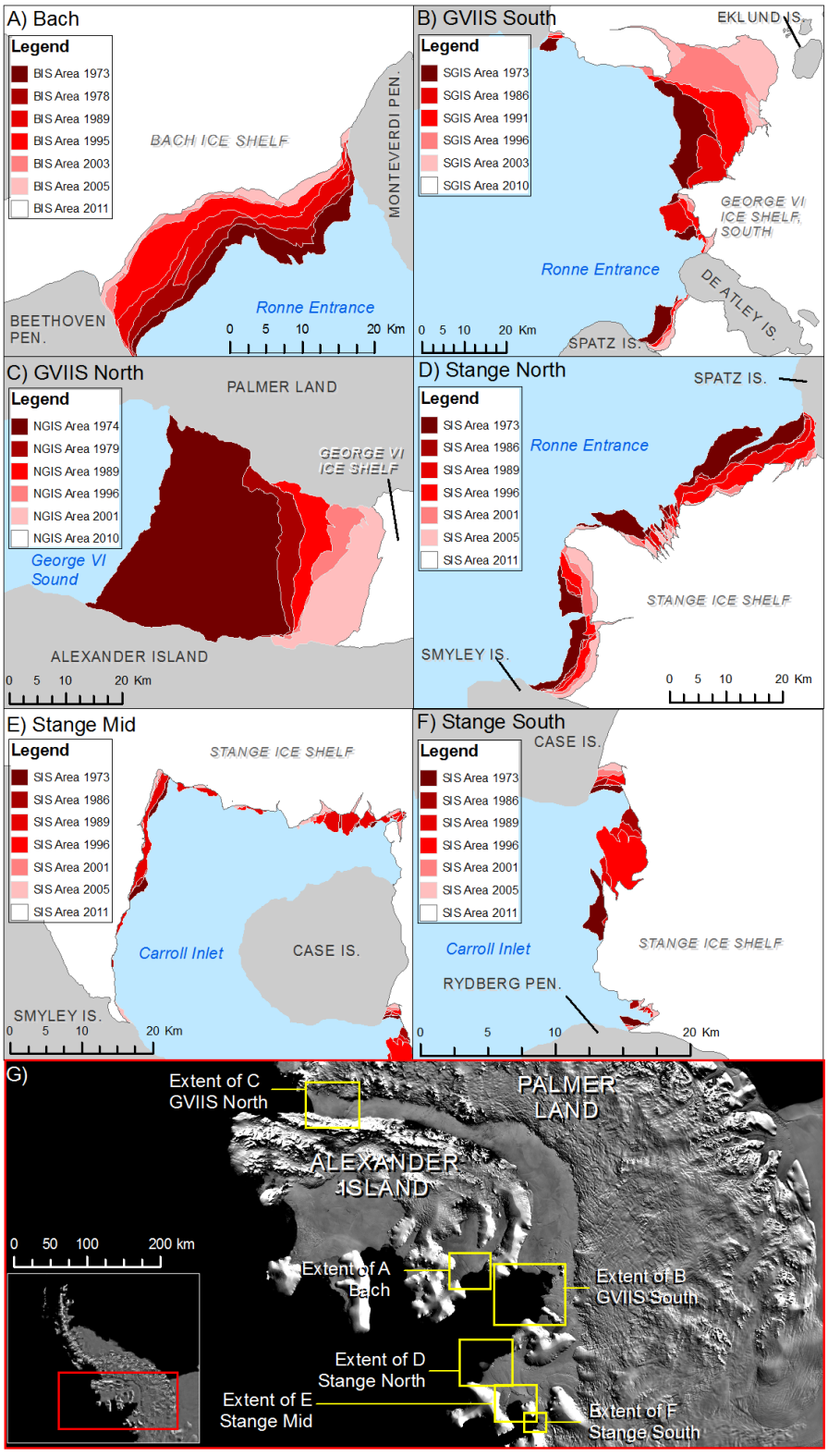

Figure 9.1. A-F Retreat of southwest Antarctic Peninsula Ice Shelves as calculated in this study from ca. 1973 to ca. 2010. G) Location of Bach, George VI and Stange ice fronts and (insert) study area on the Antarctic Peninsula.

At its northern ice front, retreat is also observed (Lucchitta and Rosanova, 1998; Smith *et al.*, 2007; Cook and Vaughan, 2010). The conditions of the ice front prior to 1947 are

uncertain, although Fleming *et al.* (1938) reported that sea-ice-filled rifts occupied the northern sections of George VI Sound, possibly extending to Cape Jeremy (Doake, 1982), some 80 km north of the present day ice front. Smith *et al.* (2007) and Cook and Vaughan, (2010) both present a 1947 extent similar to that of the 1974 limit presented in this study, but also illustrate a frontal advance between 1947 and 1960, followed by sustained retreat. If these early observations are correct, then the amount of ice loss on George VI Ice Shelf between 1936 and 1974 is similar (~40 km linear along centreline) to the loss recorded between 1974 and 2010 (~41 km linear along centreline). Interestingly, the rate of retreat over these two longer observation periods is remarkably similar (Table 9.1) and perhaps illustrates the periodic large-scale breakup of the northern ice front.

Table 9.1. Long-term retreat patterns of George VI's northern ice front

Time period	Years between observations	Total linear retreat	Rate of linear retreat	Source
1936 - 1974	38	40 km	1.05 km a^{-1}	Fleming *et al.* (1938), Doake (1982), Lucchitta and Rosanova (1998)
1974 - 2010	36	41 km	1.14 km a^{-1}	This study

*Due to the geometry of George VI Sound, the areal extent of ice loss is also likely to be similar over the two timescales.

The spatial changes at the northern ice front of George VI Ice Shelf in this study compare well with previous calculations by Lucchitta and Rosanova (1998) who identified a retreat of 993 km^2 between 1974 and 1995; here 1002 km^2 of ice was found to have been lost from the ice front from the same baseline period to 1996 (Figure 9.1C). Cook and Vaughan (2010), however, estimated the loss of ice to be much less (610 km^2 since 1947), but also commented on the difficulty of locating the true ice front prior to 1974 due to widespread sea ice and heavily rifted shelf-ice (Doake, 1982); it is likely that the large differences between their results and those presented here is due to the uncertainty in true ice front location during 1974, due to the difficulties in assessing the coarse-resolution data.

9.1.4 Regional patterns and disparity of retreat

Evidence from the retreat patterns of Jones and Müller Ice Shelves (Fox and Vaughan, 2005; Vaughan and Cook, 2010) reveal that whilst geographic location is not a controlling factor on short-term ice-shelf changes, the overall pattern of ice loss on the Antarctic Peninsula has followed the southern migration of the -9°C mean annual isotherm (Morris and Vaughan, 2003). It is perhaps not surprising therefore, that the greatest loss of ice occurred from George VI Ice Shelf, and the least amount of ice was lost from Stange Ice Shelf (Figure 9.2).

However, the retreat of the southern extent of George VI Ice Shelf precedes that of the northern ice front (Smith *et al.*, 2007), and even two or more ice fronts on the same ice shelf can respond remarkably differently over the same timescale (e.g. Cooper, 1997; Fox and Vaughan, 2005; Cook and Vaughan, 2010). Consequently, the response of each ice front investigated in this study is considered individually below.

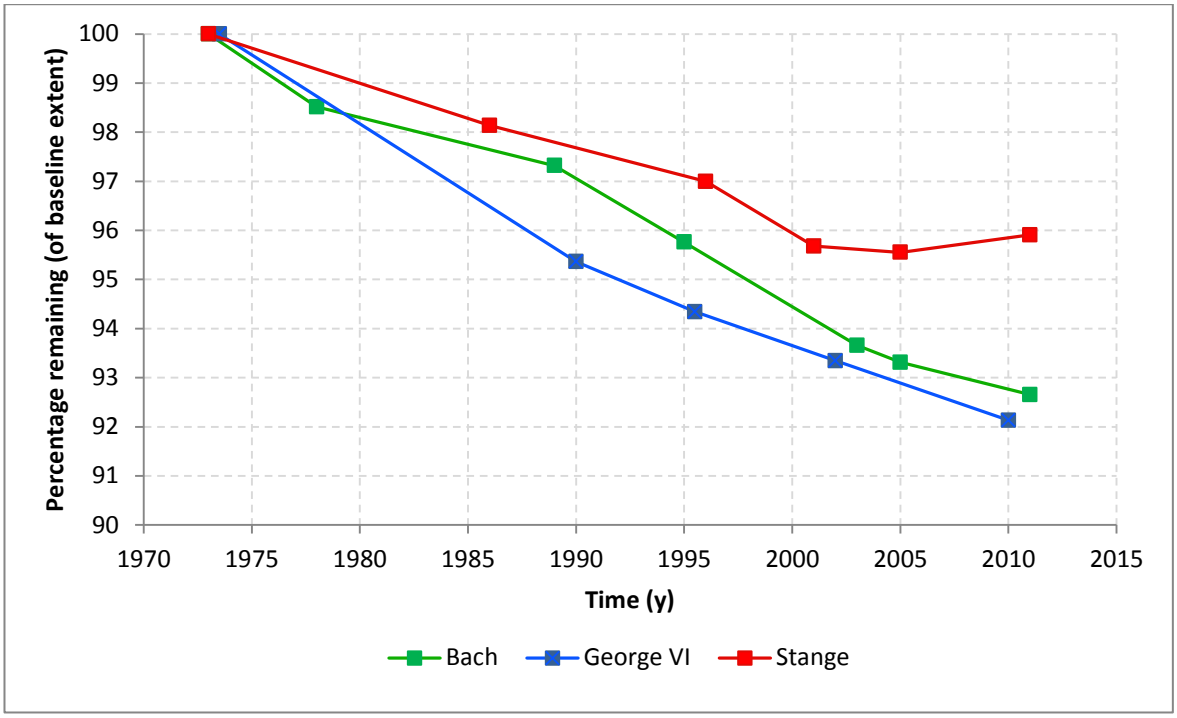

Figure 9.2. Ice-shelf area remaining following retreat between ca. 1973 and ca. 2010, illustrating that the most northern ice shelf (George VI) has undergone the most retreat, and the most southern ice shelf (Stange) the least retreat. Also note how the spatial extent of Stange Ice Shelf has remained relatively stable since ca. 2000 where as George VI and Bach Ice Shelves have continued to retreat at relatively constant rates.

Figure 9.3 displays ice front retreat data expressed as percentage loss over time to allow direct comparisons between ice fronts to be made. There are some clear disparities in the data sets: First, the large-scale retreat of George VI's north ice front between 1974 and 1979 is illustrated, followed by an extended period of regular, but reduced ice loss. This pattern is not reflected anywhere else on the south-west Antarctic Peninsula, highlighting the regional differences between ice shelves over shorter time periods. George VI's south ice front, however, shows a more cyclical pattern of increasing and decreasing retreat rates, although the timescale is too short to make any significant claims on these patterns of retreat. The ice fronts of Stange mid and Stange south also stand out, with the majority of the observed retreat occurring in one single retreat phase. For Stange mid-ice front, this observation can be neglected as there are few observations of clear retreat in this dataset,

and changes are linked to atypical ice-shelf motion adjacent to, rather than towards, the ice front. The peak in the Stange south ice front dataset can be linked to the calving event during ca. 2000 that occurred as part of its steady growth/retreat cycle.

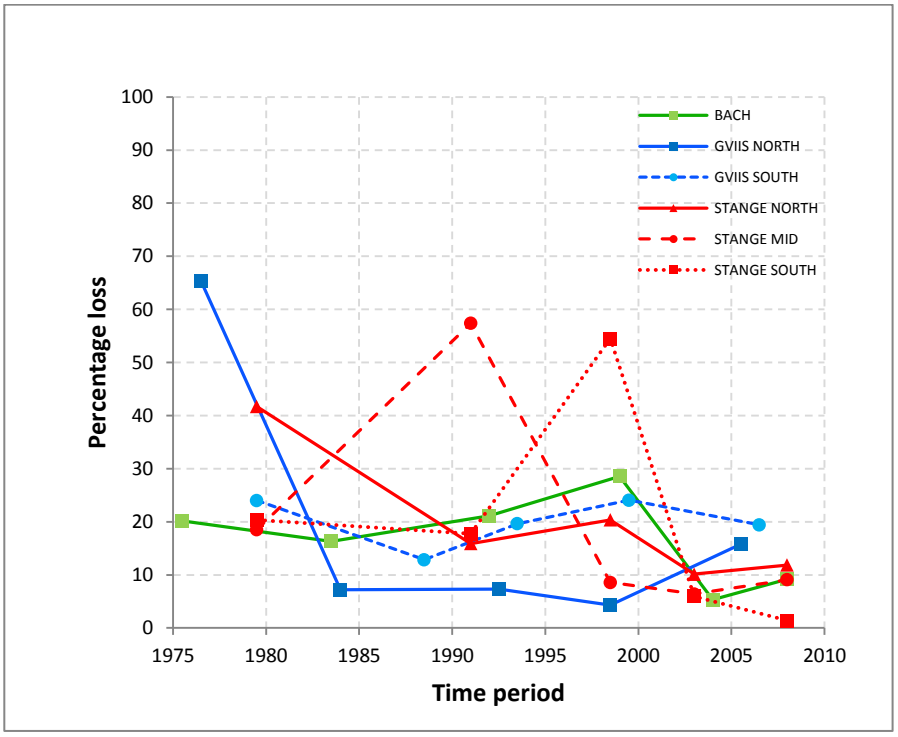

Figure 9.3. Timing of retreat (only), displayed as percentage of total loss against time period for individual ice fronts. Markers illustrate when loss occurred, interpolated lines show patterns of loss over time. (GVIIS = George VI Ice Shelf). Note the difference between GVIIS NORTH and the other ice fronts. The rate of loss for STANGE MID atypically increases leading up to 1990. BACH, GVIIS SOUTH, STANGE NORTH and STANGE SOUTH all show increases in percentage of ice loss between ca. 1990 and ca. 2003, with the latter explained by clear cyclical calving regime of a healthy ice front. BACH, GVIIS SOUTH and STANGE NORTH all show broadly similar patterns of retreat between ca. 1990 and ca. 2003 that may be as a result of their geographic proximity to localised climatic/oceanic changes that is discussed further in Section 9.1.11.

The ice fronts of Bach, George VI south and Stange north, however, do show broadly similar patterns of ice loss between ca. 1990 and ca. 2003 (Figure 9.3). (Prior to 1985-1990 there are few similarities; ice loss from Stange north and George VI south halves, whereas ice loss from Bach Ice Shelf slowly increases). These patterns are followed by enhanced retreat between ca. 1990 and ca. 2003 at all sites, and from then until ca. 2010, the amount of ice-loss recorded at each ice front decreases, albeit at different rates. The different morphologies, geometries and glaciological characteristics between each site are discussed below, but one clear relationship between each of the sites is their geographic proximity

around the Ronne Entrance area, that may, in part, be a controlling factor on the rate of retreat and ultimately the (in)stability of these ice-shelf systems.

9.1.5 Embayment geometry and characteristics

Bach Ice Shelf stands apart from the other ice shelves on the Antarctic Peninsula, as it is almost entirely enclosed by the tip of Beethoven Peninsula to the west and the tip of Monteverdi Peninsula to the east. Furthermore, the headlands of Bennett Dome and Shostakovich Peninsula play a vital role in the dynamics of the ice shelf; essentially, any ice that enters one of the four ice domains is fed to a relatively narrow 40 km-wide channel. Consequently, Bach's ice front sits in a converging embayment and is likely to have impacted the rate of retreat observed.

The north ice front of George VI Ice Shelf also sits in a unique physical setting. The long, narrow channel of George VI Sound gradually widens to Cape Jeremy, but to class it as a diverging channel is somewhat misleading due to its irregular morphology either side of the channel. The retreat of the northern ice front takes place across its entire profile, thus the ice-front pinning points along Palmer Land and Alexander Island are considered relatively instable, and it is suggested that their position is governed by something other than simply the channel geometry. Conversely, the south ice front of George VI Ice Shelf is situated in a clearly-diverging channel, opening up to widths greater than 80 km near to the ice front. Based on the assumptions of previous work, the south ice front should therefore be more susceptible to enhanced retreat, although in reality, the pinning points at the southern margin are far more stable than those of the north ice front, and only undergo a slight linear retreat throughout the observation period. Also at the southern ice front, the positioning of the Eklund Islands and De Atley Island is likely to be a controlling factor on the patterns and processes of retreat (Humbert, 2007).

There are two arguments surrounding the effect of ice rises in ice shelves; 1) their existence stabilises shelf-ice to a point where retreat is limited (Hughes, 1983; Vaughan, 1993), or 2) ice rises act as a 'wedge', contributing to the weakness of the ice shelf and thus hastening retreat (Vaughan, 1993; Cook and Vaughan, 2010). Structural assessment carried out in this study reveals high compressive stresses on the stoss-side of the ice rises and ice rumples near the southern ice front of George VI Ice Shelf. Lee-side of the ice rises, fracturing and rifting occurs, along which iceberg calving eventually takes place. The recent recession of George VI Ice Shelf at its southern margin has almost certainly been enhanced by the fracturing caused by its dynamic interaction with the Eklund Islands.

More recent imagery suggests, however, that the ice front has become pinned on some of the larger ice rises near the ice front that from now may play an important role in stabilising the southern ice front and consequently limiting future retreat rate.

Stange Ice Shelf's embayment geometry is distinct from Bach and George VI Ice Shelves, and indeed those elsewhere on the Antarctic Peninsula. It perhaps most closely resembles the Wilkins Ice Shelf in that it appears to be stabilised by large islands that ultimately control its dynamic regime. However, unlike the Wilkins Ice Shelf, ice is fed into Stange Ice Shelf from the two largest islands, Spatz and Smyley Islands, which thus actively add mass to the ice-shelf system, rather than solely acting as pinning points that do not add mass. The three ice fronts of Stange Ice Shelf also sit in markedly different channels and embayments.

Stange's northern ice front occupies a diverging channel between Spatz Island and Smyley Island, whereas its southern ice front currently sits in a converging channel between Rydberg Peninsula and Case Island. Ultimately, the northern ice front is more susceptible to retreat, as displayed in the retreat patterns since 1973. A more complex embayment geometry exists along the mid ice front, because of its ice front geometry as discussed in Section 9.1.6. However, generally, the mid ice front sits in an open embayment, pinned against Case Island along its eastern extremity.

9.1.6 Ice-front geometry

The frontal geometry of the individual ice shelves has been referred to during the interpretations of retreat in chapters 6.2, 7.2 and 8.2 so is only briefly reiterated here. Bach's ice front has both a concave and a convex portion that ultimately creates a stable, compressional geometry. Over time, however, the concave portion has become more dominant due to iceberg calving regime. Furthermore, the decoupling of the ice front from Monteverdi Peninsula has, not only increased the width of the channel that the ice front occupies, but the profile length of the ice front. If this pattern continues, then Bach Ice Shelf may soon enter a phase of enhanced retreat. Complete removal of the convex portion of the ice front will consequently weaken the structural stability of Bach Ice Shelf, similar to the interpretations of Doake *et al.* (1998) for Larsen A.

The northern margin of George VI Ice Shelf during the observation periods in this study has largely remained concave, and thus it is argued that it has always been pre-conditioned for iceberg calving. The current ice front is similarly concave, cutting back towards its centreline from the pinning points along Palmer Land and Alexander Island, and is thus similarly susceptible to further retreat.

Since 1973 the southern ice front has shown a concave profile, becoming increasingly so with concentrated retreat towards the centre of the ice front. The consequent splitting of the southern ice front during March 2010, however, created two convex configurations. South Ice Front 3, which sits between De Atley and Spatz Island, has a similar profile geometry to that of Bach Ice Shelf. Likewise, the pattern of retreat has increased the area of the concave portion and consequently reduced the structural stability; in its current form, however, this narrow ice front is still believed to be stable.

Stange's northern ice front largely protrudes beyond the extent of both of its pinning points making it broadly convex and thus stable (Doake *et al.,* 1998), whereas its southern ice front (during 2011) displayed both a convex and concave portion. The mid ice front is again difficult to assess because of its glaciological configuration. The Smyley Island ice front (see Figure 8.24) is slightly concave between its grounded pinning point and confluence with the Lidke Ice Stream ice front; over time, it becomes increasingly concave towards its eastern confluence albeit on a small scale. The Lidke Ice Stream ice front is generally convex, although again, this is atypical of an ice front system because of its dynamics. The ST06-fed portion is also convex. Thus, overall, the mid ice front of Stange Ice Shelf is considered geometrically stable (see Figure 9.1).

9.1.7 Ice-shelf thickness and elevation (thickness) changes

9.1.7.1 Ice-shelf thickness

There are few direct links made between ice-shelf thicknesses and their retreat/ breakup patterns, most likely due to the spatial absence of thickness data on Antarctic Peninsula Ice Shelves prior to major retreat phases. Measurements have mostly been confined to small areas on individual ice shelves, that whilst highly accurate (Griggs and Bamber, 2011), are spatially non-representative.

The view taken here is that if a thinning ice shelf (as discussed below) becomes increasingly susceptible to fracture and retreat (e.g. Shepherd *et al.,* 2003; Skvarca *et al.,* 2004; Rack and Rott, 2004; Fricker and Padman, 2012), then pre-existing areas of thinner ice are also more susceptible to retreat than comparatively thicker regions of ice, even in close proximity within the same ice-shelf system. One key characteristic of the retreat patterns of Bach Ice Shelf and George VI Ice Shelf in particular, is the difference in retreat patterns in areas of thinner ice. Until now, these inferences have mostly been made by assessing the relative ice-shelf surface elevations that elsewhere have been used to calculate ice-shelf thicknesses (e.g. Shuman and Fahnestock, 2005; Braun *et al.,* 2009). In a recent study, Griggs and Bamber (2011) produced 1 km-resolution thickness estimates for all of Antarctica using ERS-1 radar altimetry data from ca. 1995; Figure 9.4 presents those data for Bach, George VI and Stange Ice Shelves.

Whilst the retreat patterns of Bach Ice Shelf are similar along its frontal profile (see Figure 6.15), it is clear that the concave portion of the ice front is situated in much thinner (~70 m) ice than the convex portion to the east (~200 m; Figure 9.4). This thinner region of ice near Bach ice front extends backwards to Bennett Dome, and connects with the distinct fracture zone caused by the confluence of tributary glacier units that is inherently thinner. A similar thickness configuration has been identified along South Ice Front 3 of George VI Ice Shelf (Figure 7.41), with thinner ice to the west (~80 m) displaying a concave ice front and thicker ice (~170 m) conversely displaying a convex profile; here, enhanced retreat has been recorded in the area of thinner ice between 1973 and 2010. Additionally, the large area of thinner ice inferred around, and downstream of, the Eklund Islands is confirmed by Griggs and Bamber's (2011) thickness estimates. This area of George VI's main south ice front has clearly been more susceptible to retreat than adjacent units. Interestingly, the relatively static pinning points at the ice front of George VI south are also thicker than the ice between them, and may explain their relative stability. Consequently, it is inferred that

thinner ice is more likely to undergo retreat than thicker ice because it is more susceptible to fracturing. Thicknesses across the ice fronts of Stange Ice Shelf and George VI north, however, are relatively consistent, and do not seemingly play a role in determining retreat patterns.

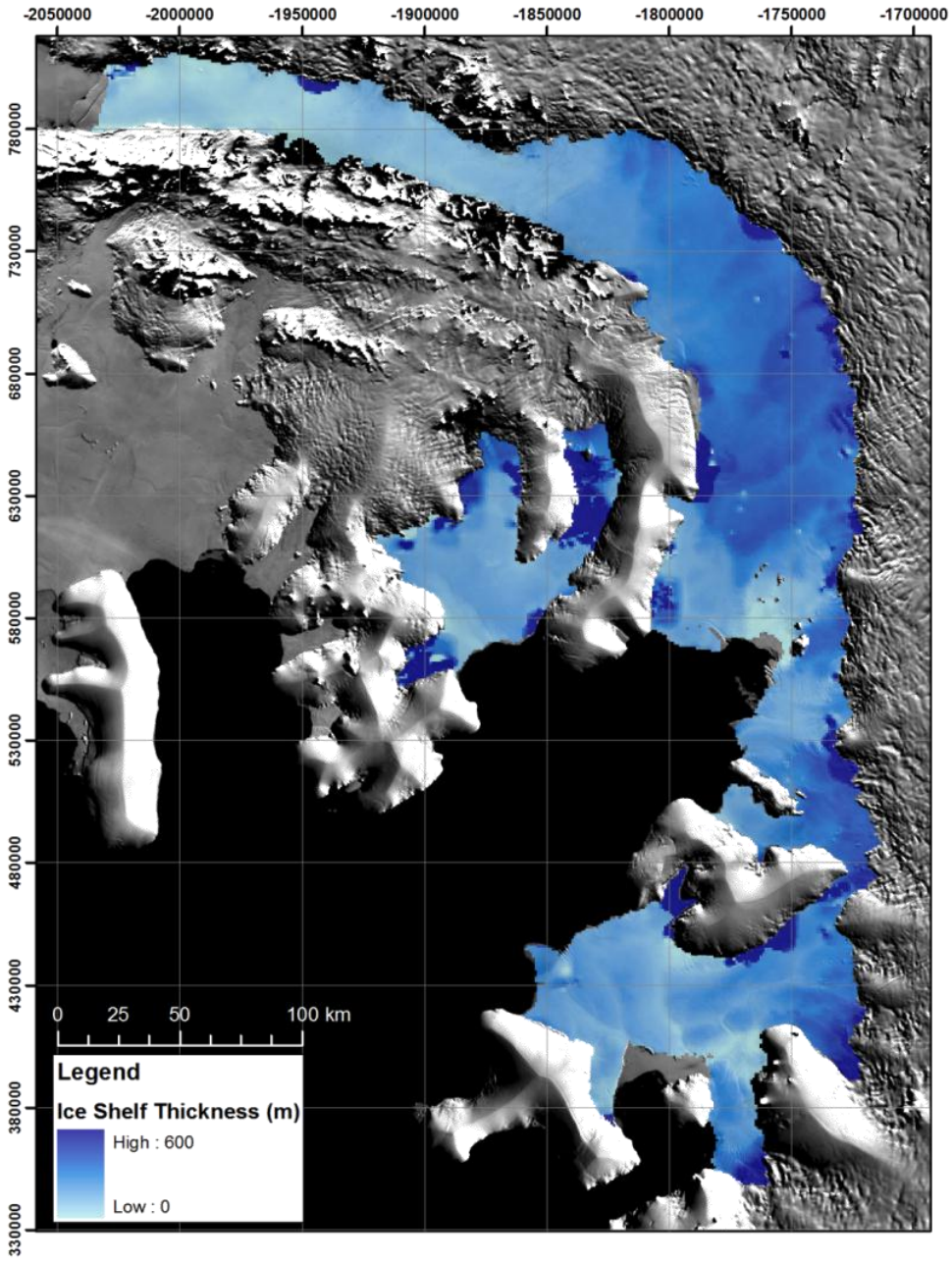

Figure 9.4. Thickness calculations for Bach, George VI and Stange Ice Shelves from 1995 ERS-1 radar altimetry data, clipped to 2010 ice-shelf extents. Note the concave portion of Bach and George VI southern ice fronts correlating with thinner regions of ice, whereas the more stable, convex portions are generally thicker in composition. Data sources: Ice thicknesses (Griggs and Bamber, 2011), MODIS MOA background image (Haran *et al.*, 2006).

9.1.7.2 Elevation changes and ice-shelf retreat

Whilst spatial thickness patterns have rarely been considered in ice-shelf retreat, thickness changes (and/ or surface elevation changes) have been studied in much greater detail (e.g. Shepherd *et al.,* 2003; Skvarca *et al.,* 2004; Zwally *et al.,* 2005; King *et al.,* 2009; Fricker and Padman, 2012; Pritchard *et al.,* 2012). Thinning has been attributed to the enhanced retreat or collapse of Antarctic Peninsula Ice Shelves (e.g. Larsen A, Larsen B), based on sub-decadal measurements of surface elevation changes. Changes in ice-shelf thickness can be driven by various processes including changes to basal and surface mass balance conditions, ice divergence, variation in ice dynamics and ice flux across the grounding zone (Khazendar *et al.,* 2011; Shuman *et al.,* 2011) and the compaction of firn overtime (Shepherd *et al.,* 2003, 2004). Elevation-change measurements obtained in this study are likely to represent variations in one or more of these components. Broadly speaking, each of the above drivers of ice thickness can be attributed to either atmospheric or oceanic forcing, which are discussed in Section 9.1.11.

Here, ICESat surface-thickness/elevation-change calculations reveal widespread thinning on each of the Bach, George VI and Stange Ice Shelves, with the greatest changes observed near the ice front of Bach Ice Shelf and the southern section of George VI Ice Shelf. There has been, however, limited surface-elevation change recorded in the northern section of George VI Ice Shelf, coinciding with a reduction in the retreat rate as observed from 1973 to 2010. Elevation changes measured on Stange Ice Shelf reveal no correlation between patterns of retreat and patterns of thinning, other than widespread, strong surface-elevation changes over much of the ice shelf.

It is known, however, that both atmospheric and oceanic variability in the Antarctic Peninsula region can range from inter-annual to decadal timescales (Meredith and King, 2005; Monaghan *et al.,* 2006; Martinson *et al.,* 2008; Holland *et al.,* 2008), thus whilst surface elevation measurements may reflect the shorter timescale, they may not be consistent with rates over longer timescales (Fricker and Padman, 2012), as illustrated over a 40-year time period on the Amery Ice Shelf (King *et al.,* 2009). The elevation change data presented in this study between 2003 and 2008, therefore only represent variations over a sub-decadal timescale. These results therefore may or may not be characteristic of a longer response of Bach, George VI and Stange Ice Shelves to either atmospheric and/or oceanic changes. Recently, Fricker and Padman (2012) published a 30-year quasi-

continuous surface-elevation change dataset for Antarctic Peninsula Ice Shelves, and therefore provide a more representative assessment of ice-shelf thickness changes. The results from that study are presented in Table 9.2 and Figure 9.5, and consequently compared to the ICESat datasets calculated here.

Table 9.2. Comparison of elevation-change data. ERS-1, ERS-2, Envisat and Seasat calculations taken from Fricker and Padman (2012). See Figure 9.5 for graphical representation.

	ERS-1	ERS-2	Envisat	Seasat to Envisat	ICESat (this study)
	1992-1996	1995-2003	2003-2008	1978-2008	2003-2008
Bach	-0.23 ± 0.05 [3]	-0.13 ± 0.01	-0.09 ± 0.03	-0.09 ± 0.01 [113]	-0.17 ± 0.09 [950]
Stange^{+}	-0.61 ± 0.19 [9]	-0.18 ± 0.09	-0.09 ± 0.18	N/A	-0.45± 0.09$^{\#}$ [1056]
GVIN	-0.11 ± 0.19 [3]	-0.17 ± 0.1	-0.24 ± 0.08	-0.13 ± 0.02 [14]	-0.03 ± 0.05* [610]
GVIC	-0.16 ± 0.07 [6]	-0.06 ± 0.02	-0.08 ± 0.04	-0.04 ± 0.00 [206]	-0.05 ± 0.12* [804]
GVIS^{+}	-0.26 ± 0.06 [14]	-0.14 ± 0.5	-0.05 ± 0.07	N/A	-0.32 ± 0.09* [1882]
GVIW	-0.44 ± 0.7 [4]	-0.01 ± 0.27	-0.20 ± 0.09	N/A	-0.12 ± 0.09* [299]

Values given represent averaged-surface elevation change in ma^{-1} over the specified time periods. Errors given for ERS-2/2 Envisat and Seasat data are standard deviations, whereas ICESat error is based on cross-over analysis. Values given in square-brackets represent number data points used; the same cross over points are used for ERS-2 and Envisat as in ERS-1 analysis.

**Recalculated surface elevation change to match spatial extent of data presented in Fricker and Padman (2012) for each of the GVIIS locations.*

$^{\#}$Uncertainty estimated from the average of all other cross-over track uncertainties on Bach and George VI Ice Shelves due to the absence of cross-over data on Stange Ice Shelf.

$^{+}$Original data presented in Table 1 of Fricker and Padman (2012) differed from that presented in Figure 4 (of the same publication). Fricker (personal communication) has since confirmed that values presented in Table 1 of their study were printed incorrectly. Figure 4 of that study was used to obtain the correct data on which this table and Figure 9.5 is based.

There are clear similarities and differences between the datasets, in particular, and most significantly, between the Envisat and ICESat results between 2003 and 2008. The clearest agreements between these two surface-elevation-change estimates are observed over Bach Ice Shelf and the central and western portions of George VI Ice Shelf (GVIC, GVIW. Figure 9.5). ICESat measurements, however, estimate greater surface lowering for Bach Ice Shelf between 2003 and 2008 than Envisat radar altimetry data, with a more conservative estimate of elevation changes recorded for the western and central regions of George VI Ice Shelf.

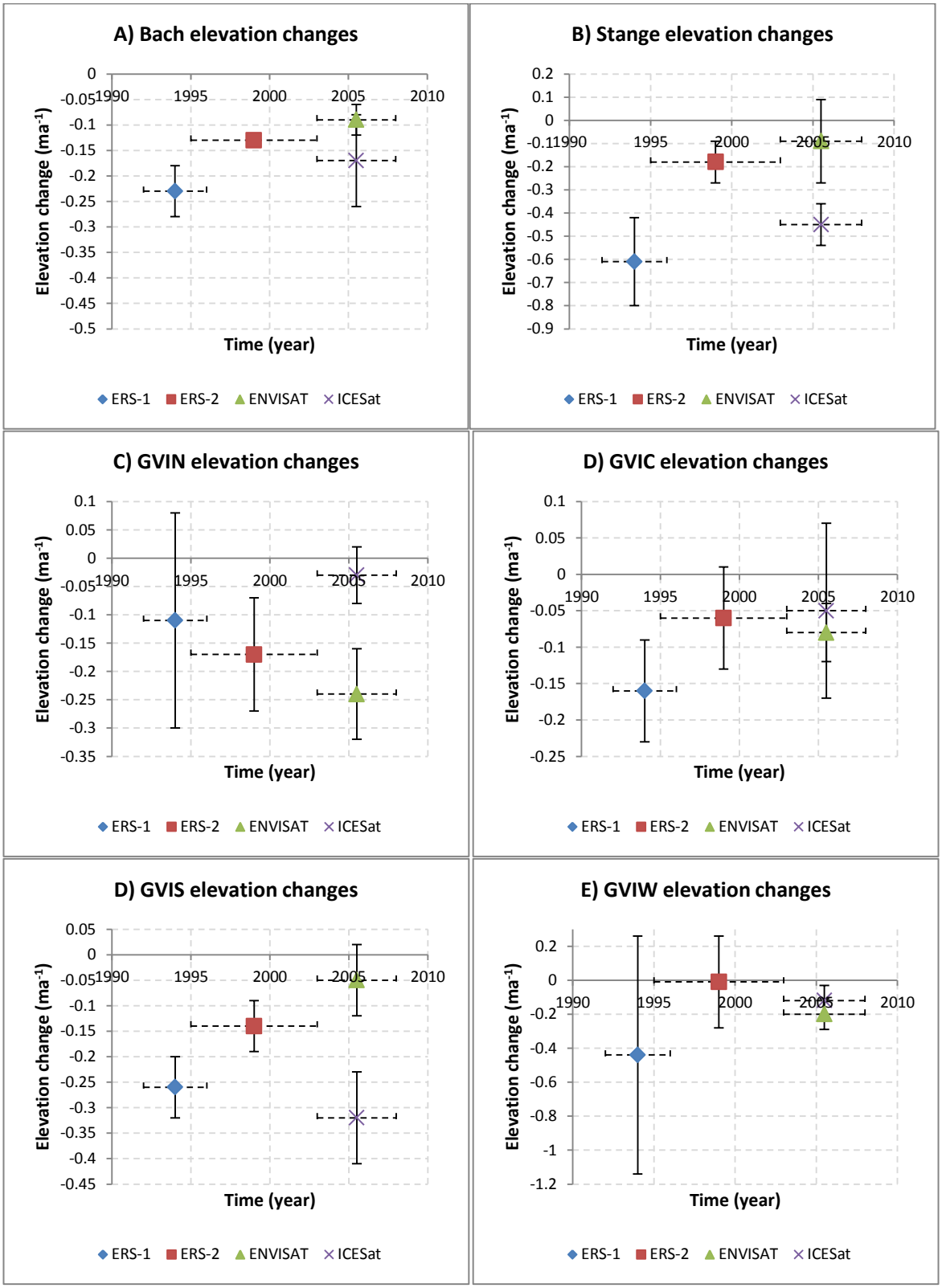

Figure 9.5. Surface elevation changes between 1992 and 2008 as recorded by Fricker and Padman (2012; ERS-1, ERS-2 and ENVISAT) and calculated in this study (ICESat). Patterns, similarities and disparities are discussed in the text below. Horizontal 'error' bar illustrates length of observations with the marker being the centre point of the acquisition period. Vertical error bars represent data displayed in Table 9.2.

Major differences are observed between Envisat and ICESat calculations in the northern section of George VI Ice Shelf (GVIN, Figure 9.5C), with ICESat measurements revealing significantly less negative surface-elevation changes than the Envisat measurements, as well as less negative change as recorded in the ERS-1 and ERS-2 phases. Greater differences still are recorded in the southern region of George VI Ice Shelf (GVIS, Figure 9.5D) and over Stange Ice Shelf (Figure 9.5B), where Fricker and Padman (2012) calculate regular, but reducing, negative surface-elevation changes, whereas ICESat measurements suggesting strong negative elevation changes between 2003 and 2008 (Table 9.2; Figure 9.5).

There are a number of possible reasons why the elevation change measurements show differences over the same time period and prohibit a direct comparison, including, 1) the ice-shelf area over which elevation measurements were taken and the location of measurements, 2) the number of repeat-measurements made to calculate elevation change, 3) the acquisitional properties of the different sensors, 4) the accuracy of data acquisition and, 5) the accuracy and precision of data processing. The latter two inaccuracies are thought to be minimal due to the relative precision of both sensors.

The elevation change measurements presented in Fricker and Padman (2012) are based solely on cross-over analysis of radar altimetry data, meaning that spatially, the elevation change measurements were somewhat restricted. Although only slight differences between surface-elevation measurements from Envisat and ICESat data exist on Bach Ice Shelf, the radar altimetry estimates were based on three points in the central portion of the ice shelf, and therefore did not consider changes at the ice front, in the Stravinsky Ice Domain or towards the Weber Ice Domain, thus missing key thickness variations as calculated in this study. The broad areas of analysis over George VI Ice Shelf and Stange Ice Shelf in Fricker and Padman (2012) are similar to those presented in this study, but their cross-over analysis technique again prevents, 1) data acquisition in key areas (for example, the centreline of George VI South), and 2) data acquisition in comparable locations in the same ‘areas’ as presented in Table 9.2 (i.e. whilst their study and this study present changes in each of the six locations, estimates were based on different locations within each area, and are therefore not directly comparable).

Furthermore, the reliance on cross-over analysis in Fricker and Padman (2012) substantially reduces the number of data points on which they base elevation-change calculations (Table 9.2, square brackets), thus they present a broad overview of changes

without necessarily assessing the finer spatial response across the ice-shelf surfaces as presented here. The ICESat data points thus enhance the spatial resolution of elevation measurements and elevation changes between 2003 and 2008.

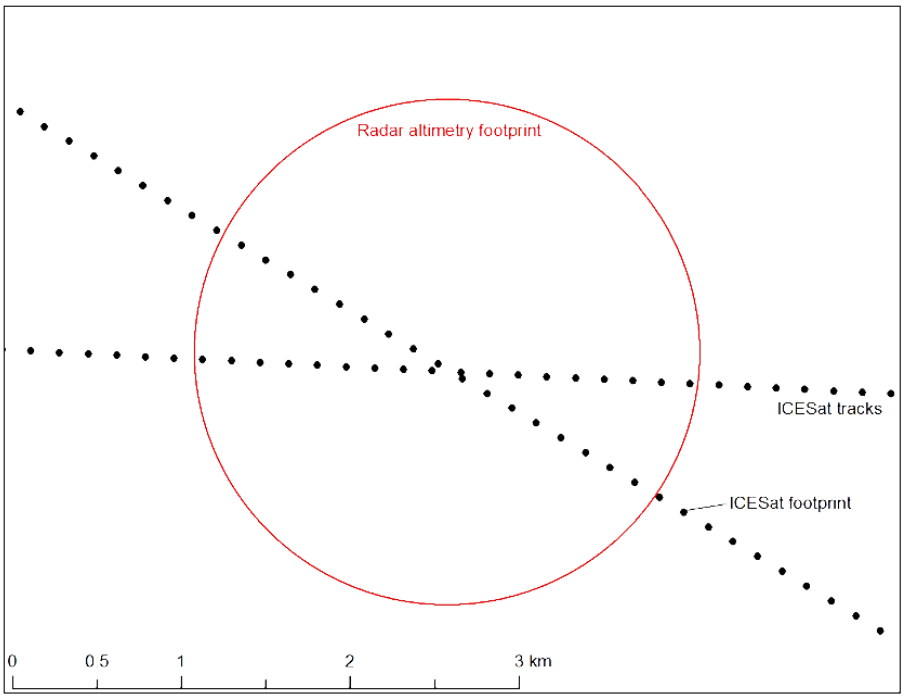

Figure 9.6. Scaled schematic illustrating the areal difference between radar altimetry and ICESat GLAS footprints over which elevation change measurements are calculated.

Additionally, the acquisitional characteristics of radar altimetry and ICESat differ considerably. First, the footprint of radar altimetry data is roughly 3 km^2 (Shepherd *et al.*, 2003; Zwally *et al.*, 2005) therefore surface elevation measurements are essentially averaged over an area of 7 km^2, whereas the approximate 40 m footprint of an ICESat GLAS pulse takes an elevation measurement over an approximate 0.0012 km^2 area (Figure 9.6). Consequently, ICESat elevation measurements have a finer spatial resolution, but only acquire data over a 40 m-wide track, whereas the spatially-limited radar altimetry data presented in Fricker and Padman (2012) have a coarser resolution over a wider swath. Resultantly, ERS-1, ERS-2 and Envisat data are less sensitive to small-scale horizontal and vertical changes on the ice-shelf surface, with ICESat measurements conversely more sensitive to small-scale changes.

The difference between the two system types may play an important role in change-detection. The radar systems of ERS-1, ERS-2 and Envisat penetrate the upper surface layer of the ice shelves (Shepherd *et al.*, 2003; Lillesand *et al.*, 2008; Humbert and Steinhage, 2011), whereas the laser pulse of ICESat records the true ice-shelf surface

(Fricker and Padman, 2012). Consequently, the two difference sensor types record two different 'elevation' measurements, with elevation-change calculations thus representing two slightly different components; the radar altimetry data represent a discrete boundary between loose ice-crystals and more compact glacier ice at depth (up to 10 m) whilst the ICESat measurements represent the actual surface elevation regardless of ice compaction, thus making the latter more sensitive to changing surface conditions related to short term weather and climatic patterns.

Consequently, it is not reasonable to compare ICESat and radar altimetry datasets directly without some prior calibration. Identifying patterns between the datasets calculated in this study against those presented elsewhere (Zwally *et al.,* 2005; Fricker and Padman, 2012) is thus largely prohibited.

However, by only considering the datasets presented by Fricker and Padman (2012) to assess the longer timescale of change, alongside the retreat rates observed here, discrete patterns are observed, and indeed each ice shelf has undergone sustained thinning over the last four decades. The greatest negative-surface-elevation changes on Bach, GVIS, GVIW and Stange were all observed during the ERS-1 observation period between 1992 and 1996, coinciding with the increased rate of retreat between ca. 1990 and ca. 2003. Interestingly, the negative-surface-elevation-change measurements generally decreased, also coinciding with the general decrease in rate of retreat over a similar timescale. Conversely, only in the northern region of George VI Ice Shelf (GVIN) does the rate of negative surface-elevation change increase, yet this does not coincide with an increased rate of retreat.

There is perhaps further evidence that the ice shelves that feed into the Ronne Entrance embayment are linked, with surface lowering (and inferred thinning) seemingly following a similar pattern. It is thus proposed that there is a clear link between thinning ice and enhanced retreat over multi-decadal timescales as observed prior to breakup of other ice shelves. The causes of increased thinning on the southwest Antarctic Peninsula are discussed in more detail in Section 9.1.11.

9.1.8 Ice-shelf dynamics and velocity changes

9.1.8.1. Dynamic configuration

The greatest control on ice-shelf retreat, breakup and collapse is arguably the dynamic configuration of an ice shelf, including flow speeds, velocities, dynamic changes (vertical and horizontal) and the interaction of different flow units. These, in part, are controlled by those criteria already discussed, including ice shelf and embayment geometry, ice thickness and thickness changes, and associated retreat characteristics. Here, only the horizontal component of dynamics is discussed.

Despite its confining embayment geometry, the flow speeds of Bach Ice Shelf typically increase towards the ice margin from the grounding zone, with the greatest speeds calculated at the centre of the ice front. Ice flow over much of the ice shelf is controlled by those tributary glaciers entering the Boccherini Ice Domain, and consequently, the majority of retreat occurs from this domain, and therefore has the greatest control on the rate of retreat.

The dynamic regime of George VI Ice Shelf is more complex. There is a dominant inflow from Palmer Land glaciers that in the northern section, often stretch across George VI Sound and turn just a few kilometres short of Alexander Island (Pearson and Rose, 1983; Reynolds and Hambrey, 1988; Humbert, 2007). Towards the southern section, flow is still dominated by Palmer Land glaciers, although the flow direction is more typical of an ice-shelf system, with flow units approaching the ice front perpendicularly.

Pearson and Rose (1983) inferred the flow direction (Figure 9.7A) of George VI Ice Shelf by analysing a combination of Landsat MSS imagery, oblique aerial photographs, USGS sketch maps (1:500000), ice flow transect data and ice thicknesses. Their flow lines in the northern and southern sections are similarly reflected in interpretations made in this study, but the location of the ice-shelf ice divide (where flow diverges to north and south ice fronts) differs markedly, and therefore the interpretations of the ice shelf's dynamics also differ (Figure 9.7B). As the longitudinal flow structures mapped in this study do not change over time, the differences between the inferred flow directions are attributed to misinterpretation of limited data by Pearson and Rose (1983). Furthermore, a modelling study by Humbert (2007) is in agreement with the location of the ice divide as presented in this study, and recently compiled velocities (Rignot *et al.,* 2011) are in good agreement with the speeds derived by feature tracking and InSAR here.

One key conclusion to emerge from numerical modelling of George VI's dynamics was that ice speeds at the northern front are dominated by the inflow of ice from Palmer Land, whereas the dynamics of the southern ice front are driven by a steep thickness gradient from the ice divide to the south ice front (Humbert, 2007). This provides a very basic overview of the dynamic regime of George VI Ice Shelf, as it is apparent in this study that ice flowing towards South Ice Front 2 is also likely to be controlled by inflow of ice, whereas only South Ice Front 1 is driven by the thickness gradient, as well as being influenced by the presence of the Eklund Island ice rises that evidently retard ice flow.

It is difficult to relate retreat patterns observed on George VI Ice Shelf with its ice-flow regime due to the lack of sufficient flow measurements at either ice front prior to 1989 (the changing surface velocities are discussed in Section 9.1.8.2). Retreat at the southern ice front since then was largely concentrated in slow-moving ice, lee-side of the Eklund Islands, whereas faster moving units to the north and west of these ice rises retreated less. Other factors controlling the spatial patterns of retreat in this location have already been discussed, but the dynamic regime may also play an important role in retreat pattern. It is evident that the potential flux of ice to the ice front lee-side of the Eklund Islands is less than the potential flux of ice alongside Monteverdi Peninsula and towards South Ice Front 2. Consequently, even if the rate of absolute calving were constant over time along the whole ice front, the amount of retreat would appear greater in regions of slower moving ice, although this would need to be analysed over finer temporal resolutions to confirm or refute calving rate/ ice flux as a principal control on retreat patterns.

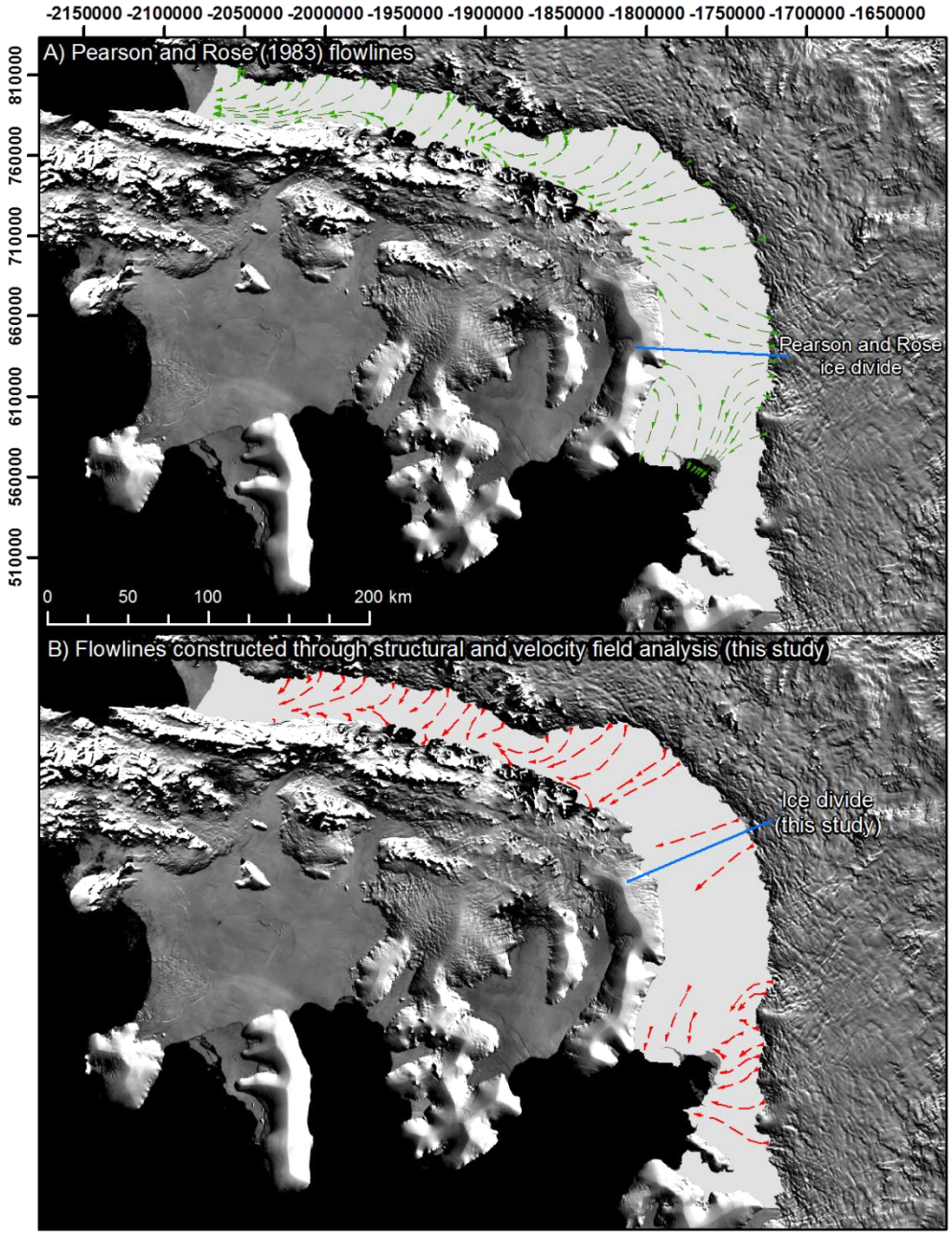

Figure 9.7. Flowlines (flow vectors) on George VI Ice Shelf as inferred by A) Pearson and Rose (1983) and, B) surface structures and calculated velocities in this study. Note the difference in positioning of the ice divide that splits ice flux to the northern and southern regions. Background image = MODIS MOA (Haran *et al.*, 2006)

At the northern ice front, calving and retreat are governed by one major flow unit that has altered after major calving events (such as between 1974 and 1979). Currently, the retreat patterns at the northern ice front are controlled by the flow dynamics of Riley Glacier.

At the northern ice front of Stange Ice Shelf, greater retreat is observed in ice fed by Spatz Island to the east and Smyley Island to the west, whereas ice towards the centre of the northern margin appears more resistant to iceberg calving. In the former location,

increasing flow around the tip of Spatz Island causes sudden fracturing that precedes iceberg calving whilst calving along the latter portion is governed by small fractures developed by tidal flexure at the grounding line that are carried to the ice front. Despite the clear difference in retreat rates along the ice front, there are no clear flow discontinuities.

The dynamics of the mid ice front vary considerably, yet the amount of absolute retreat recorded is minimal, thus changes at the mid ice front cannot be attributed to the flow speeds or dynamic regime of the ice shelf. At the southern ice front of Stange Ice Shelf, flow speeds in excess of 800 ma^{-1} are recorded. Here, regular cycles of advance followed by calving take place, with the actual ice front location fluctuating over an approximate 7 km distance; there is little difference between the ice front profile in 1973 and 2011.

9.1.8.2 Velocity changes and ice-shelf retreat

Interferometric analysis and feature tracking on Bach Ice Shelf reveal no significant increases in surface speeds between ca. 1996 and ca. 2007. Feature tracking on Stange Ice Shelf reveals a slight increase in velocities in the central portions of the northern ice front, coinciding with increased transverse fracturing, but otherwise, flow speeds remain similar between ca. 1989, ca. 2004 and ca. 2010. Interestingly, flow speeds of ice feeding the southern margin decreased, coinciding with a change in structural regime. It is also possible that strong thinning in this portion of the ice shelf led to a reduction of flow speeds as modelled by Vieli *et al.* (2007) for the Larsen B Ice Shelf.

At the northern ice front of George VI Ice Shelf, recorded velocity increases following retreat are apparent on Riley Glacier. This response is also identified at the southern ice front, particularly in ice fed to South Ice Front 2 where flow speeds have increased up to 362 ma^{-1} (181%) along the centre of the ice front between ca. 1989 and ca. 2009. These are by far greater than any other velocity increases measured on Antarctic Peninsula Ice Shelves and thus highlight the susceptibility of ice shelves beyond the inferred limit of viability.

What remains unclear, however, is whether velocity increases 1) cause enhanced retreat, 2) are a product of enhanced retreat, or 3) represent a precursor for future retreat. In modelling studies, Vieli *et al.* (2006, 2007) revealed that the retreat of Larsen B Ice Shelf between 1995 and 1999 led to a significant increase in shelf flow, although changes to the ice-front geometry could not solely explain the observed acceleration (Vieli *et al.*, 2007).

They also commented that ice-shelf speedup is not driven by enhanced pushing of tributary glaciers, but indeed 'enhanced pulling' on these glaciers from the ice front.

Flow increases at Stange's northern ice front are spatially limited, and thus it is evident that these changes are a result of enhanced 'pulling' following, or leading to fracturing. Similarly at the northern ice front of George VI Ice Shelf, 'pulling' is inferred following the retreat of the ice front as speeds of Riley Glacier along the grounding zone do not significantly alter over time. This is also typically the case at the southern ice front of George VI Ice Shelf, where flow speeds at the grounding line remain constant over time, but increasing towards the ice front. The only exception is the tributary of GT07 that increases in velocity along its entire length from the grounding line. Several authors (e.g. van der Veen, 1996; Venteris, 1999; Pritchard and Vaughan, 2007) have commented that high calving rates and consequent retreat is an effect and not the cause of fast flow, although observations here generally oppose this theory.

Perhaps most significantly, Vieli *et al.* (2007) attributed the enhanced ice flow rates to a mechanical weakening and softening of narrow flow confluences that ultimately changed the rheological properties of the ice shelf. The structures and their significance on each of the ice shelves are further discussed below.

9.1.9 Ice-shelf structures: Significance and controls on ice-shelf retreat

9.1.9.1 Flow related features (longitudinal structures, pressure ridges and flow-unit boundaries)

On Bach, George VI and Stange Ice Shelves, the most dominant features are longitudinal surface structures. These are also reported on other Antarctic Ice Shelves, illustrating their ubiquitous nature. Glasser and Gudmundsson (2012) identified two broad types of longitudinal structures, 1) those that form within glacier flow units, and 2) where there is a convergence of glacier flow. Here, the same types of features have been found, but categorised as three more distinct forms of structures based on their origin and approximate dimensions (Table 9.3).

Table 9.3. Description of longitudinal features observed on Bach, George VI and Stange Ice Shelves.

Longitudinal structure type	Origin	Characteristics
Type 1	Grounded ice confluence	10-20 km in length, largest features traced across grounding line onto ice shelf surface. Retain linearity down ice.
Type 2	Ice-shelf confluences	20-30 km in length, most striking and persistent on ice shelf surface. Few cases of shearing but mostly cohesive. Retain linearity down ice.
Type 3	Within main flow channels	3-25 km in length (on ice shelf). Can develop at the grounding line, but also traceable back upstream to zones of lateral compression. Indicative of longitudinal foliation. Retain linearity down ice.

The origin of these features on Antarctic Ice Shelves is still debatable and has previously been discussed in Section 6.2.3.1. However formed, analysis from all three ice shelves have revealed that longitudinal structures are able to endure both transverse and longitudinal compression, and transverse and longitudinal extension, whilst retaining broadly constant surface characteristics down ice. They are also capable of crossing the grounding zone and surviving substantial surface melting. Their persistence down ice, in most cases, is also a unique characteristic of these features, although their visibility on Bach, George VI and Stange Ice Shelves reduces towards the ice fronts. On other ice shelves (e.g. Larsen B, Larsen C and Filchner-Ronne) they can be traced uninterrupted to the ice margin (Swithinbank *et al.,* 1988; Hambrey and Dowdeswell, 1994; Glasser and Scambos, 2008; Glasser *et al.,* 2009). Consequently, temporal changes in the dynamic history are recorded as spatial changes in these features (Raup *et al.,* 2005) and permit assessment on the longer term stability of these systems.

Longitudinal structures on Bach and George VI remain almost equidistant down ice, with the exception of splaying on some of the most dominant tributaries flowing into George VI Sound from Palmer Land (although even these remain linear after splaying terminates). In general, the flow regime of Bach and George VI over the last 500 to 1000 years is assumed to be similar to that of today (except where clear velocity changes have been identified since 1973), and therefore indicated the long-term stability of these ice-shelf systems. The majority of longitudinal structures also remain uniform on Stange Ice Shelf, although clear longitudinal compression along flow-unit boundaries in the centre of the ice shelf suggests that at some point in its recent history, the flux of ice from the English Coast altered significantly enough for large-scale folding of shelf ice.

Pressure ridges on Antarctic Ice Shelves have also been recognised as important indicators of stress and strain rates, most strikingly along the Alexander Island grounding zone of

George VI Ice Shelf (Reynolds and Hambrey, 1988), although similar features are also found on the McMurdo Ice Shelf (Collins and McCrae, 1985) and in portions of the Ross Ice Shelf (Kehle, 1964). Pressure-ridge dimensions vary, with Wright and Priestley (1922) identifying amplitudes of 12 m and wavelengths of 3.2 km on Beardmore Glacier, Gould (1935) commenting on ridges 9 m high and 1.2 km in wavelength on Shackleton Ice Shelf, and Kehle (1964) describing pressure rollers with amplitudes of 12-15 m and wavelengths of 180-650 m on the Ross Ice Shelf.

On George VI Ice Shelf, Reynolds and Hambrey (1988) identified pressure ridges 15 m high where the dominant westward flow caused transverse foliation under increasing longitudinal compression against Alexander Island. More recently, Labarbera and MacAyeal (2011) modelled a dampening sinusoidal wave away from the confluence area, suggesting that amplitude of pressure ridges decreases back up-ice, coinciding with increasing wavelength distances upstream from 150 to 350 m, as identified here.

The structural glaciology of George VI Ice Shelf during 1973 presented by Reynolds and Hambrey (1988) identified pressure ridges along the central portion of Alexander Island. Extending this north and south of their study site, pressure ridges are found to exist at the current northern ice front, and towards the Kirwan Inlet, indicating the dominant compressional regime of the ice shelf along its northern section. Furthermore, finer spatial-resolution imagery (15 m, Landsat ETM+) reveals greater concentrations of pressure ridges along these confluence zones not identified in earlier imagery. Similar features have been identified in ice flowing towards Case Island on Stange Ice Shelf, although the spatial extent only covers a few squared kilometres.

Landsat ETM+ imagery also permitted the identification of pressure ridge zones at the confluence of glaciers along Palmer Land, most notably where at least one dominant system impinges against another. These are also present between tributary glaciers at the southern extent of George VI Ice Shelf and between Smyley Island-derived ice and the main channel of Stange Ice Shelf. Pressure ridges are also identified on the Stravinsky Domain of Bach Ice Shelf (confluence with BT02) and form distinct arcuate bands when viewed from above. One common factor governing the development of pressure ridges is the decreasing flow speeds as ice enters the shelf from a grounded location. It is inferred that increased compressive stresses in the longitudinal, horizontal plane causeice mass a vertical buckling of the ice shelf, similar to the formation of pressure ridges where ice impinges against more resistant bedrock.

The process of viscous-buckling in ice-shelf flow units so close to their upstream grounding line has rarely been studied, probably as compressive stresses on ice shelves are uncommon; flow generally extends in the horizontal plane (Thomas, 1979; LaBarbera and MacAyeal, 2011) into an open embayment. However, detailed structural analysis here suggests that this process is quite common on George VI Ice Shelf. As well as distinct pressure-ridge features, more subtle structures have been identified. In the northern section of George VI Ice Shelf, Reynolds and Hambrey (1988) identified these features as crevasse traces, emanating from the grounding zone of Palmer Land glaciers, and consequently transmitted across the ice shelf with flow. As with longitudinal structures, their identification was aided by the presence of surface meltwater during the austral summer. Here, these features have been reinterpreted as transverse pressure ridges, caused by longitudinal compression of feeder glaciers as ice enters the narrow channel of George VI Sound. During the melt season, accumulation of surface water in these narrow structures has been used to highlight their abundance across the ice shelf, particularly where a sudden reduction in flow speeds is recorded. These features are also identified in regions where upstream crevassing is not apparent, thus refuting a crevasse-trace pattern. Furthermore, observations outside of the meltwater limit again demonstrate features more likened to a buckled surface topography than healed crevasses, extending regularly, some 50 km into the ice shelf.

The importance of both longitudinal and transverse foliation structures is that they show the dynamic history and strain history of an ice-shelf system. Their spatial characteristics can be used as a proxy for long-term dynamics of ice shelves over recent centuries. In the case of Bach and George VI Ice Shelves, both longitudinal and transverse structures illustrate, 1) the relatively stable flow of ice over the late-Holocene, and 2) that the changes in velocity observed at the northern and southern ice fronts of George VI Ice Shelf are unprecedented in its recent past.

Finally, understanding the glaciological processes in zones where individual flow units coalesce is important as it has been illustrated that these boundaries are susceptible to subtle changes of ice rheology (Vieli *et al.,* 2006, 2007), and are likely to be thinner in composition (Fricker *et al.,* 2001). Glasser and Scambos (2008) highlighted the significance of these boundaries preceding the Larsen B collapse, commenting that a thinning ice-shelf system rendered these structures mechanically weak, and encouraged the rapid disintegration of the ice shelf. As with Larsen C (Glasser *et al.,* 2009), flow-unit boundaries on Bach, George VI and Stange Ice Shelves do not show any large-scale

fracturing along these sutures, with the exception of the eastern boundary of ST07 with slow moving ice that has progressively ruptured from 2001 to present. The evolution of fractures on all three ice shelves is discussed below in Section 9.1.9.3, but here, it is highlighted that the complex dynamics of George VI and Stange Ice Shelves in particular, means that there are numerous flow-unit boundaries on each ice shelf perhaps making these systems susceptible to future weakening.

9.1.9.2 Fractures, rifts and iceberg calving.

Fracturing occurs when the extensional stresses exerted on an ice mass exceed a specific temperature-dependant threshold (Vaughan, 1993), although in practice the processes of fracturing and rifting is far more complex (Rist *et al,* 2002). The physics of fracturing in ice shelves are not discussed here; instead, the broad spatial and temporal patterns of retreat are highlighted with respect to fracturing, and the possible causes of fracturing and rifting are discussed.

Fractures in shelf-ice are important for three reasons. First, their abundance, form and location give a visual impression of ice-shelf dynamics and strain regimes, representing the toughness and relative mechanical strength of an ice body. Second, their development and propagation over space and time permit an assessment of an ice shelf's response to internal or external forcings. Finally, fractures and rifts delineate iceberg dimensions, and thus play a vital role in the mass-balance of ice-sheet systems.

On Bach, George VI and Stange Ice Shelves, fractures and rifts develop in four broad areas;

S1) At a confluence of flow units, either around headlands or peninsulas, or from the grounding line.
S2) Lee-side of ice rises and ice rumples.
S3) Near the ice front, either in consolidated ice or along pre-existing lines of weakness typically developed further back upstream.
S4) Directly at the ice front cutting back into the ice shelf.

Situation 1 (S1) was also identified by Glasser and Scambos (2008), who commented that the initial fracturing and resealing of these particular zones weakened the ice-shelf flow boundaries down ice and were partially responsible for the rapid disintegration observed on Larsen B, through shearing along these boundaries. Situation 2 (S2) fractures were also deemed responsible for the poor surface conditions observed on the Wordie Ice Shelf prior

to breakup events (Reynolds, 1988) and played an important role in determining the rate of retreat of that particular ice shelf. Situation 3 (S3) is perhaps most common and has been observed on various ice shelves around Antarctica (e.g. Amery (Fricker *et al.*, 2005; Bassis *et al.*, 2005); Ronne (Hulbe *et al.*, 2010); Filchner (Swithinbank *et al.*, 1988); Larsen B (Glasser and Scambos, 2008); Larsen C (Glasser *et al.*, 2009); Prince Gustav (Glasser *et al.*, 2011); Wilkins (Braun *et al.*, 2009)), and is generally brought about either by tidal flexure (Rist *et al.*, 2002; Larour *et al.*, 2004) or plate-bending (Scambos *et al.*, 2009) at the ice front. These types of fractures and rifts control the frequency and magnitude of iceberg calving events (Weiss, 2004) that can be predicted and anticipated in advance as illustrated most strikingly at the northern margin of George VI Ice Shelf. Situation 4 (S4) fractures develop sporadically and rapidly at the ice front and rarely survive between observation periods. They probably account for a high-proportion of observed retreat through instantaneous calving, making the prediction and anticipation of retreat more difficult over longer timescales.

On Bach Ice Shelf, retreat rate and retreat patterns have been governed by calving along fractures predominantly developed near to the ice front (S3) or at the ice front (S4), although the close proximity of a fracture zone lee-side of Bennett Dome cannot be ruled out as a governing factor on retreat in the concave portion of the ice shelf (e.g. S1). Whilst the most notable change on Bach Ice Shelf was the development of two large fracture/rift features, they have not had an impact on retreat patterns to date, but are discussed further in Section 9.2.

At the northern margin of George VI Ice Shelf, retreat rate was governed predominantly by long-standing fractures and rifts that typically stretched across the whole ice front. Retreat from 1974 to 2001 was essentially as a result of heavily fractured ice migrating to the ice front and propagating over time from the Warren Ice Piedmont and the northern boundary of Riley Glacier (S1). Calving between 2001 and 2010 was dominated by one single event along a single rift developed near the ice front (S3). At the southern ice front, calving occurred predominantly along pre-existing fractures caused as ice diverged around ice rises upstream (S2), and reopening of healed fractures near the ice front (S3). Only towards its western section could small-scale calving at the ice front be seen (S4). At South Ice Front 2 (from March 2010), chaotic fracturing consisting of all four situations is observed, with the most noticeable fractures and rifts emanating from further upstream (S1, S2), and cutting back along flow-unit boundaries (S4); mostly, however, fractures cut across flow-unit boundaries rather than longitudinally along them.

At the northern ice front of Stange Ice Shelf, calving is controlled by longstanding fractures developed near the ice front in the eastern and central portions (S3), with calving at the western edge governed by pre-existing weaknesses stemming from the grounding line and carried forward to the ice front (S1). The limited calving that takes place along the mid ice front is controlled by fractures migrating from the grounding line (S1) and from small scale fractures at the ice front (S4), whereas the calving rate at the southern ice front is governed by a combination of S1 and S3, with those fractures evolving close to the ice front cross-cutting existing fractures from further upstream. Shear-induced fracturing is observed during the period 2001 to 2011, but no actual calving had taken place as a result of this.

Increased fracturing has been observed in all three ice-shelf systems on varying scales, showing reduced structural strength. On Bach Ice Shelf the most notable change occurred between 2003 and 2004 with the opening of two fracture/rift systems ~10 km sub-parallel from the ice front (S3) in previously consolidated ice. This has been qualitatively linked to enhanced tidal flexure/ plate bending at the ice front after decoupling of the ice front from Monteverdi Peninsula altered the stress fields at the ice front between the ice shelf and the ocean. Over time, the fracture/rift system has migrated towards the retreating ice front, propagating transversely at both rift tips. To date, no iceberg calving has been initiated by these structures.

Whilst the abundance of fractures and rifts has reduced at the northern ice front of George VI Ice Shelf through iceberg calving, the southern region has seen an increase in both the distribution and extent of fracturing, particularly in ice extending from the English Coast grounding line illustrating an increasing longitudinal extension consistent with increasing flow speeds in this zone. The greatest changes on Stange Ice Shelf occurred as a result of shearing between ST07 and slower moving ice to its east, although again this has had no direct influence on retreat rate to date. The evolution of fractures and significance on future retreat is discussed in Section 9.2.

9.1.9.3 Meltwater and meltwater features

Surface meltwater is abundant in the austral summer over large portions of the Bach and George VI Ice Shelves. The features on the former have not been previously studied (although mentioned briefly by Reynolds (1981)), yet those forming on the surface of George VI Ice Shelf have been scrutinised over many decades. It is clear that the distribution of surface lakes on George VI Ice Shelf is strongly linked to its structural

glaciology (Reynolds and Hambrey, 1988), forming in longitudinal troughs that show the dynamic regime of individual flow units in the shelf. Reynolds (1981) and Reynolds and Hambrey (1988) suggested that the narrow meltwater lakes (termed transverse or secondary channels here) form as a result of the prevailing wind from south to north. This wind-induced formation of the transverse channels is contested as multi-annual satellite imagery reveals that these lakes move at the same speed as the underlying ice and deform with flow; thus they are more likely to represent the surface structural of transverse pressure ridges as discussed in Section 9.1.9.2.

On other Antarctic Peninsula Ice Shelves, surface melting and increased distribution of meltwater lakes has been attributed to a rise in atmospheric temperature and a lengthening of the melt season (Vaughan *et al.,* 2003; Torinesi *et al.,* 2003; Skvarca *et al.,* 2004). It has been suggested that the increased meltwater acts as a mechanical force in crevasse penetration thus accelerating ice-shelf collapse (Scambos *et al.,* 2000, 2003; MacAyeal *et al.,* 2003; van der Veen, 2007). Therefore, understanding the evolution of meltwater lakes and their distribution is fundamental in assessing the stability of remaining ice shelves.

Meltwater has been identified on the surface of George VI Ice Shelf since at least the 1930s. Stephenson and Fleming (1940) first commented on surface melting near Ablation Point during a field expedition, with Wager (1972) also documenting surface melt on George VI Ice Shelf during 1967 and 1970. It is thus inferred that the ponds identified on the surface cannot be solely attributed to atmospheric warming from the 1950s onwards (e.g. King, 1994). In Section 7.2.2.1, an expanding northern limit of surface meltwater on George VI Ice Shelf was attributed to changing climatic conditions (increased length of melt season), yet the southern limit seemingly did not follow the expected southern migration, as recorded in similar latitudes on Bach Ice Shelf. Whilst not directly related to the current stability of George VI Ice Shelf, it is informative to consider the reasons for this observation as it may have greater implications over a longer timescale.

It has already been suggested using data available in this study, that the absence of a southern migration was down to the timing of data collection or localised changes in the surface gradient. It was also suggested that the relatively consistent southern meltwater limit represents annual weather patterns rather than climatic change, or that ice-shelf surface melting was controlled by another external factor. Indeed, Stephenson and Fleming (1940) noted a fine dust covering the surface of the ice shelf around Ablation Point that they thought responsible for lowering the local albedo sufficiently to initiate melting.

Wager (1972) took this hypothesis and applied it to the whole of the ice shelf melt zone, commenting that the prevailing wind pattern and availability of fine material around the margins of George VI Sound supplied enough 'dust' to instigate melting. This theory was contested by Reynolds (1981) who attributed the widespread melting of the ice shelf surface to climatic conditions, especially away from the western edge (Alexander Island grounding zone) where dust concentrations were seemingly absent. Reynolds (1981, 1988) and Reynolds and Hambrey (1988) commented that surface meltwater on Antarctic ice shelves occurs where the annual surface temperature is between -6 and -10 °C. Based on the most recent estimates (Morris and Vaughan, 2003), the southern meltwater limit determined here lies well within the upper threshold that extends as far south as the south ice front of George VI Ice Shelf, and therefore the surface meltwater should, theoretically at least, stretch beyond its current southern limit.

This subsequently questions the temperature control on the southern limit of surface melting on George VI Ice Shelf, and perhaps highlights other climate and/or glaciological conditions as a controlling factor on the visible meltwater. Reynolds (1981) theorised that where surface accumulation rates are greater than 0.2 Mg m^{-2} a^{-1} an ice-shelf percolation zone exists through which surface water drains. Whilst measurements of surface accumulation over ice-shelf surfaces are spatially coarse, a general increase in precipitation events (Turner *et al.*, 1995, 1997) recorded on the Antarctic Peninsula may play a role in the short-term positioning of the visible southern meltwater limit on George VI Ice Shelf, although it is recognised that this is merely a postulation based on broad spatial patterns.

Nevertheless, the abundant distribution of meltwater on the surface of George VI Ice Shelf is attributed to the compressional regime across much of the ice shelf, with drainage routes from the ice-shelf surface generally limited to distinct regions along Alexander Island. A similar situation exists on Bach Ice Shelf, where meltwater sits on the surface for longer than expected (Cook and Vaughan, 2010) as the drainage routes off or through the ice shelf are limited due to its compressional regime.

However, one potential drainage route for surface meltwater is through ice dolines that appear on the surface of both Bach and George VI Ice Shelf. Elsewhere they have been termed ice blisters (Kovacs, 1992), and ice calderas (Stephenson and Fleming, 1940) although here, the naming convention of Bindschadler *et al.* (2002) has been adopted based on their surface dimensions. Their formation is not well researched, but Bindschadler *et al.* (2002) suggest that they are the surface expression of collapsed 'ceilings' after draining

events of localised englacial pools (see Figure 7 in Bindschadler *et al.* (2002)). They also comment that ice dolines represent weak zones in the ice shelf, and perhaps link the surface of the ice shelf to the ocean below through a series of englacial conduits.

If these theories are correct, then limited drainage of surface meltwater is on-going during the austral summer on Bach and George VI Ice Shelves, and localised 'weak' points exist in mostly cohesive portions of shelf ice. Whilst common on other ice shelves that have undergone significant retreat (e.g. Larsen B, (Bindschadler *et al.,* 2002), Wilkins (Braun *et al.,* 2009)) ice dolines have not been directly linked to any major breakup or collapse phases. Furthermore, as the meltwater limits of both Bach and George VI Ice Shelves lie some distance from the current ice fronts, it is not believed that any ice-doline-induced weakness caused the retreat of the ice shelves prior to 1973.

Ultimately it has been illustrated that surface meltwater on both ice shelves does not interact with widespread regions of surface fractures as observed elsewhere (e.g. Scambos *et al.,* 2003; MacAyeal *et al.,* 2003), thus preventing hydro-fracture-induced retreat. Therefore, an increasing meltwater distribution over Bach and George VI cannot be directly linked to the patterns of retreat observed between 1973 and 2003.

9.1.10 Ice-shelf composition; meteoric ice vs marine ice

Direct measurements of the meteoric and marine ice concentrations in most ice shelves are rare. The few measurements that exist often point to a spatially complex configuration that alters depending on the physical and dynamic components of an ice shelf. Again, presenting the physics behind the accretion of marine ice onto the base of ice shelves is beyond the scope of this study, but understanding the significance of a marine ice layer is important when considering the current and future stability of these systems, especially as marine ice composition has a particularly profound effect on fracturing (Rist *et al.,* 2002) and ice-shelf rheology (Khazender *et al.,* 2009, 2011) that ultimately control iceberg calving.

On the Ronne Ice Shelf, marine ice accounts for up to 350 m of the shelf thickness (Thyssen *et al.,* 1993; Lambrecht *et al.,* 2007) compared to 140 m on the Filchner Ice Shelf (Gordfeld, 1998), 190 m on the Amery Ice Shelf (Fricker *et al.,* 2001) and only 10 m on the Ross Ice Shelf (Neal, 1979), with variations mostly due to basal geometry, ice-shelf draft, water properties and circulation (Fricker *et al.,* 2001). The thickest marine ice concentrations are located immediately downstream of ice rises, ice rumples and

peninsulas (Thyssen *et al.,* 1993; Blindow, 1994; Lambrecht *et al.,* 2007; Holland *et al.,* 2009), including at the confluences of flow units (Fricker *et al.,* 2001); marine ice tends to thin towards the ice front (Thyssen *et al.,* 1993). The common denominator between each of these locations is the existence of basal cavities that favour basal accretion of marine ice. Based on these findings, it is assumed that the marine ice concentrations of Bach, George VI and Stange Ice Shelves are greatest down-stream of peninsulas, ice rises, ice rumples and at the confluence of individual flow units, although inferences on the spatial and vertical extent cannot be made. The overriding significance of marine-ice concentrations in ice shelves is the heightened susceptibility to oceanographic warming (Williams *et al.,* 1998) that is discussed below.

9.1.11 Atmospheric or oceanic-driven changes?

Being sandwiched between atmospheric and oceanic environments, ice shelves are uniquely susceptible to variations in both, with their response to date highlighted by significant retreat (Cook and Vaughan, 2010) and thinning (Shepherd *et al.,* 2003; Zwally *et al.,* 2005; Fricker and Padman, 2012). Below, the possible causes of observed glaciological changes to Bach, George VI and Stange Ice Shelves are discussed with reference to other ice shelves on the Antarctic Peninsula that have undergone apparent atmospheric and oceanic change.

9.1.11.1 Atmospheric changes and ice-shelf retreat

Mercer (1978) first commented that if atmospheric temperatures continually increased, ice-shelf systems would respond through dramatic retreat phases, since observed from the beginning of the 1980s. He predicted that ice shelves would only be viable where summer (January) temperatures remained below 0°C, with Morris and Vaughan (2003) later revising ice-shelf viability to below the -9°C mean annual isotherm (this limit has been used through this study). Doake and Vaughan (1991) noted the impacts of small atmospheric changes on the net mass balance of ice shelves, essentially switching them from net accumulation to net ablation over a short time period. The same authors also highlighted the demise of the Wordie Ice Shelf after successive years of net ablation, and attributed the mass balance changes to these increasing atmospheric temperatures. It must be noted that whilst the ice-shelf viability is linked with the -9°C mean annual isotherm, the warming towards this ‘threshold’ is progressive, and thus mass balance changes are on-going in the years and decades up to this point, rather than being an instantaneous response. There are also no comments on how rapidly an ice shelf responds (rather than

retreats) once the -9°C mean annual isotherm is met, whether the entire ice shelf has to be at this threshold, or for how many years the -9°C threshold must be sustained before a collapse event takes place.

The northern section of Bach Ice Shelf is close to the -9°C thermal limit of ice-shelf viability (see Figure 2.3), based on year-2000 interpolated air temperatures, with a small 'pocket' of -9°C annual mean temperatures also observed towards the ice front, suggesting that the ice shelf will be the next ice shelf to be subjected to atmospherically-driven changes. The southward migration of the surface meltwater limit on Bach Ice Shelf suggests that there has been a continued southerly shift of the -9°C isotherm over recent years, and it is likely that much of the ice shelf now experiences mean annual temperatures close to this limit. The period of sustained retreat observed on Bach Ice Shelf has coincided with the period of increasing atmospheric temperatures, and thus it is suggested that changes on the ice shelf are predominantly attributed to atmospheric warming in the southwest Antarctic Peninsula region.

For George VI Ice Shelf, Smith *et al.*, (2007) hypothesised that retreat on both the northern and southern ice fronts have been governed by atmospheric warming, and that this is likely to continue if the warming trend is sustained. This is not disputed here, but enhanced (and preceding) retreat at the southern margin with annually colder temperatures perhaps suggests that other forces have played a role in the ice-loss from the southern ice front, whereas it is more likely that the patterns of loss at the northern ice front are as a result of increased atmospheric temperatures.

Humbert (2007) suggested that disintegration of George VI Ice Shelf would be instigated from its northern ice front, yet its apparent stability compared to portions of the southern ice front questions this proposal, particularly when considering the dynamic regime within the narrow channel of George VI Sound. Furthermore the pattern of retreat from the northern ice front of George VI Ice Shelf is episodic. Thus, no immediate breakup at its northern ice front is anticipated despite being situated within the -9°C mean annual isotherm limit.

Stange is the most southern ice shelf on the west Antarctic Peninsula, and is comparable in latitude to the Larsen D tributaries on the eastern side of the peninsula. Mean annual surface temperatures are typically less than -11°C at its northern front, reducing rapidly to -15°C along the English Coast tributary glaciers (Morris and Vaughan, 2003; see Figure 2.3). Consequently there is a strong negative temperature gradient across the ice shelf from

north to south; the mean annual temperature variations on the surface areas of Bach and George VI are generally less than 1°C. Whilst an increase in temperatures would still affect the overall mass balance of Stange Ice Shelf, the cryospheric response to atmospheric warming is assumed to be less due to the much lower surface temperatures experienced, although the retreat of the northern ice front (which is exposed to comparatively warmer temperatures) is evidently greater than its mid and southern counterparts. Thus the limited retreat of Stange Ice Shelf is likely to have been only affected by increasing atmospheric temperatures towards its northern ice front.

Atmospheric variation is also directly responsible for increased surface meltwater (van den Broeke, 2005) that Scambos *et al.* (2000, 2003) linked to the rapid collapse of the Larsen A and Larsen B Ice Shelves through hydro-fracture mechanisms. As already suggested, this does not seemed to have affected the retreat of either Bach or George VI Ice Shelves thus far; there are no signs of surface meltwater on Stange Ice Shelf and indeed it lies outside of the -10°C to -6°C temperature range in which surface melting is apparent (Reynolds, 1981).

9.1.11.2 Oceanic changes

Despite the clear response of Antarctic Peninsula Ice Shelves to climatic warming over recent decades, a direct link between this and a critical thermal limit is somewhat simplistic, and may only illustrate a broad pattern of ice-shelf viability. Alternatively, Shepherd *et al.* (2003) commented that increasing oceanic temperatures in the Weddell Sea encroaching beneath Larsen B caused a reduction in basal accretion and an increase in basal melting, thus initially reducing the thickness of the ice shelf and prompting further instabilities. Whilst more difficult to measure, the evidence and support for oceanic-driven changes has recently increased (e.g. Holland *et al.,* 2010; Fricker and Padman, 2012; Padman *et al.,* 2012; Pritchard *et al.,* 2012).

Variations in the oceanic regimes surrounding the Antarctic Peninsula have been well documented over recent years (e.g. Robertson *et al.,* 2002; Martinson *et al.,* 2005; Stammerjohn *et al.,* 2008) on seasonal, annual and inter-annual timescales. Uniquely to the Antarctic Peninsula, sea surface temperatures correlate well with atmospheric temperature increases and reduction of sea ice extent (Smith and Stammerjohn, 2001; Parkinson, 2002; Liu *et al.,* 2004; Parkinson and Cavalieri, 2012). The upper layers (to 100 m depth) of the oceans on the west Antarctic Peninsula have increased by up to 0.5°C $(decade)^{-1}$ in the summer between 1955 and 1998 (Meredith and King, 2005), explained by upwelling of

Circumpolar Deep Water (CDW; warmer water) (Comiso, 1997) or as a response to atmospheric climatic variation (Turner *et al.*, 1997; Thompson and Solomon, 2002; Harangozo, 2006).

In the Bellingshausen Sea, the warmer (>1°C) CDW has been shown to flood the entire continental shelf (Holland *et al.*, 2010), overlain with much cooler Winter Water (-1.5°C) and more typical Antarctic Surface Water (<-1.5°C) (Smith *et al.*, 1999; Jenkins and Jacobs, 2008). The latter two layers derive from interactions with the atmosphere, but the CDW originates from the deeper Antarctic Circumpolar Current (ACC) where typical temperatures are between 1.6 and 2.0°C, and thus episodic but persistent mixing (Moffat *et al.*, 2009) of the CDW waters with the cooler upper layers raises the regional oceanic temperatures. Jenkins and Jacobs (2008) report on the intrusion of CDW into the Ronne Entrance area of the Bellingshausen Sea, in which the ice fronts of Bach, George VI (south) and Stange Ice Shelves terminate. Potter and Paren (1985) measure CDW directly beneath George VI Ice Shelf and concluded that waters of ~1°C existed beneath the entire ice shelf. Towards the northern ice front, CDW was found to upwell and melt the underside of the ice shelf (Potter *et al.*, 1988), with more recent work by Holland *et al.* (2010) concluding that a similar process operates at the southern ice front. There are no reports of CDW and its interaction with either Stange or Bach Ice Shelves.

Holland *et al.* (2010) modelled the impact of this oceanic variability on the mass balance of George VI Ice Shelf from 1978 to 2008 and found an increase in melt rate between 1989 and 1992, followed by another increase during 2005 to 2008 (see Figure 9.8), correlating well with reducing sea ice extents. Interestingly, the first period of higher melt occurred almost immediately prior to the increased rate of retreat recorded at the ice fronts of Bach, George VI and Stange Ice Shelves, and it is possible that increased melting in the years leading up the recorded retreat, weakened the ice fronts and caused enhanced iceberg calving in the following years; the enhanced calving may have also caused further instabilities (MacAyeal *et al.*, 2003). This is particularly significant on the southern margin of George VI Ice Shelf as marine ice accretion downstream of the Eklund Islands would have been greatly reduced, on top of the increased basal melting. Elsewhere, the ice melange between open rifts is believed to be a stabilising characteristic, holding the opposing walls of the rift in place and limiting propagation (Fricker *et al.*, 2001). Destabilisation of these regions, as well as those in subglacial cavities (basal fractures, flow-unit tributaries) may have been enhanced by warming oceanic temperatures. If this link between enhanced calving and increasing melt rates is viable, then a similar response

would be expected to have taken place post-2008, yet the period of only three years since the melt rates reduced prevents the response of the ice fronts from being fully analysed.

In Section 7.2.4.2, it was briefly mentioned that the greatest surface elevation changes (and therefore thickness changes) on George VI Ice Shelf occurred in areas where the ice-shelf draft was thickest. Taking into account the thermal structure of the sub-ice-shelf oceanic regime, the central portions of the shelf would naturally sit in the warmer CDW waters (Holland *et al.,* 2010). The rest of the shelf is melted by cooler waters that are mixed with the CDW layer during the episodic variations that consequently leads to higher melting. It is thus argued that George VI Ice Shelf is already more susceptible to oceanic variations than other ice shelves on the Antarctic Peninsula.

Potter *et al.* (1984) calculated spatially averaged melt rates to be 2.1 ma^{-1} in order for the ice shelf to remain in equilibrium. The calculations of mean melt rate presented in Jenkins and Jacobs (2008), Corr *et al.* (2002), Holland *et al.* (2008) and Dinniman *et al.* (2012) (Table 9.4) are consistently above the equilibrium rates required for the ice shelf to be in mass balance, and give reason to the widespread thinning reported by Fricker and Padman (2012), Pritchard *et al.* (2012), and calculated here. Interestingly, basal melting in the northern regions of George VI Ice Shelf is distinctly less than the basal melting towards the south (Figure 9.8), thus fitting with the calculations here that suggests weak, non-significant thinning in the northern section.

Table 9.4. Published mean basal melt rates for George VI Ice Shelf

Reference	Observation year/s	Basal melt	Comments
Bishop and Walton (1981)		1-8 ma^{-1}	Range of basal melt recorded
Lennon *et al.* (1982)		>10 ma^{-1}	Maximum basal melt
Potter *et al.* (1984)		2.1 ma^{-1}	Spatially averaged for ice shelf
Corr *et al.* (2002)	2000	2.8 ma^{-1}	Over thicker southern section
Jenkins and Jacobs (2008)	1994	2.3 - 4.1 ma^{-1}	From direct measurements in the southern extents of the ice shelf
Holland *et al.* (2010)	1990 – 2008	≅ 3.0 ma^{-1}	Modelled mean melt rates for whole ice shelf
Dinniman *et al.* (2012)	2000 - 2003	≅ 6.0 ma^{-1}	Modelled mean melt rates for whole of ice shelf.

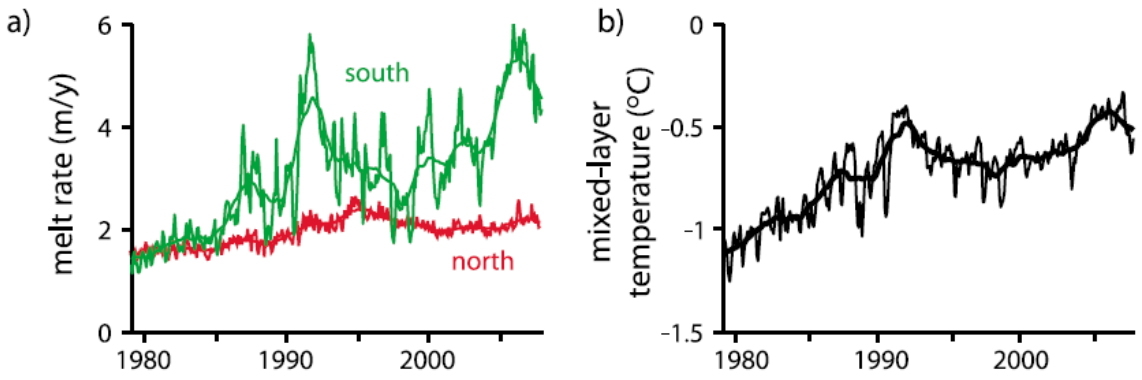

Figure 9.8. a) Mean melt rates, and b) mixed-layer temperature modelled by Holland *et al.* (2010) for George VI Ice Shelf illustrating the increasing basal melt towards the southern regions of the ice shelf between 1978 and 2008 linked with warming of underlying oceanic regime. Data sourced from Holland *et al.* (2010).

It is suggested that the similar response of Bach and Stange (north) ice fronts during the period of increased oceanic temperatures links their current stability with oceanic regime. However, the typical ice thicknesses for these ice shelves are much less than the thickest parts of George VI, and so it is likely that rather than being subjected to constantly high basal melt rates (as predicted by Holland *et al.*, 2010) from deeper warmers, these systems are only sensitive to the episodic or seasonal cycles of warm water upwelling in mixing phases. Ultimately, however, the driving force of these oceanic upwelling events is in part, atmospherically driven. What this demonstrates, however, is that ice shelves can respond rapidly to short-term oceanic variation (Pritchard *et al.*, 2012) as opposed to the more lengthy response to atmospheric warming.

9.1.12 Summary of current configurations and immediate stability

Throughout Section 9.1 the long-term glaciological configurations of Bach, George VI and Stange have been assessed against the response of other Antarctic Peninsula Ice Shelves as documented in the literature (See Chapter 2). By carrying out this analysis, the current condition of each ice shelf has been critically assessed against common characteristics of other systems that have undergone episodes of rapid retreat, breakup and collapse. Ultimately, this has enabled an assessment to be made on their immediate stability. Each diagnostic characteristic that has been linked to enhanced retreat has been discussed and is summarised specifically for each ice shelf in Table 9.5.

From the analysis above it is clear that sustained retreat and thinning is apparent on each ice shelf, albeit at varying scales. It is inferred that ice-shelf thinning, either from enhanced basal melting or in-situ surface lowering, is the cause of other glaciological changes (e.g.

dynamic response, structural changes) as these variations are not necessarily observed on each ice shelf, and therefore cannot explain the recorded ice-shelf thinning. Ultimately, this analysis illustrates that each ice shelf is preconditioned for further retreat.

Currently, however, Bach, Stange and the northern section of George VI Ice Shelves are considered relatively stable; large scale retreat and breakup is not anticipated in the immediate future. At the southern extent of George VI Ice Shelf, considerable changes to the dynamic regime and structural configuration make the ice shelf naturally more susceptible to further, enhanced retreat that arguably renders this portion of George VI unstable. The future stability is considered in the following section.

Table 9.5. Summary of the discussions on the retreat history and current stability of southwest Antarctic Peninsula Ice Shelves. Due to the disparity between George VI north and south, they are treated as two separate systems.

	Bach Ice shelf	George VI North	George VI South	Stange Ice Shelf
Retreat history	Advance and calving regime prior to 1973 before entering a period of sustained retreat. No documented collapse in Holocene or late-Pleistocene.	Sustained retreat in large episodic breakup events along pre-existing rifts and fractures. From 1979 to 2010 retreat occurred through regular calving events approximately every 10 years.	Sustained retreat since 1947 predominantly in the central portion of the ice front. Localised advance recorded between 1973 and 2010 linked to cyclical calving regime, but largely in negative mass balance. South ice front split into two during early 2010.	No documented changes prior to 1973. North ice front has undergone sustained retreat punctuated with spatially limited advance. Mid ice front has been in a period of relative stasis, and the south ice front fluctuated with calving regime.
Embayment geometry	Terminates in a converging embayment between Monteverdi and Beethoven peninsulas. No ice rises or ice rumples near ice front. Geometry limited ice retreat.	Terminates in a narrow, almost parallel embayment that diverges slightly towards Marguerite Bay. No ice rises or ice rumples near to the ice front. Geometry not thought to have a major impact on retreat history to date.	Diverging embayment punctuated with a series of ice rises and ice rumples, most significantly in the centre of the channel (Eklund Islands) and towards De Atley Island. Ice rises and ice rumples both enhanced and limited retreat, depending on location of ice front.	North ice front terminates into a diverging embayment. South ice front is held in a converging channel whereas the mid ice front is generally sat in an open embayment. No ice rises or ice rumples present near any ice front. Retreat at north ice front perhaps linked with ice front geometry.
Ice front geometry	Both concave and convex profile portions exist and have done since 1947. Concave portion increased with retreat pattern. Ice front mostly stably in current condition.	Concave throughout observation periods. Always preconditioned for further retreat.	Largely concave prior to 2010. Splitting of ice front left more stable geometries at both South Ice Front 1 and South Ice Front 2. South Ice Front 3 similar to geometry of Bach Ice Shelf.	North ice front broadly convex, with concave portions where retreat rate is greatest towards east and west pinning points. Mostly stable. Mid and southern ice fronts both stable throughout observation period.
Thickness	Retreat even across ice front although thinner concave portion increases. Thicker ice towards east historically more resistant to retreat but undergone geometric changes.	Thickest parts linked with major tributary glaciers. Ice front similar thickness across its width. No indication of ice thickness prior to ca. 1995 when most of the retreat occurred.	Greatest retreat in thinner ice downstream of Eklund Island. South Ice Front 3 concave in thinnest portion and convex in thicker ice.	No distinct links between ice thickness and retreat/ advance patterns.
Thickness change	Significant thinning at the ice front, widespread thinning across the ice shelf. Ice-shelf in negative mass balance.	Non-significant weak thinning measured between 2003 and 2008. Strong thinning in previous decades may have been responsible for retreat prior to 2003.	Significant thinning across large portions of the ice shelf weakened the ice front further causing retreat. Retreat of grounding line also indicative of enhanced retreat.	Significant negative thickness changes across the ice shelf.
Dynamics	Frontal dynamics controlled predominantly by Boccherini Ice Domain and its interaction with Weber-derived flow and the frontal pinning points.	Atypical flow regime means that the ice front is governed by one predominant flow unit at any given time (currently Riley Gl) that ultimately controls the retreat rate.	South Ice Front 1 driven by thickness gradient, South Ice Front 2 driven by glacier flux. Eklund Islands limit ice flow thus creating a steep velocity gradient laterally and longitudinally with flow.	Complex dynamic regime, mostly cohesive towards ice fronts. Flow dominated by English Coast-derived ice at all three ice fronts. Southern ice front independent of the rest of the ice shelf.
Flow changes	No flow increased reported between ca. 1996 and ca. 2007. No structural changes to suggest dynamic changes.	Flow increases are measured at the ice front across the channel. These are due to enhanced 'pulling' leading up to and following iceberg calving rather than increased 'pushing' from the grounding line.	Flow speed increases towards South Ice Front 2 after retreat, linked to enhanced 'pulling' after the removal of buttressing, slower moving ice. Evidence of enhanced fracturing perpendicular to flow rather than along flow-unit boundaries – no evidence of shearing. Little speed increase towards South Ice Front 1, probably owing to thickness-driven velocity and retarding presence of ice	Mostly confined to the southern ice front and ice feeding it. Reduction in velocity over time, but increased shearing towards the eastern margin of ST07. Both changes possibly caused by thinning shelf ice.

			rises.	
Structural stability	A cohesive ice shelf due to channel and embayment geometry. Lateral flow is prevented therefore flow discontinuities are limited to tributary glacier within the first 5 km of entering the ice shelf. Retreat to date not linked to flow instabilities. Calving took place along pre-existing fractures or rifts, or along more instantaneously-formed weaknesses at the ice front	Retreat took place along pre-existing and long-standing rifts (~ 10 years), developed through extensional flow towards ice front. Atypical flow regime behind the ice front creates a compressional regime across George VI Sound creating a largely cohesive ice shelf. No structural weaknesses observed in latest imagery.	Structurally weak behind South Ice Front 2 due to excessive fracturing that has increased since 1973 to present. Rifts developing back along flow-unit boundaries suggest weakening sutures though no shearing is evident. Structurally weak ice downstream of the Eklund Islands along South Ice Front 1. Compressive longitudinal stresses upstream create a more stable environment.	Largely cohesive across main channel. Weaknesses at ice fronts due to existing fractures and rifts that have caused iceberg calving. Weak shear zone between ST07 and slower moving ice to its east. No calving initiated along this weakness to date.
Ice-shelf composition	No direct measurements. Likely to have high concentrations of marine along major flow-unit confluences between different ice domains and downstream of fracture zones.	No direct measurements made. Likely to have high concentrations of marine ice between the numerous flow unit boundaries that stretch across George VI Sound. High basal melt rates may limit basal accretion elsewhere in the northern section.	High marine-ice concentration inferred along flow unit boundaries, lee-side of ice rises and ice rumples and in zones where a high density of fracture-traces are present. No direct measurements are reported.	No direct measurements made. Likely to have significant marine-ice concentrations in flow unit boundaries between large tributaries flowing from the English Coast, in basal crevasses at the grounding line carried forward towards the ice front, and downstream of ice rises near the grounding line of the English Coast.
Atmospheric changes	Increased surface melting overtime indicative of a warming climate. Thinning inferred to be as a result of enhanced surface ablation and increased rate of firn compaction due to increasing surface temperatures. Ice front located close to the interpolated -9°C mean annual isotherm threshold of ice-shelf viability.	Northern advance of meltwater limit driven by climatic change, although not directly responsible for ice-shelf retreat. Non-significant elevation change suggest limited thinning; ice surface shows bare ice therefore no further firn compaction. Long-term thinning possibly caused by thinning history, but fractures existed well before first thickness measurements.	South of the proposed limit of ice-shelf viability but subjected to increasing atmospheric temperatures. Unlikely to be exposed to widespread surface melting (and only significant enough for meltwater to pool along the Monteverdi Peninsula). Changes not thought to be atmospherically driven.	Strong temperature gradient from north ice front to the English Coast. Outside of the meltwater production upper limit (-10°C mean annual) and ice-shelf viability limit (-9°C mean annual). Subjected to warming temperatures but retreat not thought to be directly linked to atmospheric changes, and thinning not linked to increased surface melting or firn compaction.
Oceanic changes	Clear links to enhanced retreat rate and intrusion of warmer Circumpolar Deep Water post-1993.	Basal melt rate in the northern section steady overtime and fits with limited surface elevation change. Section thought to be in slight negative mass balance, but not directly linked to oceanic regime. Already has a high basal melt rate.	Due to inferred high concentration of marine ice and links between retreat rate and intrusion of warmer waters, George VI South is likely to have been more susceptible to oceanographic changes. Retreat of central portion of the ice front, where high concentrations of marine ice were expected fits with oceanic-driven changes hypothesis.	Linked to the same oceanic regime that caused the enhanced retreat of Bach and George VI South. Intrusion of warmer waters to the ice-shelf base caused significant thinning between 2004 and 2007. Changes most likely to represent oceanic thinning and hydrostatic rebalancing. No evidence that the mid and south ice fronts respond to oceanic warming.

9.2 Assessing the future stability of Bach, George VI and Stange Ice Shelves

Vieli *et al.* (2007) commented that glaciological changes occur well in advance of actual breakup and collapse phases, and indeed Mercer (1978) recognised the susceptibility of ice shelves prior to any major breakup events. Whilst currently stable, it is clear that each ice-shelf system has undergone some significant changes in recent decades that are believed to represent an early response to documented atmospheric and oceanic changes. Fully quantifying the probability of the future of ice shelves is challenging due to the varying parameters that effect ice-shelf stability. Thus in the following section, a semi-quantitative assessment is made on the future stability of these ice-shelf systems based on the empirical data presented in Chapters 6, 7 and 8, and the discussions in Section 9.1. The scenario projected is that of continued atmospheric and oceanic warming as documented to date (e.g. King, 1994; Vaughan *et al.,* 2003; Marshall *et al.,* 2002; Meredith and King, 2005; Turner *et al.,* 2005; Bekryaev *et al.,* 2010; Padman *et al.,* 2012; Pritchard *et al.,* 2012); the likely glaciological responses to these changes are considered.

An initial qualitative analysis is presented in Table 9.6, which is then semi-quantified in Table 9.7. This follows a similar principle used in the assessment of glacial hazards (e.g. Dyce and Reynolds, 2002; Huggel *et al.,* 2004), but is not made fully quantitative due to uncertainty in providing weightings for each of the main parameters; sufficient data are not available to be able to weight one criterion above another on our current understanding of ice-shelf response to documented atmospheric and oceanic changes.

The criteria outlined in Table 9.6 have been applied to ice shelves that have been recently studied on the Antarctic Peninsula (e.g. Cook and Vaughan, 2010; Holland *et al.,* 2010; Griggs and Bamber, 2011; Fricker and Padman, 2012), in order to judge the effectiveness of a semi-quantitative approach. The overall score and mean is only based on fulfilled criteria. For example, if an ice front is not affected by ice rises or ice rumples, then Criterion D is not considered. The total and mean mark given in Table 9.7 therefore only takes into account those criteria assessed for each individual ice front.

Table 9.6. Key characteristics for deriving qualitative prediction of future ice-front susceptibility.

Ice-shelf characteristic	Attribute	Qualitative probability of enhanced retreat	Numerical equivalent
Retreat characteristics	Sustained retreat	High	10
	Regular calving/advance	Medium	5
	Overall advance	Low	1
Ice-front geometry	Concave	High	10
	Concave/Convex	Medium	5
	Convex	Low	1
Embayment geometry	Diverging	High	10
	Linear	Medium	5
	Converging	Low	1
Ice rises near ice front	Causes fracturing	High	10
	No fracturing	Low	1
Structural weakness (fracturing, shearing)	Structurally weak and weakening	High	10
	Long history of fracture propagation	Medium	5
	Limited structural weaknesses	Low	1
Thickness/ thickness changes	Sustained thinning	High	10
	No change	Medium	5
	Sustained thickening	Low	1
Velocity changes (temporal)	Increasing speeds	High	10
	No change	Medium	5
	Decreasing speeds	Low	1
Proximity to -9°C mean annual isotherm	At thermal limit	High	10
	-1°C	Medium	5
	-4°C (or greater)	Low	1
Susceptible to oceanic warming?*	Yes	High	10
	Some evidence	Medium	5
	Unlikely	Low	1

**Based on evaluation of retreat characteristics and evidence presented in Holland et al. (2010), Fricker and Padman (2012) and assumptions on ice-shelf composition.*

Table 9.7. Ice front susceptibility assessment of other ice shelves on the Antarctic Peninsula based on key characteristics presented in Table 9.6

	Larsen A*	**Larsen B***	**Wordie***	**Wilkins**	**Larsen C**	**Larsen D**
Retreat characteristics	10	10	10	10	10	1
Ice-front geometry	10	10	10	10	1	5
Embayment geometry	10	10	10	10	10	10
Ice rises near ice front	N/A	N/A	10	N/A	1	1
Structural weakness	10	10	10	10	5	5
Thickness/ thickness changes	10	10	N/A	5	10	5
Velocity changes (temporal)	10	10	10	5	5	5
Proximity to -9°C mean annual isotherm	10	10	10	10	1	1
Susceptible to oceanic warming?	10	10	N/A	10	5	1
TOTAL	80/80	80/80	80/80	70/80	48/90	33/90
Mean	10	10	10	8.75	5.33	3.67

**Based on ice front documented prior to final major retreat phase. Only ice shelves that can be assessed against at least seven of the nine criteria are included.*

Wordie, Larsen A and Larsen B were evaluated on their documented ice fronts and conditions prior to their final breakup, with Wilkins Ice Shelf assessed based on its current configuration as presented in Padman *et al.* (2012), as one ice-shelf unit. The collapsed ice shelves of Wordie, Larsen A and Larsen B scored 'high' susceptibility on each of the considered criteria therefore obtaining a maximum mean of 10. Wilkins Ice Shelf, which is largely regarded as the next system expected to completely disintegrate, scored a mean of 8.75 and was ranked top of the remaining systems. Wilkins Ice Shelf satisfies all but two criteria with 'high' susceptibility, and interestingly, the semi-quantitative assessment suggests that it is only sensitive to future negative-thickness changes and velocity increase. Larsen C Ice Shelf is regarded as comparatively stable, agreeing with the assessment of Glasser *et al.* (2009), and Larsen D (assessed as one ice-shelf system rather than multiple ice fronts) is not expected to undergo any large-scale changes in the near future according to the semi-quantitative assessment (Table 9.6, Table 9.7). Jones, Müller and Prince Gustav Ice Shelves have not been considered as more than three of the criteria could not be fulfilled due to the absence of relevant data. The assessment of ice-shelf susceptibility is therefore in good agreement with patterns and responses of Antarctic Peninsula Ice

Shelves. Subsequently, the same criteria have been applied to Bach, George VI and Stange Ice Shelves, the results of which are presented in Table 9.8, Table 9.9 and Table 9.10.

Table 9.8. Future ice-front susceptibility based on key characteristics presented in Table 9.6. Results are summarised in Table 9.9.

	Bach	George VI				Stange		
		North	South			North	Mid	South
			SIF1	SIF2	SIF3			
A	10	10	5	10	10	10	5	5
B	5	10	5	1	5	1	1	5
C	1	5	10	10	5	10	10	1
D	N/A	N/A	10	10	N/A	N/A	N/A	N/A
E	10	5	10	10	1	5	5	10
F	10	5	10	10	10	10	10	N/A
G	5	10	5	10	N/A	5	5	1
H	5	10	10	5	5	1	1	1
I	5	5	10	10	5	5	5	5
TOTAL	51/80	60/80	75/90	76/90	31/70	47/80	32/80	28/70
Mean	6.38	7.5	8.33	8.44	5.86	5.88	4.75	4

Table 9.9. Ice-front susceptibility to future retreat/ breakup based on the criteria in Table 9.6 and scoring in Table 9.7.

Rank	Score	Ice front
1	8.44	GVIIS South Ice Front 2
2	8.33	GVIIS South Ice Front 1
3	7.50	GVIIS North Ice Front
4	6.38	Bach ice front
5	5.88	Stange North
6	5.86	GVIIS South Ice Front 3
7	4.75	Stange Mid
8	4.00	Stange South

The semi-quantitative approach highlights the susceptibility of George VI Ice Shelf, particularly at its southern ice fronts, with South Ice Front 2 most likely to undergo continued retreat. George VI's northern ice front is also highly susceptible to further retreat, with the ice fronts of Bach, Stange north and George VI's South Ice Front 3 considered the next most likely to undergo enhanced retreat, respectively. The values calculated for Stange mid and Stange south suggest that sustained retreat is less likely.

Comparing the semi-quantitative assessments of Bach, George VI and Stange Ice Shelves to others on the Antarctic Peninsula (Table 9.9) it is apparent that George VI, Bach and the northern front of Stange Ice Shelf are considered more likely to undergo retreat than Larsen C and Larsen D, situated on the eastern Antarctic Peninsula.

Table 9.10. Ice front susceptibility to enhanced retreat/ breakup based on the criteria in Table 9.6 and scoring in Table 9.8 and Table 9.9.

Rank	Score	Ice front
1	10	Wordie*[+]
=	10	Larsen A*[+]
=	10	Larsen B*[+]
4	8.75	Wilkins (as one)*[#]
5	8.44	GVIIS South Ice Front 2
6	8.33	GVIIS South Ice Front 1
7	7.50	GVIIS North Ice Front
8	6.38	Bach ice front
9	5.88	Stange North
10	5.86	GVIIS South Ice Front 3
11	5.33	Larsen C*
12	4.75	Stange Mid
13	4.00	Stange South
14	3.67	Larsen D (as one)*

**Based on published data reviewed in Chapter 2 and Section 9.1. [+]Ice shelf that has already undergone rapid retreat and breakup. [#]Ice shelf recently undergone breakup phases.*

To fully understand the semi-quantitative assessment, the anticipated weaknesses and future changes of Bach, George VI and Stange Ice Shelves are discussed in the following sections. Their future stability is considered with respect to the observed patterns and mechanisms on other ice shelf systems that have been presented in Chapter 2, Section 9.1 and Table 9.6. A spatial assessment of their instabilities is presented.

9.2.1 Bach Ice Shelf

Assuming continued retreat of the ice front and steady ice-shelf motion, the greatest risk to the stability of the system is presented by any future changes to the ice-front geometry. It has already been inferred that 'new' fracturing and rifting between March 2003 and March 2004 was caused by changing stress regimes at the ice front due to the progressive decoupling from the tip of Monteverdi Peninsula, permitting increased plate-bending by tidal action. Continued forward motion of these structures towards the ice front would almost certainly initiate large-scale calving. As the fractures are almost linear across the central portion of the ice shelf, calving will remove the stabilising convex ice-front geometry towards the east.

Recently (11 Feb 2012, Figure 9.9), the fracture/rift system was between 6.1 km and 10.1 km from the ice front, moving at roughly 0.125 km a^{-1} towards the margin. Coupled with an average retreat rate of 0.263 km a^{-1} (distance) the fracture/rift system will get 0.388 km closer to the ice front each year (on average), even if the pinning points remained stable. Therefore, in the unlikely event of no large-scale calving, these fractures will reach the central portion of the ice front within the next 15 years, ultimately removing any stabilising ice-front properties and preconditioning the ice shelf for further, enhanced retreat. This is a

conservative estimate, and it is perhaps more likely that fracture/rift-derived calving will commence within the next decade followed by a period of increased retreat, based on predictions by Doake *et al.* (1998).

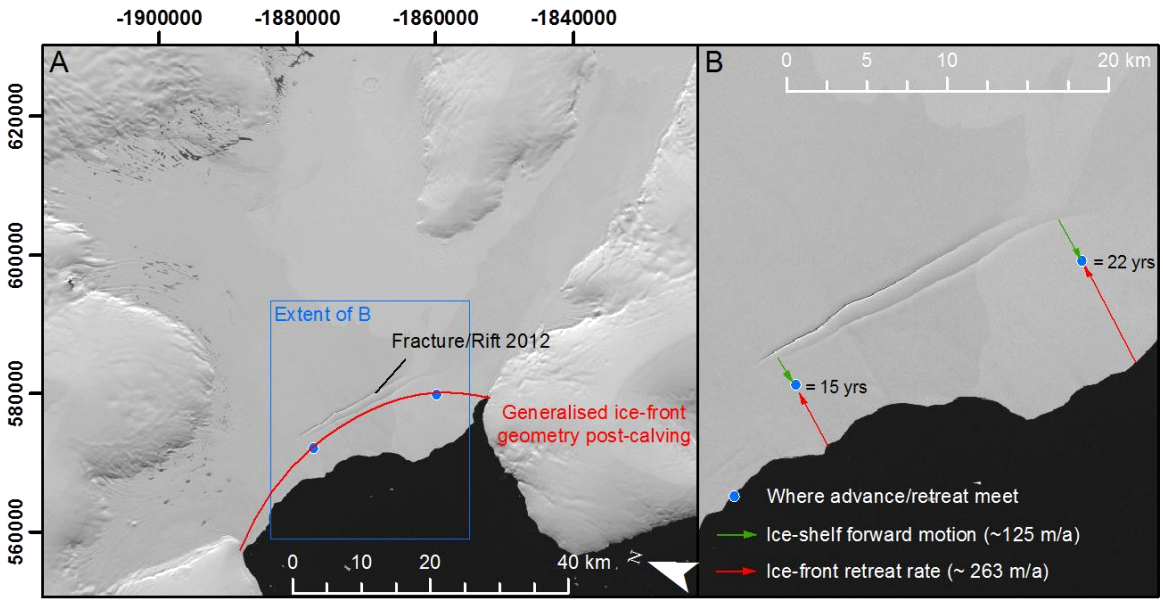

Figure 9.9. A) Generalised ice-front geometry of Bach Ice Shelf following predicted retreat along fracture/rift system with stable pinning points. B) Temporal changes in fracture/rift location and predicted time (from 2012) when they will reach the 'ice front', assuming no calving. The ice front is likely to change dimension in the next decade and become configured for irreversible retreat.

The second stabilising characteristic recognised on Bach Ice Shelf is the converging channel which the ice front occupies. However, decoupling from the eastern grounding zone occurred during the 1990s, with continued calving along the pinning point observed since. If retreat at both pinning points continues at present rates, then further decoupling is envisaged within the next 10 years. At the eastern edge along Monteverdi Peninsula, this would lead to a further expansion of the channel that cuts back upstream along the peninsula towards the Stravinsky Ice Domain. Along the western margin, the southern pinning point of Weber Ice Domain is only 2.5 km from the ice front. Continued retreat of the ice margin could severely affect the dynamics of this particular portion of the ice shelf; a fracture is observed in this zone where a long history of fracture/calving cycles has been recorded (see Figure 6.8). As a result, retreat is expected to continue here, and it is likely to reduce the back-stresses exerted on both the Weber and Boccherini ice domains, thus permitting increased flow speeds. Initially, this is most likely to affect the Weber Ice Domain particularly at the western pinning point.

Whilst presently cohesive, the boundary between Weber and Boccherini units has been shown to be thinner, and is likely to contain a significant proportion of marine ice, accreted in the basal cavity downstream of Bennett Dome and incorporated into the shelf through fracture healing. As a result, this flow unit boundary is likely to be mechanically weaker than ice in the main flow channel. Consequently, changes to the dynamic regime of Weber Ice Domain or Boccherini Ice Domain could exploit the pre-existing weaknesses along the flow confluence, potentially leading to shearing as observed prior to the collapse of Larsen B (Glasser and Scambos, 2008), resulting in increased longitudinal extension and speed up of flow ice domains towards the ice front.

Indeed this situation could be sped up with continued thinning from the surface and base of Bach Ice Shelf. With a southerly migration of warmer air temperatures predicted to continue, an increased amount of surface melting is likely to occur, enhancing thinning rates near the ice front through sustained negative mass balance. Furthermore, increasing the volume and longevity of surface meltwater in pre-existing fracture zones could potentially raise the hydraulic pressure to a critical limit where enhanced fracturing in already weak zones causes further instabilities. At the very least, it is expected that increasing atmospheric temperatures and lengthening melt seasons (Torinesi *et al.*, 2003) would reduce the amount of in-situ accumulation that perhaps provides extra stability to rift and fracture zones by limiting rift-tip propagation (Bassis *et al.*, 2005).

With the flow-unit boundary zones likely to contain a significant amount of marine ice, these areas are particularly susceptible to projected oceanic warming. Whilst Bach Ice Shelf has been shown to be responsive to episodic upwelling of deep ocean waters, general warming of the sea surface on the west Antarctic Peninsula is likely to reduce the rate of basal accretion and frazil-ice accumulation, and also increase the rate of basal melt. Consequently, the basal cavities at flow-unit confluences will become even thinner and thus prone to fracturing. Increasing oceanic temperatures would also lead to a reduction in the stability of ice melange in some of the larger rifts which elsewhere has been reported as a limiting factor on fracture propagation (Bassis *et al.*, 2005; Fricker *et al.*, 2005; Braun *et al.* 2009). Continued widespread thinning, caused by atmospheric and/or oceanic warming would thus naturally weaken the ice shelf (e.g. Shepherd *et al.*, 2003) making it vulnerable to widespread fracturing.

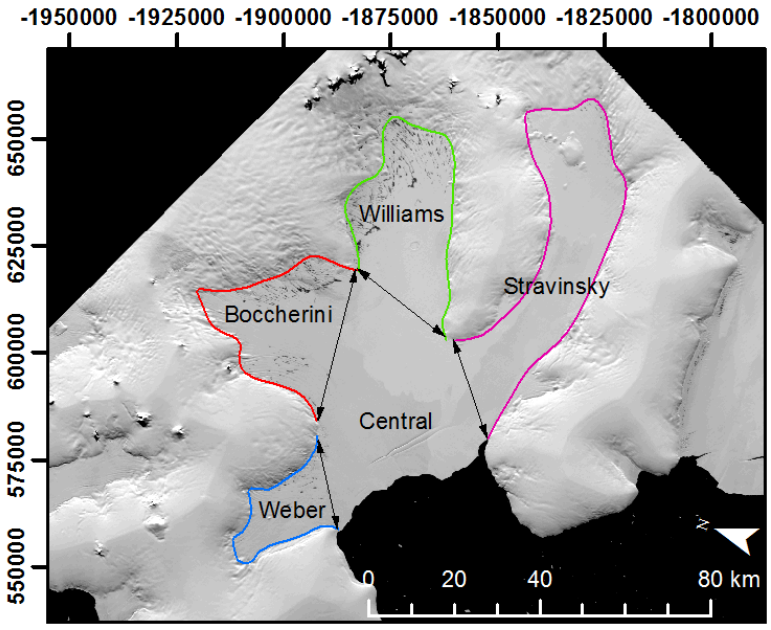

Figure 9.10. Illustrating the diverging channels of the individual ice domains of Bach Ice Shelf. In the event of ice loss in the Central section, the Weber, Boccherini, Williams and Stravinsky ice domains may become preconditioned for further retreat.

Presently, the dynamic nature of Bach Ice Shelf limits transverse fracturing except for at the ice front and between flow units. Increased longitudinal extension is likely to cause fracturing on the ice shelf surface, thus increasing the susceptibility to hydro-fracture as discussed by van der Veen (1998) and Scambos *et al.* (2000, 2003). Coupled with the extensive surface meltwater that already occupies much of Bach Ice Shelf during the austral summer, the potential of hydro-fracture must also be recognised beyond present fracture zones. It is envisaged that increased longitudinal extension together with increasing surface meltwater over space and time could weaken the ice shelf to a point where at least partial collapse is observed through hydro-fracture mechanisms.

It is anticipated that the Stravinsky Ice Domain will be more resilient to future atmospheric and oceanic changes due to its relative ice thickness and comparatively slow flow speeds. Anticipated retreat of the Boccherini Ice Domain may simply reduce the Stravinsky Ice Domain to a separate ice-shelf system, resembling the individual marine terminating glaciers observed on the west coast of the Beethoven Peninsula. The future of the Williams Ice Domain will depend on the amount of glaciological changes observed in Boccherini-derived ice as currently this domain is largely restricted by the dominant dynamics of ice to the west; Weber Ice Domain could equally become an individual ice shelf and stabilise in its embayment. One key characteristic of each separate ice domain is their diverging

channels towards the central portion (Figure 9.10), thus arguably, the strength and stability of Bach Ice Shelf is controlled by the current cohesion between all four components that will be lost during the continued retreat of the central section of the ice front.

9.2.2 George VI Ice Shelf

9.2.2.1 Northern ice front

Whilst the semi-quantitative assessment in Section 9.2.1 suggests that the southern ice front is more susceptible to further retreat, Humbert (2007) argues that any disintegration of George VI Ice Shelf will be initiated from its northern margin. It has already been discussed that this region has been ice-free during the late-Pleistocene and early-Holocene (e.g. Bentley *et al.,* 2005, 2011; Roberts *et al.,* 2008) and that the dynamics have changed in the past (Clapperton and Sugden, 1982), thus illustrating that George VI Ice Shelf is responsive to oceanic and atmospheric variation. Currently, being concavely-shaped and showing a sustained ice-loss regime, the north ice front satisfies the criteria for irreversible retreat proposed by Doake *et al.* (1998).

The retreat history of the northern ice front since ca. 1940 alludes to periodic large-scale breakup of heavily-fractured ice that stretches for some distance back upstream from the ice front. There is an apparent lengthy time period over which fractures develop and propagate, and therefore the amount of ice-loss can be anticipated well in advance of actual calving. Thus based on these historical observations, no immediate large-scale calving is expected from the northern ice front, as few fractures or rifts currently exist; iceberg calving will be governed by regular, but instantaneous calving at the ice front that is likely to reduce the retreat rate from ~0.56 km a^{-1} (linear along centreline) observed between 1979 and 2010.

Historical observations also illustrate that the structural regime at the northern ice front is governed by the dynamics of individual tributary glaciers that flow from Palmer Land. It has been shown that where there is a lack of longitudinal and transverse compression (due to the absence of flow-unit confluence), fractures and rifts are capable of propagating across the ice shelf, along which large-scale calving is initiated. It is therefore argued that the short bursts of rapid retreat are linked to the breakup of comparatively 'less-active' zones of shelf ice, with retreat rate much lower where the ice front is directly supplied by fast-flowing 'active' ice. The latter situation currently exists, with iceberg calving and

retreat rate governed by the dynamics of Riley Glacier. Figure 9.11 illustrates that George VI Ice Shelf, south of Riley Glacier, has a comparatively slow, less-active dynamic regime absent of significant glacier input. It is proposed that this zone (Zone 2, Figure 9.11) is currently exposed to a high back-stress regime by the presence of Riley Glacier, limiting longitudinal extension that ultimately restricts fracturing. Removal of Riley Glacier-derived ice (Zone 1, Figure 9.11) would reduce these back-stresses and permit fractures to open transverse-to-flow across an approximate area of 1200 km^2, rendering this entire section weak and susceptible to large scale retreat as observed between 1974 and 1979 further downstream.

Figure 9.11 also displays the meltwater distribution on George VI Ice Shelf during January 2010 in the northern region; if the proposed sequence of events detailed above takes place, then Zone 2 will become increasingly susceptible to hydro-fracture mechanisms as discussed by van der Veen (1998) and Scambos *et al.* (2000, 2003) that ultimately led to the rapid collapse of Larsen A and Larsen B Ice Shelves. Surface melting on George VI Ice Shelf in the northern region has been on-going since at least 1940 (Stephenson and Fleming, 1940) yet the compressive flow regime of the ice shelf has limited the effect of surface meltwater on its structural stability. Furthermore, the northern limit of surface meltwater has always been south of the ice front, but in recent years it has been shown to expand towards a retreating northern margin. As a result, a combination of structural weakening (longitudinal extension), abundant meltwater and intensifying surface-melt brought on by warmer temperatures (e.g. Vaughan *et al.* 2003) and a lengthening melt season (Torinesi *et al.*, 2003), creates an environment susceptible to atmospheric warming; the northern region already sits within the -9°C mean annual isotherm limit of viability, presented by Morris and Vaughan (2003).

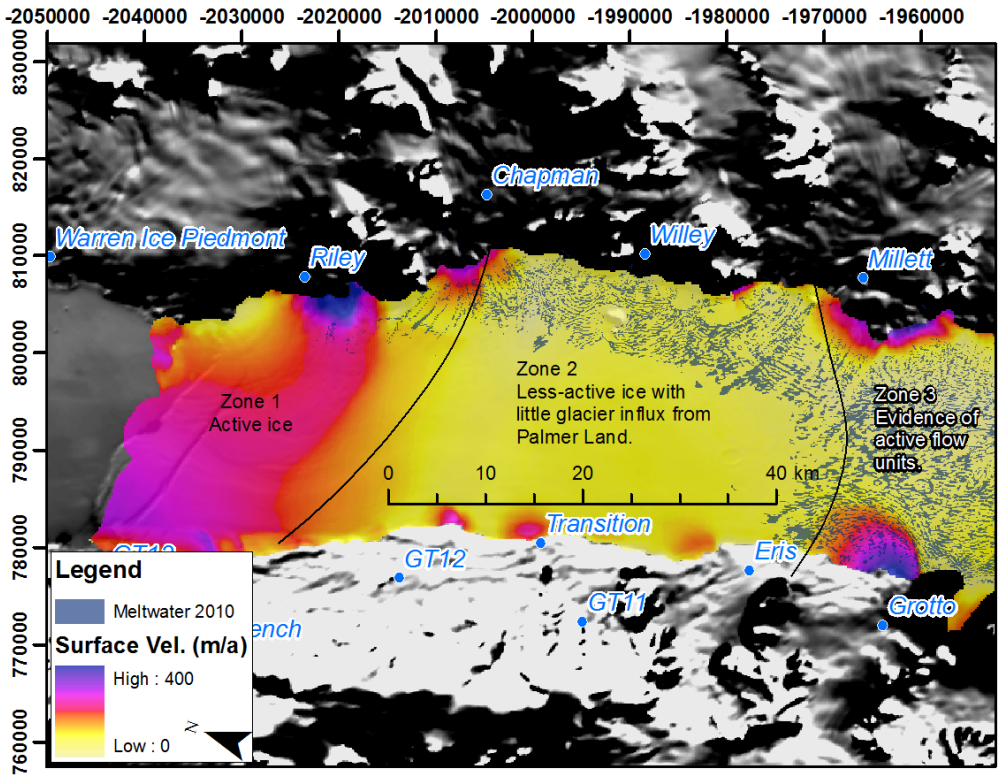

Figure 9.11. Zone 1: Active ice fed by Riley Glacier which ultimately controls the retreat rate of George VI north ice front. Zone 2: Transverse fracturing limited due to dominant ice flux downstream, preventing longitudinal extension. Removal of ice in Zone 1 could lead to an increase in longitudinal extension thus making Zone 2 susceptible to large-scale fracturing as observed during 1974-1989 further downstream. Note also, the extent of surface meltwater that currently occupies the compressive-zones of George VI Ice Shelf. Zone 3: Evidence of more active ice from Millett and Grotto glaciers marking the southern limit of proposed large-scale retreat. Velocities shown are indicative of ca. 1995 InSAR calculations, superimposed over a MODIS image (2003) courtesy of Haran *et al.* (2006).

In terms of its basal conditions, recent modelling studies (Holland *et al.*, 2010) have suggested that the rate of basal melt specific to the northern region increased from ~1.8 ma^{-1} to ~2.0 ma^{-1} since 1980. Whilst comparatively high to the other ice shelves on the west Antarctic Peninsula, basal melt remains marginally less than the 2.1 ma^{-1} rate required to switch from a positive to a negative mass balance (Potter *et al.*, 1984). The northern region of George VI Ice Shelf is therefore close to equilibrium, but currently is not losing sufficient mass from its base to instigate widespread thinning. This is further reflected in recent surface-elevation change measurements and inferred thinning rates obtained from ICESat GLAS data between 2003 and 2008. Indeed, the non-significant surface-elevation changes calculated also point to an ice-shelf surface near equilibrium. Whilst surface melting is evident for prolonged periods of the austral summer, the absence of sufficient surface drainage means that meltwater refreezes on the surface of the ice shelf and therefore the actual mass lost is considered negligible. Other surface processes such as firn

compaction are also considered negligible due to the ice-shelf surface being largely free of snow and firn during the summer (Reynolds and Hambrey, 1988; Tedesco, 2009). As a result, the northern section of George VI Ice Shelf is perhaps less susceptible to ice-shelf thinning, although Fricker and Padman (2012) commented that surface-lowering terminated on Wilkins Ice Shelf approximately 8 years prior to the two most recent breakup phases in 2008 and 2009, and thus a lack of vertical change may not necessarily point to a stable ice shelf. The northern region, however, is susceptible to regular surface melting from a structural perspective, regardless of whether mass is lost from the ice shelf. The stabilising characteristic is its unusual dynamic regime that will ultimately control the spatial and temporal retreat/ breakup patterns.

The longevity of the northern ice front in its current configuration is difficult to assess. Based on its retreat rate from 1979 to 2010 (i.e. excluding large-scale breakup between 1974 and 1979), the ice front is predicted to have retreated beyond Riley Glacier by 2030 based on its current retreat rate, although in reality this is a conservative assessment; calving to date has occurred along pre-existing rifts that are not presently observed, and the assessment does not consider dynamic instabilities of Riley Glacier. Nevertheless, within this timeframe, it is expected that significant changes would have occurred at the northern ice front that will permit more widespread and rapid retreat in the following years, by which time the ice shelf may be in negative mass balance from basal and surface melting, and also be more vulnerable to hydro-fracture-collapse mechanisms.

9.2.2.2 Southern ice fronts

The semi-quantitative assessment depicts George VI South as the most susceptible region to further retreat. This area has seen by far the greatest changes in recent decades as a response to climatic and oceanic variability. Prior to March 2010, the main south ice front underwent sustained retreat concentrated in the central portion that was inferred to be thin and have a high concentration of marine-derived ice. This sustained ice loss (horizontal and vertical) has rendered large portions of the southern margins structurally weak, and prone to iceberg calving along preconditioned fractures and rifts. The removal of the central portion of the ice front separated it into two individual ice fronts, that even despite their close proximity, have distinctly different glaciological regimes.

The thinning observed to date is linked to increasing basal melting as a result of a warming ocean (Holland *et al.,* 2010; Pritchard *et al.,* 2012). Assuming, with some confidence, that this warming will continue, the whole southern ice front of George VI Ice Shelf is particularly vulnerable to heightened retreat as a result of increased basal melting and a reduction of in situ basal accretion. The future response of South Ice Front 1 and South Ice Front 2 are discussed separately below, as it has been shown that these are now largely independent systems.

South Ice Front 1's stability is governed by its frontal geometry and thickness-driven velocity from further upstream, particularly towards the Monteverdi Peninsula. This portion has historically shown prolonged periods of advance followed by large-scale calving, and indeed, calving is anticipated in the coming years along a well-developed rift. Even after this expected loss of ice, the ice front would remain relatively stable, being convex over much of its length (Figure 9.12). It is expected that it would also maintain a similar speed as it has done in previous decades as it is seemingly non-responsive to retreat patterns as its dynamics are driven by its thickness gradient between the ice front and its tributary grounding lines.

Towards the Eklund Islands, South Ice Front 1 is structurally weak. Large areas lee-side of IR5, IR6 and IR7 are heavily fractured and rifted; the recent retreat history illustrates that these are most susceptible to further ice loss, particularly as increasing basal melting and reduced basal accretion (Holland *et al.,* 2010) will limit basal accumulation. Furthermore, the visible ice melange that fills the rifts is likely to reduce, and with it, any resistance to further propagation (Bassis *et al.,* 2005). Within the next decade it is probable that the ice directly in front of these ice rises will have disappeared, leaving the ice shelf pinned behind them, similar to the way in which it is currently pinned behind IR8, IR9, IR10 and IR11 (Figure 9.12).

The consequent response of the ice shelf further upstream to these changes at the ice front is more difficult to predict. Extra strength may be given to the ice front immediately adjacent to the Eklund Islands due to pinning and buttressing, reducing the retreat rate and consequently allowing the entire ice shelf to stabilise. Conversely, continued retreat beyond IR5-to-IR7 towards IR1-to-IR3 may occur; it has already been shown in this region that retreat is possible beyond the ice rises (IR12, IR13-to-IR17). The latter would seem more likely over a longer time period, especially as continued fracturing and thinning of

the ice shelf would naturally make these areas more vulnerable to retreat, and indeed the shelf is already thinner in this region than in the main flow channel to the north and south. Changes on this scale would then directly affect the dynamics of the more stable ice to the north, along Monteverdi Peninsula. The projected phases of retreat are displayed in Figure 9.13 and are based on a qualitative assessment of previous retreat patterns, thickness and thickness changes recorded, and inferred structural stability.

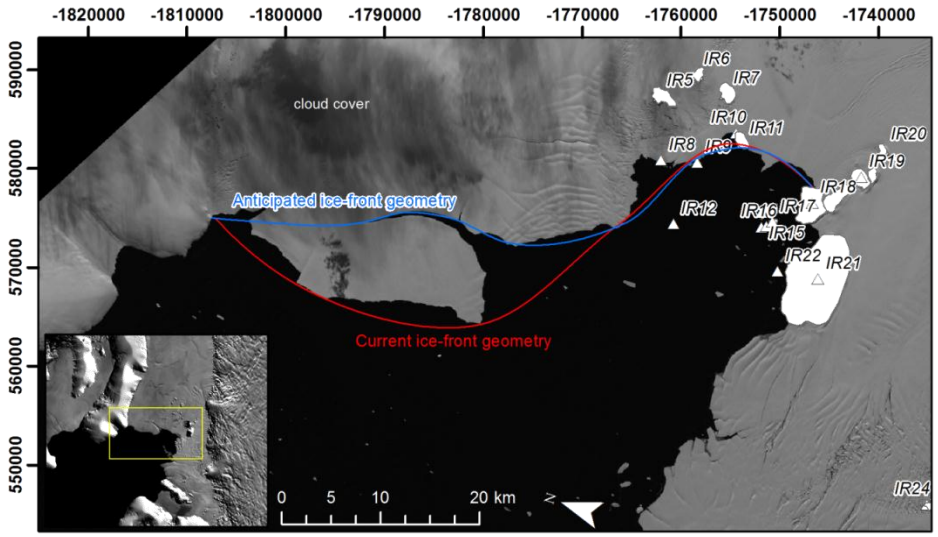

Figure 9.12. Generalised frontal geometry of South Ice Front 1 in its present configuration (Feb 2012, Red) and expected configuration post calving which is anticipated in the coming years (Blue). Note that even post-calving, the ice front remains largely convex between pinning points due to thickness-driven dynamics. The ice-front geometry acts as the main control on the stability of South Ice Front 1.

The removal of ice lee-side of ice rises and ice rumples will expose more resistant, consolidated areas of the shelf to oceanic processes that have previously been protected from, for example tidal forcing. Calving is likely to continue in regions between ice rises and ice rumples, particularly from IR11 to IR18 where calving has previously been observed (see Figure 7.26 G, H, I, J; Figure 9.13). Continued retreat in this specific location increases the vulnerability of the shelf further upstream which is marked by a distinct flow unit boundary between GT03 and GT04a, likely to be thinner, and which contains a significant concentration of marine ice. Significant thinning has taken place in this location over recent decades, highlighting the susceptibility to oceanic warming and whilst no timescale is suggested, it is proposed that this area is initially vulnerable to continued, regular calving rather than breakup along pre-existing weaknesses.

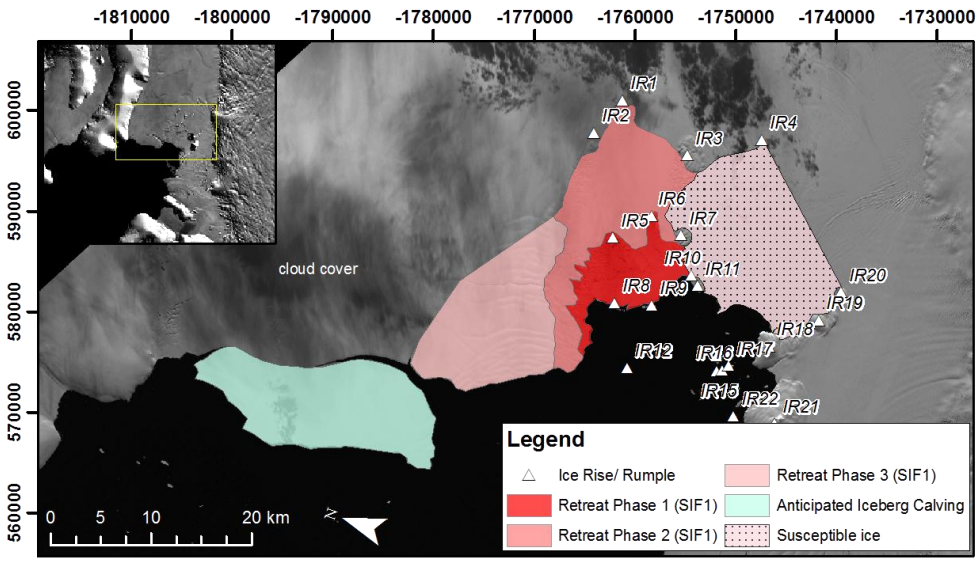

Figure 9.13. Projected changes to South Ice Front 1 (SIF1) including anticipated iceberg calving and proposed retreat phases. Ice in Retreat Phase 1 is current rifted and vulnerable to immediate retreat. Retreat Phase 2 is expected to occur following the removal of ice lee-side of IR5-IR7, and is again heavily fractured and contains a significant amount of melange-filled rifts. The timing of Retreat Phase 2 is dependent on how stable the ice becomes pinned against IR5, IR6 and IR7. Whilst the ice in Retreat Phase 3 is weakened by IR1 and IR2, the rifts and fractures generally heal with flow towards the ice front; the ice-shelf draft is thicker in this location and dynamically influenced by the main flow channel immediately to its north. It is proposed that this section is comparatively stable and will only become vulnerable to further retreat once weaker ice is removed in retreat phases 1 and 2. The stippled area of susceptible ice lies between IR11 and IR18, has a concave ice front and a history of instantaneous iceberg calving, as discussed in the text; continued, regular retreat is envisaged in this region although the projected extent of the retreat is ambiguous.

Ice feeding South Ice Front 2 has seen the greatest dynamic and structural changes of any other ice shelf either considered in this study, or reported elsewhere, and indeed is most likely to undergo further retreat based on the semi-quantitative assessment in Section 9.2.1. These changes have been linked to the removal of buttressing ice in the central portion of the former ice front that reduced the back stress on the tributary glaciers flowing off the English Coast. This region is considered highly susceptible to further retreat within the next few years, and in particular, it remains vulnerable to on-going oceanic warming.

The positioning of several ice rises close to the grounding zone (IR23, IR24, IR25 and IR26) in addition to those further downstream (IR27, IR28, IR29 and IR30) almost certainly create basal cavities, that not only result in thinner regions of the ice shelf, but also encourage basal accretion of marine ice. As a result, ice feeding South Ice Front 2 is likely to have a high concentration of marine-derived ice that naturally results in these thinner areas being more susceptible to oceanic variation. Rupturing along these already-weak zones is likely to occur if oceanic and atmospheric thinning continues. This could

lead to a further increase in flow speeds as observed on Larsen A and Larsen B prior to collapse (Shepherd *et al.*, 2003; Vieli *et al.*, 2007), and would render this entire section wholly unstable.

This portion of the ice shelf has also seen significant transverse fracturing over recent decades as a progressive response to ice-shelf thinning and velocity increase. The distribution of open rifts in particular has increased, many being filled with an ice melange that elsewhere has been shown to limit further propagation (e.g. Bassis *et al.*, 2005). Even within the last decade, the number of open rifts with visible water at their bases has increased, and as this region is outside of that which is subjected to abundant surface melting, it is clear that this is open sea water. A warming oceanic environment has effectively begun to remove the stabilising ice melange in these rifts. As a result, future widening of these rifts is almost certain to occur as they progress through the ice shelf towards the front, increasing the rate of retreat and also increasing the likelihood of rapid breakup phases.

The dynamic and structural regimes currently seen in this section of George VI Ice Shelf prevent a sequenced retreat pattern from being inferred, and indeed the whole ice front is subject to on-going iceberg calving and rapid structural change. The eastern section of South Ice Front 2 is perhaps more vulnerable to such changes, and based on its current structural configuration, vertical response to warming and consequent increase in speed, it is envisaged that this portion of the ice front is expected to see the greatest changes well within the next decade. In the central portion of South Ice Front 2 the shelf is more consolidated, yet fractures and rifts emanating from IR25 and IR26 clearly illustrate a weakening ice-shelf system that will only undergo further fracturing with increasing atmospheric and oceanic temperatures. Removal of ice to its immediate east could also promote further fracturing here and cause enhanced iceberg calving. Further west still, fractures stemming from IR29 render this portion of the ice shelf vulnerable to continued retreat, and indeed historical retreat patterns illustrate the susceptibility of this area to frontal calving. Figure 9.14 summarises the current strengths and weaknesses in ice feeding South Ice Front 2 and proposed limit of maximum retreat.

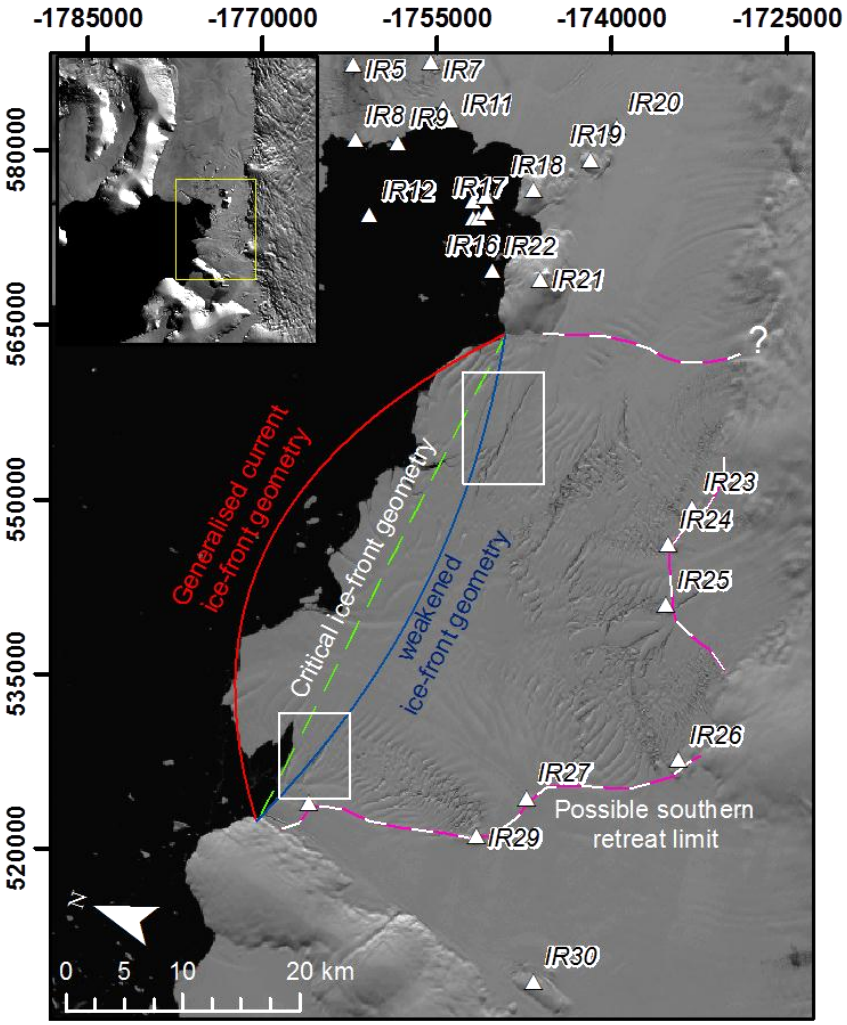

Figure 9.14. Current stabilities and inferred weaknesses at South Ice Front 2 of George VI Ice Shelf. Note in particular that the response of its feeder glaciers is mainly sensitive to future changes in its ice front geometry. At present (red line), the ice front displays a largely convex geometry and may be limiting the current rate of retreat. The critical ice front geometry (green-hashed) is linear and stretches from each of the pinning points. Any retreat beyond this (blue line) would see a shift in geometric stability. Given the rifts close to the present ice front (white boxes), a change in its shape is likely to take place as a result of continued iceberg calving. It is inferred that retreat will halt as the ice shelf becomes pinned on various ice rises in the region (purple-white line).

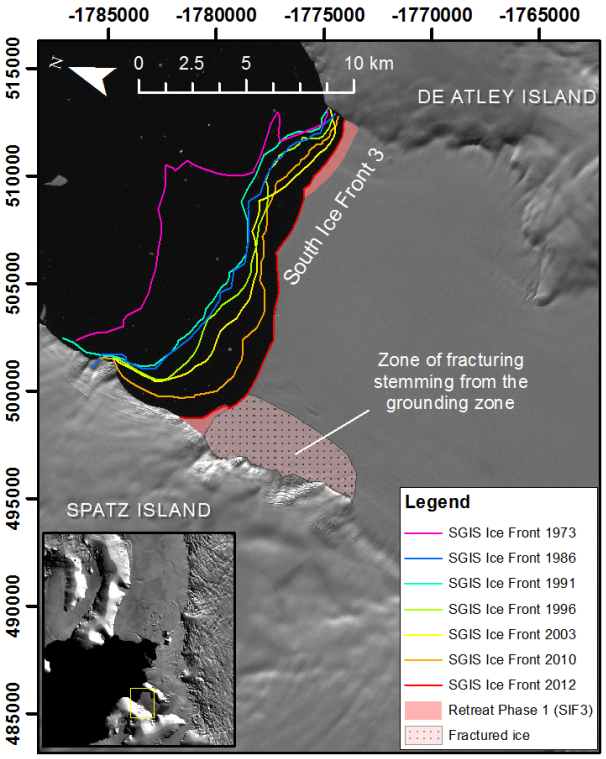

Figure 9.15. Retreat patterns illustrating increased concavity along South Ice Front 3 (SIF3). The red polygons at both pinning points show areas that are preconditioned for retreat in coming years. The stippled pink area illustrates a zone of fracturing and fracture traces stemming from the grounding zone of Spatz Island. Future retreat is likely to be concentrated in this zone.

Figure 9.14 also displays the current and critical ice-front geometries at South Ice Front 2. At present, the ice front is convex and therefore the future response of the feeder glaciers is predominantly sensitive to its geometric characteristics. Due to the extent and distribution of ice-shelf fractures and rifts in this zone, rapid changes are expected along the ice front that will ultimately increase the susceptibility to a rapid breakup event. These changes are envisaged within the next decade. Despite an increase in flow speeds recorded in GT07, the ice-shelf portion upstream of IR27 and IR29 remains largely stable. It is expected that this area will mark the southern boundary of the breakup event, although removal of buttressing ice is likely to cause further instabilities to the flow dynamics in this zone.

Conversely, South Ice Front 3 is unlikely to undergo rapid retreat. Although thinning has been calculated along this narrow portion of George VI Ice Shelf, its frontal geometry, embayment geometry and lack of any distinct fracture zones has, to date, limited its change. More recent satellite imagery (7th March 2012) illustrates that calving has continued along the concave portion of the ice front, and indeed the convex portion has

almost disappeared. Faint surface fractures at either pinning point also highlight the regions that are most susceptible to imminent calving (Figure 9.15).

The weakest zone lies towards the Spatz Island margin. Crevasses that originate above the grounding zone transmit onto the ice shelf and heal to form crevasse (fracture) traces. At the ice front, these are seen reopening and give reason to the area susceptible to future retreat at the ice front. It has already been illustrated that the concave portion of the ice front is linked to thinner and thus weaker ice, and there is no reason to believe that any other retreat pattern would exist in this area. South Ice Front 3 is currently situated south of the -9°C mean annual isotherm, and may be susceptible to further atmospheric warming. Coupled with increasing oceanic temperatures, this area is vulnerable to future thinning that could impact the long-term response of this narrow ice-shelf portion. The spatial extent over which immediate retreat is expected is minimal compared to that at South Ice Front 1 and South Ice Front 2 and it is expected that the ice feeding South Ice Front 3 is comparatively stable.

9.2.3 Stange Ice Shelf

The semi-quantitative assessment of Stange's three ice fronts illustrate the ice shelf's resistance to breakup in the near future; it is not preconditioned for enhanced retreat as observed on George VI and Bach Ice Shelves. Whilst undergoing sustained ice loss (horizontally and vertically), the northern front of Stange Ice Shelf remains stable due to its convex profile. There is a long history of iceberg calving at its eastern and western pinning points, yet the central section of the ice front only underwent limited retreat along pre-existing fractures that gradually propagate back upstream. It is clear from the historical observations that this process is a part of its natural mass balance cycle rather than a response to recent atmospheric and oceanic warming.

Even located in a diverging channel, this is not thought to impact the stability of the northern ice front unless the ice-front geometry changes significantly over a short time period. Retreat at the eastern margin has been governed by iceberg calving along fractures and rifts that initiate as Spatz Island-derived ice rounds the tip of the island and propagate transversely towards the ice front. This is likely to produce icebergs for the foreseeable future, but retreat may halt when rift production is no longer viable as the ice front becomes pinned at the tip of Spatz Island (Figure 9.16). At its western pinning point,

steady retreat is likely to continue along pre-existing fractures that migrate to the ice front from Smyley Island grounding zone. Based on historical observation, the heightened retreat rate towards both pinning points over the central portions would result in a convex profile being maintained across the Ronne Entrance embayment. The only concerning factor on future stability would be the removal of the central portion of the ice front; fractures and rifts that developed in 2001 have progressively propagated back into the ice shelf, and may promote frontal calving that alters the geometric profile of the north ice front over a longer timescale (Figure 9.16).

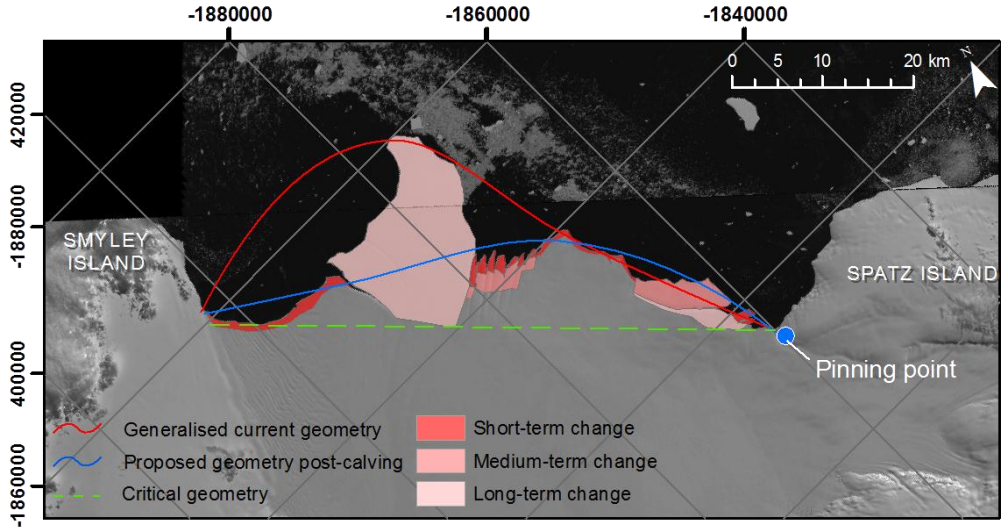

Figure 9.16. Generalised current, projected and critical geometric profiles of Stange north ice front and areas susceptible to short-term, medium-term and long-term change. Qualitatively categorised based on fracture/rift development and calving history. The ice front is likely to become pinned on the tip of Spatz Island thus limiting retreat beyond this point.

At the mid ice front, little retreat has been observed to date; historical observations show that this is a stable portion of Stange Ice Shelf. It is apparent that the multi-annual sea ice has a stabilising property on the rate of calving from all three ice-front components, not only holding distinct rifts together, but limiting wave propagation to the ice front, dampening tidal amplitude and possibly impeding shelf flow. Whilst ice flowing towards the mid ice front is heavily fractured and prone to retreat the stability of this region is governed by the longevity of sea ice, and therefore its removal is likely to have the greatest impact on the response of Stange Ice Shelf in the short-term.

The southern ice front has a long history of advance and retreat. Its stability is governed by this dynamic regime, ice front geometry and channel embayment into which it terminates.

Despite clear shearing between ST07 and slower moving ice towards its east, enhanced retreat is not expected to occur because of its already rapid dynamic regime that is able to regulate the frontal position of the southern portion. Furthermore, this section is largely independent of the rest of the shelf, and any structural and dynamic changes are unlikely to have any impact on the main portions of Stange Ice Shelf.

Considering Stange Ice Shelf as a whole, its future stability is likely to be controlled by its long-term interaction between the warming atmospheric and oceanic environments rather than short-term glaciological changes. Whilst outside of the -9°C mean annual isotherm limit of viability, a southward migration of warming temperatures is likely to have a similar effect to that which has been previously observed on its northern neighbours. More concerning, perhaps, is the potential response of the ice shelf to oceanic warming.

The complex dynamic regime of Stange Ice Shelf has created equally complex structures and features, most notably the flow unit boundaries and fracture zones that spread into the ice shelf from the grounding line (Figure 9.17). Elsewhere, these features have been shown to contain a significant portion of marine-derived ice, as well as being thinner and thus structurally weaker than the main flow channels. Indeed, their comparative thinness compared to the main channel of flow is evident in Griggs and Bamber's (2011) ice thickness data even at a 1 km resolution (Figure 9.17).

Elevation change measurements over Stange Ice Shelf have revealed substantial thinning across the whole shelf, and consequently, it is these thinner sections that are believed to be susceptible to oceanic changes (Figure 9.17). Glasser and Scambos (2008) and Vieli *et al.* (2007) both recognised the controlling nature of these suture zones on the stability of ice-shelf systems, thus thinning and weakening from the basal cavities upward is likely to impact upon the structural and dynamic stability of Stange Ice Shelf, as already observed between ST07 and slower-moving ice between the English Coast and Case Island.

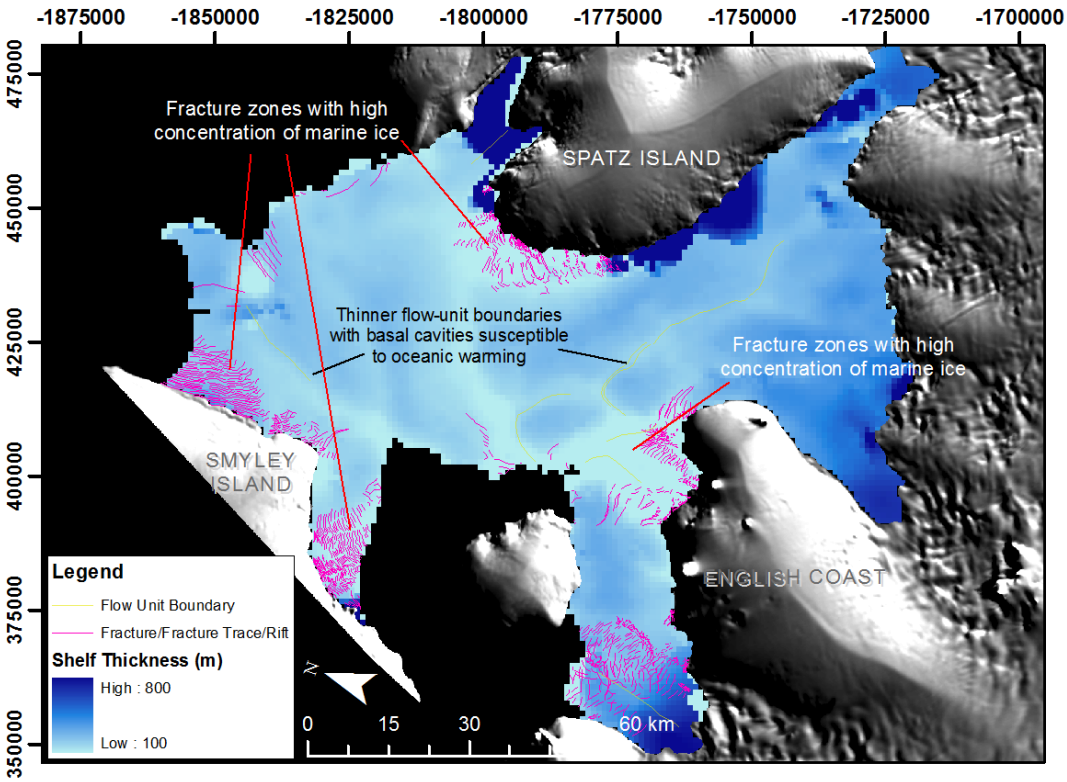

Figure 9.17. Areas on Stange Ice Shelf susceptible to oceanic warming due to inferred high marine ice concentrations, accreted in basal cavities and incorporated into the shelf through longitudinal fracture healing. Thickness data sources from Griggs and Bamber (2011) and overlain on the MOA image (Haran *et al.*, 2006).

The future of Stange Ice Shelf is largely dependent therefore, on the response of these suture zones to continued basal melting. Weakening of the ice shelf from below would almost certainly permit an increase in flow speed towards the northern ice front. Being situated in a diverging channel, there would be little transverse compression to restrict velocity increase. As seen elsewhere, an increase in flow speeds would promote transverse fracturing and create an ice-shelf system prone to collapse.

9.2.4 Consequences of ice-shelf removal

The responses of ice-shelf tributary glaciers post-collapse have been well documented. Scambos *et al.* (2004), Rignot *et al.* (2004), Hulbe *et al.* (2008), Rignot *et al.* (2011) and Glasser *et al.* (2011) have all illustrated an acceleration and thinning of former feeder glaciers after the disintegration of Antarctic Peninsula Ice Shelves, increasing the discharge of former glaciers between three and nine times (Rignot *et al.*, 2004). Whilst imminent removal of Bach, George VI and Stange Ice Shelves is unlikely, continued atmospheric

and oceanic warming over a multi-decadal timescale is likely to see a similar disintegration of these systems as observed elsewhere.

The consequences of such a response in this region have been reported by Shepherd *et al.* (2003) who commented that removal of the Larsen A and Larsen B Ice Shelves accelerated ice discharge into the oceans by ~0.07 mm a^{-1}, although the same authors note that snow-driven accumulation essentially cancelled out the increased ice discharge. Rignot *et al.* (2004) demonstrated that the total ice flux directly into the oceans from the eight former tributary glaciers of Larsen B was ~ 27 km^3 a^{-1} (~24.7 gigatonne (Gt) a^{-1}), roughly equal to the total net ice discharge from the Greenland and Antarctic ice sheets (20 Gta^{-1}, Zwally *et al.,* 2002), although again accumulation on the Dyer Plateau cancelled out much of the increased discharge. More recently, Rott *et al.* (2011) re-estimated this value at ~4.3 Gta^{-1} in 2008 and illustrated a decrease in ice discharge overtime following retreat. However, the total contribution of the Antarctic Peninsula to sea level rise is, at present, considered negligible (Shepherd *et al.* 2003; Vaughan *et al.,* 2003) because of high accumulation rates.

For each of the ice shelves considered in this study, the total ice discharge into the ocean has been calculated using ALOS PALSAR InSAR velocities from ca. 2008 (Rignot *et al.*, 2011) and thickness data at the grounding line (ca. 1995, Griggs and Bamber, 2011) (Figure 9.18; Table 9.11). The velocity data of Rignot *et al.* (2011) were used as the velocities for all of the tributary systems extend upstream of the grounding line, whereas velocity data calculated here are mostly limited to the ice fronts of each ice shelf. Uncertainty in the velocity data is less than 10%. Although the ice thickness at the grounding line from 1995/96 is likely to over-estimate the actual thicknesses in ca. 2008 due to continued thinning since, it offers the best spatial resolution that permits calculations across all of the major ice-shelf tributary systems. At most, errors are ~ 10% for ice shelf thickness estimates, and assuming an error of 10% for the width of the glacier systems at the grounding line, the overall error for discharge estimates is therefore ± 17%. An ice density of 915 kg m^3 was used to estimate the total discharge across the major glacier grounding lines, so that the total ice discharge could be calculated using Equation 9.1 (km^3a^{-1}) and Equation 9.2 (Gta^{-1}).

$$Q_i = \sum \frac{\bar{U}.\bar{H}.d}{1000^3} \qquad \text{Equation 9.1}$$

$$Q_i = \sum \frac{\bar{U}.\bar{H}.d}{1000^3} . 0.915 \qquad \text{Equation 9.2}$$

wWhere Q_i is the ice discharge, $\bar{U}$ is the interpolated velocity over a 1000 m^2 grid, $\bar{H}$ is the interpolated ice thickness over a 1000 m^2 grid, and d is the distance between points (always 1000 m). The product of $\bar{U}.\bar{H}$.d is converted from m^3a^{-1} to km^3a^{-1} using the denominator 1000^3. This is then converted to Gta^{-1} by multiplying the total discharge by 0.915 (as 1 km^3 of ice = 0.915 Gt by weight). The summation of each section (Figure 9.17) resulted in an estimate of the total ice discharge in both km^3a^{-1} and Gta^{-1} for the major tributary systems on Bach, George VI and Stange Ice Shelves across their grounding lines.

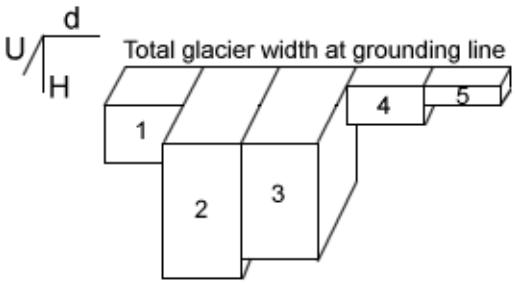

Figure 9.18. Schematic of discharge calculation across grounding zone. Each of the five 1 km-width sections are summed to obtain total discharge for each glacier.

Based on the estimates of Zwally *et al.* (2002, 2005) and Rignot *et al.* (2005), each Gigatonne of ice entering the ocean is approximately equal to 0.003 mm a^{-1} of eustatic sea level rise. Table 9.11 presents the total discharge (in km^3a^{-1}, Gta^{-1}) and estimated sea-level rise equivalent (mm a^{-1}) of the major tributary systems of Bach, George VI and Stange Ice Shelves (see Figure 9.19 for their locations). The total discharge of the main tributary glaciers of all three ice shelves is equal to ~75.1 ± 12.5 Gta^{-1}, or the equivalent eustatic sea level rise of 0.2249 ± 0.0191 mm a^{-1} (not accounting for accumulation). Based on these estimates, tributary glaciers discharge ~2.5 ± 0.4 Gta^{-1} into Bach Ice Shelf, ~14.4 ± 2.4 Gta^{-1} into George VI north, ~40.2 ± 6.8 Gta^{-1} into George VI south and ~18.0 ± 3.1 Gta^{-1} into Stange Ice Shelf (Table 9.11). Of all ice-shelf portions, George VI south is the most significant in terms of discharge, and is also the most likely to undergo sustained retreat.

Table 9.11. Major glacier influxes to Bach, George VI and Stange Ice Shelves. Eustatic sea-level rise equivalent is based on discharge only and does not take into account expected increasing accumulation inland. Locations shown in Figure 9.18.

Region/Glacier	Grounding line width (km)	$km^3 a^{-1}$	Gt a^{-1}	Sea-level rise equivalent (mm a^{-1})
George VI North				
Riley		2.572 ± 0.437	2.353 ± 0.400	0.0070
Chapman/Skinner		0.141 ± 0.024	0.129 ± 0.022	0.0004
Meiklejohn		0.282 ± 0.048	0.258 ± 0.044	0.0008
Millett		0.143 ± 0 .024	0.131 ± 0.022	0.0004
Bertram		0.404 ± 0. 069	0.37 ± 0.060	0.0011
Ryder		0.882 ± 0.150	0.807 ± 0.137	0.0024
McArthur		0.071 ± 0.012	0.065 ± 0.011	0.0002
Conchie		0.682 ± 0.116	0.624 ± 0.106	0.0019
Goodenough		5.143 ± 0.874	4.706 ± 0.800	0.0141
GT01		0.464 ± 0.079	0.425 ± 0.072	0.0013
GT01a		4.431 ± 0.753	4.054 ± 0.689	0.0122
Mars/Saturn		0.113 ± 0.019	0.103 ± 0.017	0.0003
GT10 to Eros		0.125 ± 0.021	0.114 ± 0.020	0.0003
Pluto to Jupiter		0.041 ± 0.007	0.038 ± 0.006	0.0001
Grotto		0.141 ± 0.024	0.129 ± 0.022	0.0004
Eris to Trench		0.054 ± 0.009	0.049 ± 0.008	0.0001
Sub-total		*15.689 ± 2.667*	*14.355 ± 2.44*	*0.0426 ± 0.0037*
George VI South				
GT02		9.101 ± 1.547	8.327 ± 1.416	0.0250
Sheet flow (PL)		10.042 ± 1.707	9.188 ± 1.562	0.0276
GT03		9.204 ± 1.565	8.422 ± 1.432	0.0253
GT04		2.809 ± 0.478	2.57 ± 0.440	0.0077
GT05		0.956 ± 0.163	0.875 ± 0.149	0.0026
GT06		0.845 ± 0.144	0.773 ± 0.131	0.0023
GT07		8.721 ± 1.483	7.98 ± 1.360	0.0239
GT08		2.035 ± 0.346	1.862 ± 0.317	0.0056
GT09		0.112 ± 0.019	0.102 ± 0.017	0.0003
Kirwan Inlet		0.102 ± 0.017	0.093 ± 0.016	0.0003
Sub-total		*43.927 ± 7.468*	*40.193 ± 6.833*	*0.1206 ± 0.0102*
Bach				
Lovell Glacier		0.941 ± 0.161	0.861 ± 0.146	0.0026
BT01		0.102 ± 0.017	0.093 ± 0.016	0.0003
BT02		0.104 ± 0.018	0.095 ± 0.016	0.0003
BT03/BT04		0.095 ± 0.016	0.087 ± 0.015	0.0003
BT05/BT06		0.378 ± 0.064	0.346 ± 0.058	0.0010
BT07/BT08		0.147 ± 0.025	0.135 ± 0.022	0.0004
BT09		0.099 ± 0.017	0.091 ± 0.014	0.0003
BT10 to BT12		0.106 ± 0.018	0.097 ± 0.016	0.0003
BT13		0.042 ± 0.007	0.038 ± 0.006	0.0001
BT14		0.791 ± 0.134	0.724 ± 0.123	0.0022
Sub-total		2.782 ± 0.473	2.546 ± 0.436	*0.0076 ± 0.0006*
Stange				
ST01/ Hill Glacier		0.662 ± 0.113	0.604 ± 0.103	0.0018
ST02		2.594 ± 0.441	2.375 ± 0.404	0.0071
ST03		1.075 ± 0.183	0.979 ± 0.166	0.0029
ST04		2.099 ± 0.357	1.912 ± 0.325	0.0057
ST05/Lidke		2.156 ± 0.367	1.967 ± 0.334	0.0059
ST06		0.043 ± 0.007	0.037 ± 0.006	0.0001
ST07/ST08		10.052 ± 1.709	9.196 ± 1.563	0.0276
ST09		0.552 ± 0.094	0.503 ± 0.086	0.0015
ST10		0.491 ± 0.083	0.448 ± 0.076	0.0013
Sub-total		*19.701 ± 3.349*	*18.026 ± 3.063*	*0.0541 ± 0.0046*
TOTAL		**82.099 ± 13.935**	**75.136 ± 12.75**	**0.2249 ± 0.0191**

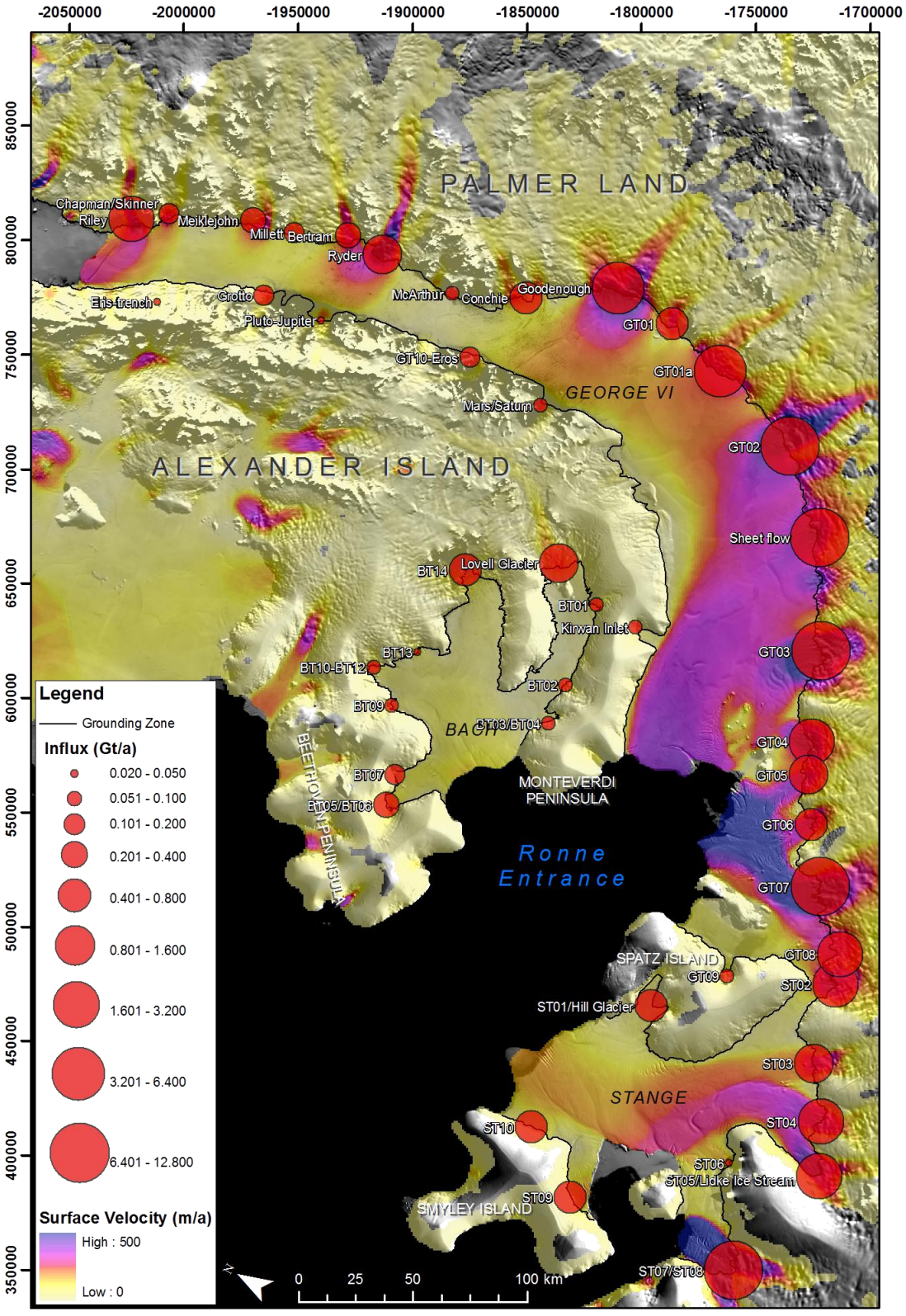

Figure 9.19. Current ice discharge into Bach, George VI and Stange Ice Shelves based on InSAR velocity measurements (Rignot *et al.*, 2011) and 1995 thickness estimates (Griggs and Bamber, 2011). Note the dominant control of Palmer Land glaciers on the total discharge in this region.

Recent estimates (Rignot, 2008; Bindschadler *et al.*, 2011) suggest that the discharge into the floating section of Pine Island Glacier increased from ~41 ± 27 Gta^{-1} to ~90 ± 27 Gta^{-1} between 1996 and 2006, attributed to a retreating and thinning ice shelf. It is also expected that the discharge calculated here for Bach, George VI and Stange Ice Shelves will increase as the back stresses exerted on the tributary glaciers reduces with further thinning and retreat, particularly from Riley Glacier and those feeding South Ice Front 2 on George VI Ice Shelf.

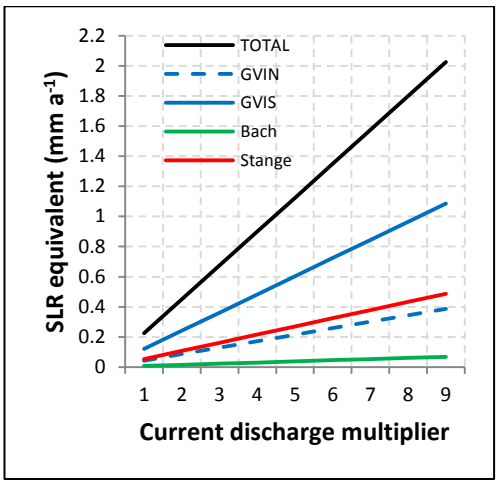

Figure 9.20. Projected maximum total sea-level rise (SLR) equivalent per annum following the complete removal of Bach, George VI and Stange Ice Shelves. Rignot *et al.* (2004) calculated a maximum nine-fold increase in the discharge of Hektoria/Green/Evans glaciers after the removal of the Larsen B Ice Shelf during 2002 and hence the range selected here as a thought experiment only. George VI south (GVIS; south of GT02) accounts for 54% of the total ice discharge from the southwest Antarctic Peninsula.

In terms of the complete removal of shelf ice in the southwest Antarctic Peninsula, accelerated discharge is also expected. The scenarios projected in Figure 9.20 are based on the maximum changes as observed on Larsen B Ice Shelf, where between three-to-nine times of the pre-collapse discharge was recorded (Rignot *et al.*, 2004). Consequently, (not accounting for accumulation) it is envisaged that complete removal of all three systems has the potential to increase global sea level by between 0.22 and 2.03 mm a^{-1}, however, it is stressed that the higher end of this estimation is unlikely to be reached because it is improbable that the discharge of each glacier system will increase by up to nine-times is current flow rate, or that the increased discharge rate will be sustainable.

9.3 Study Limitations

Throughout the thesis, the recent history of southwest Antarctic Peninsula Ice Shelves has been assessed using a range of remote sensing data, methods and analytical techniques. The limitations of each of these have been expressed where appropriate, and are summarised in Table 9.12.

Table 9.12. An overview of the major limitations of this study.

Data, process or analysis	Limitations and comments
Landsat imagery	• Spatial and temporal resolutions often prevent finer detail from being examined. • Data gap during mid-1990s. • Data loss from Landsat ETM+ imagery (2003-present) due to equipment failure created significant data gaps along the outermost edges of the satellite imagery.
ASTER	• Data acquisition mode does not favour repeat coverage, and spatial coverage is poor over large ice-shelf areas.
SAR imagery	• Noisy data unsuitable for fine resolution structural mapping.
ICESat GLAS	• Equipment failure after launch limited acquisition to three 33-day periods each year. • Patchy data due to cloud cover and atmospheric haze. • Not always an exact 12-month repeat acquisition. • Only available from between 2003-2008.
RAMP DEM	• Horizontal accuracy of 200 m, vertical accuracy over steep terrain ± 15 m (± 1 m for ice-shelf surfaces) resulting in issues removing topographic phase from InSAR derived velocities.
Structural and spatial mapping	• Scale of structural and spatial mapping dictated by pixel resolution of imagery. • Features often interpreted based on shadow/ reflectance of the Sun. Some features unidentifiable without further interpretation. • Coarser pixel resolution of earlier imagery could cause misinterpretation of 'new' structures in later imagery. • Meltwater mapping restricted to ice-shelf surfaces and non-fractured areas due to spectral similarities between water and shadow: Problematic mostly where large glacier systems enter George VI Ice Shelf.
InSAR	• Poor coherence between image pairs limited the spatial and temporal distribution of InSAR-derived velocities. • Residual errors due to topography (see 'RAMP DEM'), tidal flexure and atmospheric pressure. • Unable to unwrap interferograms from stable location due to lack of bare ground: Ice divides used – inaccuracy likely to be minimal.
Feature tracking	• Features dictated by coverage in optical satellite imagery. • Greatest inaccuracies arise from coregistration of initial images and interpolation mode selected.
Elevation-change measurements	• Errors caused by horizontal movement of surface structures through time were largely reduced, although in the northern section of George VI Ice Shelf, this was not done as explicitly as other areas due to the masking by surface meltwater. • Changes based on repeat-track acquisitions across the ice shelves – large areas therefore not assessed. • Assumed that surface elevation change was constant between 2003 and 2008 to account for incomplete data series. • Thickness change estimates calculated without exact knowledge of ice and water densities – approximations used instead.
Discharge estimations	• Based on ca. 1995 thickness estimates and ca. 2007 velocity calculations. • Grounding line thickness estimates likely to underestimate true thicknesses. • Projected discharge after removal of ice shelves a thought experiment rather than a probable outcome.

Chapter 10

Conclusions

10.1 Conclusions

This study has demonstrated that southwest Antarctic Peninsula Ice Shelves have responded to environmental changes that represent the initial stages of irreversible retreat observed elsewhere in the region. By applying established remote-sensing techniques this study has:

- Quantified the retreat rate of all ice fronts of Bach, George VI and Stange Ice Shelves, as well as providing an assessment of retreat patterns with respect to ice-shelf configuration.
- Provided detailed surface-feature and structural analysis from multi-annual satellite imagery, to:
  - Further the understanding of glaciological configurations of each ice shelf.
  - Show structural evolution and structural change of the ice-shelf systems on sub-decadal time scales.
  - Identify the variations in surface meltwater extent and distribution.
- Calculated ice-shelf flow speeds over multi-annual time periods to determine:
  - Ice-shelf flow regimes and the genesis of surface structures.
  - Variations in flow dynamics over time.
- Examined the vertical response of the ice shelves over sub-decadal timescales to illustrate widespread thinning across the region.

The key findings of this study are summarised as follows:

- Bach and George VI Ice Shelves have exhibited sustained retreat, with only a minor advance recorded at the southern margin of George VI between 1973 and 2010; even here, iceberg calving is anticipated within the coming years. The northern ice front of Stange Ice Shelf has also displayed continued retreat since 1973, whereas its mid-ice front remained relatively stable, and its southern ice front fluctuated as a result of a highly dynamic flow regime. The retreat of Bach, Stange and George VI south has been comparatively steady, whereas the northern ice front of George VI showed evidence of large-scale, rapid retreat followed by periods of progressive ice loss along preconditioned fractures and rifts.
- Each ice shelf displayed widespread and significant thinning, most notably towards the ice front of Bach Ice Shelf, in the central and southern regions of George VI Ice Shelf, and across the whole of Stange Ice Shelf. Grounding zone retreat was also

evident towards the southern margin of George VI Ice Shelf, whereas towards the northern region, weak, non-significant thinning was recorded from 2003 to 2008.

- Each ice shelf exhibited increased fracturing and rifting from 1973, in particular:
  - A large fracture/rift system which developed and propagated in the centre of Bach Ice Shelf between 2003 and 2004.
  - Widespread fracturing and rifting between the around the Eklund Island and between them and De Atley Island in the southern extent of George VI Ice Shelf.
  - Shear-induced fracturing occurred between ST07 and its eastern boundary from 2001 to present on Stange Ice Shelf.
- Meltwater extent and distribution increased on Bach Ice Shelf, migrating pole-wards since 1973, attributed to warming atmospheric temperatures. Similarly, the northern meltwater extent on George VI Ice Shelf increased, although the southern extent fluctuated; it is known that the positioning of the meltwater limits on George VI Ice Shelf is closely linked with localised temperature patterns rather than long-term climatic changes.
- At the northern and southern ice fronts of George VI Ice Shelf, flow speeds increased, which are thought to be linked to the reduction of back-stresses on the tributary glaciers as a response to ice-shelf retreat. Flow speeds towards the southern ice front of Stange Ice Shelf slowed; it is proposed that this response was linked to sustained thinning that altered its dynamic configuration. Flow speeds on Bach Ice Shelf did not significantly increase or decrease over the observation periods considered here.

By integrating secondary data sources and previously published information, this study has also been able to examine the present and future stability of Bach, George VI and Stange Ice Shelves, as well as offering a discussion on the consequence of ice-shelf removal. The key points resulting from the detailed discussions are:

- George VI Ice Shelf is an atypical system with a dominant flow regime off Palmer Land that controls the present stability of the northern ice front. Its flow regime creates a largely compressive ice shelf that limits fracturing to distinct flow confluences along both grounding zones. At present, Riley Glacier is responsible for the dynamic configuration of the north ice front, and any future changes to the rest of the northern section are closely linked to the longevity of this particular glacier. It is

envisaged that retreat beyond this system will reduce back-stresses sufficiently to prompt widespread fracturing and rifting of less active ice between Chapman Glacier and Bertram Glacier, which could see the next large-scale retreat phase at the northern ice front.

- The area between the Eklund Islands and De Atley Island at the southern ice front of George VI Ice Shelf is most likely to undergo continued and rapid retreat. Whilst its ice front is currently convex, thus providing extra stability, the ice that feeds it is heavily fractured and rifted and is therefore considered mechanically weak. Between the Eklund Islands and Monteverdi Peninsula, the ice shelf is more stable, driven by tributary glaciers ~150 km upstream. It is expected that this area of the southern ice from will show progressive, rather than rapid, changes. The whole of the southern region, however, is responsive to oceanic warming, and without a detailed understanding of ice-ocean interactions, projecting the response of this region is challenging.
- Bach Ice Shelf is considered comparatively stable, although the response of the ice shelf to calving along the distinct fractures and rifts within the next 15 years will ultimately control its long term stability. Along with Stange Ice Shelf, the retreat of Bach may be periodically enhanced by warm-water intrusion. As a result, the longevity of both systems could be most responsive to oceanic variations in the Bellingshausen Sea.
- It is expected that continued atmospheric and oceanic temperature increase will result in the complete removal of each ice-shelf system, although due to their complex configurations, the response may be more progressive than those collapse phases observed elsewhere (Larsen B, for example).

This study has provided a wealth of data to suggest that ice shelves in the southwest Antarctic Peninsula have been responding to documented environmental change. There is little evidence to suggest the ice shelves are configured for long-term, decadal stability, although it is recognised that continued monitoring of such systems is required to develop our understanding of specific atmospheric-cryospheric-oceanic interactions.

10.2 Future work

This thesis has highlighted that there is still a significant knowledge gap in our present understanding of the atmospheric, cryopheric and oceanic interactions in the Antarctic Peninsula (and therefore those regions outside the Antarctic Peninsula, also). In particular, future work should consider the interaction of surface meltwater with the upper layers of the ice shelf. With the compressive nature of both George VI and Bach Ice Shelves, and abundant, annual surface meltwater, these perhaps form the two best control sites for investigating such interactions in such a susceptible region.

Furthermore, whilst the volume of surface meltwater has been estimated (e.g. George VI Ice Shelf; Reynolds, 1981), these calculations are largely outdated and based on only a limited amount of data. With developments in LiDAR over recent years, high-precision DEMs could be produced and used to construct hydrological drainage networks of the ice-shelf surfaces, not only allowing for a more accurate estimation of the volume of surface meltwater, but also surface drainage into, or through, the ice shelves, to estimate the total amount of ablation from surface melting. Again, George VI and Bach Ice Shelves are ideal study sites for such research.

There is also a requirement for further research into the basal regimes of ice shelves. Recently, Fricker and Padman (2012) and Pritchard *et al.* (2012) identified the importance of ice thickness and basal topography on the thinning rates of Antarctic Peninsula Ice Shelves. Here, this study has also shown that where the ice-shelf draft is thickest, more significance thinning has taken place. This is most evident in the central regions of George VI Ice Shelf (Chapter 7) where vertical ice thickness reaches up to 600 m. With the release of the BEDMAP2 (see Fretwell *et al.,* 2012), more accurate datasets exist for ice thickness and basal topography. Coupled with a better understanding of the dynamics of the Circumpolar Deep Water (e.g. Holland *et al.,* 2010) and the role it plays in basal melting, future research should aim to model the spatial distribution of basal melt conditions across the Antarctic Peninsula. Projections could be appropriately tested with field measurements, going on the hypothesis that the thickest ice shelves, with the greatest bathymetric depth, are most susceptible to basal melting and therefore further retreat and collapse.

Moreover, historical radio-echo sounding (RES) profiles exist along George VI and Bach Ice Shelves (Swithinbank, 1968). The original data was collected during 1961; retracing these flight-lines would allow a much longer time period of ice-shelf thinning to be assessed.

Coupled with a better estimation of surface ablation and basal melting, as discussed above, the individual attributes that lead to ice-shelf thinning could be investigated separately, rather than being collated into a single measurement.

A significant portion of this thesis was dedicated to identifying ice-shelf structural weaknesses over time. Whilst some of the measured retreat was due to discrete calving, the most substantial ice-loss events occurred where pre-existing (and often longstanding) fractures and rifts encouraged iceberg calving. Numerical models that are capable of predicting calving regimes have become more sophisticated in recent years, yet the application of these to current ice-shelf configurations, using accurate flow velocities, thicknesses and thickness change is yet to be achieved. This is without doubt one of the most challenging steps forward in Antarctic glaciology, and with the empirical data now available, the possibilities of accurately determining calving rates, retreat patterns and the long-term stability of individual ice shelves with respect to present environmental and glaciological conditions is greater than it has previously been.

References

References

Alley, R.B., Clark, P.U., Huybrechts, P. and Joughin, I. 2005. Ice sheet sea-level changes. *Science*, **310**, 456-460.

Antarctic Temperature Datasets, available from: http://www.antarctica.ac.uk/met/gjma/temps.html [last accessed 10.02.2009].

Bamber, J.L. and Bentley, C.R. 1994. A comparison of satellite altimetry and ice thickness measurements of the Ross Ice Shelf, Antarctica. *Annals of Glaciology*, **20**, 357-364.

Bamber, J.L., Gomez-Dans, J.L. and Griggs, J.A. 2009. A New 1 km Digital Elevation Model of the Antarctic Derived from Combined Satellite Radar and Laser Data Part 1: Data and Methods. *The Cryosphere*, **3**, 101-111.

Bamber, J.L. 1994 A digital elevation model of the Antarctic ice sheet derived from ERS-1 altimeter data and comparison with terrestrial measurements. *Annals of Glaciology*, **20**, 48-54.

Bamber, J.L. and Gomez-Dans, J.L. 2005. The accuracy of Digital Elevation Models of the Antarctic Continent. *Earth and Planetary Science Letters*, **237**, 516-523.

Bassis, J.N., Coleman, R., Fricker, H.A. and Minster, J.B. 2005. Episodic propagation of a rift on the Amery Ice Shelf, East Antarctica. *Geophysical Research Letters*, **32**, L06502, doi:10.1029/2004GL022048.

Bekryaev, R.V., Polyakov, I.V. and Alexeev, V.A. 2010. Role of Polar Amplification in long-term surface air temperature variations and modern Arctic warming. *Journal of Climate*, **23**, 3888-3906.

Bentley, C.R., Clough, J.W., Jezek, K.C. and Shabtaie, S. 1979. Ice-thickness patterns and the dynamics of the Ross Ice Shelf, Antarctica. *Journal of Glaciology*, **24**, 287-294.

Bentley, M.J., Hodgson, D.A., Sugden, D.E., Roberts, S.J., Smith, J.A., Leng, M.J. and Bryant, C. 2005. Early Holocene retreat of the George VI Ice Shelf, Antarctic Peninsula. *Geology*, **33**, 173-176.

Bentley, M.J., Johnson, J.S., Hodgson, D.A., Dunai, T., Freeman, S.P.H.T. and Ó Cofaigh, C. 2011. Rapid deglaciation of Marguerite Bay, western Antarctic Peninsula in the Early Holocene. *Quaternary Science Reviews*, **30**, 23-24.

Beran, D.W. 1967. Large amplitude lee waves and Chinook winds. *Journal of Applied Meteorology*, **6**, 865-877.

Berthier, E., Scambos, T.A. and Shuman, C.A. 2012. Mass loss of Larsen B tributary glaciers (Antarctic Peninsula) unabated since 2002. *Geophysical Research Letters*, **39**, doi:10.1029/2012GL051755.

Bindschadler, R.A. 1994. Surface-velocity field of the northern Larsen Ice Shelf, Antarctica. *Annals of Glaciology*, **20**, 319-326.

Bindschadler, R.A. 1998. Monitoring ice sheet behaviour from space. *Reviews of Geophysics*, **38**, 79-104.

Bindschadler, R.A. and Scambos, T.A. 1991. Satellite-image-derived velocity field of an Antarctic ice stream. *Science*, **252**, 242-246.

Bindschadler, R.A. Scambos, T.A., Rott, H., Skvarca, P. and Vomberger, P. 2002. Ice dolines on the Larsen Ice Shelf, Antarctica. *Annals of Glaciology*, **34**, 283-290.

Bindschadler, R.A. Vaughan, D. and Womberger, P. 2011. Variability of basal melt beneath the Pine Island Glacier Ice Shelf, West Antarctica. *Journal of Glaciology*, **57**, 581-595.

Bishop, J.F. and Walton, J.L.W. 1981. Bottom melting under George VI Ice Shelf, Antarctica. *Journal of Glaciology*, **27**, 429-447.

Blindow, N. 1994. The central part of the Filchner-Ronne Ice Shelf, Antarctica: Internal structures revealed by 40 MHz monopulse RES. *Annals of Glaciology*, **20**, 365-371.

Braun, M. and Humbert, A. 2009. Recent retreat of Wilkins Ice Shelf reveals new insights in ice shelf breakup mechanisms. *Geoscience and Remote Sensing Letters*, **6**, 263-267.

Braun, M., Humbert, A. and Moll, A. 2009. Changes of Wilkins Ice Shelf over the past 15 years and inferences on its stability. *The Cryosphere*, **3**, 41-56.

Brenner, A.C., DiMarzio, J.P. and Zwally, H.J. 2007. Precision and accuracy of satellite radar and laser altimeter data over the continental ice sheets. *Geoscience and Remote Sensing*, **45**, 321-331.

Bromirski, P.D. Sergienko, O.V. and MacAyeal, D.R. 2010. Transoceanic infragravity waves impacting Antarctic Ice Shelves. *Geophysical Research Letters*, **37**, L02502 doi:10.1029/2009GL041488.

Brunt, K., Fricker, H.A. Padman, L. Scambos, T.A. O'Neel, S. 2010. Mapping the grounding zone of the Ross Ice Shelf, Antarctica, using ICESat laser altimetry. *Annals of Glaciology*, **51**, 71-79.

Budd, W. 1966. The dynamics of the Amery Ice Shelf. *Journal of Glaciology*, **6**, 335-358.

Campbell, I. Jacobel, R., Welch, B. and Pettersson, R. 2008. The evolution of surface flow stripes and stratigraphic folds within Kamb Ice Stream: Why don't they match? *Journal of Glaciology*, **54**, 421-427.

Carvalho, L.M.V., Jones, C., Ambrizzi, T. 2005. Opposite phases of the Antarctic Oscillation and relationships with intraseasonal to interannual activity in the tropics during the austral summer. *Journal of Climate*, **18**, 702–718.

Casassa, G. and Brecher, H.H. 1993. Relief and decay of flow stripes on Byrd Glacier, Antarctica. *Annals of Glaciology*, **17**, 255–261.

Casassa, G., Jezek, K.C., Turner, J., and Whillans, I.M. 1991. Relict flow stripes on the Ross Ice Shelf. *Annals of Glaciology*, **15**, 132–138.

Cavalieri, D.J. and Parkinson, C.L. 2008. Antarctic sea ice variability and trends, 1979-2006. *Journal of Geophysical Research*, **113**, C07004 doi: 10.1029/2007JC004564.

Collins, L.F. and McCrae, I.R. 1985. Creep buckling of ice shelves and the formation of pressure rollers. *Journal of Glaciology*, **31**, 242-252.

Comiso, J.C. 2000. Variability and trends in Antarctic surface temperatures from in situ and satellite infrared measurements. *Journal of Climate*, **13**, 1674-1696.

Comiso, J.C. 2002. A rapidly declining perennial sea ice cover in the Artic. *Geophysical Research Letters*, **29**, doi: 10.1029/2002GL015650.

Cook, A,J., Fox, A.J., Vaughan, D. and Ferrigno, J.G. 2005. Retreating glacier fronts on the Antarctic Peninsula over the past half-century. *Science*, **308**, 541-544.

Cook, A.J. and Vaughan, D.G. 2010. Overview of the areal changes of the ice shelves on the Antarctic Peninsula over the past 50 years. *The Cryosphere*, **4**, 77-98.

Cooper, A.P.R. 1997. Historical observations of Prince Gustav Ice Shelf. *Polar Record*, **33**, 285-294.

Corr, H.F.J., Jenkins, A., Nicholls, K.W. and Doake, C.S.M. 2002. Precise measurement of changes in ice-shelf thickness by phase sensitive radar to determine basal melt rates. *Geophysical Research Letters*, **29**, doi: 10.1029/2001GL014606.

Crabtree, R.D. and Doake, C.S.M. 1980. Flow lines on Antarctic Ice Shelves. *Polar Record*, **20**, 31-37.

Crabtree, R.D., Storey, B.C. and Doake, C.S.M. 1985. The structural evolution of George VI Sound, Antarctic Peninsula. *Technophysics*, **114**, 431-442.

Davies, B.J., Carrivick, J.L., Glasser, N.F., Hambrey, M.J. and Smellie, J.L. 2011. A new glacier inventory for 2009 reveals spatial and temporal variability in glacier response to atmospheric warming in the northern Antarctic Peninsula, 1988-2009. *The Cryosphere Discuss*, **5**, 3541-3595.

De Angelis, H. and Skvarca, P. 2003. Glacier surge after ice-shelf collapse. *Science*, **299**, 1560-1562.

Definiens. 2005. eCognition User Manual, Version 3.

DiCaprio, C.J. and Simons, M. 2008. Importance of ocean tidal load corrections for differential InSAR. *Geophysical Research Letters*, **35**, L22309, doi: 10.1029/2008GL035806.

DiMarzio, J., Brenner, A., Schutz, C., Shuman, C.A. and Zwally, H.J. 2007. GLAS/ICESat 1 km laser altimetry digital elevation model of Greenland. National Snow and Ice Data Centre, Boulder, CO.

Dinniman, M.S., Klinck, J.M. and Hofmann, E.E. 2012. Sensitivity of Circumpolar Deep Water transport and ice shelf basal melt along the west Antarctic Peninsula to changes in the winds. *Journal of Climate*, **25**. doi: 20.1175/JCLI-D-11-00307.1.

Doake, C.S.M. 1982. State of balance of the ice sheet in the Antarctic Peninsula. A*nnals of Glaciology*, **3**, 77-82.

Doake, C.S.M. 1984. Ice-shelf densities from a comparison of radio echo and seismic soundings. *Annals of Glaciology*, **5**, 47-50.

Doake, C.S.M. and Vaughan, D.G. 1991. Rapid disintegration of the Wordie Ice Shelf in response to atmospheric warming. *Nature*, **350**, 328-330.

Doake, C.S.M., Corr, H.F.J., Rott, H., Skvarca, P. and Young, N. 1998. Breakup conditions for stability of the northern Larsen Ice Shelf, Antarctica. *Nature*, **391**, 778-780.

Domack, E., Duran, D., Leventer, A., Ishman, S., Doane, S., McCallum, S., Amblas, D., Ring, J., Gilbert, R. and Prentice, M. 2005. Stability of the Larsen B Ice Shelf on the Antarctic Peninsula during the Holocene epoch. *Nature*, **436**, 681–685.

Drewry, D.J. (Ed) 1983. *Antarctica: Glaciological and Geophysical Folio*. Cambridge Scott Polar Research Institute.

Drewry, D.J., Jordan, S.R. and Janowski, E. 1982. Measured properties of the Antarctic Ice Sheet: Surface configuration, ice thickness, volume and bedrock characteristics. *Annals of Glaciology*, **3**, 83-91.

Dupont, T.K. and Alley, R.B. 2005. Assessment of the importance of ice-shelf buttressing to ice-sheet flow. *Geophysical Research Letters*, **32**, L04503 doi: 10.1029/2004GL022024.

Dyce, G. and Reynolds, J.M. 2002. Multi-Criteria Analysis and GLOF studies in Bhutan. *Water Resources Management Plan and Update of Power Systems Master Plan, Norconsult A.S., Norway, and Department of Power, Royal Government of Bhutan.*

Eineder, M., Jaber, W.A., Floricioiu, D., Rott, H. and Yague-Martinez, N. 2011. Glacier flow and topography measurements with TerraSAR-X and TanDEM-X. *Geoscience and Remote Sensing Symposium (IGARSS)*, 3835-3838.

ERSDAC (Earth Remote Sensing Data Analysis Centre). 2009. ASTER GDEM Overview, available from: http://www.gdem.aster.ersdac.or.jp/outline.jsp. [Last accessed 10.12.2008].

Falcini, F., Holt, T.O. and Davies, B.J. In prep. Speedup and thinning of Sjörgren Glacier, Trinity Peninsula, Antarctica.

Ferrigno, J.G., Cook, A.J., Mathie, A.M., Williams, R.S., Swithinbank, C., Foley, K.M., Fox, A.J., Thomson, J.W. and Sievers, J. 2009. Coastal-change and Glaciological Map of the Palmer Land Area, Antarctica: 1947-2009. *USGS Geologic Investigations Series Map I-2600-C*, 1 map sheet, pp28.

Fatland, D.R. and Lingle, C.S. 1998. Analysis of the 1993-95 Bering Glacier (Alaska) surge using differential SAR interferometry. *Journal of Glaciology*, **44**, 532-546.

Fetterer, F., Knowles, K., Meier, W., and Savoie, M. 2002. Sea Ice Index. Boulder, Colorado USA: National Snow and Ice Data Center. Digital media.

Fetterer, F., Knowles, K., Meier, W., and Savoie, M. 2009. Sea Ice Index. Boulder, Colorado USA: National Snow and Ice Data Center. Digital media.

Fleming, W.L.S. 1940. Relic glacial forms on the western seaboard of Graham Land. *The Geographical Journal*, **96**, 93-100.

Fleming, W.L.S., Stephenson, A., Roberts, B.B. and Bertram, G.C.L. 1938. Notes on the scientific work of the British Graham Land Expedition. *Geographical Journal*, **91**, 508-532.

Fletcher, J.O. 1969. Ice extent on the Southern Ocean and its relation to world climate. *Memorandum RM-5973-NSF*. Santa Monica, Rand Corporation.

Folland, C.K., Karl, TR., Christy, J.R., Clarke, R.A., Gruza, G.V., Jouzel, J., Mann, M.E., Oerlemans, J., Salinger, M.J., and Wang, S.-W. 2001. *Observed Climate Variability and Change, in Climate Change 2001: The Scientific Basis* Edited by J. T. Houghton et al., 99–181, Cambridge Univ. Press, New York, 2001.

Fox, A.J. and Cooper, P.R. 1998. Climate-change indicators from archival aerial photography of the Antarctic Peninsula. *Annals of Glaciology*, **27**, 636-642.

Fox, A.J. and Vaughan, D.G. 2005. The retreat of Jones Ice Shelf, Antarctic Peninsula. *Journal of Glaciology*, **51**, 555-560.

Francis, S.J. 1947. Survey report including a general account of country traversed for second sledge journey, 5-28 August 1947. *British Antarctic Survey Archives ref*. AD6/2D/1947/L2.

Fretwell., P., Pritchard, H.D., Vaughan, D.G., Bamber, J.L., Barrand, N.E., Bell, R., Bianchi, C., Bingham, R.G., Blankenship, D.D., Casassa, G., Catania, G., Callens, D., Conway, H., Cook, A.J., Corr, F.F.J., Damaske, D., Damm, V., Ferraccioli, F., Forsberg, R., Fujita, S., Gogineni, P., Griggs, J.A., Hindmarsh, R.C.A., Holmlund, P., Holt, J.W., Jacobel, R.W., Jenkins, A., Jokat, W., Jordan, E., King, E.C., Kohler, J., Krabill, W., Riger-Kusk, M., Langley, K.A., Leitchenkov, G., Leuschen, C., Luyendyk, B.P., Matsuoka, K., Nogi, Y., Nost, O.A., Popov, S.V., Rignot, E., Rippin, D.M. Riviera, A., Roberts, J., Ross, N., Siegert, M.J., Smith, A.M., Steinhage, D., Studinger, A., Sun, B., Tinto, B.K., Welsh, B.C., Young, D.A., Xiangbin, C. and Zirizzotti, A. 2012. Bedmap2: Improved ice bed, surface and thickness dataset for Antarctica. *The Cryosphere Discuss*, **6**, 4305-4361.

Fricker, H.A. and Padman, L. 2006. Ice-shelf grounding zone structure from ICESat laser altimetry. *Geophysical Research Letters*, **33**, doi: 10.1029/2006GL026907.

Fricker, H.A. and Padman, L. 2012. Thirty years of elevation change on Antarctic Peninsula Ice Shelves from multi-mission satellite radar altimetry. *Journal of Geophysical Research*, **117**, C02026. Doi: 10.1029/2011JC007126.

Fricker, H.A. Popov, S., Allison, I. and Young, N. 2001. Distribution of marine ice beneath the Amery Ice Shelf. *Geophysical Research Letters*, **28** (11), 2241-2244.

Fricker, H.A., Coleman, R., Padman, L., Scambos, T.A., Bohlander, J. and Brunt, K.M. 2009. Mapping the grounding zone of the Amery Ice Shelf, East Antarctica using InSAR, MODIS and ICESat. *Antarctic Science*, **21**, 515-532.

Fricker, H.A., Young, N.W., Coleman, R., Bassis, J.N. and Minster, J.-B. 2005. Multi-year monitoring of rift propagation on the Amery Ice Shelf, East Antarctica. *Geophysical Research Letters*, **32**, L02502 doi: 10.1029/2004GL021036.

Gao, J. and Liu, Y. 2001. Applications of remote sensing, GIS and GPS in glaciology: A review. *Progress in Physical Geography*, **25**, 520-540.

Gilbert, R. and Domack, E.W. 2003. Sedimentary record of disintegrating ice shelves in a warming climate, Antarctic Peninsula. *Geochemistry, Geophysics, Geosystems*, **4**, 1038-1050.

Gille, S.T. 2002. Warming of the Southern Ocean since the 1950s. *Science*, **295**, 1275-1277.

Gillet, N.P. and Thompson, D.W.J. 2003. Simulation of recent Southern Hemisphere climate change. *Science*, **302**, 273-275.

Glasser, N.F. and Gudmundsson, G.H. 2012. Longitudinal surface structure (flowstripes) on Antarctic Glaciers. *The Cryosphere*, **6**, 383-391.

Glasser, N.F. and Scambos, T.A. 2008. A structural glaciological analysis of the 2002 Larsen B Ice-Shelf collapse. *Journal of Glaciology*, **54**, 3-16.

Glasser, N.F., Kulessa, B., Luckman, A., Jansen, D., King, E.C., Sammonds, P.R., Scambos, T.A. and Jezek, K.C. 2009. Surface structure and stability of the Larsen C Ice Shelf, Antarctic Peninsula. *Journal of Glaciology*, **55**, 400-410.

Glasser, N.F., Scambos, T.A., Bohlander, J., Truffer, M., Petit, E. and Davies, B.J. 2011. From ice-shelf tributary to tidewater glacier: Continued rapid recession,

acceleration and thinning of Röhss Glacier following the 1995 collapse of the Prince Gustav Ice Shelf, Antarctic Peninsula. *Journal of Glaciology*, **57**, 397-406.

Gloersen, P., Campbell, W.J., Cavalieri, D.J., Comiso, J.C., Parkinson, C.J. and Zwally, H.J. 1992. Arctic and Antarctic Sea Ice, 1978-1987: Satellite Passive-Microwave Observations and Analysis. *NASA Special Publication*, **511**, 290.

Goldstein, R. M., Engelhardt, H., Kamb, B. and Frolich, R. 1993. Satellite radar interferometry for monitoring ice sheet motion: Application to an Antarctic ice stream, *Science*, **262**, 1525–1530.

Gordon, A.L. and Goldberg, R.D. 1970. Circumpolar characteristics of Antarctic waters. In Bushnell, V. (Ed) *Antarctic Map Folio Series*. American Geographical Society, **13**.

Gould, L.M. 1935. Structure of the Queen Maud Mountains. *Antarctica Geological Society of America Bulletin*, **46**, 973-984.

Graham, A.G.C. and Smith, J.A. 2012. Palaeoglaciology of the Alexander Island Ice Cap, western Antarctic Peninsula, reconstructed from marine geophysical and core data. *Quaternary Science Reviews*, **35**, 63-81.

Graham, A.G.C., Nitsche, F.O. and Larter, R.D. 2011. An improved bathymetry compilation for the Bellingshausen Sea, Antarctica, to inform ice-sheet and ocean models. *The Cryosphere*, **5**, 95-106.

Gray, A.L., Short, N., Mattar, K.E. and Jezek, K.C. 2001. Velocities and flux of the Filchner Ice Shelf and its tributaries determined from Speckle Tracking Interferometry. *Canadian Journal of Remote Sensing*, **27**, 193-206.

Griggs, J.A. and Bamber, J.L. 2009. A new 1 km Digital Elevation Model of Antarctica derived from combined radar and laser data – Part 2: Validation and error estimates. *The Cryosphere*, **3**, 113–123.

Griggs, J.A. and Bamber, J.L. 2011. Antarctic Ice Shelf thickness from satellite radar altimetry. *Journal of Glaciology*, **57**, 485-498.

Grumbine, R.W. 1994. A sea-ice albedo experiment with the NMC Medium Range Forecast model. *Weather Forecasting*, **9**, 453–456.

Gudmundsson, G.H., Raymond, C.F. and Bindschadler, R. 1998. The origin and longevity of flow stripes on Antarctic Ice Streams. *Annals of Glaciology*, **27**, 145–152.

Guttenberg, N., Abbot, D.S., Amundson, J.M., Burton, J.C., Cathles, M.L., MacAyeal, D.R. and Zhang, W.W. 2011. computational investigation of iceberg capsize as a driver of explosive ice-shelf disintegration. *Annals of Glaciology*, **52**, 51-59.

Hall, D.K., Riggs, G.A. and Salomonson, V.V. 1995. Development of methods for mapping global snow cover using moderate resolution imaging spectroradiometer data. *Remote Sensing of Environment*, **64**, 127-140.

Hambrey, M.J. 1977. Foliation, minor folds and strain in glacier ice. *Tectonophysics*, **39**, 397–416.

Hambrey, M.J. and Dowdeswell, J.A. 1994. Flow regime of the Lambert Glacier-Amery Ice Shelf system, Antarctica: structural evidence from Landsat imagery. *Annals of Glaciology*, **20**, 401–406.

Hambrey, M.J. and Glasser, N.F. 2003. The role of folding and foliation development in the genesis of medial moraines: Examples from Svalbard glaciers. *Journal of Geology*, **111**, 471–485.

Haran, T., Bohlander, J., Scambos, T., Painter, T. and Fahnestock, M. 2006. MODIS mosaic of Antarctica (MOA) image map, digital media, National Snow and Ice Data Centre, Boulder, CO.

Harangozo, S.A. 2006. Atmospheric circulation impacts on winter maximum sea ice extent in the west Antarctic Peninsula region (1979–2001). *Geophysical Research Letters*, **33**, L02502 doi :10.1029/2005GL024978.

Haug, T., Kääb, A. and Skvarca, P. 2010. Monitoring ice shelf velocities from repeat MODIS and Landsat data – a method study on the Larsen C Ice Shelf, Antarctic Peninsula, and 10 other ice shelves around Antarctica. *The Cryosphere*, **4**, 161-178.

Haynes, G.J. 1928. *Antarctic: A treatise on the Southern Continent.* The Richard Press, 386.

Hetland, E.A., Muse, P., Simons, M., Lin, Y.N., Agram, P.S. and DiCaprio, C.J. 2012. Multi-scale InSAR time series (MInTS) analysis of surface deformation. *Journal of Geophysical Research*, **117**, B02404 doi: 10.1029/2011JB008731.

Hjort, C., Bentley, M.J. and Ingolfsson, O. 2001. Holocene and pre-Holocene temporary disappearance of the George VI Ice Shelf, Antarctic Peninsula. *Antarctic Science*, **13**, 296-301.

Holland, D.M. and Bitz, C.M. 2003. Polar amplification of climate change in coupled models. *Climate Dynamics*, **21**, 221-232.

Holland, P.R., Corr, H.F.J., Vaughan, D.G., Jenkins, A. and Skvarca, P. 2009. Marine ice in Larsen Ice Shelf. *Geophysical Research Letters*, **36**, L11604 doi: 10.1029/2009GL038162.

Holland, P.R., Jenkins, A. and Holland, D.M. 2008. The response of ice shelf basal melting to variations in ocean temperature. *Journal of Climate*, **21**, 2558-2572.

Holland, P.R., Jenkins, A. and Holland, D.M. 2010. Ice and ocean processes in the Bellingshausen Sea, Antarctica. *Journal of Geophysical Research*, **115**, C05020 doi 10.1029/2008JC005219.

Hooke, R, Le B. and Huddleston, P.J. 1978. Origin of foliation in glaciers. *Journal of Glaciology*, **20**, 285-299.

Hooke, R, Le B. 2005. *Principles of Glacier Mechanics*. Cambridge University Press.

Horgan, H.J., Walker, R.T., Anandakrishnan, S. and Alley, R.B. 2011. Surface elevation changes at the front of the Ross Ice Shelf: Implications for basal melting. *Journal of Geophysical Research*, **116**, C02005 doi: 10.1029/2010JC006192.

Huang, L. and Li, Z. 2011. Comparison of SAR and optical data in deriving glacier velocity with feature tracking. *International Journal of Remote Sensing*, **32**, 2681-2698.

Huggel, C., Haeberli, W., Kääb, A., Bieri, D. and Richardson, S. 2004. Assessment procedures for glacial hazards in the Swiss Alps. *Canadian Geotechnical Journal*, **41**, 1068-1083.

Hughes, T. 1983. On the disintegration of ice shelves: The role of fracture. *Journal of Glaciology*, **29**, 98-117.

Hulbe, C.L. and Fahnestock, M. 2007. Century-scale discharge stagnation and reactivation of the Ross Ice Streams, West Antarctica. *Journal of Geophysical Research*, **112**, F03S27. doi: 10.1029/2006JF000603.)

Hulbe, C.L. and Whillans, I.M. 1997. Weak bands within Ice Stream B, West Antarctica. *Journal of Glaciology*, **43**, 377-386.

Hulbe, C.L., LeDoux, C. and Cruikshank, K. 2010. Propagation of long fractures in the Ronne Ice Shelf, Antarctica, investigated using a numerical model of fracture propagation. *Journal of Glaciology*, **56**, 459-472.

Hulbe, C.L., MacAyeal, D.R., Denton, G.H., Kleman, J. and Lowell, T.V. 2004. Catastrophic ice shelf breakup as the course of Heinrich event icebergs. *Palaeooceanography*, **19**, PA1004 doi: 10.1029/2003PA000890.

Humbert, A. 2006. Numerical simulations of the ice flow dynamics of Fimbulisen. *Frisp report*, **17**, 1-12.

Humbert, A. 2007. Numerical simulations of the ice flow dynamics of George VI Ice Shelf, Antarctica. *Journal of Glaciology*, **53**, 659-664.

Humbert, A. and Braun, M. 2008. The Wilkins Ice Shelf, Antarctica: Breakup along failure zones. *Journal of Glaciology*, **54**, 943-944.

Humbert, A. and Steinhage, D. 2011. The evolution of the western rift area of the Fimbul Ice Shelf. *The Cryosphere*, **5**, 931-944.

Ingólfsson, O., Hjort, C. and Humlum, O. 2003. Glacial and climate history of the Antarctic Peninsula since the Last Glacial Maximum. *Arctic, Antarctic and Alpine Research*, **35**, 175–186.

Ingolfsson, O., Hjort, C., Berkman, P.A., Bjorck, S., Colhoun, E., Goodwin, I.D., Hall, B., Hirakawa, K., Melles, M., Molle, P. and Prentice, M.L. 1998. Antarctic glacial history since the Last Glacial Maximum: An overview of the record on land. *Antarctic Science*, **10**, 326-344.

Intergovernmental Panel on Climate Change. 1990. *IPCC First Assessment Report.* UNOG Library.

Intergovernmental Panel on Climate Change. 1995. *IPCC Second Assessment Report.* UNOG Library.

Intergovernmental Panel on Climate Change. 2001. *IPCC Third Assessment Report.* UNOG Library.

Intergovernmental Panel on Climate Change. 2007. *IPCC Fourth Assessment Report.* UNOG Library.

Jacka, T. H. and Budd, W.F. 1998. Detection of temperature and sea-ice-extent changes in the Antarctic and Southern Ocean, 1949–96. *Annals of Glaciology*, **27**, 553–559.

Jacobel, R.W., Gades, AM., Gottschling, D.L., Hodge, S.M. and Wright, D.L. 1993. Interpretation of radar-detected internal layer folding in West Antarctic Ice Streams. *Journal of Glaciology*, **39**, 528–537.

Jacobs, S.S. 2006. Observations of change in the Southern Ocean. *Philosophical Transactions of the Royal Society A*, **364**, 1657– 1681.

Jacobs, S.S. and Comiso, J.C. 1993. A recent sea-ice retreat west of the Antarctic Peninsula. *Geophysical Research Letters*, **20**, doi: 10.1029/93GL01200.

Jacobs, S.S. and Comiso, J.C. 1997. Climate variability in the Amundsen and Bellingshausen Seas. *Journal of Climate*, **10**, 697–709.

Jacobs, S.S., Helmer, H.H., Doake, C.S.M., Jenkins, A. and Frolich, R.M. 1992. Melting of the ice shelves and the mass balance of Antarctica. *Journal of Glaciology*, **38**, 375-387.

Jansen, D., Kulessa, B., Sammonds, P.R., Luckman, A., King., E.C. and Glasser, N.F. 2010. Present stability of the Larsen C Ice Shelf, Antarctic Peninsula. *Journal of Glaciology*, **56**, 593-600.

Jenkins, A. and Jacobs, S.S. 2008. Circulation and melting beneath George VI Ice Shelf, Antarctica. *Journal of Geophysical Research*, **113**, C04013 doi: 10.1029/2007JC004449.

Jet Propulsion Laboratory. *Imaging Radar Information*, available from: http://southport.jpl.nasa.gov. [last accessed 21/01/2009]

Johnson, J.S., Everest, J.D., Leat, P.T., Golledge, N.R., Rood, D.H. and Stuart, F.M. 2012. The deglacial history of NW Alexander Island, Antarctica from surface exposure dating. *Quaternary Research*, **77**, 273-280.

Jones, J.M. and Widmann, M. 2004. Atmospheric science: Early peak in Antarctic oscillation index. *Nature*, **432**, 290-291.

Jones, P.D. 1995. Recent variations in mean temperatures and the diurnal temperature range in the Antarctic. *Geophysical Research Letters*, **22**, 1345–1348.

Joughin, I. and MacAyeal, D.R. 2005. Calving of large tabular icebergs from ice shelf rift systems. *Geophysical Research Letters*, **32**, L02501 doi: 10.1029/2004GL020978.

Joughin, I. and Padman, L. 2003. Melting and freezing beneath Filchner-Ronne Ice Shelf, Antarctica. *Geophysical Research Letters*, **30**, doi: 10.1029/2003GL016941.

Joughin, I., Abdalati, W. and Fahnestock, M. 2004. Large fluctuations in speed on Greenland's Jakobshavn Isbrae Glacier. *Nature*, **432**, 608– 610.

Joughin, I., Kwok, R. and Fahnestock, M. 1998. Interferometric estimation of three-dimensional ice-flow using ascending and descending passes. *IEEE Transactions on Geoscience and Remote Sensing*, **36**, 25– 37.

Joughin, I., Tulaczyk, S., Fahnestock, M. and Kwok, R. 1996. A mini-surge on the Ryder Glacier, Greenland, observed by satellite radar interferometry. *Science*, **274**, 228-230.

Joughin, I.L., Gray, L., Bindschadler, R., Price, S., Morse, D., Hulbe, C., Mattar, K. and Werner, C. 1999. Tributaries of West Antarctic Ice Streams revealed by RADARSAT Interferometry. *Science*, **286**, 283-287.

Kehle, R.O. 1964. Deformation of the Ross Ice Shelf, Antarctica. *Geological Society of America Bulletin*, **75**, 259-86.

Khazendar, A., Rignot, E. and Larour, E. 2011. Acceleration and spatial rheology of Larsen C Ice Shelf, Antarctic Peninsula. *Geophysical Research Letters*, **38**, L09502 doi: 10.1029/2011GL046775.

Khazendar, A., Rignot., E. and Larour, E. 2007. Larsen B Ice Shelf rheology preceding its disintegration inferred by a control method. *Geophysical Research Letters*, **34**, L19503 doi: 10.1029/2007GL030980.

Khazendar, A., Rignot., E. and Larour, E. 2009. Roles of marine ice, rheology, and fracture in the flow and stability of the Brunt/ Stancomb-Wills Ice Shelf. *Journal of Geophysical Research*, **114**, F04007 doi: 10.1029/2008JF001124.

King, J.C. 1994. Recent climate variability in the vicinity of the Antarctic Peninsula. *Journal of Climatology*, **14**, 357-369.

King, J.C. and Harangozo, S.A. 1998. Climate change in the western Antarctic Peninsula since 1945: Observations and possible causes. *Annals and Glaciology*, **27**, 571-575.

King, M.A. and Padman, L. 2005. Accuracy assessment of ocean tide models around Antarctica. *Geophysical Research Letters*, **32**, L23608 doi: 10.1029/2005GL023901.

King, M.A., Coleman, R., Freemantle, A-J., Fricker, H.A., Hurd, R.S., Legrésy, B., Padman, L. and Warner, R. 2009. A 4-decade record of elevation change of the Amery Ice Shelf, East Antarctica. *Journal of Geophysical Research*, **114**, F01010 doi: 10.1029/2008JF001094.

Klink, J.M. and Smith, D.A. 1993. Effect of wind changes during the Last Glacial Maximum on the circulation in the Southern Ocean. *Palaeoceanography*, **8**, 427-433.

Kovacs, A. 1992. Correspondence. Ice-blister observations on glaciers, sea ice and rivers. *Journal of Glaciology*, **38**, 314-316.

Kwok, R. and Comiso, J.C. 2002. Southern Ocean climate and sea ice anomalies associated with the southern Oscillation. *Journal of Climate*, **15**, 487-501.

L'Heureux, M.L. and Thompson, D.W.J. 2006. Observed Relationships between the El Niño–Southern Oscillation and the Extratropical Zonal-Mean Circulation. *Journal of Climate*, **19**, 276-287.

LaBarbera, C.H. and MacAyeal, D.R. 2011. Travelling supraglacial lakes on George VI Ice Shelf, Antarctica. *Geophysical Research Letters*, **38**, L24501 doi: 10.1029/20011GL049970.

Lambrecht, A., Sandhager, H., Vaughan, D.G. and Mayer, C. 2007. New ice thickness maps of Filchner–Ronne Ice Shelf, Antarctica, with specific focus on grounding lines and marine ice. *Antarctic Science*, **19**, 521-532.

Larour, E., Rignot, E. and Aubry, D. 2004. Modelling of rift propagation on Ronne Ice Shelf, Antarctica and sensitivity to climate change. *Geophysical Research Letters*, **31**, L16404 doi: 10.1029/2004GL020077.

Lennon, P.W., Loynes, J. Paren, J.G. and Potter, J.R. 1982. Oceanographic observations from George VI Ice Shelf, Antarctic Peninsula. *Annals of Glaciology*, **3**, 178-183.

Levitus, S., Antonov, J.I., Boyer, T. and Stephens, C. 2000. Warming of the World Ocean. *Science*, **287**, 2225-2229.

Lillesand, T.M., Kiefer, R.W. and Chipman, J.W. 2008. *Remote Sensing and Image Interpretation*. John Wiley and Sons.

Liu, H.W., and Miller, K.J. 1979. Fracture toughness of freshwater ice. *Journal of Glaciology*, **22**, 135-143.

Liu, J. Curry, J.A. and Martinson, D.G. 2004. Interpretation of recent Antarctic sea ice variability. *Geophysical Research Letters*, **31**, L02205 doi: 10.1029/2003GL018732.

Lucchitta, B.K. and Rosanova, C.E. 1998. Retreat of northern margins of George VI and Wilkins Ice Shelves. *Annals of Glaciology*, **27**, 41-46.

Luckman, A., Jansen, D., Kulessa, B., King, E.C., Sammonds, P., and Benn, D.I. 2012. Basal crevasses in Larsen C Ice Shelf and implications for their global abundance. *The Cryosphere*, **6**, 113–123.

Luckman, A., Quincey, D.J. and Bevan, S. 2007. The potential of satellite radar interferometry and feature tracking for monitoring flow rates of the Himalayan Glaciers. *Remote Sensing of Environment*, **111**, 172-181.

Lui, H., Jezek, K., Li, B. and Zhao, Z. 2001. Radarsat Antarctic Mapping Project Digital Elevation Model version 2. *National Snow and Ice Data Centre, digital media*, Boulder, CO.

Lui, H., Jezek, K.C. and Li, B. 1999. Development of an Antarctic Digital Elevation Model by integrating cartographic and remotely sensed data: A Geographic Information System based approach. *Journal of Geophysical Research*, **104**, doi: 10.1029/1999JB900224.

Lythe, M.A., Vaughan, D.G. and the BEDMAP consortium. 2001. BEDMAP: A new ice thickness and subglacial topographic model of Antarctica. *Journal of Geophysical Research*, **106**, 11335-11351.

MacAyeal, D.R. Scambos, T.A. Hulbe, C. and Fahnestock, M.A. 2003. Catastrophic ice-shelf break-up by an ice-shelf-fragment-capsize mechanism. *Journal of Glaciology*, **29**, 22-36.

Manabe, S. and Stouffer, R.J. 1980. Sensitivity of a Global Climate Model to an increase of CO_2 concentration in the Atmosphere. *Journal of Geophysical Research*, **85**, 5529-5554.

Marshall, G.J. 2002, Analysis of circulation and thermal advection change in the northern Antarctic Peninsula. *International Journal of Climatology*, **22**, 1557–1567.

Marshall, G.J., Orr, A., van Lipzig, N.P.M. and King, J.C. 2006. The impact of a changing Southern Hemisphere Annular Mode on Antarctic Peninsula summer temperatures. *Journal of Climate*, **19**, 5388-5404.

Marshall, G.J., Stott, P.A., Turner, A., Connolley, W.M., King, J.C. and Lachan-Cope, T.A. 2004. Causes of exceptional atmospheric circulation changes in the Southern Hemisphere. *Geophysical Research Letters*, **31**, L14205 doi: 10.1029/2004GL019952.

Martin, P.J. and Peel, D.A. 1978. The spatial distribution of 10 m temperatures in the Antarctic Peninsula. *Journal of* Glaciology, **20**, 311–317.

Martinson, D.G., Stammerjohn, S.E., Iannuzzi, R.A., Smith, R.C. and Vernet, M. 2008. Western Antarctic Peninsula physical oceanography and spatio-temporal variability. *Deep Sea Research Part II*, **55**, 1964-1987.

Maslanyj, M.P. 1988. Gravity and aeromagnetic evidence for the crustal structure of George VI Sound, Antarctic Peninsula. *British Antarctic Survey Bulletin*, **79**, 1-16.

Massom, R.A., Stammerjohn, S., Lefevre, W., Harangozo, S.A., Adams, N., Scambos, T.A., Pook, M.J. and Fowler, C. 2008. West Antarctic Peninsula sea ice in 2005: Extreme ice compaction and ice edge retreat due to strong anomaly with respect to climate. *Journal of Geophysical Research*, **113**, C02S20 doi: 10.1029/2007JC004239.

Mercer, J.H. 1978. West Antarctic Ice sheet and CO_2 greenhouse effect: A threat of disaster. *Nature*, **271**, 321-325.

Meredith M.P. and King, J.C. 2005. Climate change in the ocean to the west of the Antarctic Peninsula during the second half of the 20th Century. *Geophysical Research Letters*, **32**, L19604.5 doi:10.1029/2005GL024042.

Merry, C.J. and Whillans, I.M. 1993. Ice-flow features on Ice Stream B, Antarctica, revealed by SPOT HRV imagery. *Journal of Glaciology*, **39**, 515–527.

Michel, R. and Rignot, E. 1999. Flow of Glaciar Moreno, Argentina, from repeat-pass Shuttle Imaging Radar images: Comparison of the phase correlation method with radar interferometry. *Journal of Glaciology*, **45**, 93–100.

Mitchell, J.F.B., Manabe, S., Meleshko, V. and Tokioko, T. 1990. Equilibrium climate change - and its implications for the future. In Houghton, J.T., Jenkins, G.J. and Ephraums, J.J. (eds.). *Climate Change: The IPCC Scientific Assessment*. Cambridge University Press, 131–172.

Monaghan, A.J., Bromwich, D.H., Fogt, R.L., Wang, S-H., Mayewski, P.A., Dixon, D.A., Ekaykin, A., Frezzotti, M., Goodwin, I., Isaksson, E., Kaspari, S.D., Morgan, V.I., Oerter, H., can Ommen, T.D., van der Veen, C.J. and Wen, J. 2006. Insignificant change in Antarctic snowfall since the International Geophysical Year. *Science*, **313**, 827-831.

Moore, J. 1993. Correspondence. Ice blisters and ice dolines. *Journal of Glaciology*, **39**, 714-716.

Morris, E.M. and Mulvaney, R. 1995. Recent changes in surface elevation of the Antarctic Peninsula Ice Sheet, *Zeitschrift fur Gletscherkunde und Glazialgeologie*, **31**, 7–15.

Morris, E.M. and Vaughan, D.G. 2003. Spatial and temporal variation of surface temperature on the Antarctic Peninsula and the limit of viability of ice shelves. *Antarctic Research Series*, **79**, 61-68.

Neal, C.S. 1979. The dynamics of the Ross Ice Shelf revealed by radio echo sounding. *Journal of Glaciology*, **24**, 295-307.

Ng, F. and Conway, H. 2004. Fast-flow signature in the stagnated Kamb Ice Stream, West Antarctica. *Geology*, **32**, 481–484.

Padman, L. and Fricker, H.A. 2005. Tides on Ross Ice Shelf observed with ICESat. *Geophysical Research Letters*, **32**, L14503 doi: 10.1029/2005GL023214.

Padman, L., Costa, D.P., Dinniman, M.S., Fricker, H.A., Goebel. M.E., Huckstadt, L.A., Humbert, A., Joughin, I. Lenaerts, J.T.M., Ligtenberg, S.R.M., Scambos, T.A. and van den Broeke, M.R. 2012. Oceanic controls on the mass balance of Wilkins Ice Shelf, Antarctica. *Journal of Geophysical Research*, **117**, C01010 doi: 10.1029/2011JC007301.

Padman, L., Fricker, H.A., Coleman, R., Howard, S. and Erofeeva, L. 2002. A new tide model for Antarctic Ice Shelves and Seas. *Annals of Glaciology*, **34**, 247-254.

Palmer, S., Shepherd, A., Bjornsson, H. and Palsson, F. 2009. Ice velocity measurements of Langjökull, Iceland, from interferometric synthetic aperture radar. *Journal of Glaciology*, **55**, 834-838.

Parkinson, C.L. 2002. Trends in the length of the Southern Ocean sea-ice season, 1979–99. *Annals of Glaciology*, **34**, 435–440.

Parkinson, C.L. and Cavalieri, D.J. 2012. Antarctic sea ice variability and trends, 1979-2010. *The Cryosphere Discuss*, **6**, 931-956.

Payne, A.J., Vieli, A., Shepherd, A.P., Wingham, D.J. and Rignot, E. 2004. Recent dramatic thinning of largest West Antarctic Ice Stream triggered by oceans. *Geophysical Research Letters*, **31**, L23401 doi:10.1029/2004GL021284.

Pearson, M.R. and Rose, I.H. 1983. The dynamics of George VI Ice Shelf. *British Antarctic Survey Bulletin*, **52**, 205-220.

Potter, J.R. and Paren, J.G. 1985. Interaction between ice shelf and ocean in George VI Sound, Antarctica. *Antarctic Research Series*, **43**, 35-58.

Potter, J.R., Paren, J.G. and Loynes, J. 1984. Glaciological and oceanography calculations of the mass balance and oxygen isotopes ratio of a melting ice shelf. *Journal of Glaciology*, **30**, 161-170.

Pritchard, H.D. and Vaughan, D. 2007. Widespread acceleration of tidewater glaciers on the Antarctic Peninsula. *Journal of Geophysical Research*, **112**, F03S29.1-F03S29.10 doi: 10.1029/2006JF000567.

Pritchard, H.D., Anthern, R.J., Vaughan, D.G. and Edwards, L.A. 2009. Extensive dynamic thinning on the margins of the Greenland and Antarctic ice sheets. *Nature*, **461**, 971-975.

Pritchard, H.D., Ligtenberg, S.R.M., Fricker, H.A., Vaughan, D.G. van den Broeke, M.R. and Padman, L. 2012. Antarctic Ice Sheet loss driven by basal melting of ice shelves. *Nature*, **484**, 502-505.

Pudsey, C.J. and Evans, J. 2001. First survey of Antarctic sub-ice shelf sediments reveals mid-Holcene ice-shelf retreat. G*eology*, **29**, 787-790.

Quincey, D.J. and Luckman, A. 2009. Progress in satellite remote sensing of ice sheets. *Progress in Physical Geography*, **33**, 647-687.

Rack, W. 2000. Dynamic behaviour and disintegration of the northern Larsen Ice Shelf, Antarctic Peninsula. (Ph.D. thesis, University of Innsbruck).

Rack, W. and Rott, H. 2004. Pattern of retreat and disintegration of Larsen B Ice Shelf, Antarctic Peninsula. *Annals of Glaciology*, **39**, 505-510.

Rack, W., Doake, C.S.M., Rott, H., Siegel, A. and Skvarca, P. 2000. Interferometric analysis of the deformation pattern of the northern Larsen Ice Shelf, Antarctic Peninsula, compared to field measurements and numerical modelling. *Annals of Glaciology*, **31**, 205-210.

Racoviteanu, A.E., Williams, M.W. and Barry, R.G. 2008. Optical Remote Sensing of Glacier Characteristics: A Review with Focus on the Himalaya. *Sensors*, **8**, 3355-3383.

Raper, S.C.B., Wigley, T.M.L., Mayes, P.R., Jones, P.D. and Salinger, M.J. 1984. Variations in surface air temperature. Part 3. The Antarctic 1957–82. *Monthly Weather Review*, **112**, 1341–1353.

Rau, F., Mauz, F., De Angelis, H., Jana, R., Arigony-Neto, J., Skvarca, P. Vogt, S., Saurer, H. and Gossmann, H. 2004. Variations of glacier frontal positions on the Northern Antarctic Peninsula. *Annals of Glaciology*, **39**, 525-530.

Raup, B.H., Scambos, T.A. and Haran, T. 2005. Topography of streaklines on an Antarctic Ice Shelf from photoclinometry applied to a single Advanced Land Imager (ALI) image. *Transaction on Geoscience and Remote Sensing*, **43**, 736–742.

Reece, A. 1949. The ice of Crown Prince Gustav Channel, Graham Land, Antarctica. *Journal of Glaciology*, **1**, 404-409.

Reeh, N. 1968. On the calving of ice from floating glaciers and ice shelves. *Journal of Glaciology*, **7**, 215–232.

Remy, F. and Parouty, S. 2009. Antarctic Ice Sheet and radar altimetry: A review. *Remote Sensing*, **1**, 1212-1239 doi: 10.3390/RS1041212.

Reynolds, J.M. 1981. Lakes on George VI Ice Shelf, Antarctica. *Polar Record*, **20**, 425-432.

Reynolds, J.M. and M.J. Hambrey. 1988. The structural glaciology of George VI Ice Shelf, Antarctic Peninsula. *British Antarctic Survey Bulletin*, **79**, 79–95.

Reynolds, J.M. 1988. The structure of the Wordie Ice Shelf, Antarctic Peninsula. *British Antarctic Survey Bulletin*, **80**, 57-64.

Ridley, J.K. 1993. Surface melting on Antarctic Peninsula Ice Shelves detected by passive microwave sensors. *Geophysical Research Letters*, **20**, 2639-2642 doi: 10.1029/93GL02611.

Rignot, E. 1998. Fast recession of a West Antarctic Glacier. *Science*, **281**, 549–551.

Rignot, E. 2008. Changes in West Antarctic Ice Stream dynamics observed with ALOS PALSAR data. *Geophysical Research Letters*, **35**, L12505 doi: 10.1029/2008GL033365.

Rignot, E. and Kanagaratnam, P. 2006. Changes in the velocity structure of the Greenland Ice Sheet. *Science*, **311**, 986–990.

Rignot, E. Casassa, G., Goginen, P., Krabill, W., Rivera, A. and Thomas, R. 2004. Accelerated ice discharge from the Antarctic Peninsula following the collapse of Larsen B Ice Shelf. *Geophysical Research Letters*, **31**, doi: 10.1029/2004GL020697.

Rignot, E., Buscarlet, G., Csatho, B., Gogineni, S., Krabill, W. and Schmeltz, M. 2000. Mass balance of the northeast sector of the Greenland Ice Sheet: A remote-sensing perspective. *Journal of Glaciology*, **46**, 265–73.

Rignot, E., Forster, R. and Isacks, B. 1996. Mapping of glacial motion and surface topography of Hielo Patagonico Norte, Chile, using satellite SAR L-band interferometry data. *Annals of Glaciology*, **23**, 209-215.

Rignot, E., Mouginot, J. and Scheuchl, B. 2011. Ice Flow of the Antarctic Ice Sheet. *Science*, **333**, 1427-1430. (Documentation).

Rignot, E., Mouginot, J. and Scheuchl, B. 2011. *MEaSUREs InSAR-Based Antarctica Velocity Map*. Boulder, Colorado USA. NASA EOSDIS Distributed Active Archive Center at NSIDC. http://nsidc.org/data/nsidc-0484.html [last accessed 20.12.11] (Digital Media).

Rignot, E., Vaughan, D.G., Schmeltz, M., Dupond, T. and MacAyeal, D.R. 2002. Accelaration of Pine Island and Thwaites Glaciers, West Antarctica. *Annals of Glaciology*, **34**, 189-194.

Rind, D., Healy, R., Parkinson, C. and Martinson, D.G. 1995. The role of sea ice in 2 x CO_2 climate model sensitivity. Part I: The total influence of sea ice thickness and extent. *Journal of* Climate, **8**, 449– 463.

Rippin, D.M., Siegert, M.J., Bamber, J.L., Vaughan, D. and Corr, H.F.J. 2006. Switch-off of a major enhanced ice flow unit in East Antarctica. *Geophysical Research Letters*, **33**, L15501 doi: 10.1029/2006GL026648.

Rist, M.A., Sammonds, P.R., Oerter, H. and Doake, C.S.M. 2002. Fracture of Antarctic Shelf Ice. *Journal of Geophysical Research*, **107**, doi: 10.1029/2000JB000058.

Roberts, S.J., Hodgson, D.A., Bentley, M.J., Smith, J.A. Millar, I.L., Olive, V. and Sugden, D.E. 2008. The Holocene history of George VI Ice Shelf, Antarctic Peninsula, from clast-provenance analysis of epishelf lake sediments. *Palaeogeography, Palaeoclimatology, Palaeoecology*, **269**, 258-283.

Robertson, R. Visbeck, M., Gordon, A.L. and Fahrbach, E. 2002. Long-term temperature trends in the deep waters of the Weddell Sea. *Deep-Sea Research Part II*, **49**, 4791-4806.

Robin, G. de Q. and Adie, R.J. 1964. The ice cover. In Priestley, R., Adie, R.J. and Robin, G. de Q. (Eds) *Antarctic Research*. Butterworths, London. 100-117.

Rott, H., Müller, F., Nagler, T. and Floricioiu. 2010. The imbalance of glaciers after disintegration of Larsen B Ice Shelf, Antarctic Peninsula. *The Cryosphere Discuss*, **4**, 1607-1633.

Rott, H., Müller, F., Nagler, T. and Floricioiu. 2011. The imbalance of glaciers after disintegration of Larsen B Ice Shelf, Antarctic Peninsula. *The Cryosphere*, **5**, 125-234.

Rott, H., Nagler, T., Eineder, M., and Floricioiu, D. 2008. New results on dynamic instability of Antarctic Peninsula glaciers detected by TerraSAR-X ice motion analysis. *Proceedings of 7th EUSAR Conference 2008*, **4**, 159-162.

Rott, H., Rack, W. and Nagler, T. 2007. Increased export of grounded ice after the collapse of the northern Larsen Ice Shelf, Antarctic Peninsula, observed by Envisat ASAR. *Geoscience and Remote Sensing Symposium 2007*, 1174-1176.

Rott, H., Rack, W., Nagler, T. and Skvarca, P. 1998. Climatically induced retreat and collapse of the northern Larsen Ice Shelf, Antarctic Peninsula. *Annals of Glaciology*, **27**, 86-92.

Rott, H., Rack, W., Skvarca, P. and De Angelis, H. 2002. Northern Larsen Ice Shelf, Antarctica: Further retreat after collapse. *Annals of Glaciology*, **34**, 277–282.

Rott, H., Skvarca, P. and Nagler, T. 1996. Rapid collapse of the northern Larsen Ice Shelf, Antarctica. *Science*, **271**, 788-792.

Scambos, T.A. Bohlander, J.A. Shuman, C.A. and Skvarca, P. 2004. Glacier acceleration and thinning after ice-shelf collapse in the Larsen B embayment, Antarctica. *Geophysical Research Letters*, **31**, L18402 doi: 10.1029/2004GL020670.

Scambos, T.A. Hulbe, C. Fahnestock, M. and Bohlander, J. 2000. The link between climate warming and break-up of ice shelves in the Antarctic Peninsula. *Journal of Glaciology*, **46**, 516-530.

Scambos, T.A., Dutkiewitcz, M.J., Wilson, J.C. and Bindschadler, R.A. 1992. Application of image cross-correlation software to the measurement of glacier velocity using satellite image data. *Remote Sensing of Environment*, **42**, 177–186.

Scambos, T.A., Fricker, H.A., Liu, C-C., Bohlander, J., Fastook, J., Sargent, A., Masson, R. and Wu, A.M. 2009. Ice shelf disintegration by plate bending and hydro-fracture: Satellite observations and model results of the 2008 Wilkins Ice Shelf break-ups. *Earth and Planetary Science Letters*, **280**, doi:10.1016/j.epsl.2008.12.027.

Scambos, T.A., Haran, T.M., Fahnestock, M.A., Painter, T.H. and Bohlander, J. 2007. MODIS-based Mosaic of Antarctica (MOA) datasets: Continent-wide surface morphology and snow grain size. *Remote Sensing of Environment*, **111**, 242-257.

Scambos, T.A., Hulbe, C. and Fahnestock, M.A. 2003. Climate induced ice-shelf disintegration in the Antarctic Peninsula. *Antarctic Research Series*, **79**, 79-92.

Scambos, T.A., Ross, R., Bauer, R., Yermolin, Y., Skvarca, P., Long, D., Bohlander, J. and Haran, T. 2008. Calving and ice-shelf break-up processes investigated by proxy: Antarctic tabular iceberg evolution during northward drift. *Journal of Glaciology*, **54**, 579-591.

Scharroo, R. and Visser, P.N.A.M. 1997. ERS Tandem mission orbits: Is 5 cm still a challenge? *Proceedings of the Third ERS Symposium, ESA Special Publication*, **SP-414**.

Schmitz, W.J. 1995. On the interbasin-scale thermohaline circulation. *Reviews of Geophysics*, **33**, 151-173.

Schutz, B.E., Zwally, H.J., Shuman, C.A., Hancock, D. and DiMarzio, J.P. Overview of the ICESat mission. *Geophysical Research Letters*, **32**, L21S01 doi: 10.1029/2005GL024009.

Shepherd, A., Wingham, D., Payne, T. and Skvarca, P. 2003. Larsen Ice Shelf has progressively thinned. *Science*, **302**, 856-859.

Shepherd, A., Wingham, D.J., Mansley, J.A.D. and Corr, H.F.J. 2001. Inland thinning of Pine Island Glacier, West Antarctica. *Science*, **291**, 862–864.

Shindell, T., and Schmidt, G.A. 2004. Southern Hemisphere climate response to ozone changes and greenhouse gas increases. *Geophysical Research Letters*, **31**, L18209 doi:10.1029/2004GL020724.

Shuman, C.A. and Fahnestock, M.A. 2005. ICESat elevation profiles, inversion for ice shelf thickness. *Geophysical Research Abstracts*, **7**, 08323.

Shuman, C.A., Berthier, E. and Scambos, T.A. 2011. Glacier elevation and mass loss, 2001–2009, in the Larsen A and B embayments, Antarctic Peninsula. *Journal of* Glaciology, **57**, 737–754.

Shuman, C.A., Zwally, H.J., Schultz, B.E., Brenner, A.C., DiMarzio, J.P., Suchdeo, V.P. and Fricker, H.A. 2006. ICESat Antarctic elevation data: Preliminary precision and accuracy assessment. *Geophysical Research* Letters, **33**, L07501 doi: 10.1029/2005GL025227.

Siegfried, M.R., Hawley, R.L. and Burkhart, J.F. 2011. High-resolution ground-based GPS measurements show intercampaign bias in ICESat elevation data near Summit, Greenland. *IEEE Transaction on Geoscience and Remote Sensing*, **49**, 3393-3400.

Simmons, D.A. 1986. Flow of the Brunt Ice Shelf, Antarctica, derived from Landsat images, 1974–85. *Journal of Glaciology*, **32**, 252–254.

Simmons, D.A. and Rouse, J.R. 1984. Geomagnetic measurements made on the moving ice shelf at Halley, Antarctica. *Survey Geophysics*, **6**, 407–417.

Skvarca, P. 1993. Fast recession of the northern Larsen Ice Shelf monitored by space images. *Annals of Glaciology*, **17**, 317-321.

Skvarca, P. 1994. Change and surface features on the Larsen Ice Shelf, Antarctica, derived from Landsat and Kosmos mosaics. *Annals of Glaciology*, **20**, 6-12.

Skvarca, P., De Angelis, H. and Zakrajsek, A. 2004. Climatic conditions, mass balance and dynamics of Larsen B Ice Shelf, Antarctic Peninsula, prior to collapse. *Annals of Glaciology*, **39**, 557–562.

Skvarca, P., Rack, W., Rott, H. and Donangelo, T.I.Y. 1999. Climate trend and the retreat and disintegration of ice shelves on the Antarctic Peninsula: An overview. *Polar Research*, **18**, 151-157.

Smith, D.A., Hofmann, E.E., Klinck, J.M., and Lascara, C.M. 1999. Hydrography and circulation of the west Antarctic Peninsula continental shelf. *Deep Sea Research Part I*, **46**, 925–949.

Smith, J.A., Bentley, M.J., Hodgson, D.A. and Cook, A.J. 2007. George VI Ice Shelf: Past history, present behaviours and potential mechanisms for future collapse. *Antarctic Science*, **19**, 131-142.

Splettoesser, J.1992. Antarctic Global Warming? *Nature*, **355**, 503.

Stammerjohn, S.E. and Smith, R.C. 1997. Opposing Southern Ocean climate patterns as revealed by trends in regional sea ice coverage. *Climate Change*, **37**, 617–639.

Stammerjohn, S.E., Martinson, D.G., Smith, R.C., Yuan, X. and Rind, D. 2008. Trends in Antarctic annual sea ice retreat and advance and their relation to El Nino–Southern Oscillation and Southern Annular Mode variability. *Journal of Geophysical Research*, **113**, C03S90 doi: 10.1029/2007JC004269.

Steinhage, U., Nixdorf, U., Mayer, U. and Miller, H. 2001. Subglacial topography and internal structure of central and western Dronning Maud Land, Antarctica, determined from airborne radio echo sounding. *Journal of Applied Geophysics*, **47**, 183-189.

Stephenson, A. and Fleming, W.L.S. 1940. King George The Sixth Sound. *The Geographical Journal*, **96**, 153-164.

Strozzi, T., Luckman, A., Murray, T., Wegmuller, U. and Werner, C.L. 2002. Glacier motion estimation using SAR offset-tracking procedures. *IEEE Transactions on Geoscience and Remote Sensing*, **40**, 2384–2391.

Sugden, D. 1982. *Arctic and Antarctic. A Modern Geographical Synthesis.* Basil Blackwell.

Swithinbank, C. 1968. Radio echo sounding of Antarctic Glaciers from light aircraft. *International Association of Scientific Hydrology*, **79**, 405-14.

Swithinbank, C., Brunt, K. and Sievers, J. 1988. A glaciological map of Filchner-Ronne Ice Shelf, Antarctica. *Annals of Glaciology*, **11**, 150-155.

Swithinbank, C.W.M. and Lucchitta, B.K. 1986. Multispectral digital image mapping of Antarctic ice features. *Annals of Glaciology*, **8**, 159-163.

Talbot, M.H. 1988. Oceanic environment of George VI Ice Shelf, Antarctic Peninsula. *Annals of Glaciology*, **11**, 161-164.

Tedesco, M. 2009. Assessment and development of snowmelt retrieval algorithms over Antarctica from K-band spaceborne brightness temperature (1979-2008). *Remote Sensing of Environment*, **113**, 979-997.

Thomas, R.H. 1979. Ice shelves: A review. *Journal of* Glaciology, **24**, 273–286.

Thomas, R.H., Stephenson, S.N., Bindschadler, R.A., Shabtaie, S., and Bentley, C.R. 1988. Thinning and grounding line retreat on the Ross Ice Shelf. *Annals of* Glaciology, **11**, 165–172.

Thompson, D.W.J. and Solomon, S. 2002. Interpretation of recent Southern Hemisphere climate change. *Science*, **296**, 895–899.

Thyssen, F. 1988. Special aspects of the central part of the Filchner-Ronne Ice Shelf. *Annals of Glaciology*, **11**, 173-179.

Thyssen, F., Bombosch, A. and Sandhager. 1993. Elevation, ice thickness and structure mark maps of the central part of the Filchner-Ronne Ice Shelf. *Polarforschund,* **62**, 17-26.

Torinesi, O., Fily, M., and Genthon, C. 2003. Interannual variability and trend of the Antarctic Ice Sheet summer melting period from 20 years of spaceborne microwave data. *Journal of* Clmate, **16**, 1047–1060.

Turner, J. Colwell, S.R., Marshall, G.J. and Lachlan-Cope, T.A. 2005. Variability of precipitation over the western Antarctic Peninsula from synoptic observations. *International Journal of Climatology*, **25**, 279-294.

Turner, J., Colwell, S.R., and Harangozo, S. 1997. Variability of precipitation over the coastal western Antarctic Peninsula from synoptic observations. *Journal of Geophysical Research*, **102**, 13,999–14,007.

Turner, J., Lachlan-Cope, T.A., Thomas, J.P. and Colwell, S.R. 1995. The synoptic origins of precipitation over the Antarctic Peninsula. *Antarctic Science*, **7**, 327–337.

Van den Broeke, M.R. 2005. Strong surface melting preceded collapse of Antarctic Peninsula Ice Shelf. *Geophysical research Letters*, **32**, doi: 10.1029/2005GL02347.

Van den Broeke, M.R. and van Lipzig, N.P.M. 2003. Factors controlling the near-surface wind field in Antarctica. *Monthly Weather Review*, **131**, 733-743.

Van der Veen, C.J. 1998. Fracture mechanics approach to penetration of surface crevasses on glaciers. *Cold Regions Science and Technology*, **27**, 31–47.

Van der Veen, C.J. 2007. Fracture propagation as means of rapidly transferring surface meltwater to the base of glaciers. *Geophysical Research Letters*, **34**, L01501 doi: 10.1029/2006GL028385.

Van Lipzig, N.P.M.,. Marshall, G.J., Orr, A. and King, J.C. 2008. The relationship between the Southern Hemisphere annular mode and Antarctic Peninsula summer temperatures: Analysis of a high-resolution model Climatology. *Journal of Climate*, **21**, 1649–1668.

Vaughan, D.G. 1993. Implications of the break-up of the Wordie Ice Shelf, Antarctica for sea level. *Antarctic Science*, **5**, 403-408.

Vaughan, D.G. 1994. Investigating tidal flexure on an ice shelf using kinematic GPS. *Annals of Glaciology*, **20**, 372-276.

Vaughan, D.G. and Doake, C.S.M. 1996. Recent atmospheric warming and retreat of ice shelves on the Antarctic Peninsula. *Nature*, **379**, 328-331.

Vaughan, D.G., Marshall, G.J., Connolley, W.M., King, J.C. and Mulvaney, R. 2001. Climate change: Devil in the detail. *Science*, **293**, 1777-1779.

Vaughan, D.G., Marshall, G.J., Connolley, W.M., Parkinson, C., Mulvaney, R., Hodgson, D.A., King, J.C., Pudsey, C.J. and Turner, J. 2003. Recent rapid regional climate warming on the Antarctic Peninsula. *Climate Change*, **60**, 243-274.

Venteris, E.R. 1999. Rapid tidewater glacier retreat: A comparison between Columbia Glacier, Alaska, and Patagonian calving glaciers. *Global Planetary Change*, **22**, 131-138.

Vieli, A., Payne, A., Shepherd, A. and Du, Z. 2007. Causes of pre-collapse changes of the Larsen B Ice Shelf: Numerical modelling and assimilation of satellite observations. *Earth and Planetary Science Letters*, **259**, 297-306. doi: 10.1016/j.epsl.2007.04.050.

Vieli, A., Payne, A.J., Du, Z.J. and Shepherd, A. 2006. Numerical modelling and data assimilation of the Larsen B Ice Shelf, Antarctic Peninsula. *Philosophical Transactions of the Royal Society A*, **364**, 1815-1839.

Wager, A.C. 1972. Flooding of the ice shelf in George VI Sound. *British Antarctic Survey Bulletin*, **28**, 71-74.

Walsh, J.E. 1983. The role of sea ice in climate variability: Theories and Evidence. *Atmosphere-Ocean*, **21**, 229–242.

Ward, C.G. 1995. The mapping of ice front changes on Müller Ice Shelf, Antarctic Peninsula. *Antarctic Science*, **7**, 197-198.

Watson, D.F. 1992. *Contouring: A Guide to the Analysis and Display of Spatial Data*. Oxford, Pergamon.

Weatherley, J., Walsh, J. and Zwally, H.J. 1991. Antarctic sea ice variability and seasonal air temperature relationships. *Journal of Geophysical Research*, **96**, 15119–15130.

Weertman, J. 1973. Can a water-filled crevasse reach the bottom of a glacier? *International Association of Scientific Hydrology*, **95**, 139-145.

Weiss, J. 2004. Subcritical crack propagation as a mechanism of crevasse formation and iceberg calving. *Journal of Glaciology*, **50**, 109–115.

White, W.B. and Peterson, R.G. 1996. An Antarctic circumpolar wave in surface pressure, wind, temperature and sea-ice extent. *Nature*, **380**, 699-702.

Williams, M.J.M., Warner, R.C. and Budd, W.F. 1988. The effects of ocean warming and ocean circulation under the Amery Ice Shelf, East Antarctica. *Annals of* Glaciology, **27**, 75-80.

Williams, R.S., Ferrigno, J.G., Swithinbank, C, Lucchitta, B.K. and Seekins, B.A. 1995. Coastal-change and glaciological maps of Antarctica. *Annals of Glaciology*, **21**, 284-290.

Williams, R.S.J. and Ferrigno, J.G. 1998. USGS Fact sheet FS, 2005-3055. USGS.

Woodruff, A.H.W. and Doake, C.S.M. 1979. Depolarization of radio waves can distinguish between floating and grounded ice sheets. *Journal of* Glaciology, **23**, 223–232.

Wright, C.S. and Priestley, R.E. 1922. *Glaciology, British (Terra Nova) Antarctic Expedition, 1910–1913*. Harrison, London.

Wuite, J. and Jezek, K.C. 2009. Evidence of past fluctuations on Stanscomb-Wills Ice Tongue, Antarctica, preserved by relict flow stripes. *Journal of Glaciology*, **55**, 239-244.

Yamanokuchi, T., Doi, K., Shibuya, K. and Aoki, S. 2011. Monitoring of East Antarctic marginal zone using ALOS PALSAR data. *SAR 2011 3rd International Asia-Pacific Conference*, **3**.

Yaun, X. and Martinson, D.G. 2000. Antarctic sea ice extent variability and its global connectivity. *Journal of Climate*, **13**, 1697-1717.

Yuan, X. and Li, C. 2008. Climate modes in southern high latitudes and their impacts on Antarctic sea ice. *Journal of Geophysical Research*, **113**, C06S91 doi: 10.1029/2006JC004067.

Zotikov, I.A., Zagorodnov, V.S. and Raikovsky, J.V. 1980. Core drilling through the Ross Ice Shelf (Antarctica) confirmed basal freezing. *Science*, **207**, 1463-1465.

Zwally, H.J. Giovinetto, M.B., Li, J., Cornejo, H.C., Beckley, M.A. and Brenner, A. 2005. Mass changes of the Greenland and Antarctic ice, its sheets and shelves and contribution to sea-level rise: 1992-2002. *Journal of Glaciology*, **51**, 509-527.

Zwally, H.J., Comiso, J.C., Parkinson, C.L., Cavalieri, D.J. and Gloersen, P. 2002. Variability of Antarctic sea ice 1979– 1998. *Journal of Geophysical Research*, **107**(C5), 3041, doi: 10.1029/2000JC000733.

Zwally, H.J., Parkinson, C. and Comiso, J.C. 1983. Variability of Antarctic sea ice and changes in carbon dioxide. *Science*, **220**, 1005–1012.

Appendices

Appendix 1a – Bach Ice Shelf velocity transect plots

Refer to Figure 6.2 and Table 6.1

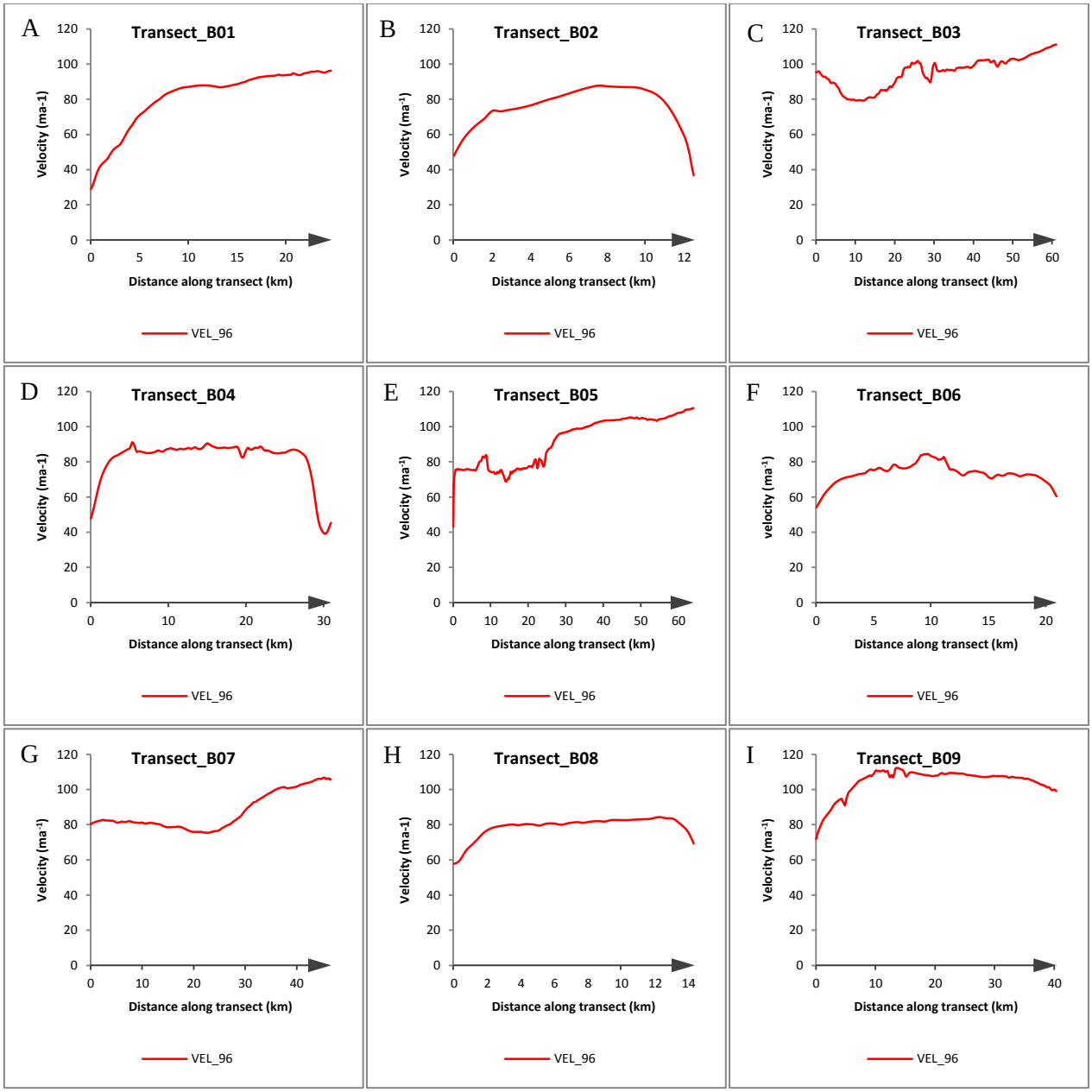

Appendix 1a. InSAR-derived surface speeds for ca. 1996 (VEL_96) across Weber Ice Domain (A, B), Boccherini Ice Domain (C, D), Williams Ice Domain (E, F), Stravinsky Ice Domain (G, H) and across the ice front (I). All transects illustrate an increase in surface speeds along the centreline of each ice domain and towards the ice front. X-axis arrow corresponds to transect direction in Figure 6.2. Minimum, maximum and average surface speeds for each transect is presented in Table 6.1.

Appendix 1b – Bach Ice Shelf surface elevation and elevation change plots

Refer to Figure 6.11 and Table 6.5

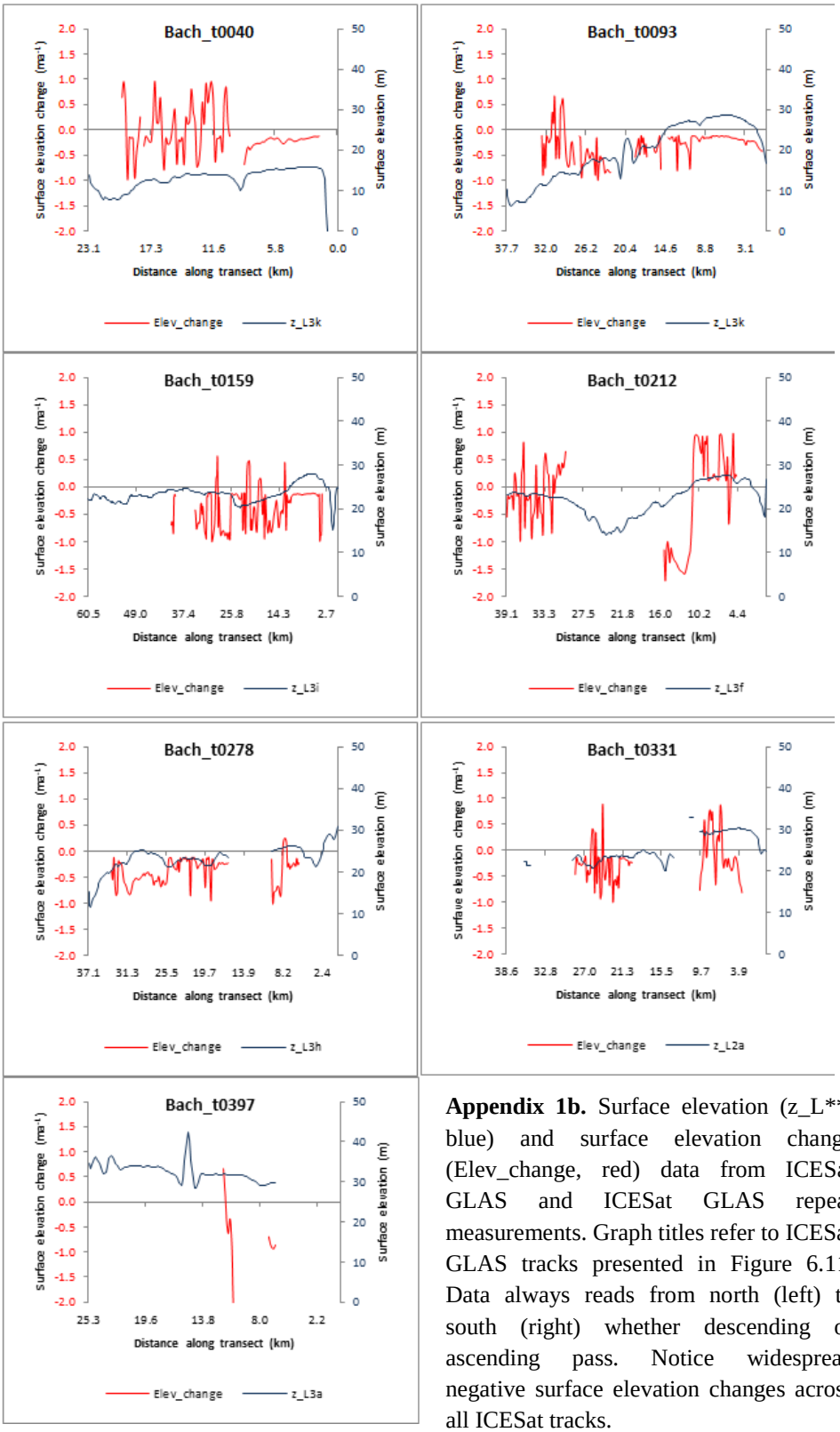

Appendix 1b. Surface elevation (z_L**, blue) and surface elevation change (Elev_change, red) data from ICESat GLAS and ICESat GLAS repeat measurements. Graph titles refer to ICESat GLAS tracks presented in Figure 6.11. Data always reads from north (left) to south (right) whether descending of ascending pass. Notice widespread negative surface elevation changes across all ICESat tracks.

Appendix 2a – George VI Ice Shelf north velocity transects plots

Refer to Figure 7.3 and Table 7.2.

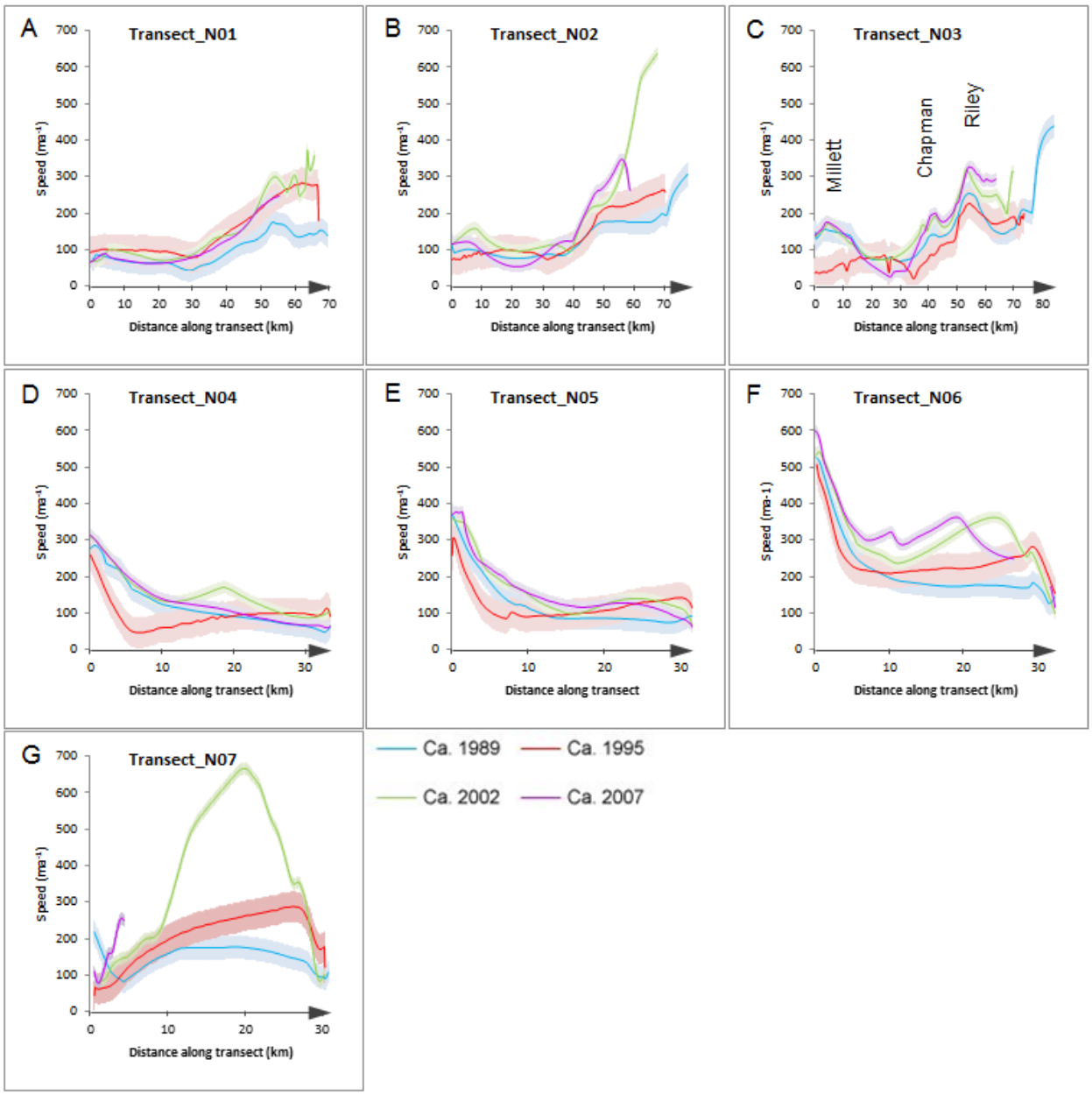

Appendix 2b. Velocity transects illustrating the temporal changes in surface speeds from ca. 1989, ca. 1995, ca. 2002 and ca. 2007. X-axis direction corresponds to the transect direction displayed in Figure 7.3. Note in particular the increase in surface speeds over time at the north ice front as displayed in Transect_N01, Transect_N02, Transect_N03 and Transect_N07. Corresponding transect statistics are displayed in Table 7.2. Uncertainties illustrated by shaded areas.

Appendix 2b. George VI Ice Shelf south velocity transects plots

Refer to Figure 7.4 and Table 7.3.

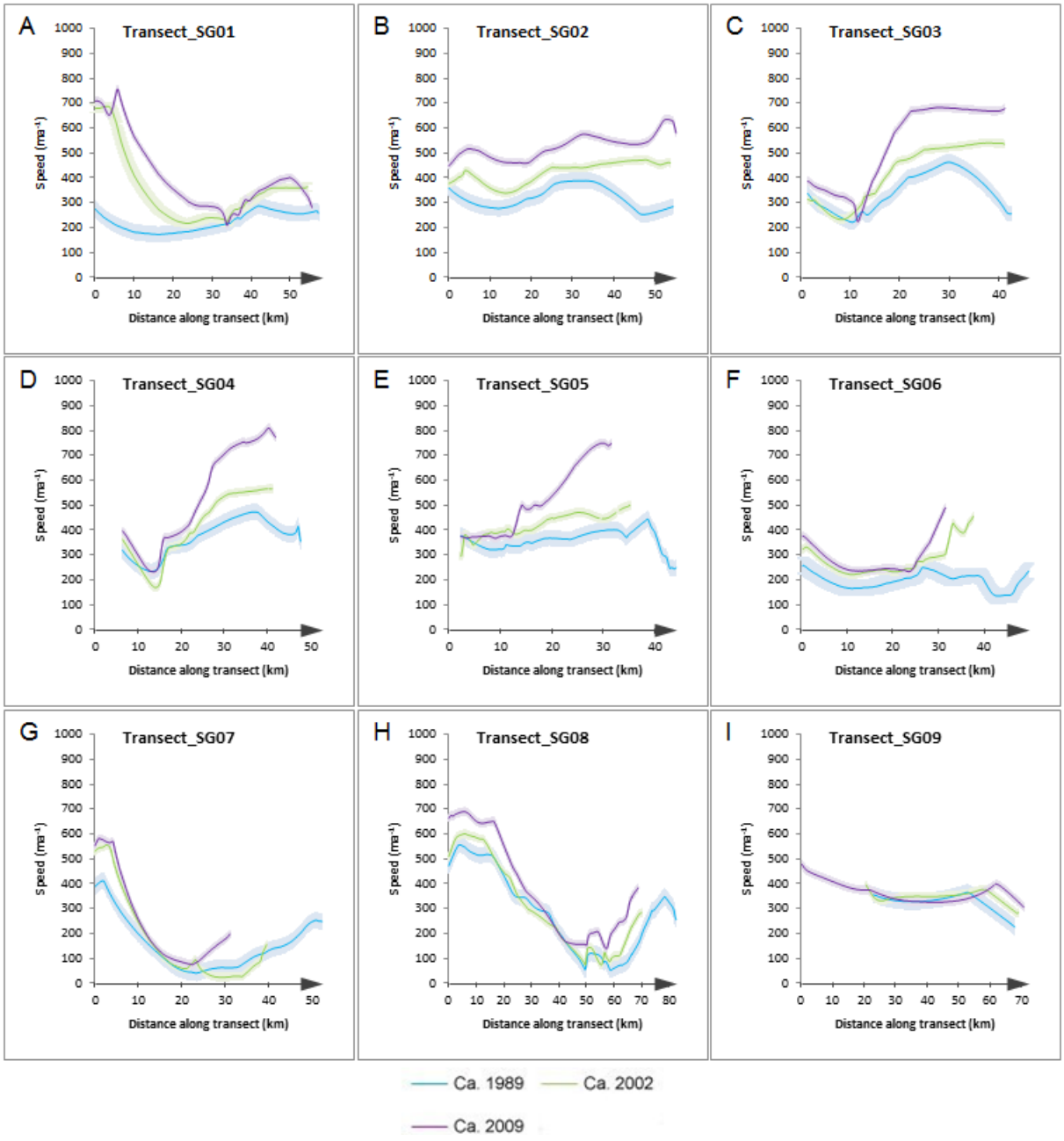

Appendix 2b. Velocity transects corresponding to Figure 7.4 illustrating the temporal changes in surface speeds for ca. 1989, ca. 2002 and ca. 2009 at the southern ice front. X-axis direction corresponds to the transect direction displayed in Figure 7.4. Note in particular the increase in surface velocities over time extracted over transects SG01 to SG06 and the steady flow regime over SG07, SG08 and SG09. Velocity transects statistics displayed in Table 7.3. Uncertainties shown by shaded areas.

Appendix 2c. George VI Ice Shelf surface elevation and elevation change plots

Refer to Figure 7.31 and Table 7.11.

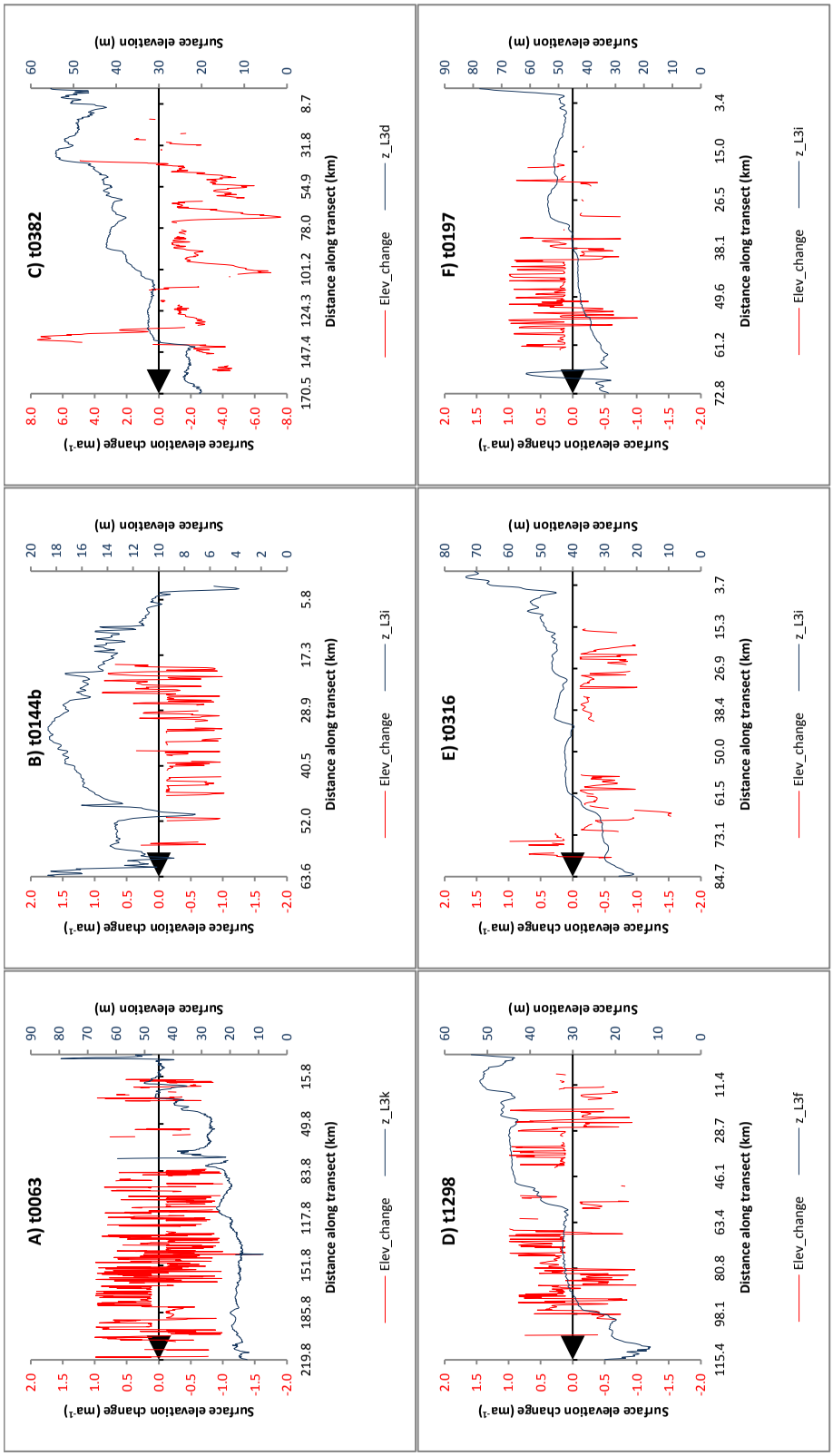

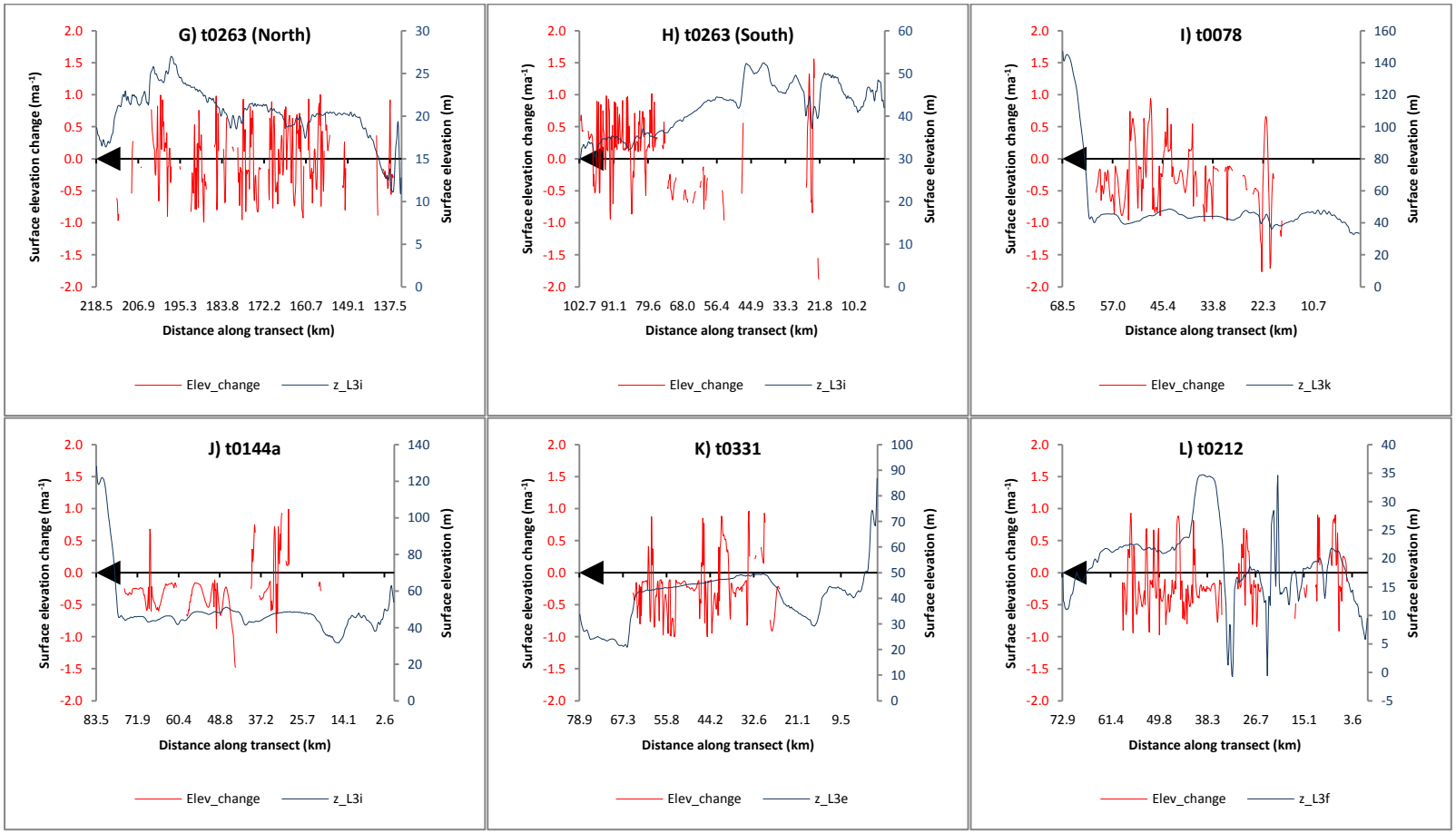
G) t0263 (North)
Surface elevation change (ma-1)
Surface elevation (m)
218.5 206.9 195.3 183.8 172.2 160.7 149.1 137.5
Distance along transect (km)
Elev_change
z_L3i
H) t0263 (South)
102.7 91.1 79.6 68.0 56.4 44.9 33.3 21.8 10.2
Distance along transect (km)
Elev_change
z_L3i
I) t0078
68.5 57.0 45.4 33.8 22.3 10.7
Distance along transect (km)
Elev_change
z_L3k
J) t0144a
83.5 71.9 60.4 48.8 37.2 25.7 14.1 2.6
Distance along transect (km)
Elev_change
z_L3i
K) t0331
78.9 67.3 55.8 44.2 32.6 21.1 9.5
Distance along transect (km)
Elev_change
z_L3e
L) t0212
72.9 61.4 49.8 38.3 26.7 15.1 3.6
Distance along transect (km)
Elev_change
z_L3f

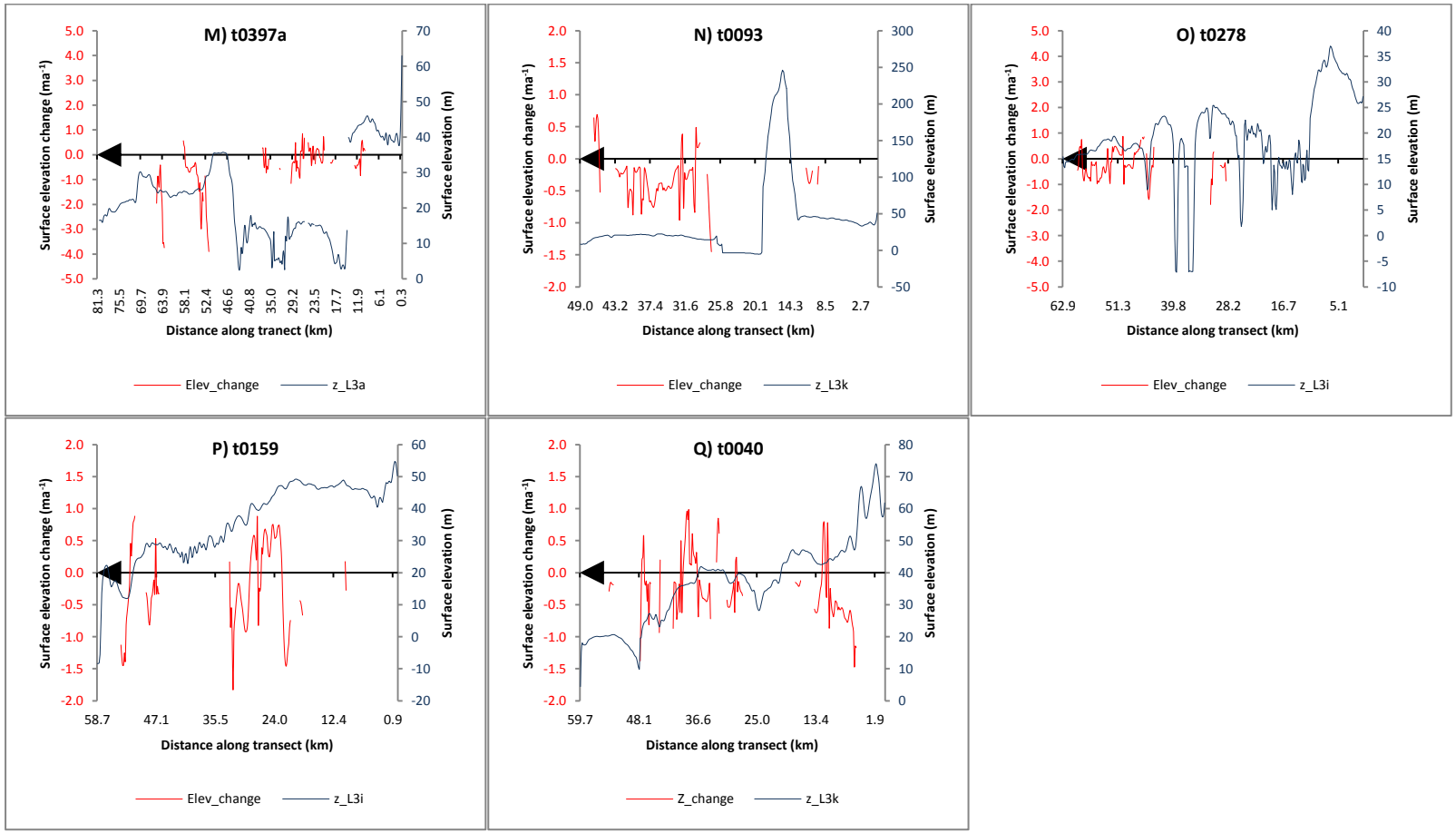

Appendix 2c. Surface elevations (z_L**, blue) and surface elevation change (Elev_change, red) data from ICESat GLAS and ICESat GLAS repeat measurements. Graph titles refer to ICESat GLAS tracks presented in Figure 7.31 and discussed in Table 7.11. X-axis arrow illustrates northward direction of ICESat GLAS track.

Appendix 3a. Stange Ice Shelf velocity transects plots

Refer to Figure 8.3 and Table 8.2.

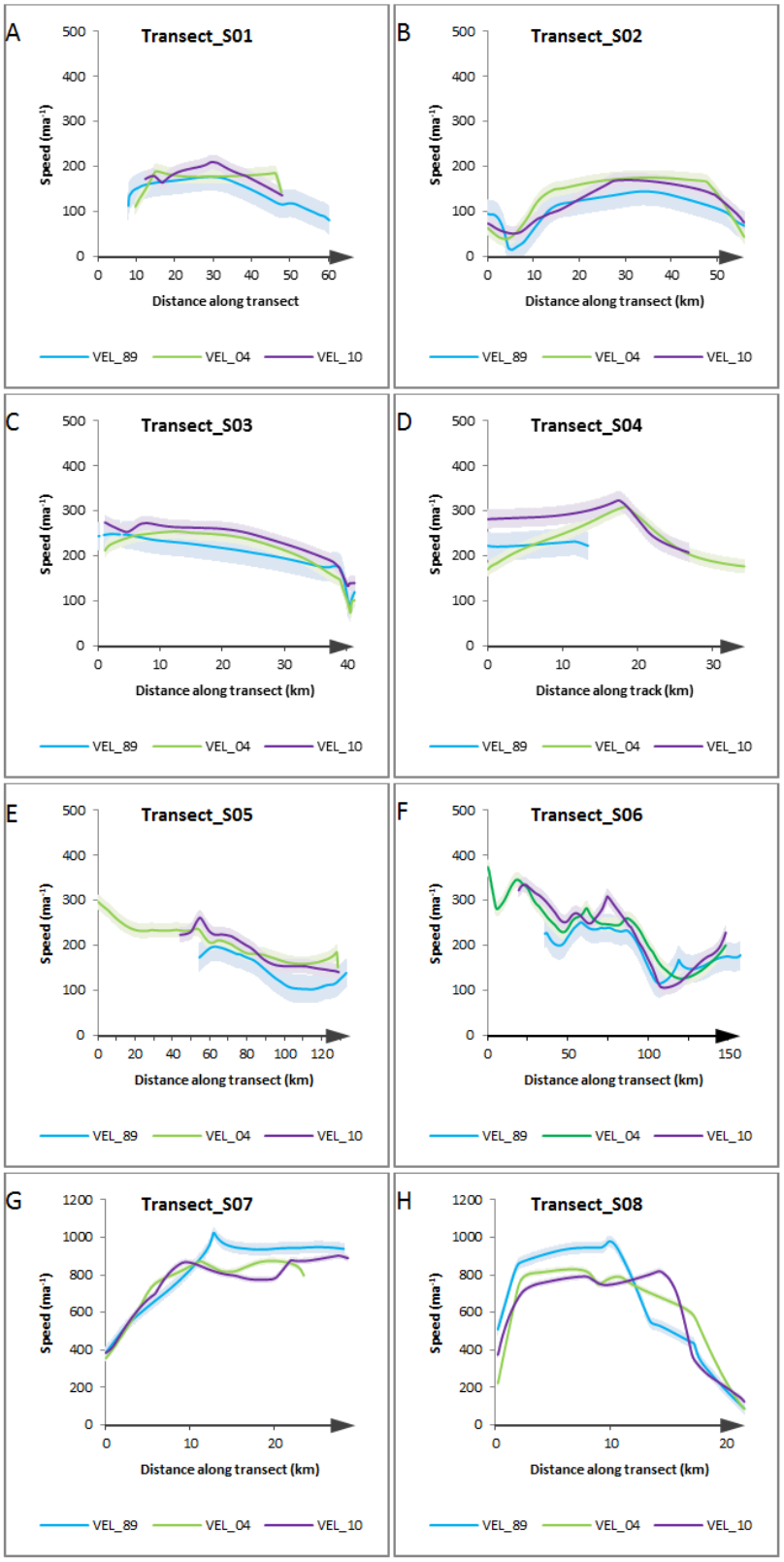

Appendix 3a. Velocity transects corresponding to Figure 8.3B displaying the slight increase in surface velocities between ca. 1989 (VEL_89), ca. 2004 (VEL_2004) and ca. 2010 (VEL_10). X-axis direction corresponds to transect direction displayed in Figure 8.3B. Basic statistics are provided in Table 8.2 for each time period along each individual transect. Uncertainties are shown by shaded areas.

Appendix 3b – Stange Ice Shelf surface elevation and elevation change plots

Refer to Figure 8.19 and Table 8.10

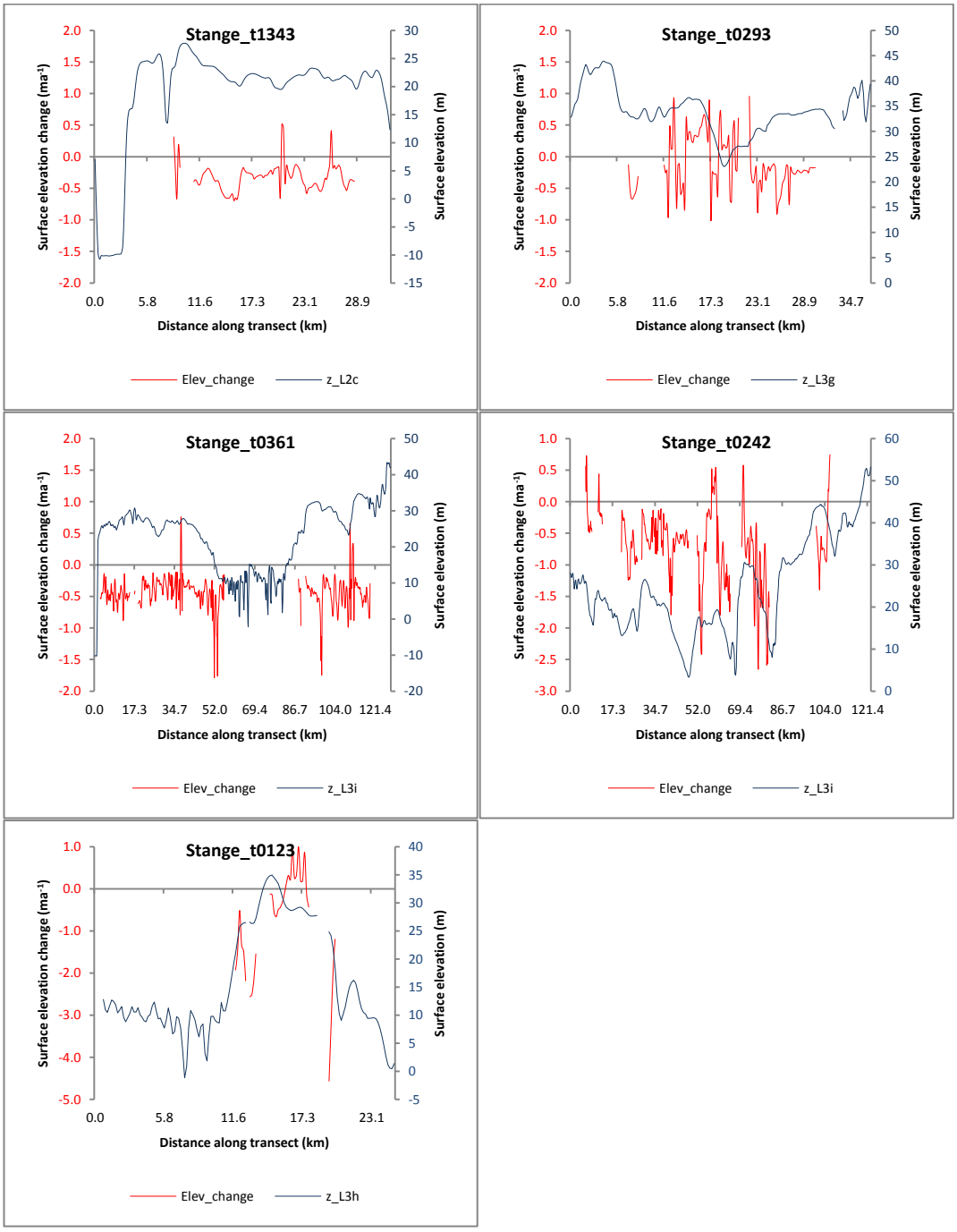

Appendix 3b. Surface elevation (Blue) and surface elevation changes (Red) calculated from ICESat GLAS and ICESat GLAS repeat measurements. Surface elevation measurements taken from single laser campaign (e.g. L2c = Laser 2, campaign 'c'), with change detection calculated from repeat measurements as described in Table 8.10. Graph titles correspond to tracks in Figure 8.19, and X-axis distance always reads from left to right across the corresponding track.